

Where Visions Become Reality

AD-A260 821



3

(2)

1992

S DTIC
ELECTE
FEB 5 1993 **D** =
C



ROME LABORATORY

93-02064



232128

93 2 3 072

APPROVED FOR PUBLIC RELEASE; DISTRIBUTION UNLIMITED.

Journal

The Rome Laboratory Journal is published by Rome Laboratory, Griffiss AFB NY 13441-4514. It is distributed free of charge to qualified recipients (government employees and contractors, libraries, and R&D laboratories). Requests for individual copies should be sent to RL/CD, 26 ELECTRONIC PARKWAY, GRIFFISS AFB NY 13441-4514. Requests to reprint individual articles should be addressed to the author.

This report has been reviewed by the Rome Laboratory Public Affairs Office (PA) and is releasable to the National Technical Information Service (NTIS). At NTIS it will be releasable to the general public, including foreign nations.

**THE ROME LABORATORY
JOURNAL**

TABLE OF CONTENTS

I. INTRODUCTION.	1
II. JOURNAL PUBLICATIONS.	5
OPTICAL SWITCHING WITH PHOTOREFRACTIVE POLARIZATION HOLOGRAMS Q.W. Song, M.C. Lee, and P.J. Talbot	7
OPTICAL BAND GAP OF THE TERNARY SEMICONDUCTOR $\text{Si}_{1-x-y}\text{Ge}_x\text{C}_y$ Richard A. Soref	15
PREDICTED BAND GAP OF THE NEW SEMICONDUCTOR SiGeSn Richard A. Soref and Clive H. Perry	18
LARGE SINGLE-MODE RIB WAVEGUIDES IN GeSi-Si and Si-on-SiO_2 Richard A. Soref, Joachim Schmidtchen, and Klaus Petermann	21
FORCES ON THREE-LEVEL ATOMS INCLUDING COHERENT POPULATION TRAPPING M.S. Prentiss, N.P. Bigelow, M. S. Shahriar, and P.R. Hemmer	25
ROOM-TEMPERATURE OPTICAL NONLINEARITIES OF GaInAs/AlInAs AND GaAlInAs/AlInAs MULTIPLE QUANTUM WELLS AND INTEGRATED-MIRROR ETALONS AT $1.3\ \mu\text{m}$ C.C. Hsu, B.P. McGinnis, J.P. Sokoloff, G. Khitrova, H.M. Gibbs, N. Peyghambarian, S.T. Johns, and M.F. Krol	28
SELF-PUMPED OPTICAL PHASE CONJUGATION WITH A SODIUM RAMAN LASER J. Donoghue, M. Cronin-Golomb, J.S. Kane, and P.R. Hemmer	32
OPTICAL FINGERPRINT IDENTIFICATION BY BINARY JOINT TRANSFORM CORRELATION Kenneth H. Fielding, Joseph L. Horner, and Charles K. Makekau	35
ELECTRO-OPTIC MODE-DISPLACEMENT SILICON LIGHT MODULATOR Thomas Pimat, Lionel Friedman, and Richard A. Soref	39
OPTICAL WAVEGUIDES IN SIMOX STRUCTURES B.L. Weiss, G.T. Reed, S.K. Toh, R.A. Soref, and F. Namavar	44
VERTICALLY INTEGRATED SILICON-ON-INSULATOR WAVEGUIDES R.A. Soref, E. Cortesi, F. Namavar, and L. Friedman	47
ACTIVE SEMICONDUCTOR OPTICAL SWITCHES WITH BLUE-SHIFTED CHANNEL WAVEGUIDES Richard A. Soref	50
NXN AND IXN SWITCHING WITH CHIRAL NEMATIC LIQUID CRYSTALS Richard A. Soref	56
OPTICAL WAVEGUIDING IN $\text{Si/Si}_{1-x}\text{Ge}_x/\text{Si}$ HETEROSTRUCTURES F. Namavar and R. A. Soref	58

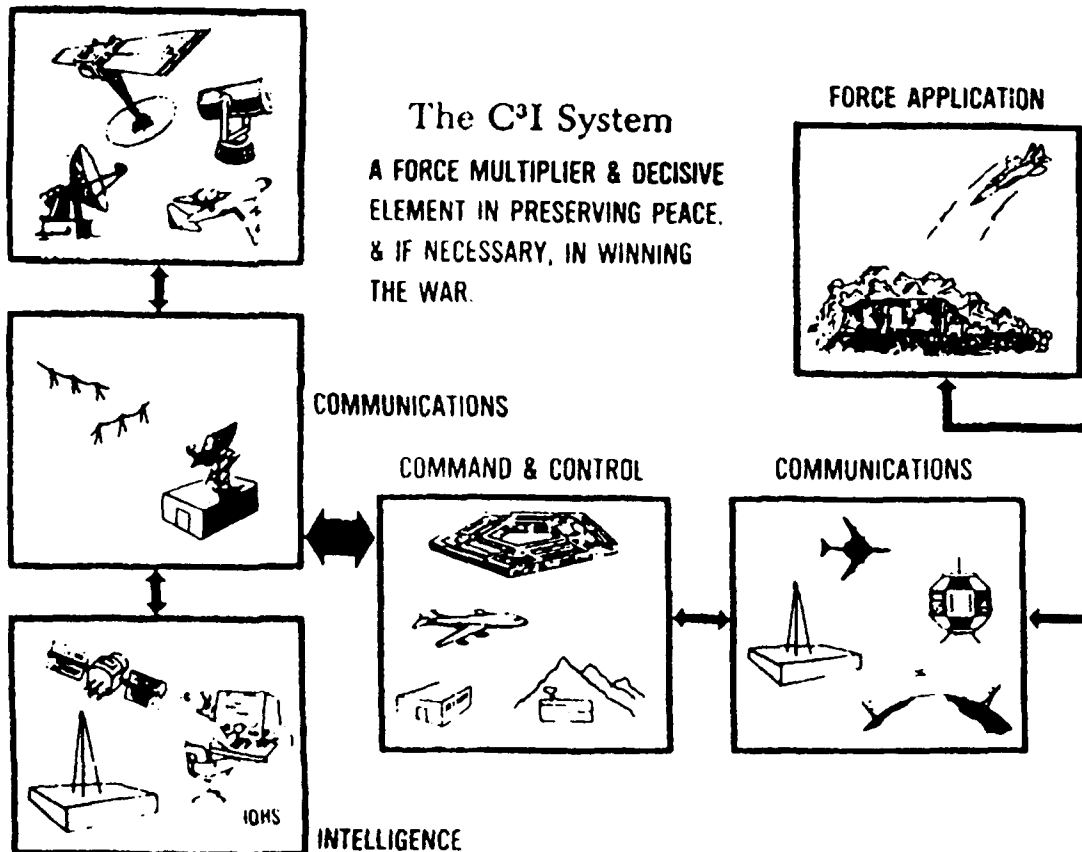
PHOTOREFRACTIVE TIME CORRELATION MOTION DETECTION	61
Jehad Koury, Vincent Ryan, Mark Cronin-Golomb, and Charles Woods	
NOISE REDUCTION USING ADAPTIVE SPATIAL FILTERING IN PHOTOREFRACTIVE TWO-BEAM COUPLING	66
Jehad Khoury, Charles L. Woods, and Mark Cronin-Golomb	
PHOTOREFRACTIVE OPTICAL LOCK-IN DETECTOR	69
Jehad Khoury, Vincent Ryan, Charles Woods, and Mark Cronin-Golomb	
SPHERICAL-WAVE EXPANSIONS OF PISTON-RADIATOR FIELDS	73
Ronald Wittman and Arthur D. Yaghjian	
DUAL-SERIES SOLUTION TO SCATTERING FROM A SEMICIRCULAR CHANNEL IN A GROUND PLANE	85
M.K. Hinders and A.D. Yaghjian	
EXCIMER LASER-INDUCED DEPOSITION OF COPPER FILMS	89
Suryadevara V. Babu, Raghunath Padiyath, Moses David, and Lois Walsh	
THREE-DIMENSIONAL MULTIREGION S_n SOLUTIONS OF THE SPENCER-LEWIS ELECTRON TRANSPORT EQUATION	94
W.L. Filippone, S.P. Monahan, S. Woolf, and J.C. Garth	
HIGH-PURITY InP GROWN ON Si BY ORGANOMETALLIC VAPOR PHASE EPITAXY	100
O. Aina, M. Mattingly, J.R. Bates, A. Coggins, J. O'Connor, S.K. Shastry, J.P. Salerno, A. Davis, J.P. Lorenzo, and K.S. Jones	
ELECTRON-ACOUSTIC PHONON SCATTERING IN SiO ₂ DETERMINED FROM A PSEUDO-POTENTIAL FOR ENERGIES OF $E > E_{BZ}$	103
J.N. Bradford and S. Woolf	
IMPACT IONIZATION IN THE PRESENCE OF STRONG ELECTRIC FIELDS IN SILICON DIOXIDE	106
J.N. Bradford and S. Woolf	
MLEK CRYSTAL GROWTH OF (100) INDIUM PHOSPHIDE	110
David F. Bliss, Robert M. Hilton, Stephen Bachowski, and Joseph A. Adamski	
COUPLED LONG JOSEPHSON JUNCTIONS AND THE N SINE-GORDON EQUATION	115
Stanford P. Yukon and Nathaniel Chu H. Lin	
THE INFLUENCE OF DISLOCATION DENSITY ON ELECTRON MOBILITY IN InP FILMS ON Si	129
T.E. Crumbaker, M.J. Hafich, C.Y. Robinson, K.M. Jones, M.M. Al-Jassim, A. Davis, and J.P. Lorenzo	
SIGNAL-TO-NOISE POWER OR SIGNAL-TO-NOISE ENERGY FOR MAXIMIZING DECISION PERFORMANCE? ..	134
Vincent C. Vannicola	
MEASURING THE QUALITY OF KNOWLEDGE WORK	138
Anthony Coppola	
BOUNDS ON THE SIZES OF IRREDUNDANT TEST SETS AND SEQUENCES FOR COMBINATIONAL LOGIC NETWORKS	144
Warren H. Debany, Jr. and Carlos R.P. Hartmann	

AN EXTENSION OF PROBABILISTIC SIMULATION FOR RELIABILITY ANALYSIS OF CMOS VLSI CIRCUITS	157
Farid N. Najm, P. Yang, and Ibrahim N. Hajj	
APPLICATION OF AUDIO/SPEECH RECOGNITION FOR MILITARY REQUIREMENTS	167
Edward J. Cupples and Bruno Beek	
III. ABSTRACTS OF PUBLICATIONS	177
A. SURVEILLANCE	179
B. COMMUNICATIONS	184
C. COMMAND & CONTROL	187
D. INTELLIGENCE	191
E. ELECTROMAGNETICS	193
F. PHOTONICS	202
G. SIGNAL PROCESSING	207
H. COMPUTER SCIENCE	211
I. RELIABILITY SCIENCE	217
IV. PATENTS	221
V. ROME LABORATORY TECHNICAL REPORTS	227

DTIC QUALITY INSPECTED 3

Accession For	
NTIS General	<input checked="" type="checkbox"/>
DTIC TAB	<input type="checkbox"/>
Unannounced	<input type="checkbox"/>
Justification	
By	
Distribution/	
Availability Codes	
Dist	Avail and/or Special
A-1	

1. INTRODUCTION



The Rome Laboratory is the Air Force's center of expertise for advancing the state-of-the-art in command, control, communications, and intelligence (C³I). This mission is accomplished by:

1. Conducting vigorous research, development, and test programs in all applicable technologies.
2. Transitioning technology to current and future Air Force systems to improve operational capability, readiness, and supportability.
3. Providing a full range of technical support to AFSC product divisions and other Air Force organizations.
4. Conducting selected acquisition programs for low volume, limited quantity intelligence and software systems.

The Laboratory maintains leading edge technological expertise in the following areas: surveillance, communications, command & control, intelligence, reliability science, electromagnetic technology, photonics, signal processing, and computational science.

The Laboratory is organized into four major staff directorates and four mission directorates: Surveillance and Photonics, Command Control & Communications, Intelligence & Reconnaissance and Electromagnetics & Reliability. We recognize

that a system approach, integrating efforts across the Laboratory organizational structure, is required to develop effective C³I systems.

As an Air Force laboratory, we are committed to provide the technical leadership in the transition of new technology to warfighting systems. This is accomplished by:

- Conducting long-term, high-payoff research
 - Developing technologies for product development and maintenance, and
 - Providing in-house technical expertise for the Air Force.
- We create Science and Technology (S&T) programs in response to our users' requirements, higher headquarters guidance, and our own enlightened view of high-payoff technologies.

The Rome Laboratory Journal is published annually to acquaint the technical community with the outstanding research and development carried out by this laboratory. The papers contained in Section II are reprints of publications that appeared in refereed journals in 1991. We have also included in the Journal abstracts of other publications (Section III), abstracts of patents issued to Rome Laboratory personnel in 1991 (Section IV), and a listing of Rome Laboratory Technical Reports (Section V).

II. JOURNAL PUBLICATIONS

OPTICAL SWITCHING WITH PHOTOREFRACTIVE POLARIZATION HOLOGRAMS

Q.W. Song, M.C. Lee, and P.J. Talbot, Department of Electrical and Computer Engineering, Syracuse University

Published in Optics Letters, 16, #16, 1228, 15 August 1991

Abstract - A switching technique using the polarization sensitivity of photorefractive holograms in crystals is experimentally demonstrated. The design is capable of handling a large number of 2x2 switching channels with only four holograms. The concept is applicable to either synchronous or asynchronous switching and also to a variety of photorefractive materials.

1. INTRODUCTION

As the needs for more complex and higher bandwidth networks in communication and computing continues, the research into high performance optical interconnection networks has become more and more active^(1,2). The unique features of optical interconnection such as high bandwidth and parallelism make it very attractive for many applications. Currently, many practical interconnection architectures are based on a large number of 2x2 switches⁽³⁾.

In this paper we describe a massive switching architecture which can implement a large number of 2x2 switches in a single crystal. The method of switching is based upon the polarization sensitivity of crystal volume holograms. The advantage of a polarization switch is its symmetry with respect to binary logic and its theoretical cascability and energy conservation⁽⁴⁾. While the reconfiguration time of the system is limited by the speed of available spatial light modulators (currently in ms to μ s range), the large bandwidth (GHz) and the simplicity of the architecture makes it applicable to a number of applications.

2. PROPERTIES OF CRYSTAL VOLUME HOLOGRAMS

We first discuss some basic properties of crystal volume holograms. For transmission holograms, we assume that two writing beams, R (reference beam) and S (signal beam), enter a photorefractive (Z cut) material as shown in Fig. 1 (a).

In the recording process, two vertically polarized laser beams (ordinary light), represented by their wave vector K_1 and K_2 respectively, interfere within the photorefractive crystal. A volume hologram represented by the wave vector K_3 is generated as shown in Fig. 1 (a). In the reading process, if we read the hologram with beam K_1 then the beam represented by the wave vector K_2 is reconstructed. However, if the polarization of the reading beam is changed to the horizontal direction

(extraordinary light) then the corresponding wave vector inside the crystal will be K_1' . The K_1' beam reads the hologram K_3 . Bragg's condition requires that the diffracted wave vector K_2' form a closed triangle with K_1' and K_3 (i.e., momentum conservation). However, the normal surface of the crystal prohibits K_2' . This mismatch, ΔK as indicated in Fig. 1 (a), results in a sharp decrease in diffraction efficiency. Referring to the coupled-wave theory derived by Kogelnik⁽⁵⁾, the dephasing measurement ϑ is given as

$$\vartheta = K_3 \cos(\phi - \theta_s) - \frac{K_3^2}{4\pi n_s} \lambda = K_3 \cos(\phi - \theta_s) - \frac{K_3^2}{2K} \quad (1)$$

where ϕ is the angle between grating K_3 and the propagation direction (y axis in Fig. 1), θ_s is the angle between the signal beam and the propagation axis, k is the diffracted wave vector K_2' in Fig. 1 (a). Note that when the Bragg condition is satisfied, ϑ equals zero. When the Bragg condition is not met, we can expand ϑ in a Taylor expansion to the first order. Therefore, ϑ in the above case can be approximated as

$$\vartheta = \frac{K_3^2}{2K^2} \Delta k \quad (2)$$

Let's further assume that the multiple diffraction process can be neglected for a multi-exposure hologram. The problem can be treated with the weak coupling approximation. Thus the normalized diffraction efficiency for transmission holograms can be expressed as

$$\eta = \frac{\sin^2 \sqrt{v^2 + \zeta^2}}{1 + \frac{\zeta^2}{v^2}} \quad (3)$$

where $v = \pi n_1 d / \lambda \sqrt{\cos \theta_s \cos \theta_R}$, $\zeta = \vartheta d / 2 \cos \theta_s$, n_1 is the amplitude of the spatial modulation of the refraction index, λ is the wavelength, θ_R and θ_s are the angles between propagation direction and reference and signal beams respectively, d is the thickness of crystal, and ϑ is the dephasing measurement as defined in equation (1). For the weak coupling approximation (i.e., $|v| \ll |\zeta|$) equation (3) can be simplified, giving

$$\eta = v^2 \operatorname{sinc}^2 \zeta \quad (4)$$

In designing an optical switch using the polarization sensitivity of the crystal hologram the parameter of interest is the diffraction efficiency ratio, that is, the ratio of the diffraction efficiency for vertical polarization vs. that for horizontal

polarization. Note that the Bragg condition is perfectly matched when writing and reading using the same reference beam. Referring to Fig. 1 (a), if we read the hologram using the K_1 beam (vertical polarization) then ΔK equals zero and so does ζ_{\perp} . On the other hand, if we read the hologram using K_1' (horizontal polarization), ΔK does not equal zero. So we can write the diffraction efficiency ratio as

$$\frac{\eta_{||}}{\eta_{\perp}} = \frac{v_{||}^2 \sin^2 \zeta}{v_{\perp}^2 \sin^2 \theta} = \frac{v_{||}^2 \sin^2 \zeta}{v_{\perp}^2} \quad (5)$$

In order to use the holograms as binary optical switches, we must find the angle where the diffraction efficiency ratio is as small as possible. In other words, when the polarization is changed from vertical to horizontal the diffracted light is "turned off". The selectivity of the hologram can be obtained as follows. For transmission holograms, referring to Fig. 1 (a) and using Snell's law, we can calculate the y and z component (K_y , K_z) for grating K_3 as

$$(K_y, K_z) = (\sin \alpha_S - \sin \alpha_R, \sqrt{n_0^2 - \sin^2 \alpha_S} - \sqrt{n_0^2 - \sin^2 \alpha_R}) \quad (6)$$

Let the y and z component of the desired vector K_2' be (P_y , P_z); using vector algebra we find (P_y , P_z) easily

$$(P_y, P_z) = K_1' + K_3 = \{ \sin \alpha_S, \sqrt{n_0^2 - \sin^2 \alpha_S} + (\frac{n_c}{n_0} - 1) \sqrt{n_0^2 - \sin^2 \alpha_R} \} \quad (7)$$

However, the normal surface of the refractive index ellipse allows only the wave vector OB . The index ellipse is given as⁽⁶⁾

$$\frac{Z^2}{n_0^2} + \frac{Y^2}{n_c^2} = 1 \quad (8)$$

Solving the equations (7) and (8), we have

$$|OB| = n_0 n_c \sqrt{\frac{P_z^2 + P_y^2}{n_c^2 \sin^2 \alpha_S + n_0^2 P_y^2}}$$

and

$$|OP| = \sqrt{P_z^2 + P_y^2}$$

The mismatch Δk can be expressed as

$$|\Delta k| = |OB| - |OP| = \sqrt{P_z^2 + P_y^2} \left[\sqrt{\frac{1}{n_c^2 P_z^2 + n_0^2 P_y^2} - 1} \right] \quad (9)$$

The first null of the diffraction efficiency ratio occurs at $\zeta = \pi$ and is given by

$$\frac{dK_3^2}{4 \cos \theta_s k^2} \Delta k = \pi \quad (10)$$

where $K_3^2 = K_z^2 + K_y^2$ is the amplitude square of the grating vector. From equation (6), (7) and (9) we can calculate the incident angles, α_S and α_R , where the diffraction efficiency ratio is zero. For example, with $n_0 = 2.286$, $n_c = 2.200$ for a LiNbO_3 crystal of $d = 1$ cm and $\lambda = 633$ nm the first null occurs at $\alpha_S = 30^\circ$, $\alpha_R = 34.1^\circ$.

Similarly, for reflection holograms, the normalized diffraction efficiency can be expressed as

$$\eta = \frac{1}{1 + \frac{1 - \zeta^2/v^2}{\sinh \sqrt{v^2 - \zeta^2}}} \quad (11)$$

where

$$v = j n_1 \pi d / \lambda \sin \theta_s, \quad \zeta = \theta d / 2 [C_s] = d K_3^2 \times \Delta k / 4 \cos \theta_s k^2$$

For the weak coupling case (i.e., $|v| \ll |\zeta|$), equation (8) can be reduced to the following expression

$$\eta = |v|^2 \sin^2 \zeta \quad (12)$$

Referring to Fig. 1 (b), the selectivity of the hologram can be derived as for the transmission hologram. The resulting equations follow

$$(P_z, P_y) = [\sin \alpha_S, \sqrt{n_0^2 - \sin^2 \alpha_S} - \sqrt{n_0^2 - \sin^2 \alpha_R} + \frac{n_0}{n_c} \sqrt{n_c^2 - \sin^2 \alpha_R}]$$

$$|OB| = n_0 n_c \sqrt{\frac{P_z^2 + P_y^2}{n_0^2 P_z^2 + n_c^2 P_y^2}}$$

$$|OP| = \sqrt{P_z^2 + P_y^2}$$

and

$$|\Delta k| = |\mathbf{OB}| - |\mathbf{OP}| = \sqrt{P_x^2 + P_y^2} \left[\sqrt{\frac{1}{n_0^2 P_x^2 + n_c^2 P_y^2}} - 1 \right]. \quad (13)$$

The nulls of diffraction efficiency ratio occurs at $\zeta = n\pi$ and is given by

$$\frac{dK_3}{4\cos\theta_s k^2} \Delta k + n\pi.$$

Again the first null of the sinc function of reflection hologram occurs at $\zeta = \pi$. For example, with $n_0=2.286$, $n_c=2.200$ for a LiNbO₃ crystal of $d=1$ cm and $\lambda=633$ nm the first null occurs at $\alpha_s=30^\circ$ and $\alpha_R=32.2^\circ$. From the above calculations, we see that the width of the first lobe of the transmission hologram is a little larger than that of reflection hologram at $\alpha_s=30^\circ$. This is due to the fact that the orientation of the refractive index ellipse of transmission and reflection holograms are different. As we can see from the above discussion, the diffraction efficiency of crystal volume hologram is very sensitive to the polarization of the reading beam. If the wave vector of the hologram and that of the reading beam are carefully chosen, the diffracted beam's intensity virtually drops to zero when the polarization of the reading beam is changed. This phenomenon is exactly what we want to achieve from an optical directional coupling switch.

3. OPTICAL POLARIZATION DIRECTIONAL COUPLING SWITCH

The principle of an optical polarization coupling switch using holograms is illustrated in Fig. 2. The grating vectors AP and BP are written in the photorefractive crystal with vertical and horizontal polarizations, respectively. When the grating AP is read out with wave vector OA using vertical polarization, the diffracted beam is denoted by its wave vector PC. On the other hand, this vertically polarized reading beam contributes almost no light in the PD direction. This results because the mismatch ΔK is so large that the diffraction efficiency in the PD direction is virtually zero. Similarly, if the grating BP is read out with the same reference beam R but in the horizontal polarization, the

wave vector inside the crystal is OB and the corresponding diffracted wave vector is changed to PD.

Thus, by changing the polarization of the reading beam, we can read different gratings inside the crystal. Since different gratings result in diffracted beams in different directions, an optical directional coupling switch can be realized in this simple fashion. Notice that in the above process, the direction of the reading beam before entering the crystal is unchanged. Currently, there exist a number of spatial light modulators available to achieve this end, such as electrically addressed MOD, LCTV, and optically addressed LCLV and MSLM. Referring to Fig. 3(a), we have expanded the above concept in recording four such gratings in the crystal. They are designed in such a way that by changing the polarization of reading beam R₁, the diffracted beam goes in the A or B direction, respectively. Similarly, by changing the polarization of reading beam R₂, the diffracted beam also goes to A or B direction, respectively.

Therefore, by changing the polarization of a single beam, we can switch (or direct) it to either one of the two predetermined directions. In other words, the crystal holograms function as a 2x2 switch that can connect any one of the two inputs to any one of the two outputs. The circuit analogy of the above is given in Fig. 3(b). The total number of switch channels that can be handled by the crystal hologram is basically limited by the number of resolvable spots of the diffracted beams. According to the Rayleigh criterion⁽⁷⁾, the minimum angle, α_{\min} , between two resolvable beams is $0.61\lambda/r$, where λ is the wavelength, and r is the diameter of the diffracted beam. Consider two parallel circular optical beams that are incident on a crystal surface. Assume that the output beams emerging from the other side of the crystal are also parallel. If an observation plane is placed at a distance z from the back plane of the crystal then the minimum separation between these two circular beams is given by $d_{\min}=0.61\lambda z/r$. The number of optical switch channels is determined by the radius of the optical beam, the size of the crystal, the distance between the crystal and the observation plan, and the wavelength. For example, if we require the observation plane to be 5 mm away from the crystal, the resolution on the plane to be $d_{\min}=0.01$ mm, and use an Argon laser ($\lambda=512$ nm) the diameter of the signal beams would be $r=150$ μ m. Therefore, for a crystal of area 1.5 cm x 1.5 cm about 10^4 signal channels can be achieved. Further, the number of channels could be dramatically increased by using a larger crystal.

Because of the storage capacity and resolution of a crystal hologram, millions of 2x2 switches can be built on a small crystal. These switches can be addressed either synchronously by a thick beam of light, or asynchronously through spatial light modulators. The former method has the advantage of massive parallelism while the latter is more flexible.

4. EXPERIMENTAL MEASUREMENTS

To illustrate the feasibility of the above discussed concept, we measured the switching behavior of the crystal hologram using the experimental setup as shown in Fig.4. The laser beam is divided into two parts by a polarizing beam splitter. Two half-wave plates were placed at the two outputs of the beam splitter to rotate the polarization of the optical beams. In the recording process, the polarization of both reference and signal beams are the same. In the reading process, we first blocked out the signal beam; then, we measured the diffracted light from the reference beam in vertical and horizontal polarizations, respectively. A piece of Z cut LiNbO₃ crystal (1 cm³) was employed as the recording medium. Because of the sensitivity and high accuracy of volume holograms two parameters were being used to describe the incidental laser beams instead of α_S and α_R in figure 1. One is the write-in angle which is the angle between the reference beam R and the signal beam S (2α in Fig. 4). The other parameter is the normal angle which is the angle between the crystal surface and the line that bisects R and S (β in Fig.4).

The write-in angle was confined at between 18.4° and 23.2°. This angle limitation is due to the diameter of the laser beam (0.5 cm) and the size of the crystal (1 cm³). For each of the write-in angles given above, seven measurements were conducted by rotating the crystal at 2° steps. The wavelength was 633 nm (He-Ne Laser). The intensity of diffracted beam was measured by a power detector.

Figure 5 plots the theoretical and experimental diffraction efficiency ratio of vertical polarization over horizontal polarization vs normal angle β . Eq.(5) modified by the transmittance behavior at the two boundary planes is employed to provide the theoretical prediction as given by

$$\frac{\eta_{||}}{\eta_{\perp}} = \frac{T_{air \rightarrow nc} \times T_{nc \rightarrow air} \times v_{||}^2 \text{sinc}^2 \zeta}{T_{air \rightarrow no} \times T_{no \rightarrow air} \times v_{\perp}^2} \quad (14)$$

where $T_{air \rightarrow no}$ is the transmittance for a vertical polarized reference beam from air to crystal, $T_{no \rightarrow air}$ is the transmittance for a vertical polarized signal beam from crystal to air, $T_{air \rightarrow nc}$ is the transmittance for a horizontal polarized reference beam from air to crystal, and $T_{nc \rightarrow air}$ is the transmittance for a horizontal polarized signal beam from air to crystal. Referring to Fig. 1 (a), these values can be obtained as following

$$T_{air \rightarrow no} = \frac{\sin 2\alpha_R \times \sin 2\theta_R}{\sin 2(\alpha_R + \theta_R)}$$

$$T_{no \rightarrow air} = \frac{\sin 2\alpha_S \times \sin 2\theta_S}{\sin 2(\alpha_S + \theta_S)}$$

$$T_{air \rightarrow ne} = \frac{\sin 2\alpha_R \times \sin 2\theta_R}{\sin 2(\alpha_R + \theta_R) \times \cos^2(\alpha_R - \theta_R)}$$

$$T_{ne \rightarrow air} = \frac{\sin 2\alpha_S \times \sin 2\theta_S}{\sin 2(\alpha_S + \theta_S) \times \cos^2(\alpha_S - \theta_S)}$$

The optimum performance for switching is achieved by finding the minimum of the above equation. For clarity and due to the window size of the crystal only two sets of data are presented in Fig. 5, $2\alpha=18.4^\circ$ and $2\alpha=23.2^\circ$.

The two curves in Fig.5 follow essentially the sinc function. As can be see from equation (14), the diffracted efficiency ratio is about one when the normal angle is at 90° and it decreases rapidly to zero when the normal angle approaches 105°. That the experimental values are less than the theoretical ones is due to assumptions made in the associated coupling wave theory. The assumption is that there is a small absorption loss and a slow energy interchange between the coupled waves (R and S) and the theory does not consider the second order terms in the wave equations (R" and S"). Furthermore the laser beam is Gaussian; where as, the coupled wave theory assumes plane waves.

The significant role of ΔK in the evaluation of the diffraction efficiency ratio is apparent from our results. At a fixed normal angle the larger the write-in angle the higher the ΔK which in turn gives a smaller efficiency ratio. Also, at a fixed write-in angle the larger the difference between the normal angle and 90° the larger the ΔK which again gives a smaller efficiency ratio. In this polarization optical switch, a small efficiency ratio results in a the large signal to noise ratio, that is a large distinction between signal "on" and noise "off". In practice, the choice is limited by the configuration of the optical system and the size of the crystal. As demonstrated in our experiment for a 1 cm² LiNbO₃ crystal, an efficiency ratio of less than 0.01 (i.e., the "on" and "off" ratio larger than 100) can be easily achieved. This is adequate for many binary operations.

5. CONCLUSIONS

The technique of using polarization sensitive holograms to implement a large number of 2x2 optical switches on a single crystal has been described. The method has several positive attributes. First, polarization optical switching provides theoretical cascability and energy conservation. Second, the free space optics offers a very large bandwidth. Finally, the design requires only four holograms which can yield high diffraction efficiency. The development of better and larger photorefractive crystals may further improve the technique.

6. REFERENCES

1. J. Goodman, F. Leonberger, S. Kung, and R. Athale, "Optical Interconnections for VLSI systems", Proc. IEEE Vol. 72, 850(1984)
2. Shudong Wu, Qiwang Song, Andy Mayers, Don A. Gregory and Francis T. S. Yu, "Reconfigurable interconnections using photorefractive holograms", Applied Optics Vol. 29, 1118(1990).
3. G. Almasi, and A. Gottlieb, "Highly parallel computing", Benjamin and Cummings Publishing Company, Inc., Redwood city, CA. 1989.
4. A. Lohmann, and J. Weigelt, "Spatial filtering logic based on polarization", Applied Optics, Vol. 26, 131(1987).
5. Herwig Kogelnik, "Coupled Wave Theory for Thick Hologram Gratings", The-Bell System Technical Journal, pp 2909-2947, Nov. 1969.
6. Pochi Yeh and Amnon Yariv, "Optical waves in crystals", John Wiley and Sons, New York. 1984.
7. P.P. Benerjee and T. C. Poon, "Principles of Applied Optics", Richard Irwin, Inc., 1991.

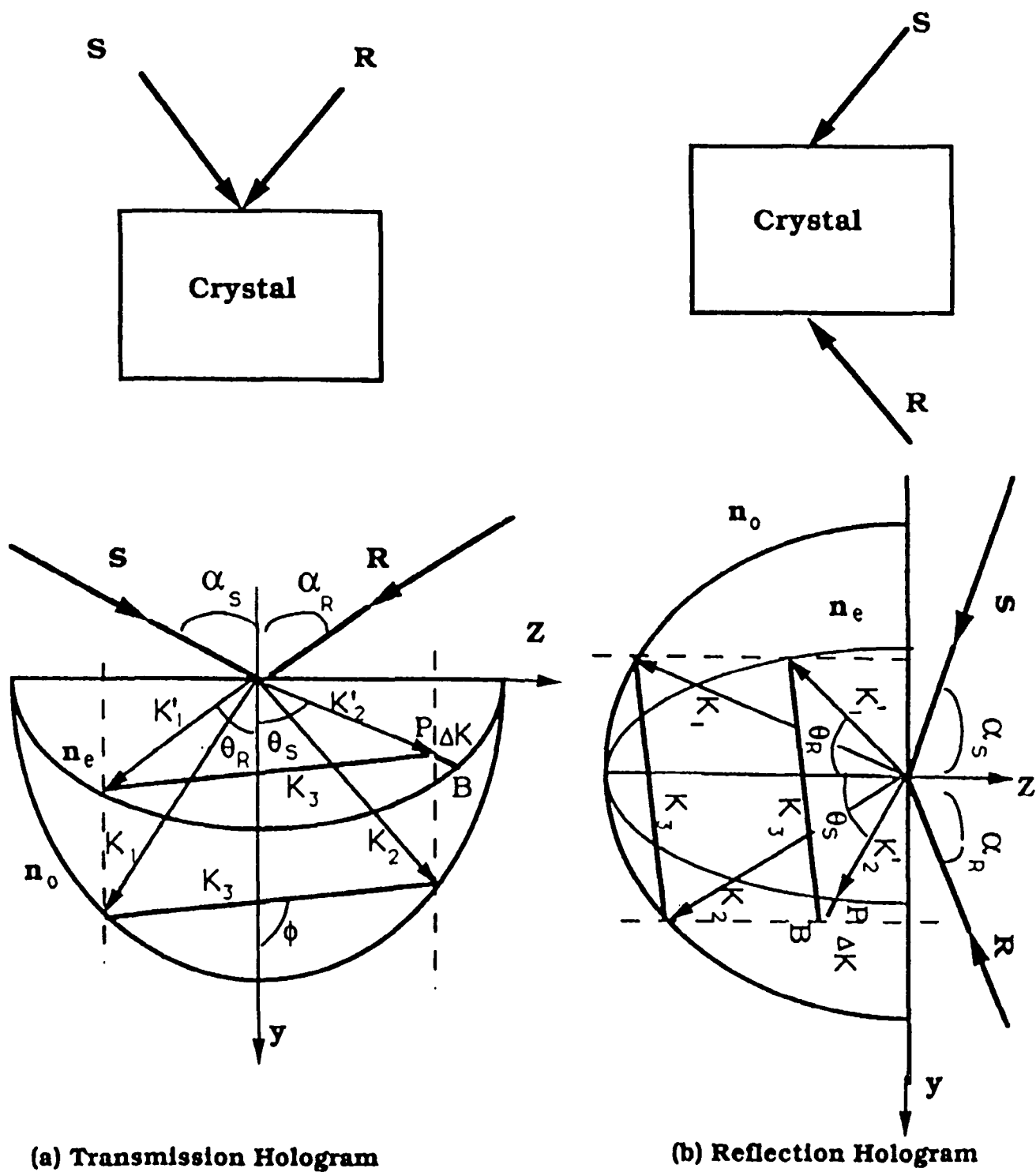


Fig. 1 Wave vector diagram of a crystal volume hologram: (a) transmission hologram; (b) reflection hologram.

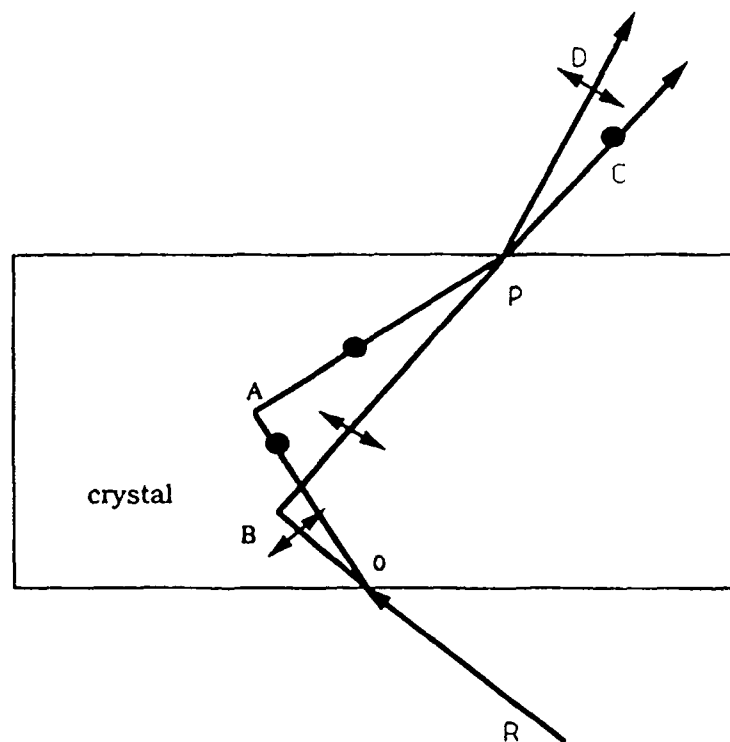


Fig. 2 One to two optical coupling switch configuration.

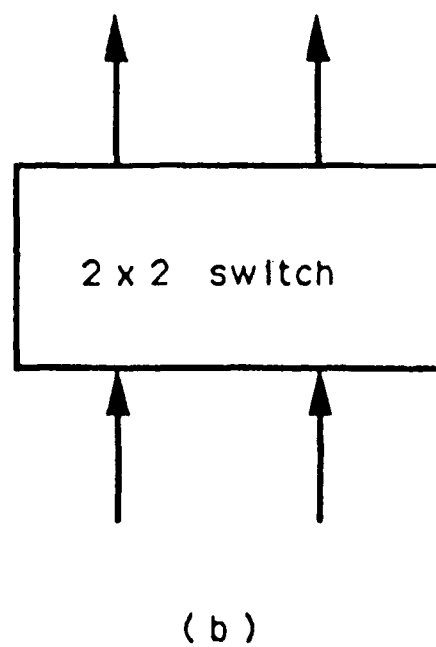
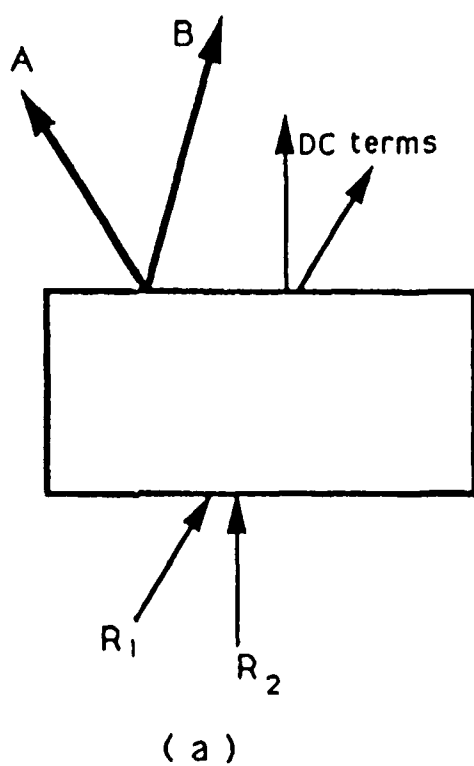


Fig. 3 An optical 2x2 switch: (a) optical configuration; (b) circuit analogy.

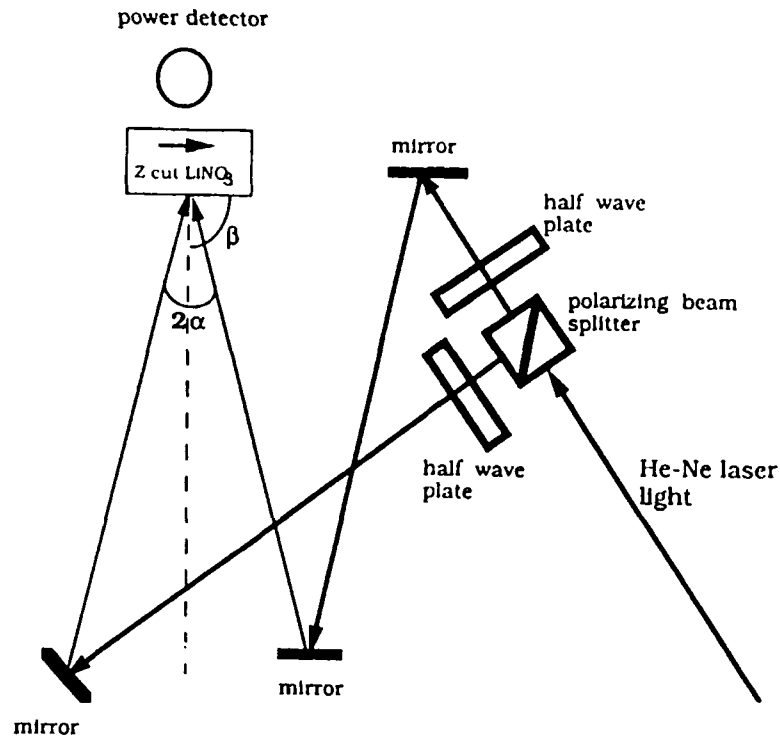


Fig. 4 Experimental setup for the measurement of diffraction efficiency ratio.

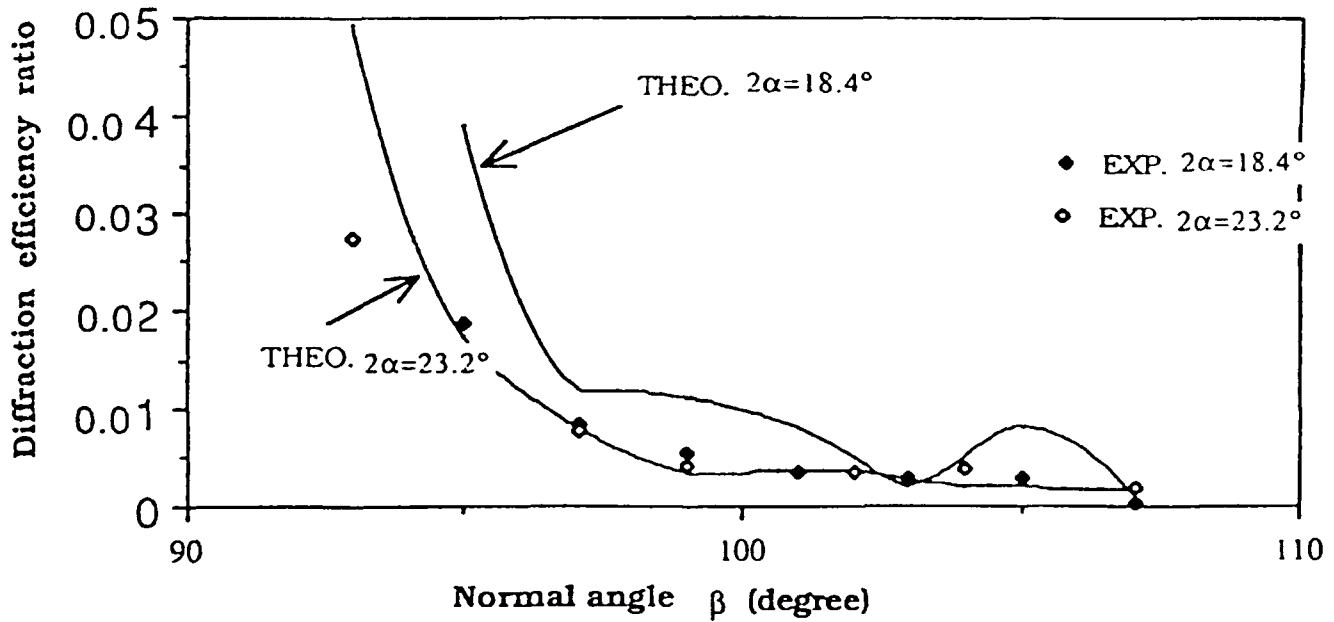


Fig. 5 Diffraction efficiency ratio of vertical polarization over horizontal polarization: solid-line theoretical prediction; dots-experimental results.

OPTICAL BAND GAP OF THE TERNARY SEMICONDUCTOR $\text{Si}_{1-x-y}\text{Ge}_x\text{C}_y$

Richard A. Soref, Electromagnetics & Reliability Directorate, Rome Laboratory

Published in Journal of Applied Physics, Vol. 70, No. 4, 15 August 1991

Abstract—Single-crystal alloys of diamond with Si and Ge are investigated theoretically. An indirect band gap $\Gamma_{25'}^v \rightarrow \Delta_1^c$ is found for the new semiconductor $\text{Si}_{1-x-y}\text{Ge}_x\text{C}_y$ over most compositions x and y , with an indirect $\Gamma_{25'}^v \rightarrow L_1^c$ gap found for the remaining compositions. The estimated band gaps span the 0.62–5.5-eV-range. Predictions are made for band gap versus lattice parameter in the new alloy semiconductors $\text{Si}_{1-x}\text{C}_x$ and $\text{Ge}_{1-x}\text{C}_x$.

Diamond is an elemental group-IV insulator (wide-gap semiconductor) with a lattice parameter of 3.545 Å, a parameter much smaller than the lattice size of Si (5.431 Å) or Ge (5.646 Å). In this communication, we investigate an optical property (the minimum-energy gap) of crystalline alloys of diamond with Si and Ge, including the new ternary semiconductor $\text{Si}_{1-x-y}\text{Ge}_x\text{C}_y$. The interpolation approach of Soref and Perry,¹ which was developed for $\text{Si}_{1-x-y}\text{Ge}_x\text{Sn}_y$, is used here, with the energy bands of diamond replacing the α -Sn bands in the calculation.

Although the semiconductor $\text{Si}_{1-x-y}\text{Ge}_x\text{C}_y$ has never been grown, modern heteroepitaxy techniques will probably allow a thin layer of crystal SiGeC to be grown on a Si, Ge, or diamond substrate. The epilayer would be commensurately strained, or strain relieved, depending upon its composition and thickness. Coherent strain in a $\text{Si}_{1-x-y}\text{Ge}_x\text{C}_y$ epilayer might be facilitated by growing the layer on an alloy buffer layer of $\text{Si}_{1-x}\text{C}_x$ or $\text{Si}_{1-p-q}\text{Ge}_p\text{C}_q$, etc. In this communication we shall investigate the properties of bulk unstrained SiGeC at room temperature. The band-gap narrowing or dilation that occurs due to strain is a subject for future study.

The energy-band structure of diamond was calculated in 1975 by Brener² using the screened-exchange-plus-Coulomb-hole method. His approach gave good agreement between theory and experiment, especially for the important $\Gamma_{25'}^v - \Gamma_{15}^c$ transition [7.6 eV (theory) versus 7.3 eV (experiment)] and the $\Gamma_{25'}^v - \Delta_1^c$ transition [5.6 eV (theory) versus 5.5 eV (experiment)]. Therefore, starting with Fig. 3 of Brener,² we obtained realistic valence- and conduction-band energies at several critical points in the Brillouin zone, as listed in Table I. [The 1983 calculation of Jones and King³ gives an incorrect value (6 eV) for the direct gap of diamond, but their L_1^v , X_1^v , L_1^c , Γ_2^c eigenvalues may be more accurate than those in Table I.] The table also contains the corresponding energies for Si and Ge that were taken from Li and Lin-Chung⁴ as explained in Ref. 1. In Si and C, the conduction-band minimum is in the (100) direction

near Δ_1 and X_1 with the minimum lying ~5% lower than the X_1 zone boundary value. In Table I we use the experimental indirect gaps of 1.13 eV for Si and 5.5 eV for C to represent the X_1 - Δ_1 saddle point, while 0.72 eV is assumed for Ge at X_1 - Δ_1 . Germanium has a (111) conduction-band minimum at the L -zone boundary (0.62 eV). The light- and heavy-hole valence bands are degenerate at the $\Gamma_{25'}^v$ valence-band maximum in Si, C, and Ge. Now, we follow the same procedure as in Ref. 1 to generate diagrams of critical-point energies, estimated band gap versus lattice parameter, and ternary band gap versus composition.

In Fig. 1 the critical-point energies are arrayed in a vertical column for each elemental semiconductor. Then, the corresponding points are connected by straight lines to yield the interpolated values for the binary semiconductor alloys $\text{Ge}_{1-x}\text{Si}_x$, $\text{Si}_{1-x}\text{C}_x$, and $\text{C}_{1-x}\text{Ge}_x$. We take $\Gamma_{25'}^v$ as the zero reference for each material, a procedure that is acceptable for determining the forbidden band. However, in a heterostructure device it would be important to know the Si/Ge, Si/C, and C/Ge valence-band offsets, as well as the conduction-band offsets.

Next, in Fig. 2, we show a magnified view of Fig. 1 that includes only the highest-lying valence band and lowest-lying conduction band. Again, a linear fit between the elemental data points was used. The lightly shaded areas in Fig. 2 reveal that the gap is indirect $\Gamma_{25'}^v \rightarrow \Delta_1^c$ for most compositions (x) of the three binary alloys. The darkly shaded areas near the Ge line show that the gap is indirect $\Gamma_{25'}^v \rightarrow \Delta_1^c$ for the compositions $0 < x < 0.16$ in $\text{Ge}_x\text{Si}_{1-x}$ and $0.96 < x < 1.00$ in $\text{Ge}_x\text{C}_{1-x}$.

Having estimated the energy gap versus composition x for the three alloys, we employ the well-known approximation that the lattice constant α_x of the binary alloy $A_{1-x}B_x$ is $(1-x)\alpha_A + x\alpha_B$. This rule enabled us to plot the fundamental gap as a function of lattice parameter for the crystalline alloys $\text{Ge}_{1-x}\text{Si}_x$, $\text{Si}_{1-x}\text{C}_x$, and $\text{C}_{1-x}\text{Ge}_x$. To check the accuracy of our method, we plotted E_g vs α_x on linear-versus-linear scale, and we compared the calculated value of E_g for $\text{Si}_{0.5}\text{C}_{0.5}$ material with the experimental E_g value (at 300 K) for the stoichiometric IV-IV semiconductor β -SiC. It was found that the calculated value of 3.4 eV was 50% larger than the observed⁵ 2.25-eV indirect gap of cubic SiC, which called into question the validity of the linear interpolation.

TABLE 1. Conduction- and valence-band energies (eV) at critical points in Brillouin zone. Γ_{25}^v is used as the zero of energy.

	L_3^v	X_4^v	Γ_{25}^v	Γ_{15}^c	$X_1^c - \Delta_1^c$	L_1^c	Γ_2^c
Ge	-2.28	-3.10	0.00	2.66	0.72	0.62	0.75
Si	-2.44	-3.37	0.00	2.66	1.13	1.71	2.88
C	-3.50	-7.50	0.00	7.60	5.50	13.50	18.10

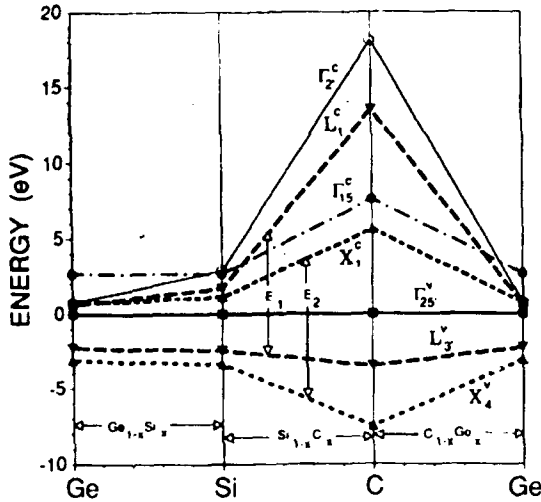


Fig. 1. Composite energy-band diagram for Ge, Si, and diamond, showing critical-point energies arrayed on one line for each elemental material. Energies for binary alloy semiconductors are also indicated.

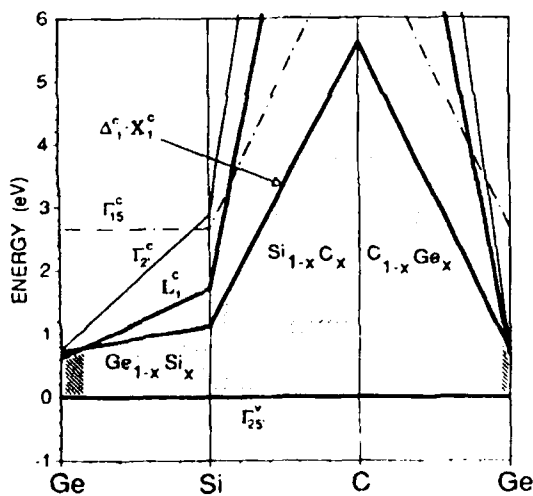


Fig. 2. Enlarged view of Fig. 1 showing the indirect gaps $\Gamma_{25}^v \rightarrow \Delta_1^c$ and $\Gamma_{25}^v \rightarrow L_1^c$.

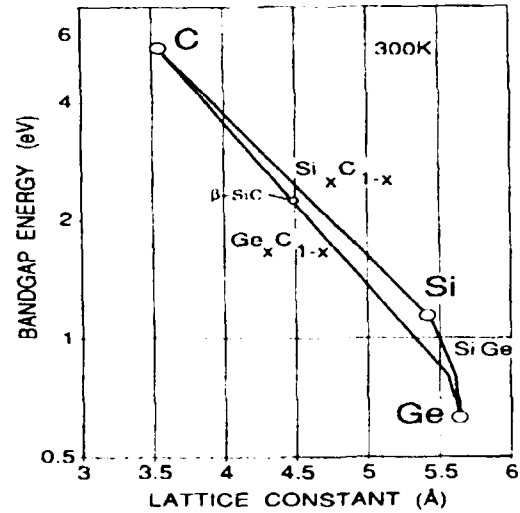


Fig. 3. Indirect band gap of the alloy semiconductors $\text{Ge}_x\text{C}_{1-x}$, $\text{Si}_x\text{C}_{1-x}$, and $\text{Ge}_x\text{Si}_{1-x}$ as a function of lattice parameter. An exponential fit of Ge-C-Si data was used.

To obtain better agreement between theory and practice, we tried a nonlinear curve fitting of the elemental Δ_1 -gap data points. We plotted E_g as a function of α_x , on logarithmic-versus-linear scales, and we used straight-line segments to connect the Δ_1 gap points, with the result shown in Fig. 3. Here, the gap increases exponentially with increasing carbon concentration. In Fig. 3 it is seen that $\text{Si}_{0.5}\text{C}_{0.5}$ material (whose lattice constant is 4.488 Å) has a predicted gap of 2.5 eV, which is close to the actual β -SiC value of 2.25 eV. This agreement gave us confidence in the validity of the Fig. 3 exponential approach; thus we attempted to predict the band gap of a new semiconductor,

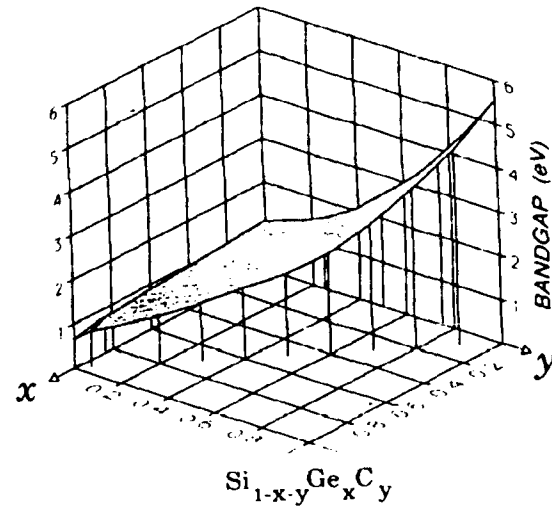


Fig. 4. Indirect energy gap of the new ternary semiconductor $\text{Si}_{1-x-y}\text{Ge}_x\text{C}_y$ (diamond lattice) as a function of composition x and y .

cubic GeC, which has never been grown⁶. If we examine the $\text{Ge}_{0.5}\text{C}_{0.5}$ alloy in Fig. 3, whose lattice constant is 4.596 Å, we predict a band gap of 2.1 eV for cubic GeC. Further, if we apply the exponential fit to an alloy of diamond and tin we find that $E_g(\Delta_1) \sim 1.2$ eV for cubic SnC at the 5.017-Å lattice.

Finally, we can estimate the band gap of the ternary semiconductor $\text{Si}_{1-x-y}\text{Ge}_x\text{C}_y$ from our Fig. 3 result for the gaps of binary alloys. On a three dimensional (3D) graph (Fig. 4), the band gap of the ternary is displayed on the vertical axis, while the horizontal axes represent composition x and y . All compositions are located within an (x,y) triangle: The line $(0,y)$ signifies $\text{Si}_{1-y}\text{C}_y$, the line $(x,0)$ signifies $\text{Si}_{1-x}\text{Ge}_x$, and the line $x+y=1$ represents $\text{Ge}_x\text{C}_{1-x}$. The 3D surface of ternary gap in Fig. 4 consists of a "wire frame" with an elastic sheet stretched between the three wires. Each wire is a 2D representation of E_g for one of the three binary alloys. We find in Fig. 4 that all ternary gaps are indirect, primarily to Δ_1 , the remainder being indirect to L_1 . Since visible light spans the photon energies of 1.77-3.10 eV, we see that the absorption edges of the materials in Figs. 3 and 4 cover the near-infrared, visible, and near-ultra-

violet ranges, a property that should be useful for electro-optical device applications.

In summary, we have used interpolation between the critical-point band energies of diamond, silicon, and germanium to estimate the fundamental band gap of a new crystalline semiconductor alloy $\text{Si}_{1-x-y}\text{Ge}_x\text{C}_y$.

I wish to thank F. Namavar of Spire Corporation for helpful and stimulating discussions of ternary diamond alloys. I am also grateful to C. H. Perry of Northeastern University for helpful comments on the manuscript.

REFERENCES

1. R. A. Soref and C. H. Perry, *J. Appl. Phys.* **69**, 539 (1991).
2. N. E. Brener, *Phys. Rev. B* **11**, 929 (1975).
3. R. Jones and T. King, *Philos. Mag.* **B 47**, 481 (1983).
4. Y. Li and P. J. Lin-Chung, *Phys. Rev. B* **27**, 3465 (1983).
5. H. R. Phillip and E. A. Taft, in *Silicon Carbide, A High Temperature Semiconductor*, edited by J. O'Connor and J. Smultens (Pergamon, New York, 1960), pp. 366-370.
6. A. Morimoto, T. Kataoka, M. Kumeda, and T. Shimizu, *Philos. Mag.* **B 50**, 517 (1984).

PREDICTED BAND GAP OF THE NEW SEMICONDUCTOR SiGeSn

Richard A. Soref and Clive H. Perry^{a)}, Electromagnetics & Reliability Directorate, Rome Laboratory

Published in Journal of Applied Physics, Vol. 69, No. 1, 1 January 1991

Abstract - The direct and indirect band gaps of $\text{Si}_{1-x-y}\text{Ge}_x\text{Sn}_y$ are inferred from the calculated energy-band structure of $\alpha\text{-Sn}$ and from the known structures of Ge and Si. Our assumptions are: that the energy-band shapes of the binaries $\text{Sn}_{1-x}\text{Ge}_x$, $\text{Ge}_{1-y}\text{Si}_y$, and $\text{Si}_{1-z}\text{Sn}_z$ change smoothly with x and y , and that the energy gap of SiGeSn can be estimated by interpolation from the gaps of SnGe, GeSi, and SiSn. The optical indices of refraction of SiGeSn are also estimated.

Efforts have been made in recent years to alloy $\alpha\text{-Sn}$ with Ge or Si, but it has been difficult to stabilize Sn in the alloy lattice because the lattice parameter of grey tin is 6.489 Å compared to 5.646 Å for Ge and 5.431 Å for Si. Nevertheless, there is hope of stabilizing Sn by growing a thin, strained layer of SnGe or SiSn on a substrate of Si or Ge or Sn. Such growth would probably require chemical beam epitaxy or metalorganic chemical vapor deposition.

Strained layers of Sn-alloy semiconductors would undoubtedly find application in optoelectronics, judging from the success of the related material $\text{Ge}_{1-x}\text{Si}_x$, which has been grown on (100) Si.¹ We speculate in this communication that the new ternary semiconductor SiGeSn will prove to be a useful material in both optics and electronics. We propose that $\text{Si}_{1-x-y}\text{Ge}_x\text{Sn}_y$ could be grown on Si or Ge (with or without buffer layers to take up some of the strain), and we suggest that heteroepitaxy could be used to make ternary heterostructures $\text{Si}_{1-x-y}\text{Ge}_x\text{Sn}_y/\text{Si}_{1-p-q}\text{Ge}_p\text{Sn}_q$ (including superlattices) for optoelectronic devices. Recently, Wegscheider *et al.*² have reported the growth, structure, and optical properties of single-crystal SnGe superlattices on Ge(100) substrates.

In assessing the usefulness of SiGeSn for optoelectronics, it is important to understand the energy-band structure of the ternary, and to predict the compositional dependence of the fundamental optical band gap (E_g), including the range over which the gap is indirect (E'_g). The second step is to determine the optical properties of SiGeSn, especially the index of refraction (n), so that the prospects for optical waveguiding can be assessed. We shall make theoretical predictions for both E_g and n in this paper. The case of bulk, unstrained SiGeSn is investigated, and the modifications due to strain are discussed.

Energy-band calculations for $\alpha\text{-Sn}$ were made by Li and Lin-Chung³ using the Slater-Koster parameter (SKP) model. In order to check their technique, they reproduced the known band

structure of Ge and Si.⁴ From their results (Figs. 1-3 of Ref. 3), we have constructed in Fig. 1 the energy-band diagram of $\alpha\text{-Sn}_{1-x}\text{Ge}_x$, $\text{Ge}_{1-y}\text{Si}_y$, and $\text{Si}_{1-z}\alpha\text{-Sn}_z$ as a function of composition x , y , and z . In this figure, we show the energies of the highest lying valence bands (v.b.) and the lowest lying conduction bands (c.b.) for the $\alpha\text{-Sn-Ge-Si}$ system at the Γ -, X -, and L -critical points, respectively. For each element ($\alpha\text{-Sn}$, Ge, Si), the eigenvalues are displayed on a vertical line. Line segments are used to connect the corresponding critical-point energies, a procedure that reveals our assumption that the v.b. and c.b. shapes change smoothly with composition; x , y , and z .

By convention, $\Gamma_{25'}^v$ is taken to be zero eV. In Fig. 1, the solid lines show the E_g direct gap ($\Gamma_2^c - \Gamma_{25'}^v$), while the E_1 gap ($L_1^c - L_3^v$) is encompassed by the dashed lines and the E_2 gap ($X_1^c - X_4^v$) by the dotted lines. The E'_g indirect gap is defined as the lowest point of the conduction band not at the Γ point with respect to the zero-energy $\Gamma_{25'}^v$ point. The E_1 gap is very close to the L point in all three elements.⁵ The E_2 gap is situated in a saddle point between Δ_1 and X_1 along the $[100]$ direction for $0 < y < 1$.^{3,4,6} This E_2 behavior holds for $\alpha\text{-Sn}$ (Ref 5) and presumably for compositions x and z .

Dispersion curves similar to those calculated by Li and Lin-Chung³ have been obtained by a number of authors using local density theory of electron systems. Wang and Klein⁶ compare

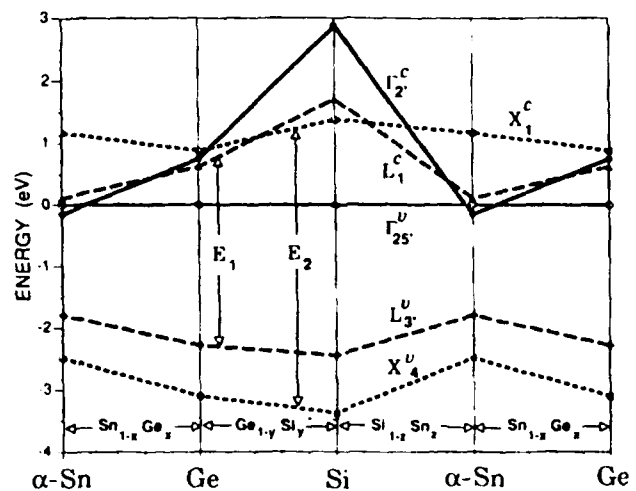


Fig. 1. Composite energy-band diagram for three elemental semiconductors, Si, Ge, and $\alpha\text{-Sn}$, showing projection of critical-point eigenvalues on one line for each material. Energies for binary semiconductors are also indicated.

^{a)} Permanent Address: Physics Department, Northeastern University, Boston, MA 02115.

their calculations with others and with the experimentally measured⁴ indirect gaps for Si and Ge. In both cases, the theoretical gaps fall below the experimental values. The same is true for Li and Lin-Chung³; they point out that they have not compared the energy values from the SKP model for α -Sn with the optical data^{5,7} as their calculations include no spin-orbit interaction, which is larger in Sn than in Ge or Si. However, the SKP approach allows a meaningful interpolation scheme from material to material.

In Fig. 2, we have slightly modified their data to make the Γ_2' conduction band degenerate with the Γ_{25}' valence band.⁵ However, the electroreflectance data of Cardona *et al.*⁵ indicate some discrepancy with our zero-gap assumption as they suggest a spin-orbit splitting of -0.35 eV between the top two valence bands. It should be understood that there is a margin of uncertainty in the relative locations of the L_1^c and Γ_2' points with respect to Γ_{25}' .

The indirect gap of Si originates from the 1.13-eV conduction band minimum located between Δ_1 and X_1 , while the corresponding c.b. minimum for Ge is at 0.68 eV. In order to obtain good estimates of the indirect gap values from Fig. 2, we shall multiply the X_1 values of Ref. 3 (1.32, 0.88, and 1.17 eV in Fig. 1) by the scale factor 0.82 in Fig. 2, which gives 1.13, 0.72, and 0.96 eV for the saddle-point $\Delta_1 - X_1$ in Si, Ge, and α -Sn, respectively. From Fig. 2 we now determine the direct and indirect energy gaps of the binary materials. The estimated band gaps are illustrated by the shaded regions in Fig. 2. The Fig. 2 plots imply that E_g would be situated near the L_1 point in $\text{Ge}_{1-y}\text{Si}_y$ for $0 < y < 0.16$, in $\text{Si}_{1-z}\text{Sn}_z$ for $0.4 < z < 0.9$, and in $\text{Sn}_{1-x}\text{Ge}_x$ for $0.45 < x < 1$. However, E_g would be at the $\Delta_1 - X_1$, saddle point for $0.16 < y < 1$ in $\text{Ge}_{1-y}\text{Si}_y$ and for

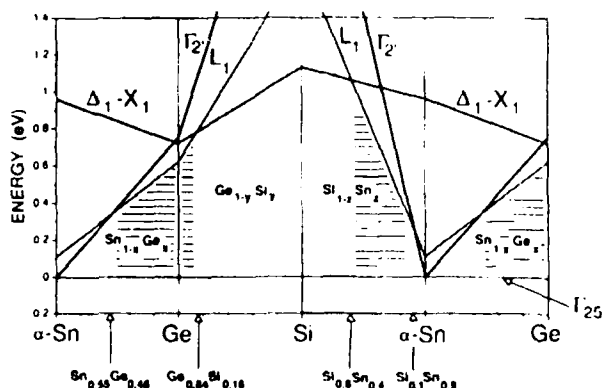


Fig. 2. Same as Fig. 1 except that the X_1 values for Si, Ge, and α -Sn are scaled to 1.13, 0.72, and 0.96 eV, respectively, and Γ_{25}' for α -Sn is set to 0 eV. This figure shows E_g vs composition for the binaries.

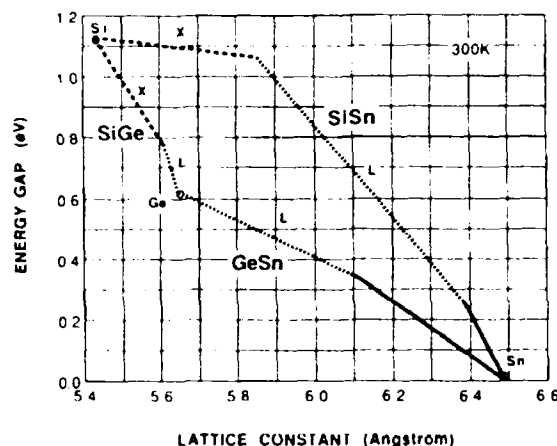


Fig. 3. Calculated band gap of the binary semiconductors $\text{Ge}_{1-x}\text{Sn}_x$, $\text{Si}_{1-y}\text{Ge}_y$, and $\text{Si}_{1-z}\text{Sn}_z$ in bulk unstrained alloy crystals. Solid lines: direct gap. Dashed lines: indirect gap with X representing $\Delta_1 - X_1$ to Γ_{25} and L signifying L_1 to Γ_{25} .

$0 < z < 0.4$ in $\text{Si}_{1-z}\text{Sn}_z$ only. The gap is "direct" for the ranges $0.9 < z < 1$ and $0 < x < 0.45$ in $\text{Si}_{1-z}\text{Sn}_z$ and $\text{Sn}_{1-x}\text{Ge}_x$, respectively. However, Tufte and Ewald⁸ suggest that the electrons in α -Sn at room temperature belong mostly in the conduction band minima centered close to the L_1 point along the $[111]$ direction. Also, a value of 0.08 eV for the thermal energy gap of α -Sn at 0 K has been found from galvanometric studies.⁸ Consequently, it takes only a small modification of the L_1 and Γ_2' lines in Fig. 2 for the direct gap to become indirect close to L_1 for all x and z .

Using the result of Fig. 2, we have constructed in Fig. 3 (a) plot of energy gap as a function of lattice constant for the com-

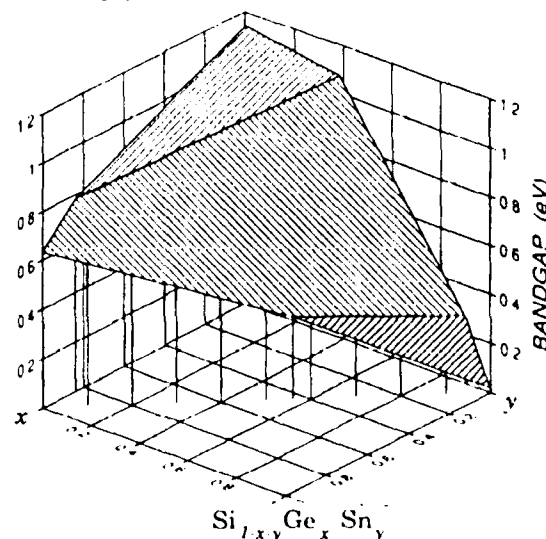


Fig. 4. Predicted band gap of the ternary semiconductor $\text{Si}_{1-x}\text{Ge}_x\text{Sn}_y$ as a function of composition x, y . The upper sheet is the indirect $\Delta_1 - X_1$ to Γ_{25} gap. The middle sheet is the L_1 to Γ_{25} indirect gap, and the lower sheet is the Γ_2 to Γ_{25} direct gap. The vertical lines show E_g along the composition line $x + y = 1$.

pound semiconductors $\text{Sn}_{1-x}\text{Ge}_x$ and $\text{Si}_{1-z}\text{Sn}_z$ (not previously known), and for $\text{Ge}_{1-y}\text{Si}_y$ (known from the literature). In Fig. 3, we used a piece-wise linear approximation for the E_g values taken from Fig. 2. The lattice constant of each binary alloy was assumed to follow Vegard's law.

The Fig. 3 predictions now form the basis for determining E_g in the ternary $\text{Si}_{1-x-y}\text{Ge}_x\text{Sn}_y$. We have constructed a three-dimensional diagram in which the z axis represents E_g of the ternary, the x axis represents Ge concentration, and the y axis shows Sn concentration. All possible ternarys are found within the triangle bounded by the $x = 0$ line, the $y = 0$ line and the $x + y = 1$ line. Starting with a display of the binary results of Fig. 3 on the 3D plot, we then connected the perimeters of the E_g sheet with a set of planes (a piece-wise planar approximation). The planes represent regions of direct gap, indirect Δ -X gap, and indirect L gap. This is shown in Fig. 4, which illustrates the linear interpolations between our SnGe, GeSi, and SiSn findings.

Turning to the optical properties of SiGeSn, we can estimate the refractive index using a simplified Lorentz oscillator model for the electrons at subgap photon energies $h\nu \ll E_d$. We can write $n^2 = 1 + \Omega^2/E_d^2$, where E_d is the effective value of the direct gap⁹ and Ω is the effective value of the plasma frequency of the valence band electrons. According to Figs. 2(a) and 2(b) of Wang and Klein,⁹ $n^2 = 11.8$ and $E_d = 4.0$ eV for Si, $n^2 = 16$ and $E_d = 3.6$ eV for Ge, yielding an average value of $\Omega^2 = 184$ (eV)² for the two materials ($E_d = 0$ for α -Sn). This relation is valid for low-to-moderate concentrations of tin. Consequently, we shall consider only the cases for which $E_d > 2$ eV. Using interpolated E_d values, we predict (for example) that $n = 4.46$ for $\text{Si}_{0.6}\text{Ge}_{0.2}\text{Sn}_{0.2}$, $n = 4.63$ for $\text{Si}_{0.3}\text{Ge}_{0.5}\text{Sn}_{0.2}$, $n = 3.70$ for $\text{Si}_{0.5}\text{Ge}_{0.5}$, $n = 4.36$ for $\text{Si}_{0.8}\text{Sn}_{0.2}$, and $n = 4.82$ for $\text{Ge}_{0.8}\text{Sn}_{0.2}$.

Coherent strain in GeSi is known to reduce the indirect band gap compared to E'_g , of the unstrained alloy. A thin GeSi layer on Si will be coherently strained if its thickness lies below a critical thickness t_c given by an empirical relation $t_c = t_0 M^{3.6}$,

where M is the lattice misfit (in percent) of SiGe relative to Si and t_0 is a curve-fitting parameter. The value $t_0 = 1200$ Å gives a good fit to the experimental data.¹⁰ If we postulate that this t_c relation holds for $\text{Ge}_{1-x}\text{Sn}_x/\text{Si}$ and for $\text{Si}_{1-x}\text{Sn}_x/\text{Si}$ (where M can reach 19.4%), then the critical thickness will fall rapidly from 3.6 μm to 9 Å as the Sn content is increased from 2% to 20%. Thus, for Sn concentrations greater than 20% in SiGeSn, it is likely that a ternary epilayer on Si will be relaxed rather than coherently strained for film thicknesses greater than a few monolayers.

In summary, we have calculated the direct and indirect band gaps of the new ternary semiconductor $\text{Si}_{1-x-y}\text{Ge}_x\text{Sn}_y$. Interpolation between the critical-point energies of Si, Ge, and α -Sn was used to estimate the gaps of the binary semiconductors $\text{Sn}_{1-x}\text{Ge}_x$, $\text{Ge}_{1-y}\text{Si}_y$, and $\text{Si}_{1-z}\text{Sn}_z$, and the ternary gap was found from interpolation on the binaries. The gap was determined as a function of composition and lattice constant. The calculation was for unstrained crystals, although strain is expected to play an important role in optoelectronic applications where strained-layer heterostructures would be constructed on a Si or Ge substrate. C. H. Perry was supported by an National Research Council Associateship (Air Force Systems Command).

REFERENCE

1. R. A. Soref, F. Nannavar, and J. P. Lorenzo, *Opt. Lett.* **5**, 270 (1980).
2. W. Wegscheider, K. Eberl, U. Menzinger, and G. Abstreiter, *Appl. Phys. Lett.* **57**, 875 (1990).
3. Y. Li and P. J. Lin-Chung, *Phys. Rev. B* **27**, 3465 (1983).
4. W. A. Harrison, *Electronic Structure and the Properties of Solids* (Freeman, San Francisco, 1980).
5. M. Cardona, P. McElroy, F. H. Pollack, and K. L. Shaklee, *Solid State Commun.* **4**, 319 (1966).
6. C. S. Wang and B. M. Klein, *Phys. Rev. B* **24**, 3393 (1981).
7. M. Cardona and D. L. Greenaway, *Phys. Rev.* **125**, 1291 (1961).
8. O. N. Tufte and A. W. Ewald, *Phys. Rev.* **122**, 1431 (1961).
9. C. S. Wang and B. M. Klein, *Phys. Rev. B* **24**, 3417 (1981).
10. G. Abstreiter, K. Eberl, E. Friess, W. Wegscheider, and R. Zachai, *J. Cryst. Growth* **95**, 431 (1989).

LARGE SINGLE-MODE RIB WAVEGUIDES IN GeSi-Si AND Si-on-SiO₂

Richard A. Soref, Electromagnetics & Reliability Directorate, Rome Laboratory
Joachim Schmidtchen and Klaus Petermann, Technische Universität Berlin, Institut für Hochfrequenztechnik

Published in IEEE Journal of Quantum Electronics, Vol. 27, No. 8, August 1991 (IEEE Log Number 9101351)

Abstract: Mode-matching and beam-propagation methods are used to analyze single-mode operation of optical GeSi-Si and Si-SiO₂ semiconductor rib waveguides. We determined the waveguide dimensions that will allow only the fundamental HE₀₀ or EH₀₀ mode to propagate. For both material systems, we find that the rib can be several microns wide and several microns high, thus allowing efficient coupling to single-mode fibers.

1. INTRODUCTION

It is often assumed that the cross-section dimensions of a 3-D rib waveguide must be similar to the thickness of a single-mode slab waveguide (made from the same material) in order to allow only the lowest-order optical mode to propagate. This assumption is incorrect, as demonstrated in this letter. The single-mode-slab condition is quite restrictive; hence, it is fortunate that the slab criterion is not essential for monomode rib propagation. For example, if the slab criterion were applied to a Si-on-SiO₂ rib guide, the Si guiding layer would be less than 0.3 μm thick, which would prevent low-loss coupling of light from a single-mode glass fiber into the semiconductor rib.

The problem of finding single-mode rib conditions is similar to the task of determining single-mode propagation in single-material fibers. Such fibers were investigated about 15 years ago [1]-[4], showing that indeed single-mode waveguides with "large" cross sections are possible even for a large index step between core and cladding. The fact that a single-mode rib guide can be several microns high and several microns wide has not been recognized generally in the optics literature. To remedy this deficiency, we shall present illustrations that reveal the specific dimensions of large single-mode ribs in real semiconductor systems.

2. ANALYSIS

We shall focus on two types of semiconductor waveguides: silicon-on-insulator (SOI) and GeSi-Si hetero-structures. Numerical examples will be given for mono-mode guiding in group-IV materials, but the results apply with little modification to III-V semiconductor ribs. Generally, we find that monomode propagation of the HE₀₀ or EH₀₀ mode is feasible at multi-micron dimensions provided that the ratio of rib width to rib height is properly chosen.

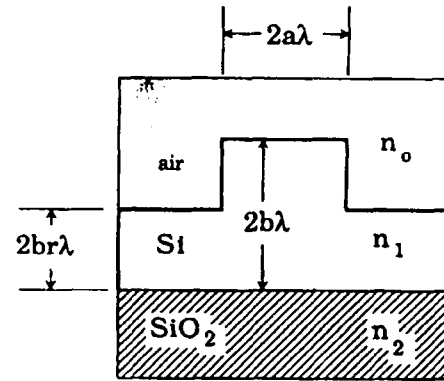


Fig. 1. Cross-section of rib waveguide.

Fig. 1 shows the cross section of the rib guide analyzed here. The rib width is designated as $2a\lambda$ and the inner rib height is $2b\lambda$ where λ is the free-space optical wavelength. The outer regions of the rib have a thickness of $2br\lambda$ where r is the fractional height of the side regions compared to the rib center (the outer-inner ratio). The three dielectric materials have refractive indices of n_0 , n_1 , and n_2 , respectively, at the wavelength of interest. The 3-D rib-guide modes are denoted as HE_{*nm*} or EH_{*nm*} where $n = 0, 1, 2, \dots$, $m = 0, 1, 2, \dots$, with HE being horizontally polarized and EH being vertically polarized.

Rib waveguides have been analyzed in [4], [5] using a mode-matching technique. Petermann's results [4] have been given in a simple normalized form which will be used for the analysis in this letter. The analysis is applicable to rib guides with a large cross section satisfying the condition $2b\sqrt{n_1^2 - n_2^2} \geq 1$ which is assumed in this letter. The rib height parameters w_1 and w_2 were defined in [4]. Here, we shall also define an effective rib height h_i inside of the rib, and an effective rib height h_o outside of the rib. These quantities, which account for decaying optical fields in the cladding, are given by: $h_i = 2b\lambda/w_1$ and $h_o = 2br\lambda/w_2$. For the rib guide, it is convenient to introduce an effective waveguide parameter [4]:

$$V = \frac{\pi}{2} \frac{aw_1}{b} \sqrt{\delta}. \quad (1)$$

Here, δ is a geometric parameter relating the effective inner and outer rib heights as follows:

$$\delta = \left(\frac{h_i}{h_o} \right)^2 - 1 = \left(\frac{w_2}{rw_1} \right)^2 - 1. \quad (2)$$

By manipulating (5) and (6) of [4], we find that

$$w_1 = \frac{4\pi b}{q + 4\pi b} \quad (3)$$

$$w_2 = \frac{4\pi rb}{q + 4\pi rb} \quad (4)$$

$$q = \frac{\gamma_0}{\sqrt{n_1^2 - n_0^2}} + \frac{\gamma_2}{\sqrt{n_1^2 - n_2^2}} \quad (5)$$

where $\gamma_{0,2} = 1$ for HE modes and $\gamma_{0,2} = (n_{0,2}/n_1)^2$ for EH modes.

The V -guiding parameter in the rib arises from an effective-index approach that takes into account the fundamental slab modes of the central ridge slab and the two side slabs (Fig. 1). Thus, for sufficiently small V , the second-order modes HE_{01} and EH_{01} will not fit laterally under the rib. Those modes will be cut off, assuring singlemode behavior in the horizontal direction. We will restrict our consideration to rib guides with $0.5 \leq r < 1.0$. Bearing this assumption in mind, higher-order modes in the vertical direction will be cut off because the higher-order modes in the central rib section will be coupled to the fundamental mode of the slab section, which becomes leaky for $r \geq 0.5$. This happens at $r \geq 0.5$ because the effective index of the fundamental slab mode becomes higher than the effective index of any higher-order vertical mode in the central rib region.

Intuitively speaking, the second-order modes in the vertical direction, HE_{10} and EH_{10} , have a double-peaked intensity distribution along the vertical axis. For $r \geq 0.5$, one of the two peaks (the lobe near the bottom of the guide) will couple out into the fundamental slab mode of the rib side regions. This lateral leakage ensures that the HE_{10} and EH_{10} modes will not propagate. That is why the condition $0.5 \leq r < 1.0$ guarantees single-mode operation of the rib in the vertical direction.

Actually, single-mode rib guides may also arise for $r < 0.5$ [2]. However, the analysis becomes much more complicated and therefore we restrict our considerations to ribs with $r \geq 0.5$. In other words, deeply etched ribs are not treated here.

For $r \geq 0.5$, it is found that the EH_{01} , HE_{01} , modes and the higher-order EH_{0n} , HE_{0n} modes will cease to propagate if the parameter V is less than a critical value V_s where the V_s solution

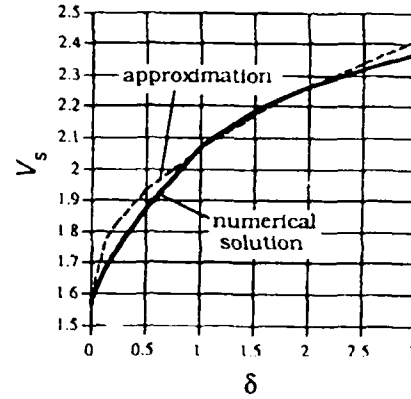


Fig. 2. Maximum waveguide parameter for single-mode operation.

[4] is plotted in Fig. 2 as a function of δ using the solid-line curve. We can make a good approximation to this curve using the relation

$$V_s = \frac{\pi}{2} (1 + 0.3\sqrt{\delta}) \quad (6)$$

as indicated by the dashed-line curve in Fig. 2. Equation (6) will aid us below. Using the $V < V_s$ single-mode condition, we can solve (1) for the aspect ratio a/b as follows:

$$\frac{a}{b} \leq \frac{2V_s}{\pi w_1 \sqrt{\delta}} \quad (7)$$

This equation can be rewritten by substituting (2)-(4) and (6) into (7) as follows:

$$\frac{a}{b} \leq \left(\frac{q + 4\pi b}{4\pi b} \right) \frac{1 + 0.3 \sqrt{\left(\frac{q + 4\pi b}{q + 4\pi b} \right)^2 - 1}}{\sqrt{\left(\frac{q + 4\pi b}{q + 4\pi rb} \right)^2 - 1}} \quad (8)$$

yielding

$$\frac{a}{b} \leq 0.3 + \frac{r}{\sqrt{1 - r^2}} \quad (9)$$

in the limit of large b .

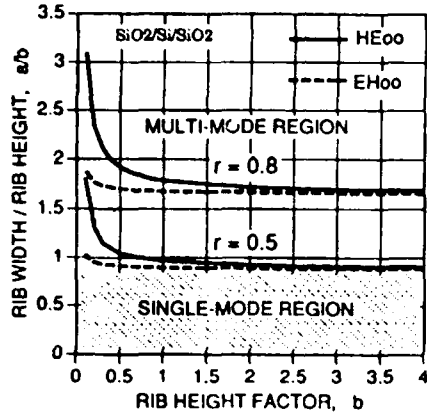


Fig. 3. Critical a/b ratio versus b for an SiO_2 -Si- SiO_2 rib guide.

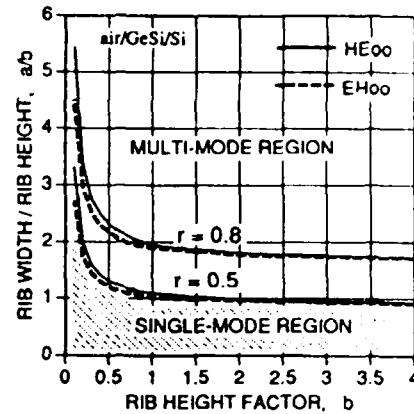


Fig. 6. Critical a/b ratio versus b for an air- $\text{Ge}_{0.1}\text{Si}_{0.9}$ -Si rib guide.

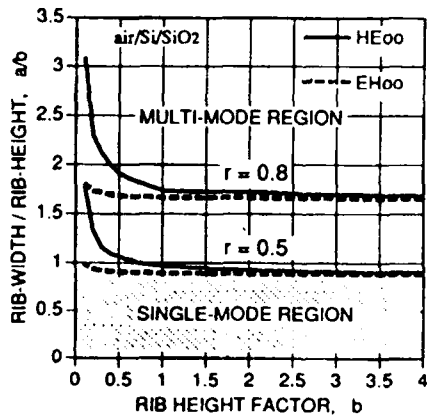


Fig. 4. Critical a/b ratio versus b for an air₂-Si- SiO_2 rib guide.

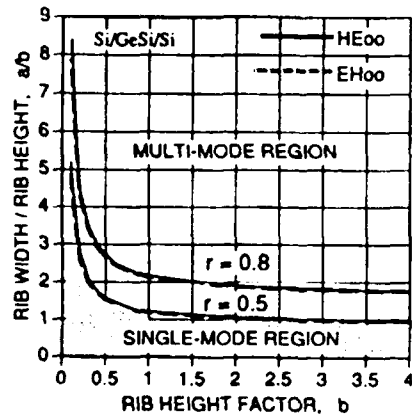


Fig. 5. Critical a/b ratio versus b for an Si- $\text{Ge}_{0.1}\text{Si}_{0.9}$ -Si rib guide.

3. NUMERICAL EXAMPLES

Equation (8) is our main result. Now we shall give numerical examples of (8) that illuminate the consequences of this relation. Four cases are considered: 1) Si-on- SiO_2 with an SiO_2 capping

layer; 2) Si-on- SiO_2 with air cladding; 3) $\text{Ge}_x\text{Si}_{1-x}$ -on-Si with an Si capping layer; 4) $\text{Ge}_x\text{Si}_{1-x}$ -on-Si with air cladding. At the $1.3 \mu\text{m}$ wavelength, the n_0, n_1, n_2 indexes are as follows: case 1 (1.45, 3.5, 1.45); case 2 (1.00, 3.5, 1.45); case 3 (3.5, 3.6, 3.5); case 4 (1.00, 3.6, 3.5). Considering the HE_{00} and EH_{00} modes in turn, we obtain from (5) the following q -values: case 1 (0.628, 0.108); case 2 (0.612, 0.078); case 3 (2.37, 2.24); case 4 (1.48, 1.14).

In cases 3 and 4, the 3.6 index corresponds to a waveguide core layer of $\text{Ge}_{0.1}\text{Si}_{0.9}$, an alloy that is transparent at $1.3 \mu\text{m}$. This $\text{Ge}_{0.1}\text{Si}_{0.9}$ layer is assumed to be thick enough ($2b\lambda > 1.4 \mu\text{m}$) so that the strain induced at the Si substrate interface is relieved within the layer (the layer is essentially unstrained). Note in case 3 that the 0.1 index step between the core and upper-lower claddings is of the same magnitude as that found in GaAs-AlGaAs-GaAs or InGaAs-InAlAs-InP waveguides. So, our calculations apply to III-V rib waveguides. The SOI cases are examples of ribs with a very large (2.05) core-clad index step.

Taking the rib-height factor b to be the independent variable in the right-hand side of (8), we have plotted in Figs. 3-6 the critical value of the ratio a/b as a function of b , using the ridge step factor r as a parameter (either $r = 0.5$ or $r = 0.8$). Predictions are given for cases 1-4. The guide is single mode for a/b less than a critical value as shown by the shaded region for $r = 0.5$. (For $r = 0.8$, the single-mode region is intended to extend from $a/b = 0$ up to the upper curves). When b is increased above 2.0, the critical width-height ratio a/b approaches an asymptote according to (9). Previous studies of single-mode ribs have considered values of $b \approx 0.1$ for which a width factor $a \approx 2b$ or $3b$ was predicted. Fig. 3-6 agree with those studies; thus, our results connect with the prior art.

The results from Figs. 3-6 show that there is a simple way to end-couple a single-mode glass fiber to a singlemode semiconductor channel waveguide. The semiconductor rib would be

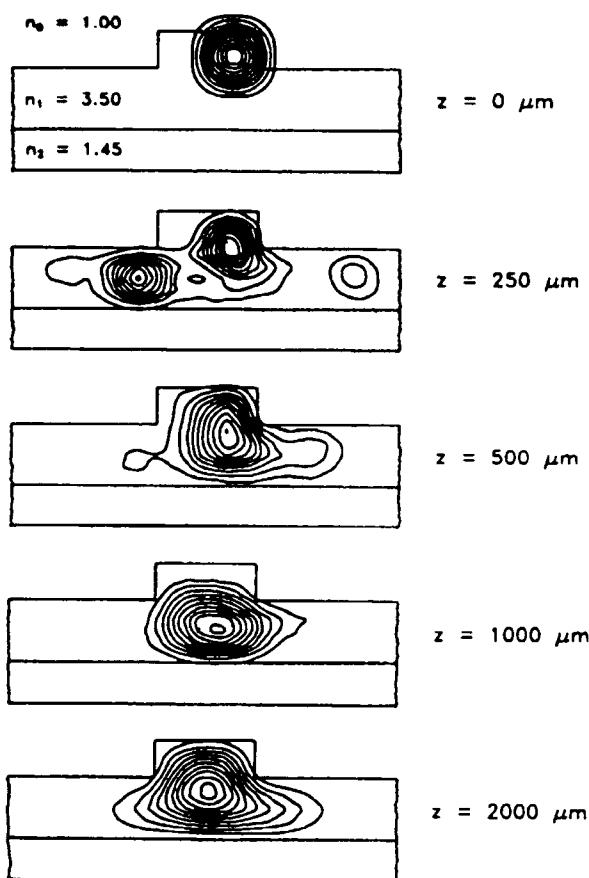


Fig. 7. Beam-propagation evaluation of a rib guide with $2a\lambda = 4 \mu\text{m}$ and $a/b = 1$.

built with a "square" aspect ratio of $a/b \approx 1$, producing a nearly circular mode profile, and, for efficient coupling, the mode sizes would be matched by choosing the rib factors $2a\lambda$ and $2b\lambda$ to be comparable to the fiber core diameter. Propagation losses of the monomode semiconductor ribs are expected to be low because the inherent losses of the basic slab guides are known to be low. Results for the HE_{00} and EH_{00} modes in Figs. 3-6 are essentially identical except for the region $b < 1$ in Figs. 3 and 4. Figs. 3-6 also indicate that it makes little difference in the critical a/b ratio as to whether the rib has symmetric or asymmetric cladding.

4. STABILITY OF THE SINGLE-MODE BEHAVIOR

Even though we have presented a single-mode condition for rib guides with large cross sections, the question remains as to

whether the leakage loss of the higher-order modes is sufficient to make these rib guides useful in practical integrated-optic networks. To resolve this issue, we have applied a newly developed efficient beam-propagation algorithm [6] which can easily handle large index steps. We used a 3-D formalism with 32×32 grid points and $0.5 \mu\text{m}$ grid spacing. An SOI rib waveguide was investigated, with $n_0 = 1.00$, $n_1 = 3.5$, $n_2 = 1.45$ as in Fig. 4, and $2b\lambda = 4 \mu\text{m}$, $r = 0.625$, $a/b = 1$, and $\lambda = 1.3 \mu\text{m}$. The propagation distance in the guide is denoted as z .

In a nominally single-mode rib, we deliberately launched a high-order mode by off-axis excitation as shown in Fig. 7. The drawing for $z = 0 \mu\text{m}$ shows the launch. In the Fig. 7 BPM calculation, contours of constant optical intensity ($10 \dots 100\%$ of maximum intensity) are shown for different propagation distances z . It can be clearly recognized that energy is leaking out laterally along the slab until at $z = 2000 \mu\text{m}$ the field intensity is close to the fundamental mode of the rib waveguide. Thus, it is shown that single-mode rib guides with large cross sections are really feasible, as long as the waveguide is at least several millimeters long, which is satisfied for most integrated-optic applications.

5. CONCLUSION

In summary, we have used a mode-matching technique and a beam-propagation analysis of $\text{Ge}_x\text{Si}_{1-x}$ -on-Si and Si-on-SiO₂ rib waveguides to predict that single-mode HE_{00} or EH_{00} propagation will occur for rib width/height ratios less than a critical value in the range 1-5 for guides whose rib side regions are more than 50% of the inner rib height. The rib width/height ratio is less than $0.3 + r/\sqrt{1-r^2}$ for rib heights greater than about 4λ .

6. REFERENCES

1. P. Kaiser, E. A. J. Marcatili, and S. E. Miller, "A new optical fiber," *Bell Syst. Tech. J.*, vol. 52, pp. 265-269, Feb. 1973.
2. E. A. J. Marcatili, "Slab-coupled waveguides," *Bell Syst. Tech. J.*, vol. 53, pp. 645-674, Apr. 1974.
3. J. A. Arnaud, "Transverse coupling in fiber optics, part II: Coupling to mode sinks," *Bell Syst. Tech. J.*, vol. 53, pp. 675-696, Apr. 1974.
4. K. Petermann, "Properties of optical rib-guides with large cross-section," *Archiv fur Elektronik und Übertragungstechnik*, (Germany), vol. 30, pp. 139-140, 1976.
5. N. Dagli and C. G. Fonstad, "Analysis of rib dielectric waveguides," *IEEE J. Quantum Electron.*, vol. QE-21, pp. 315-321, Apr. 1985.
6. A. Splett, M. Majd, and K. Petermann, "A novel beam propagation method for large refractive index steps and large propagation distances," *IEEE Photon. Technol. Lett.*, vol. 3, Mar. 1991.

FORCES ON THREE-LEVEL ATOMS INCLUDING COHERENT POPULATION TRAPPING

M. G. Prentiss, Jefferson Physical Laboratory, Harvard University
 N.P. Bigelow, Department of Physics and Astronomy, Laboratory for Laser Energetics, University of Rochester
 M.S. Shahriar, Research Laboratory of Electronics, Massachusetts Institute of Technology
 P.R. Hemmer, Electromagnetics & Reliability Directorate, Rome Laboratory

Published in Optics Letters, Vol. 16, No. 21, 1 November 1991

Abstract - We present a calculation of the force on a stationary three-level atom excited by a nearly resonant Raman light field, which may be composed of an arbitrary combination of standing- and traveling-wave fields. The effects of the ground-state coherences are explicitly included and are shown to play a crucial role in the nature of the force on the atom. We show that the force contains terms that vary on length scales both shorter and longer than the optical wavelength and that the magnitude of these terms can be made arbitrarily large.

Recently there has been considerable interest in the force due to the interaction between three-level atoms and nearly resonant optical fields.¹⁻⁴ It has been suggested that three-level forces may explain some of the differences between observations on real trapped atoms and predictions for two-level atoms^{1,5} (TLA) or incoherent processes in multilevel atoms. The three-level Λ system is of particular interest because of the effects of coherent population trapping. Recently, velocity-selective coherent population trapping has been used to cool atoms below the single-photon recoil limit.⁶ In this Letter we calculate the net average force F on a stationary atom in a Λ configuration excited by two fields E_1 and E_2 each in an arbitrary combination of standing and traveling waves. We calculate F by solving the optical Bloch equations (OBE's) in the steady-state limit. For pure traveling waves, F is spatially invariant, and the direction of the spontaneous force F_{sp} depends only on the wave vectors of E_1 and E_2 . For pure standing waves, the solutions predict that the stimulated force can have spatial components that vary on scales both shorter and longer than the optical wavelength (λ_{opt}).⁷ For experimentally attainable parameters, the size of these force terms can be substantially larger than the maximum F_{sp} on a TLA. We interpret our results in a dressed atom picture and show that many important aspects of F can be attributed to the effects of the ground-state coherences.

We consider the Λ system shown in Fig. 1 (left), which interacts with two fields $E_1 = |E_1| \times \exp[i(\omega_1 t + \phi_1)]$ and $E_2 = |E_2| \times \exp[i(\omega_2 t + \phi_2)]$ that have frequencies ω_1 and ω_2 , where the Λ system is closed and $\Gamma = 2\gamma_{ea} = 2\gamma_{eb}$. We confine ourselves to the case where E_1 (E_2) interacts only with the $|a\rangle \rightarrow |e\rangle$ ($|b\rangle \rightarrow |e\rangle$) transition. We derive F using the Lorentz expression $F_j = \mathbf{P} \cdot \nabla_j \mathbf{E}$, where $j = x, y, z$.

$\mathbf{P} = \mathbf{P}(E_1, E_2) = \text{tr}(\hat{\rho}\boldsymbol{\mu})$ is the polarization induced in the atom, where $\hat{\rho}$ and $\boldsymbol{\mu}$ are the density-matrix and vector dipole operators, respectively. Thus we solve for F by solving the OBE's⁸ for the off-diagonal elements of $\hat{\rho}$ in the steady-state limit by using the rotating-wave approximation. However, the physical significance of F may be more easily interpreted in terms of states $|-\rangle$, $|+\rangle$, and $|e\rangle$ derived from $|a\rangle$, $|b\rangle$, and $|e\rangle$ by a unitary transformation R_1 where

$$R = \begin{bmatrix} \cos(\theta) & -\sin(\theta) & 0 \\ \sin(\theta) & \cos(\theta) & 0 \\ 0 & 0 & 1 \end{bmatrix}. \quad (1)$$

Here θ is a measure of the relative strengths of E_1 and E_2 , given by $g_1 = |\langle \mu_{ea} \cdot E_1 \rangle / \hbar| = g_1(x) = g \sin \theta$, and $g_2 = |\langle \mu_{eb} \cdot E_2 \rangle / \hbar| = g_2(x) = g \cos \theta$ are the Rabi frequencies, with $g = (g_1^2 + g_2^2)^{1/2}$.

The $|+\rangle$ and $|-\rangle$ states are the eigenstates of the atom field system in the absence of spontaneous emission and are sometimes referred to as the dressed states.⁹ The OBE's can then be derived by applying R to all the matrices that describe the time evolution of the $|a\rangle$, $|b\rangle$, $|e\rangle$ system. In the dressed-state basis the Hamiltonian for the OBE's,⁸ H_{TD} , is

$$H_{TD} = \frac{\hbar}{2} \begin{bmatrix} \Delta \cos(2\theta) & \Delta \sin(2\theta) & 0 \\ \Delta \sin(2\theta) & -\Delta \cos(2\theta) & -g \\ 0 & -g & -2\delta \end{bmatrix}, \quad (2)$$

where ω_a (ω_b) is the resonant frequency of the $|a\rangle \rightarrow |e\rangle$ ($|b\rangle \rightarrow |e\rangle$) transition. $\Delta = (\omega_1 - \omega_a) - (\omega_2 - \omega_b)$ is the differential detuning, and $\delta = 1/2[(\omega_1 - \omega_a) + (\omega_2 - \omega_b)]$ is the common detuning (see Fig. 1). The dressed-state source and decay matrices⁸ can be obtained by a similar transformation.

Since the only important components of F are $P_{ea}(E_1, E_2) \cdot \nabla E_1$ and $P_{eb}(E_1, E_2) \cdot \nabla E_2$, F can be expressed in terms of the field gradients $\alpha_j = (1/g_j)(\delta g_j / \delta x)$, $\beta_j = (\delta \phi_j / \delta x)$,

$$F = [C_{\text{stim}}(\alpha_1 + \alpha_2) + C_{\text{dif}}(\alpha_1 - \alpha_2) + C_{\text{sp}}(\beta_1 + \beta_2)], \quad (3)$$

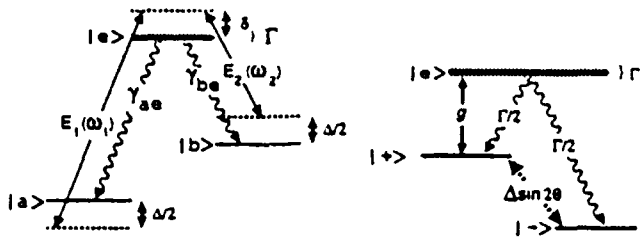


Fig. 1. Left: three-level A system in Raman excitation field. Right: coupling between the states of the A system in the dressed-state basis [see Eq. (2)].

and $C_{sp} = 2\Delta^2 \Gamma C_0$.

Here $C_0 = 4\hbar g_1^2 g_2^2 / D$ and $D = g^6 +$

$8\delta\Delta[(g_2^4 - g_1^4) + 2\Delta^2(g_1^2 - g_2^2)] + 4\Delta^2[g^2(4\delta^2 + \Gamma^2 + \Delta^2) - (g_1^4 - 4g_1^2 g_2^2 + g_2^4)]$.¹⁰ The α 's are normalized gradients of the field amplitudes. The α terms are associated with stimulated processes¹¹ and are not proportional to Γ . C_{sum} and C_{dif} are derived from the different contributions of $\hat{\rho}$ to \mathbf{P} . C_{dif} is derived from P_{-e} , which is a weighted average of the components of P_{ae} that are 180° out of phase with P_{be} . This term is associated with ρ_{-e} and thus is related to the correlation between the populations in $|-\rangle$ and $|e\rangle$. In contrast, C_{sum} , which is associated only with ρ_{+e} , is derived from P_{+e} . P_{+e} is a weighted average of the components of P_{ae} that are in phase with P_{be} ,^{9,12} and it is related to the correlation between the populations in $|+\rangle$ and $|e\rangle$. The $|+\rangle$ population also contributes a force term proportional to $(\beta_1 + \beta_2)$, which can be associated with spontaneous processes.¹¹ There is no $\beta_1 - \beta_2$ term.

We can gain some physical insight into F by considering C_{sum} , C_{dif} , and C_{sp} , which are determined by the correlations between the steady-state population distributions among the dressed states. We can estimate these correlation by considering the coupling (i.e., the population transfer rate) between the $|+\rangle$, $|-\rangle$, and $|e\rangle$ states.

Consider first the coupling between $|+\rangle$ and the other states. The Rabi flopping rate between the $|+\rangle$ and $|e\rangle$ states is given by g , and $\Gamma/2$ is the rate at which spontaneous emissions returns atoms from $|e\rangle$ to $|+\rangle$ (see Fig. 1, right). This is analogous to the coupling between the TLA states. The force on a TLA is $F_{TLA} \sim \rho_{ee}[\Gamma\beta_0 - 2(\omega - \omega_0)\alpha_0]$, where ω_0 is the TLA resonant frequency. Similarly, the contribution to F associated with $|+\rangle$ can be written as $F_{sum} = \hbar \rho_{ee}[\Gamma(\beta_1 + \beta_2) - 2\delta(\alpha_1 + \alpha_2)]$.

Thus, just as there is no semiclassical stimulated force on a TLA when $\omega - \omega_0 = 0$, in the A system, $C_{sum} = 0$ if $\delta = 0$. Note that the C_{sum} force component will be zero if E_1 and E_2 have opposite gradients.

In contrast, the contribution to F associated with $|-\rangle$ does not have a simple TLA analogy. It is not directly proportional to the

excited-state population ρ_{ee} , and it will be zero if the two fields have the same gradient. Consider the $|-\rangle$ and $|+\rangle$ to $|e\rangle$ couplings. Unlike $|+\rangle$, which is directly coupled to $|e\rangle$, $|-\rangle$ is never coupled directly to $|e\rangle$. Since $\gamma_{ea} = \gamma_{eb}$, if $\Delta = 0$, the only coupling is a source term that transfers population from ρ_{ee} to ρ_{-} at a rate $\Gamma/2$. Thus, independent of any other parameter, if $\Delta = 0$, an atom will be optically pumped into $|-\rangle$ and will remain there forever. This is why $|-\rangle$ is often referred to as the trapped or dark-resonance state.¹³ In the steady state, then, there is no population in $|e\rangle$; therefore the off-diagonal matrix elements are all zero (i.e., $\rho_{-e} = 0 = \rho_{+e}$). Thus $F = 0$ independent of the field gradients (i.e., α and β) and of δ , g_1 , and g_2 .

If $\Delta \neq 0$, then there is a coupling between $|-\rangle$ and $|+\rangle$, given by an effective Rabi flopping rate $\Delta \sin(2\theta)$. The $|-\rangle$ state is no longer a trapped state, since atoms in $|-\rangle$ can precess into $|+\rangle$, which is in turn coupled to $|e\rangle$ by g . Thus $\rho_{ee} \neq 0$ and there can be a force associated with the population in the $|-\rangle$ state. In fact, F can be dominated by the C_{dif} term. For example, this occurs if $\delta = 0$.

If both fields are traveling waves, then $\alpha_j = 0$ and $F = C_{sp}(\beta_1 + \beta_2)$, a purely spontaneous force. If the fields are counterpropagating, $F = \hbar(k_1 - k_2)g_1^2 g_2^2 \Delta^2 \Gamma / D$. Surprisingly, the direction of F is determined entirely by $(k_1 - k_2)$. The atom is not necessarily pushed in the direction of propagation of the stronger field or the field nearer resonance. If $|k_1| = |k_2|$, then $F = 0$ is independent of Δ , δ , g_1 , and g_2 . This result can be understood by noting that when one of the transitions (say $|a\rangle \rightarrow |e\rangle$) is much more strongly driven than the other ($|E_1| \gg |E_2|$), almost all of the population accumulates in the ground state of the weakly driven transition, $|b\rangle$.

Hence the $P_{ea} \rightarrow 0$ such that $P_{ea}\nabla E_1 = -P_{eb}\nabla E_2$ and $F = 0$. If g is increased while Δ is held fixed, then $C_{sp} \rightarrow 0$ since all the population will accumulate in $|-\rangle$. This is in striking contrast to F_{sp} for a TLA, which approaches $\hbar k \Gamma / 2$.

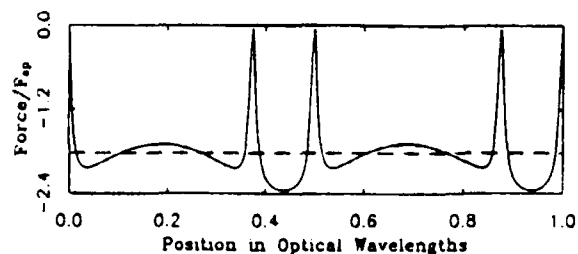


Fig. 2. Simulated force for $\delta = 0$, $\Delta = g_0/2 - 4\Gamma$, and $X = \pi/4$. $F_{sp} = \hbar \Gamma / \lambda_{opt}$. The dashed line is the spatially averaged force. Note that the force is completely rectified (unipolar). For other choices of parameters, the force is not completely rectified, and there are potential minima associated with the sharp features

population will accumulate in $|- \rangle$. This is in striking contrast to F_{sp} for a TLA, which approaches $\hbar k \Gamma / 2$.

Now consider the case where E_1 and E_2 are standing waves ($\beta_1 = 0 = \beta_2$) with equal maximum Rabi frequencies g_0 .

If $|k_1 - k_2| \ll |k_1 + k_2|$, then let $k = k_1$ and $k_2 x = (k_2 - k_1)x + k_1 x = x + kx$. Thus $g_1 = g_0 \cos(kx)$ and $g_2 = g_0 \cos(kx + x)$. Then

$$F = \frac{2\hbar k g_0^4}{D(x, x)} [\cos(x) + \cos(2kx + x)] (F_{dif} + F_{sum}), \quad (4)$$

where

$F_{sum} = 4\Delta^2 \delta \sin(2kx + x)$, $F_{dif} = -\Delta \sin(x) (g^2 - 2\Delta^2)$, and x is assumed constant over several λ_{opt} . Note that F can have a substantial nonzero average over λ_{opt} . The contribution to F from the out-of-phase component of \mathbf{P} , F_{dif} , is associated with $|- \rangle$ and has terms that do not change sign over λ_{opt} . For $\Delta^2 = g_0^2 \sin^2(x)/2$ this component is completely rectified. If $\delta = 0$, F is completely rectified (i.e., $|F|$ is positive definite¹⁴; see Fig. 2). The term associated with the real, in-phase components of \mathbf{P} , F_{sum} , is not completely rectified but can still have a nonzero spatial average over λ_{opt} . Thus both F_{dif} and F_{sum} have unbounded stimulated components that vary in space with a period $2/|k_1 - k_2|$.

It is possible to integrate Eq. (3) to form an expression for a pseudopotential that appears to become infinitely deep as $|k_1 - k_2| \rightarrow 0$. However, since F is approximately constant over a long distance, an atom will simply accelerate to a velocity for which these equations are no longer valid. In order to predict the motion of an atom accurately, the effects of nonconservative forces¹⁵⁻¹⁷ as well as force fluctuations due to the interaction with the vacuum field^{11,18} must be included.

Another remarkable feature of Eq. (3) is that F can have components that vary on a scale much shorter than λ_{opt} , even in the absence of saturation. The spacing between the features can be controlled by varying x . Although Eq. (3) does not predict any limit for the narrowness of the features in F , the motion of an atom may not necessarily be accurately predicted. Eventually, motion due to F will produce a velocity that is not consistent either with the zero-velocity approximation or the assumption that the internal state of the atom is in equilibrium at a particular point. We also note that for sufficiently low velocities the atom will have a large de Broglie wavelength, and a fully quantum-mechanical treatment of atomic coordinates will be needed. Still, the possibility of such narrow resonances in the force may merit further investigation.

In sum, we have shown that for a stationary atom¹⁹ a steady-state solution to the OBE's predicts that there can indeed be a finite force associated with the population in the antisymmetric ($|- \rangle$) ground state and that, moreover, this force component can dominate the total force on the atom.

This research was supported in part through Office of Naval Research grant ONR-N0014-91-J-1808 and Rome Laboratory contract F19628-89-K-0300. We are grateful to S. Ezekiel and AT&T Bell Laboratories.

REFERENCES

1. J. Javanainen, Phys. Rev. Lett. **64**, 519 (1990).
2. F. Mauri and E. Arimondo, in *Abstracts of 12th International Conference on Atomic Physics* (University Microfilms, Ann Arbor, Mich., 1990), p. IV 21.
3. S. Chang, B. M. Garraway, and V. G. Minogin, Opt. Commun. **77**, 19 (1991).
4. V. G. Minogin, M. A. Olshany, and S. U. Shulga, J. Opt. Soc. Am. B **6**, 2108 (1989).
5. N. P. Bigelow and M. G. Prentiss, Opt. Lett. **15**, 1479 (1991).
6. A. Aspect, E. Arimondo, R. Kaiser, N. Vansteenkiste, and C. Cohen-Tannoudji, Phys. Rev. Lett. **61**, 826 (1988).
7. M. S. Shahriar, P. R. Hemmer, N. P. Bigelow, and M. G. Prentiss, in *Quantum Electronics and Laser Science*, Vol. 11 of 1991 OSA Technical Digest Series (Optical Society of America, Washington, D.C., 1991), p. 118.
8. See, e.g., M. Sargent, M. Scully, and W. Lamb, eds., *Laser Physics* (Addison-Wesley, Reading, Mass., 1974), Chap. 7.
9. We note that a correspondence has been established between the dressed states and the normal modes of a coupled pendulum system. See P. R. Hemmer and M. G. Prentiss, J. Opt. Soc. Am. B **5**, 1613 (1988).
10. Note that D can depend on position, but it is always positive definite; consequently, the sign of F is determined entirely by the numerator.
11. J. P. Gordon and A. Ashkin, Phys. Rev. A **21**, 1606 (1980).
12. We note that p_{+e} contributes to both C_{dif} and C_{sum} , whereas p_{-e} contributes only to C_{dif} , and that it may be possible to obtain an increased appreciation of this correspondence by considering the analogy between the Raman system and a system of three-coupled pendulums, which is discussed in detail in Ref. 9.
13. H. J. Gray, R. M. Whitley, and C. R. Stroud, Jr., Opt. Lett. **3**, 218 (1978).
14. We note the introduction of the term rectified in the context of the TLA. See A. P. Kazantsev and I. V. Krasov, JETP Lett. **46**, 420 (1987); V. S. Voitskhovich, D. M. Danileiko, A. M. Negrijko, V. I. Romanenko, and I. P. Yatsenko, Zh. Tekh. Fiz. **58**, 1174 (1988); also recent TLA experiments of R. Grimm, Yu. B. Ovchinnikov, A. I. Sidorov, and V. S. Lethokov, Phys. Rev. Lett. **65**, 1415 (1990). See also Ref. 1.
15. A. Aspect, J. Dalibard, A. Heidmann, C. Solomon, and C. Cohen-Tannoudji, Phys. Rev. Lett. **57**, 1688 (1986).
16. J. Dalibard, C. Solomon, A. Aspect, E. Arimondo, R. Kaiser, N. Vansteenkiste, and C. Cohen-Tannoudji, in *Proceedings of Eleventh International Conference on Atomic Physics* (World Scientific, Singapore, 1989), p. 199.
17. S. Chu, D. S. Weiss, Y. Shevy, and P. J. Ungar, in *Proceedings of Eleventh International Conference on Atomic Physics* (World Scientific, Singapore, 1989), p. 636.
18. R. J. Cook, Phys. Rev. A **20**, 224 (1979).
19. We have calculated the first-order velocity dependence of F and find that the atomic motion can be strongly damped.

ROOM-TEMPERATURE OPTICAL NONLINEARITIES OF GaInAs/AlInAs AND GaAlInAs/AlInAs MULTIPLE QUANTUM WELLS AND INTEGRATED-MIRROR ETALONS AT 1.3 μm

C.C. Hsu, B.P. McGinnis, J.P. Sokoloff, G. Khitrova^{a)}, H.M. Gibbs, and N. Peyghambarian, Optical Sciences Center, University of Arizona
S.T. Johns and M.F. Krol, Surveillance & Photonics Directorate, Rome Laboratory

Published in Journal of Applied Physics, Vol. 70, No. 10, 15 November 1991

Abstract – The room-temperature nonlinear absorption spectra of a 40 Å GaInAs/AlInAs and a 90 Å GaAlInAs/AlInAs multiple quantum well (MQW) were measured near 1.3 μm using a pump and probe technique. Saturation carrier densities at the heavy-hole exciton peak were determined to be 1.2×10^{18} and $1.0 \times 10^{18} \text{ cm}^{-3}$ with carrier recovery times of $\sim 5 \text{ ns}$ and $\sim 750 \text{ ps}$ for the two samples, respectively. These measured saturation carrier densities are close to the reported values for GaAs/AlGaAs MQWS. Fabry-Perot etalons with integrated mirrors grown by molecular beam epitaxy with GaInAs/AlInAs MQWs as spacer layers were also fabricated as optical logic gate devices. We demonstrate a 125-ps recovery time for the etalon switching device at room temperature.

1. INTRODUCTION

Semiconductor materials have been studied extensively for potential applications in optoelectronic and all-optical devices.¹ Because GaInAs and its related materials are expected to have large optical nonlinearities in the wave-length region from 1.3 to 1.55 μm , their nonlinear optical properties are crucially important for designing opto-electronic devices in optical fiber communication systems. Previous studies have been made of optical nonlinearities in both GaInAs/AlInAs (Ref. 2) and GaInAs/InP (Refs. 3 and 4) multiple quantum wells (MQW) near 1.5 μm . Transient nonlinear absorption spectra of GaInAs/AlInAs near 1.3 μm at 10 K have been reported.^{5,6} An optical logic etalon of a GaInAs/InP MQW at 1.55 μm operating at 77 K has also been demonstrated with a 20:1 contrast and nanosecond recovery time.⁷ A room-temperature optically bistable device in a GaInAs/AlInAs MQW etalon at 1.5 μm was also demonstrated.⁸ However, there has been no report to date on the room-temperature optical nonlinearities of GaInAs/AlInAs and GaAlInAs/AlInAs MQWs and optical logic devices made from these materials at 1.3 μm . In this letter we report room-temperature measurements of the nonlinear absorption spectra, saturation carrier densities and carrier recovery times for both a 40-Å GaInAs/AlInAs and a 90-Å GaAlInAs/AlInAs MQW sample and demonstrate a high-speed, all integrated GaInAs/AlInAs optical logic Fabry-Perot etalon device at 1.3 μm .

^{a)} Present address: Physics Department, University of Toronto, Ontario, Canada.

2. EXPERIMENT

With modern crystal growth techniques such as molecular beam epitaxy (MBE), growth of high quality MQW structures with precise layer thickness and high uniformity is possible. MBE-grown Ga_{0.47}In_{0.53}As/Al_{0.48}In_{0.52}As, Ga_{0.376}Al_{0.094}In_{0.53}As/Al_{0.48}In_{0.52}As MQW structures and an integrated mirror Fabry-Perot etalon were used in this experiment. The detailed growth conditions of the samples were previously described.^{9,10} The GaInAs/AlInAs MQW consists of 100 periods of 40-Å GaInAs wells and 68-Å AlInAs barriers. The quaternary GaAlInAs/AlInAs MQW sample has 100 periods of 90-Å GaAlInAs wells and 69-Å AlInAs barriers. Both MQWs have heavy-hole exciton peaks near 1.3 μm at room temperature. In the ternary system, the transition energy of the exciton can be adjusted mainly by changing the quantum well thickness. For the quaternary system, both the well thickness and the Ga/Al ratio can be used to shift the exciton absorption peak. The latter affords the opportunity to tailor other parameters such as the carrier lifetime or exciton sharpness while maintaining the exciton at the same wavelength.⁹

The absorption spectra of both samples were examined in a pump-probe geometry. The 1.064- μm line from a Q-switched Nd:YAG laser with a 10-Hz repetition rate was used for the pump beam. The pump-beam frequency was far enough above the absorption band edge of all samples to efficiently generate electron and hole pairs. The probe was generated by difference frequency mixing of the 1.064 μm line of a YAG laser and the output of a tunable Rhodamine 6G dye laser in a LiIO₃ crystal. The tunable range of the infrared beam, from 1220 to 1350 nm, covered the band-edge region of all samples. The pump pulse and probe pulse were 10 and 4 ns in duration, respectively. The samples were mounted on a rotation stage which was adjusted for Brewster's angle to minimize Fabry-Perot oscillations in the absorption spectra. The pump and probe beams were overlapped on the sample in both space and time with spot diameters of 135 and 37 μm , respectively. The large pump beam eliminated diffusion of the carriers from the probed region. The polarization of the pump beam was orthogonal to that of the probe beam so that an analyzer could selectively block the pump

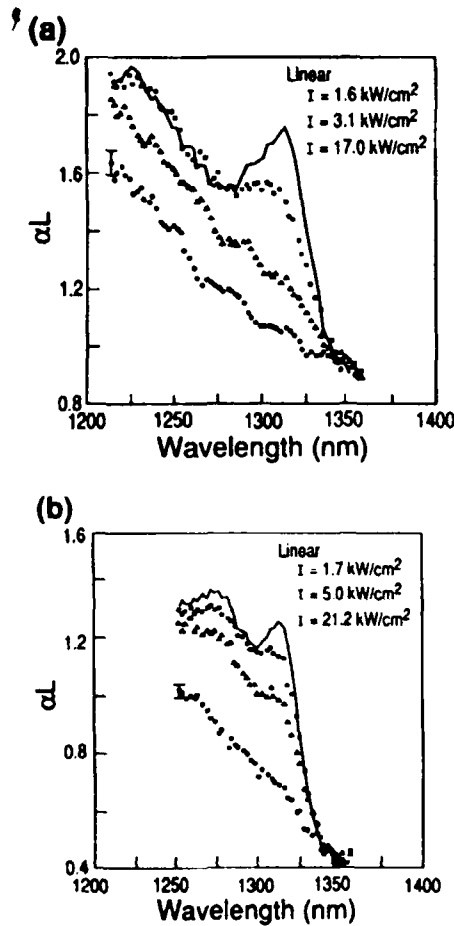


Fig. 1. (a) The absorption spectra of the 40-Å GaInAs/AlInAs MQW for various pump-beam intensities. (b) The absorption spectra of the 90-Å GaInAs/AlInAs MQW for various pump-beam intensities.

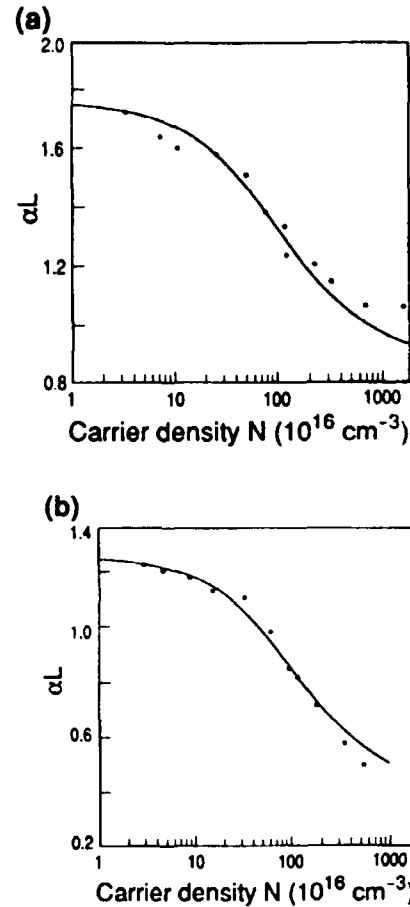


Fig. 2. (a) Optical absorption dependence of carriers density in the 40-Å GaInAs/AlInAs MQW. The black points are experimental data and the solid curve is the best fit of the experimental data. (b) Same as (a) but for the 90-Å GaInAs/AlInAs MQW.

beam. The probe beam was divided with one beam focused on a Ge detector as the reference signal and the other beam focused on the sample, then imaged onto another Ge detector which measured the transmitted signal. The reference and transmitted signals were averaged over 100 laser shots by a boxcar integrator. The relative transmission values for the samples were obtained from the ratios between the transmitted and the reference signals. The absolute transmission value for the samples was obtained from the ratio of the relative transmission with and without the sample.

The nonlinear absorption spectra measured at room temperature with pump intensities of 0, 1.6, 3.1, and 17.0 kW/cm² on the 40-Å GaInAs/AlInAs MQW are shown in Fig. 1 (a). The latter three pump-beam intensities correspond to photogenerated carrier densities of 6.4×10^{17} , 1.2×10^{18} , and 6.7×10^{18} cm⁻³ using the well-known rate equation. For this calculation, we used our measured electron-hole pair lifetime values τ and the reflection loss of pump beam at the sample surface was taken into account.

3. DISCUSSION

In the linear absorption spectrum of the 40-Å MQW, we observed well-resolved heavy-hole and light-hole excitonic resonances located at 1315 and 1225 nm, respectively. The half-width of the lowest exciton peak is about 14 meV.⁹ As shown in Fig. 1 (a), the exciton resonances bleach and broaden with increasing pump-beam intensities. Phase-space filling and exchange effects are believed to be the dominant nonlinear mechanisms for saturation of the excitons in MQWs.^{2,11} Note that the influence of Coulomb screening in quasi two-dimensional MQWs is relatively weak in comparison to the three-dimensional case.¹¹

Because the changes of absorption at the exciton peak depend on the pump-beam intensity only through photogenerated carriers, we computed the saturation carrier densities for these samples instead of the saturation intensities. The saturation carrier density at the heavy-hole exciton peak was determined by

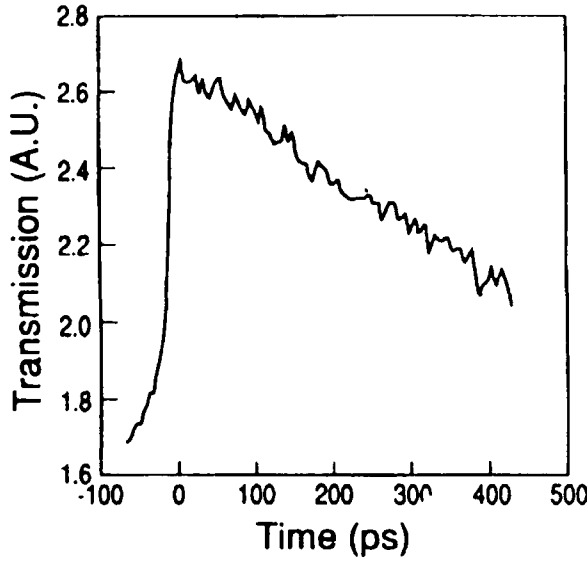


Fig. 3. The probe transmission as a function of the pump-probe time delay for the 90-Å GaAlInAs/AlInAs MQW.

the best fit of the experimental data to the following Lorentzian equation:

$$\alpha L(N) = \alpha_b L + \frac{\alpha_0}{1 + N/N_s} \quad (1)$$

where α_0 and α_b are the linear and background absorption coefficients at the heavy-hole exciton peak, respectively, L is the well thickness of the MQW and N_s is the saturation carrier density. As shown in Fig. 2(a), the optical absorption decreases as the carrier density increases. The solid curve is the best fit to the experimental data. The saturation carrier density, linear absorption ($\alpha_0 L$), and background absorption ($\alpha_b L$) were found to be $1.2 \times 10^{18} \text{ cm}^{-3}$, 0.88, and 0.88, respectively. The computed saturation carrier density for the GaInAs/AlInAs MQW is close to the reported values for GaAs/AlGaAs MQWs.¹²

Figure 1(b) shows the room temperature nonlinear absorption spectra of the GaAlInAs/AlInAs MQW sample for pump-beam intensities of 0, 1.7, 5.0, and 21.2 kW/cm². These pump-beam intensities generated carrier densities of 2.1×10^{17} , 6.2×10^{17} , and $2.6 \times 10^{18} \text{ cm}^{-3}$, respectively. Note that in Figs. 1(a) and 1(b), the residual background absorption of $\alpha_b \sim 0.8$ and 0.4, respectively, at energies below the exciton originates from the reflection and scattering from the sample surfaces. The linear absorption spectrum of the sample also shows two well resolved exciton peaks. The half-width of the lowest exciton peak is about 12 meV.⁹ The exciton peaks of the quaternary MQW are less pronounced than those of the ternary, presumably because 90-Å wells have less confinement than 40-Å wells.⁹ As in the GaInAs/AlInAs MQW case, the presence of

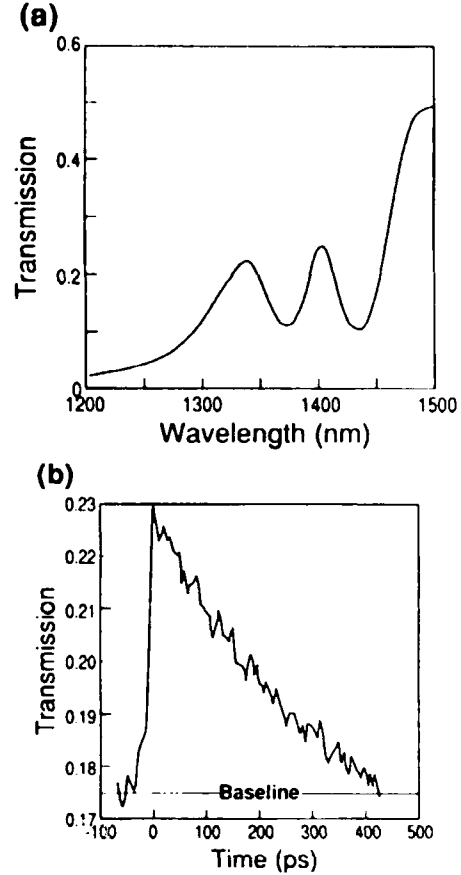


Fig. 4. Transmission of the MBE-grown integrated GaInAs/AlInAs etalon device. (b) Measured switching time of the room-temperature optical logic gate of (a).

increasing pump-beam intensity bleaches exciton peaks of GaAlInAs/AlInAs MQW as a result of phase-space filling and exchange effects. The saturation carrier density, linear absorption, and background absorption were determined to be $1.0 \times 10^{18} \text{ cm}^{-3}$, 0.84, and 0.43, respectively. The computed saturation carrier density for the GaAlInAs/AlInAs MQW is close to the GaInAs/AlInAs MQW. The dependence of optical absorption on the carrier density in the 90-Å GaAlInAs/AlInAs MQW is shown in Fig. 2(b).

The carrier recovery dynamics of the samples were measured with a picosecond pump-probe setup. The experiments were performed with a pulse compressed mode-locked Nd:YAG laser at a 100-MHz repetition rate. Both pump and probe beams had a 2-ps duration at a wavelength of 1319 nm which coincides with the heavy-hole exciton peak. The pump and probe beams were overlapped on the samples with a 26 μm diameter. The pump beam was polarized orthogonal to the probe beam. The time delay between the pump beam and probe beam was varied from -50 to 450 ps. Figure 3 shows the probe transmission as a function of the pump probe delay for a pumping power of 20 mW of the 90-Å GaAlInAs/AlInAs MQW. This

pumping power corresponds to a photogenerated carrier density of $1.7 \times 10^{18} \text{ cm}^{-3}$. The exponential fit of the data resulted in a 750-ps lifetime for the 90-Å MQW. The lifetime for the 40-Å ternary MQW is longer with a value of $\approx 5 \text{ ns}$. The lifetime for the quaternary MQW is shorter than that for the ternary MQW, probably due to the presence of aluminum in the quaternary MQW, which may affect the carrier lifetime.¹⁰ To check the effects of lateral diffusion on the absorption recovery time, the diffusion equation¹³ was used to determine changes in the average carrier density. In this calculation, the ambipolar diffusion constant $D \approx 15 \text{ cm}^2/\text{s}$ was determined by carrier mobilities of $10\,500 \text{ cm}^2/\text{Vs}$ for electrons and $300 \text{ cm}^2/\text{Vs}$ for holes.¹⁴ The diffusion calculation indicates that 500 ps after excitation, the average carrier density decreases less than 1% for a 26- μm diameter spot. Thus, the small lateral diffusion of the carrier does not play an important role in the pico-second recovery of the absorption changes.

We also designed and grew nonlinear Fabry-Perot etalons with MBE-grown integrated mirrors for room-temperature operation at 1.3 μm . The etalons consist of two integrated mirrors, each with 12 pairs of GaAlInAs/AlInAs quarter-wave layers and a spacer of 108 periods of GaInAs/AlInAs MQWs consisting of 35-Å wells and 58-Å barriers, grown lattice-matched on an InP substrate.¹⁰ The etalon transmission spectrum is shown in Fig. 4(a). Non-linear switching on and off times of the devices were measured using the 2-ps 1319-nm pulses. As shown in Fig. 4(b), the GaInAs/AlInAs Fabry-Perot etalon has a 125-ps recovery time, with a fast switch-on speed. Due to the limited translation from the positioning equipment available, we could not measure the delay beyond 500 ps. It is probable that the transmission drops below the baseline as a result of heating of the sample (which shifts the transmission fringe to a longer wavelength) by the high repetition rate pulses laser in our experiment. The faster recovery of the etalon compared with the MQWs may be associated with poorer quality MQWs in the etalon grown on top of 12 pairs of quarter-wave layers.

4. CONCLUSION

In conclusion, we have measured optical nonlinearities and recovery time of carriers at 1.3 μm for two MQW structures of

epitaxially-grown GaAlInAs/AlInAs and GaInAs/AlInAs at room temperature. Nonlinear integrated Fabry-Perot etalon logic gates were fabricated and a high-speed switching time was demonstrated. These devices are potentially useful for development of multi-giga-bit optical time-division demultiplexed interconnection system at 1.3 μm where ultrafast optical processing elements are needed.

5. ACKNOWLEDGMENTS

The Arizona group would like to acknowledge support from Rome Laboratory, Photonics Center, AFOSR, ARO, NSF Lightwave Technology, and the Optical Circuitry Co-operative of the University of Arizona. C. C. Hsu acknowledges fruitful discussions with S. G. Lee and the preparation of samples by C. L. Chuang. S.T.J. gratefully thanks E. Toughlian for useful discussions.

6. REFERENCES

1. H. M. Gibbs, G. Khitrova, and N. Peyghambarian, *Nonlinear Photonics* (Springer, Berlin, 1990).
2. J. S. Weiner, D. B. Pearson, D. A. B. Miller, and D. S. Chemla, D. Sivco, and A. Y. Cho, *Appl. Phys. Lett.* **49**, 531 (1986).
3. A. M. Fox, A. C. Maciel, M. G. Schorthose, J. E. Ryan, M. D. Scott, J. I. Davies, and J. R. Ruffat, *Appl. Phys. Lett.* **51**, 30 (1987).
4. M. A. Fisher, *J. Appl. Phys.* **67**, 543 (1990).
5. T. Elsaesser, R. J. Bauerle, W. Kaiser, H. Lobentanzer, W. Stolz, and K. Ploog, *Appl. Phys. Lett.* **54**, 256 (1989).
6. H. Lobentanzer, W. Stolz, K. Ploog, R. J. Bauerle, and T. Elsaesser, *Solid State Electron.* **32**, 1875 (1989).
7. K. Tai, J. L. Jewell, W. T. Tsang, H. Temkin, M. Panish, and Y. Tzu, *Appl. Phys. Lett.* **50**, 796 (1987).
8. H. Kawaguchi and Y. Kawamura, *Electron. Lett.* **23**, 1013 (1987).
9. G. Khitrova, T. Iwabuchi, and H. M. Gibbs, *Superlatt. and Microstruct.* **8**, 439 (1990).
10. G. Khitrova, T. Iwabuchi, C. L. Chang, T. Yoon, R. Pon, and H. M. Gibbs, C'MH2, CLEO '91 (Optical Society of American, Washington, DC) 1991 Technical Digest Series **10**, 54 (1991).
11. S. Schmitt-Rink, D. S. Chemla, and D. A. B. Miller, *Phys. Rev. B* **32**, 601 (1985).
12. S. H. Park, J. E. Morhange, A. D. Jeffery, R. A. Morgan, A. Chavez-Pirson, H. M. Gibbs, S. W. Koch, N. Peyghambarian, M. Derstine, A. C. Gossard, J. H. English, and W. Weigmann, *Appl. Phys. Lett.* **52**, 1201 (1988).
13. C. Kittel, *Introduction to Solid State Physics* (Wiley, New York, 1966).
14. *GaInAsP Alloy Semiconductors*, edited by T. P. Pearsall (Wiley, New York, 1982).

SELF-PUMPED OPTICAL PHASE CONJUGATION WITH A SODIUM RAMAN LASER

J. Donoghue And M. Cronin-Golomb, Electro-optics Technology Center, Tufts University
J.S. Kane and P.R. Hemmer, Electromagnetics & Reliability Directorate, Rome Laboratory

Published in Optics Letters, Vol. 16, No. 17, 1 September 1991

Abstract - We report self-pumped optical phase conjugation in which the pumps are self-induced as standing waves in a linear Raman laser. Self-pumped reflectivities approaching 5% are obtained for input intensities of 20 W/cm^2 . This low optical input intensity combined with predicted sub-microsecond response times suggests that the resonant Raman interaction may provide the basis for a promising new class of nonlinear-optical material.

Recently there has been increased interest in the use of resonant atomic systems for performing optical wave-front conjugation.¹ This is because resonant atomic systems are inherently fast. However, resonant systems tend to have lower efficiency and greater optical power requirements than photorefractive crystals such as BaTiO_3 . To trade a portion of the speed for higher efficiency and much lower optical power requirements, we propose the use of a three-level atomic system in the resonance Raman configuration. This system is expected to have advantages over conventional two-level atomic systems because it is possible to induce total transparency² while still maintaining gratinglike sensitivity³ to the relative phases of the two exciting fields. To demonstrate the feasibility of resonance Raman systems for nonlinear-optics applications, we have performed self-pumped optical phase conjugation, with pumps self-induced, in a sodium-vapor Raman laser.

The sodium Raman laser was first demonstrated by Kumar and Shapiro⁴ with a ring laser geometry. In this demonstration, Raman-shifted unidirectional lasing was observed at pump powers of less than 40 W/cm^2 . We adapted this Raman ring laser to a standing-wave configuration similar to that used by Gaeta *et al.*⁵ in their initial demonstration of self-pumped phase conjugation using two-level interactions in sodium vapor.

A schematic of our experiment is shown in Fig. 1. The sodium cell is a heat-pipe oven of 13-cm active length, with a 6.4-mm-diameter optical aperture. The Raman laser cavity has a length of 2.6 m with a 2-m focal-length lens inserted to make the resonator stable. Both lenses and cell windows are multilayer antireflection coated to reduce cavity losses. The measured cavity loss is 6% per round trip (including the loss from the 98% Raman laser output coupling mirror shown in the figure). A 2-m lens is also placed in the pump-beam path to limit divergence. The pump laser beam has a 1-mm FWHM spot size at the sodium cell, and its angle of incidence relative to the cavity optic axis is typically 0.2° . Standard operating condi-

tions are 10 mTorr of He buffer gas pressure and a high enough temperature to obtain approximately 50% absorption at resonance for the input pump power of 240 mW.⁶

To evaluate system performance, we simultaneously monitor four beams as shown in Fig. 1. The measured optical power in these four beams as a function of pump laser detuning to the blue of the sodium D_1 line is shown in Fig. 2. From top to bottom, the data traces in this figure are the transmitted pump beam, the diffracted beam (discussed below), the Raman laser output beam, and the phase-conjugate beam. Optical powers in all four beams are expressed as a percentage of the input pump power of 240 mW.

Examination of Fig. 2 shows that a peak conjugate reflectivity of nearly 5% occurs at approximately 2 GHz from resonance.⁷ Again, these data were obtained for an input pump power of 240 mW, which translates to a peak intensity of approximately 20 W/cm^2 , assuming a Gaussian laser beam of 1-mm FWHM spot size. Of course, the exact intensity inside the sodium cell is not known owing to the competing effects of resonant absorption and mild self-focusing.

Further examination of Fig. 2 shows a matching comblike structure in optical power versus laser frequency in both the conjugate and Raman laser beams. This comblike structure, which was first observed by Kumar and Shapiro,⁴ is attributed to the fact that the Raman gain curve is more narrow band than the cavity free spectral range of 52 MHz. When the cavity output is beat against the pump beam, a single 3-MHz-wide beat note is observed near 1772 MHz. This single narrow beat note at the Raman frequency⁸ is the characteristic signature of a Raman laser in sodium. The conjugate beam in our experiment was found to be doubly Raman shifted from the pump frequency in the same sense as the Raman laser beam (farther from resonance).

Finally, for a linearly polarized pump beam, the Raman laser beam polarization was predominantly linear but perpendicular to the pump, whereas the conjugate polarization was linear and parallel to the pump. This is expected for a Raman interaction in sodium owing to the selection rules for the dipole transitions.

The circulating optical power in the Raman resonator (Fig. 2, third trace) is as much as twice the input pump power. Since the measured spot size of the Raman laser output beam is the same as that of the input pump (1 mm FWHM), the intensity of the

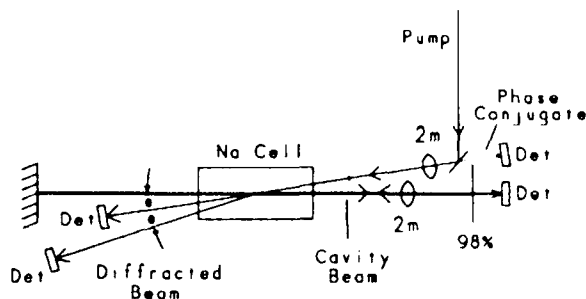


Fig. 1. Schematic diagram of the experimental Det's, detectors.

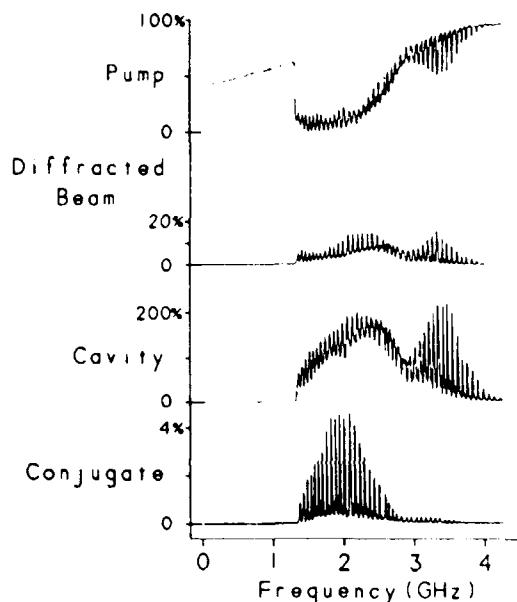


Fig. 2. Data showing optical power versus pump laser (blue) detuning from D_1 in each of four monitored laser beams. From top to bottom the traces are the transmitted pump beam, the diffracted beam, the Raman laser output beam, and the phase-conjugate beam. The traces were obtained by scanning the stabilized pump frequency (5-MHz linewidth).

intracavity oscillation is actually twice that of the input pump. This illustrates the high efficiency of the Raman interaction at these low pump intensities. Also of interest is the transmitted pump-beam power (Fig. 2, top trace). In the absence of lasing, the resonance pump absorption is approximately 55%. However, when lasing and phase conjugation commence, the pump absorption abruptly increases to nearly 100%. This indicates that the Raman laser transfers energy out of the pump at least as efficiently as does resonant absorption. Finally, the optical power in the diffracted beam (see Fig. 1) is shown in the second trace of Fig. 2. As can be seen, this diffracted beam contains as much as 20% of the input pump power and therefore acts as a loss for the phase conjugate process. This diffracted beam has been observed only in the forward direction. Its frequency is Raman shifted in the opposite sense to that of the Raman laser and is therefore consistent with first order Bragg diffraction

from a moving grating. Its intensity-versus-frequency characteristics most closely resemble those of the Raman laser.

The mechanism responsible for the Raman laser, as proposed by Kumar and Shapiro,⁴ is illustrated in Fig. 3. In this figure the pump beam interacts simultaneously with both ground states of the three-level system and generates two additional laser fields at the frequencies indicated. One of these is Raman shifted farther from resonance than the pump and produces the Raman laser output. The other is Raman shifted closer to resonance and has the same frequency as the diffracted beam (Figs. 1 and 2). Figure 3 suggests that the Raman gain process is the result of a nondegenerate four-wave mixing process wherein the pump beam provides two of the waves. This has yet to be shown theoretically. If the above mechanism is correct, the phase-conjugate output would be viewed as the result of a nondegenerate six-wave mixing process (not shown) wherein the pump and Raman laser beams provide four of the six fields.

One of the major advantages of being able to perform self-pumped optical phase conjugation with an unfocused pump

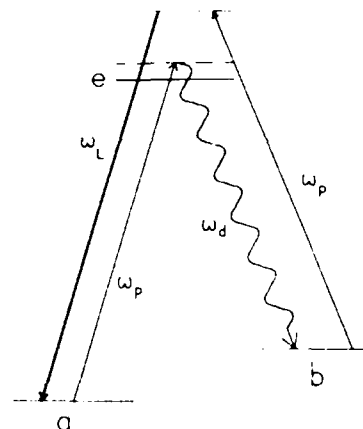


Fig. 3. Level diagram illustrating proposed mechanism for the Raman laser (from Ref. 4).



Fig. 4. Conjugate image showing the numeral 3, which denotes the start of series 3 on an Air Force resolution chart (8 lines/mm).

beam is the ability to conjugate images easily. Self-pumped image conjugation at these low optical intensities has been previously demonstrated only in photorefractives. To demonstrate self-pumped image conjugation in our system, we imaged a positive U.S. Air Force resolution chart into the sodium cell. This was accomplished using a 40-cm focal-length lens and a $4f$ object to image distance. A positive rather than a negative resolution chart was used to keep the total input laser power above the 100-mW threshold needed for the production of a conjugate beam. The conjugate image produced by this system is shown in Fig. 4. The numeral 3 marks the start of series 3 on the bar chart, which has a resolution of 8 lines/mm. The conjugate reflectivity was only approximately 0.5% for the image shown in the figure. To obtain higher reflectivity, it was necessary to tune closer to resonance. However, in this case, resolution was degraded because of the absorption of higher diffraction orders in the 13-cm-long cell. Mild aberrators were also inserted in the pump-beam path after the input image. The resulting conjugate output image (not shown) was free of aberrations, but the intensity envelope was no longer a smooth Gaussian. Here it must be emphasized that the data in Fig. 4 are only preliminary. The experimental setup was not specifically designed to produce images. In fact, some of the higher diffraction orders actually missed the input mirror. Nonetheless it is significant that an image can be conjugated at all with a self-pumped geometry in a strongly absorbing medium at such low intensities.

In summary, we have achieved a phase-conjugate reflectivity of nearly 5% using a self-pumped Raman laser in sodium vapor. This relatively high reflectivity was accomplished with only 20 W/cm² of input pump intensity. This represents a factor-of-50 reduction in pump intensity for comparable reflectivity in previous sodium vapor experiments.⁵ Moreover, the low-intensity

threshold allowed us to conjugate images easily. Thus we have demonstrated the potential of the resonant Raman system as the basis for a new class of high-speed nonlinear-optical material. In addition, we expect similar reductions in laser power requirements for non-self-pumped geometries wherein the pump beams are generated by an acousto-optic or electro-optic modulator. Finally, the resonant Raman processes in Li, Rb, or Cs vapors can be excited with semiconductor lasers for which the low laser power requirements are especially important. In fact, non-self-pumped schemes would be much simpler for semiconductor laser excitation because the Raman-shifted frequencies needed could be easily produced by high-speed modulation of the lasers.

The authors acknowledge the invaluable contribution of John Kierstead of Parke Mathematical Laboratories to this research. This research was performed at the Rome Laboratory electro-optics facility at Hanscom Air Force Base. The Tufts University portion was funded by Rome Laboratory contract F19628-88-K-0043.

REFERENCES

1. P. F. Liao, O. M. Bloom, and N. P. Economou, *Appl. Phys. Lett.* **32**, 813 (1978).
2. H. R. Gray, R. M. Whitley, and C. R. Stroud, Jr., *Opt. Lett.* **3**, 218 (1978).
3. M. S. Shahriar and R. R. Hemmer, *Phys. Rev. Lett.* **15**, 1865 (1990).
4. P. Kumar and J. H. Shapiro, *Opt. Lett.* **10**, 226 (1985).
5. C. J. Gaeta, J. F. Lam, and R. C. Lind, *Opt. Lett.* **14**, 245 (1989).
6. The exact temperature inside a heat-pipe cell depends on the position. In our experiments the temperature of the outer surface of the cell was 360° C near the cell midpoint.
7. For these data, resonance is defined as the laser frequency at which minimum absorption is obtained in a Doppler-broadened reference cell.
8. P. Kumar and S. T. Ho, *J. Opt. Soc. Am. A* **2**(13), 113 (1985).

OPTICAL FINGERPRINT IDENTIFICATION BY BINARY TRANSFORM CORRELATION

Kenneth H. Fielding (member SPIE), Joseph L. Horner (fellow SPIE), and Charles K. Makekau, Electromagnetics & Reliability Directorate, Rome Laboratory

Published in Optical Engineering, Vol. 30, No. 12, December, 1991

Abstract - We describe an optical fingerprint identification system that optically reads a latent fingerprint for correlation using a binary joint transform correlator. The fingerprint is read using the total internal reflection property of a prism. The system was built, tested, and the experimental results are presented.

1. INTRODUCTION

The purpose of research efforts in optical signal processing is to develop techniques leading to systems that optically process data at very high rates of speed, preferably with smaller volume and low power requirements. Image processing systems based on the joint Fourier transform correlator¹ (JTC) have been shown to perform well.²⁻⁵ Binarizing the joint power spectrum of the JTC provides significantly higher peak intensity, larger peak-to-secondary ratios, delta-like correlations, and better cross-correlation discrimination.⁶ We present a system that uses a prism operating in the total internal reflection mode to generate optically a high-contrast image of a fingerprint^{7,8} that is used as an input to the binary JTC (BJTC) for comparison with a data base. Our system is compact, operates in near real time, and has good discrimination capability. This system is ideally suited for secure entry systems to identify individuals for access to a restricted area or for mobile and remote surveillance by law enforcement agencies.

2. THEORY

2.1. Prism: total internal reflection

High-contrast images of a fingerprint can be read optically using a standard 90-deg prism where the read beam is directed at the critical angle.^{7,8} When the laser beam enters one side of a 90-deg prism and strikes the hypotenuse at an angle given by

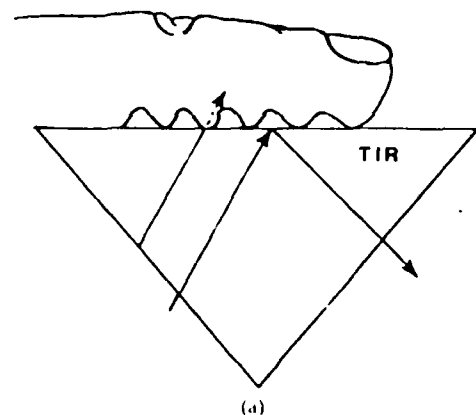
$$\theta_c = \arcsin(n_t/n_i), \quad (1)$$

the transmitted light will travel tangential to the glass medium interface. Incident angles beyond θ_c will cause the light to be totally internally reflected in the prism and pass out the opposing side. This assumes $n_i > n_t$ where n_i and n_t are the indices of refraction of the prism glass and external medium.

Placement of a finger on the hypotenuse side of the prism, shown in Fig. 1(a), changes the boundary conditions such that where the ridges of the fingerprint make contact with the glass, the natural oils of the skin make a good optical bond and the light wave is transmitted and largely attenuated by the skin. Where the ridges do not make contact, the light is totally internally reflected by the interface and captured by the input camera. An example of the captured print is shown in Fig. 1(b). Figure 1(c) shows the print binarized around its mean value. This print is sent to the BJTC for comparison with a data base of fingerprints to determine the individual's identity.

2.2. Binary joint transform correlator

For the JTC architecture shown in Fig. 2, the reference and target images are placed on their respective halves of the input spatial light modulator (SLM) and are denoted by $r(x + x_0, y)$ and $s(x - x_0, y)$. The Fourier transform of this input, called the joint power spectrum (JPS), is captured by a square law detector



(a)



(b)



(c)

Fig. 1. (a) An exaggerated view of the finger in contact with the prism, (b) typical fingerprint image, and (c) the fingerprint binarized around its mean value.

and Fourier transformed. The resulting correlation signal is given by

$$h(x_1, y_1) = R_{R,R}(x_1, y_1) + R_{S,S}(x_1, y_1) + R_{R,S}(x_1 - 2x_0, y_1) + R_{S,R}(x_1 + 2x_0, y_1) \quad (2)$$

The first two terms are on-axis autocorrelation terms, the correlation of reference and target signals with themselves, and the third and fourth terms are the correlations of the reference with the target.

Javidi⁶ was the first to binarize the JPS and formalize the k 'th law nonlinearity, revealing an interesting family of correlation types varying in sensitivity.⁹ Although our work is performed using a binary SLM, the full potential of the fingerprint correlator should probably be realized by means of a gray-scale device. By applying a nonlinear operation on JPS and following the theoretical development of Ref. (9), we find that the output field of the nonlinear system is made up of harmonics with the first term containing the correct phase information and largest intensity. The general equation for this first harmonic is given by⁹

$$g_{1k}(E) = \frac{2\Gamma(k+1) [R(\alpha, \beta)S(\alpha, \beta)]^k}{\Gamma[1 - (1 - k/2)]\Gamma[1 + (1 + k/2)]} + \phi_s(\alpha, \beta) - \phi_R(\alpha, \beta) \quad (3)$$

To understand the nonlinear process better, let us vary k and compare the field in Eq. (3) to the field exiting the filter of a frequency plane correlator.^{9,10} Assuming the target and reference to be identical and letting $k = 1$, Eq. (3) reduces to the field expected to leave the Fourier plane of a frequency plane correlator employing a classical matched filter. If $k = 0.5$ the field is similar to a phase-only filter based correlator; if $k = 0$, the hardclip binarization we use here, the analogy is to the inverse filter correlator since all amplitude information of both the input and reference signals has been eliminated. These filters are successively more sensitive to input object distortions, so by vary-

ing the nonlinearity k , the sensitivity of the system to target image distortions can be changed. We feel this concept of varying the sensitivity is extremely important in this system. Comparison of images at either extreme of the scale presented here is probably not ideal. If $k = 1$, the system is likely to be fairly insensitive and false alarms will occur, while if $k = 0$ the system will be too sensitive, requiring the target print to be extremely similar to the reference for correct identification. In the next section, we describe the experimental results derived from comparing fingerprints from several individuals. We have successfully identified individuals using a system employing a binary SLM, encouraging us to pursue this research with a gray-scale device.

3. EXPERIMENTAL METHOD AND RESULTS

The compact optical BJTC system is shown in Fig. 2. A 10-mW He-Ne laser is the source and the SLM used is the Semetex 128 x 128 binary electrically addressed device. A dc block is used in the Fourier plane to capture the JPS more accurately.¹⁰ We have previously shown that the correlation peak intensity can increase by a factor of 2 using the dc block. A comparison of the fingerprints of five individuals is done to evaluate the effectiveness of this system. Two distinct fingerprints from the right-hand index finger of each individual are obtained. Each print is separately frame-grabbed after cleaning the prism surface and stored in 128 x 128 binary data files. Each fingerprint is compared with all other fingerprints in the data base. The two fingerprint images to be compared are separately binarized around their respective average value and reduced to 64 x 64 images that are placed together on the SLM. The JPS is captured by a CCD camera and binarized around its average value. The binarized JPS is displayed on the SLM, and the resulting correlation observed.

Table 1 shows the results; each entry F1 through F5 represents the two distinct fingerprints taken from each test individual. A plus sign indicates a proper identification while a minus sign indicates a correct "no match" response. The indication was simply the presence or lack of a clear and distinguishable

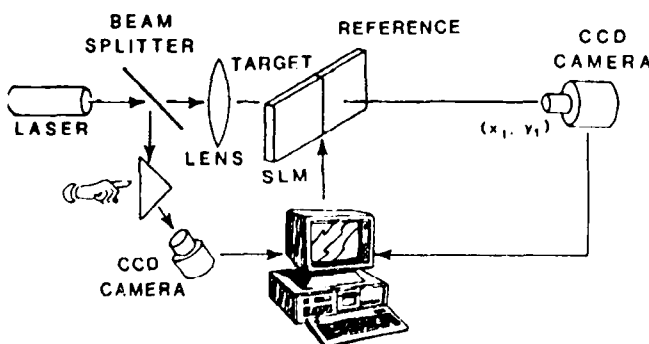


Fig. 2 Compact BJTC correlator configuration.

Table 1 Fingerprint comparison results. Entries F1 through F5 represent the two fingerprints obtained from each test individual. No false alarms were observed during these trials.

Fingerprint	F1A	F2A	F3A	F4A	F5A
F1B	+	-	-	-	-
F2B	-	+	-	-	-
F3B	-	-	+	-	-
F4B	-	-	-	+	-
F5B	-	-	-	-	+



Fig. 3 Plexiglass fingerguide used to assist individuals in placing their finger on the prism in nearly the same angular orientation.

correlation peak. In our limited trials, we had no false alarms. We should mention that a guide was fashioned on the prism to help the individuals place their finger in nearly the same angular orientation for each measurement. A guide, such as the one shown in Fig. 3, is essential when dealing with the sensitive BJTC.

Figure 4(a) shows the binarized fingerprints of an individual placed on the SLM. The print on the left is the stored reference while the fingerprint on the right is optically read and fed into the system. The binarized JPS of this input is shown in Fig. 4(b) with the corresponding correlation shown in 4(c). The correlation nearest the dc block are from the zeroth order while the outside correlations are from the first replicated orders. The peak-to-secondary ratio of the correlation is 3-to-1 while the signal-to noise ratio (SNR) is 27 using the metric¹⁰

$$SNR = \frac{C_0}{N_{rms}} \quad (4)$$

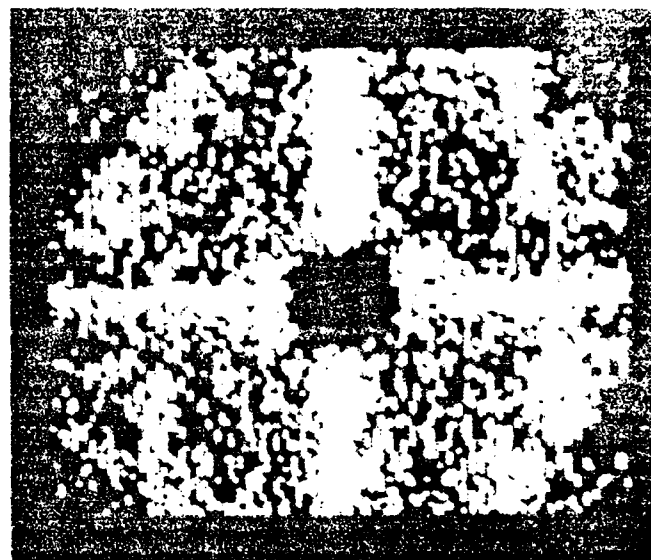
where C_0 and N_{rms} are the peak height and rms of the noise in the correlation plane whose mean has been subtracted. To simplify the calculation, we considered all points except the correlation peak as noise. The typical peak is only a few pixels wide at its base so counting these points as noise does not appreciably affect the calculation.

Figure 5(a) shows the binarized fingerprints of two different individuals displayed on the SLM. Figure 5(b) shows the resulting cross correlation pattern with energy distributed in the correlation plane with no discernible peak observed. The experimental conditions for this response are the same as Fig. 4(c). The response in Fig. 5(b) is representative of all cross-correlations we experimentally observed.

In attempting to reduce the sensitivity of the BJTC we tried a new approach. We applied a k 'th law nonlinearity on the JPS



(a)



(b)



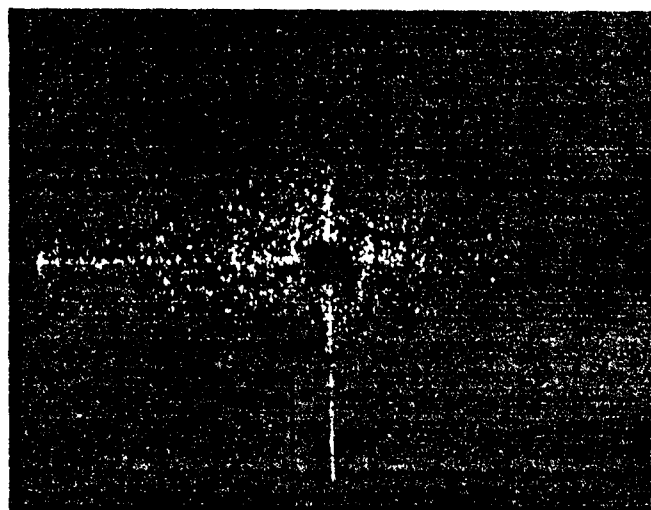
(c)

Fig. 4 (a) Binarized reference and target print of the same individual placed on the SLM, (b) the joint power spectrum binarized around the mean value, and (c) the resulting correlations

before binarizing. Raising the JPS to powers greater than unity should accentuate the lower, more intense, spatial frequencies while suppressing higher ones yielding less sensitivity in the correlation plane. Computer simulations showed a peak in the SNR as k was varied, but it was only improved by a few percent. Further investigation of this approach is under way.



(a)



(b)

Fig. 5. (a) Binarized fingerprints of two individuals displayed on the SLM and (b) correlation response typical of all cross-correlations.

4. CONCLUSIONS

We have demonstrated experimentally a simple system that optically reads a fingerprint and optically compares it with a data base for identification purposes. We have combined the previously demonstrated method of reading the fingerprint with a prism with the binary JTC technique for correlating reference

and target images. The hybrid optical/digital system uses a PC to store the reference data base and control the electrically addressed SLM. This system operates well using the binary SLM and we had no false alarms in our trials. Using a gray-scale SLM would unlock the full potential of this system permitting the sensitivity of this system to be varied to enhance performance.

5. REFERENCES

1. C. S. Weaver and J. W. Goodman, "A technique for optically convolving two functions," *Appl. Opt.* **5**, 1248 (1966).
2. F. T. S. Yu, S. Jutamulia, T. W. Lin, and D. A. Gregory, "Adaptive real-time pattern recognition using a liquid crystal TV based joint transform correlator," *Appl. Opt.* **26**, 1370 (1984).
3. J. Florence, "Joint-transform correlator systems using deformable-mirror spatial light modulators," *Opt. Lett.* **14**, 341 (1989).
4. B. Javidi and J. L. Homer, "Multifunction nonlinear signal processor: deconvolution and correlation," *Opt. Eng.* **28**(8), 837-843 (1989).
5. E. D. Tam, F. T. S. Yu, D. A. Gregory, and R. D. Juday, "Autonomous real-time object tracking with an adaptive joint transform correlator," *Opt. Eng.* **29**(4), 314-320 (1990).
6. B. Javidi and C. Kuo, "Joint transform image correlation using a binary spatial light modulator at the Fourier plane," *Appl. Opt.* **27**, 663 (1988).
7. A. Shimizu and M. Hase, "Entry method of fingerprint image using prism," *Trans. Inst. Electronic Comm. Engineers Japan, Part D*, **J67D**(5), 627 (1984).
8. L. A. Gerhardt, J. B. Attali, D. H. Crockett, and A. M. Presler, "Fingerprint imagery using frustrated total internal reflection," in *Proc. 1986 International Carnahan Conference on Security Technology*, 251 (1986).
9. B. Javidi, "Nonlinear joint power spectrum based optical correlation," *Appl. Opt.* **28**, 2358 (1989).
10. K. H. Fielding and J. L. Homer, "1-f binary joint transform correlator," *Opt. Eng.* **29**(9), 1081-1087 (1990).

ELECTRO-OPTIC MODE-DISPLACEMENT SILICON LIGHT MODULATOR

Thomas Pimat and Lionel Friedman, Department of Electrical Engineering, Worcester Polytechnic Institute
Richard A. Soref, Electromagnetics & Reliability Directorate, Rome Laboratory

Published in Journal of Applied Physics, Vol. 70, No. 6, 15 September 1991

Abstract - A new type of guided-wave electro-optical intensity modulator is proposed and analyzed. The waveguide consists of an N-type Si core layer on a P-type Si substrate. Forward bias on the N⁺-N-P-P⁺ diode decreases the refractive index of the core and displaces the fundamental guided mode downward into the substrate. However, the mode is not extinguished because the substrate is bounded by a P⁺ contact. A spatial filter at the output converts the mode displacement into optical intensity modulation. A Poisson and continuity equation solver and multilayer waveguide simulation were used to obtain numerical estimates of mode displacement in a realistic structure.

1. INTRODUCTION

It has been established that elemental silicon can be used for optical waveguiding at the optical communication wavelength of 1.3 μm .^{1,2} Several active devices have been proposed as light modulators. These have generally been of two kinds: phase and amplitude modulators. In the former, a large change in phase ideally occurs for a minimal increase in attenuation. When used with an interferometer or coupler, this can provide amplitude modulation or optical switching. For the amplitude modulator, a voltage-controlled free-carrier absorption is used.

The present paper concerns a different means of controlling the optical mode. The original idea was that of the mode-extinction modulator. Here, an optical mode is weakly confined by an adjacent substrate whose index of refraction is slightly less than that of the "core"-guided wave region. If charge injection is mainly into the guided region, the core-substrate index difference may be reduced sufficiently by the plasma dispersion effect that the mode is no longer confined but radiates into the substrate. However, for the specific device structure investigated below, mode extinction does not strictly occur under conditions of high injection. Rather, the mode is displaced towards the substrate such that a significant loss of intensity is seen for propagation in the core. Hence this device is called the mode-displacement modulator.

2. DEVICE STRUCTURE AT EQUILIBRIUM

The all-silicon device geometry is shown in the perspective view of Fig. 1 (a) and the cross-section end view of Fig. 1 (b). An ohmic contact at voltage V_2 is in contact with a 1- μm N⁺ layer at $2 \times 10^{18} \text{ cm}^{-3}$. This is followed by a 5- μm N layer doped to $3.5 \times 10^{17} \text{ cm}^{-3}$ in the ridge geometry shown, then a

34- μm P layer at $6 \times 10^{17} \text{ cm}^{-3}$ is followed by a 4- μm P⁺ layer at $4 \times 10^{18} \text{ cm}^{-3}$ and a lower contact maintained at voltage $V_1 = 0$.

At equilibrium ($V_1 = V_2 = 0$), the index of refraction and absorption coefficient of crystalline silicon at 1.3 μm are given by the free-carrier plasma relations

$$n(1.3) = n_0 - 6.2 \times 10^{-22} (\text{cm}^3) N - 6.0$$

$$\times 10^{-18} (\text{cm}^2) P^{0.8},$$

$$\alpha(1.3, \text{cm}^{-1}) = \alpha_0 + 5.9 \times 10^{-18} (\text{cm}^2) N + 2.8$$

$$\times 10^{-20} (\text{cm}^2) P^{1.13}, \quad (1)$$

where N and P are the electron and hole concentrations, respectively, and $n_0 = 3.504$, $\alpha_0 = 0.1 \text{ cm}^{-1}$. Thus, for uniform doping profiles given, the permanent index and absorption coefficient profiles vertically through the device (i.e., normal to the junctions) are as shown in Figs. 2(a) and 2(b). From the figure it is seen that the fundamental mode in the guided n layer is confined by an index difference of $\Delta n \approx 8 \times 10^{-4}$.

The question of the existence of higher-order modes in a structure of such large dimensions is of importance and has been investigated. To investigate this question, we employ a three-layer model. Denoting the N⁺, N, and P regions by 1, 2, and 3 respectively, at equilibrium we have

$$n_1(1.3 \mu\text{m}) = 3.502760,$$

$$n_2(1.3 \mu\text{m}) = 3.503783,$$

$$n_3(1.3 \mu\text{m}) = 3.502998,$$

and so

$$\Delta n_{12} = n_2 - n_1 = 1.023 \times 10^{-3},$$

$$\Delta n_{23} = n_2 - n_3 = 7.85 \times 10^{-4},$$

$$\Delta n_{31} = n_3 - n_1 = 2.38 \times 10^{-4}.$$

So, approximately, we have a symmetric waveguide ($n_1 \approx n_3$). For this case, the condition for a guided mode is

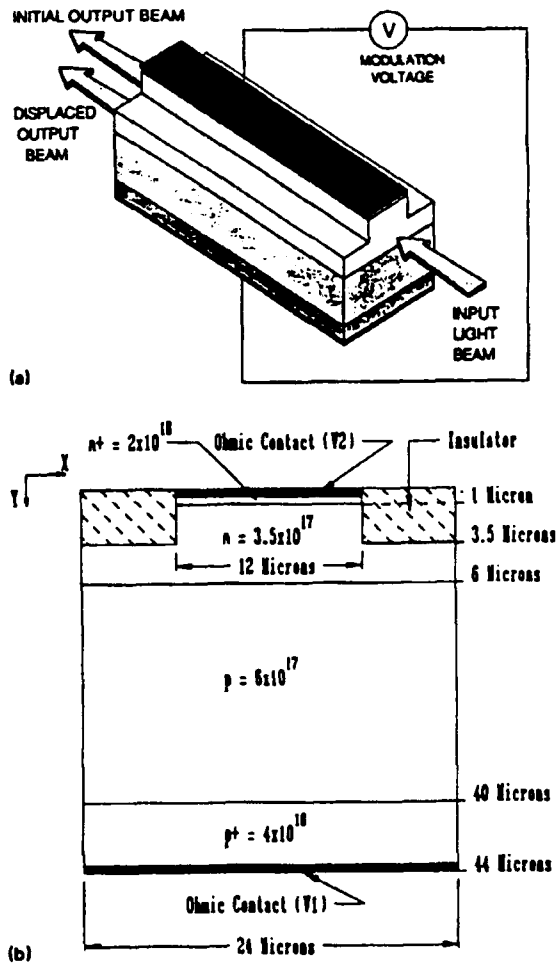


Fig. 1. (a) Perspective view of mode-displacement modulator. (b) Cross-sectional view of device geometry with dimensions and dopant concentrations.

$$\Delta n = \delta n_2 - \delta n_1 > m^2 / 4t^2 (n_2 - n_1), \quad m = 0, 1, 2, \dots, \quad (2)$$

where λ is the wavelength of light in vacuum, and t is the thickness of the guiding layer (layer 2). In the approximation of a symmetric guide, the fundamental ($m = 0$) mode is always supported. Substituting $\lambda = 1.3 \mu\text{m}$, $t = 5 \mu\text{m}$, and n_1 and n_2 given above, the first excited mode ($m = 1$) is supported if

$$\Delta n_{21} > 2.41 \times 10^{-3}.$$

This is not satisfied, though only barely, suggesting that only the fundamental ($m = 0$) mode is supported. This argument is only approximate, however. The plane-waveguide simulations reveal the possible existence of higher-order modes with many zeros in intensity uniformly distributed throughout the structure. However, these higher-order modes are believed to be of subsidiary importance because (i) the relative intensity of the mode in the guided N region is small, and (ii) the attenuation is

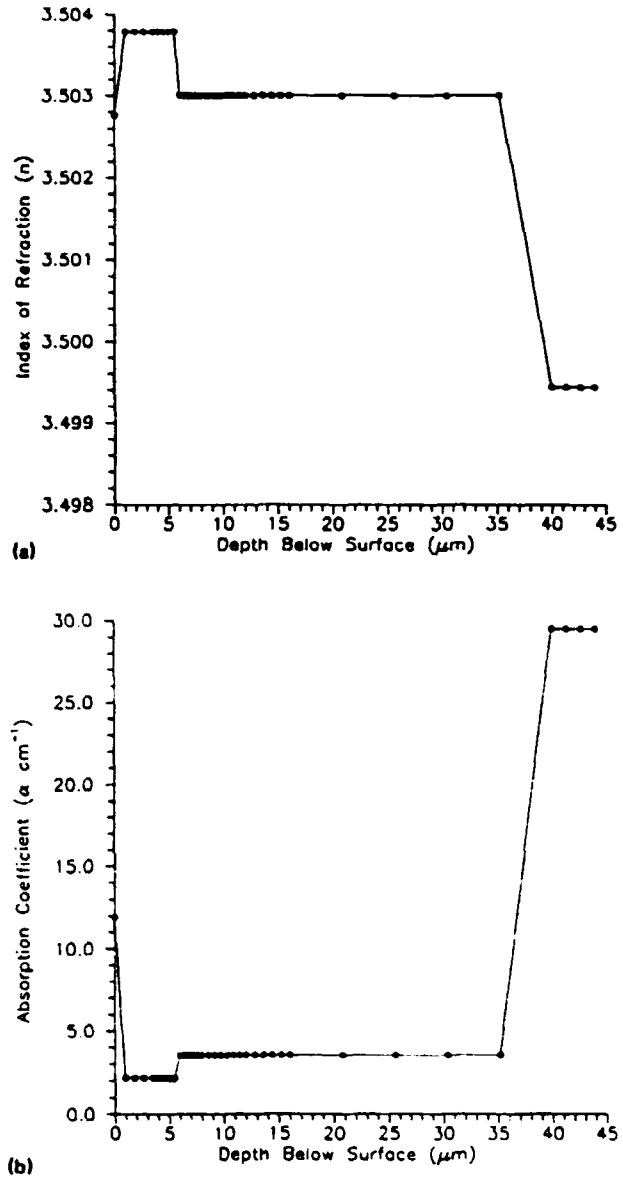


Fig. 2. (a) Index of refraction at $V_2 = 0$ and $\lambda = 1.3 \mu\text{m}$ as a function of depth below the surface. (b) Absorption coefficient at $V_2 = 0$ and $\lambda = 1.3 \mu\text{m}$ as a function of depth below surface.

higher than that of the fundamental mode, similar to the attenuation of the fundamental displaced mode discussed below.

3. ELECTRICAL AND OPTICAL SIMULATIONS

Next, the situation under forward bias ($V_1 = 0$, $V_2 < 0$) will be examined. Increasing forward biases ranging from 0.8 to 1.1 V in 0.05-V steps were applied. The two-dimensional device structure shown in Fig. 1 (b) was simulated on PISCES-2B at each value of forward bias.¹ For the purposes of the present

study, the output data of importance are the two-dimensional electron and hole concentrations at each mesh point, $N(x,y)$ and $P(x,y)$, respectively. At each mesh point (x,y) the local index and absorption coefficient $n(x,y)$ and $\alpha(x,y)$ at $1.3 \mu\text{m}$ are given by Eq. (1) with $N = N(x,y)$ and $P = P(x,y)$.

The subsequent optical simulations were performed on the plane-waveguide program³ provided to us by Ritter of the Martin Marietta Corporation. This program calculates the modes of a multilayer slab waveguide and is therefore one dimensional. Each slab is characterized by a thickness (except for the semi-infinite boundary layers), an index of refraction n_i , and an absorption coefficient α_i . In order to obtain these input data from the PISCES-2B simulations, the electron and hole concentrations were spatially averaged over the horizontal x dimension of each row to obtain

$$\begin{aligned}\bar{N}(y) &= \frac{1}{L(y)} \int_0^{L(y)} dx N(x,y), \\ \bar{P}(y) &= \frac{1}{L(y)} \int_0^{L(y)} dx P(x,y),\end{aligned}\quad (3)$$

where $L(y)$ is the length of the slab at point y . In discretized form,

$$\begin{aligned}\bar{N}(y_i) &= \frac{1}{m_j} \sum_j N(x_i, y_j), \\ \bar{P}(y_i) &= \frac{1}{m_j} \sum_j P(x_i, y_j).\end{aligned}\quad (4)$$

For each y_i , the local index of refraction $n(y_i)$ and absorption coefficient $\alpha(y_i)$ are then obtained as

$$\begin{aligned}n(y_i) &= n_0 - a\bar{N}(y_i) - \bar{P}(y_i)^{0.8}, \\ \alpha(y_i) &= \alpha_0 - c\bar{N}(y_i) - d\bar{P}(y_i)^{1.13},\end{aligned}\quad (5)$$

where, at $1.3 \mu\text{m}$, $n_0 = 3.504$, $a = 6.2 \times 10^{-22} \text{ cm}^3$, $b = 6.0 \times 10^{-18} \text{ cm}^{2.4}$, $\alpha_0 = 0.1 \text{ cm}^{-1}$, $c = 5.9 \times 10^{-20} \text{ cm}^2$, and $d = 2.8 \times 10^{-20} \text{ cm}^{2.3}$.

The values of $n(y_i)$ and $\alpha(y_i)$ so generated serve as input parameters to the plane-waveguide program. A five-layer system was simulated, the layers being: air ($n = 1.0$, $\alpha = 0$), N^+ , N , P , and P^+ . The bounding air and P^+ regions are semi-infinite in extent. As output, the program provides the structure's modal index (propagation constant) β , the attenuation constant α , and the spatial distribution of the optical intensity as a function of y_i . Forward biases of 0.9 and 1.1 V will be examined. As noted earlier, smaller voltages were also employed, but appreciable perturbations of the carrier densities only occurred for voltages less than, but of the order of, the built-in voltage V_{bi} . Figures 3

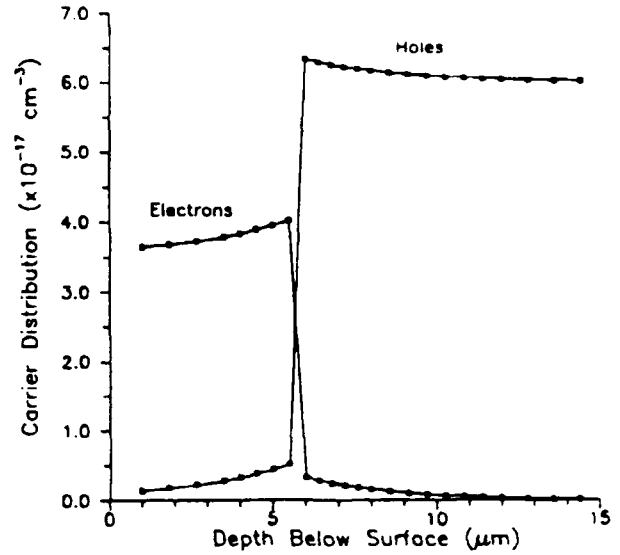


Fig. 3. Electron and hole concentrations at $V_2 = -0.9 \text{ V}$ and at $\lambda = 1.3 \mu\text{m}$ as a function of depth below surface.

and 4 show $N(y_i)$ and $P(y_i)$ at $1.3 \mu\text{m}$ at 0.9 and 1.1 V, respectively, in the vicinity of the $p-n$ junction. The enhanced values of these quantities are noted. It is also noted that under conditions of high-level injection operative here ($V \leq V_{bi}$), majority-carrier injection is as important as minority-carrier injection, i.e., the majority-carrier distribution follows the minority-carrier distribution in order to insure local charge neutrality. Figures 5(a), 5(b), 6(a), and 6(b) show the index and absorption coefficient at $1.3 \mu\text{m}$, as obtained from Eq. (5), at 0.9 and 1.1 V. The pointwise index and absorption coefficient data shown in these figures served as input data to the plane-waveguide optical simulations. Also, the data described by Eq. (1) and shown

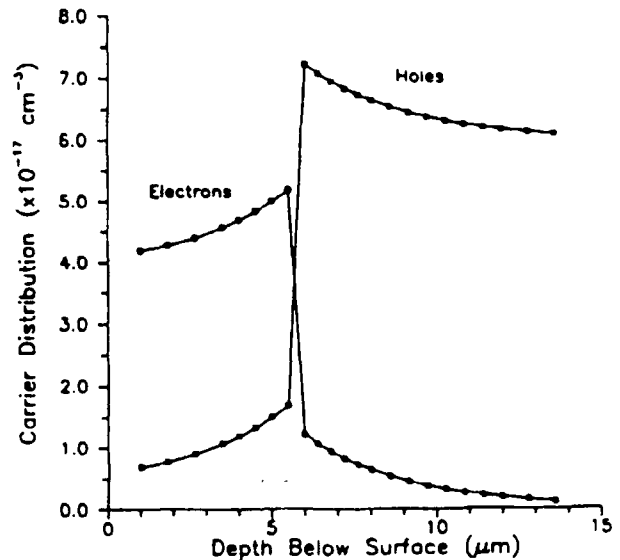
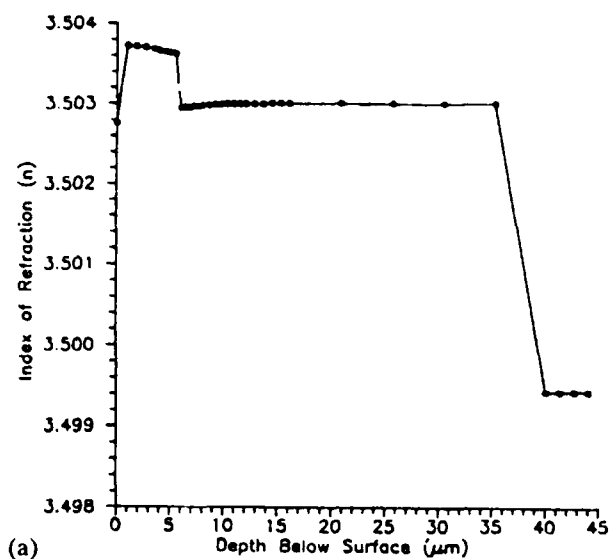
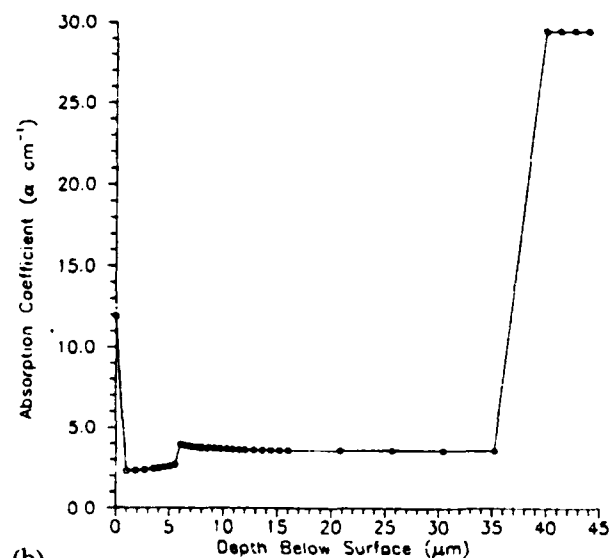


Fig. 4. Electron and hole concentrations at $V_2 = -1.1 \text{ V}$ and at $\lambda = 1.3 \mu\text{m}$ as a function of depth.



(a)



(b)

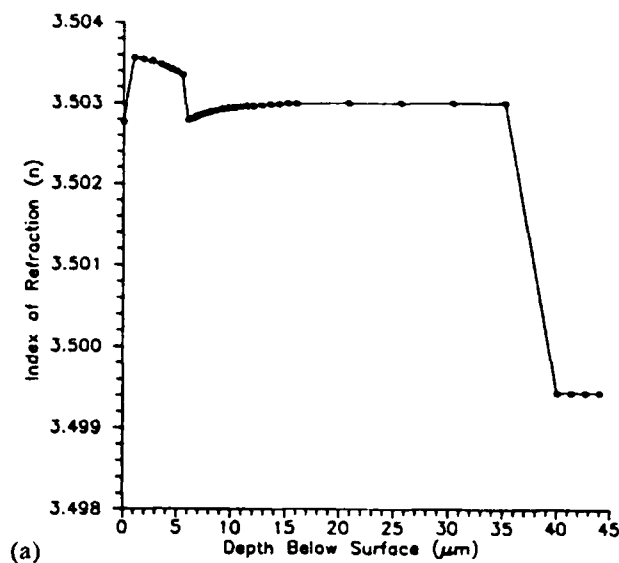
Fig. 5. (a) Index of refraction for $V_2 = -0.9$ V and $\lambda = 1.3$ μm as a function of depth. (b) Absorption coefficient for $V_2 = -0.9$ V and $\lambda = 1.3$ μm as a function of depth.

in Figs. 2(a) and 2(b) served as input for the device structure at equilibrium ($V_1 = V_2 = 0$)

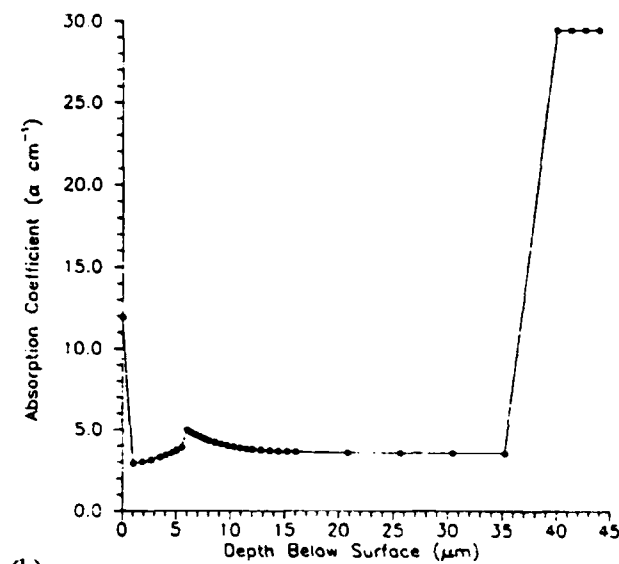
4. RESULTS AND DISCUSSION

The results of the optical simulations are shown in Fig. 7. Figure 7 shows the optical intensity distribution of the TE_0 fundamental mode at the modulation voltages of zero and 1.1 V. Considering first the zero-bias case, the intensity is seen to be largely confined to the waveguiding N layer. The modal index here is $\beta = 3.50312$ and the attenuation is 12.36 dB/cm.

Only the larger forward bias of 1.1 V will be considered here. (Forward bias is here achieved by setting $V_1 = 0$ and setting V_2 ,



(a)



(b)

Fig. 6. (a) Index of refraction for $V_2 = -1.1$ V and $\lambda = 1.3$ μm as a function of depth. (b) Absorption coefficient for $V_2 = -1.1$ V and $\lambda = 1.3$ μm as a function of depth.

the voltage applied to the N^+ contact, negative.) For this bias, it is seen in Fig. 7 that the optical intensity of the fundamental mode is substantially displaced from the N -waveguiding region into the P substrate. The modal index is decreased to $\beta = 3.50292$ and the attenuation is increased to 15.62 dB/cm. The behavior of the TM_0 mode was essentially identical to that of the TE_0 mode.

The important effect of the applied bias is the displacement of the fundamental mode over a distance sufficiently large (≈ 19 μm) that the loss of optical intensity in the N -waveguiding region is easily detected. Higher-order modes were not seen in the present example, but it has been argued that their possible existence would not obviate our conclusions. The effect of the applied

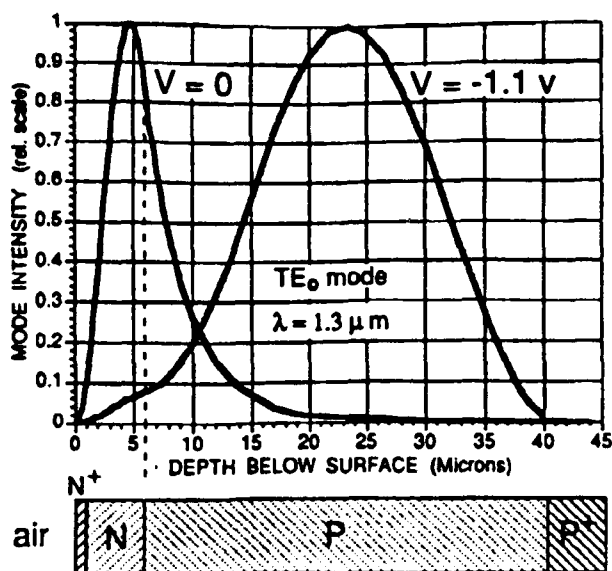


Fig. 7. TE₀ mode intensity for $\lambda = 1.3 \mu\text{m}$ at $V_2 = 0$ and $V_2 = -1.1 \text{ V}$ as a function of depth below surface.

bias on the modulation of the phase and intensity are of lesser importance. The change in modal index is $\Delta\beta = 2 \times 10^{-4}$, corresponding to $L(\pi) = 3.25 \text{ mm}$, while the attenuation increase is 3.26 dB/cm. Neither of these would qualify the device as an effective phase or amplitude modulator.

The electrical current density is an important electrical characteristic that must be checked to insure that there is not excessive dissipation. The I - V characteristic of the diode is shown in Fig. 8. A forward bias of 0.9 V corresponds to a current density of

$$j = 10^{-4} / 12 \times 10^{-8} = 833 \text{ A/cm}^2.$$

At 1.1 V, this will increase by approximately a factor of 4 corresponding to a current density of 3333 A/cm^2 . To limit j to 2000 A/cm^2 , the bias would have to not exceed 1.0 V.

5. CONCLUSIONS

Using PISCES-2B software and multilayer waveguide theory, we have analyzed a new type of semiconductor guided-wave electro-optic intensity modulator. We simulated electron and

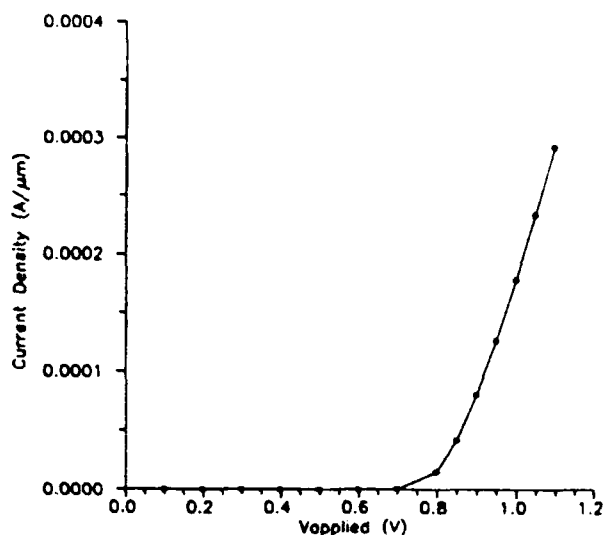


Fig. 8. Current density ($\text{A}/\mu\text{m}$) vs applied voltage ($-V_2$).

hole injection into a planar air-clad silicon $N^+-N-P-P^+$ diode rib guide during forward bias. The carrier-induced index decrease in the N -type core displaces the fundamental guided mode downward into the substrate, but the mode is not cut off because the P -type substrate is bounded by a lower-index P^+ contact. At zero bias, the mode's core-substrate intensity distribution is about 55%/45%, while at full bias ($V_{\text{applied}} \approx V_{\text{bi}} \approx 1 \text{ V}$) the distribution changes to about 5%/95%. A spatial filter at the end of the active electroded region will transform the mode's spatial displacement into optical intensity modulation. For example, an aperture that blocks the substrate light but passes the core light is a suitable filter. Alternatively, the active guide could be end coupled to a more tightly bound guide with a similar core height, such as a silicon-on-insulator or GeSi/Si guide. The second guide would discriminate against substrate light. Dual-aperture filters would produce 1×2 optical switching.

6. REFERENCES

1. S. Giguere, L. Friedman, R. A. Soref, and J. P. Lorenzo, *J. Appl. Phys.* **68**, 4970 (1990).
2. R. D. Lareau, L. Friedman, and R. A. Soref, *Electron. Lett.* **26**, 1653 (1990).
3. R. A. Soref and K. J. Ritter, *Opt. Lett.* **15**, 792 (1990).

OPTICAL WAVEGUIDES IN SIMOX STRUCTURES

B.L. Weiss, G.T. Reed, and S.K. Toh, Department of Electronic and Electrical Engineering, University of Surrey
R.A. Soref, Electromagnetics & Reliability Directorate, Rome Laboratory
F. Nanavar, Spire Corporation

Published in IEEE Photonics Technology Letters, Vol. 3, No. 1, January 1991 (IEEE Log Number 9041575)

Abstract – Planar optical waveguides have been formed in SIMOX structures and their propagation characteristics have been determined. All the samples were found to support both TE and TM modes at both 1.15 μm and 1.523 μm with a lowest propagation loss of 8 dB/cm. This loss was measured at a wavelength of 1.15 μm for the TE₀ mode of a planar waveguide with a 2.0- μm -thick Si guiding layer.

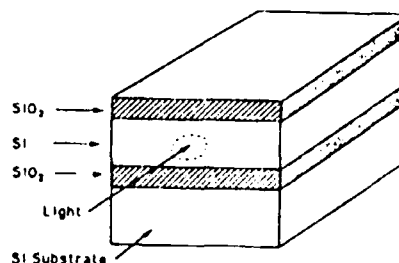


Fig. 1. SIMOX sample structure

1. INTRODUCTION

Optical waveguiding in SIMOX structures was first demonstrated by Soref *et al.* [1] in 1989. With silicon (Si) being transparent above a wavelength of 1.05 μm and with the refractive indexes of Si and silicon dioxide (SiO₂) being 3.5 and 1.5, respectively, this material system is suitable for strongly confined passive optical waveguiding structures. Active devices, such as modulators based on carrier injection, have been proposed [2] and developed [3] although they have yet to reach the point where they are useful for communications applications. This technology is also suitable for the development of intrachip optical interconnects.

SIMOX structures are Si-based and have a surface silicon layer isolated from the Si substrate by a layer of SiO₂, which is formed by the high dose implantation of oxygen. Post implantation annealing is required to remove the implantation induced damage by regrowth from the top Si layer, resulting in the formation of a high quality epitaxial Si layer. It has been shown that this Si layer has extremely good electrical properties and has been used to fabricate some state of the art devices [4].

In this work SIMOX waveguide structures have been fabricated and the propagation characteristics have been determined both experimentally and theoretically and it is the first report of waveguiding being obtained in SIMOX structures at a wavelength above 1.15 μm . The results show that the waveguides support both TE and TM modes at wavelengths of 1.15 and 1.52 μm with the lowest propagation loss of 8 dB/cm being obtained for the TE₀ mode at a wavelength of 1.15 μm .

2. EXPERIMENTAL METHOD

Samples of Si were implanted with 160 keV oxygen ions to a dose of $1.6 \times 10^{18} \text{ cm}^{-2}$ and annealed at 1300°C for 6 h, which produced a buried oxide layer thickness of 0.4 μm and a top Si

layer thickness of 0.15 μm [5]. Subsequently a 2 μm thick layer of epitaxial Si, with a carrier concentration of $\sim 10^{15} \text{ cm}^{-3}$, was grown by chemical vapor deposition (CVD) on the sample surface. In order to investigate the effect of the thickness of the top silicon layer (i.e., the guiding layer) on the propagation characteristics of the waveguide, the samples were annealed at 1000°C in N₂ for periods up to 18 h in dry oxygen to oxidize varying thicknesses of the top Si layer. This sample structure is shown in Fig. 1.

Waveguide measurements were carried out using He-Ne lasers operating at 1.15 and 1.523 μm , respectively. The samples were cleaved and the endfaces were polished to produce flat parallel surfaces through which the light was coupled into and out of the waveguide using X40 microscope objectives. The output beam intensity and mode profile were measured using a Ge diode and an IR camera interfaced to a video analyzer, respectively, to enable the waveguide loss and intensity profile of the propagating modes to be determined. The number of modes was predicted from a simple computer simulation of the waveguide structure, assuming abrupt Si/SiO₂ interfaces. The waveguide excitation was optimized to excite a single propagating mode, which was confirmed by examination of the waveguide output beam using the camera.

The number of modes supported by the waveguides and their intensity profiles were predicted by a solution of Maxwell's equations, assuming abrupt Si-SiO₂ interfaces and uniform Si and SiO₂ refractive indexes.

3. RESULTS AND DISCUSSION

The results of the modeling showed that all the waveguides studied here were multimode for the wavelengths used. It showed that they support three TE modes for a 0.55 μm thick-

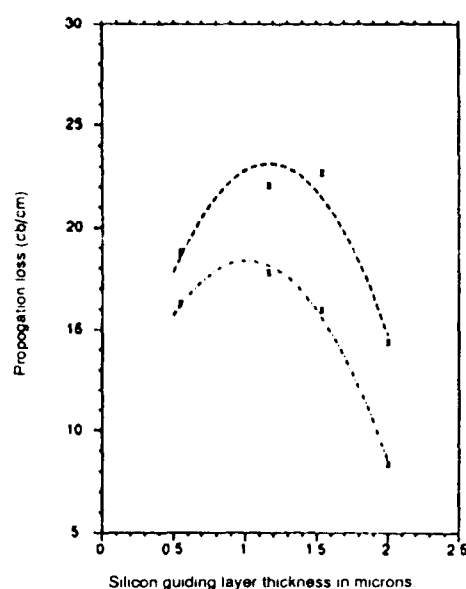


Fig. 2. The variation of TE₀ and TM₀ propagation loss with silicon guiding layer thickness at a wavelength of 1.15 μm. (----TM₀,TE₀)

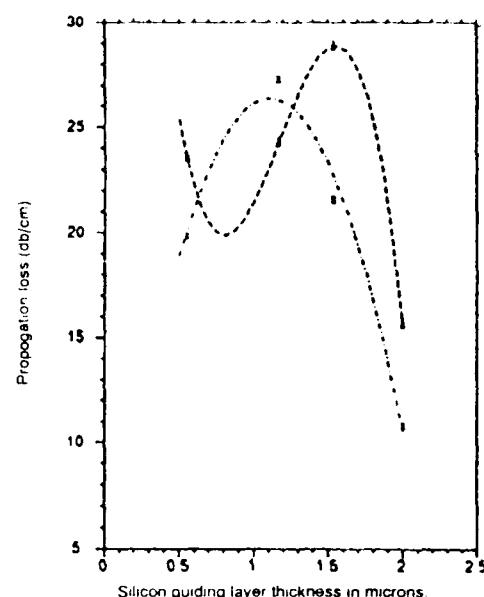


Fig. 3. Same as Fig. 2, but for a wavelength of 1.523 μm. (----TM₀,TE₀)

Si-guiding layer and eleven TE modes for a 2 μm thick Si-guiding layer at a wavelength of 1.15 μm. At a wavelength of 1.523 μm these values decreased to two and nine for the 0.55 and the 2.0 μm Si guiding layer thicknesses respectively.

The profile of the waveguide mode at the output is basically that of a single mode waveguide. However, with regard to studying the waveguide propagation loss, since the mode profile has an approximately Gaussian shape, the approximate mode overlap loss between the input laser beam and the propagating mode for one dimension (the depth) only has been made. This enables a more accurate calculation of the propagation loss to be made.

The variation of the fundamental mode propagation loss with Si-guiding layer thickness is shown in Figs. 2 and 3 for wavelengths of 1.15 and 1.523 μm, respectively. These results have been calculated by subtracting the Fresnel reflection loss (~ 3 dB) and an estimate of the mode overlap loss from the measured insertion loss. Due to the very large numerical aperture of the Si waveguide, the angle of divergence of the waveguide output beam is very large, making it very difficult in practice to collect all of the waveguide output beam and measure its intensity. Consequently, it is likely that the intensity of the output beam is greater than the measured value, in which case the measured values of insertion loss, and therefore propagation loss will be higher than the actual value in the waveguide due to the measurement technique.

A comparison of the insertion loss of the waveguides, given in Table 1, and their propagation loss, given in Figs. 2 and 3, indicate that the mode overlap loss and the waveguide coupling

Table 1. The insertion loss values for waveguides with various values of Si-Guiding layer thickness.

Sample Length (mm)	Guiding Layer Thickness (μm)	Wavelength (μm)	Insertion Loss (dB)	
			TE ₀ Mode	TM ₀ Mode
2.0	2.0	1.15	9.6	10.8
2.2	1.54	1.15	12.0	13.4
2.0	1.17	1.15	12.0	12.8
2.1	0.55	1.15	12.4	12.9
2.0	2.0	1.523	10.0	11.0
2.2	1.04	1.523	13.1	14.6
2.0	1.17	1.523	13.8	14.3
2.1	0.55	1.523	13.1	13.8

loss are considerably greater than the waveguide propagation loss. Therefore, any changes in the coupling of the laser beam into the waveguide, which is difficult for the reason described above, would result in an increase in the propagation loss of the waveguide because of the method used to calculate the propagation loss. Thus, the values of the propagation loss presented here are probably larger than the actual values in the waveguide.

We believe that the observed waveguide propagation loss is caused primarily by the optical scattering loss, including volume scattering due to crystal lattice defects in the Si-guiding layer (mainly threading dislocations) and surface scattering due to roughness at the Si-SiO₂ interfaces. Our samples had a defect density of approximately 10^9 cm^{-2} , a density that can be

reduced below 10^5 cm^{-2} by using multiple low-dose O^+ implants [6]. Our samples also had Si twinning defects extending 200 Å from the buried Si-SiO₂ interface. These twins can be avoided by different sample processing. The reasons for the higher losses found at 1.523 μm wavelength are not fully understood. There are two loss contributions which increase with increasing wavelength. The first is free carrier absorption in the Si-guiding layer. The second is the finite thickness of the buried oxide layer which results in some energy of the propagating mode being coupled into the Si substrate. In other words, the evanescent field penetration into the oxide layer increases with increasing wavelength, as reported by Kurdi *et al.* [7]. The absorption and mode penetration factors offer a partial explanation of the 1.523 μm results.

The effect of the surface oxide layer is not expected to be significant because the refractive index difference between air

($n = 1.0$) and SiO₂ ($n = 1.5$) is not nearly as large as is the refractive index difference between Si ($n = 3.5$) and these materials. Computer simulation of the TE₀ mode profiles shows that this assumption is correct. They also show that the amount of light coupled into the Si substrate is small since the amplitude of the evanescent field at the Si-SiO₂ interface is small.

4. CONCLUSIONS

The results show that low loss single mode waveguides may be fabricated in SIMOX structures. These waveguides support both TE and TM modes at both 1.15 and 1.523 μm and have a minimum propagation loss of 8 dB/cm for the TE₀ polarization at 1.15 μm.

VERTICALLY INTEGRATED SILICON-ON-INSULATOR WAVEGUIDES

R.A. Soref, Electromagnetics & Reliability Directorate, Rome Laboratory

E. Cortesi and F. Namavar, Spire Corporation

L. Friedman, Department of Electrical Engineering, Worcester Polytechnic Institute

Published in IEEE Photonics Technology Letters, Vol. 3, No. 1, January 1991 (IEEE Log Number 9041748)

Abstract - A new $\text{SiO}_2\text{-Si-SiO}_2\text{-Si-SiO}_2\text{-Si}$ structure produced by the SIMOX process is used for dual, vertically integrated waveguiding in silicon at $\lambda = 1.3 \mu\text{m}$. Independent waveguiding is observed when $2\text{-}\mu\text{m}$ -thick Si cores are separated by $0.36\text{-}\mu\text{m}$ -thick SiO_2 . Coupled waveguiding is found for an $0.12 \mu\text{m}$ intercore oxide thickness.

1. INTRODUCTION

Techniques for three-dimensional (3-D) integration of waveguides are needed to expand the capabilities of silicon-based integrated optics. This paper reports waveguiding in vertically integrated pairs of Si guides in a new six-layer $\text{SiO}_2\text{-Si-SiO}_2\text{-Si-SiO}_2\text{-Si}$ structure. Dual waveguiding in Si at $1.3 \mu\text{m}$ was observed. Vertical directional couplers and uncoupled guides were examined. The multilayer structure was fabricated by a repeated sequence of oxygen-ion implantation, annealing, and Si epitaxy. Vertical 3-D integration of silicon-on-insulator (SOI) waveguides has potential applications in opto-electronic integration, including wafer-scale optical interconnects.

Fig. 1 shows our double SOI structure in which optical guiding occurs in two Si levels. In this structure, the layer thickness is designated as t_0 for the SiO_2 cap layer, d_1 for the first Si core layer, t_1 for the first buried oxide layer, d_2 for the second Si core layer, and t_2 for the second buried oxide layer.

2. THEORY

A range of physical behavior occurs when intercore oxide thickness t_1 is increased from 50 to 500 \AA , and then from 500 to 5000 \AA . At 50 \AA , leaky mode guiding occurs [1]. The confinement at 500 \AA changes to conventional-mode guiding with strong mutual coupling of the Si cores. Finally, at 5000 \AA , the cores become independent and the guides are uncoupled. The computer program of Soref and Ritter [1] was used to calculate the effect of t_1 upon coupling strength. Results for the Fig. 1 structure are presented in Fig. 2 for the TE and TM polarizations at the optical wavelengths of 1.3 and $1.55 \mu\text{m}$. Fig. 2, the predicted coupling length (the propagation length needed to transfer 100% of the optical power from core 1 to core 2) is plotted as a function of t_1 . In this calculation, it was assumed that both cores were $2 \mu\text{m}$ thick, that $t_0 = 1 \mu\text{m}$, and that $t_2 = 3700 \text{ \AA}$. These numbers correspond to experimental samples

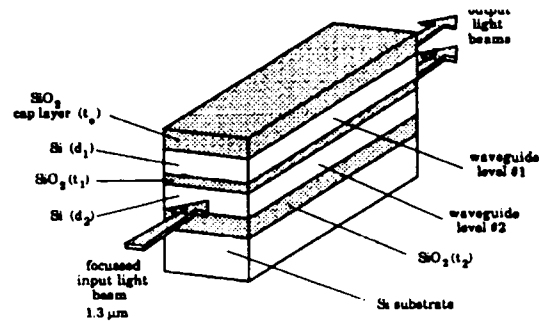


Fig. 1. Six-layer structure for vertical 3-D integration of SOI waveguides.

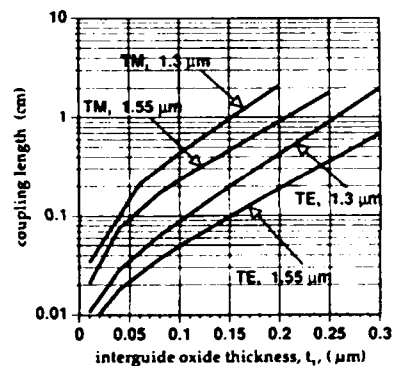


Fig. 2. Calculated coupling length versus t_1 for dual waveguiding in Fig. 1 with $t_0 = 1 \mu\text{m}$, $d_1 = d_2 = 2 \mu\text{m}$, and $t_2 = 0.37 \mu\text{m}$.

discussed below. It is found that TE modes couple more strongly than TM modes, which agree with an earlier finding that the rate of optical leakage into the substrate of a simple SOI waveguide is greater for TE light than for TM light when $d_1 > 0.4 \mu\text{m}$ [2]. For samples with $t_1 = 1200 \text{ \AA}$ (discussed below) the coupling lengths in Fig. 2 range from 0.6 to 1.2 mm (TE) and $3\text{-}6 \text{ mm}$ (TM). The calculation of coupling length L_c was repeated for thinner cores, $d_1 = d_2 = 1 \mu\text{m}$, and it was found that the ratio L_c/t_1 was $1/9$ of that for $2 \mu\text{m}$ cores. Our calculations also show that intrinsic propagation losses due to leakage of light through t_0 and t_2 are less than 0.02 db/cm for Fig. 2.

3. SAMPLE PREPARATION

The SIMOX process produced good results. Starting with a 100-mm-diam p-type (100)-Si substrate, an ion fluence of $1.6 \times$

$10^{18} \text{ O}^+ \text{ cm}^{-2}$ was implanted at 160 keV. The wafer was annealed at 1300°C in N_2 for 6 h, then $\sim 2 \mu\text{m}$ of epitaxial Si was grown by chemical vapor deposition (CVD) on the implanted wafer. This was followed by a second 160 keV O^+ implanted at the $1.6 \times 10^{18} \text{ cm}^{-2}$ dose, by another 6 h 1300°C anneal, and by a second Si epitaxy $\sim 2 \mu\text{m}$ thick. Then an SiO_2 cap layer $1 \mu\text{m}$ thick was deposited atop the wafer. The result was a Fig. 1 structure with $t_0 = 1 \mu\text{m}$, $d_1 = 2 \mu\text{m}$, $t_1 = 0.37 \mu\text{m}$, $d_2 = 1.6 \mu\text{m}$, $t_2 = 0.37 \mu\text{m}$, designated sample type A. Here, the two Si guides are essentially uncoupled. To make a vertical directional coupler (sample type B), we repeated the above fabrication process, except that the second implant(s) consisted of $4 \times 10^{17} \text{ O}^+ \text{ cm}^{-2}$ anneal + $2 \times 10^{17} \text{ O}^+ \text{ cm}^{-2}$ anneal. This produced an interguide oxide thickness of only $0.12 \mu\text{m}$ which produced strong coupling. Samples B had $t_0 = 1 \mu\text{m}$, $d_1 = 2 \mu\text{m}$, $t_1 = 0.12 \mu\text{m}$, $d_2 = 1.9 \mu\text{m}$, and $t_2 = 0.39 \mu\text{m}$.

The presence of the $1 \mu\text{m}$ SiO_2 cap layer was found to be helpful because in that case the first core layer was buried $1 \mu\text{m}$ below the top surface of the wafer. The buried core proved to be beneficial when the wafer ends were polished after dicing. During polishing, micron sized chips frequently appear in the top corner of the sample end, and those chips are now located in the upper cladding rather than in waveguide core 1, facilitating a smoother launch of light in the core.

Earlier, we demonstrated waveguiding in simple SOI [3]. The experimental work of Davies *et al.* [4] and Weiss *et al.* [5] on simple SOI guides shows that the fundamental-mode propagation loss in practice is much higher than the intrinsic leakage loss, and that the actual loss is governed by the presence of defects, such as threading dislocations, in the Si layer. It was found that the annealing process played a role in minimizing both the defect density and mode loss. In this connection, we used transmission electron microscopy to examine a cross section of our samples (XTEM). Fig. 3 shows the XTEM of sample type A (minus the oxide cap). The defect density in this sample is in the range of 10^7 cm^{-2} . Based on other experiments [6], [7], we believe that it is possible to reduce the defect density in the six layer SOI wafers to less than 10^4 cm^{-2} using multiple low dose O^+ implants [6] or high temperature implants [7].

4. EXPERIMENTAL RESULTS

Batches of rectangular samples, types A and B, with propagation lengths (L) of 7 to 15 mm, were prepared. For etal fire optical launch, the sample ends were polished with 1- and $0.25 \mu\text{m}$ diamond paste. Using a $40\times$ microscope objective, $1.3 \mu\text{m}$ laser light was focused into one core of the sample. The input focal spot had an e^{-1} diameter of about $1.6 \mu\text{m}$, which allowed individual excitation of the dual cores. To excite the cores in se-

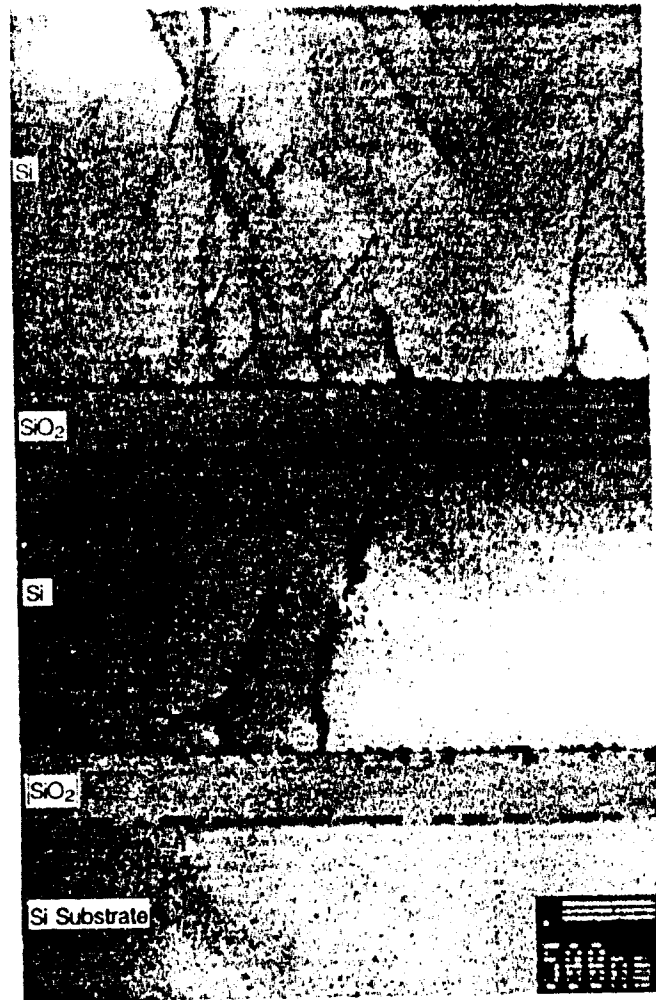


Fig. 3. XTEM of Fig. 1 sample type A.

quence, the sample was moved vertically in submicron increments at right angles to the fixed input beam. The near field radiation pattern of both waveguide outputs was imaged at high magnification onto an infrared vidicon.

For samples A, it was found that 95% of the light remained in the original excited guide, either guide 1 or guide 2, implying that the guides were not coupled. The small fraction of light in the adjacent guide was attributed to optical tail excitation by the Gaussian input beam. For samples B, excitation of 1 produced simultaneous emission from both cores with an approximate 60/40% power distribution. As the optical input changed from 1 to 2 during the mechanical scan, the outputs switched from 60/40 to 40/60, implying coupling between Si levels 1 and 2. A video line scan of the dual TE output from sample B with $L = 9 \text{ mm}$ is shown in Fig. 4. Similar results were obtained for TM modes.

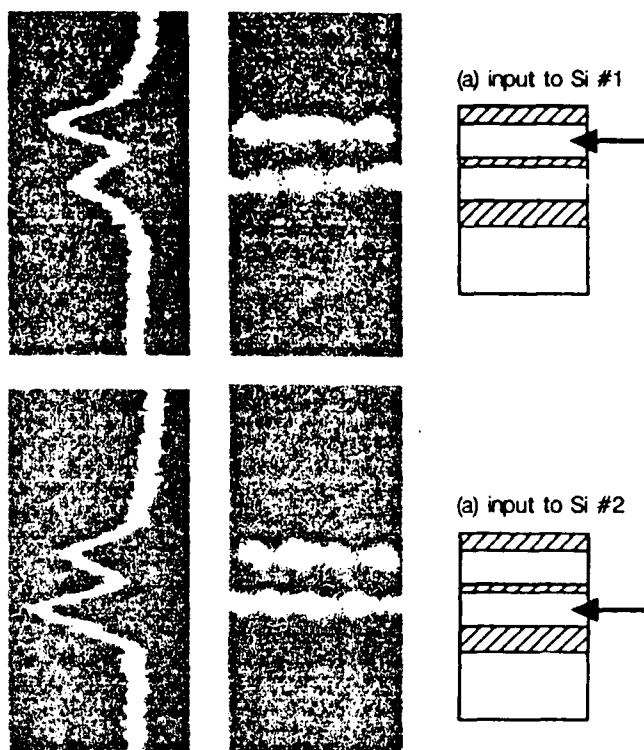


Fig. 4. Coupled, vertically stacked $2\ \mu\text{m}$ Si guides with $t_1 = 0.12\ \mu\text{m}$. Photos on right show near-field radiation pattern at output. Photos at left show video line scan of output intensity. (a) is for laser input to number 1. (b) is for input to number 2.

5. DISCUSSION

The experimental coupling results are in good agreement with the theoretical model. Thus, the designer of the double SOI structure has the option of making the optical levels coupled or independent. Note that our samples have the same layer sequence as the six layer ARROW-C of [2], although the Si ARROW-C would be constructed with much thinner t_1 , t_2 and with $d_1 = 2d_2$.

A recent patent [8] shows explicitly the manufacturing steps required to transform the planar Si guides of Fig 1 into networks of Si channel waveguides: one network in level 1 and the other in level 2, with the guides in 1 being optically isolated from those in 2. Another transformation of the Fig. 1 structure is described in a second patent [9] that introduces the idea of a localized optical coupling between levels. Beginning with $t_1 \approx 5000\ \text{\AA}$ over most of the device area, a small region of the oxide is thinned to $t_1 \approx 1000\ \text{\AA}$ to give local coupling of cores. In that thinned region, two Si channels in adjacent levels run parallel to each other and couple over $\sim 1\ \text{mm}$. This vertical coupler can be used for passive interlevel power division or for active 2×2 interlevel optical switching. The 2×2 switch (Fig. 8 of [9]) is a $\Delta\beta$ device in which the group velocity of one Si core is changed

by injection, accumulation, depletion, or inversion of charge (the free carrier plasma effect). The voltage-controlled charge-carrier manipulation is produced by an MOS or pn diode.

Optical interconnects are another potential application for the dual SOI. One can envision a two-level interconnect in which electronic circuits are located in the top Si layer. Optical channel waveguides situated in the lower Si layer would pass beneath the circuits. There could also be channel waveguides in the top Si layer, and those guides could communicate at selected locations with circuits in the top level or with guides in the lower level, shuttling light from 1 to 2 and/or from 2 to 1. In this manner, a complex 3-D optoelectronic interconnect could be created.

6. CONCLUSION

We have demonstrated simultaneous waveguiding at $1.3\ \mu\text{m}$, either coupled or uncoupled, in two Si layers of a new SiO_2 -Si SiO_2 -Si-Si- SiO_2 -Si structure. Coupled mode theory has been worked out for this structure. The 3-D vertically integrated structure is believed to have applications in two-level optical networks, interlevel optical switches, and optoelectronic integration including optical interconnects.

7. REFERENCES

1. R. A. Soref and K. J. Ritter, "Silicon antiresonant reflecting optical waveguides," *Opt. Lett.*, vol. 15, pp. 792-794, 15 July 1990.
2. S.T. Peng, NY Inst. Technol., private communication, 1988.
3. F. Namavar, E. Cortesi, R.A. Soref, and P. Siwashani, "On the formation of thick and multiple layer SIMOX structures and their applications," *Mat. Res. Soc. Symp. Proc.*, vol. 147, pp. 235-246, Apr. 25, 1989.
4. D.E. Davies, M. Burnham, T.M. Benson, N. Mohd Kassim, and M. Seifouri, "Optical waveguides and SIMOX characterization," in *Proc. 1989 IEEE SOI/SOI Technol. Conf.*, Stateline, NV, Oct. 3, 1989, pp. 160-161.
5. B.L. Weiss, G.T. Reed, S.K. Toh, R.A. Soref, and F. Namavar, "Optical waveguides in SIMOX structures," *IEEE Photon. Technol. Lett.*, vol. 3, pp. 19-21, Jan. 1991.
6. F. Namavar, E. Cortesi, and P. Siwashani, "Low-defect high-quality SIMOX produced by multiple oxygen implantation with sub-stoichiometric total dose," *Mat. Res. Soc. Symp. Proc.*, vol. 128, pp. 623-628, 1989.
7. M.K. El-Ghor, S.J. Pennycook, F. Namavar, and N.H. Karam, "Formation of low dislocation density silicon-on-insulator by a single implantation and annealing," *Appl. Phys. Lett.*, vol. 57, pp. 156-158, July 9, 1990.
8. J.P. Lorenzo and R.A. Soref, "Method for fabricating low-loss crystalline silicon waveguides by dielectric implantation," U.S. Patent 4 789 642, Dec. 6, 1988.
9. ---, "Electro-optical silicon devices," U.S. Patent 4 787 691, Nov. 29, 1988.

ACTIVE SEMICONDUCTOR OPTICAL SWITCHES WITH BLUE-SHIFTED CHANNEL WAVEGUIDES

Richard A. Soref, Electromagnetics & Reliability Directorate, Rome Laboratory

Published in *Fiber and Integrated Optics*, Vol. 9, pp 313-321

Abstract - This paper presents a theoretical design study of active optical switches constructed from III-V semiconductor multiple-quantum-well waveguides. New designs are given for 4 X 4 matrix switches, 1 X 4 tree switches, and 4-delay optical transversal filters. The designs feature ~ 0 dB insertion loss and ~ 30 dB crosstalk isolation. Low injection currents are predicted because pumping is eliminated on ~ 70 percent of the channel waveguide area by an induced-disorder treatment that blue-shifts the material's absorption edge. The active networks also feature etched facet reflectors that facilitate the dense packing of guides.

1. INTRODUCTION

The use of erbium-doped fiber-optical amplifiers in fiber-optic communication networks is an important and growing trend. A related trend is the coupling of glass fibers with discrete semiconductor optical amplifiers [1-3], although an all-fiber gain network includes a more natural marriage of components. When integrating gain elements and optical circuit functions on a semiconductor chips, the best approach is to integrate semiconductor amplifiers with semiconductor channel waveguides. All-semiconductor networks like these are discussed in this paper.

We shall present new designs for 4 X 4 and 1 X 4 optical switches that use traveling-wave optical amplifiers to compensate for any optical losses incurred in the network, thereby restoring the optical signal levels to their input values. All of the designs are scaleable to higher order, which suggests that active semiconductor networks are capable of large-scale optical integration on a small chip. Switching networks 32 X 32 in size, or larger, should be feasible. The packing density and the scale of integration are larger than in Ti:LiNbO₃ integrated optics, and the semiconductor networks feature ~ 0 dB insertion loss with ~ 30 dB crosstalk isolation.

Electric current consumption and electrical power dissipation can be uncomfortably large in some semiconductor active networks. We propose to minimize current and power by using quantum-well gain media, and by interconnecting gain regions with unpumped blue-shifted waveguides. The manufacturing of such interconnects can be done with a simple process in which a uniformly microlayered wafer is treated in selected areas to induce disorder in the wells. This treatment shifts the unbiased absorption edge of the wells to shorter wavelengths.

2. A BRIEF HISTORY

Active optical switching in monolithic semiconductor structures was discussed in previous papers by Ikeda [4-6] and Thylen et al. [7-9]. Soref and Lau elaborated on those ideas in their 1988 proposal [10] for 2 X 2 and N X N optical switches in III-V multiple quantum-well (MQW) material. White et al. [11] built and tested an active 2 X 2 switch in bulk InGaAsP/InP operating at the 1.5 μ m wavelength. These authors introduced the use of etched facet reflectors on the rib waveguide structures, that produced a very compact device. The layout of their switch is similar to that given in Soref and Lau (compare Fig. 1 of Ref. 11 with Figs. 5 and 6 of Ref. 10). A problem in White's switch is the dc pumping (injection current) required on ~ 70 percent of the waveguide area in order to attain transparency for the guided lead-ins and lead-outs to the switch. This problem is overcome in the designs discussed here.

Lindgren et al. [12] constructed an InP-based Y-branched 1 X 2 switch containing active waveguides whose core was an 0.6 μ m layer of bulk InGaAsP ($E_g = 0.96$ eV). The core was bundled with an 0.3 μ m passive cladding of wide-gap InGaAsP ($E_g = 1.08$ eV). Outside the active zones, the 1.08 eV layer was expanded to become core material. The problem with Lindgren's switch is the complicated manufacturing process needed to bind active and passive materials together. The solution is the simple process proposed here.

3. QUANTUM WELLS

We pointed out in Ref. 10 that MQW waveguides give more optical gain per unit of injection current than bulk heterostructure guides. In addition, when active switching stages are cascaded, the spontaneous emission noise builds up at a slower rate in MQW gain stages than in active bulk stages. Consequently, more switching stages can be cascaded in the MQW case before the final amplifier stages become saturated by optical noise [10]. For these reasons, MQW construction is preferred for the networks.

Semiconductor laser media are highly attenuating at the laser wavelength when the pumping current is turned off. To modify the residual absorption, Tang et al. [13] performed experiments on a single-quantum-well AlGaAs/GaAs laser waveguide.

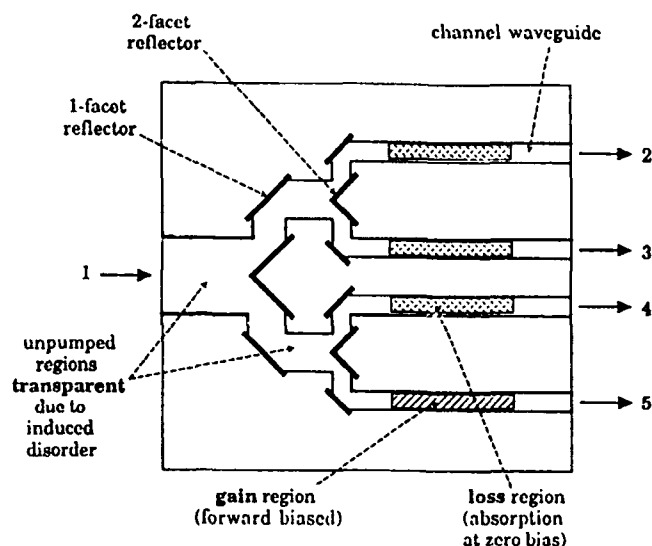


Fig. 1. Tree-structured 1 X 4 electro-optical guided-wave switch.

They used a combination of impurity-induced layer disordering and vacancy-induced disordering of the native quantum wells. They found that the absorption edge of the waveguide could be shifted from 800 nm to 860 nm while preserving very high transmission in the guide for $\lambda > 860$ nm. Their work proves that a simple manufacturing process is available for inducing transparency at zero bias in III-V MQW gain guides at the central gain wavelength.

4. DESIGN RULES

Here is a list of thirteen design rules that were used in this paper:

- (1) The cross-section of the channel waveguides closely resembles that of a $p-i-n$ III-V index-guided MQW laser diode.
- (2) The same microlayering is used throughout the wafer.
- (3) The electroded regions on these gain guides are 50 to 100 μm long in densely packed switches.
- (4) The integrated network is monolithic and planar.
- (5) The switches do not use mode interference or mode evaluation.
- (6) The waveguides are multimode.
- (7) Optical beam splitting and optical beam combining are obtained with Y-branched guides or with pairs of etched facet mirrors [14] that give total internal reflection of light.
- (8) Optical amplitude is routed by absorption-induced blocking of undesired optical paths and gain-induced selection of desired paths.
- (9) Waveguide bends of 90° are used wherever possible, as provided by 45° facet mirrors.
- (10) All of the lead-in waveguides and all of the waveguide lengths connecting active regions are treated with impurity-in-

duced disorder, or with vacancy induced disorder, making those sections highly transmissive at zero bias at the gain wavelength.

(11) The width of a channel guide can be varied within the switch without affecting the switch's operation.

(12) The guides are continuous between active and passive regions.

(13) Antireflection coatings are applied to the input and output ends of the chip.

Now, we shall apply these rules and give eight examples of 4 X 4 and 1 X 4 electro-optical guided-wave switches in Figs. 1-8. All of these are space division switches. In all figures, we see a top view of the channel-waveguide network. The shaded areas represent active $p-i-n$ electroded areas, and all shaded areas have the same construction. Either forward-bias or zero-bias can be applied to *any* electroded area. To avoid cluttering the diagram, we did not show the electrical connections to the active zones. There are three possibilities for electrical leads: (1) a

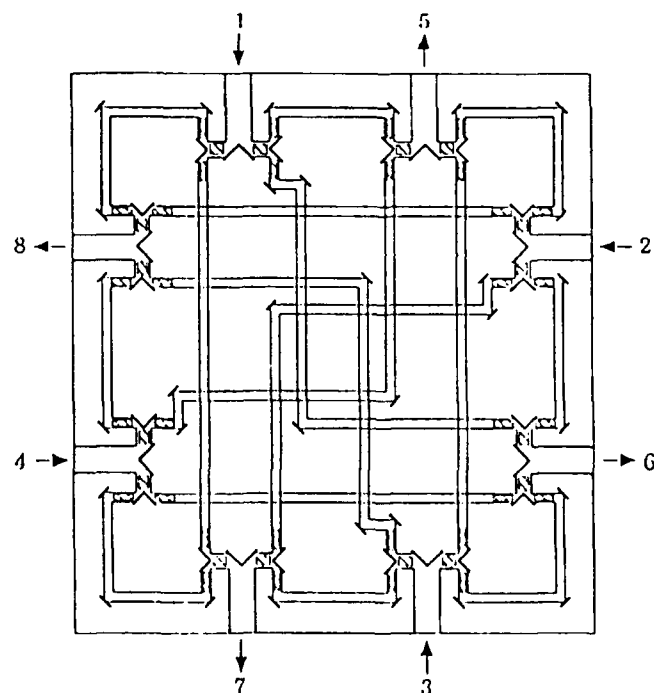


Fig. 2. Tree-structured 4 X 4 matrix switch with central symmetry.

metalization extends from each active area to an individual wire-bond pad at the periphery of the chip; (2) a drive transistor is integrated opto-electronically on the chip next to each active optical zone; (3) an array of drive transistors on a separate chip is bump-solder-bounded to the optical chip. The drawings also do not show opto-electronic tap-off components and sensor components that could be integrated on the chip for self-routing [6] of optical signals.

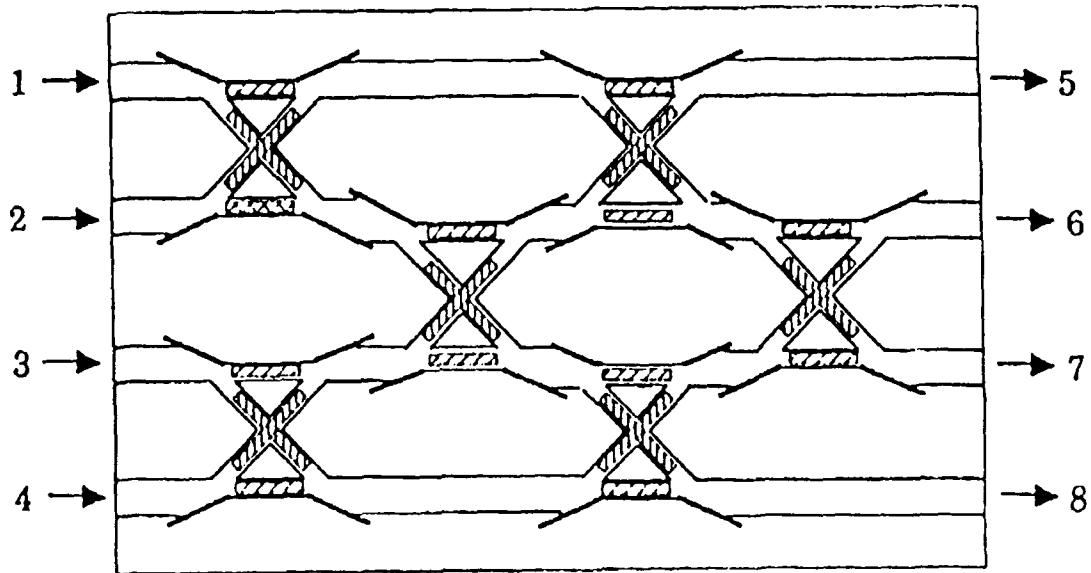


Fig. 3. 4 X 4 permutation-matrix switch using 2 X 2 crosspoints with 90° waveguide crossovers.

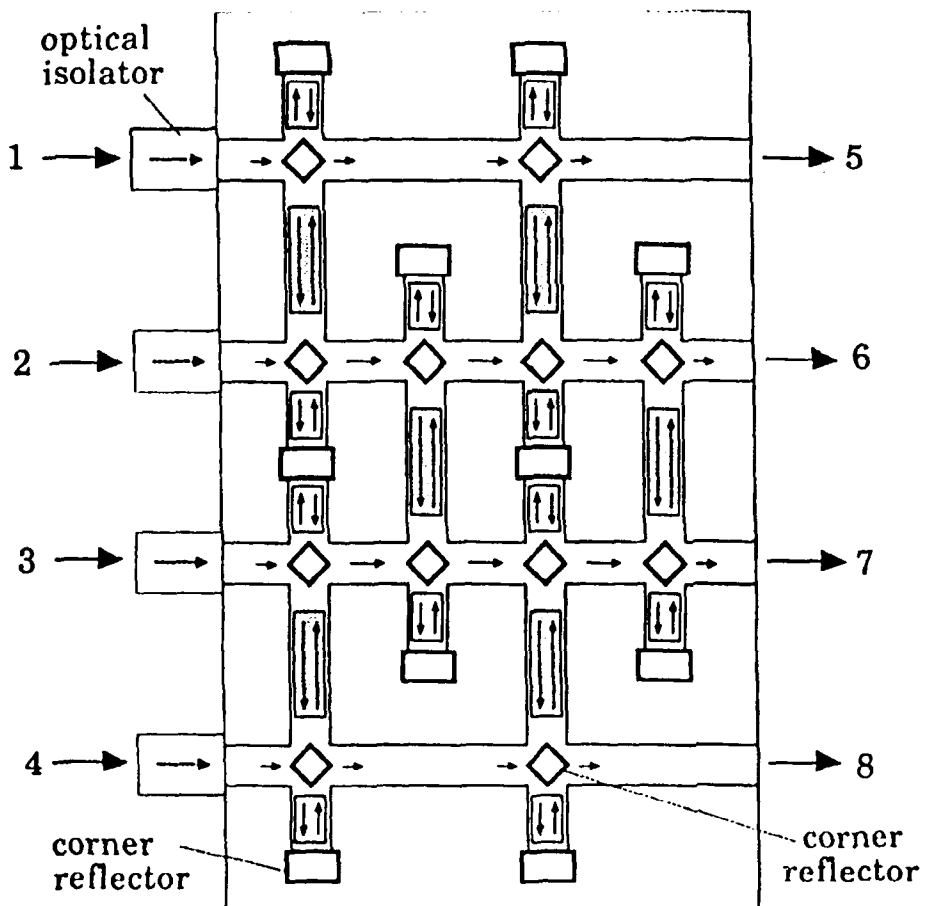


Fig. 4. 4 X 4 permutation-matrix switch using new bidirectional 2 X 2 switches.

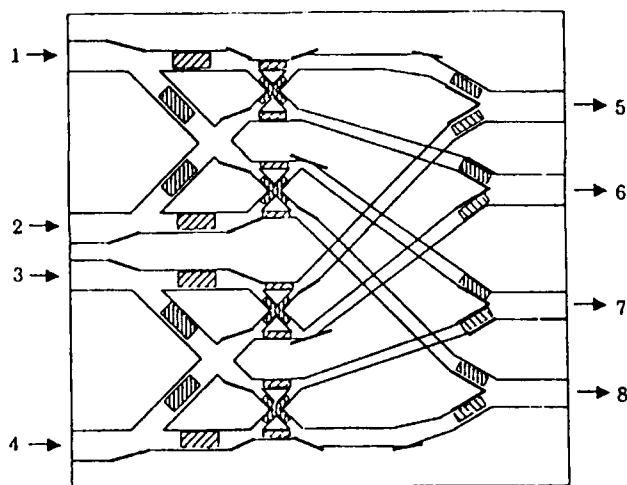


Fig. 5. 4 X 4 shuffle-exchange matrix switch with 1 X 2, 2 X 2, and 2 X 1 constituent switches.

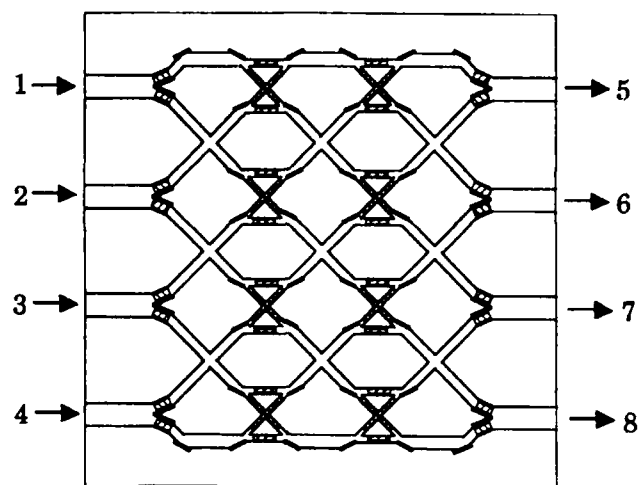


Fig. 6. 4 X 4 Sawaki-architecture matrix switch with 1 X 2, 2 X 2, and 2 X 1 components.

5. PROPOSED NETWORKS

To begin, let us look at the operation of the simplest device, the 1 X 4 binary tree switch as shown in Fig. 1. We have labeled the transparent channel waveguides (that require no current) and the active lengths of waveguide (that are switched between a ~ 6 dB amplifying condition and a ~ 30 dB attenuating condition, the latter requiring no current). Each of the right-angle waveguide bends is given a 45° internal-reflection facet mirror. Two successive divisions of the input optical beam (port 1) give four-fold splitting. A trio of 2-facet internal reflectors divides the guided beam. The four optical outputs (ports 2-5) can be individually selected by the four independent electroded regions.

Figs. 2-6 show 4 X 4 optical matrix switches, three of which are nonblocking networks. Fig. 2 is a centrally symmetric tree-structured network. We start with four 1 X 4 switches at input

ports 1-4 and four 4 X 1 switches at output ports 5-8. Each of these building-block switches is tree-structured like Fig. 1. However, unlike Fig. 1, each branch of the tree is deployed 90° to the preceding thicker branch. Having arrayed the 1 X 4s and the 4 X 1s around the perimeter of a square, we then interconnect the eight trees with a perfect-shuffle exchange network of channel waveguides, thereby completing the 4 X 4 matrix.

The permutation-matrix architecture is a simple architecture with simple addressing algorithms. This matrix is constructed from 2 X 2 exchange switches (crosspoints). There are only N stages and $(1/2)N(N - 1)$ crosspoints in an $N \times N$, although the network is blocking. For the 4 X 4, we draw upon the 2 X 2 switch design from Refs. 10 and 11, which includes a 90° waveguide crossover oriented at 45° to the input/output channels. The two outer arms of the 2 X 2 are addressed with a bias opposite to the crossover bias. Using transparent interconnects,

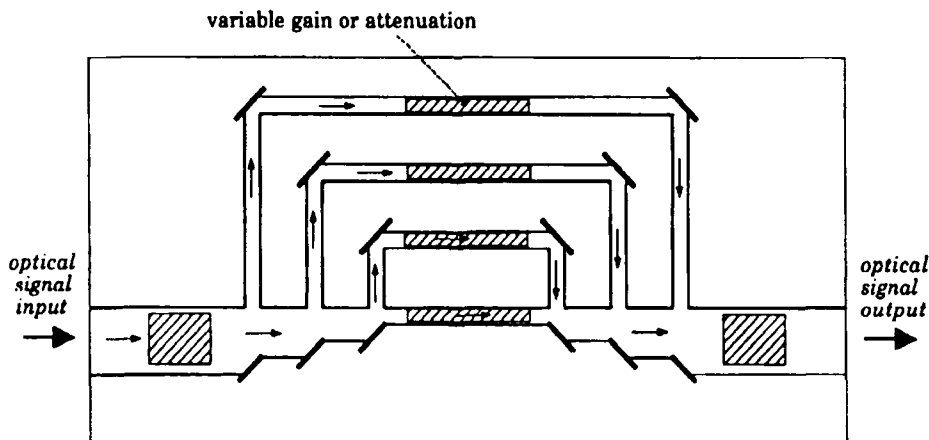


Fig. 7. Programmable optical transversal filter with finite impulse response.

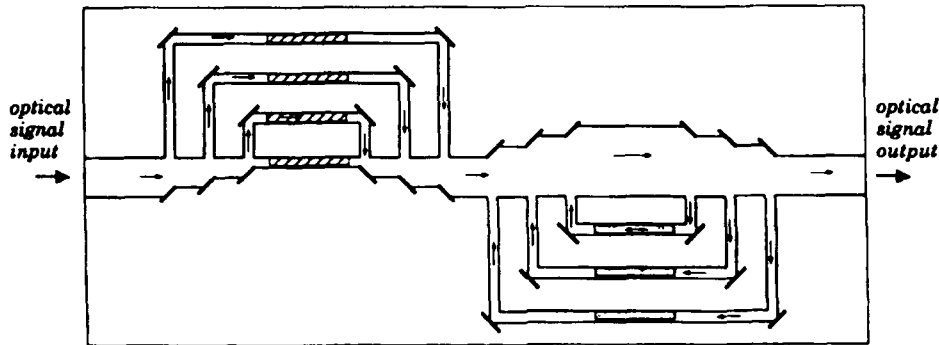


Fig. 8. Programmable optical transversal filter with infinite impulse response.

we cascade these 2×2 s to make the 4×4 optical switch of Fig. 3, a simple and cost-effective structure.

Recently, we conceived of a new 2×2 bidirectional active switch, and we found that those bidirectional exchange switches could be used to cast the $N \times N$ permutation matrix into a more compact form. Figure 4 shows the compact 4×4 matrix switch. Each 2×2 switch is oriented vertically with short horizontal input and output leads. Each 2×2 includes a pair of four-facet corner reflectors [14] and a pair of waveguide end reflectors (rectangular trenches). The middle waveguide segment in the 2×2 is equivalent to an unusual 0° waveguide crossover in which up-traveling and down-traveling light beams pass through each other (without interaction) in the same waveguide. The other two waveguide segments are folded up-and-down paths. An input light beam in the 2×2 is split into up-and-down beams. If the folded path is transmissive (forward bias), the end-mirror returns one beam to the same four-facet mirror, where it exits the switch. (Half of the light is deflected back to the input where it is absorbed by an optical isolator). If the fold is opaque (zero bias), the beam launched into the transmissive 0° crossover (forward bias) is sent to the adjacent 4-facet mirror where the beam goes out the adjacent port. So, the light is exchanged at the 2×2 's output ports if the folded guides are opaque and the crossover is transparent. Alternatively, light is not exchanged if the folds are clear and the crossover is opaque. As in prior-art 2×2 active crosspoints, the 3 dB splitting and combining losses in the bidirectional 2×2 are compensated by the active areas whose gain is approximately 6 dB.

Now, we turn to other architectures for a 4×4 matrix: the shuffle-exchange [15] and Sawaki [16] architectures. These networks use an interconnection of 1×2 , 2×2 , and 2×1 functional building blocks. The latter architecture was proposed by Sawaki et al. [16] as a rectangular rearrangement of an $N \times N$ crossbar. Figure 5 shows our version of an active 4×4 shuffle-exchange switch. The 1×2 switches are stacked in an input

column, the 2×2 s (of the 90° crossover type) are stacked in a central column, and the 2×1 s are stacked in an output column. A series of facet mirrors direct the guided light within the interconnect pattern. Some of the waveguide crossovers are at $\sim 60^\circ$ while others are at 90° . The facet pairs in the 2×1 switches are oriented at $\sim \pm 30^\circ$. This matrix is a fairly simple compact structure with 12 constituent switches.

Figure 6 shows our proposal for an active 4×4 switch based on Sawaki's architecture. There are 16 constituent switches: one column of 1×2 s, two columns of 2×2 s (of the 90° crossover type), and one column of 2×1 s. This network has a regular structure with 90° crossovers.

Our last two designs deal with programmable optical transversal filters. In the filters, light is routed among parallel spatial paths, but the primary function of these devices is optical signal processing rather than matrix switching. Goodman and Dias [17] have proposed filters with finite impulse response (FIR) or with infinite impulse response (IIR). Those authors are presently constructing filters in single-mode glass fibers, but, we show how FIR and IIR filters could be implemented in a monolithic integrated-optic chip using III-V semiconductors. In Figs. 7 and 8, the Goodman-Dias architecture serves as a guideline for the layout of agile active filter networks. Figures 7 and 8 have four active parallel optical paths of different lengths (time delays of T , $2T$, $3T$, $4T$), and the variable-gain region within each path offers adjustable tap weighting for the filter as well as optical amplification.

Figures 7 and 8 show the FIT and IIR filters, respectively. The filter's input channel is narrowed or expanded by a staircase of facets that extract or insert a series of optical signals. In Fig. 8, a set of $N - 1$ feed-backward channels with gain act as optical feedback paths for the first stage of delays. The second stage of delays recirculates the forward-traveling light pulses. As pulses circulate repeatedly in the filter, the various amplifiers maintain constant amplitude within the optical pulse train.

6. CONCLUSION

Monolithic active networks of III-V quantum-well channel waveguides offer some unique opportunities for building $N \times N$ space-division switches with zero insertion loss, excellent crosstalk isolation, large-scale integration, and reasonable injection currents for controlling the network.

7. REFERENCES

1. J.D. Evankow and R.A. Thompson, *IEEE J. on Selec. Areas in Commun.*, **6**, 1987-1095, Aug 1988.
2. R. Kishimoto, K. Yoshino and M. Ikeda, *IEEE J. on Selec. Areas in Commun.*, **6**, 1079-1086, Aug. 1988.
3. E. Eichen, W.J. Miniscalco, R. Boudreau, and P. Melman, *OE3.2, LEOS'90 Tech. Dig.*, Boston, Nov. 1990.
4. M. Ikeda, *Elect. Lett.*, **17**, 899-900, 1981.
5. M. Ikeda, *Trans. IECE Japan*, **E69**, 1072-1074, 1986.
6. R. Kishimoto and M. Ikeda, *IEEE J. on Selec. Areas in Commun.*, **6**, 1248-1254, Aug. 1988.
7. L.H. Thylen, U.S. Patent 4,717,228, issued Jan. 1988.
8. C.J. Setterlind and L. Thylen, *IEEE J. Quantum Elect.*, **QE-22**, 595, 1986.
9. L. Thylen, P. Granstrand and A. Djupsjobacka, **PDP-8**, *Proc. First, Top. Meet. on Photonic Switching*, Incline Village, NV, 1987.
10. R.A. Soref and K.Y. Lau, *SPIE Proceedings*, Vol. **993** (Integrated Optical Circuit Engineering IV), 126-136, 7 Sept. 1988. (U.S. Patent 5,004,447, issued Apr. 2, 1991; U.S. Patent 5,013,113, issued May 7, 1991).
11. I.H. White, J.J.S. Watts, J.E. Carroll, C.J. Armistead, D.J. Moule and J.A. Champelvier, *Elect. Lett.* **26**, 617-618, 10 May 1990.
12. S. Lindgren, M.G. Oberg, J. Andre, S. Nilsson, B. Broberg, B. Holmberg, and L. Backbom, *IEEE J. of Lightwave Tech.* **8**, 1591-1595, Oct. 1990.
13. T. Tang, P. Swanson, C. Herzinger, L.M. Miller, T.M. Cockerill, R.P. Bryan, T.A. DeTemple, and J.J. Coleman, *Appl. Phys. Lett.*, **57**, 741-743, 20 Aug. 1990.
14. W.J. Grande, J.E. Johnson and C.L. Tang, *LEOS'90 Tech. Dig.*, **OE10.4**, Boston, Nov. 1990. [See also *Appl. Phys. Lett.*, **57**, 2537-2539, 10 Dec. 1990].
15. J. Skinner and C.H.R. Lane, *IEEE J. on Selec. Areas in Commun.*, **6**, 1178-1185, Aug. 1988. [See also C.J. Smyth, *Ibid*, 1060, Fig. 16].
16. I. Sawaki, T. Shimoe, H. Nakamoto, T. Iwama, T. Yamane and H. Nakajima, *IEEE J. on Selec. Areas in Commun.*, **6**, 1267-1272, Aug. 1988.
17. J.W. Goodman and A.R. Dias, *Final Report on RADC/ES contract Number F19628-89-C-0114 (Phase 1)*, Dec. 1989 (unpublished).

N X N AND 1 X N SWITCHING WITH CHIRAL NEMATIC LIQUID CRYSTALS

Richard A. Soref, Electromagnetics & Reliability Directorate, Rome Laboratory

Published in Applied Optics, Vol. 30, No. 2, 10 January 1991

ABSTRACT - New designs are presented for 4 X 4, 1 X 4, and 1 X 16 electro-optical switches that utilize chiral nematics.

A recent publication by Shankar *et al.*¹ reported a new 2 X 2 fiber optic switch using selective reflection from a layer of chiral nematic liquid crystal (CLC) and voltage-variable retardation from homogeneous layers of nematic liquid crystal (NLC). The purpose of this Technical Note is to show how Shankar's structure can be extended to higher-order switching functions. New designs for 4 X 4, 1 X 4, and 1 X 16 electro-optical (EO) switches are presented.

The principle of cascading and interconnecting 2 X 2 elements in a rectangular array is illustrated in Fig. 1, which shows a proposed 4 X 4 permutation switch. Here all the optical paths lie on one plane. The input and output beams are unpolarized. A disadvantage of Fig. 1 is that $3(N - 1)$ liquid crystal layers are required. (An alternative switch that uses fewer layers is discussed.) Each passive CLC layer selectively reflects right circular polarized (RCP) light and transmits left circular polarized (LCP) light, a beam splitting operation discussed in Ref. 1. Each NLC layer is sandwiched between glass plates that are coated with transparent electrode material such as indium-tin oxide (ITO). Photolithographic etching of the ITO is used to bracket each NLC layer in Fig. 1 with several pairs of localized electrodes.

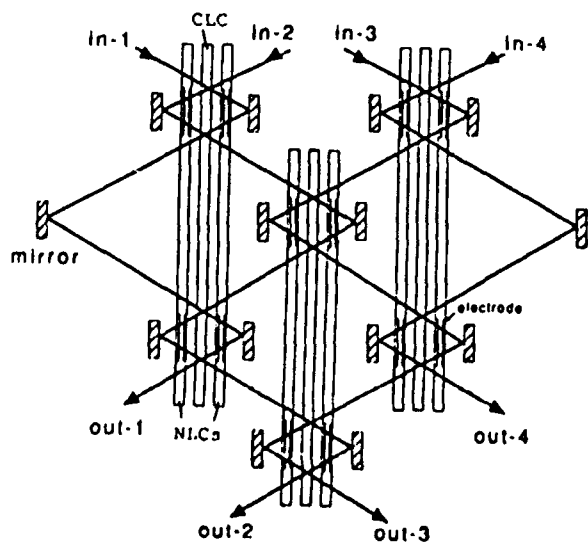


Fig. 1. Layout of EO 4 X 4 permutation matrix switch. This cross-sectional side view shows liquid crystal layers, electrodes, mirrors, and collimated light paths.

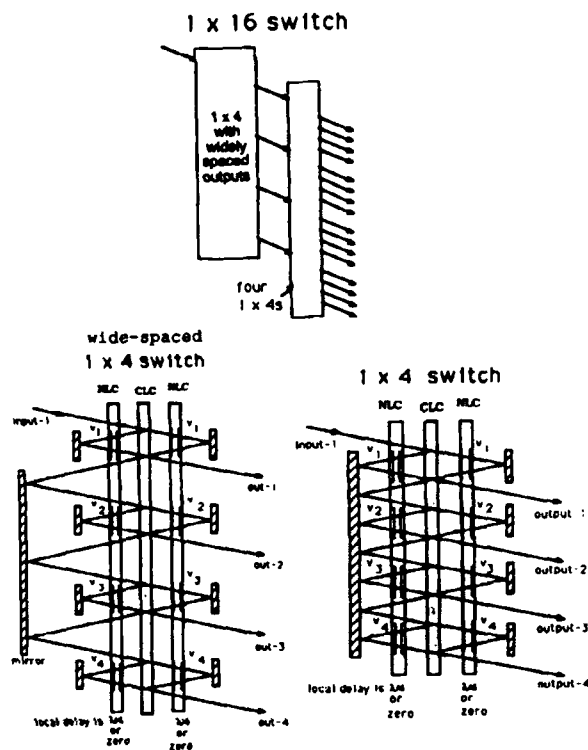


Fig. 2. Schematic diagram of a 1 X 16 EO switch and its constituent 1 X 4 switches. The lower drawings show cross-sectional side views of wide spaced and compact 1 X 4 switches. The LC layers, electrodes, mirrors, and light paths are illustrated.

Within a 2 X 2 cell in Fig. 1, the same voltage is applied to electrode pairs in both NLC layers. However, the six 2 X 2 cells in the Fig. 1 matrix are addressed by six independent voltage sources (not shown in Fig. 1 to keep the diagram simple). Each 2X2 cell has two switching states. To select either state, a voltage of either $V_a \approx 2V_{rms}$ or $V_b \approx 6V_{rms}$ is applied to the NLCs. At $V = V_a$, the NLC has parallel alignment, which produces a quarterwave delay in the light transmitted through the NLC. At $V = V_b$, the NLC becomes homeotropic (perpendicular), which changes the delay to zero delay. On reflection from the 180° mirror and passage through two zero delay NLCs, an RCP beam is converted to LCP and vice versa. Alternatively, a double pass through a quarterwave NLC layer plus the 180° mirror retardation leaves the RCP and LCP unchanged. Hence the NLC addressing allows RCP and LCP beams to be recombined at their second CLC encounter as either a forward-traveling or reverse-traveling unpolarized beam.

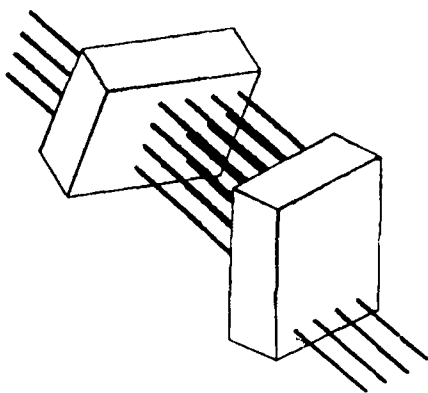


Fig. 3. Layout of a 4 X 4 matrix switch based on the 1 X 4 switches of Fig. 2.

We note in Fig. 1 that the input and output beam as well as the interstage beams pass through parallel aligned ($V = 0$) regions of nematic liquid. This is acceptable because the unpolarized light beams are not affected by the homogeneous liquid. In addition to the Fig. 1 architecture, it is possible to construct a chiral 4 X 4 crossbar matrix switch. However, the CLC crossbar does not appear to be practical because it requires twenty-one liquid layers for the 4 X 4 switch and $3(2N - 1)$ layers for an N X N device.

Our proposed 1 X 4 switch is shown in Fig. 2 (lower diagrams). Here only three LC layers are needed because the architecture is a folded unbalanced tree. Again we split and recombine collimated RCP and LCP components using the CLCs, mirrors, and tunable NLCs. There are four independent voltage sources $V_1 \dots V_4$, which drive four sets of transparent localized electrodes spaced at regular intervals on the NLCs.

Each 1 X 2 switching cell in Fig. 2 is actuated by a two-level supply, V_a or V_b for each of the four sources $V_1 \dots V_4$. This gives a localized delay of $\lambda/4$ or zero at each NLC pair, which enables the combined RCP and LCP beams to travel to the next 1 X 2 element or exit the 1 X 4 switch at that point. The upper diagram in Fig. 2 shows a 1 X 16 switch comprised of a widely spaced 1 X 4 switch that feeds a quartet of compact 1 X 4 switches. The four 1 X 4s are integrated end to end in the same three LC layers.

Finally, in Fig. 3, we show a nonblocking 4 X 4 matrix switch that relies on replicated versions of the 1 X 4 switches in Fig. 2. The matrix uses a 3-D architecture similar to the 3-D perfect shuffle switch in Ref. 2. The 4 X 4 switch consists of a 4 X 16 switch in optical cascade with a 16 X 4 switch. The 16 X 4 is spatially rotated 90° with respect to the 4 X 16, so that rows of the 4 X 16's output array are mapped onto columns of the 16 X 4's input array. Both the 4 X 16 and the 16 X 4 are constructed monolithically in three LC layers using a plane-parallel array of four 1 X 4s. Thus there are only six LC layers in this N X N matrix switch.

The collimated light beam devices of Figs. 1-3 can be converted easily to fiber optic switches by inserting a quarter-pitch grinrod lens at each input port and at each output port in Figs. 1-3. Each grinrod would be pigtailed to a fiber.

References

1. N.K. Shankar, J.A. Morris, C. P. Yakymyshyn, and C.R. Pollock, "A 2 X 2 Fiber Optic Switch Using Chiral Liquid Crystals," *Photon. Technol. Lett.* **2**, 147-149 (1990).
2. R. A. Soref, "Electrooptic 4 X 4 Matrix Switch for Multimode Fiber-Optic Systems," *Appl. Opt.* **21**, 1386-1393 (1982).

OPTICAL WAVEGUIDING IN Si/Si_{1-x}Ge_x/Si HETEROSTRUCTURES

F. Namavar, Spire Corporation

R.A. Soref, Electromagnetic & Reliability Directorate, Rome Laboratory

Published in Journal of Applied Physics, Vol. 70, No. 6, 15 September 1991

Abstract – Waveguiding at 1.3 μm has been observed in a submicrometer strained layer of Si_{1-x}Ge_x sandwiched between a Si capping layer and a Si substrate. This structure is a precursor of the waveguided Si/Si_{1-x}Ge_x/Si heterojunction bipolar transistor. The buried alloy layer, grown by chemical vapor deposition, had a Ge content of either 8% or 18%. The SiGe layer was ~1500 Å thick beneath a 2- μm Si cap. The observed TE₀ mode profile agreed with theory.

The ultrafast Si/Si_{1-x}Ge_x/Si heterojunction bipolar transistor (HBT) now being developed for large-scale integration¹ has an optical counterpart: the waveguided HBT proposed and analyzed by Lareau, Friedman, and Soref.² This elongated transistor offers high-speed optical phase and amplitude modulation by carrier injection or depletion in the Si_{1-x}Ge_x base layer. (A waveguided HBT has already been demonstrated in III-V semiconductors.³) It is shown in this communication that the infrared guidedmode power will peak in the Si_{1-x}Ge_x base region of the Si/Si_{1-x}Ge_x/Si HBT, even though that region is only 1200-1500 Å thick. We present theoretical and experimental results on the 1.3 μm waveguide profile in Si/Si_{1-x}Ge_x/Si grown by high-temperature chemical vapor deposition (CVD). To our knowledge, this is the first demonstration of waveguiding in a buried, submicrometer layer of Si_{1-x}Ge_x in Si.

Figure 1 illustrates the waveguide samples. Epitaxial Si/Si_{1-x}Ge_x/Si thin-layer structures were grown by CVD on Si(100) substrates using an Applied Materials 1200 vertical epitaxy reactor. Silane (SiH₄) and germanium tetrachloride (GeCl₄) were used as the Si and Ge sources, respectively. SiGe layers were grown with concentrations from 0-20 at. % and with layer thicknesses from 1000 to 1500 Å. The growth temperature typically ranged from 800 to 1000°C and the growth rate varied from 0.5 to 1.0 $\mu\text{m}/\text{min}$, both depending upon Ge concentration. The growth rate for the 2- μm Si capping layer was about 1 $\mu\text{m}/\text{min}$. Waveguiding was attempted and observed in two groups of samples: one batch with $x = 0.08$, and the other with $x = 0.18$.

Si/SiGe/Si samples were studied using RBS/ channeling, transmission electron microscopy (TEM), Raman spectroscopy, and high-resolution x-ray diffractometry. Also, cross-sectional electron-diffraction measurements at the SiGe/Si interfaces were performed to determine changes in the d spacing of the SiGe layer with respect to the Si.

The defect density in a sample with 8% Ge was less than 10^4 cm^{-2} , as determined by plan view TEM of a 100 X 100-

μm^2 area.^{4,5} High-resolution electron and x-ray diffraction as well as Raman spectroscopy⁶ clearly indicate that the Si_{0.92}Ge_{0.08} layer is nearly 100% strained. Raman and electron-diffraction results for a sample with 18% Ge show that the Si_{0.82}Ge_{0.18} layer is 80% strained and 20% relaxed. Small area plan view TEM of the 18% sample shows no defects; a large area has yet to be evaluated. We believe that the SiGe layers in both types of samples are commensurately strained because identical strained layers have been used to confine the threading dislocations in SIMOX material.⁷

In theory, the Si_{1-x}Ge_x layer will be coherently strained if its thickness t is less than a critical value t_c given by the empirical relation $t_c = t_0 x^{-3.6}$, where $t_0 = 8.2 \text{ Å}$ and x is the Ge fraction.⁸ Thus, our samples $x = 0.08$, $t = 1200 \text{ Å}$ and $x = 0.18$, $t = 1500 \text{ Å}$ are below the critical thickness and should be strained. The experiments agreed with this theory.

The optical index of refraction of coherently strained and bulk unstrained Si_{1-x}Ge_x alloy material is plotted in Fig. 2 versus the mole fraction of Ge. We estimated the index values from the band-gap interpolation formula presented in Ref. 2 using strained-layer band-gap values for the top curve and bulk unstrained gaps for the lower curve. The SiGe index can be written as $n(\text{Si}_{1-x}\text{Ge}_x) = n(\text{Si}) + \Delta n(x)$, and for $x < 0.25$, the linear approximation $\Delta n(x) = ax$ is useful. An oscillator model for $n(\text{SiGe})$ was introduced by Soref and Perry⁸ who found that $\Delta n(x) = 0.33x$. This index increase is smaller than the $\Delta n(n) = 0.8x$ result given by the Fig. 2 band-gap model for relaxed material. A red-shift model for $n(\text{SiGe})$ presented in Ref 9 gave an even smaller index enhancement, $\Delta n(x) = 0.09x$, for unstrained alloys. Turning to strained layers, the Fig. 2 index difference between a strained alloy core and the Si claddings ($\Delta n = 1.45x$) ranges from 0.015 at $x = 0.01$ to 0.36 at $x = 0.25$; hence, the waveguide designer has a choice of strongly or weakly confining guides. An example of the latter is the Si/Si_{0.99}Ge_{0.01}/Si waveguide which would be suitable for a mode extinction modulator because $\Delta n \sim 0.01$.

The planar Si/Si_{1-x}Ge_x/Si guide is symmetric and the $m = 0$ mode (TE₀ or TM₀) is not cut off, even though the SiGe core layer thickness is only ~10% of the free-space optical wavelength. Classical theory, and the indices of Fig. 2, indicate that the guide is single moded at $t \approx 1500 \text{ Å}$ since the $m = 1, 2, 3, \dots$, modes are cut off for $t < 0.46 \mu\text{m}$ in Si_{0.82}Ge_{0.18} and for $t < 0.7 \mu\text{m}$ in Si_{0.92}Ge_{0.08}. The multilayer waveguide theory of Soref and Ritter,¹⁰ together with Fig. 2, was used to calculate the TE₀

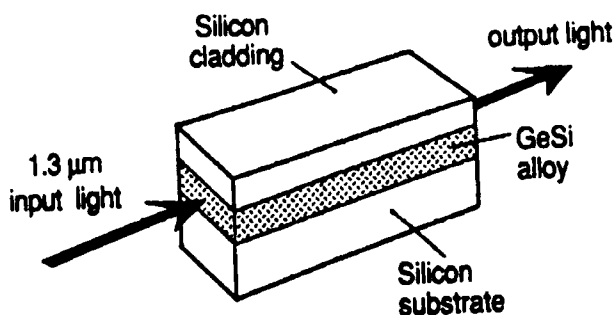


Fig. 1. Perspective view of Si/Si_{1-x}Ge_x/Si heterostructure waveguide.

and TM₀ intensity profiles in the four-layer air/Si/SiGe/Si guide. The result for TE₀ at $\lambda = 1.3 \mu\text{m}$ is shown in Fig. 3 for the examples of $x = 0.08$ and 0.18 .

Our samples were 8-15 mm long. For end-fire coupling, the sample ends were polished with diamond paste. Polarized light from a 1.3- μm semiconductor laser was focused into one end of the sample, and the light emerging from the waveguide was imaged onto an infrared vidicon. A video line analyzer was used to determine the optical power distribution across the waveguide.

For the 8% Ge samples, the numerical aperture (NA) of the guide was not large enough to capture all of the incoming light focused by the 0.66 NA 40X lens, and some light traveled unguided in the substrate. At the output, the depolarized substrate light complicated the loss measurement. We did not measure the propagation loss in these samples. However, because our samples were not intentionally doped, we anticipate that the losses will be similar to the 2-3 dB/cm losses measured for non-buried SiGe/Si in Ref. 9.

As shown in Fig. 4, the experimental TE₀ mode widths (FWHM) of 0.7 and 0.35 μm for the 8% and 18% samples are in fairly good agreement with the theoretical curve obtained from both the band-gap model of Fig. 2 and the multilayer the-

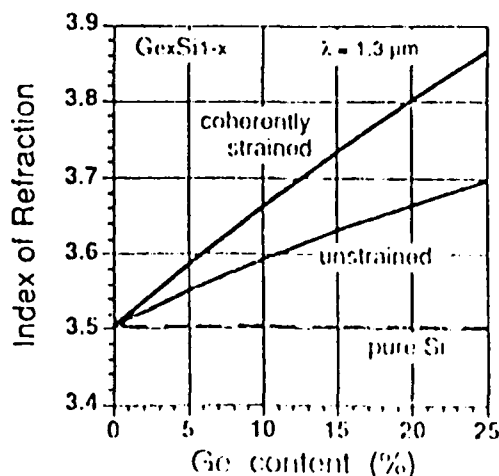


Fig. 2. Optical index of refraction of Si_{1-x}Ge_x at $1.3 \mu\text{m}$ as a function of Ge content.

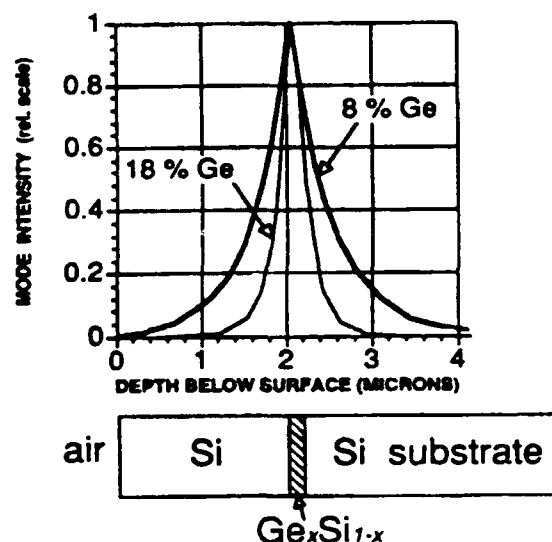


Fig. 3. Calculated mode-intensity profile of a Si/Si_{1-x}Ge_x/Si planar guide with a 0.15- μm buried Si_{1-x}Ge_x alloy layer and a 2- μm Si cap layer

ory of Ref. 10. There is little difference between the widths of TE₀ and TM₀. We see from Figs. 3 and 4 that more than 50% of the guided optical energy is located in the upper and lower Si claddings. Thus, in an HBT, the free-carrier absorption loss of the doped emitter and doped collector regions will play a role in determining the waveguide propagation loss. In Ref. 2, it is estimated that the TE₀ loss reaches nearly 20 dB/cm in a fully doped npn device at 1.55 μm . An actual HBT would have a Si cap layer much thinner than the 2- μm cap used here (2 μm was

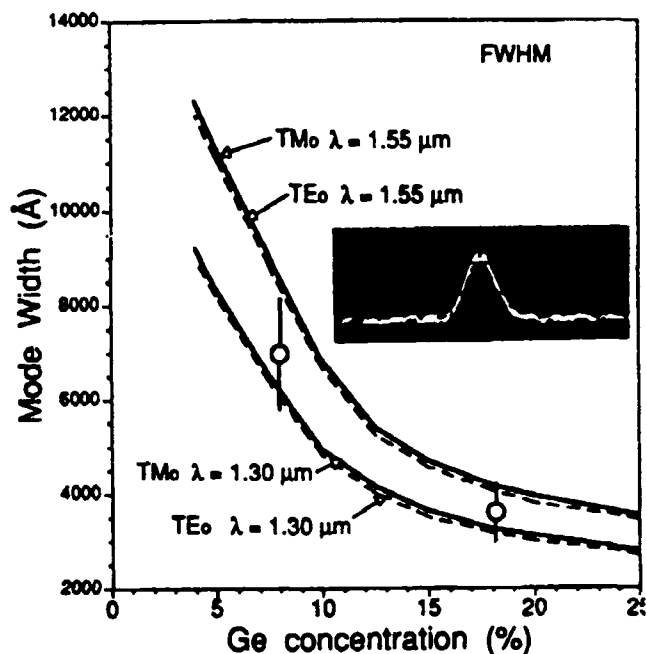


Fig. 4. Theory (---) and experiment (O) for the mode-intensity width as a function of x in the Si/Si_{1-x}Ge_x/Si waveguide of Fig. 3. The experimental points are for TE₀ at $1.3 \mu\text{m}$. The photo insert shows the observed mode profile for the 18% Ge sample.

chosen to facilitate our waveguide measurements), but the guided mode would still fill the transistor in the manner of Fig. 3.

In summary, we have developed CVD growth techniques to produce high-quality Si/Si_{1-x}Ge_x/Si heterostructures that are precursors of the waveguided HBT. We observed the first waveguiding in submicrometer Si_{1-x}Ge_x buried in Si and the 0.35-0.70- μ m mode widths agreed with theoretical predictions.

The authors are grateful to M.C. Blythe and A.O. DeSilvestre of Spire Corporation for their help in growing the materials. Work at Spire was supported in part by an SBIR phase-I grant from the National Science Foundation.

REFERENCES

1. J.M.C. Stork, G.L. Patton, B.S. Meyerson, J.H. Comfort, E.F. Crabbe, D.L. Harame, and J.Y.C. Sun, paper 1A-2, IEEE Device Research Conference, Santa Barbara, CA, 25 June 1990.
2. R.D. Lareau, L. Friedman, and R.A. Soref, *Electron. Lett.* **26**, 1653, (1990).
3. Y. Okada and K. Tada, *J. Appl. Phys.* **69**, 73 (1991).
4. F. Namavar, E. Cortesi, J.M. Manke, N.M. Kalkhoran, E.A. Johnson, O.A. DeSilvestre, M.C. Blythe, M.H. Johnson, and D.L. Perry, *Proceedings of the Second International Conference on Electronic Materials*, Newark, NJ, 17 September 1990, p. 403.
5. F. Namavar, E.P. Kvan, D.L. Perry, E. Cortesi, N.M. Kalkhoran, and J.M. Manke, *Materials Research Society Symposium on Electronic, Optical, and Device Properties of Layered Structures*, edited by Hayes and Hybrsten, Boston, MA, 26 November, 1990, pp. 249-252.
6. F. Namavar, N.M. Kalkhoran, J.M. Manke, E. Cortesi, C.H. Perry, and D.M. Pease, *Mater. Res. Soc. Symp.*, **220**, 285 (1991).
7. F. Namavar, E. Cortesi, D.L. Perry, E.A. Johnson, N.M. Kalkhoran, J.M. Manke, N.H. Karam, R.F. Pinizotto, and H. Yang, *Mater. Res. Soc. Symp.*, **198**, 503 (1990). SIMOX refers to separation by implantation of oxygen.
8. R.A. Soref, C.H. Perry, *J. Appl. Phys.* **69**, 539 (1991).
9. R.A. Soref, F. Namavar, and J.P. Lorenzo, *Opt. Lett.* **15**, 270 (1990); see also *SPIE Proc.* **1177**, 175 (1989).
10. R.A. Soref and K.J. Ritter, *Opt. Lett.* **15**, 792 (1990).

PHOTOREFRACTIVE TIME CORRELATION MOTION DETECTION

Jehad Khoury, Vincent Ryan, and Mark Cronin-Golomb, Electro-Optical Technology Center, Tufts University
Charles Woods, Electromagnetics & Reliability Directorate, Rome Laboratory

Published in Optics Communications, Vol. 85, No. 1, 15 August 1991

Abstract - A photorefractive time correlation motion detector is demonstrated. This device overcomes the material response time limitation associated with other photorefractive motion detectors. Two techniques have been proposed to increase and tune the bandwidth of the motion detection device.

1. INTRODUCTION

Motion detection has been achieved, in the last few years, by using photorefractive novelty filters. Some of these novelty filters need phase images as an input and others can work with amplitude and phase images [1-3]. One significant shortcoming in all of these novelty filters is that none of them can respond to sustained fast motions which exceed the limitation imposed by the response time of the material. In this paper we present a time correlation motion detector which can detect moving phase objects without any limitations placed on it by the response of the material.

The time correlation motion detector operates through nearly degenerate four-wave mixing where a reference beam and a signal beam interact within a photorefractive medium to generate a hologram. The hologram is read by a beam that is (i) incoherent with respect to the two writing beams, and (ii) counterpropagating with respect to the reference beam. The diffracted readout beam travels in the phase conjugate direction of the signal beam. In this scheme, a fast phase modulation is placed on the reference beam so the hologram is destroyed and no phase conjugate beam is generated. However, by introducing moving phase objects in the signal beam the phase conjugate reappears.

The theory of this method, developed from time varying photorefractive theory for a general signal, shows that the operation results from the cross correlation in time between the two input signals. The sensitivity of this device to object velocities is a function of a system dependent resonant frequency response which can be tuned through the use of an electric field applied to the crystal and through changing the phase modulation frequency in the reference beam.

We demonstrated this device using a square wave temporal signal to piezoelectrically modulate the phase in the reference beam. In addition we introduced two techniques to increase the bandwidth of the motion detector.

2. THEORY

Consider three input beams of the same wavelength A_1 , A_2 , and A_4 intersecting within a photorefractive medium as shown in Fig. 1. A_1 and A_4 are coherent so they combine to induce a hologram within the material: while A_2 and A_3 are coherent with themselves, but not with A_1 and A_4 .

Mathematically the amplitudes are

$$A_1 = E_1(t) \exp [i(k_1 r - \omega t)], \quad (1)$$

$$A_2 = E_2(t) \exp [i(k_2 r - \omega t)], \quad (2)$$

$$A_4 = E_4(t) \exp [i(k_4 r - \omega t)]. \quad (3)$$

In the steady state case (i.e. beam A_1 and A_4 not varying in time) a hologram is written, and a phase conjugate is generated. This phase conjugate is counterpropagating with respect to beam A_4 . Treatment of time varying input beams necessitates the solution of the photorefractive space charge field in the dynamic regime. For the sake of simplicity we will assume that the total intensity of the beams incident on the crystal is constant. (i.e. Any amplitude variation in the input beams is considered small compared to the summation of the intensities of all the beams.)

The development of the space charge field (E_{sc}) within the crystal is described by [4.5]

$$\frac{\partial E_{sc}}{\partial t} + \frac{E_{sc}}{\tau} = \frac{G}{\tau} \frac{A_1(t) A_4^*(t)}{I_0} \quad (4)$$

where τ is the response time for grating formation, G is a parameter related to the photorefractive characteristics and I_0 is the total intensity. Eq. (4) assumes that the readout beam is sufficiently weak so that it does not affect the grating.

The general solution of eq. (4) is

$$E_{sc}(t) = C e^{+1/\tau} + e^{+1/\tau} \int_0^t \frac{G A_1(t) A_4^*(t)}{\tau} e^{-1/\tau} dt. \quad (5)$$

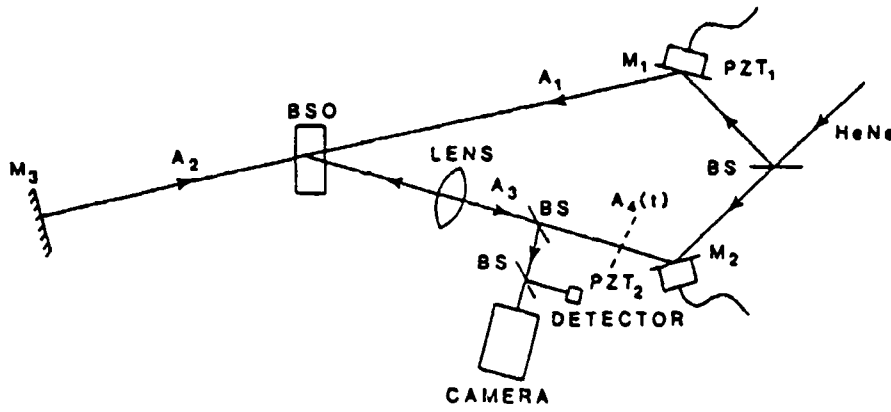


Fig. 1. Schematic diagram of the experimental arrangement.

Eq. (5) can be treated by assuming that $A_1(t)$ and $A_4(t)$ are signals with Fourier transforms such that

$$A_1(t) = \int_{-\infty}^{\infty} S_1(\omega_1) \exp(-i\omega_1 t) d\omega_1, \quad (6)$$

$$A_4(t) = \int_{-\infty}^{\infty} S_4(\omega_2) \exp(-i\omega_2 t) d\omega_2. \quad (7)$$

Substituting eqs. (6) and (7) into eq. (5) yields

$$E_{sc}(t) = \frac{G}{l_0 \tau} \int_{-\infty}^{\infty} \int_{-\infty}^{\infty} \frac{S_1(\omega_1) S_4^*(\omega_2)}{-i(\omega_1 - \omega_2) + 1/\tau} \times \exp[-i(\omega_1 - \omega_2)t] d\omega_1 d\omega_2 \quad (8)$$

in the diffusion limit where τ is real number. With a dc electric field applied to the crystal, τ becomes complex [4]:

$$1/\tau = 1/\tau_1 + i\omega_g. \quad (9)$$

This yields

$$E_{sc} = [(G/I_0)(1/\tau_1 + i\omega_g)]$$

$$\times \int_{-\infty}^{\infty} \int_{-\infty}^{\infty} \frac{S_1(\omega_1) S_4^*(\omega_2)}{-i(\omega_1 - \omega_2 + \omega_g) + 1/\tau_1} \times \exp[-i(\omega_1 - \omega_2 + \omega_g)t] d\omega_1 d\omega_2. \quad (10)$$

In the context of motion detection, eq. (10) signifies the following. When motion of the object induces a temporal frequency component in the signal beam that matches the difference in carrier frequencies of the two writing beams, a dc component to

the space charge field described by eq. (10) above will be induced. The associated photorefractive grating reveals the motion by diffraction of the read out beams. The applied field has two additional effects: first it increases the diffraction efficiency and second it shifts the operating point by ω_g .

In order to enlarge the bandwidth of the motion detector, it is necessary to increase the overlap between the motion spectrum $S_4(\omega_2)$ and the grating destroying spectrum of the reference beam $S_1(\omega_1)$. This may be achieved in at least two ways. For example we can choose $S_1(\omega_1)$ to be a bandlimited spectrum of white noise. Another method is to choose $S_1(\omega_1)$ to be a comb function of frequencies which are separated by intervals equal to $(2\pi)/\tau$ (which is twice the spread in the spectrum associated with finite material response). This choice for a comb separation was made to prevent beating between signal components riding on neighboring comb teeth, i.e.

$$S_1(\omega_1) = A \sum_{n=-\infty}^{\infty} \delta(\omega_1 + 4\pi n/\tau). \quad (11)$$

Increasing the bandwidth of the device in these ways will decrease the reflectivity. To explain this, we consider the second technique. With $S_1(\omega_1)$ depicted as a comb function, assume without loss of generality that the output is generated from the overlap of the first delta function with the signal spectrum. It is clear that the other delta functions will tend to destroy the grating and decrease the reflectivity.

3. EXPERIMENTAL RESULTS

Fig. 1 shows the experimental arrangement used. Essentially, it was the standard configuration for four-wave mixing modified by two piezoelectric transducers (PZT). The two PZTs

were driven by two separate function generators. The source was a HeNe laser operating in multilongitudinal mode with an output power of 30 mW and wavelength $\lambda = 632.8$ nm. The beam was expanded to a diameter of 2 mm. Beam splitter BS1 divided the source beam into two beams A_1 (reference beam) and A_4 (signal beam). Read beam A_2 was generated by retroreflection of A_1 from mirror M3. A lens ($f = 100$ mm) was used in beam A_4 to image the input object plane to the BSO. The measured intensities of the beams I_1 , I_2 , I_4 were 10 mW, 5 mW, and 7 mW respectively.

This experiment, as previously mentioned, relied on destroying the grating through rapid phase variations in the beams. We chose π square phase shifts for our modulation to maximize the erasing tendency of the modulation as in coherent erasure techniques [6-8]. For static objects under continuous flipping of the phase, the phase conjugate beam intensity will average to zero. However, for moving objects, the phase conjugate will not average to zero, reappearing under the constraints of time correlation detection.

Fig. 2 illustrates the basic operation of the device when the PZT in the reference beam (PZT₁) was driven with a square wave of voltage V_π to produce π phase shifts at a frequency of 416 Hz. For a comparison Fig. 2a shows the full stationary phase conjugate beam, almost saturating the camera, and Fig. 2b illustrates the result while operating PZT₁ with a square wave, almost no conjugate appears. However, by introducing arbitrary phase shifts in the signal beam (accomplished by moving a microscope slide in the beam), the grating inside the photorefractive was no longer washed out and the phase conjugate beam reappeared, as shown in Fig. 2c. It is clear then that phase changes in the signal beam may be detected and observed in the output image plane.

We studied the performance of this device when a resolution chart was placed in the input object plane. Fig. 3a is the conjugate image of the chart while operating a square wave signal on PZT₁. When the chart was twisted in the plane, a transient image appeared which disappeared with the static chart. This is shown in Fig. 3b. (The horizontal lines in the figures are video scan lines.) However, for transverse motion of the chart in the input plane nothing was detected because the resultant phase variations were not sufficiently fast.

We were able to observe the transverse amplitude motions, by attaching a phase diffuser to the resolution chart. With this technique any transverse motion caused amplitude and phase variations. These results were extremely smeared due to the fast motions; therefore we present the results with the diffuser alone.

Fig. 4a is the conjugate image of the diffuser. Fig. 4b shows the results under conditions similar to those in Fig. 3a. When

the diffuser is translated in any direction, a phase conjugate image appears as shown in Fig. 4c. The irradiance of the output image is very much dependent on the speed of motion. Slow translations were very faint. With increasing speed the output irradiance increased until the frequencies of the variations in the input image no longer matched the reference beam frequencies. It is possible to design these systems to measure motion of certain speeds exceeding some present threshold that has no upper bound.

The last experiment we performed was to measure the effect of the bandwidth increase on the device reflectivity. First we operated PZT₁ in the reference beam with a square wave at a frequency of $f_1 = 200$ Hz (which was the minimum frequency capable of destroying the grating). We then introduced continuously increasing phase delays in the signal beam (again by twisting a microscope slide) and measured the resulting output intensity.

We operated the device by driving a second PZT (PZT₂) in the signal beam with a square wave at $f_2 = 416$ Hz (which was also capable of destroying the grating with or without modulation of PZT₁). It was expected that this would increase the bandwidth while decreasing the reflectivity. We only examined the effect of this process on the reflectivity without concern to the effect on bandwidth (due to a lack of a third modulator). Our results show that introduction of the second PZT produced a factor two decrease in the intensity compared to the experiment with only one PZT. The reason is explained below.

The amplitude of the reference beam A_1 resulting from modulating its phase with a square wave is

$$A_1(t) = \frac{4 |A_1|}{\pi} \sum_{m=0}^{\infty} \frac{\sin[(2m+1)(\omega_1 t)]}{2m+1} \quad (12)$$

The fundamental frequency of the reference beam A_1 , and hence the interference pattern is $f_1 = 200$ Hz. When the frequency of the phase delays in the signal beam A_4 is contained within this spectrum a phase conjugate beam is generated with intensity proportional to $(2/\pi)^2$. When the second PZT is introduced, mixing of the signal and reference produced large harmonics in the interference pattern at the sum and difference of the signal and reference fundamental frequencies, $f_2 + f_1 = 616$ Hz and $f_2 - f_1 = 216$ Hz, respectively. Here when the frequency of the phase delays is contained within this expanded spectrum, particularly when it is at the fundamental difference frequency $f_2 - f_1$, the output beam had an intensity proportional to $(4/\pi^2)^2$. Taking a ratio of the intensities for both cases we get a theoretical reduction factor of 2.5 which is close to experimental ratio of 2.

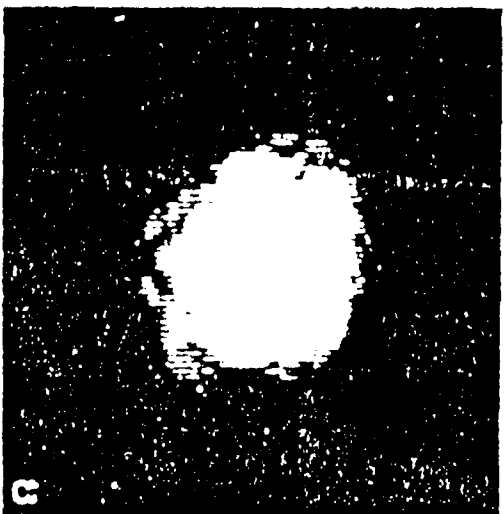
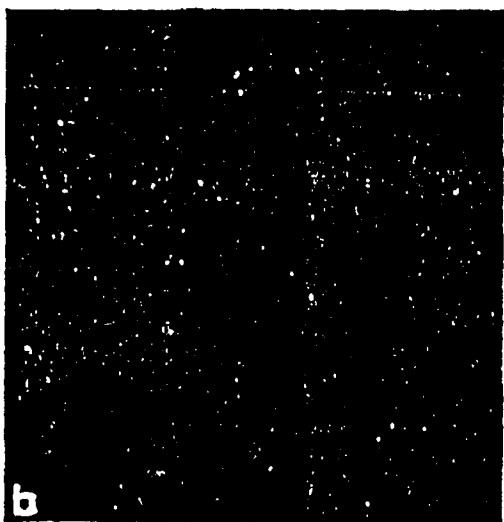


Fig. 2. Illustration of the principle of phase motion detection. (a) The phase conjugate beam. (b) The phase conjugate with the operation of phase modulation in the reference beam. (c) The phase conjugate beam as a microscopic slide is twisted in the signal beam.

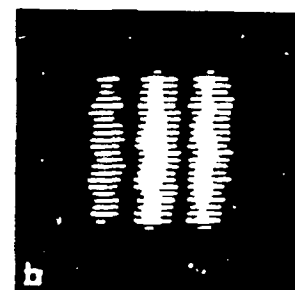


Fig. 3. (a) The phase conjugate image of a static resolution chart when a square phase modulation is operated in the reference beam. (b) The phase conjugate as a resolution chart is twisted.

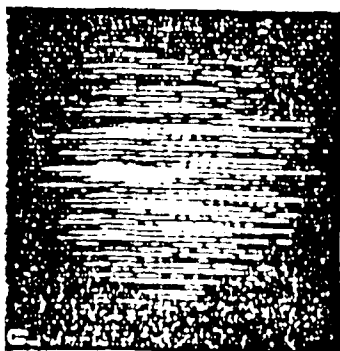
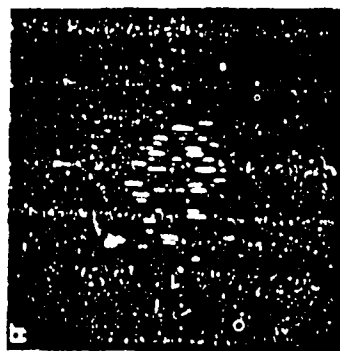
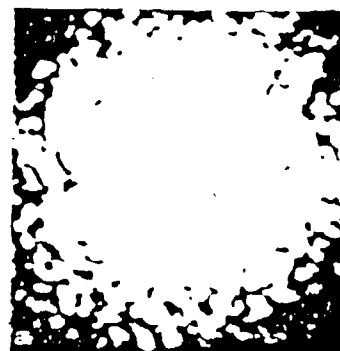


Fig. 4. Illustration of transverse motion detection of phase objects. (a) The phase conjugate image with a static diffuser. (b) With square phase modulation operated on PZT. (c) The regenerated phase conjugate with transverse motion of the diffuser.

In further examination of this effect, we operated PZT₁ with white noise and PZT₂ with a square wave. No signal was detected at the output for this case. This result was independent of the frequency of the square wave.

4. CONCLUSION

We have proposed and demonstrated a tunable time correlation motion detector. This detector has the advantage that it can detect motions faster than the material response time. Two techniques were given to increase the bandwidth of the device with experimental results that indicate the trade off between the reflectivity and the bandwidth. This device detects phase objects: therefore, using the device in combination with real-time phase spatial light modulators is more feasible. Also, the objects can

be Fourier transformed so that any transverse motion of the object results in detectable phase motions in the Fourier plane.

5. REFERENCES

1. D. Anderson and J. Feinberg, *IEEE J. Quantum Electron.*, QE **25** (1989) 635.
2. J. Khoury, G. Hussain, and R.W. Eason, *Optics. Comm.* **71** (1989) 137.
3. J. Khoury, C.L. Woods and M. Cronin-Golomb, *Optics. Comm.* **82** (1981) 533.
4. T.J. Hall, R. Jaura, L.M. Connors and P.C. Foote, *Prog. Quant. Electron.* **77** (1985) 10.
5. M. Cronin-Golomb, Digest of Topical Meeting on Photorefractive materials, effects, and devices. (Optical Society of America, Washington, D.C., 1987) p. 142.
6. Y.H. Ja, *Optics. Comm.* **42** (1988) 377.
7. J.P. Huignard, J.P. Herriau and F. Micheron, *Appl. Phys. Lett.* **26** (1975) 256.
8. A. Marrakchi, *Optics. Lett.* **14** (1989) 326.

NOISE REDUCTION USING ADAPTIVE SPATIAL FILTERING IN PHOTOREFRACTIVE TWO-BEAM COUPLING

Jehad. Khoury, Charles L. Woods, and Mark Cronin-Golomb, Electromagnetics & Reliability Directorate, Rome Laboratory

Published in Optics Letters, Vol. 16, No. 10, 15 May 1991

Abstract - We present an optical signal-processing technique for additive noise reduction that uses the noisy signal and a Gaussian reference beam to produce an adaptive Wiener filter. We experimentally demonstrate an improvement from 1 to 8 in the signal-to-noise ratio by using nonlinear gain in two-beam coupling in barium titanate to transmit 50% of the signal and 6% of the noise.

Photorefractive two-beam coupling has been used to perform a variety of optical processing functions. Examples include edge enhancement,¹ beam cleanup,^{2,3} optical differentiation in time,⁴ novelty filtering,⁵ and contrast enhancement.⁶

In this Letter we introduce a new optical implementation for reducing additive noise in images that utilizes the difference in energy distribution of the signal and the noise at the Fourier plane. In many cases, the spatial noise spectrum is broadly spread at a low intensity relative to the intense signal spectrum peaks. This occurs even when the signal-to-noise ratio is low at the input plane. Here we propose what is to our knowledge the first use of any phase-preserving thresholding mechanism (holographic materials or other optically addressed spatial light modulators) in the Fourier plane to reduce the noise. Nonlinear gain in two-beam coupling is experimentally demonstrated to reduce additive speckle in bar-chart images by implementing a self-adaptive Wiener filter.

Beam cleanup by photorefractive two-beam coupling is an amplification and not a noise-reduction technique because it pumps a pure seed beam.^{2,3} Other nonlinear-optical methods exist for reducing noise in special cases.^{7,9} Fast multiplicative speckle is removed by time-averaging holography.⁷ Slowly developing beam fanning backgrounds are removed by moving the crystal.⁸ Additive noise may be reduced by using a noise-free reference signal to write a Wiener filter in combination with the noisy signal.⁹ None of these techniques can separate an unknown signal embedded in a high-noise background. For any timevarying coherent signal, our new approach reduces additive noise that varies more slowly than the beam fanning response time by writing a noise-canceling hologram.

Figure 1 shows the configuration of two-beam coupling. The gain experienced by the signal beam can be found from the solution of the coupled wave equation under the slowly varying envelope approximation. If we assume negligible absorption, the solution is given by¹

$$G = \frac{I_s(L)}{I_s(0)} = \frac{(r + 1) \exp(\Gamma L)}{1 + r \exp(\Gamma L)}, \quad (1)$$

and, for a negative coupling coefficient, the limits become

$$G = \begin{cases} 1 & r \gg \exp(-\Gamma L) > 1 \\ \exp(\Gamma L) & r \ll 1 < \exp(-\Gamma L) \end{cases}$$

Here r is the beam intensity ratio of the input (beam 5) relative to the reference beam (beam 4) at the front surface of the crystal, Γ is the two-beam coupling coefficient, and L is the effective interaction length within the crystal.

The sign of the coupling coefficient in the diffusion case depends on the crystal orientation and the sign of the photoinduced space charge. The magnitude of the coupling coefficient depends on the effective electro-optic coefficient and trap density. For the barium titanate crystal shown in Fig. 1, the orientation of the c axis gives a negative coupling coefficient, which attenuates the signal beam. For this measurement, a signal beam that is more intense than the reference beam will pass through without loss, while a signal beam that is less intense will lose intensity exponentially. This physical process may be used for additive noise reduction.

When the image is embedded in additive speckle noise, the noisy input $i(x, y)$ is the sum of the signal $s(x, y)$ produced by the object transparency and a noise background $n(x, y)$. The Fourier transform of the signal and noise are $S(u_x, u_y)$ and $N(u_x, u_y)$, respectively.

The Fourier transform of speckle noise is speckle $N(u_x, u_y)$ whose spatial spectrum bandwidth is determined by the grain size of the speckle $n(x, y)$ in the input plane. An example of the Fourier transform of fully developed speckle is shown in Fig. 2A. The speckle in the Fourier plane is spread uniformly up to

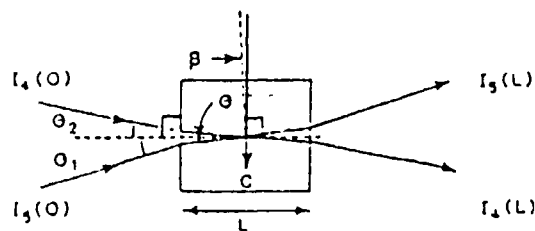


Fig. 1 Geometry for two-wave mixing in barium titanate specifying both the reference and signal beams.

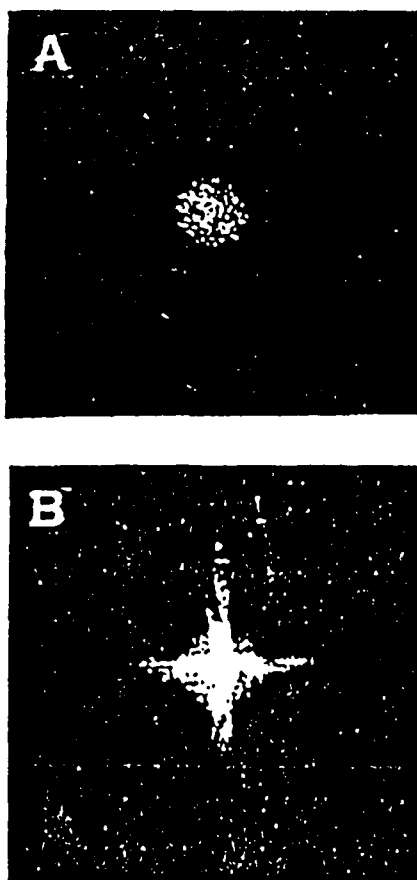


Fig. 2. Fourier transforms. (A) for fully developed speckle and (B) for the input information (signal plus noise).

a certain spatial frequency. A photograph of the Fourier transform of a noisy resolution chart input (Fig. 4B) is shown in Fig. 2B. The signal Fourier transform is seen to be a diffraction pattern of high intensity relative to the noise. It is clear, therefore, that by beam coupling the spectrum of the information in the Fourier plane with a relatively low-intensity reference beam it is possible to remove most of the noise from the signal. The signal will pass through with little attenuation, while the speckle noise will be coupled into the reference beam.

The experimental arrangement is shown in Fig. 3. It is essentially a standard configuration of two-beam coupling. The laser used is an argon laser operating at $\lambda = 514.5$ nm with an intracavity étalon. Beam splitter BS1 divides the input intensity into two beams (beams 1 and 2). Beam 1 is the noise beam, which passes through a diffuser to generate speckle noise and then through an aperture with the same size as the signal beam. The object beam (beam 3) has its intensity adjusted by the variable neutral-density filter and produces the signal image by illuminating a portion of a U.S. Air Force lens resolution chart. The reference beam (beam 4) also passes through a variable neutral-density filter and has the same size as the object beam. The signal beam and the noise beam were combined by a beam

splitter with careful alignment to overlap the signal and noise beams in both the near and far fields. All the input information (speckle and signal) was then Fourier transformed by a lens (L) of 11-cm focal length into a barium titanate crystal of width 4.2 mm, height 4.6 mm, length 4.9 mm.

The orientation of the reference and signal beams relative to the barium titanate crystal is shown in Fig. 1. The crystal was oriented such that $\theta_1 = 11^\circ$, $\theta_2 = 17^\circ$, and $\beta = 2.5^\circ$. For our crystal, the measured transmittance of a weak-intensity signal beam by an equal-diameter reference beam was 33%. The coupling coefficient for our crystal as determined by Eq. (1) is 0.25/mm, which is consistent with published data.¹ In this noise-reduction configuration, approximately 20% of the signal energy in the steady state is lost from the signal-beam images in Fig. 4.

Figure 4 gives characteristic results for this technique of additive noise (speckle) reduction. Figure 4A shows the input signal information from the fine features in the center of the resolution chart. Figure 4B is the input information (signal embedded in additive speckle noise). The initial signal-to-noise ratio was equal to unity as defined by the ratio of the binary signal peak to the noise peak intensities. Figure 4C shows the result of noise reduction using two-beam coupling. It can be seen that the signal has passed through with little change, while the noise has experienced a large attenuation. The result is that the image contrast is enhanced with an improvement in signal-to-noise ratio from 1 to 8 by transmitting (reflection corrected) 50% and 6% of the signal and speckle, respectively. If we divide the output image energy by the total input energy of both pump and signal (after correcting for reflection losses), a total optical efficiency of 2% for steady-state coupling is calculated. In device operation, the energy cost of this noise reduction is proportional to the energy in the noise, and the optical efficiency improves for inputs with less noise. For our high noise input, a maximum optical efficiency of approximately 50% would occur for noise

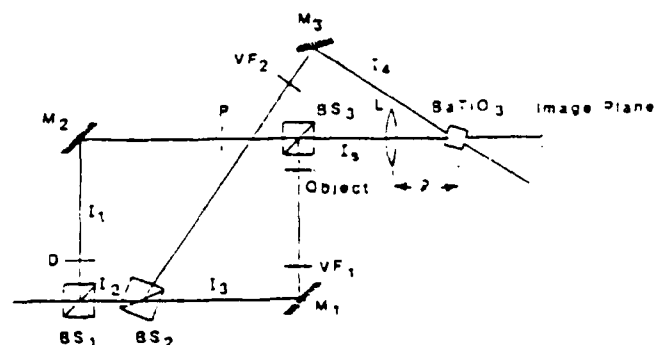


Fig. 3. Experimental arrangement for additive noise reduction. VF1, VF2, variable neutral-density filters, M1-M3, mirrors, D, diffuser, P, aperture.

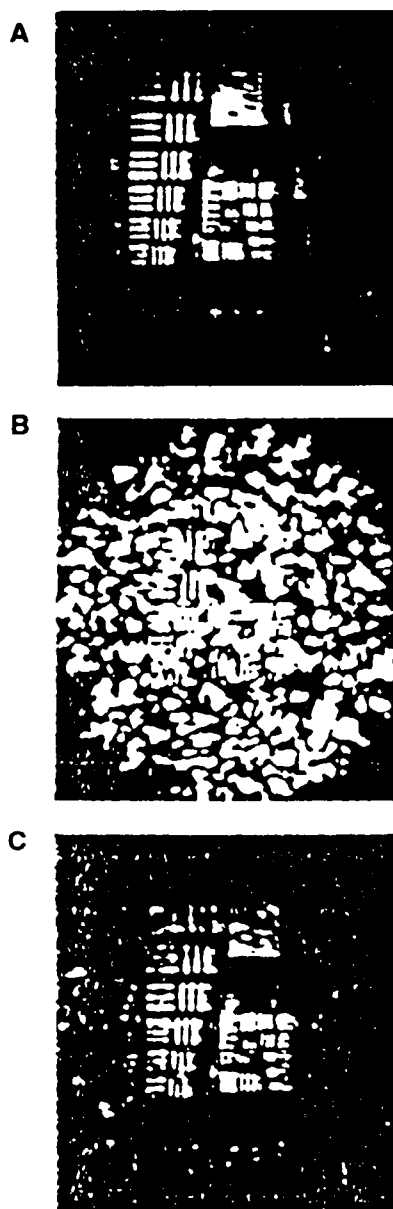


Fig. 4. Additive noise (speckle) reduction. (A) The signal, (B) the input information (signal and noise), (C) the noise-reduced version of B using two-beam coupling

removal using a fixed spatial filter, i.e., with zero pump beam energy and no adaptive capability.

This noise-reduction technique is based on the difference between the spatial spectra of the noise and the signal and can be analyzed as an adaptive optical implementation of a digital Wiener filter. The digital Wiener filter¹⁰ is widely used for additive noise reduction. Comparing the adaptive optical noise reduction filter G of Eq. (1) with the Wiener (transmission) filter for additive noise reduction F , one has

$$F(v_x, v_y) = \frac{|S|^2}{|S|^2 + (N)^2}, \quad (2)$$

and the limits become

$$F = \begin{cases} 1 & |S|^2 \gg (N)^2 \\ 0 & |S|^2 \ll (N)^2 \end{cases}.$$

Here $|S|^2$ is the signal spectral density and $(N)^2$ is the statistical noise spectral density. In Eq. (1), self-adaptive Wiener filtering occurs when the Fourier spectrum of the signal is greater than the pump intensity, which is in turn greater than (and possibly proportional to) the noise intensity. One significant difference between our photorefractive adaptive Wiener filter and the classical Wiener filter is that the photorefractive version adaptively thresholds out a particular noise spectral pattern, while the classical Wiener filter attenuates according to the statistical probability of the noise spectrum.¹⁰

In summary, we have described an energy-efficient nonlinear-optical technique that enhances the contrast of a signal that is embedded in additive noise. Our specific implementation relies on thresholding the Fourier transform of the input information by using photorefractive two-beam coupling. Fourier transforms of many additive noises have broadly spread low-intensity spatial spectra. This is sufficient to produce the spectral separation of noise and signal patterns required by this technique. Our results show that it is possible to increase the signal-to-noise ratio from 1 to 8 while enhancing features that are both smaller and larger than the speckle grain size at the input.

Jehad Khoury and Mark Cronin-Golomb are also with the Electro-Optics Technology Center, Tufts University, Medford, Massachusetts. Their research was supported by Rome Laboratory contract F30602-88-D-0026.

REFERENCES

1. Y. Fainman, E. Klineck, and S. H. Lee, *Opt. Eng.* **25**, 228 (1986).
2. A. E. Chou and P. Yeh, *Opt. Lett.* **10**, 621 (1985).
3. A. E. Chou and P. Yeh, *Opt. Lett.* **11**, 461 (1986).
4. M. Cronin-Golomb, A. M. Biernacki, C. Lin, and H. Kong, *Opt. Lett.* **12**, 1029 (1987).
5. M. Cronin-Golomb, in *Digest of Meeting on Photorefractive Materials, Effects and Devices* (Optical Society of America, Washington, D.C., 1987), p. 142.
6. J. A. Khoury, G. Hussain, and R. W. Eason, *Opt. Commun.* **70**, 272 (1989).
7. J. P. Hugnard, J. P. Herman, L. Pichon, and A. Marrakchi, *Opt. Lett.* **5**, 436 (1980).
8. H. Rajbetch, A. Delboulbe, and J. P. Hugnard, *Opt. Lett.* **14**, 1275 (1989).
9. N. A. Vamos, *Opt. Lett.* **14**, 128 (1989).
10. K. Tazuke, *Engineering Optics*, Vol. 36 of Springer Series on Applied Sciences (Springer-Verlag, Berlin, 1985).

PHOTOREFRACTIVE OPTICAL LOCK-IN DETECTOR

Jehad Khoury, Vincent Ryan, Charles Woods, and Mark Cronin-Golomb, Electromagnetics & Reliability Directorate, Rome Laboratory

Published in Optics Letters, Vol. 16, No. 18, 15 September 1991

Abstract - An optical lock-in detector has been proposed and demonstrated. This scheme utilizes the multiplicative and low-pass filtering characteristics of four-wave mixing in Bi₁₂SiO₂₀.

In many scientific, commercial, and industrial applications it is necessary to detect and recognize signals that are embedded in a high-noise environment. Some of these applications may include communications, spectroscopy, and measurement of the Hall effect and may further include biomedical applications.^{1,2} One of the more useful instruments for these applications is the lock-in amplifier. In certain cases, such as in the study of noisy images for which the signal and the noise have different temporal frequencies and in interferometric techniques for thin film analysis³ when the signal is already optical, it is better to develop an all-optical device that would be parallel in its performance.

Traditionally a lock-in detector is a combination of a frequency mixer followed by a low-pass filter. Mixing two signals of frequencies f_1 and f_2 generates signals of frequencies $f_1 + f_2$ and $f_1 - f_2$ and their integer multiples. Low-pass filtering yields a signal with the beat frequency $f_1 - f_2$.

Both multiplication and lock-in detection can be realized optically by using photorefractive four-wave mixing (FWM).⁴ The multiplicative characteristic of FWM is used for mixing, and the response time of the photorefractive medium is used for low-pass filtering.⁵

In this scheme one reference beam is temporally phase modulated at a frequency f_1 , which is much higher than the reciprocal of the crystal response time. The signal beam is phase modulated at a slightly different frequency, f_2 . The modulation in both beams results in the phase-conjugate beam's oscillating in amplitude at the frequency $f_1 - f_2$. The amplitude of the oscillating phase conjugate is higher at low beat frequencies and vanishes when the beat period becomes much shorter than the photorefractive response time. When both the signal and the reference beams are modulated with the same period by similar or different waveforms, the result is a nonoscillating phase conjugate whose intensity is determined by the phase difference between the two input modulating signals. We show that this parallel optical lock-in detector is analogous to the serial electronic phase-sensitive detector or lock-in detector.

Another device that operates on the principle of processing signals that vary faster than the response time of the material is the time-integrating optical correlator.⁶

Consider a photorefractive material in which three beams, A_1 , A_4 (the reference and the signal beams, respectively), and A_2 interact through FWM. A space-charge field (E_{sc}) is built up, and a phaseconjugate beam, A_3 is generated.⁷ The photorefractive equation that describes the development of the space-charge field within the crystal, assuming that A_1 and A_4 are coherent, is given by

$$\frac{\partial E_{sc}}{\partial \tau} + \frac{E_{sc}}{\tau} = \frac{G}{\tau} \frac{A_1(t)A_4^*(t)}{I_0}, \quad (1)$$

where τ is the response time of writing the grating, G is a parameter that can be found from standard theories of the photorefractive effect,⁸ and I_0 is the total intensity of the interacting beams:

$$I_0 = |A_1|^2 + |A_2|^2 + |A_3|^2 + |A_4|^2 = \text{const.}$$

For weakly absorbing materials with small electrooptic coefficients, constant I_0 , and a time-independent readout beam, the Kogelnik⁹ theory yields a phase-conjugate amplitude that is proportional to the space-charge field:

$$A_3 \propto E_{sc}.$$

Assuming that the specific case in which the two input beams A_1 and A_4 are sinusoidally phase modulated at frequencies large compared with the reciprocal response time of the material, one has

$$\begin{aligned} A_1 &= |A_1| \exp[-i \delta_1 \sin(\omega_1 t + \phi_1)] \\ &= |A_1| \sum_{n=-\infty}^{\infty} J_n(\delta_1) \exp[-in(\omega_1 t + \phi_1)], \end{aligned} \quad (2a)$$

$$\begin{aligned} A_4 &= |A_4| \exp[-i \delta_2 \sin(\omega_2 t + \phi_2)] \\ &= |A_4| \sum_{n=-\infty}^{\infty} J_n(\delta_2) \exp[-in(\omega_2 t + \phi_2)], \end{aligned} \quad (2b)$$

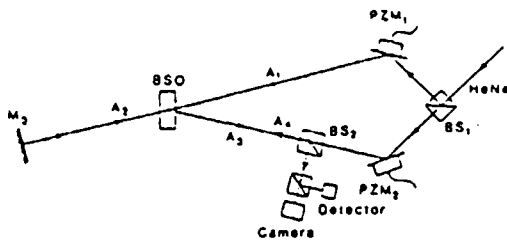


Fig. 1. Experimental arrangement used for frequency mixing and optical lock-in detection.

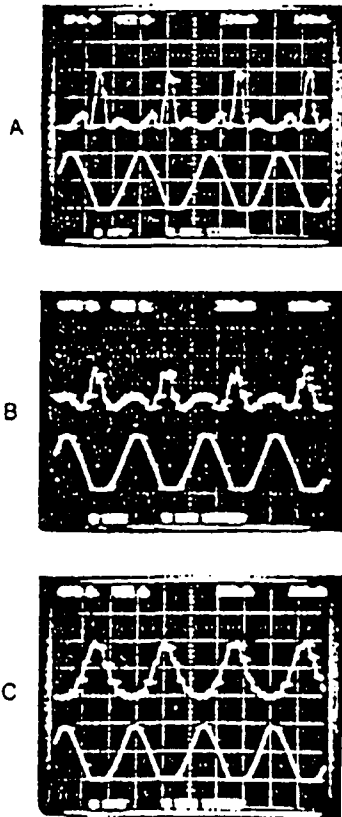


Fig. 2. Six oscilloscope traces displaying the results of sinusoidal phase modulation. The bottom trace of each pair shows the electronic results. A. Both inputs are modulated at 10.8 rad. B. The two inputs modulated simultaneously by 10.8 and 5.4 rad. C. Both of the inputs are modulated by 5.4 rad. The horizontal axis in all cases is 100 ns/division.

where δ_1 and δ_2 are the amplitudes of the phase modulations in beams A_1 and A_4 , respectively, and ω_1 and ω_2 are the phase-modulation frequencies. The signal phases are ϕ_1 and ϕ_2 and J_n is the n th-order Bessel function. Substituting Eqs. (2) into the solution for Eq. (1) yields

$$E_{sc} = \frac{G |A_1| |A_4|}{I_0 \tau} \sum_{n=-\infty}^{\infty} \sum_{m=-\infty}^{\infty} \left\{ \frac{J_n(\delta_1) J_m(\delta_2)}{i(n\omega_1 - m\omega_2) + 1/\tau} \right. \\ \left. \times \exp[-i(n\omega_1 - m\omega_2)t] \exp[-i(n\phi_1 - m\phi_2)] \right\}. \quad (3)$$

Because of the low-pass-filtering characteristics of the photorefractive medium, the only terms that have significant contributions are the terms that satisfy the relation

$$(n\omega_1 - m\omega_2)\tau \ll 1.$$

Since the oscillation frequencies are assumed to be large compared with the reciprocal response time of the photorefractive material, the only terms that contribute are the $n = m$ terms, and

$$E_{sc} = \frac{G |A_1| |A_4|}{I_0 \tau} \sum_{n=-\infty}^{\infty} \left\{ \frac{J_n(\delta_1) J_n(\delta_2)}{in(\omega_1 - \omega_2) + 1/\tau} \right. \\ \left. \times \exp[-in(\omega_1 - \omega_2)t] \exp[-in(\phi_1 - \phi_2)] \right\}. \quad (4)$$

For reference frequencies, $\omega_1 = \omega_2$,

$$E_{sc} = \frac{G |A_1| |A_4|}{I_0} \sum_{n=-\infty}^{\infty} J_n(\delta_1) J_n(\delta_2) \exp[-in(\phi_1 - \phi_2)]. \quad (5)$$

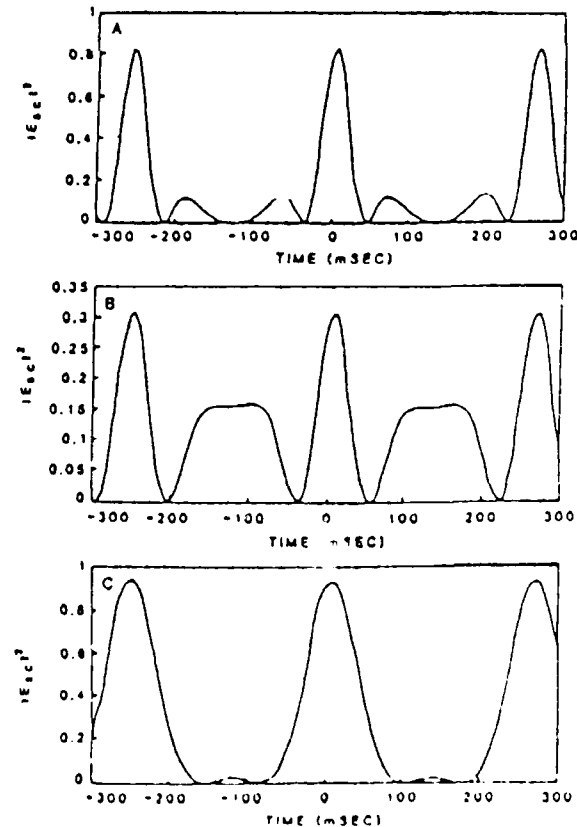


Fig. 3. Theoretical prediction of the oscilloscope traces in Fig. 2

For $\omega_1 = 2\omega_2$ it is possible to show that the second harmonic of A_1 couples with the first harmonic of A_4 , as is the case in electronic lock-in detectors.¹

It is clear from Eq. (5) that, when the fields A_1 and A_4 are modulated at frequencies higher than the reciprocal response time of the material, the output is dependent on the phase difference between the two input signals and their amplitudes. This is the principle of optical phase-sensitive detection.

The experimental arrangement for demonstration of the underlying ideas and comparison with theory is shown in Fig. 1. It is essentially a standard configuration of FWM modified by two mirrors mounted upon piezoelectric transducers (PZM₁ and PZM₂) in the reference and signal beams. A 30-mW He-Ne laser beam was expanded to a radius of 2 mm and divided into two input beams by beam splitter BS₁. The intensity of the reference beam was $I_1 = 59 \text{ mW/cm}^2$, and the intensity of the signal beam was $I_4 = 82 \text{ mW/cm}^2$. The beams intersect in a Bi₁₂SiO₂₀ (BSO) crystal at an angle of 18°. The reference beam after its passage through the crystal was reflected back to the BSO crystal to generate a readout beam of $I_2 = 38 \text{ mW/cm}^2$. The phase-conjugate beam A_3 was detected simultaneously by a photodetector and a camera.

Figure 2 shows three oscilloscope traces of frequency mixing between two sinusoidal phase modulations. The modulation on PZM₁ was at a frequency of 161 Hz, and the modulation on PZM₂ was at a frequency of 165 Hz. In Fig. 2A the top trace shows the result when both piezoelectric transducers were modulated so that the total phase modulation was 10.8 rad. We emphasize that any one of the phase modulations alone was able to destroy the phase-conjugate beam. The output signal consists of a high peak intensity with two low peak intensities. When the phase modulation of any one of the beams was reduced to half of its original amplitude, the previous two low peaks in Fig. 2A merged into one low peak, as illustrated in the top trace of Fig. 2B. By changing the modulation in both inputs to 5.4 rad, we observed a significant change and the result of the frequency mixing, which looks like the distorted sine wave shown in Fig. 2C.

Corresponding theoretical solutions are shown in Fig. 3. These are calculated from Eq. (4), assuming that $\tau = 10 \text{ ms}$ and $\Delta\omega = 0.02416 \text{ rad/ms}$. To show that the frequency of the mixed signal is the beat frequency, we fed the two triggers of the driving signals to an electronic multiplier. The electronic results are illustrated in any one of the bottom traces of Figs. 2A-2C. A semiquantitative agreement between the theory and the experiment has been achieved.

Figure 4 shows the results of the phase-sensitive detector when it is operated simultaneously with two phase-locked sinusoidal phase modulations with shifts of 10.8 rad in both piezoelectric modulators at a frequency of 162.5 Hz. The solid

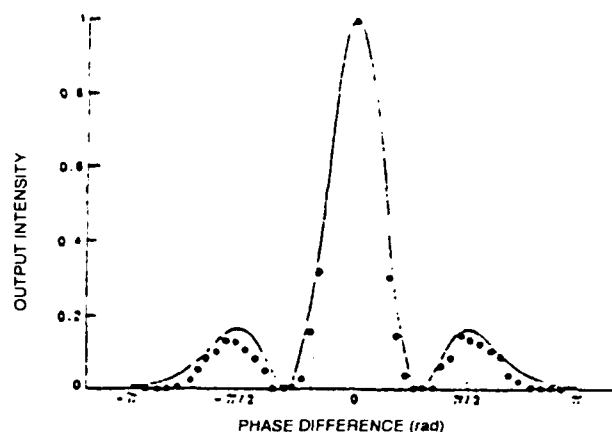


Fig. 4. Intensity of the phase-conjugate return as a function of the phase difference in the two electronic driving signals. The dots represent the experiment, and the solid curve represents the theory.

curve is the theoretical plot from Eq. (3). In these calculations it was assumed that the response time of the material is 10 ms, which corresponded to the faster of the two response times of BSO.¹⁰ Nine pairs of Bessel functions were included in the calculations. A good agreement between the experiment and the theory was achieved.

The object of this study is to introduce and demonstrate the principle of the optical lock-in detector. Even though the use of sine waves to modulate the phase of the reference and the signal beams is not optimal for self-referencing of the output, an exact self-reference can be obtained with a square wave modulating the phase of the reference beam and a sinusoidal amplitude modulation of the signal beam. In this sense, the output is linearly proportional to the amplitude of the input, which is the case in the electronic analog.¹

An obvious follow-up to these experiments would be to design a device with pulse-width modulation in the reference beam to avoid coupling in the second harmonic. In addition, heterodyne detection would be possible by applying an external electric field across the crystal, resulting in a complex response time.⁸

In conclusion, we have proposed and demonstrated what is to our knowledge the first optical lock-in detector. This scheme utilizes the multiplicative characteristic of the real-time holographic medium as well as the low-pass-filtering property imposed by the response time of the material. Developing this device with the use of diode lasers and semiconducting photorefractive materials may open up the possibility of a new generation of optical phase-sensitive detectors that can process spatial and serial information. Using a material with a large electro-optic coefficient (such as BaTiO₃ or SBN) will provide gain, therefore permitting consideration of use of some real-time holographic media in an optical lock-in amplifier.

J. Khoury, V. Ryan, and M. Cronin-Golomb are also with the Electro-Optics Technology Center, Tufts University, Medford, Massachusetts 02155.

REFERENCES

1. M. L. Meade, *Lock-in Amplifiers: Principles and Applications* (Peregrinus, London, 1983).
2. A. B. Carlson, *Communication Systems: An Introduction to Signals and Noise in Electrical Communication*, 2nd ed. (McGraw-Hill, New York, 1975).
3. E. Parshall and M. Cronin-Golomb, "Phase-conjugate interferometric analysis of thin films," *Appl. Opt.* (to be published).
4. M. Cronin-Golomb, B. Fisher, J. O. White, and A. Yariv, *IEEE J. Quantum Electron.* **QE-20**, 12 (1984).
5. J. F. Lam, *Appl. Phys. Lett.* **42**, 155 (1983).
6. D. Psaltis, J. Yu, and J. Hong, *Appl. Opt.* **24**, 3860 (1985).
7. N. V. Kukhtarev, V. B. Markov, S. G. Odulov, M. S. Soskin, and V. I. Vinetskii, *Ferroelectrics* **22**, 949 (1979).
8. T. J. Hall, R. Jaura, L. M. Connors, and P. D. Foote, *Prog. Quantum Electron.* **10**, 77 (1985).
9. H. Kogelnik, *Bell Syst. Tech. J.* **48**, 2909 (1969).
10. G. C. Valley, *Appl. Opt.* **22**, 1160 (1983).

SPHERICAL-WAVE EXPANSIONS OF PISTON-RADIATOR FIELDS

Ronald Wittman, National Institute of Standards and Technology •
Arthur D. Yaghjian, Electromagnetics & Reliability Directorate, Rome Laboratory

Published in J. Acoust. Soc. Am., Vol. 90, No. 3, September 1991

Abstract – Simple spherical-wave expansions of the continuous-wave fields of a circular piston radiator in a rigid baffle are derived. These expansions are valid throughout the illuminated half-space and are useful for efficient numerical computation in the near-field region. Multipole coefficients are given by closed-form expressions which can be evaluated recursively.

1. INTRODUCTION

The subject of this paper first came to our attention regarding a similar electromagnetic problem: In order to test the robustness of algorithms for determining far-field patterns from near-field data,¹⁻³ we have been studying radiation problems for which fields can be calculated accurately and efficiently throughout free space. We realized that the fields of a uniformly excited circular aperture can be expanded in spherical waves, and a natural first step in solving this electromagnetic problem is to solve the corresponding acoustic problem.⁴

While searching for comparable results, we were surprised to find that spherical-wave expansions for piston-radiator fields seem not widely known. The 1969 review paper of Gitis and Khimunin⁵ briefly mentions papers of Backhaus,^{6,7} and Stenzel,⁸ who give spherical-wave expansions for the region $r > a$, where a is the piston radius and r is the distance to the observation point, measured from the center of the piston. The range of validity exceeds that of better known expressions such as those of Carter and Williams⁹ or of Seki *et al.*¹⁰ We know of no recent substantive reference to the spherical-wave expansions of Backhaus and Stenzel, although calculation of piston-radiator fields has continued to generate much interest (for examples, see Refs. 11-21).

In Sec. 2 we give spherical-wave expansions for piston-radiator fields in the interior region ($r < a$), as well as in the exterior ($r > a$) region. In Secs. 3 and 4 we derive expressions for the multipole coefficients in a form suitable for recursive calculation. In Sec. 5 we present numerical results as a point of comparison for anyone wishing to apply our formulation.

2. SPHERICAL-WAVE EXPANSIONS

Throughout a source-free region, the acoustic pressure p and particle velocity \mathbf{v} are related by

$$\nabla p = i\omega\rho_0\mathbf{v} \quad (1a)$$

$$\nabla \cdot \mathbf{v} = \frac{ik}{\rho_0 c} p \quad (1b)$$

where ρ_0 is the equilibrium density, c is the speed of sound, and $k = \omega/c$. The time harmonic factor $\exp(-i\omega t)$ is suppressed here and in the remaining discussion.

Pressure and the Cartesian components of the velocity also obey the Helmholtz equation

$$\nabla^2 u + k^2 u = 0. \quad (2)$$

Spherical waves are elemental (multipole) solutions which arise naturally when Eq. (2) is separated in spherical coordinates. We define

$$\mathbf{u}_{nm}^{(1)}(\mathbf{r}) = i^n j_n(kr) Y_{nm}(\hat{\mathbf{r}}), \quad (3a)$$

$$\mathbf{u}_{nm}^{(3)}(\mathbf{r}) = i^n h_n^{(1)}(kr) Y_{nm}(\hat{\mathbf{r}}). \quad (3b)$$

The Y_{nm} are spherical harmonics, and j_n and $h_n^{(1)}$ are spherical Bessel and Hankel functions (Ref. 22, Chaps. 3 and 16).

Consider the problem of a uniformly vibrating, infinitesimally thin disk as depicted in Fig. 1. The velocity at the surface $z = 0^+$ is $+V\hat{\mathbf{z}}$, and the velocity at the surface $z = 0^-$ is $-V\hat{\mathbf{z}}$. From symmetry considerations, the z component of the particle velocity is 0 on the aperture plane; thus, when $z > 0$, the fields

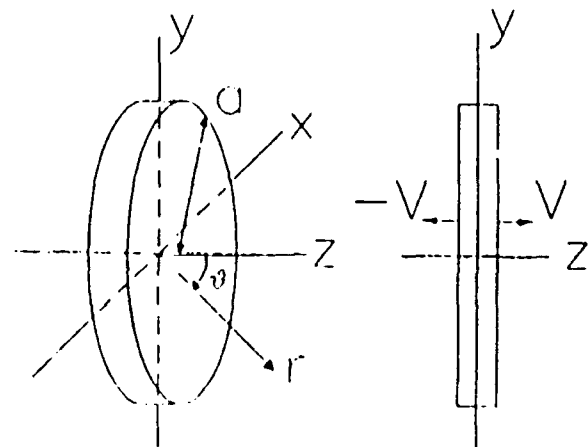


Fig. 1. A disk radiator, perspective and edge views.

of the disk radiator correspond to the fields of a piston radiator in a rigid baffle. With this understanding, we will use the terms "piston" and "disk" interchangeably. Since disk-radiator fields are defined for all directions, natural orthogonalities of spherical harmonics can be exploited in developing field expansions.

We divide space into two regions: The interior region is the spherical volume ($r < a$) which contains the disk radiator. The exterior region ($r > a$) is the remaining (infinite) volume. The $u_{nm}^{(1)}$ are finite at the origin and are used for expanding fields in the interior region. The $u_{nm}^{(3)}$ obey the radiation condition and are used for expanding fields in the exterior region.

Spherical-wave expansions for the pressure and z component of the velocity have the form

$$\bar{p}(r) = \exp(ik|z|) - \sum_{v=0}^{\infty} v_{2v}^{(i)} u_{2v,0}^{(1)}(r), \quad r \leq a, \quad (4a)$$

$$\bar{p}(r) = \sum_{v=0}^{\infty} v_{2v}^{(e)} u_{2v,0}^{(3)}(r), \quad r \geq a, \quad (4b)$$

$$\bar{v}_z(r) = \text{sgn}(z) \exp(ik|z|)$$

$$- \sum_{v=0}^{\infty} v_{2v+1}^{(i)} u_{2v+1,0}^{(1)}(r), \quad r \leq a, \quad (5a)$$

$$\bar{v}(r) = \sum_{v=0}^{\infty} v_{2v+1}^{(e)} u_{2v+1,0}^{(3)}(r), \quad r \geq a. \quad (5b)$$

Normalized pressure and velocity are $\bar{p} = p/(\rho_0 c V)$ and $\bar{v} = v/V$, and $\text{sgn}(z)$ is 1, 0, or -1, depending on whether z is positive, 0, or negative. The superscripts i and e on the multipole coefficients refer to interior and exterior. Together with expressions for the coefficients given in Secs. 3 and 4, Eqs. (4) and (5) are the fundamental results of this paper.

The expansions Eqs. (4) and (5) reflect the symmetries of the disk radiator: The second spherical-wave index is 0 due to invariance on rotation about the z axis, and since

$$u_{nm}^{(q)}(-r) = (-)^n u_{nm}^{(q)}(r), \quad (6)$$

$\bar{p}(r)$ is an even function of z and $\bar{v}_z(r)$ is an odd function of z , as required by symmetry of rotation of 180° about the y axis.

In the source-free exterior region ($r > a$) fields can be expanded using the spherical waves $u_{n0}^{(3)}(r)$ (Ref. 23, theorem

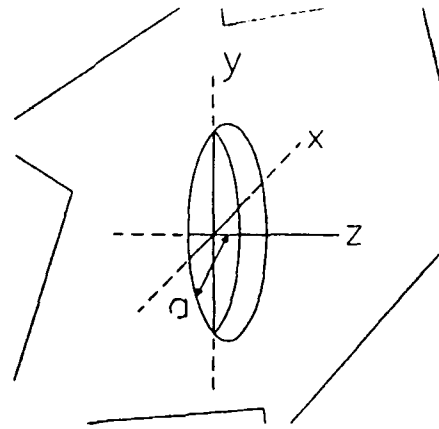


Fig. 2. A hole of radius a in a disk radiator of arbitrarily large radius.

16). The form of the interior region ($r < a$) expressions can be motivated using Fig. 2. Here, a circular hole of radius a is cut in an infinite disk radiator (that is, a disk radiator of arbitrarily large radius). Within this opening ($r < a$) fields can be expanded using the spherical waves $u_{n0}^{(1)}(r)$ (Ref. 23, theorem 13). When the hole of Fig. 2 is filled in by the disk radiator of Fig. 1, the fields are plane waves. Therefore, for the disk alone, the fields ($r < a$) can be expressed as the difference between a plane-wave part and a spherical-wave expansion of what may be termed an edgewave part.²⁴ Validity of Eqs. (4) and (5) at $r = a$ is discussed in the Appendix.

The plane-wave parts of Eqs. (4a) and (5a) satisfy the inhomogeneous Helmholtz equations

$$(\nabla + k^2) \exp(ik|z|) = 2ik \delta(z), \quad (7a)$$

$$(\nabla + k^2) \text{sgn}(z) \exp(ik|z|) = 2 \delta'(z), \quad (7b)$$

and account for the source in the aperture plane.

Spherical-wave functions have been defined so that

$$u_{nm}^{(3)}(r) \underset{r \rightarrow \infty}{\sim} Y_{nm}(\hat{r}) \frac{\exp(ikr)}{ikr}. \quad (8)$$

Thus

$$\hat{p}(r) \underset{r \rightarrow \infty}{\sim} v^\infty(\hat{r}) \frac{\exp(ikr)}{ikr}. \quad (9)$$

where

$$v^\infty(\hat{r}) = \sum_{v=0}^{\infty} v_{2v}^{(e)} Y_{2v,0}(\hat{r}). \quad (10)$$

Similarly,

$$\bar{v}(\mathbf{r}) \xrightarrow{r \rightarrow \infty} v^\infty(\hat{\mathbf{r}}) \hat{\mathbf{r}} \frac{\exp(ikr)}{ikr} \quad (11)$$

3. FORMULAS FOR THE EXTERIOR REGION COEFFICIENTS

In this section we will obtain formulas for the exterior coefficients:

$$v_{2n}^e = \sqrt{4\pi(4n+1)} (1 - \alpha_{2n}^{(1)}) \quad (12)$$

$$\alpha_{2n}^{(1)} = ka \sum_{\mu=0}^n \frac{(2\mu-1)!!}{(2\mu)!!} \frac{4\mu-1}{2\mu-1} j_{2\mu-1}(ka) \quad (12)$$

$$v_{2n+1}^e = \sqrt{4\pi(4n+3)} (1 - \beta_{2n+1}^{(1)}) \quad (13)$$

$$\beta_{2n+1}^{(1)} = \sum_{\mu=0}^n \frac{(2\mu-1)!!}{(2\mu)!!} (4\mu+1) j_{2\mu}(ka) \quad (13)$$

Here, $(2n)!! = 2 \cdot 4 \cdot 6 \cdots (2n)$, $(2n-1)!! = 1 \cdot 3 \cdot 5 \cdots (2n-1)$, and $(0)!! = (-1)!! = 1$.

We begin with the familiar spectral representation²⁵

$$\bar{v}_z(\mathbf{r}) = \frac{1}{2\pi} \int \frac{\gamma}{K} v^\infty(\hat{\mathbf{k}}) \exp(ik \cdot \mathbf{r}) \frac{dK}{\gamma k}, \quad z > 0, \quad (14)$$

where

$$\int dK = \int_{-\infty}^{\infty} dk_x \int_{-\infty}^{\infty} dk_y, \quad K = k_x \hat{x} + k_y \hat{y}, \quad K = |K|,$$

and since $|k| = k = \omega/c$,

$$\gamma = k_z = \begin{cases} \sqrt{k^2 - K^2}, & K \leq k, \\ \sqrt{K^2 - k^2}, & K > k. \end{cases}$$

The spectrum can be determined if the z component of the velocity is known on the aperture plane:

$$v^\infty(\hat{\mathbf{k}}) = \frac{1}{2\pi} \int \bar{v}_z(\mathbf{R}) \exp(-i\mathbf{K} \cdot \mathbf{R}) k^2 d\mathbf{R}, \quad (15)$$

$$\int d\mathbf{R} = \int_{-\infty}^{\infty} dx \int_{-\infty}^{\infty} dy, \quad \mathbf{R} = x\hat{x} + y\hat{y}, \quad R = |\mathbf{R}|.$$

In our case, $\bar{v}_z = 1$ on the surface of the disk, and

$$v^\infty(\hat{\mathbf{k}}) = \frac{1}{2\pi} \int_{r < a} \exp(-i\mathbf{K} \cdot \mathbf{R}) k^2 d\mathbf{R} \quad (16a)$$

$$= (ka)^2 \frac{J_1(Ka)}{Ka} \quad (16b)$$

Here J_n is cylindrical Bessel function. Substitution of Eq. (16b) into Eq. (9) gives Airy's famous far-field formula (Ref. 26, pp. 395-398).

The coefficients in Eq. (10) can be found using the orthonormality of the spherical harmonics:

$$v_n^e = \int v^\infty(\hat{\mathbf{k}}) Y_{n0}(\hat{\mathbf{k}}) d\hat{\mathbf{k}}, \quad (17)$$

$$\int d\hat{\mathbf{k}} = \int_0^{2\pi} d\phi \int_0^\pi \sin \theta d\theta.$$

From Eqs. (16a) and (17),

$$v_n^e = 2 \int_{R < a} k^2 d\mathbf{R} \frac{1}{4\pi} \int Y_{n0}(\hat{\mathbf{k}}) \exp(-i\mathbf{k} \cdot \mathbf{R}) d\hat{\mathbf{k}}$$

$$= 2 \int_{R < a} u_{n0}^{(1)}(R) k^2 dR$$

$$= 4\pi \int_0^a u_{n0}^{(1)}(R) k^2 R dR. \quad (18)$$

We have used the spectral representation²⁷

$$u_{nm}^{(1)}(\mathbf{r}) = \frac{1}{4\pi} \int Y_{nm}(\hat{\mathbf{k}}) \exp(ik \cdot \mathbf{r}) d\hat{\mathbf{k}}. \quad (19)$$

Because

$$u_{2n,0}^{(1)}(R) = \sqrt{\frac{4n+1}{4\pi}} \frac{(2n-1)!!}{(2n)!!} j_{2n}(kR),$$

$$u_{2n+1,0}^{(1)}(R) = 0,$$

we can write Eq. (18) as

$$v_{2n}^e = \sqrt{4\pi(4n+1)} (1 - \alpha_{2n}^{(1)}), \quad (20a)$$

$$v_{2n+1}^e = 0, \quad (20b)$$

with

$$1 - \alpha_{2n}^{(1)} = \frac{(2n-1)!!}{(2n)!!} \int_0^{ka} x j_{2n}(x) dx. \quad (21)$$

Equations (10), (20), and (21) can also be obtained by integrating a well-known spherical-wave expansion of $J_0(Ka)$ [Ref. 28, Eq. (10.1.48)].

Using recursion formulas for the spherical Bessel functions, we can easily show that

$$\alpha_0^{(1)} = \cos(ka) = kaj_{-1}(ka), \quad (22a)$$

$$\alpha_{2n}^{(1)} = \frac{(2n-1)!!}{(2n)!!} \frac{4n-1}{2n-1} kaj_{2n-1}(ka) + \alpha_{2n-2}^{(1)}. \quad (22b)$$

These formulas are useful for recursive calculation of the multipole coefficients. Equations (22) lead directly to the closed-form expression Eq. (12). We can also show that

$$1 - \alpha_{2n}^{(1)} = ka \sum_{\mu=n+1}^{\infty} \frac{(2\mu-1)!!}{(2\mu)!!} \frac{4\mu-1}{2\mu-1} j_{2\mu-1}(ka). \quad (23)$$

Since $\alpha_{2n}^{(1)}$ approaches 1, Eq. (23) is preferable to Eq. (12) for calculating $1 - \alpha_{2n}^{(1)}$ for large n .

In a 1930 paper,⁶ Backhaus obtained the result (in our notation)

$$\alpha_{2n}^{(1)} = 2^{-n} \sum_{\mu=0}^n (-)^{n+\mu} \times \frac{(2n+2\mu-1)!!}{\mu!(n-\mu)!} (ka)^{-\mu+1} j_{\mu-1}(ka). \quad (24)$$

This can be shown (with some difficulty) to satisfy Eqs. (22). In subsequent papers, Stenzel²⁹ and Backhaus⁷ essentially derived Eq. (21) and demonstrated the equivalence of Eq. (24); however, they did not note the recursion formula Eq. (22b).

The expansion (5b) for the z component of the velocity field can be obtained using Eqs. (1a) and (4b). We find that

$$v_{2n}^z = 0, \quad (25a)$$

$$v_{2n+1}^z = \sqrt{4\pi(4n+3)} (1 - \beta_{2n+1}^{(1)}), \quad (25b)$$

where

$$\beta_{2n+1}^{(1)} = \alpha_{2n}^{(1)} + \frac{(2n-1)!!}{(2n)!!} kaj_{2n+1}(ka). \quad (26)$$

From Eqs. (22) and (26), we have

$$\beta_1^{(1)} = \frac{\sin(ka)}{ka} = j_0(ka), \quad (27a)$$

$$\beta_{2n+1}^{(1)} = \frac{(2n-1)!!}{(2n)!!} (4n+1) j_{2n}(ka) + \beta_{2n-1}^{(1)}. \quad (27b)$$

These formulas are useful for recursive calculation of the multipole coefficients. Equations (27) lead directly to the closed-form expression Eq. (13). We can also show that

$$1 - \beta_{2n+1}^{(1)} = \sum_{\mu=n+1}^{\infty} \frac{(2\mu-1)!!}{(2\mu)!!} (4\mu+1) j_{2\mu}(ka). \quad (28)$$

Since $\beta_{2n+1}^{(1)}$ approaches 1, Eq. (28) is preferable to Eq. (13) for calculating $1 - \beta_{2n+1}^{(1)}$ for large n .

The method used to determine the coefficients in Eqs. (4b) and (5b) can be generalized for aperture velocity profiles of the form $\bar{v}_z(R) = (kR)^n, n=0,1,2,\dots$

Before leaving this discussion of exterior coefficients, we will write our results in a form more suitable for comparison with the interior coefficient results of Sec. 4. We define spherical-wave operators as follows:

$$\Phi_{nm} = Y_{nm} \left[\frac{1}{ik} \nabla \right]. \quad (29)$$

Φ_{nm} is an n th order differential operator involving the spatial derivatives ∂_x, ∂_y , and ∂_z . In particular,

$$\Phi_{n0} = \sqrt{\frac{2n+1}{4\pi}} P_n(\eta), \quad \eta = \frac{1}{ik} \partial_z. \quad (30)$$

That is, in the Legendre polynomial $P_n(\cos \theta)$, we replace $\cos \theta = z/r$ by the operator η . In the following discussion, we will use the facts

$$\Phi_{nm} \exp(ik \cdot r) = Y_{nm}(\hat{k}) \exp(ik \cdot r), \quad (31a)$$

$$\Phi_{nm} j_0(kr) = u_{nm}^{(1)}(r), \quad (31b)$$

$$\Phi_{nm} h_0^{(1)}(kr) = u_{nm}^{(3)}(r). \quad (31c)$$

These and other properties of the spherical-wave operators are discussed more fully in Ref. 27.

Now let us generalize Eq. (18) by making v_n^e a function of z :

$$v_n^e(z) = 4\pi \int_0^R u_{n0}^{(1)}(r) k^2 R dR, \quad r = \hat{z}z + R, \quad (32)$$

with the understanding that $v_n^e = v_n^e(0)$. Applying Eqs. (31), we have

$$\begin{aligned} v_n^3(z) &= 4\pi \int_0^R \Phi_{n0} j_0(kr) k^2 R dR \\ &= 4\pi \Phi_{n0} \int_0^R \frac{\sin(kr)}{kr} k^2 R dR \\ &= 4\pi \Phi_{n0} [\cos(kz) - \cos(k\sqrt{z^2 + a^2})]. \end{aligned} \quad (33)$$

The integral may be preformed by changing the variable of integration from R to r and noting that $R dR = r dr$. Similarly, we can define

$$v_n^{ze}(z) = 4\pi \eta \Phi_{n0} [\cos(kz) - \cos(k\sqrt{z^2 + a^2})], \quad (34)$$

where $v_n^{ze} = v_n^{ze}(0)$. The bracketed quantity in Eqs. (33) and (34) is the real part of the familiar expression for pressure on the z axis:³⁰

$$\bar{p}(\hat{z}z) = \exp(ik|z|) - \exp(ik\sqrt{z^2 + a^2}). \quad (35)$$

Equations (33) and (34) can be put in the form of Eqs. (20) and (25) using Eqs. (30) and (31a) and the definitions

$$\alpha_n^{(1)}(z) = P_n(\eta) \cos(k\sqrt{z^2 + a^2}), \quad (36)$$

$$\beta_n^{(1)}(z) = \eta P_n(\eta) \cos(k\sqrt{z^2 + a^2}), \quad (37)$$

with $\alpha_n^{(1)} = \alpha_n^{(1)}(0)$ and $\beta_n^{(1)} = \beta_n^{(1)}(0)$.

4. FORMULAS FOR THE INTERIOR REGION COEFFICIENTS

In this section we will obtain formulas for the interior coefficients:

$$v_{2n}^i = \sqrt{4\pi(4n+1)} \alpha_{2n}^{(3)}, \quad (38)$$

$$\alpha_{2n}^{(3)} = ka \sum_{\mu=0}^n \frac{(2\mu-1)!!}{(2\mu)!!} \frac{4\mu-1}{2\mu-1} h_{2\mu-1}^{(1)}(ka),$$

$$v_{2n+1}^i = \sqrt{4\pi(4n+3)} \beta_{2n+1}^{(3)}, \quad (39)$$

$$\beta_{2n+1}^{(3)} = \sum_{\mu=0}^n \frac{(2\mu-1)!!}{(2\mu)!!} (4\mu+1) h_{2\mu}^{(1)}(ka),$$

Our derivation of Eqs. (38) and (39) uses the fact that

$$(-)^m 4\pi [\Phi_{n,-m} u_{\nu\mu}^{(1)}](0) = \int Y_{nm}(\hat{k}) Y_{\nu\mu}(\hat{k}) d\hat{k} = \delta_{n\nu} \delta_{m\mu}, \quad (40)$$

which is based on Eqs. (19) and (31a). Thus spherical-wave operators can be used to determine multipole coefficients if the field and all of its derivatives are known at a point in space. Because of the axial symmetry of the piston problem, it is necessary to know only derivatives along the z axis, and these may be calculated from Eq. (35). The first term in Eq. (35) evidently gives the plane-wave part of Eq. (4a); the second term gives the edge-wave contribution. Applying Eq. (40) to Eqs. (4a) and (5a), we have

$$v_n^i(z) = 4\pi \Phi_{n0} \exp(ik\sqrt{z^2 + a^2}), \quad (41)$$

$$v_n^{zi}(z) = 4\pi \eta \Phi_{n0} \exp(ik\sqrt{z^2 + a^2}), \quad (42)$$

$$\alpha_n^{(3)}(z) = P_n(\eta) \exp(ik\sqrt{z^2 + a^2}), \quad (43)$$

$$\beta_n^{(3)}(z) = \eta P_n(\eta) \exp(ik\sqrt{z^2 + a^2}), \quad (44)$$

where $v_n^i = v_n^i(0)$, and so on. A comparison of Eqs. (43) and (44) with Eqs. (36) and (37) confirms the fact that Eqs. (12) and (13) are the real parts of Eqs. (38) and (39).

First, we evaluate the operator expression Eq. (44):

$$\beta_n^{(3)}(z) = P_n(\eta) ikz h_0^{(1)}(k\sqrt{z^2 + a^2}). \quad (45)$$

Now

$$P_n(\eta) ikz - ikz P_n(\eta) = P_n'(\eta), \quad (46)$$

$$P_{2n}'(\eta) = \sum_{\mu=1}^n (4\mu-1) P_{2\mu-1}(\eta), \quad (47)$$

$$P_{2n+1}(\eta) = \sum_{\mu=0}^n (4\mu+1) P_{2\mu}(\eta). \quad (48)$$

In addition, from Eq. (31c),

$$P_n(\eta) h_0^{(1)}(k\sqrt{z^2 + a^2}) = \sqrt{\frac{4\pi}{2n+1}} u_{n0}^{(3)}(z\hat{z} + a\hat{R}). \quad (49)$$

Equations (46)-(49) can be used to evaluate Eq. (45) for arbitrary z . When $z = (0)$, $\beta_{2n+1}^{(3)}$ is given by Eq. (39) and $\beta_{2n}^{(3)} = 0$.

Next, we evaluate the operator expression Eq. (43). The relation

$$2n\alpha_{2n}^{(3)}(z) - (4n-1)\beta_{2n-1}^{(3)}(z) + (2n-1)\alpha_{2n-2}^{(3)}(z) = 0 \quad (50)$$

follows from Eqs. (43) and (44) and a familiar recursion formula for Legendre polynomials. With Eq. (50) and the starting value

$$\alpha_0^{(3)}(z) = \exp(ik\sqrt{z^2 + a^2}), \quad (51)$$

the $\alpha_n^{(3)}$ can be calculated from the known $\beta_n^{(3)}$. When $z = 0$, it is not difficult to show that

$$\alpha_{2n}^{(3)} = \beta_{2n+1}^{(3)} - \frac{(2n-1)!!}{(2n)!!} kah_{2n+1}^{(1)}(ka), \quad (52a)$$

$$\alpha_{2n+1}^{(3)} = 0. \quad (52b)$$

Equations (39) and (52a) lead directly to Eq. (38).

The method used to determine the coefficients in Eqs. (4a) and (5a) can be generalized for aperture velocity profiles of the form $\bar{v}_z(R) = (kR)^n$, $n = 0, 2, 4, \dots$.

In his classic 1934 paper, King³¹ stated that he had been able to reproduce Backhaus's formulas by a procedure which also enabled him to calculate the coefficients of the interior expansion; however, he neither elaborated on his methodology nor gave his results. Instead, he claimed that the spherical-wave representation was invalid because pressure and velocity could not be continuous at $r = a$. From the viewpoint of the disk problem, King's objection is flawed because he did not account for the source term [see Eqs. (7)].

Nevertheless, since the coefficients of Eqs. (4) and (5) were obtained by ensuring a match with the known fields on the z axis, it is appropriate to check the behavior at $r = a$. We find that

a necessary condition for the continuity of pressure and velocity is

$$\sin(k|z|) = \sum_{v=0}^{\infty} (-)^v (4v+1) \xi_{2v}(kr) P_{2v}(\hat{r} \cdot \hat{z}), \quad (53a)$$

$$- \operatorname{sgn}(z) \cos(kz)$$

$$= \sum_{v=0}^{\infty} (-)^v (4v+3)$$

$$\times \xi_{2v+1}(kr) P_{2v+1}(\hat{r} \cdot \hat{z}), \quad (53b)$$

where

$$\xi_0(x) = -\frac{1}{x}(\cos x - 1),$$

$$\xi_1(x) = -\frac{1}{x^2}(\cos x - 1) - \frac{1}{x} \sin x,$$

$$\xi_n(x) = \frac{2n-1}{x} \xi_{n-1}(x) - \xi_{n-2}(x)$$

$$+ \frac{1}{x} \frac{2n-1}{n-1} i^n P_n(0).$$

Also,

$$j_n(x) + i\xi_n(x) = i^{-n} \int_0^{\pi/2} P_n(\cos \theta)$$

$$\times \exp(ix \cos \theta) \sin \theta d\theta,$$

$$\xi_n(kz) = i^{-n} P_n(\eta) \xi_0(kz).$$

In obtaining Eqs. (53) we have used the spherical-wave expansion for $\exp(i\mathbf{k} \cdot \mathbf{r})$ [Ref. 22, Eq. (16.127)] [which can be derived easily with Eqs. (31a) and (40)]. It is an interesting exercise to verify that the series of Eqs. (53a) and (53b) are formal solutions of Eqs. (7a) and (7b).

The coefficients in Eqs. (53) can also be obtained directly by exploiting the orthonormality of spherical harmonics. According to Hobson (Ref. 32, p. 345), these are valid representations. Equation (53a) converges uniformly with respect to \hat{r} and Eq. (53b) converges uniformly with respect to \hat{r} in any closed interval that excludes $\theta = \pi/2$. It can be shown that

$$\xi_{2n}(x)_{n \rightarrow \infty} = \frac{x}{(2n-1)(2n+2)} \frac{(2n-1)!!}{(2n)!!},$$

$$\xi_{2n+1}(x)_{n \rightarrow \infty} = \frac{1}{(2n+2)} \frac{(2n-1)!!}{(2n)!!},$$

and so Eqs. (53) converge slowly.

Stenzel²⁹ obtained a solution for $r \leq a$ by dividing the disk into a smaller disk with radius r and a ring with inner radius r and outer radius a . In our notation,

$$\bar{p}(r) = \sum_{v=0}^{\infty} \left[\left(4\pi \int_0^r u_{2v,0}^{(1)}(R) k^2 R dR \right) u_{2v,0}^{(3)}(r) + \left(4\pi \int_r^a u_{2v,0}^{(3)}(R) k^2 R dR \right) u_{2v,0}^{(1)}(r) \right]. \quad (54)$$

Thus also follows from Eq. (4a) if $\sin(k|z|)$ is replaced by the series in Eq. (53a). Because of slow convergence, Eq. (54) is of limited computational usefulness; however, Stenzel did give numerical results which are valuable for comparison.^{29,33}

Poor convergence of Eqs. (4) and (5) for $r = a$ can be overcome by expanding the fields about a point, say, $z_0 \hat{z}$, other than the origin. We have actually provided the machinery to accomplish this efficiently. For example,

$$\bar{p}(r) = \exp(ik|z|) - \sum_{v=0}^{\infty} v_{2v}^{(1)}(z_0) u_{2v,0}^{(1)}(r - z_0 \hat{z}). \quad (55)$$

If $z_0 = a$, then Eq. (55) will converge uniformly when $|r - a\hat{z}| < \sqrt{2}a$.

5. NUMERICAL RESULTS

For numerical evaluation, it is convenient to divide the pressure expansion Eq. (4) into real and imaginary parts:

$$\text{Re } \bar{p}(r) = \sum_{v=0}^{\infty} (-)^v (4v+1) (1 - \alpha_{2v}^{(1)}) j_{2v}(kr) P_{2v}(\hat{r} \cdot \hat{z}), \quad (56)$$

$$\text{Im } \bar{p}(r) = \sin(k|z|) - \sum_{v=0}^{\infty} (-)^v (4v+1) \alpha_{2v}^{(2)}$$

$$\times j_{2v}(kr) P_{2v}(\hat{r} \cdot \hat{z}), \quad r \leq a, \quad (57a)$$

$$\text{Im } \bar{p}(r) = \sum_{v=0}^{\infty} (-)^v (4v+1) (1 - \alpha_{2v}^{(1)}) \times y_{2v}(kr) P_{2v}(\hat{r} \cdot \hat{z}), \quad r \geq a, \quad (57b)$$

[See also Eqs. (A1) and (A2).] Here,

$$h_n^{(1)}(x) = j_n(x) + i y_n(x),$$

$$\alpha_n^{(3)} = \alpha_n^{(1)} + i \alpha_n^{(2)}.$$

As discussed in the Appendix, we use the average of Eqs. (57a) and (57b) to improve convergence when $r = a$.

Algorithms for computing Legendre polynomials and spherical Bessel functions based on three-term recursion relations are well known and extremely efficient,³⁴ requiring no further discussion here.

The $\alpha_{2n}^{(2)}$ may be calculated by applying Eq. (38) recursively for successively larger n values. It is best to compute $1 - \alpha_{2n}^{(1)}$ using Eq. (23) beginning with some large value of n . [The terms in Eq. (23) decrease rapidly when $2n > ka$.] Then Eq. (22b) may be used to compute $1 - \alpha_{2n}^{(1)}$ for successively smaller n values. Correct determination of the coefficients may be verified with the sums

$$\sum_{v=0}^{\infty} (4v+1) (1 - \alpha_{2v}^{(1)}) = \frac{1}{2} (ka)^2, \quad (58)$$

$$\sum_{v=0}^{\infty} (4v+1) (1 - \alpha_{2v}^{(1)})^2 = \frac{1}{2} (ka)^2 \left[1 - \frac{1}{a} J_1(2ka) \right], \quad (59)$$

$$\sum_{v=0}^{\infty} (4v+1) (1 - \alpha_{2v}^{(1)}) \alpha_{2v}^{(2)} = \frac{1}{2} ka H_1(2ka), \quad (60)$$

where H_n is Struve function (Ref. 28, Chap. 12). Equation (58) follows on evaluating Eqs. (10) and (16b) on the z axis. Equations (59) and (60) are consequences of an exact expression for the complex power:³⁰

$$\begin{aligned} & \frac{1}{2} \int p(R) v^*(R) \cdot \hat{z} dR \\ &= \rho_0 c V^2 \frac{\pi a^2}{2} \left[1 - \frac{1}{ka} [J_1(2ka) + i H_1(2ka)] \right]. \end{aligned} \quad (61)$$

Table 1. Values of $1 - \alpha_n^{(1)}$ and $\alpha_n^{(2)}$ for selected n , $ka = 10$.

n	$1 - \alpha_n^{(1)}$	$\alpha_n^{(2)}$
0	1.839 071 529 1E+00	-5.440 211 108 9E-01
2	6.620 674 021 0E-01	3.978 712 848 1E-01
4	1.007 656 045 7E+00	-4.362 441 553 6E-01
6	1.389 455 813 1E+00	2.088 614 436 8E-01
8	7.250 833 678 6E-01	4.579 219 839 6E-01
10	2.050 512 401 3E-01	-1.260 612 187 4E-01
12	3.725 395 116 2E-02	-1.304 066 719 9E+00
14	4.774 284 322 9E-03	-4.589 471 290 4E+00
16	4.578 614 220 1E-04	-2.079 142 506 8E+01
18	3.423 292 507 8E-05	-1.408 637 535 0E+02
20	2.056 703 810 6E-06	-1.356 186 578 6E+03
22	1.016 370 035 0E-07	-1.730 097 926 2E+04
24	4.208 889 732 2E-09	-2.791 777 234 1E+05
26	1.482 969 446 0E-10	-5.527 330 387 4E+06
28	4.502 636 666 5E-12	-1.313 388 136 9E+08
30	1.190 849 831 2E-13	-3.681 930 243 3E+09
32	2.769 063 563 1E-15	-1.201 003 919 8E+11
34	5.706 917 203 5E-17	-4.506 045 546 1E+12
36	1.049 890 971 9E-18	-1.925 683 367 8E+14
38	1.734 966 197 3E-20	-9.295 163 839 9E+15
40	2.589 876 394 2E-22	-5.030 657 908 1E+17
42	3.509 924 097 8E-24	-3.033 054 868 4E+19
44	4.338 359 188 0E-26	-2.025 482 464 2E+21
46	4.910 880 224 8E-28	-1.490 513 391 4E+23
48	5.110 212 525 5E-30	-1.203 067 410 7E+25
50	4.905 315 150 5E-32	-1.060 637 778 2E+27
100	4.572 370 070 5E-91	-6.928 278 505 5E+84
500	6.703 434 072 8E-789	-7.571 819 662 6E+779
1000	1.595 461 674 7E-1873	-1.991 413 212 3E+1863

Equation (59) results when the radiated power [twice the real part of Eq. (61)] is computed by integrating the intensity over a sphere in the far-field region using Eqs. (9) and (11). Equation (60) results when the integral in Eq. (61) is evaluated using Eqs. (4a) and (21). Table I is a listing of $1 - \alpha_n^{(1)}$ and $\alpha_n^{(2)}$ for $ka = 10$ and selected values of n . Note that $1 - \alpha_n^{(1)}$ decreases sharply when $2n > 10$.

The number of terms needed to sum the series of Eqs. (4) and (5) is on the order of ka . The exception occurs when $r = a$, where convergence becomes much poorer. It is difficult to give a precise assessment, since behavior depends strongly on required accuracy, and so we illustrate by example. Equations (57) ($ka = 10$) were summed on the z axis from $kz = 0$ to 20 at 0.01 increments. The number of terms needed to obtain relative accuracies of 0.01, 0.001, and 0.0001 was recorded with the following results: (1) The percentage of points where ten or fewer terms were required was 88%, 74%, and 59%. (2) The number

Table 2. Normalized pressure, $ka = 10$, on the plane $kz = 5$.

kR	Real \bar{p}	Imaginary \bar{p}
0.0	9.994 605 730 8E - 02	2.405 506 604 3E - 02
0.5	1.133 588 520 6E - 01	-2.367 178 245 3E - 02
1.0	1.516 043 124 4E - 01	-1.598 154 260 5E - 01
1.5	2.089 645 827 4E - 01	-3.644 948 034 1E - 01
2.0	2.767 503 658 9E - 01	-6.084 343 885 0E - 01
2.5	3.444 611 857 2E - 01	-8.579 648 897 1E - 01
3.0	4.012 162 787 0E - 01	-1.080 617 973 4E + 00
3.5	4.372 807 718 1E - 01	-1.250 258 762 7E + 00
4.0	4.454 892 734 0E - 01	-1.350 826 746 4E + 00
4.5	4.223 685 326 6E - 01	-1.378 054 597 7E + 00
5.0	3.687 863 522 7E - 01	-1.338 958 646 8E + 00
5.5	2.900 064 275 7E - 01	-1.249 341 329 5E + 00
6.0	1.951 048 893 1E - 01	-1.129 925 039 2E + 00
6.5	9.579 578 402 1E - 02	-1.001 970 424 6E + 00
7.0	4.806 817 560 3E - 03	-8.832 771 573 0E - 01
7.5	-6.597 211 267 5E - 02	-7.853 208 161 0E - 01
8.0	-1.072 924 220 3E - 01	-7.119 867 800 9E - 01
8.5	-1.140 156 987 0E - 01	-6.599 934 213 9E - 01
9.0	-8.599 734 750 8E - 02	-6.207 390 854 2E - 01
9.5	-2.821 635 828 2E - 02	-5.830 400 061 6E - 01
10.0	4.990 048 541 9E - 02	-5.361 019 985 1E - 01
10.5	1.358 780 899 7E - 01	-4.720 996 305 3E - 01
11.0	2.161 075 019 7E - 01	-3.878 934 001 6E - 01
11.5	2.779 702 284 7E - 01	-2.856 416 408 4E - 01
12.0	3.118 210 365 4E - 01	-1.722 987 611 1E - 01
12.5	3.124 927 801 6E - 01	-5.819 004 951 7E - 02
13.0	2.800 629 290 7E - 01	4.500 735 623 8E - 02
13.5	2.197 469 178 5E - 01	1.264 749 861 3E - 01
14.0	1.409 362 777 7E - 01	1.782 469 038 2E - 01
14.5	5.555 173 788 2E - 02	9.66 365 609 1E - 01
15.0	-2.399 568 002 9E - 02	1.828 586 039 1E - 01

of terms required at 95% of the points was less than or equal to 14, 24, and 39. (3) The largest number of terms required at any one point was 24, 86, and 297. As Table I shows, computation near $r = a$ can tax standardly available dynamic ranges.

Figures 3-5 show pressure ($ka = 10$) at three radii, $kr = 6$, 10, and 20. Figure 5 also shows the far-field pattern [Eq. (10) normalized to 2 on the z axis] for reference. Computation at $r = a$ may be checked against the exact result³¹

$$p(\alpha R) = \frac{1}{2} [1 - J_0(2ka)] - \frac{i}{2} H_0(2ka). \quad (62)$$

Figures 6 and 7 give pressure on the aperture plane $kz = 0$ and on the plane $kz = 5$. These figures illustrate, graphically, that pressure is continuous at $r = a$. (The slight roughness in the curves is a consequence of plotter resolution.) To allow closer comparison, Table II gives numerical data at $kz = 5$.

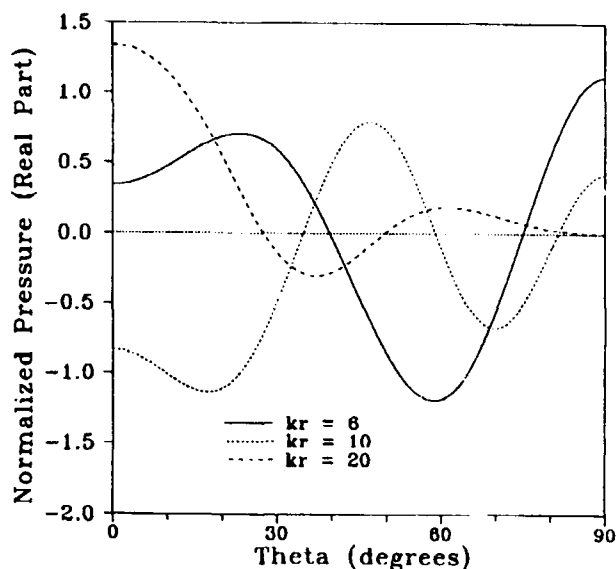


Fig. 3. Real part of the pressure, $ka = 10$, $kr = 6, 10$, and 20 .

Finally, the more complicated fields of a disk with $ka = 50$ are shown in Fig. 8, where the pressure is plotted for $kr = 30, 50$, and 100 . Much larger disks can be treated since computational effort per field point is a roughly linear function of the piston radius.

6. SUMMARY

We have developed a complete solution for the acoustic fields of a uniformly excited circular disk (and for the equivalent

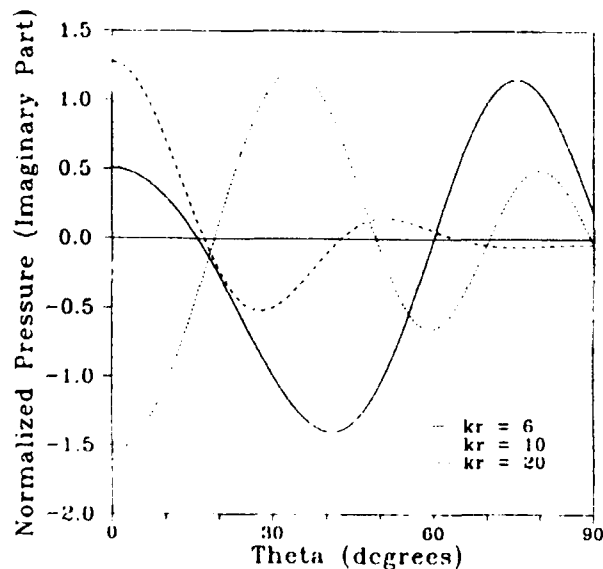


Fig. 4. Imaginary part of the pressure, $ka = 10$, $kr = 6, 10$, and 20 .

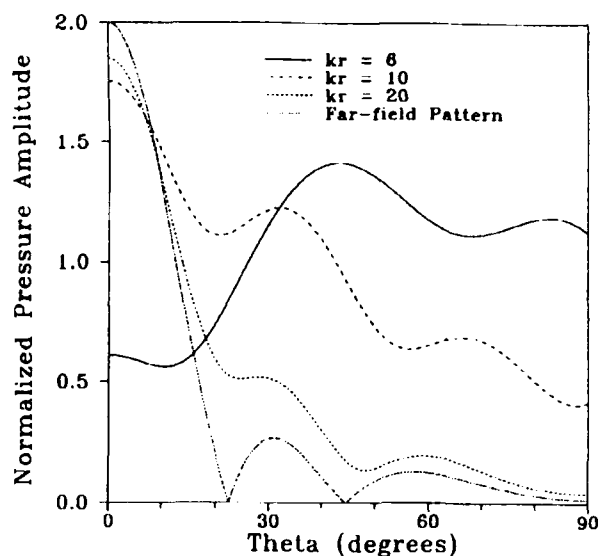


Fig. 5. Amplitude of the pressure, $ka = 10$, $kr = 6, 10$, and 20 . The far-field pattern (normalized to 2 on the z axis) is shown for reference.

lent piston radiator). Spherical-wave expansions are given in Eqs. (4) and (5). Expressions for the multipole coefficients are given in Eqs. (12), (13), (38) and (39). This solution is suitable for efficient and accurate numerical computation throughout the near-field region. We hope that our results will be useful in the evaluation of numerical and analytical techniques which are applicable for a wider range of geometries.

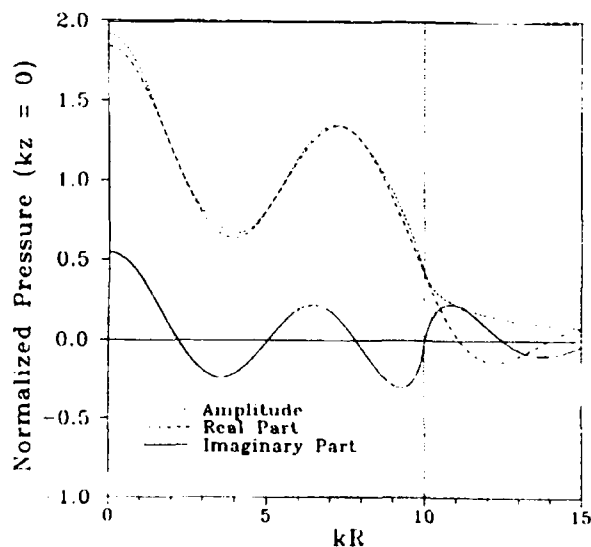


Fig. 6. Pressure, $ka = 10$, on the aperture plane $kz = 0$. The vertical line at $kR = 10$ locates the point for which $r = a$.

7. ACKNOWLEDGMENT

The authors thank Douglas P. Kremer of NIST for his help in preparing the figures.

APPENDIX: VALIDITY OF THE SPHERICAL-WAVE EXPANSIONS AT $r = a$

Here, we establish the validity of Eqs. (4) and (5) when $r = a$. We first show that the interior and exterior expansions converge to the same result at $r = a$. Then, we show that \bar{p} and \bar{v}_z are continuous $r = a$.

For the purpose of the discussion, it is convenient to divide the velocity expansion Eqs. (5) into real imaginary parts:

$$\text{Re } \bar{u}_z(r) = \text{sgn}(z) \cos(kz) + \sum_{v=0}^{\infty} (-)^v \times u_v^-(kr) P_{2v+1}(\hat{r} \cdot \hat{z}), \quad r \leq a, \quad (\text{A1a})$$

$$\text{Re } \bar{u}_z(r) = \sum_{v=0}^{\infty} (-)^v u_v^+(kr) P_{2v+1}(\hat{r} \cdot \hat{z}), \quad r \geq a,$$

$$\text{Im } \bar{u}_z(r) = \sum_{v=0}^{\infty} (-)^v (4v+3) (1 - \beta_{2v+1}^{(1)})$$

$$\times j_{2v+1}(kr) P_{2v+1}(\hat{r} \cdot \hat{z}), \quad (\text{A2})$$

where

$$u_v^-(kr) = (4v+3) \beta_{2v+1}^{(2)} j_{2v+1}(kr),$$

$$u_v^+(kr) = (4v+3) (1 - \beta_{2v+1}^{(1)}) y_{2v+1}(kr),$$

$$\beta_{2v+1}^{(3)} = \beta_{2v+1}^{(1)} + i \beta_{2v+1}^{(2)}.$$

The expansion for the imaginary part of \bar{u}_z Eq. (A2) is uniformly convergent with respect to r (Ref. 23, theorem 13) and is continuous at $r = a$ since the spherical waves are continuous (Ref. 35, theorem 13-8).

Convergence of the expansions Eqs. (A1) for the real part of \bar{u}_z can be demonstrated as follows: From Eq. (53b) we have that, for $z = a \cos \theta$,

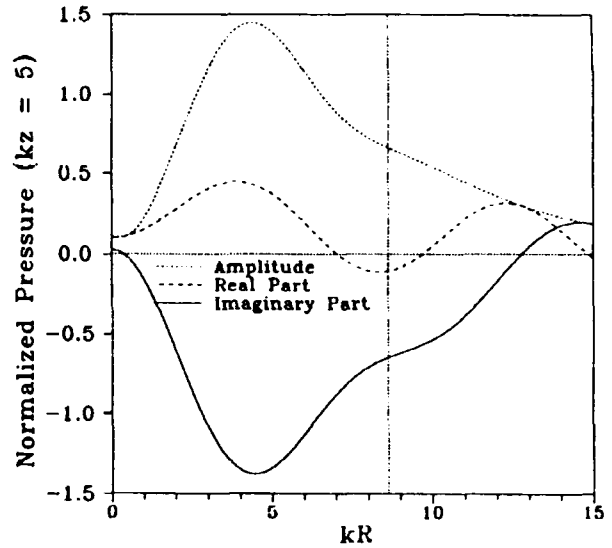


Fig. 7. Pressure, $ka = 10$, on the plane $kz = 5$. The vertical line at $kR = \sqrt{75} \approx 8.660$ locates the point for which $r = a$.

$$- \text{sgn}(z) \cos(kz) = \sum_{v=0}^{\infty} (-)^v$$

$$\times [u_v^-(ka) + u_v^+(ka)] P_{2v+1}(\hat{r} \cdot \hat{z}). \quad (\text{A3})$$

Thus $\text{Re } \bar{u}_z(a\hat{r})$, from either Eq. (A1a) or (A1b), equals the average

$$\text{Re } \bar{u}_z(a\hat{r}) = \frac{1}{2} \text{sgn}(z) \cos(kz)$$

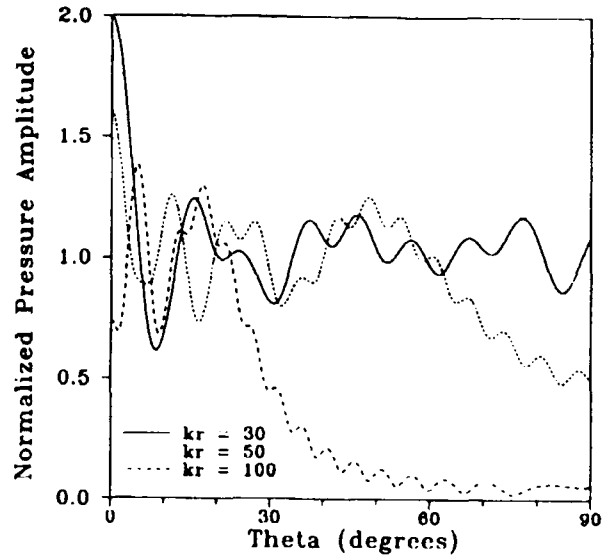


Fig. 8. Amplitude of the pressure, $ka = 50$, $kr = 30, 50$, and 100 .

$$+ \frac{1}{2} \sum_{v=0}^{\infty} (-)^v [v_v^-(ka) - v_v^+(ka)] \quad (A4)$$

$$\times P_{2v+1}(\hat{r} \cdot \hat{z}),$$

provided that Eq. (A4) is convergent. With the aid of Eqs. (28) and (39), it can be shown that

$$v_n^-(ka) - v_n^+(ka) = - \frac{(2n-1)!!}{(2n)!!}$$

$$\times \frac{1}{(2n+2)} \left[1 + O\left(\frac{1}{n^2}\right) \right] \quad (A5)$$

and

$$\frac{v_{n+1}^-(ka) - v_{n+1}^+(ka)}{v_n^-(ka) - v_n^+(ka)} = 1 - \frac{3}{2n} + O\left(\frac{1}{n^2}\right), \quad (A6)$$

which implies absolute and uniform (with respect to \hat{r}) convergence (Ref. 36, p. 46). The series in Eqs. (A1) converge at $r = a$, since both the difference of the series Eq. (A3) and the sum of the series Eq. (A4) converge.

Continuity at $r = a$ is a consequence of the fact that, if

$$f(r) = \sum_{v=0}^{\infty} f_v j_v(kr), \quad 0 \leq r < a, \quad (A7)$$

and the series converges at $r = a$, then

$$f(a^-) = \sum_{v=0}^{\infty} f_v j_v(ka). \quad (A8)$$

The proof of Eq. (A8) rests on the observation that it is possible to choose a value of n such that, when $v > n$,

$$1 \geq j_v(kr)/j_v(ka) \geq j_{v+1}(kr)/j_{v+1}(ka) \geq 0,$$

for $0 \leq r \leq a > 0$. Abel's test (Ref. 37, p. 50) establishes uniform convergence for $0 \leq r \leq a$, and this leads directly to the conclusion Eq. (A8). (A similar theorem involving y_n instead of j_n can be used to verify continuity as r approaches a^+ .)

Equation (A4) has been obtained from Eqs. (A1) by using Eq. (A3) to sum a relatively slowly converging subseries. Consequently, Eq. (A4) is preferable to Eqs. (A1) for numerical computation at $r = a$. Because the sum in Eq. (A4) is a continuous function of θ (Ref. 35, theorem 13-8), which is 0 at

$\theta = \pi/2$, we see that

$$\lim_{\theta \rightarrow (\pi/2)^-} \bar{v}_z(a\hat{r}) = 1/2, \quad (A9)$$

as expected.¹⁸

The validity of Eqs. (5) at $r = a$ can also be established using the approach of this appendix. The expansions converge absolutely and uniformly.

REFERENCES

1. D. M. Kerns, "Plane-wave scattering-matrix theory of antennas and antenna interactions," Natl. Bur. Stand. (U.S.) Monograph 162, June 1981.
2. A. D. Yaghjian, "Near-field antenna measurements on a cylindrical surface: A source scattered-matrix approach," Natl. Bur. Stand. (U.S.) Technical Note 696, Sept. 1977.
3. J. E. Hansen, editor, *Spherical Near-Field Antenna Measurements* (Pergamon, London, 1988).
4. R. C. Wittmann and C. F. Stubenrauch, "Spherical near-field scanning: Experimental and theoretical studies," Natl. Inst. Stand. Tech. NISTIR 3955, July 1990.
5. M. B. Gitis and A. S. Khimunin, "Diffraction effects in ultrasonic measurements (review)," Sov. Phys. Acoust. **14**, 413-431 (1969).
6. H. Backhaus, "Das Schallfeld der kreisförmigen Kolbenmembran," Annalen der Physik Ser. **55**, 1-35 (1930).
7. H. Backhaus, "Zur Berechnung des Schallfeldes der kreisförmigen Kolbenmembran," Z. Tech. Phys. **24**, 75-78 (1943).
8. H. Stenzel, "Über die Berechnung des Schallfeldes von kreisförmigen Membranen in starrer Wand," Annalen der Physik Ser. **6** **4**, 301-324 (1949).
9. A. H. Carter and A. O. Williams, "A new expansion for the velocity potential of a piston source," J. Acoust. Soc. Am. **23**, 179-184 (1951).
10. H. Seki, A. Granato, and R. Truell, "Diffraction effects in the ultrasonic field of a piston source and their importance in the accurate measurement of attenuation," J. Acoust. Soc. Am. **28**, 230-238 (1956).
11. R. V. DeVore, D. B. Hodge, and R. G. Kouyoumjian, "Radiation by finite circular pistons imbedded in a rigid circular baffle. I. Eigenfunction solution," J. Acoust. Soc. Am. **48**, 1128-1134 (1970).
12. J. Zemanek, "Beam behavior within the nearfield of a vibrating piston," J. Acoust. Soc. Am. **49**, 181-191 (1971).
13. J. C. Lockwood and J. G. Willette, "High-speed method for computing the exact solution for the pressure variations in the nearfield of a baffled piston," J. Acoust. Soc. Am. **53**, 735-741 (1973).
14. J. A. Archer-Hall and D. Gee, "A single integral computer method for axisymmetric transducers with various boundary conditions," NDT Int. **13**, 95-101 (1980).
15. G. R. Harris, "Review of transient field theory for a baffled planar piston," J. Acoust. Soc. Am. **70**, 10-20 (1981).
16. R. New, R. I. Becker, and P. Wilhelm, "A limiting form for the nearfield of the baffled piston," J. Acoust. Soc. Am. **70**, 1518-1526 (1981).
17. E. G. Williams and J. D. Maynard, "Numerical evaluation of the Rayleigh integral for planar radiators using the FFT," J. Acoust. Soc. Am. **72**, 2020-2030 (1982).
18. D. A. Hutchins, H. D. Mair, P. A. Puhach, and A. J. Osci, "Continuous-wave pressure fields of ultrasonic transducers," J. Acoust. Soc. Am. **80**, 1-12 (1986).

19. H. D. Mair, D. A. Hutchins, and P. A. Pulach, "Intensity fields of continuous-wave axisymmetric transducers," *J. Acoust. Soc. Am.* **81**, 328-334 (1987).
20. R. I. Becker and R. New, "The approximation of exterior Neumann problems in a halfspace by means of problems with compact boundary," *Proc. R. Soc. Edinburgh* **111A**, 285-300 (1989).
21. J. Backman, "Computations of diffraction for loudspeaker enclosures," *J. Audio Eng. Soc.* **37**, 353-362 (1989).
22. J. D. Jackson, *Classical Electrodynamics*, 2nd ed. (Wiley, New York, 1975).
23. C. Muller, *Foundations of the Mathematical Theory of Electromagnetic Waves* (Springer, Berlin, 1969).
24. H. D. Mair, L. Bresse, and D. A. Hutchins, "Diffraction effects of planar transducers using a numerical expression for edge waves," *J. Acoust. Soc. Am.* **84**, 1517-1525 (1988).
25. D. M. Kerns, "Scattering-matrix description and nearfield measurements of electroacoustic transducers," *J. Acoust. Soc. Am.* **57**, 497-507 (1975).
26. M. Born and E. Wolf, *Principles of Optics*, 5th ed. (Pergamon, Oxford, 1975).
27. R. C. Wittmann, "Spherical wave operators and the translation formulas," *IEEE Trans. Antennas Propagat.* **AP-36**, 1078-1087 (1988).
28. *Handbook of Mathematical Functions*, edited by M. Abramowitz and I. A. Stegun (Dover, New York, 1968).
29. H. Stenzel, "Über die Berechnung des Schallfeldes einer kreisförmigen Kolbenmembranen," *Elektr. Nachr.-Tech.* **12**, 16-30 (1935).
30. M. Greenspan, "Piston radiator: Some extensions of the theory," *J. Acoust. Soc. Am.* **65**, 608-621 (1979).
31. L. V. King, "On the acoustic radiation field of the piezoelectric oscillator and the effect of viscosity on transmission," *Can. J. Res.* **11**, 135-155 (1934).
32. E. W. Hobson, *Spherical and Ellipsoidal Harmonics* (Chelsea, New York, 1955).
33. H. Stenzel and O. Brosz, *Leitfaden zur Berechnung von Schallvorgängen* (Springer, Berlin, 1958).
34. W. Gautschi, "Computational aspects of the three-term recurrence relations," *SIAM Rev.* **9**, 25-82 (1967).
35. T. M. Apostol, *Mathematical Analysis* (Addison-Wesley, Reading, MA, 1964).
36. J. Mathews and R. L. Walker, *Mathematical Methods of Physics*, 2nd ed. (Benjamin, New York, 1970).
37. E. T. Whittaker and G. N. Watson, *Modern Analysis*, 4th ed. (Cambridge U.P., London, 1958).

DUAL-SERIES SOLUTION TO SCATTERING FROM A CHANNEL IN A GROUND PLANE

M.K. Hinders and A.D. Yaghjian, Electromagnetics & Reliability Directorate, Rome Laboratory

Published in IEEE Microwave and Guided Wave Letters, Vol. 1, No. 9, September 1991 (IEEE Log Number 9102354)

Abstract - Exact dual-series eigenfunction solutions, and simple closed-form low-frequency asymptotic approximations are determined for the problems of TM and TE scattering from a semicircular channel in a perfectly conducting ground plane. The eigenfunction solutions provide benchmarks for channel scattering, and the low-frequency solutions can be used to determine directly incremental length diffraction coefficients for narrow channels.

ALTHOUGH the scattering of plane waves from semicircular protuberances [1] and slits [2] have long been solved exactly, neither an exact eigenfunction solution nor a closed-form low-frequency solution exists, as far as we are aware, to the problem of scattering from a channel in a ground plane. We thus present in this letter dual-series eigenfunction solutions, and their low-frequency asymptotic approximations in closed form, to the 2-D problems of TM and TE scattering by a semicircular channel in a ground plane [3]. (A series representation for the low-frequency TM solution was found previously by Sachdeva and Hurd [4].) As shown in Fig. 1, a normally incident plane wave makes an angle ϕ^{inc} with the positive x axis, the channel along the z axis is of radius $r = a$, and the direction of scattering is given by the angle ϕ with the x axis. Harmonic time dependence of the form $e^{i\omega t}$ is assumed throughout.

For the incident TM plane wave, the z -component of the electric field can be expanded in cylindrical waves as [5]

$$E_z^{inc} = e^{i k r \cos(\phi - \phi^{inc})} = \sum_{n=-\infty}^{\infty} i^n J_n(kr) e^{in(\phi - \phi^{inc})} \quad (1)$$

The scattered field for $r \geq a$ may be expressed as the sum of two parts, the reflected TM plane wave given by

$$E_z^{refl} = e^{i k r \cos(\phi + \phi^{inc})} = - \sum_{n=-\infty}^{\infty} i^n J_n(kr) e^{in(\phi + \phi^{inc})} \quad (2)$$

and the "diffracted" field expanded with Hankel functions as

$$E_z^{diffr} = \sum_{n=1}^{\infty} A_n H_n^{(2)}(kr) \sin(n\phi) \quad (r \geq a), \quad (3)$$

where the A_n are the unknown modal coefficients. The diffracted field vanishes on the ground plane so that the total field for $r \geq a$ also vanishes there.

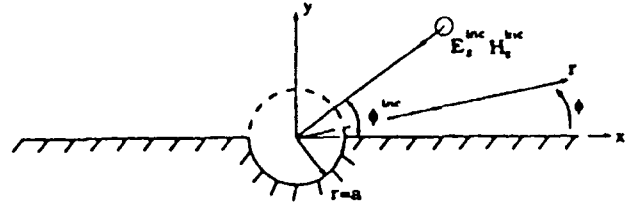


Fig. 1. Geometry of semicircular channel in perfectly conducting ground plane.

In the interior region ($r \leq a$) the electric field can be expanded with Bessel functions as

$$E_z^{int} = \sum_{n=0}^{\infty} J_n(kr) [B_n \cos(n\phi) - C_n \sin(n\phi)] \quad (C_0 = 0) \quad (r \leq a), \quad (4)$$

where B_n and C_n are two more sets of modal coefficients which, along with A_n , will be determined from the boundary conditions at $r = a$. From Maxwell's equations we write the ϕ -component of the magnetic field as $H_\phi = (1/i\omega\mu)\partial_r E_z$, so that the boundary conditions at $r = a$ of zero tangential electric field on the channel ($\pi < \phi < 2\pi$) and continuous fields across the aperture circular ($0 < \phi < \pi$) become

$$\begin{aligned} \sum_{n=0}^{\infty} B_n J_n(ka) \cos(n\phi) + \sum_{n=1}^{\infty} C_n J_n(ka) \sin(n\phi) &= 0 \quad (\pi < \phi < 2\pi), \\ \sum_{n=0}^{\infty} B_n J_n'(ka) \cos(n\phi) + \sum_{n=1}^{\infty} C_n J_n'(ka) \sin(n\phi) \\ &= \sum_{n=1}^{\infty} [4i^n J_n(ka) \sin(n\phi^{inc}) + A_n H_n^{(2)}(ka)] \sin(n\phi) \\ &\quad (0 < \phi < \pi), \\ \sum_{n=0}^{\infty} B_n J_n'(ka) \cos(n\phi) + \sum_{n=1}^{\infty} C_n J_n'(ka) \sin(n\phi) \\ &= \sum_{n=1}^{\infty} [4i^n J_n(ka) \sin(n\phi^{inc}) + A_n H_n^{(2)'}(ka)] \sin(n\phi) \\ &\quad (0 < \phi < \pi). \end{aligned} \quad (5)$$

By making a simple change of variables $\phi \rightarrow \phi - \pi$ in the first equation, each equation in (5) can be written in the form

$$\sum_{n=0}^{\infty} g_n(ka) \cos(n\phi) = \sum_{n=1}^{\infty} f_n(ka) \sin(n\phi) \quad (0 < \phi < \pi). \quad (6)$$

Partial orthogonality of the sinusoids over 0 to π gives the following relations between $f_m(ka)$ and $g_n(ka)$

$$f_m(ka) |_{m=0,2,4} + \frac{4}{\pi} \sum_{n=1,3,5}^{\infty} \frac{mg_n(ka)}{m^2 - n^2} \\ f_m(ka) |_{n=1,3,5} = \frac{4}{\pi} \sum_{n=0,2,4}^{\infty} \frac{mg_n(ka)}{m^2 - n^2}. \quad (7)$$

These relations can then be used to derive the following two equations

$$\sum_{\substack{n=0 \\ (n-m \text{ odd})}} \left(\frac{B_n}{m^2 - n^2} \right) \left\{ J_n(ka) + i \frac{\pi}{2} ka \right. \\ \left. \cdot [J_n(ka) H_m^{(2)'}(ka) J_m(ka) - J_n'(ka) H_m^{(2)}(ka) J_m(ka)] \right\} \\ = \frac{\pi}{m} i^m J_m(ka) \sin(m\phi^{\text{inc}}), \quad m = 1, 2, 3, \dots, \\ A_1 = \left[\frac{8l}{\pi} \sum_{\substack{n=0 \\ n-l \text{ odd}}}^{\infty} \left(\frac{B_n J_n(ka)}{l^2 - n^2} \right) \right. \\ \left. - 4i^l J_l(ka) \sin(l\phi^{\text{inc}}) \right] \frac{1}{H_l^{(2)'}(ka)}; \\ l = 1, 2, 3, \dots \quad (8)$$

The first can be solved numerically to give the B_n and these can be inserted in the second to give A_l . This constitutes an eigenfunction solution of our TM problem.

For narrow channels (small ka) we can employ the small argument approximations for the cylinder functions to write (8) as

$$\sum_{\substack{n=0 \\ (n-m \text{ odd})}}^{\infty} \left(\frac{b_n}{m^2 - n^2} \right) \left[\frac{3m + n}{2} \right] \\ = i \frac{\pi}{2} ka \sin \phi^{\text{inc}} \delta_{lm} \quad m = 1, 2, 3, \dots, \\ A_1 = 4il \frac{(ka/2)^l}{l!} \left[\pi i^l \frac{(ka/2)^l}{l!} \sin(l\phi^{\text{inc}}) \right. \\ \left. - \sum_{\substack{n=0 \\ n-l \text{ odd}}}^{\infty} \left(\frac{2lb_n}{l^2 - n^2} \right) \right] \quad l = 1, 2, 3, \dots \quad (9)$$

Solving (9) numerically, we then find the following closed-form expression for TM scattered from a small semicircular channel

$$E_z^{\text{dif}} \underset{r \rightarrow \infty}{\sim} 0.185 \sqrt{2\pi} (ka)^2 e^{i 3\pi/4} \frac{e^{-ikr}}{\sqrt{kr}} \sin \phi \sin \phi^{\text{inc}} \quad (ka \text{ small}), \quad (10)$$

which has the same functional form as that for TM scattering from a narrow slit in a conducting plane [2], [6]. In the expression (10) we have found the constant 0.185 by a single numerical matrix inversion since (9) shows that for narrow channels the ka -dependence is removed from the matrix, and only the coefficient A_1 is needed to determine the diffracted fields.

The transverse electric case can be solved in a similar fashion by expressing z -components of the incident, reflected, and diffracted H -fields as

$$H_z^{\text{inc}} = e^{ikr \cos(\phi - \phi^{\text{inc}})} = \sum_{n=-\infty}^{\infty} i^n J_n(kr) e^{in(\phi - \phi^{\text{inc}})} \\ H_z^{\text{ref}} = e^{ikr \cos(\phi + \phi^{\text{inc}})} = \sum_{n=-\infty}^{\infty} i^n J_n(kr) e^{in(\phi + \phi^{\text{inc}})} \\ H_z^{\text{dif}} = \sum_{n=0}^{\infty} A'_n H_n^{(2)}(kr) \cos n\phi \quad (r \geq a), \quad (11)$$

and the magnetic field in the interior region as

$$H_z^{\text{int}} = \sum_{n=0}^{\infty} J_n(kr) [B'_n \cos(n\phi) + C'_n \sin(n\phi)], \\ (C'_0 = 0) \quad (r \leq a), \quad (12)$$

where A'_n , B'_n and C'_n are the unknown modal coefficients to be determined from the boundary conditions. Proceeding as in the TM case, we find

$$\sum_{\substack{n=1 \\ (n-m \text{ odd})}}^{\infty} \left(\frac{nC'_n}{n^2 - m^2} \right) \left\{ J'_n(ka) - i \frac{\pi}{2} ka \right. \\ \left. \cdot [J'_n(ka) H_m^{(2)'}(ka) J'_m(ka) \right. \\ \left. - J_n(ka) H_m^{(2)'}(ka) J'_m(ka)] \right\} \\ = \pi i^m J'_m(ka) \cos(m\phi^{\text{inc}}) \quad m = 0, 1, 2, \dots, \\ A'_0 = \left[\frac{4}{\pi} \sum_{\substack{n=1,3,5}}^{\infty} \left(\frac{nC'_n J'_n(ka)}{n} \right) - 2J'_0(ka) \right] \frac{1}{H_0^{(2)'}(ka)} \\ A'_l = \left[\frac{8}{\pi} \sum_{\substack{n=1 \\ n-l \text{ odd}}}^{\infty} \left(\frac{C'_n J'_n(ka)}{n^2 - l^2} \right) - 4i^l J'_l(ka) \cos(l\phi^{\text{inc}}) \right] \\ \cdot \frac{1}{H_l^{(2)'}(ka)} \quad l = 1, 2, 3, \dots, \quad (13)$$

The first of (13) allows us to solve for the C'_n , which can then be substituted into the others to get A'_l .

For small ka (13) can be shown to reduce to

$$\sum_{n=1}^{\infty} \frac{nc'_n}{n^2 - m^2} \left(\frac{3n+m}{2} \right) = i\pi \cos \phi^{\text{inc}} \delta_{lm} \quad (n-m \text{ odd})$$

$$m = 1, 2, 3, \dots,$$

$$\sum_{n=1,3,5} c'_n = -2\pi(ka/2)^2 \left(1 - \frac{1}{2}(ka)^2 \ln(ka) \right) \quad m = 0,$$

$$A'_0 = \frac{\pi}{2i} (ka)^2 \left[1 - \frac{1}{2}(ka)^2 \ln(ka) \right],$$

$$A'_l = \pi i \frac{(ka/2)^l}{l!} \left[\frac{8}{\pi} \sum_{n=1}^{\infty} \left(\frac{n^2 c'_n}{n^2 - l^2} \right) \right. \\ \left. - 4li^l \frac{(ka/2)^l}{l!} \cos(l\phi^{\text{inc}}) \right] \quad l = 1, 2, 3, \dots, \quad (14)$$

from which is found the closed-form expression of the diffracted magnetic field for TE scattering from a narrow semicircular channel

$$H_z^{\text{dif}} \rightarrow \infty \sqrt{2\pi} (ka)^2 e^{i3\pi/4} \frac{e^{-ikr}}{\sqrt{kr}}$$

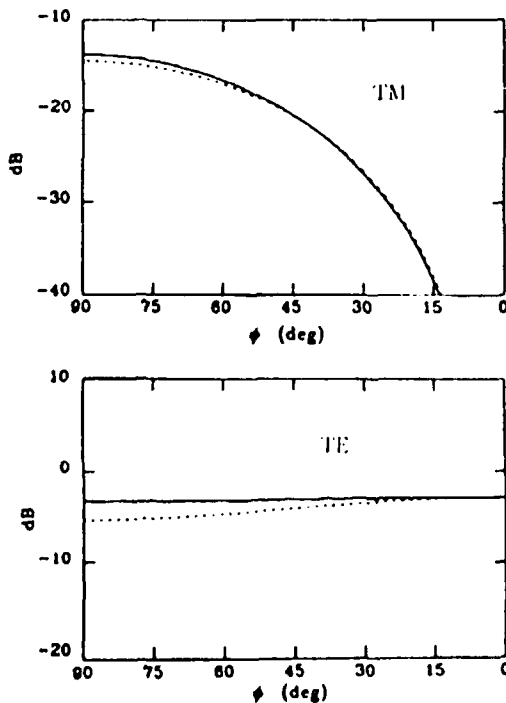


Fig. 2. Backscatter width / λ vs. scatter angle, $a/\lambda = 0.1$, — eigenfunction, - - moment method, . . . low frequency

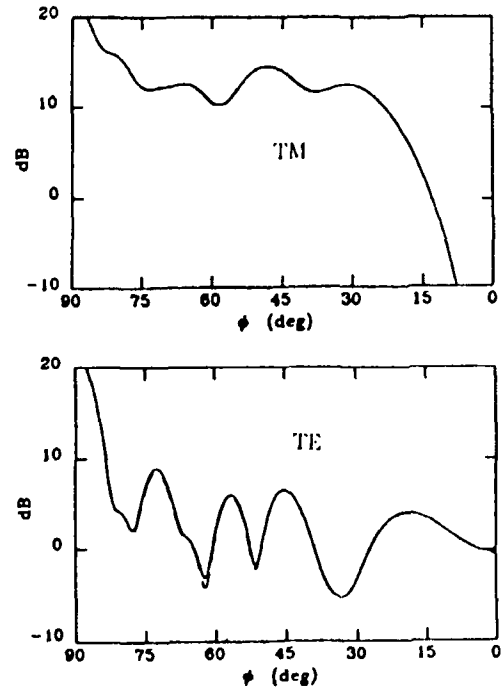


Fig. 3. Backscatter width / λ vs. scatter angle, $a/\lambda = 2$: — eigenfunction, - - moment method.

$$\left[-\frac{1}{2} + \frac{(ka)^2}{4} \ln(ka) - 0.185 \cos \phi \cos \phi^{\text{inc}} \right]. \quad (15)$$

The leading term in (15) differs from the $1/\ln(ka)$ dependence of the leading term for TE scattering from a thin slit in a conducting plane [2], [6]. Note that we have once again found the numerical constant 0.185 via a single numerical matrix inversion, since (14) shows that the ka -dependence is removed from the matrix for narrow channels.

It has been shown recently [7] that the constants multiplying the TM magnetic dipole field in (10) and the TE electric dipole field in (15), are the same not just for the semicircular channel (where they are equal to 0.185) but for any cylindrical channel or ridge in a ground plane. Also the leading term in the TE low-frequency diffracted far magnetic field is always given by

$$\pm k^2 \sqrt{2/\pi} \frac{e^{-i(kr + \pi/4)}}{\sqrt{kr}} A,$$

where A is the area of the channel or ridge [7]. Since the small-channel results show the k -dependence explicitly, they can be generalized immediately to obliquely incident plane waves, and be used to determine incremental length diffraction coefficients [6].

Plots of the backscattering width versus angle computed from the TM and TE eigenfunction solutions, (8) and (13), as well as from a numerical moment-method integral equation solution [9], are shown in Figs. 2 and 3. The low-frequency approximations, (10) and (15) are also plotted in Fig. 2. The

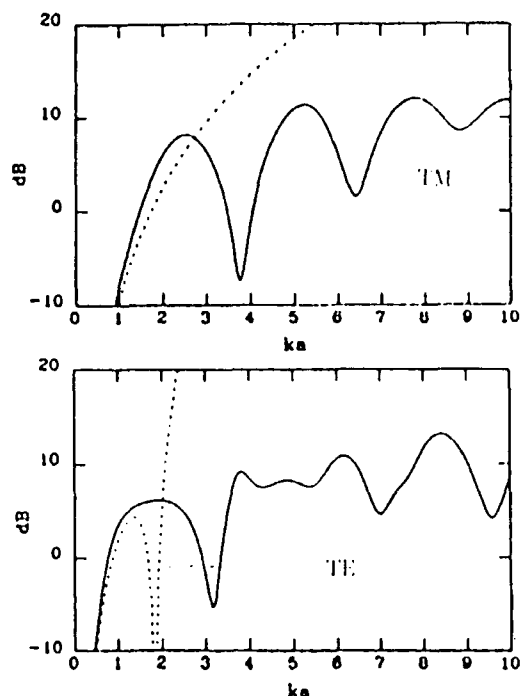


Fig. 4. Total scattering width / λ vs. ka , $\phi^{inc} = 90^\circ$; — eigenfunction, - - low frequency.

eigenfunction and moment-method solutions agreed well at all computed angles and frequencies. The low-frequency solutions are a good approximation to the exact eigenfunction solutions for a/λ smaller than about 0.1.

Fig. 4 shows the total scattering width versus ka in the TM and TE cases computed from the eigenfunction solutions and the low-frequency approximations. The clearly defined resonances displayed in Fig. 4 are not present in the total scattering width of the slit or the semicircular ridge on a ground plane.

ACKNOWLEDGMENT

M. B. Woodworth programmed the computation of the eigenfunction and low-frequency solutions and plotted the curves.

REFERENCES

1. J. W. Strutt (Lord Rayleigh), "On the light dispersed from fine lines ruled upon reflecting surfaces or transmitted by very narrow slits," *Phil. Mag.*, vol. 14, p. 350, 1907.
2. J. I. Bowman, T. B. A. Senior, P. L. E. Uslenghi, *Electromagnetic and Acoustic Scattering by Simple Shapes*. Amsterdam: North Holland, 1969, ch. 4 and section 1.2.9.
3. M. K. Henders, "Scattering of a plane electromagnetic wave from a semi-circular crack in a perfectly conducting ground plane," RADC Tech. Rep., TR-89-12, Apr. 1989.
4. B. K. Sachdeva and R. A. Hurd, "Scattering by a dielectric-loaded trough in a conducting plane," *J. Appl. Phys.*, vol. 48, no. 4, p. 1473, 1977.
5. J. A. Stratton, *Electromagnetic Theory*. New York: McGraw-Hill, 1941, ch. 6.
6. R. A. Shore and A. D. Yaghjian, "Incremental diffraction coefficients for planar surfaces," *IEEE Trans. Antennas Propagat.*, vol. 36, no. 1, p. 55, Jan. 1988.
7. T. B. Hansen and A. D. Yaghjian, "Low-frequency scattering from two-dimensional perfect conductors," *IEEE/AP-S Symp. Dig.*, London, ON, Canada, June 1991; also Rome Laboratory Tech. Rept., TR-91-49, Jan. 1991.
8. —, "Incremental diffraction coefficients for cylinders of arbitrary cross section: Application to diffraction from ridges and channels in perfectly conducting surfaces," in *IEEE/AP-S Symp. Dig.*, London, ON, Canada, June 1991, pp. 794.
9. H. Ling, private communication, Dept. Elect. and Comput. Eng., Univ. of Texas at Austin, 1990.

EXCIMER LASER-INDUCED DEPOSITION OF COPPER FILMS

Suryadevara V. Babu, Raghunath Padiyath, Moses David, Department of Chemical Engineering, Center for Advanced Materials Processing, Clarkson University
Lois Walsh, Electromagnetics & Reliability Directorate, Rome Laboratory

Published in AIChE Journal, Vol. 37, No. 1, January 1991

Rapid advances in the speed and integration of electronic devices and associated reliability concerns have resulted in an increasing demand for new and improved manufacturing processes and materials. High-performance interconnect materials are especially needed at the submicron device level. Copper is an excellent interconnect material because of its very low resistivity, high resistance to electromigration, and low cost (Jensen et al., 1984). However, aluminum has remained the interconnect material of choice at the device level until recently because of process difficulties associated with deposition and subsequent patterning of copper films (Saxena and Pramanik, 1990).

Sputtering (Susa et al., 1985), thermal (resistance-heated) evaporation (Osaka et al., 1985), electron-beam evaporation (Bunshah and Deshpandey, 1988), chemical vapor deposition (CVD) (Sherman, 1987), laser-induced chemical vapor deposition (LCVD) (Bauerle, 1984), and laser-induced evaporation (Cheung and Sankur, 1988) are widely used for the deposition of films of pure elements as well as compound materials and superlattices. Thin film deposition by sputtering or evaporation requires high vacuum (typically $< 1.3 \times 10^{-4}$ Pa) and selective deposition is not possible with these techniques. CVD with organometallic precursors having high vapor pressure is carried out at temperatures exceeding the decomposition temperature of the precursor (typically $> 300^\circ\text{C}$). Since copper-containing precursors with high vapor pressures are few in number, progress in depositing thin copper films with this technique has been slow. Only recently, CVD studies on Cu have been carried out using copper (II) hexafluoroacetylacetonate [Cu(II) (hfac)₂] (Temple and Riesman (1989); Kaloyeros et al., 1990).

A number of studies have been conducted on laser-induced deposition of copper using both pulsed and continuous-wave lasers. Thin copper lines as well as films have been deposited from a paste of copper formate and glycerol using an excimer laser (Ritz et al., 1987), from copper formate films on silica and glass using an Ar⁺ laser (Gupta and Jagannathan, 1987), and from copper acetate using an Nd:YAG laser (Harish et al., 1988). Conducting films and lines have also been obtained by decomposing Cu(II) (hfac)₂ photothermally in the gas phase (Houle et al., 1985; Markwalder et al., 1989). However, the films were heavily contaminated with carbon. Similarly, films produced by RF plasma reduction of copper formate were rich in copper only at the surface; the bulk of the film was contaminated with carbon (Padiyath et al., 1990).

In the present study, a new technique for deposition of thin copper films was investigated. Copper was deposited by reactive ablation of copper formate using a partially focused excimer (KrF, $\lambda = 248$ nm) laser beam in a flowing hydrogen gas or a hydrogen plasma ambient. Copper was deposited on a substrate located in close proximity to the target copper formate. A key feature of this laser deposition process is the laser-induced decomposition of target material, followed by evaporation/sputtering of the products and reaction in the gas phase. In contrast to the conventional laser evaporation technique (Cheung and Sankur, 1988), organometallic compound, instead of pure copper target, was used to obtain the copper deposit. Furthermore, a much smaller fluence was adequate (the laser focus spot on the target was about 20 mm^2) to deposit copper starting from copper formate. The laser deposition technique described here is somewhat similar to the activated reactive evaporation (ARE) method (Bunshah and Raghuram, 1972) and reactive sputterings (RS) method (Al-Jaroudi et al., 1989), with a key difference that a hydrogen ambient was necessary to reduce the oxygen content in the deposited copper film and to improve its purity.

1. EXPERIMENTAL SYSTEM AND METHODS

An excimer laser (Lambda Physik model EMG 101) operating at 248 nm (krypton-fluorine gas mixture) was used in the deposition studies. The laser was operated at a repetition rate of 10 Hz with an average-pulse energy of 300 mJ, measured with a Gentec joulemeter. The beam was focused to a 20 mm^2 area on the copper formate target using a fused silica biconvex lens ($f = 150$ mm). The laser beam entered a parallel plate plasma reactor (PlasmaTherm model 730) through a fused silica window. The arrangement is shown in Figure 1. RF power was supplied to the chamber through the upper electrode (0.28 m dia.), which was cooled by a water/ethylene glycol coolant mixture circulated from a heat exchanger. Heating of substrates placed on the lower, grounded electrode was achieved by a resistance heater and controller.

The copper formate target was placed at an angle of 45° to the incident beam. The substrate to be coated with copper film was placed making a small angle (20 – 40°) with the target, as shown in Figure 1. The reducing atmosphere of a hydrogen plasma or

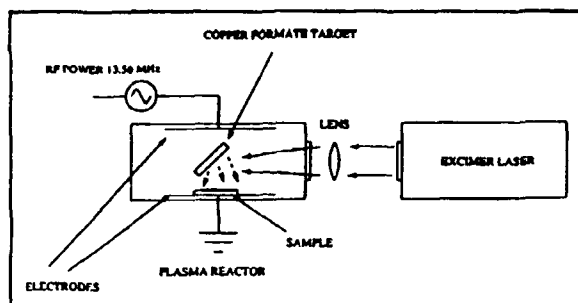


Fig. 1. Experimental arrangement for laser-induced deposition process.

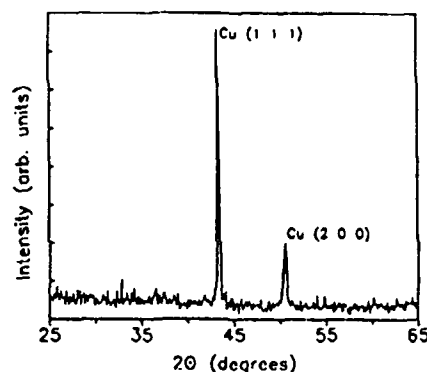


Fig. 2. X-ray diffraction pattern of a copper film deposited by excimer laser reduction.

a hydrogen gas was maintained during the deposition. The discharge was sustained by 600 W RF power and a hydrogen flow rate in the range 35-500 sccm at 2 torr (266.6 Pa). The average pulse energy of the laser beam during the deposition process was held constant at 300 mJ, corresponding to a fluence of 1.5 J/cm^2 on the target. The deposition area on the substrate surface under these conditions was about 3 cm^2 .

The deposited films were heat treated in the presence of a hydrogen plasma at 200°C for 30 min. The plasma was maintained with 200 sccm of hydrogen at a pressure of 3 torr (400 Pa) and 600 W RF power in a reactor that has been described earlier (David et al., 1990). All the samples were stored in a vacuum desiccator prior to any analysis. Film crystallinity was determined by an X-ray diffractometer (Siemens model D500). Elemental analysis and depth profiling of the deposited film was performed by Auger spectroscopy (Perkin Elmer model PHI 600 with a differentially pumped ion gun (04-303)). Atomic concentrations were determined from peak areas using sensitivity factors provided with the spectrometer by the manufacturer. A beam voltage of 3 kV and a beam current of 100 nA were used in Auger electron spectroscopy (AES) measurements while the ion gun was operated at 2 kV and $3 \mu\text{A}$. Under these conditions, the sputter rate of the copper films was about 9 nm/min. Since AES is incapable of detecting hydrogen, the elemental composition of the films is reported on a "hydrogen-free" basis.

2. RESULTS AND DISCUSSION

The copper films obtained by this process displayed excellent deposit morphology. The deposit thickness was found to be in the range of 0.2 to $0.5 \mu\text{m}$. The resistivity of the films, as measured by a four-point probe, improved from $18 \mu\Omega\text{cm}$ for the as-deposited films to $5 \mu\Omega\text{cm}$ after heat treatment. This value is comparable to that reported for copper films deposited by other

techniques (Gupta and Jagannathan, 1987; Temple and Riesman, 1989; Harish et al., 1988) but higher than the $1.9 \mu\Omega\text{cm}$ reported by Kaloyeros et al. (1990) when the substrate temperature was in the range of $300\text{--}450^\circ\text{C}$.

The X-ray diffractogram of a heat-treated copper film deposited by the laser reduction technique, shown in Figure 2, contains only the peaks of copper. The peak intensities increased after heat treatment. AES depth profiles of as-deposited and heat-treated copper films are shown in Figures 3 and 4, respectively. The as-deposited films contained small amounts of carbon and oxygen as impurities. Heat treatment in a hydrogen plasma eliminated most of the oxygen from the bulk of the film. The reduction in the carbon content as a result of heat treatment was not as appreciable as the reduction in oxygen content. Post-heat-treatment oxidation was responsible for the observed surface oxygen content.

Copper formate absorbs the 248 nm UV radiation of the excimer laser strongly (Ritz et al., 1987), which leads to dissociation. In the absence of a hydrogen atmosphere, it is possible to envision several reaction pathways for the dissociation of the formate:

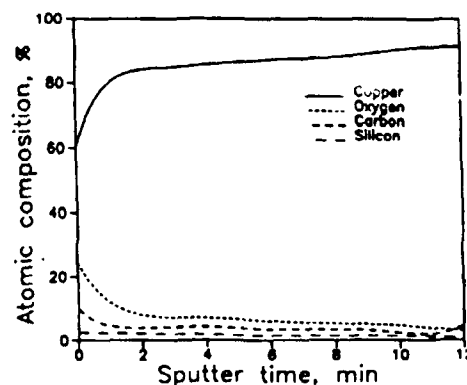


Fig. 3. AES depth profile of an as-deposited copper film deposited by excimer laser reduction.

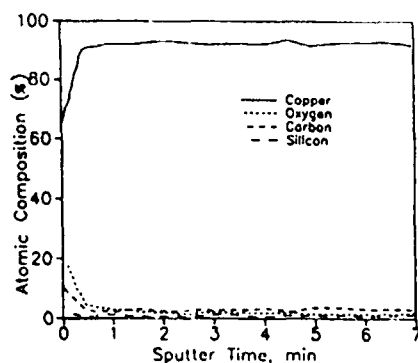
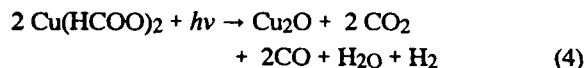
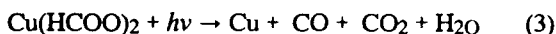
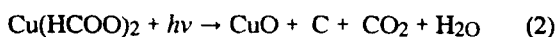
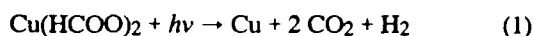
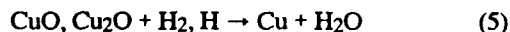


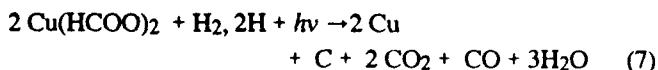
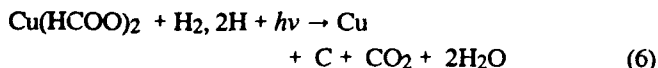
Fig. 4. AES depth profile of a copper film deposited by excimer laser reduction and heat-treated for 30 min.



Here $h\nu$ represents the 248 nm excimer laser photons. The photons may initiate a photochemical dissociation and/or the dissociation follows the heating of the film by the laser. In the presence of hydrogen, the reduction of the oxides of copper formed during reactions 2, 4, or both can occur in the laser plume or on the target surface according to the following reaction:



The dissociation of the hydrogen molecules themselves is perhaps catalyzed by the metallic copper or its oxides in the laser heated zone. The hydrogen atoms for this reduction are also available from the ambient when a hydrogen discharge is maintained. Thus, complete reduction of copper formate might be a two-step process. Alternatively, hydrogen may take part in the dissociation of the copper formate on the surface of the target under the influence of excimer laser pulses according to the following reactions:



It is not known what intermediate reaction steps, if any, may be involved in each of the reactions 1-7. Also it has not been determined if one or more of these reactions dominate. Analysis of gas phase products by mass spectrometry should be helpful in this connection.

In any case, it is quite likely that during the reduction of the copper formate, the composition of the target film changes to mostly Cu, CuO, Cu₂O, and C. The large power densities of the pulsed excimer laser beam lead to elevated surface temperatures (of the order of 1,000°C) (Kotecki and Herman, 1988), resulting in the evaporation of a large part of the products formed by reactions 1-7. While most of the decomposition products evaporate to deposit on the substrate, an extremely thin film of copper is left behind on the target due to product depletion to the vapor phase. The copper film remaining on the target does not conduct electrically. Interestingly enough, Houle et al. (1986) were able to deposit only very thin (< 50 nm) copper films from Cu(hfac)₂ using an excimer laser beam ($\lambda = 248$ nm) incident perpendicularly on a quartz or silicon substrate. However, they obtained much thicker (0.05 to 1.0 μm) films when an argon ion laser was used.

The deposition rates of the various vapor phase species generated by the laser pulse depend on their rates of nucleation, which in turn depend on supersaturation, among other things. Since the vapor pressure of carbon is much lower than that of copper and oxides of copper, evaporation of carbon is the least probable. However, volatilization of carbon can occur by the formation of high vapor pressure oxides of carbon. Hydrocarbon species having high vapor pressures may also form if sufficient reactive hydrogen is available. The plume generated by a laser beam targeted on copper formate will, therefore, comprise mostly Cu, CuO, Cu₂O, H₂O, CO₂, CO, C_mH_n, and H species. Of these, oxides of carbon, hydrocarbons, and water have relatively high vapor pressure and less supersaturation. Consequently, a cold substrate placed in the laser plume will be coated preferentially with copper and oxides of copper due to their higher supersaturation. Hence, films deposited by laser decomposition in the presence of hydrogen should consist of mostly Cu and O. The very small amount of carbon in the films confirms that a significant amount of carbon is being transformed into high vapor pressure oxides or hydrocarbons.

In order to study the role of the ambient during the deposition, films were deposited in the absence of the glow discharge. Since the plasma environment is richer in highly reactive species, the films deposited in plasma ambient were expected to display better quality. However, the films deposited with and without the plasma ambient displayed almost identical compositions, indicating very little influence of the plasma environ-

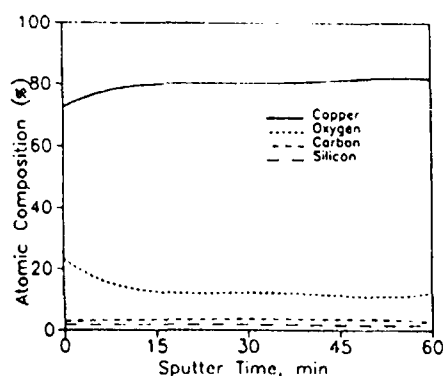


Fig. 5. AES depth profile of a copper film deposited by excimer laser reduction in an argon ambient.

ment on the deposition process. Several plausible conclusions may be drawn based on this observation:

- The residence time of the evaporated species in the laser plume [estimated as 10^{-5} s based on the measured velocities of species ejected from polymer surfaces by excimer laser ablation and the spacing between the target and the substrate (Srinivasan, 1984)] is not sufficient for gas phase reactions to occur prior to the condensation on the substrate.
- The nature of the processes occurring during the laser pulse and afterward must be such that atomic hydrogen or excited hydrogen molecules are not essential for them.
- The reactivity of the carbon-containing species and the oxides of copper, generated during the laser pulse, with molecular hydrogen is high enough to facilitate their conversion into high vapor pressure species.
- Freshly formed oxides of copper (from reactions 2 and 4) are sufficiently energetic to be reduced by molecular hydrogen to atomic copper according to reaction 5, accounting for the low oxygen content in the films deposited in the absence of plasma.
- The minimal impact of the plasma discharge on the carbon concentration in the deposited films suggests that the formation of oxides of carbon, and not hydrocarbon formation, is the primary process for the consumption of carbon.

In-situ probing by optical emission spectroscopy or laser-induced fluorescence should facilitate the identification of reaction pathways and produce more evidence to support these conclusions.

To further understand the role of hydrogen during the deposition process, copper films were deposited in a pure argon atmosphere under conditions that were otherwise identical to those with hydrogen. The AES depth profile of such a film is shown in Figure 5. The resulting films contain similar amounts of carbon but a higher concentration of oxygen, and have much lower

electrical conductivity. The similar amounts of carbon in the films deposited with and without hydrogen ambient supports the argument that volatilization of carbon occurs primarily due to the formation of oxides of carbon. Hydrocarbon formation, if any, should be minimal. The crystallographic orientation of the formate molecules in the target film must be such that the hydrogen and oxygen necessary for the volatilization of carbon are supplied by the dissociating formate molecules themselves. The films deposited in the absence of hydrogen have a higher concentration of oxygen, since, in the presence of argon the decomposition of formate resulting in CuO or Cu₂O is not succeeded or accompanied by reduction to metallic copper. Finally, the sputter time for the film deposited in the presence of argon is much higher, perhaps because the film is somewhat thicker and the sputter yield of CuO and Cu₂O is lower than that of Cu.

The laser deposition technique described here, when combined with laser patterning (Brannon, 1989) or other forms of patterning (Jensen et al., 1984), should be an efficient way to create submicron copper patterns over large areas. The ability to process uneven topography as well as temperature-sensitive substrates is one of the advantages of this technique. Furthermore, this deposition method should be more efficient than direct laser-writing of the pattern, especially for complex submicron patterns. The minimum feature size for copper metallization obtained so far by direct laser-writing is only about 5 microns. Preliminary experiments indicate that the laser/plasma reduction technique can be utilized to deposit other metals, such as silver and titanium, as well.

3. ACKNOWLEDGEMENT

This research was supported in part by the Center for Advanced Materials Processing (CAMP) at Clarkson University through a grant from the New York State Science Foundation.

4. LITERATURE CITED

1. Al-Jaroudi, M. Y., H. T. G. Hartzell, and S. E. Homstrom, "Deposition of Titanium Nitride on Surface-Hardened Structural Steel by Reactive Magnetron Sputtering," *Thin Solid Films*, **182**, 153 (1989).
2. Bäuerle, D., "Laser-Induced Chemical Vapor Deposition," *Laser Processing and Diagnostics*, D. Bäuerle, ed., Springer-Verlag (1984).
3. Brannon, J. H., "Micropatterning of Surfaces by Excimer Laser Projection," *J. Vac. Sci. Technol.*, **B7**(5), 1064 (1989).
4. Bunshah, R. F., and C. Deshpandey, "Evaporation Processes," *MRS Bulletin*, **12**, 33 (1988).
5. Bunshah, R. F., and A. C. Raghuram, "Activated Reactive Evaporation for High Rate Deposition of Compounds," *J. Vac. Sci. Technol.*, **9**(6), 1385 (1972).
6. Cheung, J. T., and H. Sankur, "Growth of Thin Films by Laser Induced Evaporation," *CRC Crit. Rev. Solid State Mat. Sci.*, **15**(1), 63 (1988).

7. David, M., S. V. Babu, and D. H. Rasmussen, "RF Plasma Synthesis of Amorphous AlN Powder and Films," *AIChE J.*, **36**, 871 (1990).
8. Gupta, A., and R. Jagannathan, "Direct Writing of Copper Lines from Copper formate Film," *Appl. Phys. Lett.*, **51**, 2254 (1987).
9. Harish, C. M., V. Kumar, and A. Prabhakar, "Direct Writing of Copper Film Patterns by Laser-Induced Decomposition of Copper Acetate," *J. Electrochem. Soc.*, **135**, 2903 (1988).
10. Houle, F. A., C. R. Jones, T. Baum, C. Pico, and C. A. Kovak, "Laser Chemical Vapor Deposition of Copper," *Appl. Phys. Lett.*, **46**, 204, (1985).
11. Houle, F. A., R. J. Wilson, and T. H. Baum, "Surface Processes Leading to Carbon Contamination of Photochemically Deposited Copper Films," *J. Vac. Sci. Technol.*, **A4**(6), 2452 (1986).
12. Jensen, R. J., J. P. Cummings, and H. Vora, "Copper/Polyimide Materials System for High Performance Packaging," *IEEE Trans. Components, Hybrids, Manufac. Technol.*, **CHMT-7**, 384 (1984).
13. Kaloyeros, A. E., A. Feng, J. Garhart, K. C. Brooks, S. K. Ghosh, A. N. Saxena, and F. Luchrs, "Low-Temperature Metal-Organic Chemical Vapor Deposition (LTMOCVD) of Device-Quality Copper Films for Microelectronic Applications," *J. Electron. Mater.*, **19**, 271 (1990).
14. Kotecki, D. E., and I. P. Herman, "A Real-Time Monte Carlo Simulation of Thin Film Nucleation in Localized-Laser Chemical Vapor Deposition," *J. Appl. Phys.*, **64**(10), 4920 (1988).
15. Markwalder, B., M. Wichner, D. Braichotte, and H. van den Bergh, "High-Speed Laser Chemical Vapor Deposition of Copper: A Search for Optimum Conditions," *J. Appl. Phys.*, **65**, 2470 (1989).
16. Osaka, T., I. Koiwa, and L. G. Svendsen, "Behavior of Evaporated Palladium Catalyst for Electroless Nickel Phosphorus Film Formation," *J. Electrochem. Soc.*, **132**, 2081 (1985).
17. Padiyath, R., M. David, and S. V. Babu, "RF Plasma Induced Deposition of Copper Films on Polymer Surfaces," Paper 50, *Proc. 177th Meet. Electrochem. Soc.*, Montreal (1990).
18. Ritz, M., S. V. Babu, V. Srinivasan, and R. C. Patel, in *Photon, Beam and Plasma Stimulated Processes at Surfaces*, V. M. Donnelly et al., eds., Mat. Res. Soc., Pittsburg, **75**, 433 (1987).
19. Saxena, A. N., and D. Pramanik, "Aluminum Metallization for ULSI," *Solid State Technol.*, **33**(3), 73 (1990).
20. Sherman, A., *Chemical Vapor Deposition for Microelectronics*, Noyes, Park Ridge, NJ (1987).
21. Srinivasan, R., "Ultraviolet Laser Ablation of Organic Polymer Films," *Laser Processing and Diagnostics*, D. Bäuerle, ed., Springer-Verlag (1984).
22. Susa, N., S. Ando, and S. Adachi, "Properties of Tungsten Film Deposited on GaAs by RF Magnetron Sputtering," *J. Electrochem. Soc.*, **132**, 2245 (1985).
23. Temple, D., and A. Reisman, "Chemical Vapor Deposition of Copper from Copper(II) Hexafluoroacetylacetonate," *J. Electrochem. Soc.*, **136**, 3525 (1989).

THREE-DIMENSIONAL MULTIREGION S_n SOLUTIONS OF THE SPENCER-LEWIS ELECTRON TRANSPORT EQUATION

W.L. Filippone and S.P. Monahan, Department of Nuclear and Energy Engineering, University of Arizona
S. Woolf, Arcon Corporation

J.C. Garth, Electromagnetics & Reliability Directorate, Rome Laboratory

Published in Nuclear Science and Engineering, Vol. 105, May 1990

Abstract – The S_n method for solving the Spencer-Lewis equation for electron transport has been extended to treat three-dimensional multiregion problems. The flux continuity condition, which holds when the flux is expressed as a function of path length for single material region problems, is generalized for multiregion problems by reexpressing the flux as a function of energy. Expressing the fluxes in terms of fixed energy increments, independent of material, rather than fixed path length increments, results in a set of S_n /diamond-difference equations that are nearly identical in form to conventional S_n /diamond-difference equations. The S_n method is then applied to calculate electron energy deposition due to 200-keV electron beams incident on problem geometries typical of silicon and gallium-arsenide semiconductor microelectronic devices. The energy deposition results were found to compare well with results of ACCEPT Monte Carlo calculations. Computer run times required for the S_n calculations were found to be lower than that required for Monte Carlo by factors ranging from 30 to 50.

1. INTRODUCTION

The Spencer-Lewis equation¹⁻³ models the transport of electrons when continuous slowing down theory applies. This equation has recently been solved for the electron flux in one- and two-dimensional homogeneous media using the SMART scattering model,⁴ with the streaming ray^{5,6} and S_n (Ref. 7) methods. Here we extend the S_n method to three-dimensional multiregion problems.

The extension from two to three dimensions is straightforward; however, extension to multiregion problems introduces a complication. In the Spencer-Lewis equation, the path length s is used to specify the electron energy E . For homogeneous media, the continuous slowing down approximation (CSDA) implies a one-to-one correspondence between E and s . With multiregion problems, this one-to-one correspondence is lost (since the spotting power is spatially dependent), and s no longer uniquely determines E .

Therefore, we redefine s to denote the path length value that would correspond to electron energy E if the material composition that characterizes the scattering medium at the current position (x, y, z) of the electron were instead assumed to characterize an infinite homogeneous medium about that point. With this definition, E is determined by s and the electron's location. However, another problem is introduced. The electron flux, when expressed as a function of path length s rather than energy E , is no longer continuous across material interfaces, and the S_n

equations cannot be solved in the conventional manner. Although the electron flux is not continuous, this same flux integrated over a path length step will be continuous, provided that the path length steps represent the same energy intervals in each region. By using integrated quantities in place of the cell center fluxes and some of the edge fluxes, we are able to cast our equations in the standard S_n form.

Electron transport S_n solutions need not be based on the Spencer-Lewis/SMART scattering model. Some S_n calculations have also been carried out using a Boltzmann multigroup approach^{8,9} for the one-dimensional case, and two- and three-dimensional results should soon be available. To model electron slowing down efficiently, a special set of group-to-group transfer cross sections is defined that make the differenced multigroup equations equivalent to the differenced Spencer-Lewis equations. As an alternative to SMART scattering theory, scattering matrices based on Fokker-Planck,¹⁰ the extended transport correction,¹¹ or Galerkin quadrature¹² are used. Unlike SMART scattering matrices, these other scattering matrices are not positive; neither are the special group-to-group transfer cross sections. However, the multigroup Boltzmann-approach has the advantage that it can be implemented in existing neutral particle transport codes by simply adjusting the cross sections.

2. THEORY

We consider the transport of electrons in a three-dimensional medium consisting of a number of homogeneous material regions. The rectangular geometry form of the Spencer-Lewis equation valid within a homogeneous region r is³

$$\left[\frac{\partial}{\partial s} + \Omega_x \frac{\partial}{\partial x} + \Omega_y \frac{\partial}{\partial y} + \Omega_z \frac{\partial}{\partial z} + \sigma_T(s) \right] \phi(x, y, z, s, \hat{\Omega}) = Q(x, y, z, s, \hat{\Omega}), \quad (1)$$

where

$$Q(x, y, z, s, \hat{\Omega}) = \int_{4\pi} d\Omega' \sigma_T(s, \hat{\Omega}' \rightarrow \hat{\Omega}) \phi(x, y, z, s, \hat{\Omega}') + q(x, y, z, s, \hat{\Omega}) \quad (2)$$

$\phi(x, y, z, s, \hat{\Omega})$
= electron flux at position (x, y, z) , path length s , and direction $\hat{\Omega}$.

$q(x, y, z, s, \hat{\Omega})$
= fixed electron source

$\sigma_r(s)$
= total (scattering) cross section

$\sigma_r(s, \hat{\Omega}' \rightarrow \hat{\Omega})$
= differential (in angle) scattering cross section.

In region r , we define the path length for an electron of energy E as

$$s = \int_0^E \frac{dE'}{\left| \frac{dE}{ds}(E') \right|_r}, \quad (3)$$

where $|dE/ds|(E')|_r$ is the stopping power in region r . Thus, s is not the true path length for an electron that has traveled in more than one region. With s defined by Eq. (3), there is a one-to-one correspondence between s and E for each region, making it possible to define path-length-dependent cross sections. For example,

$$\sigma_r(s) = \sigma_r[E(s)]. \quad (4)$$

Integrating Eq. (1) over a mesh cell Δs_i^r (the need for the superscript r on Δs_i^r is explained below), we obtain

$$\begin{aligned} \phi_{i+1/2}(x, y, z, \hat{\Omega}) - \phi_{i-1/2}(x, y, z, \hat{\Omega}) \\ + \left(\Omega_x \frac{\partial}{\partial x} + \Omega_y \frac{\partial}{\partial y} + \Omega_z \frac{\partial}{\partial z} + \sigma_i^r \right) \phi_i(x, y, z, \hat{\Omega}) \Delta s_i^r \\ = Q(x, y, z, \hat{\Omega}) \Delta s_i^r, \end{aligned} \quad (5)$$

where

$$\phi_{i \pm 1/2}(x, y, z, \hat{\Omega}) = \phi(x, y, z, s_{i \pm 1/2}^r, \hat{\Omega}), \quad (6)$$

$$\phi_i(x, y, z, \hat{\Omega}) = \frac{1}{\Delta s_i^r} \int_{s_i^r - 1/2}^{s_i^r + 1/2} ds \phi(x, y, z, s, \hat{\Omega}), \quad (7)$$

$$Q_i(x, y, z, \hat{\Omega}) = \frac{1}{\Delta s_i^r} \int_{s_i^r - 1/2}^{s_i^r + 1/2} ds Q(x, y, z, s, \hat{\Omega}), \quad (8)$$

and $s_{i \pm 1/2}^r$ are the edges of cell Δs_i^r .

The S_n algorithm cannot be applied directly to Eq. (5) because $\phi_i(x, y, z, \hat{\Omega})$ is not continuous across material interfaces. However, when multiplied by Δs_i^r , this flux is continuous, provided the Δs_i^r define the same energy interval in each region; that is,

$$\Delta s_i^r = \int_{E_i - 1/2}^{E_i + 1/2} \frac{dE'}{\left| \frac{dE}{ds}(E') \right|_r}, \quad (9)$$

where the energies $E_i \pm 1/2$ defining the edges of the i 'th path length step are identical in every material region.

Multiplying by Δs_i^r and defining

$$\bar{\phi}_i(x, y, z, \hat{\Omega}) = \phi_i(x, y, z, \hat{\Omega}) \Delta s_i^r \quad (10)$$

and

$$\bar{Q}_i(x, y, z, \hat{\Omega}) = Q_i(x, y, z, \hat{\Omega}) \Delta s_i^r, \quad (11)$$

Eq. (5) becomes

$$\begin{aligned} \bar{\phi}_{i+1/2}(x, y, z, \hat{\Omega}) - \bar{\phi}_{i-1/2}(x, y, z, \hat{\Omega}) \\ + \left(\Omega_x \frac{\partial}{\partial x} + \Omega_y \frac{\partial}{\partial y} + \Omega_z \frac{\partial}{\partial z} + \sigma_i^r \right) \bar{\phi}_i(x, y, z, \hat{\Omega}) \\ = \bar{Q}_i(x, y, z, \hat{\Omega}). \end{aligned} \quad (12)$$

To put this equation in discrete ordinates form, we set $\hat{\Omega}$ equal to discrete direction $\hat{\Omega}^m$ and integrate over mesh cell $\Delta x_j \Delta y_k \Delta z_l$, obtaining

$$\begin{aligned} \bar{\phi}_{i+1/2}^{m,jkl} + \bar{\phi}_{i-1/2}^{m,jkl} - \frac{\Omega_x^m}{\Delta x_j} \left(\bar{\phi}_{ij}^{m,j+1/2,kl} - \bar{\phi}_{ij}^{m,j-1/2,kl} \right) \\ + \frac{\Omega_y^m}{\Delta y_k} \left(\bar{\phi}_{ij}^{m,j+1/2,k+1/2,l} - \bar{\phi}_{ij}^{m,j+1/2,k-1/2,l} \right) \\ + \frac{\Omega_z^m}{\Delta z_l} \left(\bar{\phi}_{ij}^{m,j+1/2,k+1/2,l+1/2} - \bar{\phi}_{ij}^{m,j+1/2,k+1/2,l-1/2} \right) + \sigma_i^r \bar{\phi}_{ij}^{m,jkl} \\ = \sum_{m'=1}^M S_{imm'}^r \bar{\phi}_{ij}^{m',jkl} + \bar{q}_{ij}^{m,jkl}, \end{aligned} \quad (13)$$

where

$$\begin{aligned} \bar{\phi}_{i \pm 1/2}^{m,jkl} = \frac{1}{\Delta x_j \Delta y_k \Delta z_l} \int_{x_j-1/2}^{x_j+1/2} dx \int_{y_k-1/2}^{y_k+1/2} dy \\ \times \int_{z_l-1/2}^{z_l+1/2} dz \phi_{i \pm 1/2}(x, y, z, \hat{\Omega}^m), \end{aligned} \quad (14)$$

$$\begin{aligned} \bar{\phi}_{ij}^{m,j+1/2,kl} = \frac{1}{\Delta y_k \Delta z_l} \int_{y_k-1/2}^{y_k+1/2} dy \\ \times \int_{z_l-1/2}^{z_l+1/2} dz \bar{\phi}_i(x_{j \pm 1/2}, y, z, \hat{\Omega}^m), \end{aligned} \quad (15)$$

$$\begin{aligned} \bar{\phi}_{ijk \pm 1/2}^m = \frac{1}{\Delta x_j \Delta z_l} \int_{x_j-1/2}^{x_j+1/2} dx \\ \times \int_{z_l-1/2}^{z_l+1/2} dz \bar{\phi}_i(x, y_{k \pm 1/2}, z, \hat{\Omega}^m), \end{aligned} \quad (16)$$

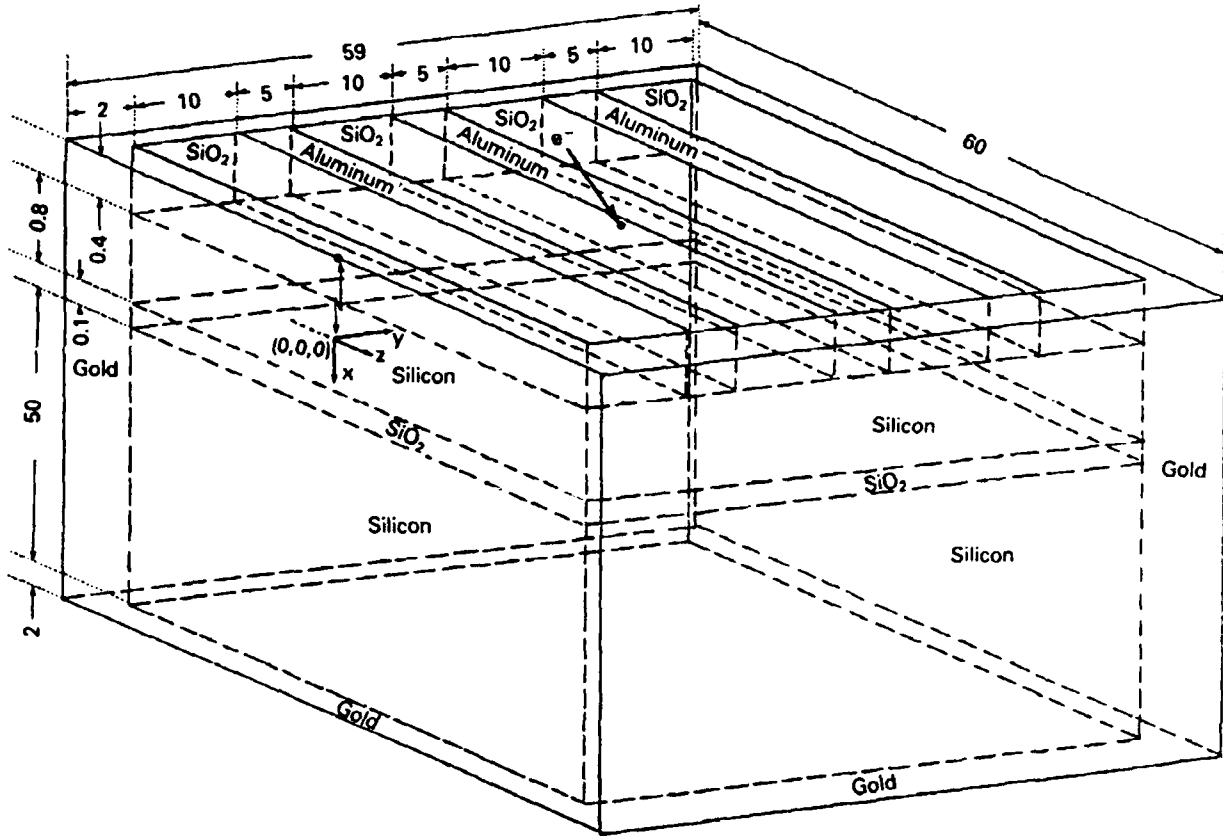


Fig. 1. Silicon device geometry (not drawn to scale). Units of lengths are in micrometres.

$$\bar{\Phi}_{ijkl\pm 1/2}^m = \frac{1}{\Delta x_j \Delta y_k} \int_{x_j-1/2}^{x_j+1/2} dx \times \int_{y_k-1/2}^{y_k+1/2} dy \bar{\Phi}_i(x, y, z_{l\pm 1/2}, \hat{\Omega}^m), \quad (17)$$

$$\bar{\Phi}_{ijkl}^m = \frac{1}{\Delta x_j \Delta y_k \Delta z_l} \int_{x_j-1/2}^{x_j+1/2} dx \int_{y_k-1/2}^{y_k+1/2} dy \times \int_{z_l-1/2}^{z_l+1/2} dz \bar{\Phi}_i(x, y, z, \hat{\Omega}^m), \quad (18)$$

$$\bar{q}_{ijkl}^m = \frac{1}{\Delta x_j \Delta y_k \Delta z_l} \int_{s_i-1/2}^{s_i+1/2} ds \int_{x_j-1/2}^{x_j+1/2} dx \times \int_{y_k-1/2}^{y_k+1/2} dy \int_{z_l-1/2}^{z_l+1/2} dz q(x, y, z, s, \hat{\Omega}^m), \quad (19)$$

$$x_{j\pm 1/2}, y_{k\pm 1/2}, z_{l\pm 1/2} \\ = \text{edges of cell } \Delta x_j \Delta y_k \Delta z_l$$

S_{imm}^r = mm 'th element of the scattering matrix for region r and path length step i
 M = total number of discrete directions.

To model the extreme anisotropy of the electron scattering kernel, we use SMART scattering theory⁴ to generate the S_{imm}^r .

Except for the numerical treatment of the scattering term, Eq. (13) is exact, but contains five unknowns, the cell center flux and the four cell exit fluxes. To obtain a solvable system of equations, we use the diamond-difference approximation:

$$\begin{aligned} 2\bar{\Phi}_{ijkl}^m &= (\bar{\Phi}_i^{m+1/2 jkl} + \bar{\Phi}_i^{m-1/2 jkl}) \Delta s_i^r \\ &= \bar{\Phi}_{ij}^{m+1/2 kl} + \bar{\Phi}_{ij}^{m-1/2 kl} \\ &= \bar{\Phi}_{ijk}^{m+1/2 l} + \bar{\Phi}_{ijk}^{m-1/2 l} \\ &= \bar{\Phi}_{ijkl}^{m+1/2} + \bar{\Phi}_{ijkl}^{m-1/2}. \end{aligned} \quad (20)$$

With the exception of the appearance of Δs_i^r in Eq. (20) and its absence from Eq. 13, these two equations are identical in form to the conventional S_N /diamond-difference equations.^{7,13}

Making a minor adjustment for Δs_i^r , we solve these equations using the usual S_N /diamond-difference algorithm.

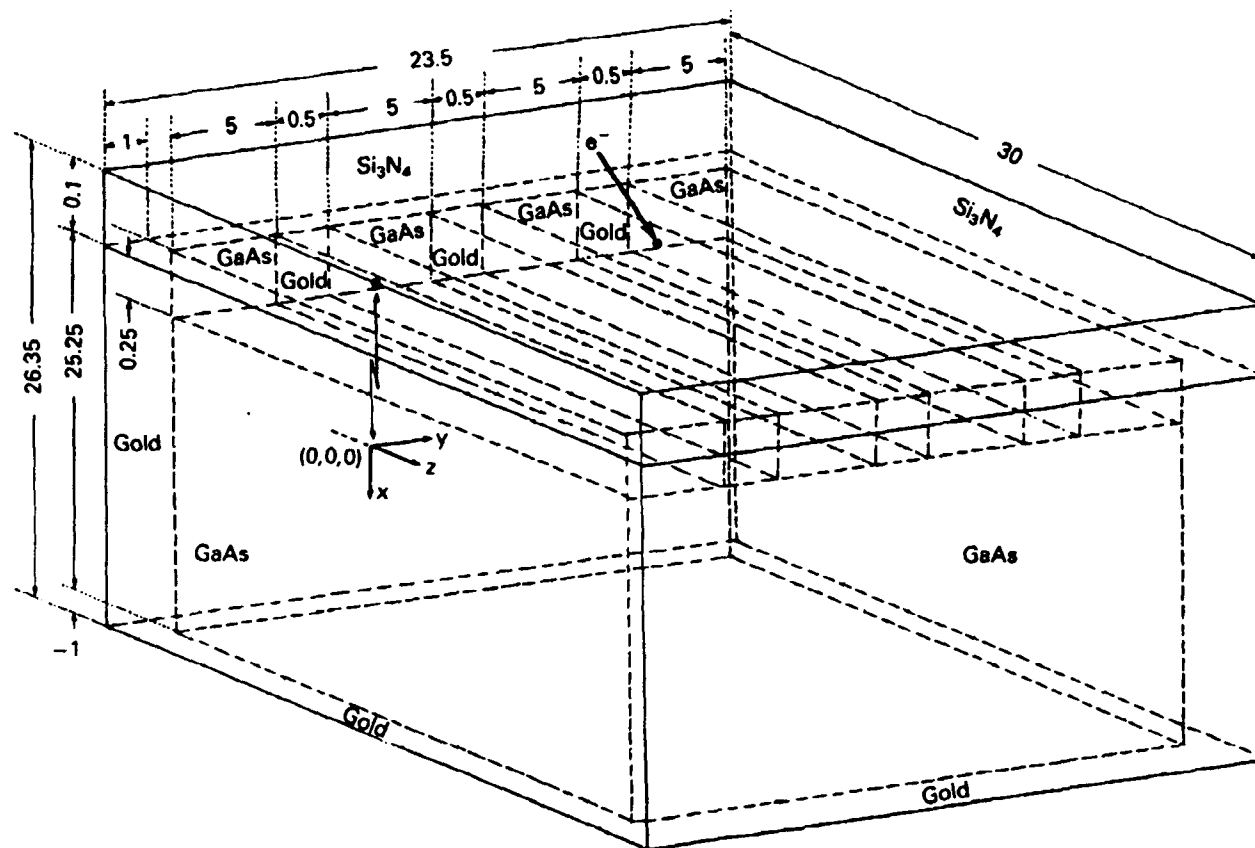


Fig. 2. Gallium-arsenide device geometry (not drawn to scale). Units of lengths are in micrometres.

3. SAMPLE CALCULATIONS

The S_n electron transport method outlined above was used to calculate energy deposition resulting from the incidence of electron beam sources on problem geometries typical of semiconductor microelectronic devices. The configurations we chose to work with are based on fairly detailed descriptions of (a) a silicon hybrid diode-resistor¹⁴ and (b) a gallium-arsenide (GaAs) field-effect transistor.¹⁵ The final configurations for the device geometries used in our calculations are simplified versions of these; however, their essential geometrical character and material compositions were preserved. The silicon and GaAs devices are shown in Figs. 1 and 2, respectively.

For both devices, the S_n transport code was run for 200-keV electron beams incident at a slightly off-center point: $x = 0 \mu\text{m}$, $y = 28 \mu\text{m}$, $z = 0 \mu\text{m}$ for the silicon device (see Figs. 1 and 3) and $x = 0 \mu\text{m}$, $y = 11.75 \mu\text{m}$, $z = 0 \mu\text{m}$ for the GaAs device (see Figs. 2 and 4). The incident beam orientation is given by $\theta = 90 \text{ deg}$, $\phi = 45 \text{ deg}$, where θ is the polar obliquity with respect to the z axis and ϕ is the azimuthal angle in the x - y plane (see Figs. 1 through 6). The scattering cross sections σ_s were taken to be screened Rutherford.²

Table 1. Exit currents from an Al/SiO₂ Block.

Surface	S_4	S_6	S_8	Monte Carlo ¹⁶
$x = 16 \mu\text{m}$	0.1089	0.1029	0.1010	0.09878
$y = 18 \mu\text{m}$	0.09864	0.08762	0.08504	0.08570
$z = 14 \mu\text{m}$	0.1215	0.1210	0.1199	0.1179
$x = 0 \mu\text{m}$	0.2201	0.2277	0.2291	0.2291
$y = 0 \mu\text{m}$	0.1955	0.1976	0.1980	0.2001
$z = 0 \mu\text{m}$	0.2553	0.2631	0.2669	0.2685

Independent calculations of energy deposition were made using the ACCEPT module of the Integrated TIGER Series¹⁶ of coupled electron-photon Monte Carlo codes. The ACCEPT code was run using the screened-Rutherford cross section with the CSDA (no-straggling) option. In this way, it was possible to ensure that both the S_n and Monte Carlo calculations were based on the same physical model. Sufficient Monte Carlo case histories (10^6) were run so that valid benchmark results could be obtained. The estimated standard error was $\leq 1\%$ in all of the

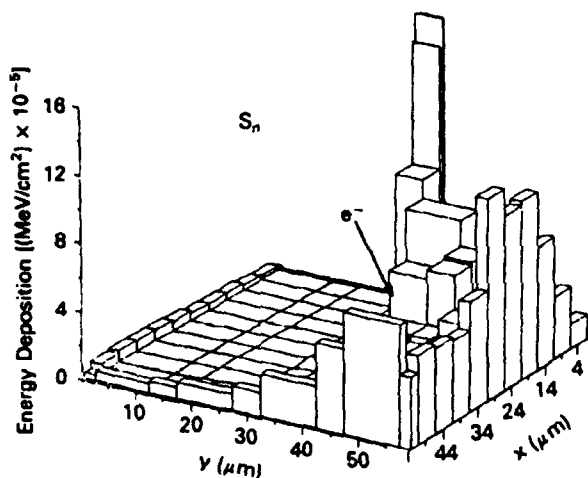


Fig. 3. Three-dimensional S_n calculation of energy deposition resulting from a 45-deg electron beam incident on a silicon device: source energy = 200 keV.

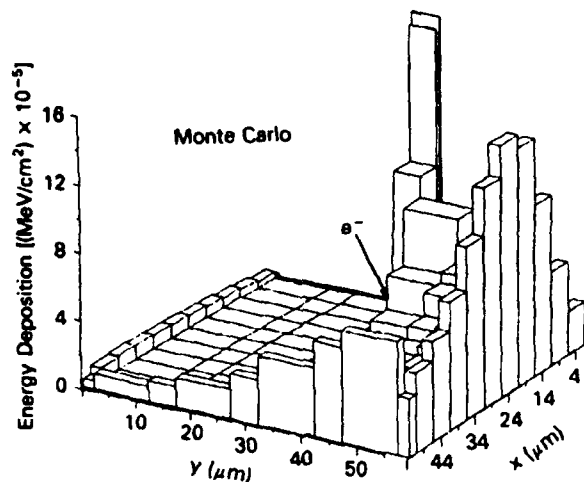


Fig. 4. ACCEPT (ref. 16) Monte Carlo calculation of energy deposition resulting from a 45-deg electron beam incident on a silicon device: source energy = 200 keV.

Monte Carlo tally cells for which the energy deposition exceeded 1% of the maximum value. The worst cases, 5 to 6% error estimates, were encountered in only 2 of 129 cells for the silicon calculation and 1 of 120 cells for the GaAs calculation. In these instances, the energy deposition values were < 0.1% of the peak value.

The energy deposition results, S_n and Monte Carlo, for the silicon device mock-up are shown in Figs. 3 and 4, respectively. The data shown result from integration, over the z coordinate, of the energy deposited per unit volume in the region bounded by the gold cap, and are therefore given in units of MeV/cm^2 . Similarly, the S_n and Monte Carlo results for the GaAs device

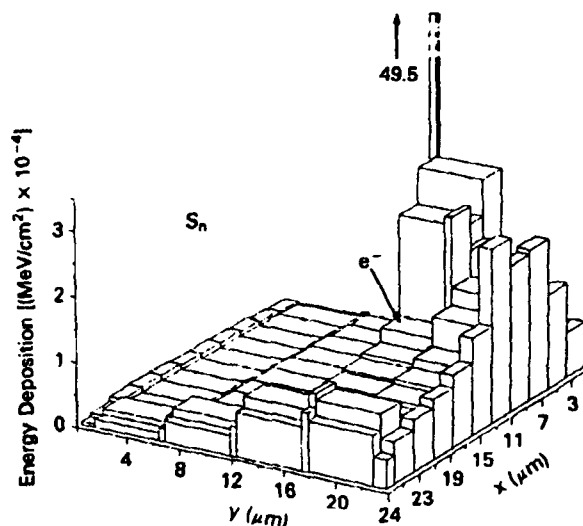


Fig. 5. Three-dimensional S_n calculation of energy deposition resulting from a 45-deg electron beam incident on a GaAs device: source energy = 200 keV.

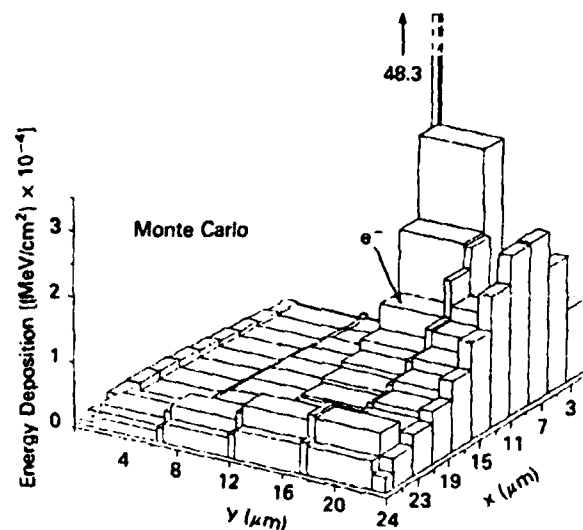


Fig. 6. ACCEPT (ref. 16) Monte Carlo calculation of energy deposition resulting from a 45-deg electron beam incident on a GaAs device: source energy = 200 keV.

configuration are shown in Figs. 5 and 6. The results obtained by the two methods seem to be in good agreement. Both S_n calculations used S_4 angular quadrature. For the silicon device, we used 60 path length steps, 14 x -mesh intervals, 9 y -mesh intervals, and 9 z -mesh intervals. The corresponding numbers for the GaAs device were 64, 13, 9, and 11. The S_n calculations consumed 29.5 min (silicon) and 35.25 min (GaAs) of VAX 8650 computer time. In contrast, the ACCEPT runs consumed 24 h (silicon) and 17.5 h (GaAs) using the same computer. We expect that the S_n calculation speed will be increased through the use of acceleration methods. As yet, none has been implemented. The use of coarse spatial mesh cells contributed

significantly to the speed of calculation. Typically, a mesh cell would have linear dimension in the range 25 to 50 (screened-Rutherford) means-free-paths. This was made possible by the use of the SMART cross-section,⁴ which provided a significant reduction in effective mean-free-path, particularly at the higher energies where a factor of 200 reduction was typical. Furthermore, use of the SMART cross section enabled us to model the extremely anisotropic scattering kernel with an S_4 quadrature set.

To test the sensitivity to S_n quadrature order, we have also analyzed the case of an isotropic electron source embedded in a simple two-region block consisting of aluminum ($0 \leq x \leq 16 \mu\text{m}$, $0 \leq y \leq 12 \mu\text{m}$, $0 \leq z \leq 14 \mu\text{m}$) and silicon dioxide (SiO_2) ($0 \leq x \leq 16 \mu\text{m}$, $12 \mu\text{m} \leq y \leq 18 \mu\text{m}$, $0 \leq z \leq 14 \mu\text{m}$). An isotropic source of 200-keV electrons is uniformly distributed in the region ($0 \leq x \leq 10 \mu\text{m}$, $0 \leq y \leq 12 \mu\text{m}$, $0 \leq z \leq 8 \mu\text{m}$). Table 1 shows S_4 , S_6 , and S_8 calculations of the currents exiting the six surfaces of the block. Also shown are the corresponding Monte Carlo results. As seen, there is very little sensitivity to the S_n quadrature order. The Monte Carlo results were obtained with the ACCEPT code (6×10^5 case histories). The estimated standard error was $< 1\%$ for all quantities calculated. While the agreement between the Monte Carlo and the S_8 calculations is excellent, the agreement with S_4 and S_6 is also good.

4. DISCUSSION

Three-dimensional multiregion S_n electron transport calculations have been carried out with good results. These calculations were made feasible through the use of SMART scattering matrices and the Spencer-Lewis model of electron slowing down.

With SMART scattering matrices, the effective mean-free-path is increased by two to four orders of magnitude, thereby reducing the required number of source iterations. The SMART scattering matrices also enable us to use a low S_n quadrature order. In spite of the severe scattering anisotropy, the calculations are insensitive to the S_n quadrature order even down to S_4 , as is evident from Table 1. The average cosine of the scattering

angle of 200-keV electrons in aluminum is 0.998. To model such scattering directly with a conventional scattering matrix, the angle between adjacent quadrature directions would have to be comparable to the average angular deflection per collision. For 200-keV electrons in aluminum, this works out to be roughly an S_{64} quadrature set!

Associated with the small deflections in angle are small energy decrements. These small decrements are well modeled by the CSDA, but not the multigroup method.^{5,8,10} The Spencer-Lewis approach has the advantage that the CSDA is built into the model.³ To apply the S_n algorithm to the Spencer-Lewis equation, it is necessary to replace cell center fluxes and some of the cell edge fluxes with integrated quantities; however, this in no way complicates the algorithm.

5. REFERENCES

1. H. W. LEWIS, *Phys. Rev.*, **78**, 526 (1950).
2. L. V. SPENCER, *Phys. Rev.*, **98**, 1597 (1955).
3. W. L. FILIPPONE, *Transport Theory Stat. Phys.*, **15**, 5, 629 (1986).
4. W. L. FILIPPONE, *Nucl. Sci. Eng.*, **99**, 232 (1988).
5. W. L. FILIPPONE, M. S. SMITH, S. WOOLF, and J. C. GARTH, *Nucl. Sci. Eng.*, **95**, 22 (1987).
6. M. S. SMITH and W. L. FILIPPONE, *Trans. Am. Nucl. Soc.*, **55**, 361 (1987).
7. W. L. FILIPPONE, S. WOOLF, and J. C. GARTH, *IEEE Trans. Nucl. Sci.*, **NS-34**, 1564 (1987).
8. W. L. FILIPPONE, S. WOOLF, and J. C. GARTH, "A Comparison of Two Discrete Ordinates Methods for Electron Transport Calculations," *Proc. Topl. Mtg. Advances in Reactor Computations*, Salt Lake City, Utah, March 28-31, 1983, Vol. 2, p. 649, American Nuclear Society (1983).
9. J. E. MOREL, *Nucl. Sci. Eng.*, **91**, 324 (1985).
10. J. E. MOREL, *Nucl. Sci. Eng.*, **79**, 340 (1981).
11. J. E. MOREL, *Nucl. Sci. Eng.*, **71**, 64 (1979).
12. J. E. MOREL, *Nucl. Sci. Eng.*, **101**, 72 (1989).
13. B. G. CARLSON and K. D. LATHROP, "Transport Theory-The Method of Discrete Ordinates," *Computing Methods in Reactor Physics*, Gordon and Breach Science Publishers, New York (1968).
14. S. VERGHESE, J. J. WORTMAN, and S. E. KERNS, *IEEE Trans. Nucl. Sci.*, **NS-34**, 1641 (1987).
15. W. T. ANDERSON et al., *IEEE Trans. Nucl. Sci.*, **NS-34**, 1326 (1987).
16. J. A. HALBLEIB and T. A. MELHORN, "TTS: The Integrated TIGER Series of Coupled Electron/Photon Monte Carlo Transport Codes," SAND84-0573, Sandia National Laboratories (Nov. 1984).

HIGH-PURITY InP GROWN ON Si BY ORGANOMETALLIC VAPOR PHASE EPITAXY

O. Aina, M. Mattingly, J.R. Bates, A. Coggins, and J. O'Connor, Allied-Signal Aerospace Company
S.K. Shastry and J.P. Salerno, Kopin Corporation
A. Davis and J. P. Lorenzo, Electromagnetics & Reliability Directorate, Rome Laboratory
K.S. Jones, Department of Materials Science, University of Florida

Published in Appl. Phys. Lett., Vol. 58, No. 14, 8 April 1991

Abstract - We have grown by organometallic vapor phase epitaxy high-purity InP on Si substrates using a GaAs intermediate layer. The InP layers exhibit residual electron concentration as low as $5 \times 10^{14} \text{ cm}^{-3}$ and electron mobilities as high as 4000 and 25 000 cm^2/Vs at 300 and 77 K, respectively. The achieved InP quality is dependent on the GaAs intermediate layer thickness. These excellent electrical properties are due to high crystal qualities as evidenced by x-ray rocking curve half width as low as 215 arcsec and defect densities on the order 10^8 cm^{-2} . *p/n* junctions, with ideality factors as low as 1.6 and low leakage currents, confirm the device quality of this material.

Heteroepitaxial growth of InP on Si continues to be a subject of intense investigation because of the potential of integration of optical and other III-V devices with Si-based electronic devices on the same chip. Monolithic integration of Si and III-V devices is desirable for a variety of applications, such as optical communications and optical control of Si devices in fly-by-light systems for avionics, radars, and flight control.

Two III-V on silicon materials have been studied more than others; GaAs-on-Si and InP-on-Si. Of these two, InP-on-Si is of interest because optical sources and detectors can be fabricated with it, and because of the close thermal expansion match between InP and Si.^{1,2} This allows the growth of thick layers of InP on Si without cracking and with a reduction of thermal stress-related defects. Recent results on long-life lasers and photodetectors on InP-on-Si have confirmed these expectations.^{3,4} Despite these device results, high purity, and high mobility InP-on-Si with properties approaching those of InP have not yet been demonstrated.

We report here the growth of high-purity, high mobility InP-on-Si by organometallic vapor phase epitaxy (OMVPE). We also outline the conditions necessary for the growth of InP-on-Si with high crystalline qualities needed for excellent optical, electrical, and *p/n* junction characteristics.

These layers were grown by organometallic vapor phase epitaxy. A layer of GaAs was first grown on Si by low-pressure OMVPE, followed by InP grown in a separate system at atmospheric pressure. The reactants for the GaAs growth were trimethylgallium and arsine, while for the InP trimethylindium and phosphine were used. For the *p/n* junctions, the *p* layers were doped with zinc using diethylzinc. Layers grown for Hall measurements were grown on 50 $\Omega \text{ cm}$ *p*-type Si while the ones

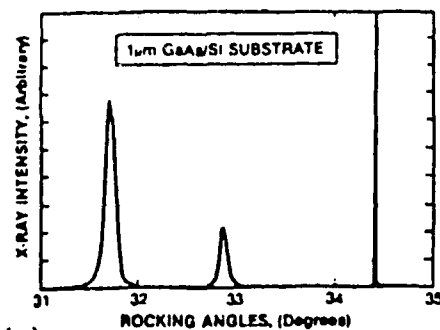
for the *p/n* junctions were on n^+ -Si substrates. A typical growth sequence for both GaAs and InP involves growth of a thin layer at low temperatures ($\sim 400^\circ\text{C}$), growth of the epilayer at 600-650°C.

We evaluated the crystal qualities of the InP epitaxial layers (using x-ray diffraction) that were grown on GaAs/Si substrates with GaAs thicknesses ranging from 200 Å to 1 μm . Figure 1 (a) show a typical rocking curve for 3 μm InP grown on 1 μm GaAs/Si substrates. Materials grown with thinner GaAs intermediate layers have larger InP rocking curve half widths. The separation of the InP and Si peaks is also smaller for the InP-on-Si layer with the thinner intermediate layer. This indicates that this material is under a higher stress than the more optimized layer. The stress for the layers with 1 μm GaAs intermediate layers is estimated to be as low as $1.3 \times 10^9 \text{ dynes/cm}^2$.

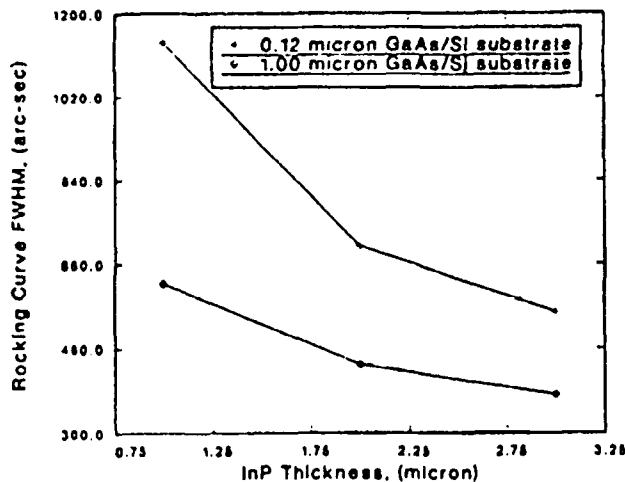
Figure 1 (b) further shows that the rocking curve full width at half maximum (FWHM) decreased with increasing GaAs and InP thickness. From this, it can be concluded that the higher the GaAs thickness, the better the quality of the InP grown on it. Since the rocking curve FWHM correlates with the defect density of the material. Further study is required to identify the optimum GaAs thickness. However, we believe 1 μm of GaAs is sufficient to optimize the InP quality since the GaAs layer quality is optimized after 0.5 μm growth. We also found that the rocking curve FWHM decreased with post-growth annealing of the InP layer at 750-800°C for 10 min. It decreased from 363 arcsec for layers annealed at 750°C to 215 arcsec for layers annealed at 800°C for 6 μm InP epitaxial layers. These half widths are the lowest that we are aware of for InP layers of similar thickness grown on Si.

Transmission electron microscopy (TEM) was used to examine these layers and showed no evidence of stacking faults. Defect densities as low as 10^8 cm^{-2} were estimated from the TEM micrographs. Etch pit densities (EPDs) were determined from HBr: H_3PO_4 acid delineation and were as low as 10^6 cm^{-2} . The discrepancy between the EPD and TEM values may be due to incomplete delineation of the variety of the defects in the InP by the HBr: H_3PO_4 solution.

The electrical properties of our InP-on-Si were assessed by Hall measurement and differential Hall profiling. The room-



(a)



(b)

Fig. 1. Crystal properties of 3 μm InP on 1 μm GaAs/Si substrates. (a) X-ray diffraction rocking curve, (b) variation of rocking curve linewidth with GaAs/Si and epitaxial InP thicknesses.

temperature Hall mobility values were 710, 3300, and 3000 cm^2/V with corresponding electron concentrations of 5×10^{15} , 2.5×10^{15} , and $4 \times 10^{15} \text{ cm}^{-3}$ for 1, 3, and 6 μm InP layers on 1 μm GaAs/Si substrates. The 77 K electron mobility was as high as 25000 cm^2/V s for 6- μm -thick layers. The electron mobility of a 2 μm InP layer grown on InP in the same system and using the same reactant is 4300 and 31 000 cm^2/V s at 300 and 77 K, respectively, with electron concentration of $6.2 \times 10^{14} \text{ cm}^{-3}$. Therefore the InP layers grown on Si have electrical properties that are close to those of InP control layers grown on bulk InP substrate. When purer metalorganics were used, the electron concentration of InP grown on Si were as low as $6.2 \times 10^{14} \text{ cm}^{-3}$.

Differential Hall profiling not only confirms these results, but shows that the 300 K electron mobility in the InP-on-Si layer is as high as 4000 cm^2/V s (Fig. 2). The slight variation in mobility in Fig. 3(a) is responsible for the lower average electron mobilities determined from Hall measurements. The electron mobilities does not decrease with depth as drastically as has been reported for InP-on-Si grown by gas source molecular

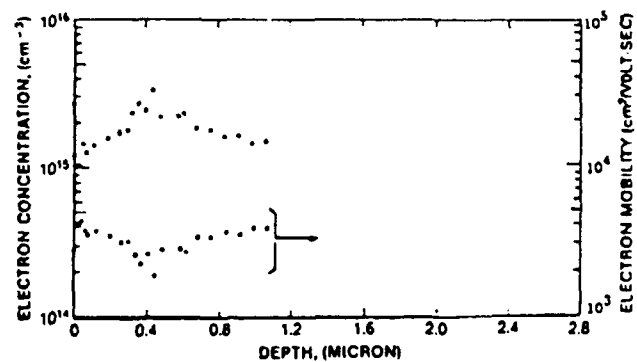


Fig. 2. Electron mobility and concentration profiles of InP-on-Si at 300 K as determined from differential Hall measurements.

beam epitaxy (MBE).⁵ The electrical properties of these InP-on-Si are the best reported to date.

The InP/GaAs/Si layers show good optical properties that are comparable to control material grown on InP substrates. As Fig. 3 shows, the photoluminescence spectra for the InP-on-Si at 10 K exhibit bound exciton and acceptor-related emissions at the same energy as the InP layer grown on InP. This indicates that

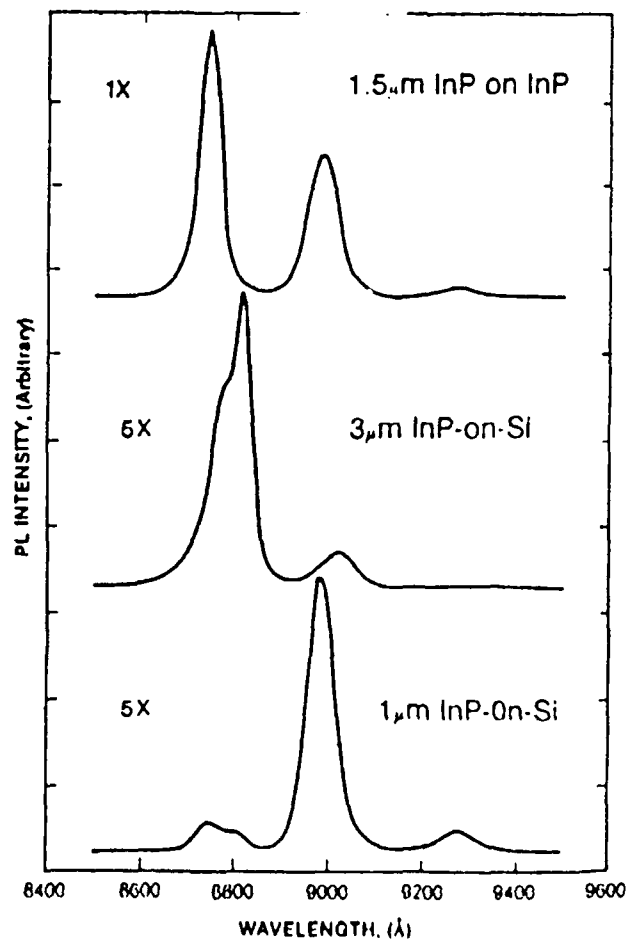


Fig. 3. Photoluminescence spectra of InP-on-Si at 10 K.

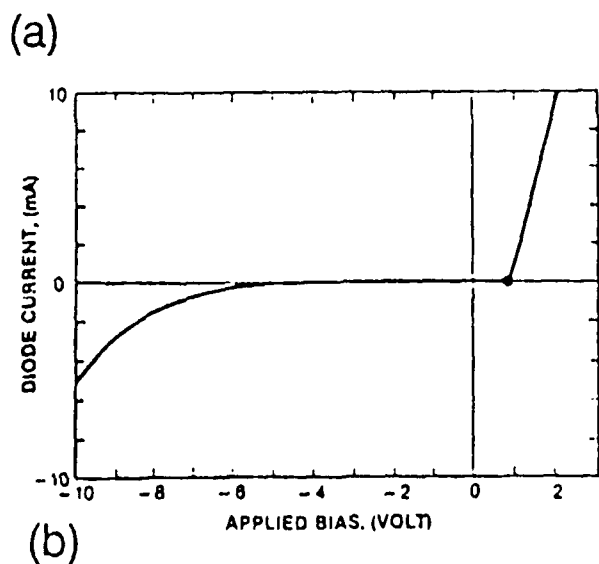
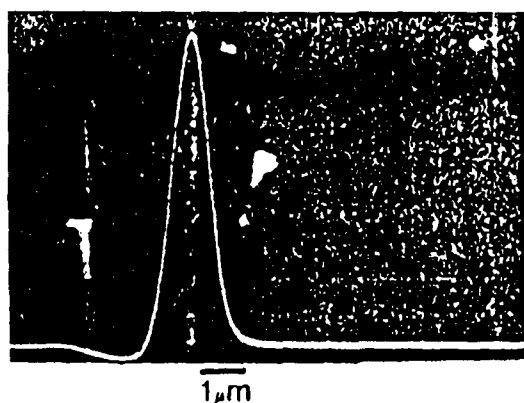


Fig. 4. Junction properties of $1\mu\text{m } p^+ \text{InP}/2\mu\text{m } n\text{-InP}$ grown on GaAs/Si. (a) SEM micrograph and EBIC scan of junction cross section, (b) I - V characteristic of the p/n junction.

there is little built-in stress in this material unlike typical GaAs-on-Si results, perhaps because of the better thermal expansion match between InP and Si.

Finally, the device quality of the material was evaluated by growing p/n junctions. Figure 4(a) shows the scanning electron microscope (SEM) micrograph of a $1\mu\text{m } p^+ \text{InP}/2\mu\text{m } n\text{-InP}$ layer grown on a $1\mu\text{m}$ GaAs/Si substrate. The superimposed electron beam induced current (EBIC) trace shows a sharp p/n junction. The minority-carrier diffusion length was estimated from the EBIC trace to be $1.6\mu\text{m}$ which is lower than the $3\mu\text{m}$ typically measured for low threshold laser structures grown on InP. The p/n junctions have an ideality factor of 1.6 as estimated from the current-voltage (I - V) characteristic in Fig. 4(b).

In summary, we have grown high-purity InP-on-Si using GaAs intermediate layers, with electron mobilities as high as $4000\text{ cm}^2/\text{V s}$ and $25\,000\text{ cm}^2/\text{V s}$ at 77 K which are the best reported so far for this kind of material. We have shown that these excellent electrical results were enabled by high crystal qualities of the InP films as evidenced by rocking curve FWHMs as low as 215 arcsec and defect densities on the order of 10^8 cm^{-2} . p/n junctions with ideality factors as low as 1.6 confirm the device quality of this material.

The authors would like to thank Dr. John McKitterick and Dr. John Lin for useful comments and suggestions, and Mary Baker for manuscript preparation. This work was supported by Rome Air Development Center/ Hanscom AFB through contract No. F19628-88-C-0119.

REFERENCES

1. M. Raseghi, *Prog. Cryst. Growth Charact.* **19**, 21 (1989).
2. H. Honkawa, Y. Kawai, M. Akiyama, and M. Sakuta, *J. Cryst. Growth* **93**, 523 (1988).
3. M. Raseghi, M. Defour, F. Onnes, Ph. Maurel, J. Chazelas, and F. Brilouet, *Appl. Phys. Lett.* **53**, 725 (1988).
4. M. Raseghi, F. Onnes, R. Blondeau, Ph. Maurel, M. Defour, O. Archer, E. Vassilakis, G. Mesquida, J. C. C. Fan, and J. P. Salerno, *J. Appl. Phys.* **65**, 4066 (1989).
5. T. E. Crumbaker, M. J. Hafich, G. Y. Robinson, A. Davis, and J. P. Lorenzo, 2nd International Conference on Indium Phosphide and Related Materials, IEEE Conference Proceedings, No. 90CH2859-7, 131 (1990).

ELECTRON-ACOUSTIC PHONON SCATTERING IN SiO₂ DETERMINED FROM A PSEUDO-POTENTIAL FOR ENERGIES OF $E > E_{BZ}$

J.N. Bradford, Electromagnetics & Reliability Directorate, Rome Laboratory
S. Woolf, Arcon Corporation

Published in Journal of Applied Physics, Vol. 70, No. 1, 1 July 1991

Abstract – The existing description of hot electron transport in silicon dioxide contains the deficiency that the resulting electron inverse mean free paths and loss rates associated with electron-acoustic phonon scattering continue to increase in an unphysical way at energies above E_{gap} . One can remove that discrepancy by introducing a pseudo potential which reflects the screened atom characteristic of higher energy electron-lattice interactions. The low energy, low q scattering, described in terms of the deformation potential, is then recovered, intact, in the low q limit. The use of the screened Coulomb potential introduces no adjustable parameters and results in an acoustic scattering cross section which approaches the phase shift derived elastic scattering cross section at $E > E_{gap}$.

1. INTRODUCTION

The transport of low energy electrons in SiO₂ has been a subject of interest in recent years due to the success of the theory of electron-acoustic phonon scatter as developed by Fischetti¹ from the ionic crystal based work of Sparks *et al.*² The addition of that acoustic phonon scatter to the LO scatter described in the theory and calculations of Fröhlich,³ Garwin,⁴ and Fitting⁵ revealed several characteristics of the electron motion. Among these were the trend toward saturation of the drift velocity, the increase in the mean value of the transport kinetic energy spectrum and the mitigation of electron velocity runaway, all in the presence of strong applied electric fields. Experimental^{6,7} and Monte Carlo results^{8,9} have been in agreement in most cases.

The continuation of the transport to energies above E_{gap} presented new challenges and emphasized a basic deficiency in the underlying theory. First, as has been pointed out elsewhere,¹⁰ the deformation potential approach is a low k, q theory and contains approximations not valid above k_{BZ} . The carrying up of this low energy theory to energies greater than E_{BZ} manifests itself in the deficiency that the predicted inverse mean free paths and energy loss rate (dE/dx), continue to increase unabated at energies $E > E_{gap}$. Second, the current theory does not naturally transform toward the elastic atomic scattering process at energies several times E_{BZ} .

The transport parameters (inelastic inverse mean free paths, elastic scattering cross sections from phase shift calculations) for electron energies greater than 10 eV in SiO₂ have been available for some time.^{11,12} A complete transport calculation requires a coupling of the low energy electron-phonon scatter

theory to the energy domain above E_{gap} where the transport is dominated by elastic scatter and impact ionization. We achieved such a Monte Carlo calculation with credible results.¹³ In order to overcome the difficulties above we terminated use of the acoustic scatter cross section in favor of the elastic cross section at 10eV. We present in this paper a way to avoid that artifice by the use of the screened Coulomb pseudo-potential in the electron-acoustic phonon interaction formalism.

2. THE PSEUDO-POTENTIAL

The prescription for creating the interaction potential between an electron and a unit cell as set forth by Ziman¹⁴ is to sum over the contribution from each cell site and then, in the calculation of the matrix element for the scatter, resolve the result into the product of two factors: a structure factor and an atomic form factor. Thus, summing over lattice sites at locations s_i ,

$$V(r) = \sum_i V_a(r - s_i), \quad (1)$$

the matrix element between the inbound electron wave vector, k , and scattered wave vector, j , is

$$M_{jk} = \int e^{i \cdot j \cdot r} \sum_i V_a(r - s_i) e^{i \cdot k \cdot r} dr, \quad (2)$$

and with scattering vector $q = k - j$ and interaction distance $x = r - s_i$,

$$= \sum_i e^{i \cdot q \cdot s_i} \int e^{i \cdot q \cdot x} V_a(x) dx. \quad (3)$$

The first factor is the structure factor and is left unchanged. The second factor, the Fourier transform of the interaction potential, is to be determined from a screened Coulomb potential which appropriately describes the q dependent scattering with the lattice seen by higher energy electrons in high q (umklapp) collisions. So, with

$$V_a(x) = \frac{1}{4\pi\epsilon_0} Z_1 Z_2 e^2 e^{-\alpha x}/x, \quad (4)$$

and its Fourier transform, including the unit cell volume, Ω_c , in the manner of Ziman,¹⁴

$$V_a(q) = \frac{4\pi}{U_c} \left(\frac{1}{4\pi\epsilon_0} Z_1 Z_2 e^2 \right) \frac{1}{\alpha^2 + q^2} \quad (5)$$

One can recover the low q deformation potential evaluation of the matrix element by requiring the $\lim_{q \rightarrow 0} V_a(q) = C$, the deformation potential. This determines the value for α^2 . Numerical evaluation based on $C = 3.5 \text{ eV}^1$ and $Z_2 = 8$ for the dominant oxygen scatterer, and $U_c = 113 \text{ \AA}^3$ yields $\alpha^2 = 3.65 \text{ \AA}^{-2}$. Thus, α is approximately equal to $2k_{BZ}$. The form for the square of the matrix element is then given by

$$|M_{jk}|^2 = C^2 q^2 / (1 + q^2/\alpha^2)^2. \quad (6)$$

In this way one retains the deformation potential description for the unit cell interaction for $q < \alpha$ but obtains a more credible behavior at $q > \alpha$. Additionally, the matrix element square in this form leads to a rollover and decline in the acoustic scatter cross section as seen in recent photoelectron line broadening experiments,¹⁵ γ and dE/dx .

The integral relations, based on the pseudo-potential, for the scattering rate, γ , and the energy loss rate dE/dx are, derived from the format of Ashley:¹⁶

$$\gamma^\pm = \frac{3C^2}{4\pi M_p N_c \hbar v} \int_0^{q_{\max}} dq \frac{q^3}{\omega(q)} \times [n(q) + 1/2 \pm 1/2] \frac{f(q)}{(1 + q^2/\alpha^2)^2}, \quad (7)$$

$$-dE/dx = \frac{3C^2}{4\pi M_p N_c v^2} \left\{ \int_0^{q_{\max}} dq q^3 \frac{f(q)}{(1 + q^2/\alpha^2)^2} \times [n(q) + 1] - \int_0^{q_{\max}} dq q^3 \times \frac{f(q)}{(1 + q^2/\alpha^2)^2} n(q) \right\}, \quad (8)$$

where M_p and N_c are mass and density of unit cell, $n(q)$ is Bose function at room temperature, $f(q)$ alters mass of unit cell to mass of heaviest constituent, $\omega(q)$ = phonon frequency,

$$q_{\max}^\pm = \begin{cases} 2k \mp 2m^* c_s / \hbar & ; \quad q < k_{BZ} \\ k [1 + (1 \mp c_s k_{BZ} \hbar / E)^{1/2}] & ; \quad q \geq k_{BZ} \end{cases}$$

Thus, the effect of the pseudo-potential form is to introduce the factor $(1 + q^2/\alpha^2)^2$ into the denominator of each of the

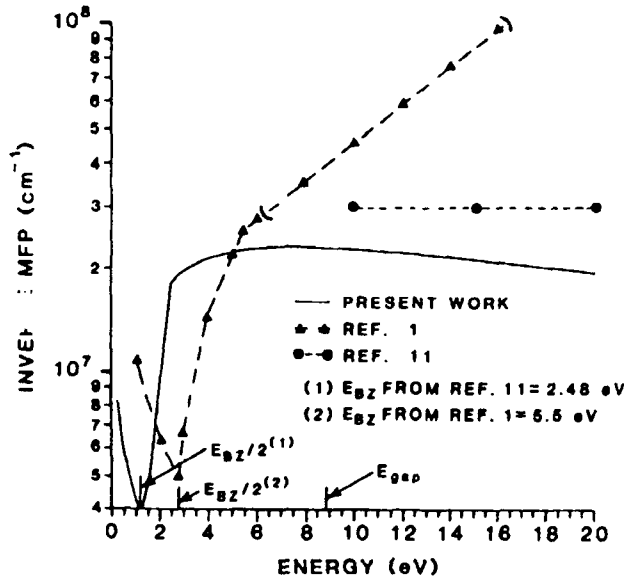


Fig. 1 Total electron-phonon scattering cross section, $1/\lambda = \gamma/v$, vs electron kinetic energy from the results of Fischetti (see Ref. 8), including extension within brackets, compared with the results from the pseudo-potential calculation and with the phase shift derived elastic scattering cross sections (see Ref. 11). Lowest energy values reflect I.O. photon scatter. The sharp break at 2.48 eV is caused by changing the mass value on the sublattice via the ramp function, $f(q)$.

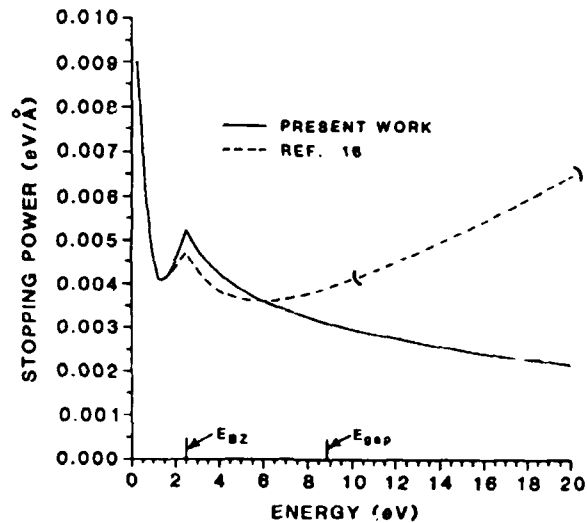


Fig. 2 Total electron-phonon dE/dx values derived from Ashley (see Ref. 16), including extension within brackets, based upon deformation potential theory compared to results from the pseudo-potential calculation. The required downturn in magnitude above E_{gap} corrects a deficiency of that original theory. Lowest energy values reflect loss to I.O. phonons. Peaks are caused by changing the mass values on the sublattice via $f(q)$.

deformation potential based expressions. For high energies and $q > k_{BZ}$, and apart from the constants, each integrand becomes $q^3/(1 + q^2/\alpha^2)^2$, which is analytically integrable. The high energy behavior of the integrated result is easily seen to be logarithmic and leads to a $(\log E)/E$ dependence for both the inverse mean free path, $\lambda^{-1} = \gamma/v$, and for the loss rate. Finally, the relationship of the differential scattering cross section in the first Born approximation has been previously utilized^{1,2} to evaluate C , the deformation potential. That relation becomes

$$\sigma(q) = 4\pi d\sigma/d\Omega = 4\pi \left(\frac{m^*}{\pi \hbar^2 N} \right)^2 |V_d(q)|^2$$

$$= \frac{4m^{*2}}{\pi \hbar^4 N^2} \frac{C^2}{(1 + q^2/\alpha^2)^2}$$

which leads to

$$\sigma(q) \rightarrow 0 \text{ for } q > \alpha,$$

$$\sigma = \frac{4m^{*2}}{\pi \hbar^4 N^2} C^2 \text{ for } q \rightarrow 0,$$

which recovers the form used by Fischetti.¹

3. NUMERICAL RESULTS

In the evaluation of γ , $1/\lambda$, and dE/dx the following numerical values were used:¹⁶

$$n(k_{BZ}) = 0.773$$

$$f(k_{BZ}) = 12.1$$

$$c_s = 3.56 \times 10^5 \text{ cm/s},$$

$$\omega(k_{BZ}) = c_s k_{BZ}$$

$$k_{BZ} = 8.15 \times 10^7 \text{ cm}^{-1}$$

$$m^*/m_0 = \begin{cases} 1/2, & E < E_{BZ}/2 \\ E/E_{BZ}, & E_{BZ}/2 < E < E_{BZ} \\ 1, & E \geq E_{BZ} \end{cases}$$

The impact of the pseudo-potential is clearly evident in Figs. 1 and 2 where the present calculations are compared to previous results. For purposes of comparison of results for all E , the in-

verse mean free path shown, λ^{-1} , includes the low energy LO phonon scatter contribution. Detailed agreement between the inverse mean free paths shown in Fig. 1 should not be expected. Two different values of E_{BZ} exist. Ashley's value¹⁶ is 2.48 eV and follows from the volume of the rhombohedral primitive cell with sides 4.913 Å and height 5.404 Å. The resulting volume, 113 Å³, and $m^* = m_0$ for the electron mass yields $E_{BZ} = 2.48$ eV. Fischetti has consistently used 5.5 eV, but without derivation. A smooth match of the scattering cross sections could be obtained by a suitable choice for E_{BZ} and suitable choices of the unknown parameters involved [e.g., C , $f(k_{BZ})$]. The declining values of dE/dx in the 10-20 eV range shown in Fig. 2 agree with the decline in line broadening described in Ref. 15. The important point is that the screened Coulomb potential satisfies much of the high and low energy requirements of acoustic phonon scatter and does so without the introduction of any new undetermined parameters.

4. REFERENCES

1. M. V. Fischetti, Phys. Rev. Lett. **53**, 1755 (1984).
2. M. Sparks, D. L. Mills, R. Warren, T. Holstein, A. A. Maradudin, L. J. Sham, E. Loh, Jr., and D. F. King, Phys. Rev. B **24**, 3519 (1981).
3. H. Fröhlich, Adv. Phys. **3**, 325 (1954).
4. J. Llacer and E. L. Garwin, J. Appl. Phys. **40**, 2766 (1969).
5. H. J. Fitting and J. U. Friemann, Phys. Status Solidi A **69**, 349 (1982).
6. S. D. Brorson, D. J. DiMaria, M. V. Fischetti, F. L. Pesaventa, P. M. Solomon, and D. W. Dong, J. Appl. Phys. **58**, 1302 (1985).
7. D. J. DiMaria, M. V. Fischetti, and E. Tierney, Phys. Rev. Lett. **56**, 1284 (1986).
8. M. V. Fischetti, D. J. DiMaria, S. D. Brorson, T. N. Theis, and J. R. Kirtley, Phys. Rev. B **31**, 812 (1985).
9. S. Woolf and J. N. Bradford, IEEE Trans. Nucl. Sci. NS-**34**, 1392 (1987).
10. S. I. Zakharov and Y. D. Fivelsky, Solid State Commun. **66**, 1251 (1988).
11. R. N. Hamm, Oak Ridge National Laboratory (private communication).
12. J. C. Ashley and V. E. Anderson, IEEE Trans. Nucl. Sci. NS-**28**, 4132 (1981).
13. J. N. Bradford and S. Woolf, Proceedings of the 13th Werner Brandt Conf., Nov. 13-16, 1990, Nara, Japan.
14. J. M. Ziman, *Principles of the Theory of Solids* (Cambridge University Press, Cambridge, 1972), pp. 55-59, 152-154, and 205-207.
15. F. R. McFeely, E. Cartier, L. J. Terminello, A. Santoni, and M. V. Fischetti, Phys. Rev. Lett. **65**, 1937 (1990).
16. J. C. Ashley, R. Ritchie, and O. H. Crawford, Proceedings of the 10th Werner Brandt Conf., Alicante, Spain, Jan 7-10, 1987, Oak Ridge National Laboratory Report CONF-870155, p. 329 (1988).

IMPACT IONIZATION IN THE PRESENCE OF STRONG ELECTRIC FIELDS IN SILICON DIOXIDE

J.N. Bradford, Electromagnetics & Reliability Directorate, Rome Laboratory
S. Woolf, Arcon Corporation

Published in Radiation Effects and Defects in Solids, 1991, Vol. 117, pp. 227-233

Abstract - This paper reports the results of Monte Carlo transport calculations for electrons in strong electric fields in silicon dioxide based on new choices for the deformation potential in acoustic phonon scatter and for the ionization threshold. Impact ionization is described on the basis of cross sections derived from many body dielectric theory coupled to a model insulator. The electron-acoustic and electron-elastic scattering rates are matched at 8eV in order to provide appropriate limitation on the electron-phonon scattering. The sensitivity of secondary electron production to these parameters is described. Also described is the important role of bulk trapped negative charge in affecting secondary electron production by changing the local field value. The results show that suitable choices for these parameters lead to appropriate levels of impact ionization and vacuum emission spectra.

1. INTRODUCTION

The electron energy domain $E_{\text{gap}} (= 8.9\text{eV}) < E < 20\text{eV}$ in SiO_2 is the meeting ground of two theories of energy loss: (1) Ionization based on the exact dielectric function (Ritchie, Ashley) and (2) Electron phonon scatter based on longitudinal optical phonon (Fröhlich) and acoustic phonon (Sparks, Fischetti, Ashley) processes. In a calculation in which energy spectra from (2) above are coupled with ionization cross sections from (1), prediction of substantial secondary electron production can result. Experimental studies^{1,2} of electrons transported in the presence of a strong applied field show spectra with high energy tails extending well beyond E_{gap} , but do not reveal accompanying secondary electron production. The missing impact ionization is one of the continuing problems in electron transport in SiO_2 . This paper reports the results of transport calculations for electrons and fields in the oxide of an idealized MOS slab structure arrangement, performed with the Monte Carlo code LOWEND, based on new choices for the deformation potential in acoustic phonon scatter and for the ionization threshold. The sensitivity of the above theories to these parameters in secondary electron production is described. Also described in this paper is the highly important role of bulk trapped negative charge in affecting secondary electron production by changing the local field value. Bulk trapping of electrons is a technique that has been used to achieve high anode fields, ostensibly without changing the cathode field. To facilitate comparison with experimental vacuum emission data, we have included a 200 Å aluminum layer at the anode and

have represented the uniformly distributed bulk charge by a spatially linear dependent form for the electric field.

2. THE MODEL

Previous calculations^{4,6,7} of electron energy gain and loss in SiO_2 in the presence of an applied electric field have emphasized the electron kinetic energy spectra and their first moments to characterize the transport. However, the kinetic energy spectrum is changing continuously in a spatially varying field so that no one spectrum can be used to characterize the impact ionization rate. Instead, we have chosen two other collective features of the transport on which we focus our attention in this paper. These are: 1) the mean total path traveled by the electrons; and 2) the secondary electron count.

The heating and stabilized transport of electron spectra in the presence of an applied electric field, \mathcal{E} , can be understood on a simple (average power in-average power out) basis, i.e.

$$\langle \text{POWER IN} \rangle = F \cdot v = e \mathcal{E} (k \cdot v) = e \mathcal{E} v_z, \quad (1)$$

$$\langle \text{POWER OUT} \rangle = v(dE/dx), \quad (2)$$

where dE/dx is the stopping power, or averaged energy loss per unit pathlength, resulting from electron scattering with longitudinal (LO) and acoustic (AC) mode phonons. Specifically, is developed by Ashley,¹² the contribution to dE/dx from LO phonon scatter is calculated from

$$-dE/dx = \frac{c^2 \omega^2}{v^2} \left(\frac{1}{\epsilon_\infty} - \frac{1}{\epsilon_0} \right) \left\{ (n_\omega + 1) \ln \left(\frac{W_2^*}{W_1^*} \right) - n_\omega \ln \left(\frac{W_2}{W_1} \right) \right\}, \quad (3)$$

where

$$W_2^* = \min \{ k(1 + \sqrt{1 \mp \hbar \omega / E}), k_{BZ} \}, W_1^* = \pm k \{ 1 - \sqrt{1 \mp \hbar \omega / E} \}$$

and from acoustic phonon scatter

$$-dE/dx = \frac{3C^2}{4\pi M N v^2} \left\{ \int_0^{q_{\text{max}}} dq q^3 f(q) (n_q + 1) - \int_0^{q_{\text{max}}} dq q^3 f(q) n_q \right\}, \quad (4)$$

where

$$q_{\max}^* = \begin{cases} 2k_F 2m^* C_s / \hbar, & q < k_{BZ} \\ k[1 + (1 \mp C_s K_{BZ} \hbar / E)^{1/2}], & q \geq k_{BZ} \end{cases}$$

where C is the deformation potential, M is the mass of a unit cell and N is the density of unit cells, $f(q)$ provides for the transform of the unit cell mass to the heaviest constituents of the cell, n_q is the Bose phonon occupation number at room temperature.

The underlying theory does not contain provision for saturation of the acoustic phonon scattering rate. We have, therefore, clamped this rate at the value equal to the elastic scattering rate at 10 eV. (Elastic scatter cross section is constant from 10 to ~ 30 eV.)

Two key parameter values govern the rate of and amount by which electron energies are increased to values in the impact ionization domain: 1) the value of the deformation potential (defined as the coupling constant for the phonon wave vector q in the electron-acoustic phonon interaction); and 2) the presence of trapped negative charges in the SiO₂. This second feature has been found in this work to be important in relating the calculated secondary production to experimental data.

The final parameters which govern secondary electron production are the threshold energy and the cross section for the process itself. We have utilized the cross section for secondary electron creation generated by J. Ashley and R. Ritchie^{8,9} based on the exact dielectric constant of the solid. We have investigated the modification of those published values based upon the work of C. Anderson and C. Crowell,¹⁰ whose principal result is that the threshold, E_{th} , for ionization is dependent upon the electron effective mass values, m_{val}^* , m_{con}^* , for the valence and conduction bands respectively, and is given by

$$E_{th} = E_{gap}(2 + \gamma)/(1 + \gamma), \quad (5)$$

where

$$\gamma = m_{val}^* / m_{con}^*. \quad (6)$$

The values of inverse mean free path⁹ were recalculated based upon this result using $m_{con}^* = m_0/2$ (where m_0 is the electron rest mass) at the bottom of the conduction band, consistent with the LO phonon model, and, with no guidance in the literature, $m_{val}^* = m_0$. The results are shown in Figure 1 where the threshold for ionization is seen shifted from E_{gap} to 11.9 eV. Secondary electron yield is reduced about 40% by use of these new values.

The value of the deformation potential in the electron-acoustic phonon matrix element is not known. The value argued for

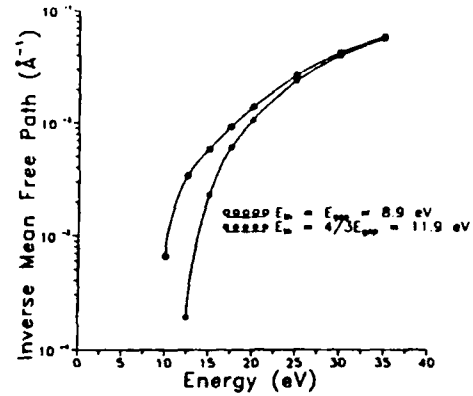


Fig. 1. Change in inverse mean free path for impact ionization according to the Anderson-Crowell formula.¹⁰ Results for threshold energy of E_{gap} as calculated by Ashley.⁹

by the IBM group⁴ in 1984 was 3.5 eV. This value for the deformation potential, C , was derived from the integrated atomic cross section through the relation $C^2 = \pi N^2 \hbar^4 \sigma / (m^*)^2$, where N is the atomic density of oxygen (the larger dominating scatterer) and σ is the cross section. More recently the value 5 eV was taken to be a better choice.¹¹ It is the square of the deformation potential that enters the formalism and, therefore, such a change in its value has the effect of doubling the dE/dx_{AC} loss rate, e.g. $(5/3.5)^2 \approx 2$.

The presence of uniform bulk trapped charge is accounted for in Monte Carlo transport calculations by assuming a spatially linear dependent form for the electric field. The actual values of δ_{anode} and δ_{avg} follow from the IBM work¹ wherein

$$\delta_{anode} = \delta_{avg} + \bar{x} Q_1 / l_{ox} \epsilon = (V(0)_g + 2\Delta V_g) / l_{ox}, \quad (7)$$

where \bar{x} is the charge centroid, Q_1 is the trapped charge/area, l_{ox} is the oxide thickness, ϵ is the permittivity of the oxide and ΔV_g is the applied voltage shift required to restore the cathode field (hence, current).

3. RESULTS

The sensitivity of mean total path and secondary count to these effects is shown in Figures 2 and 3. These results were obtained from the code LOWEND⁵ and use the unmodified secondary electron creation cross sections of Figure 1. It is clear that a reduction in secondary production by a factor of thirty occurs from a choice of 5 eV for the deformation potential and from the charged oxide condition for an 8 MV/cm anode field. The values of secondary count and mean total path obtained in the charged oxide cases are seen by projection back to the original uncharged oxide curves to intersect near those values arising from an uncharged oxide field whose strength is equal to

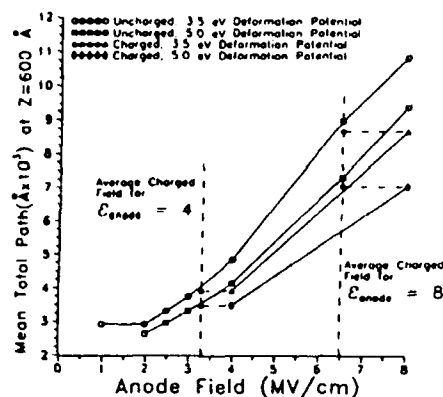


Fig. 2. Mean total paths for indicated conditions. All cases are for 600 Å total penetration depth and are based on 5000 case histories. Reductions are caused by the increased dE/dx associated with the 5 eV deformation potential and by the reduced field strength in the charged oxide.

the *average* value of the charged oxide field. That is, mean total path and secondary count are determined by the average field. We have repeated this finding for a bulk charge distributed quadratically along the field, Z , axis. To understand the origin of these results one must examine the response of the kinetic energy spectrum to different field values.

In previous works it has been emphasized that it was the anode field which determined the vacuum emission kinetic energy spectrum. Figure 4 shows this to be true for two cases with the same anode field but with differing average fields. Conversely, Figure 5 shows the spectra when the average fields are equal but the anode fields differ. Figure 6 shows the spatial distribution along the Z axis of secondary electron production by impact ionization for the constant (uncharged) and linear (charged) field cases which have the same average field value, i.e. the same conditions that produced the spectra shown in Figure 5. In the reduced (due to bulk negative charging) field

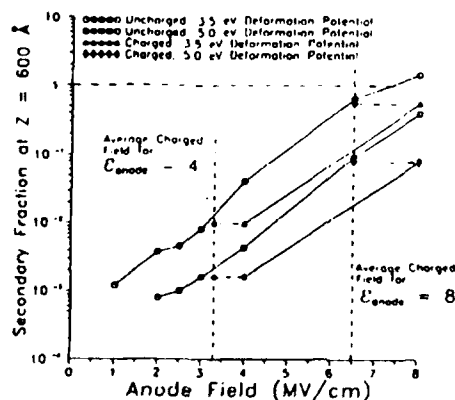


Fig. 3. Fraction of secondary electrons produced by 5000 primary electron case histories in traversing 600 Å penetration depth. Charged oxide values are shown, by backward projection, to equal those from uncharged oxide with field equal to average of charged oxide field.

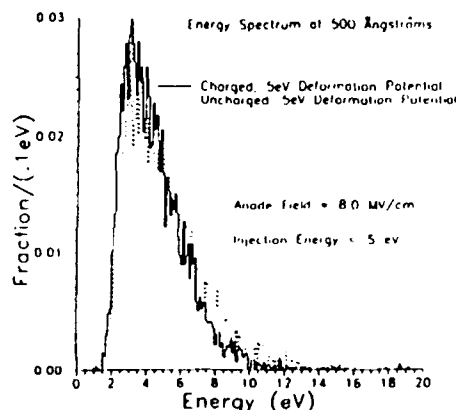


Fig. 4. Kinetic energy spectra from charged and uncharged oxides with same anode field.

region of the cathode no secondary production takes place. In the final 250 Å, additional secondary production in the linear field case is induced by the increased local field value and the resulting spectrum broadening to include more electrons in the high energy tail. This spectrum broadening to high energy while traveling through a linearly increasing field is displayed in Figure 7. The rapidly increasing impact ionization cross section and the increased population above E_{gap} leads to approximately the same number of secondary electrons being produced as in the constant field case with the same average field value.

The calculations reveal the sensitivity of the transport to the factors described above. These factors, when taken together, provide a quantitative basis for understanding the reason for the surprisingly small amount of secondary electron production seen by vacuum emission experiments¹ which utilized loading of bulk distributed electron traps. It is important to observe that the values used for deformation potential and threshold are not well established by definitive measurement. The uncharged

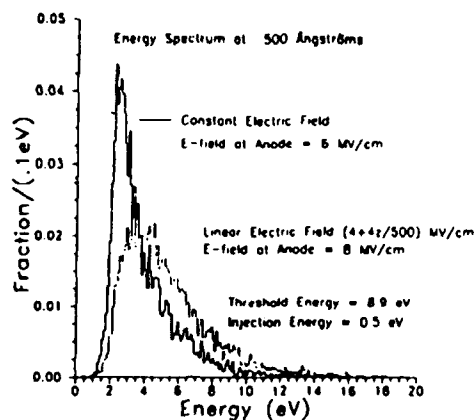


Fig. 5. Comparison of kinetic energy spectra with same average field values (6 MV/cm) but differing anode fields, 6 (-----) and 8 (----) MV/cm.

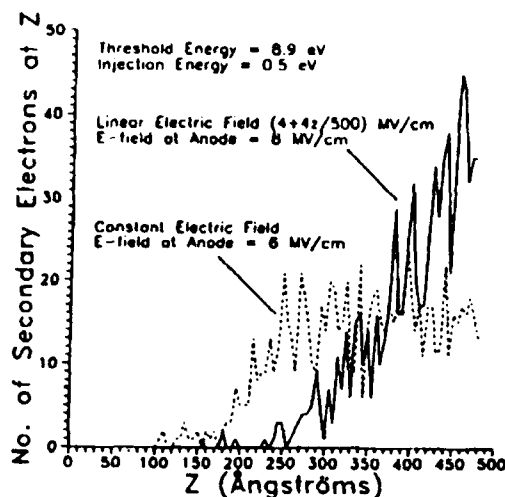


Fig. 6. Comparison of first generation secondary electron spatial distributions for same average field values (6 MV/cm), but differing anode fields, 6 and 8 MV/cm. Total number of secondaries generated in each case is nearly the same.

oxide calculations also provide a basis for understanding the quite different results on electron runaway found in experiments³ which do not use an electron trap loading technique.

Vacuum Emission Spectra

Experimental measurements of vacuum emission spectra have been reported^{1,3} which utilized either aluminum or gold anodes of ~ 200 Å thickness. We have performed a Monte Carlo calculation of the transmission spectrum through a 200 Å thick aluminum anode, based upon the cross section formalism developed in the electron gas model of Tung and Ritchie.¹³ The input spectrum from the SiO₂ was characteristic of an 8 MV/cm anode field (see Figure 4). The bottom of the conduction band

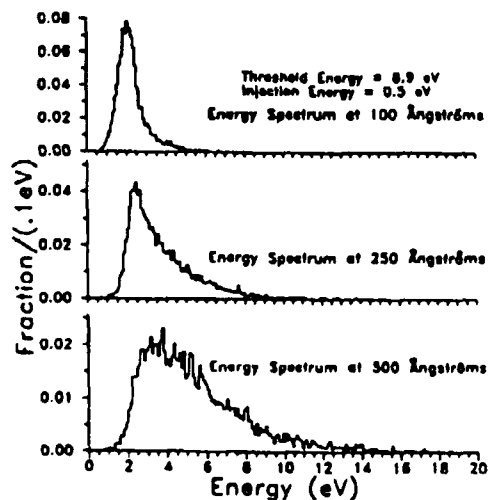


Fig. 7. Illustration of energy spectrum modification occurring in a linearly varying electric field. Secondary production does not occur until the spectrum tail overlaps the ionization threshold. This first occurs at about 250 Å.

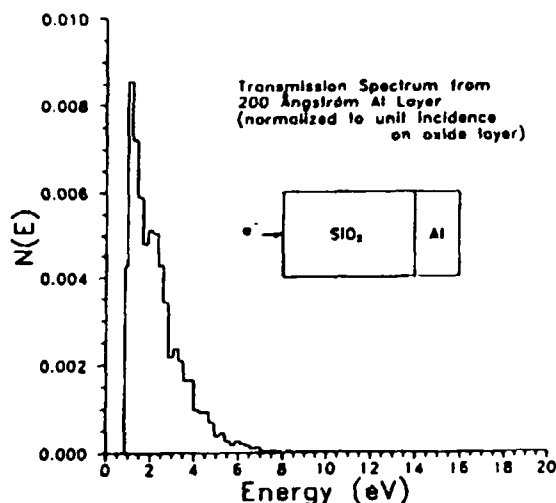


Fig. 8. Transmission spectrum through a 200 Å aluminum anode adjoining 600 Å SiO₂ layer, as shown. Input spectrum, SiO₂ → Al, is characteristic of an 8 MV/cm anode field.

in SiO₂ sits 3.2 eV above the Fermi level in aluminum and the vacuum sits 4.1 eV above the Fermi level. The resulting vacuum emission spectrum is shown in Figure 8. The integral transmission fraction is 0.064 including energetic secondaries from the aluminum. No high energy tail exists in this spectrum like that seen in experimental data. There is considerable discussion of that experimental data in Ref. 1 based upon the existence of pinholes in the aluminum layer, and indeed, one can reproduce those experimental data by small admixtures (~ 0.08) of the anode spectra, viz Figure 4, to the transmission spectrum, viz Figure 8.

4. REFERENCES

1. S. D. Brorson, et al., *J. Appl. Phys.*, **58**, 1302 (1985).
2. D. J. DiMaria, et al., *J. Appl. Phys.*, **57**, 1214 (1995).
3. H. Fitting and A. Czarnowski, *Phys. Stat. Sol.*, **83**, 385 (1986).
4. M. Fischetti, et al., *Phys. Rev. B*, **31**, 8124 (1985).
5. S. Woolf and J. N. Bradford, *IEEE Trans. Nuc. Sci.*, **NS-34**, 1392 (1987).
6. M. Fischetti, *Phys. Rev. Lett.*, **53**, 1755 (1984).
7. M. Sparks, et al., *Phys. Rev. B*, **24**, 3519 (1981).
8. R. Ritchie, *Phys. Rev.*, **114**, 644 (1959).
9. J. Ashley and V. Anderson, *IEEE Trans. Nuc. Sci.*, **NS-28**, 4132 (1981).
10. C. Anderson and C. Crowell, *Phys. Rev. B*, **5**, 2267 (1972).
11. M. Fischetti and D. Di Maria, *Physics and Technology of Amorphous SiO₂*, Plenum Press, N.Y. (1988).
12. J. Ashley, R. Ritchie and O. H. Crawford, 10th Werner Brandt Conf. (1987).
13. C. Tung and R. Ritchie, *Phys. Rev. B*, **16**, 4302 (1977).

MLEK CRYSTAL GROWTH OF (100) INDIUM PHOSPHIDE

David F. Bliss, Robert M. Hilton, and Stephen Bachowski, Electromagnetics & Reliability Directorate, Rome Laboratory
Joseph A. Adamski, Parke Mathematical Laboratories

Published in Journal of Electronic Materials, Vol. 20, No. 12, 1991

Abstract – We have used a combined magnetic liquid encapsulated Kyropoulos/Czochralski (MLEK/ MLEC) technique to produce twin-free indium phosphide (InP) crystals. This technique has advantages over the standard LEC method used for commercial production of InP. By stabilizing convective flows with a magnetic field and controlling the angle between solid and liquid, one can grow large diameter twin-free (100) InP crystals; they are shaped with a flat top as is typical for Kyropoulos growth, and then pulled from the magnetically stabilized melt as in Czochralski growth. This shaping method has the benefit of maximizing the number of single crystal wafers which can be sliced from the boule. MLEK InP growth is distinguished from other methods such as LEC and MLEC with respect to solid-liquid interface shape, dislocation density, and impurity distribution. This process has demonstrated that twin-free InP (100) crystals can be consistently grown.

1. HISTORICAL DEVELOPMENT

In 1926 Spyro Kyropoulos¹ reported on a method of growing "large" crystals from the melt. Kyropoulos was able to demonstrate single crystal growth of many alkali halides from their respective melts. His technique involved dipping an air-cooled shaft into the melt to nucleate a clump of multi-crystalline material and then raising the shaft until only a single crystal remained. By cooling the melt slowly, a flat-topped crystal was grown and subsequently lifted out of the melt. The main advantage of his technique over boat growth was that crystals grown in this manner were free from the possibility of fracture due to container confinement of the crystal. In 1938 at the Physical Institute of Danzig (now Gdansk, Poland) Morgenstern² added crystal lift and rotation to Kyropoulos growth: "The vertical growth from the melt as shown in Fig. 1 (ibid) has three definite stages. (I) The rod is dipped into the melt and withdrawn immediately. Part of the melt adheres to the rod and draws itself into a thin thread, which through a necking procedure similar to Bridgman growth, becomes a single crystal. (II) The rod with the attached crystal slowly is pulled upward. The single crystal begins to grow and forms a tetragonal cross-section. (III) The third stage becomes the finished single crystal." Figure 1 is from this 1938 journal publication.

In a survey of crystal growth written in 1946, A. F. Wells³ referred to three general methods for obtaining single crystals: Bridgman growth, Kyropoulos growth, and solid state recrystallization. Not mentioned was the Czochralski technique, which until the 1950's was mainly used for rapid growth of thin metal wires. Czochralski growth, with its inherently steep temperature gradient became the preferred method for growing

germanium and silicon in the 1950's. These elemental semiconductors can sustain large temperature gradients without plastic deformation or fracture.

After a lapse of several years, Kyropoulos growth was revived as new materials with less forgiving physical properties came into demand. Bonner and van Uiter⁴ used the Kyropoulos method to grow strain-free crystals of lead oxide compounds. It was also used to grow compound semiconductors with low thermal conductivity by Jacob⁵ and later by Ahern⁶ *et al.* Their methods involved cooling the melt until the crystal came into contact with the container walls, a departure from the original aim of Kyropoulos growth.

2. KYROPOULOS GROWTH OF INDIUM PHOSPHIDE

We have adapted the Kyropoulos method to indium phosphide growth in the (100) direction making use of a magnetic field to increase the radial temperature gradient. The axial magnetic field creates a more stable environment for crystal growth by reducing turbulence in the melt, as has been demonstrated for magnetic liquid encapsulated Czochralski (MLEC).⁷ Combining magnetic liquid encapsulated Kyropoulos (MLEK) with MLEC, the crystal is grown with a flat top roughly two inches in diameter, and then slowly pulled as a cylinder 60 mm in length. A top view of a (100) InP crystal grown by this technique is shown in Fig. 2. Controlling the shape of the growing crystal (a side view is shown in Fig. 3) is a major factor in preventing twin formation.

3. EXPERIMENTAL

The apparatus consists of a non-magnetic stainless steel chamber (see Fig. 4) containing a graphite susceptor, powered by an rf generator and coil. Outside the chamber a toroidal magnet provides an axial magnetic field up to 4kG at the center of the hot zone. Fused quartz crucibles 70 mm dia. by 65 mm high are used to contain a 450 g charge of indium encapsulated with 80 g of dry boron oxide. This is converted to 570 g of InP using the injector process⁸ at 550 psi of N₂. A (100) seed 6 mm square is used, rotating at 4 rpm in a 2kG axial magnetic field to initiate growth of a two inch flat crown. This is accomplished over a 60 min period by increasing the water flow through the

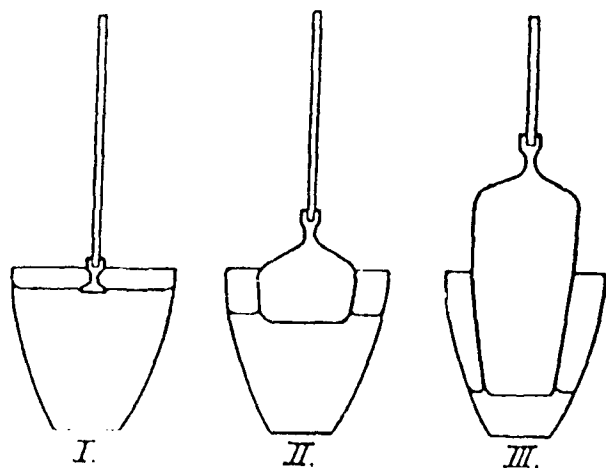


Fig. 1 Schematic of Kyropoulos Growth Method, from Morgenstern, 1938

seed holder and decreasing the rf power, no pulling is employed during this initial period. Twins are easily detected by viewing reflected light off the flat crystal crown using a high intensity light and a CCD camera (Dage MTI). When a twin is detected, the crystal is backmelted and regrown. In this fashion twin free crystals can be repeatably grown. After the crown is formed a



Fig. 2 MLEK Crystal (100) InP, Top View

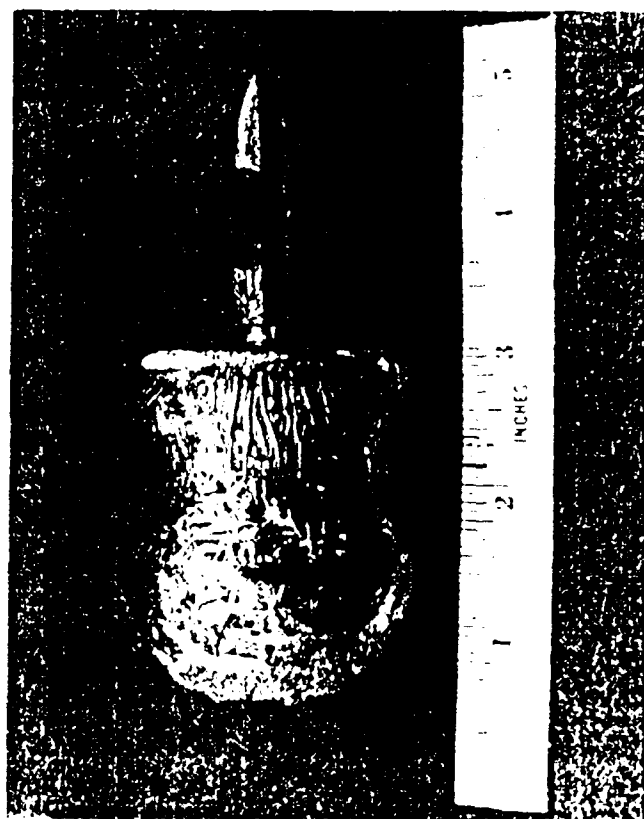


Fig. 3 MLEK Crystal (100) InP, side view

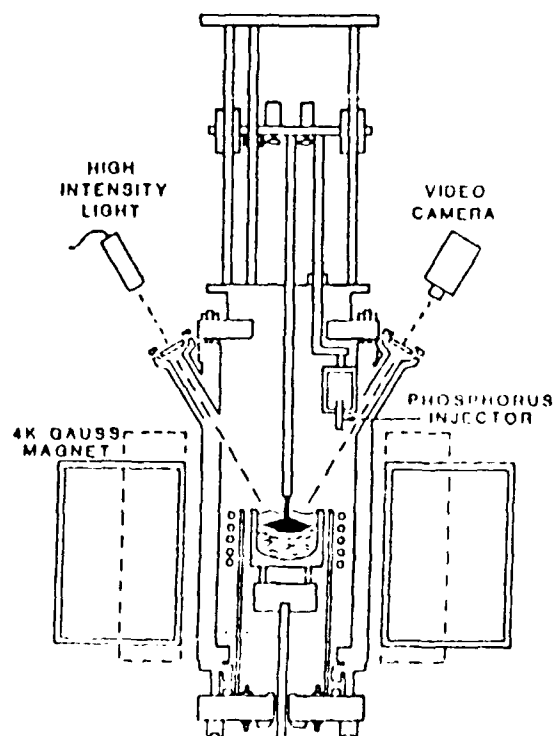


Fig. 4 Crystal Growth Apparatus for MLEK/MLFC growth method

pulling rate of 12 mm/hr is employed to pull the crystal to completion.

4. RESULTS AND DISCUSSION

InP crystals grown by the MLEK technique have been characterized and compared to LEC growth to determine the influence of the growth environment on crystal shape and dislocation density as well as dopant distribution. Unlike MLEC crystal growth, where a cone-shaped top is pulled upward through the encapsulating layer until the crystal reaches the desired diameter, the crown of the MLEK crystal is grown completely beneath the B_2O_3 , where the axial thermal gradient has been measured at $19^\circ\text{C}/\text{cm}$ in contrast to $135^\circ\text{C}/\text{cm}$ within the encapsulant. We have found that twins often form on the shoulders of MLEC crystals when pulled up through the encapsulant; however, twins are rarely found on MLEK crystals after a twin-free crown is formed. If a twin does occur on the flat top it can be quickly detected because of the crystal's specular surface, whereas the shape of an MLEC crystal cone makes it difficult to discern twin formation during growth.

A crystal was cross-sectioned and prepared for NIR transmission analysis as described previously.⁹ The solid-liquid interface shape is indicated by the striation pattern in Fig. 5, following a single striation line from the center of the crystal to the outer edge at the two-inch crystal periphery. The crystal forms

an ellipsoid of rotation with an aspect ratio $x/z = 1.6/1$. The curvature of the interface indicates a steep radial gradient, caused in part by the applied magnetic field. Unlike the interface shape of LEC crystals, which flattens out at the edge, the interface shape shown in Fig. 5 remains convex to the periphery of the growing crystal. We have observed that this shape is more conducive to single crystal growth than the sigmoidal shaped interface which is typical for LEC and MLEC growth.

In other respects, such as dislocation density and dopant distribution, MLEK/MLEC crystals are very similar to MLEC. After the flat crown is formed, crystal pulling conditions are essentially the same as MLEC growth. The dislocation density was determined on an etched (100) wafer cut from a (100) InP boule. The etch pits observed on micrographs indicate the dislocation density. A high dislocation density has been observed on commercial InP crystals grown by LEC,¹⁰ and the radial distribution varies by an order of magnitude. By comparison, MLEK/MLEC material has a lower overall dislocation density uniformity. Figure 6 shows a comparison of the radial EPD distribution between MLEK and LEC crystals grown without a magnetic field.

A tin-doped InP combined MLEK/MLEC crystal was grown using a Sn concentration in the melt of $5E19\text{ cm}^{-3}$ to determine the effect of the applied magnetic field on dopant distribution. A 4kG magnetic field was applied during the initial stages of growth until a crystal length of 22 mm had been grown. Then

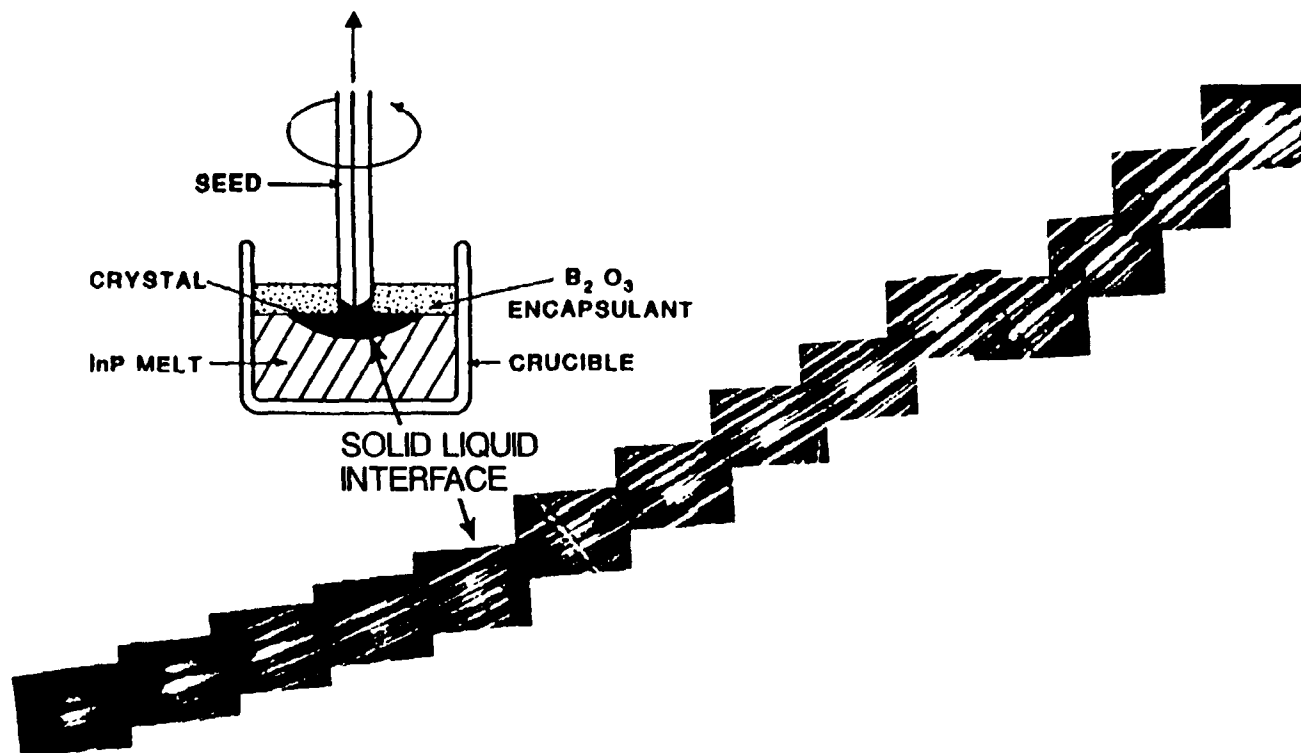


Fig. 5 NIR striagraph and schematic showing MLEK growth interface shape

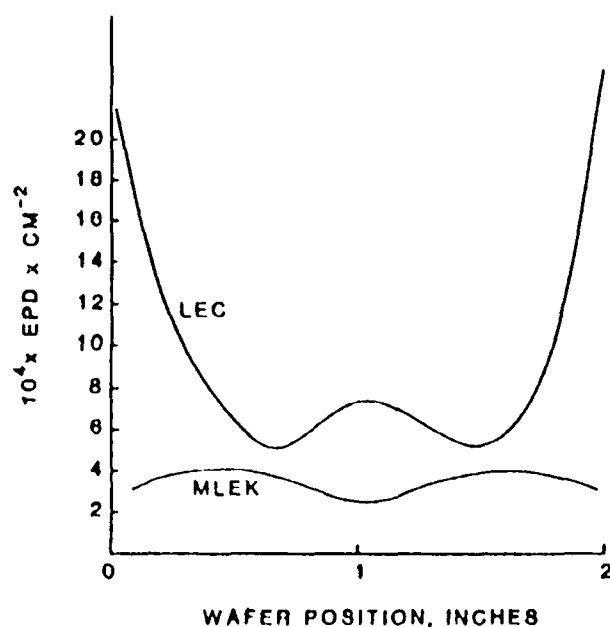


Fig. 6 Dislocation density for (100) InP Sn doped

the magnet was turned off and the crystal was pulled to completion. This crystal was sliced into Hall segments 2.5 mm apart along the crystal axis to determine the net free carrier concentration, n , as a function of crystal length. Figure 7 shows n as a function of slice position in the boule. For high carrier concentration and reasonable mobility ($> 2000 \text{ cm}^2/\text{v}\cdot\text{sec}$) the value of n is approximately N_D , the shallow donor concentration, indicating the level of tin dopant. Tin incorporation has been studied in LEC crystals grown without a magnetic field, and we have found an effective distribution coefficient, $k = 0.02$. The concentration of tin expected in the first-to-freeze InP crystal

grown by standard LEC growth is shown on Fig. 7 as $k C_L$. The dopant concentration in the MLEK InP crystal is higher than for LEC and remains uniform until the magnetic field is turned off. With the field off, the concentration increases in the typical manner of non-magnetically stabilized LEC crystals. The applied magnetic field, rather than the crystal shape, seems to control dopant incorporation as this result is similar to results obtained on MLEC InP crystals.

Controlling the thermal geometry of the crystal growth environment makes it possible to grow (100) InP by the MLEK/MLEC process. The physical shape of InP crystals grown by the combined MLEK/MLEC technique is the means by which twin formation is controlled. There are several advantages for MLEK growth of twin-free InP crystals. (1) With magnetic stabilization, it is possible to control the shape of the solid liquid interface. Twin nucleation is less likely when a convex interface is maintained, and it appears that an aspect ratio of 1.6 is sufficient to reduce the probability of twinning, although this may not be the optimized growth condition. (2) The MLEK growth environment induces a smaller amount of thermal stress than non-magnetic LEC. Since the growth interface is below the encapsulating layer, the axial temperature gradient is low during the first stages of growth, and becomes higher only when pulling is initiated. Despite the effect of a steep radial gradient, MLEK crystals show a uniform dislocation density, a factor of two lower than LEC material. (3) Magnetically stabilized InP melts contribute to a homogeneous dopant distribution, both for MLEK and MLEC growth, with an effective segregation coefficient closer to unity than is found for standard LEC growth.

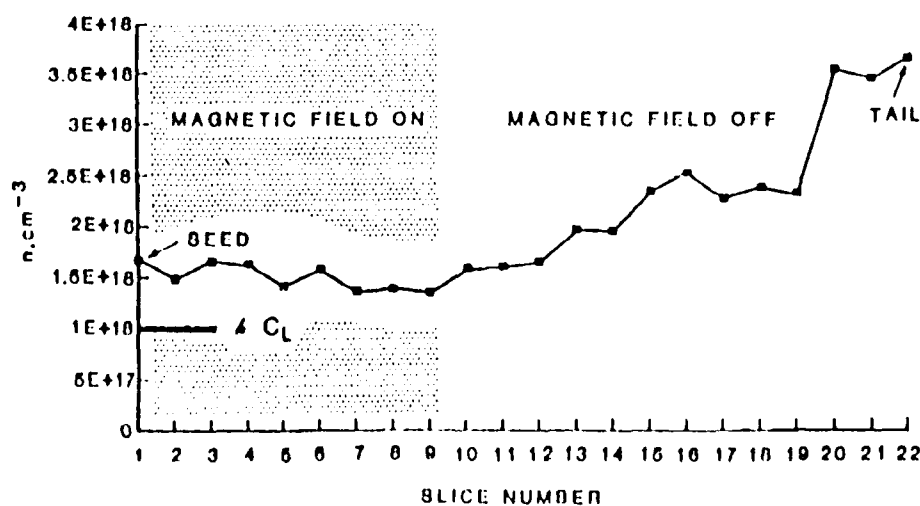


Fig. 7 Carrier concentration (77K) along axis of Sn doped MLEK/MLEC InP

5. CONCLUSION

Since its invention in 1926, Kyropoulos growth has succeeded in producing crystals not easily grown by other methods. Crystals which are prone to plastic deformation at high temperatures are naturally suited to this technique. We have demonstrated the MLEK technique for producing InP (100) crystals with uniform dislocation density. The flat top growth is shown to be favorable for twin-free growth of InP, and also maximizes the yield of single crystal wafers from each boule. MLEK growth is distinguished from MLEC growth primarily by the shaping technique, which is made possible only by magnetic stabilization of the melt. The applied magnetic field aids in growth control, which is essential for obtaining twin-free crystals with low dislocation density.

6. REFERENCES

1. S. Kyropoulos, *Z. anorg. Chem.* **154**, 308 (1926).
2. H. Morgenstern, *Z. Kristallographie*, **100**, 221 (1938).
3. A. F. Wells, Chemical Society; Annual Reports, 1946, pp. 62-87.
4. W. A. Bonner, L. G. van Uitert, *Mater. Res. Bull.* **2**, 131 (1967).
5. G. Jacob, *J. Cryst. Growth* **58**, 455 (1982).
6. B. S. Ahern *et al.*, *Mater. Lett.* **8**, 486 (1989).
7. H. Miyairi *et al.*, *J. Cryst. Growth* **79**, 291 (1986).
8. S. Bachowski *et al.*, *Mat. Res. Soc. Symp. Proc. Vol. 163* (1990) 1007.
9. S. Bachowski *et al.*, *Proc. Second Annual Conf. on InP and Related Mater.* (1990) p. 30.
10. K. P. Quinlan, *J. Electrochem. Soc.* **137**, 1991 (1990).

COUPLED LONG JOSEPHSON JUNCTIONS AND THE SINE-GORDON EQUATION

Stanford P. Yukon, Electromagnetics & Reliability Directorate, Rome Laboratory
Nathaniel Chu H. Lin, Arcon Corporation

Published in IEEE Magnetics, Vol. 27, No. 2, pg. 2736, March 1991

Abstract - We derive the Lagrangians and equations of motion for the junction phase differences for a family of coupled Josephson junction devices. These can be considered as the long junction versions and generalizations of the three coupled Josephson device first introduced by Likharev. The possible two-field kink solutions for the long three coupled Josephson junction device and three field kinks for the long six coupled junction device are derived. The two field kinks are found to exist in equal mass families having SU(3) and SU(4) symmetries respectively. With an external magnetic flux present of magnitude $\Phi = \Phi_0/2$, where $\Phi_0 = h/2c$ is the flux quantum, the kinks of the 3 junction system have 1/3 and 2/3 fluxon subkinks that behave like quarks, e.g., exhibiting permanent confinement. A collective coordinate description and time-dependent one dimensional numerical solutions for various kink collision, conversion, decay, and internal excitation processes are presented.

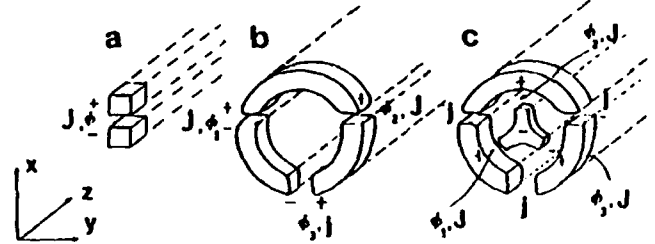


Fig. 1. Configuration of coupled superconducting elements for a) N=2, b) N=3, c) N=4 elements.

1. INTRODUCTION

The coupling of small Josephson junctions (JJ's) in various topological configurations has led to a variety of interesting and useful devices e.g., DC and AC Squids, phase locked arrays¹, the DC flux parametron², and other logic devices. In the present work we will consider what are essentially the long junction versions of squid type devices. The equations governing their behavior consist of coupled sine-Gordon equations. We solve the set of coupled equations numerically using an explicit leap-frog method and by a simple collective coordinate model. Other systems such as the model for mechanical vibrations of DNA³, lines of coupled pendula, the SU(n) Thirring model⁴, and the chiral invariant Gross Neveu model⁵ can be cast into the same form as the JJ systems. What emerges from the study of these systems is an array of new kink types and interactions, among them fractional fluxon subkinks that act like permanently confined lines rather than points of degenerate vacuum.

2. N= 3 COUPLED SUPERCONDUCTING ELEMENTS ENCLOSING FLUX $\Phi = 0$

Some possible configurations for N= 2, 3, 4 coupled superconductors and the JJ's formed by placing oxide layers between all pairs of proximate superconductors are shown in Fig. 1. The case N= 2 is that of a single JJ. Elongating this configuration in the z direction yields the long junction shown in Fig. 1a. The potential energy in terms of the phase difference $\phi(z,t)$ across the junction is given by

$$J_c \left(\frac{\Phi_0}{2\pi} \right) U[\phi], \text{ with } U[\phi] = 1 - \cos[\phi(z,t)], \quad (1)$$

where J_c is the critical current density for the long JJ and $\Phi = h/2c$ is the magnetic flux quantum. The Lagrangian density can be written as

$$\begin{aligned} \mathcal{L}[\phi] &= \frac{1}{2} C_0 \left(\frac{\Phi_0}{2\pi} \phi_t \right)^2 - \frac{1}{2L_0} \left(\frac{\Phi_0}{2\pi} \phi_z \right)^2 - J_c \left(\frac{\Phi_0}{2\pi} \right) U[\phi] \\ &= J_c \left(\frac{\Phi_0}{2\pi} \right) \left\{ \frac{1}{2\omega_p^2} \phi_t^2 - \frac{1}{2\lambda_J^2} \phi_z^2 - U[\phi] \right\}, \end{aligned} \quad (2)$$

where C_0 and L_0 are the capacitance and inductance per unit length of the junction and ω_p and λ_J are the plasma frequency and Josephson penetration depth of the junction. Variation of the Lagrangian density then yields the sine-Gordon equation of motion for ϕ as

$$\phi_{,tt} - \phi_{,zz} = \sin[\phi(z,t)], \quad (3)$$

where we have taken ω_p^{-1} and λ_J to be the unit time and length. With these units the Swihart velocity \bar{c} is given by

$$\bar{c} = \omega_p \lambda_J = 1/\sqrt{C_0 L_0} = 1.$$

The single kink solution can be derived by assuming a Lorentz invariant form

$$\phi(z,t) = \phi(\zeta) \text{ where } \zeta = \gamma(z - vt) \text{ and } \gamma = \frac{1}{\sqrt{1 - v^2}}. \quad (4)$$

The equation of motion for a single kink can then be written as

$$\phi, \zeta \zeta = -\frac{d}{d\phi}(-U[\phi]) = -\frac{d}{d\phi} V[\phi], \quad (5)$$

which can be looked upon as the Newtonian equation of motion for the "spatial" coordinate $\phi[\zeta]$ of a point particle of unit mass⁶ as a function of the "time" coordinate ζ . The kink solutions that connect two adjacent minima of the potential $U[\phi(\zeta)]$ as ζ goes from $\zeta = -\infty$ to $\zeta = +\infty$, can thus be thought of as describing the motion of a point particle in the potential $V[\phi]$ as it travels from one peak of $V[\phi]$ at $\zeta = -\infty$ down and up to an adjacent peak at $\zeta = +\infty$. For the sine-Gordon equation these solutions, determined by a simple integration, are the well known kink and antikink given by

$$\begin{aligned} \phi_k(\zeta) &= 4 \tan^{-1} \exp[(z-vt)/l] \\ \phi_{\bar{k}}(\zeta) &= 4 \tan^{-1} \exp[-(z-vt)/l] \end{aligned} \quad (6)$$

with $l = \gamma^{-1} = \sqrt{1-v^2}$,

where we have re-expressed the ζ coordinate anticipating a generalization of $l = \gamma^{-1}$.

The system consisting of $N=3$ coupled superconductors was first considered by Likharev⁷. The system was subsequently studied by Strenski and Doniach⁸ who derived the Lagrangian and equations of motion assuming negligible circuit and self inductances and investigated the non-zero voltage, zero external magnetic field case. The Lagrangian for the system of three small coupled JJ's as shown in Fig. 1b, is given as

$$\begin{aligned} L[\phi] &= \frac{1}{2} C \left[\left(\frac{\Phi_0}{2\pi} \phi_{1,t} \right)^2 + \left(\frac{\Phi_0}{2\pi} \phi_{2,t} \right)^2 + \eta \frac{\Phi_0}{2\pi} (\phi_{1,t} - \phi_{2,t})^2 \right] \\ &- \frac{\Phi_0}{2\pi} [J_{c1}(1 - \cos\phi_1) + J_{c2}(1 - \cos\phi_2) + j_c(1 - \cos(\phi_1 - \phi_2))] \end{aligned} \quad (7)$$

where we shall take $J_{c1} = J_{c2} = J_c$ and j_c as the critical Josephson currents for the three junctions, and C , C , and ηC as the capacitances of junctions 1, 2, 3 respectively. In what follows we assume that all circuit and self inductances can be neglected.

The Lagrangian in Eq. 7 may also be derived by considering it as the sum of the Lagrangians for each of the three junctions, along with the Bohm-Aharonov constraint that the line integral of the canonical momentum taken around a circuit passing within the interior of each of the superconductors equal $2\pi n$. This constraint may be written in terms of the gauge invariant phase ϕ as⁹

$$\phi_1 - \phi_2 - \phi_3 + 2 \oint \vec{A} \cdot d\vec{l} = 2\pi n. \quad (8)$$

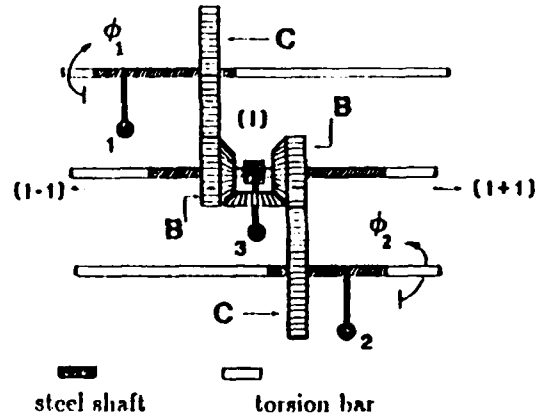


Fig. 2. Segment (i) of a differential/pendulum line (note: Pendula 1, 2, 3, and gears C are secured to shafts, all differential gears and B gears are on bearings).

Using Stoke's theorem to reexpress the line integral of the vector potential \vec{A} in terms of the total enclosed magnetic flux Φ gives

$$\phi_3 = \phi_1 - \phi_2 + 2\pi\Phi/\Phi_0 - 2\pi n. \quad (9)$$

Including this constraint by means of a Lagrange multiplier λ , then yields the Lagrangian

$$\begin{aligned} L[\phi] &= \frac{C}{2} \left[\left(\frac{\Phi_0}{2\pi} \phi_{1,t} \right)^2 + \left(\frac{\Phi_0}{2\pi} \phi_{2,t} \right)^2 + \eta \left(\frac{\Phi_0}{2\pi} \phi_{3,t} \right)^2 \right] \\ &- \frac{\Phi_0}{2\pi} [J_c(1 - \cos\phi_1) + J_c(1 - \cos\phi_2) + j_c(1 - \cos\phi_3)] \\ &+ \lambda(\phi_3 + \phi_2 + \phi_1 - \frac{2\pi\Phi}{\Phi_0} + 2\pi n) \end{aligned} \quad (10)$$

and the equations of motion

$$\begin{aligned} \ddot{\phi}_1 &= -\left(\frac{1+\eta}{1+2\eta}\right)J\sin\phi_1 - \frac{\eta J}{(1+2\eta)}\sin\phi_2 - \frac{j}{(1+2\eta)}\sin(\phi_1 - \phi_2 + \frac{2\pi\Phi}{\Phi_0}) \\ \ddot{\phi}_2 &= -\left(\frac{1+\eta}{1+2\eta}\right)J\sin\phi_2 - \frac{\eta J}{(1+2\eta)}\sin\phi_1 - \frac{j}{(1+2\eta)}\sin(\phi_2 - \phi_1 - \frac{2\pi\Phi}{\Phi_0}) \end{aligned} \quad (11)$$

where we have taken $\omega_p = (\frac{2\pi J_{c0}}{\Phi_0 C})^{\frac{1}{2}}$ as the unit of time and $J = J_c/J_{c0}$ and $j = j_c/J_{c0}$ as junction critical currents with respect to the reference current J_{c0} appearing in ω_p . For $\Phi = 0$ the above equations of motion are identical to those following from the Lagrangian $L[\Phi]$ in Eq 7.

A. Coupled pendula model.

The mechanical equivalent for the single junction is a simple pendulum¹⁰ with rotation angle ϕ . The mechanical equivalent

for the $N=3$ case is a system of two pendula coupled by a differential gear with an attached pendulum, to yield the term $(1 - \cos(\phi_1 - \phi_2 + 2\pi\Phi/\Phi_0))$ in the potential energy, as shown in Fig. 2. The external magnetic flux Φ is included by setting the initial phase relation between the three pendula [an extra 2 to 1 coupling gear C is necessary since one revolution of gear B results in only $1/2$ a revolution of the differential pendulum].

B. Long junction equation of motion.

Both the mechanical and superconducting junction systems may be considered as elements in a line of connected elements in analogy with the sine-Gordon case⁹. Taking the limit of a line of such junction elements yields the long junction shown in Fig. 1b. We shall assume that the capacitances per unit length of the long junctions 1, 2, and 3 are C_0 , C_0 , and ηC_0 respectively while the corresponding inductances per unit length are L_0 , L_0 , and L_0/η . The Swihart velocity $\bar{c} = \sqrt{C_0 L_0}$ will thus be the same for all three junctions. The equations of motion will then be given by Eq 11 with d^2/dt^2 replaced by the D'Alembertian $\partial^2/\partial t^2 - \partial^2/\partial z^2$. The ratios J and j retain the same meaning as in the short junction case when j_c , J_c , and J_{c0} are replaced by the corresponding current densities j_c , J_c , and J_{c0} . The constraint equation

$$\phi_3(z,t) = \phi_1(z,t) - \phi_2(z,t) + 2\pi\Phi/\Phi_0 + 2\pi n \quad (12)$$

is thus maintained at each field point z along the length of the line.

Taking into account the constraint of Eq 12, the Lagrangian density for the long system for $N=3$ may be written as

$$\begin{aligned} \mathcal{L}[\phi(z,t)] = J_{c0} \left(\frac{\Phi_0}{2\pi} \right) & \left\{ \frac{1}{2} [(\phi_{1,t})^2 + (\phi_{2,t})^2 + \eta(\phi_{1,t} - \phi_{2,t})^2] \right. \\ & - \frac{1}{2} [(\phi_{1,z})^2 + (\phi_{2,z})^2 + \eta(\phi_{1,z} - \phi_{2,z})^2] \\ & \left. - J(1 - \cos\phi_1) - J(1 - \cos\phi_2) - j(1 - \cos(\phi_1 - \phi_2 + 2\pi\Phi/\Phi_0)) \right\} \end{aligned} \quad (13)$$

with the equations of motion as stated above being given by Eq 11 with

$$\ddot{\phi}_i \rightarrow (\phi_{i,tt} - \phi_{i,zz}), \quad i = 1, 2. \quad (14)$$

C. Flux loop picture of kink excitations.

The simplest equation for the $N=3$ system with $\Phi = 0$ is that with $\Phi_2 = 0$ on line 2 and a sine-Gordon kink on line 1. Since an equivalent situation can be maintained on line 2 with $\Phi_1 = 0$, an

initial state of kinks $[K_1]$ or antikinks $[K_1]$ on line 1 well separated from K_2 's and \bar{K}_2 's on line 2 can be written down as an exact initial solution. In what follows we shall take $\eta = j$. A schematic drawing of a kink on line 2 colliding with an oppositely directed antikink on line 1 is shown in Fig. 3. Since the magnetic field due to a spatial gradient in the phase of a junction is given by

$$\vec{B} \propto -\vec{n} \times \vec{\nabla} \phi, \quad (15)$$

where \vec{n} is a unit vector directed from the $\phi(-)$ to the $\phi(+)$ superconductor, the magnetic field of the ϕ_2 kink is in the $+y$ direction while that of the ϕ_1 antikink is in the $-y$ direction. The phase difference across junction 3 is given by the constraint condition of Eq. 12. Since we are assuming that the external B field is constant along the z direction, taking the z derivative of Eq 12 yields the magnetic field in the third junction as

$$B_3 = B_1 - B_2 \quad (16)$$

where the directions for the flux lying within the third junction are indicated in Fig. 3. By connecting up the contribution of the flux of K_2 in junction 3 with the K_2 flux in junction 2, the K_2 kink may be thought of as a flux loop traveling down superconductor 2 with similar considerations holding for the \bar{K} flux loop on superconductor 1. The interaction of the two flux loops may then be considered as taking place in junction 3 where the interaction energy is the sum of a magnetic interaction term

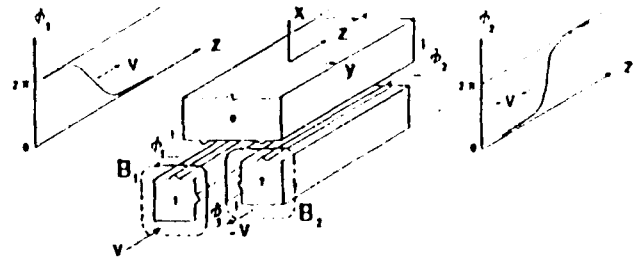


Fig. 3. Fluxon loop picture of an antikink \bar{K}_1 and kink K_2 collision.

$-\eta \phi_{1,z} \phi_{2,z}$ and a term coming from the junction potential energy $j(1 - \cos(\phi_1 - \phi_2 + \Phi))$. For a \bar{K}_1 - K_2 interaction, the magnetic interaction term will be positive resulting in repulsion of the two magnetic flux loops, while a K_1 - K_2 interaction will be attractive. The flux loop picture is also consistent with two kinks on the same line having a repulsive interaction and with a kink and antikink interaction being attractive, as is well known from the sine-Gordon case.

We have numerically solved the equations of motion for the coupled JJ systems using a modified version of the explicit leapfrog method developed for the double sine-Gordon equation by Ablowitz, Kruskal, and Ladik¹¹. The results for a sine-Gordon kink on line 1 with velocity $v = +.35c$ colliding with a sine-Gordon kink on line 2 with $v = -.35c$ are shown in a surface plot of $\phi_1(z,t)$ in Fig. 4. At the moment of impact, a burst of radiation is emitted, which subsequently travels along the light cone to the boundary where an absorbent boundary condi-

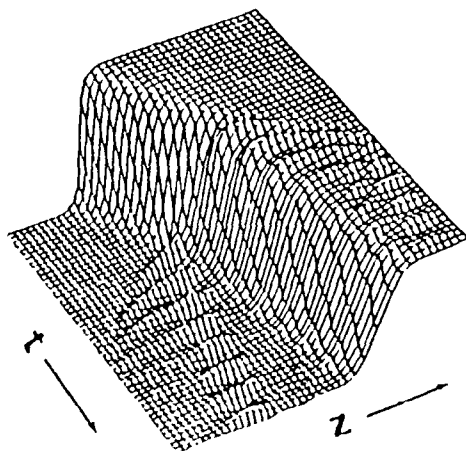


Fig. 4. Surface plot of $\phi_1(z,t)$ for K_1K_2 collision, $v = -.35$, $0 < \phi_1 < 2\pi$, $-20 < z < 20$, $0 < t < 40$. Times increases toward the viewer.

tion has been imposed. This is followed by a slower moving wake filling in the light cone. The two kinks appear as though they have become excited internally by the collision, exhibiting a teetering motion. The teetering motion is essentially what is modeled by the collective coordinate $\ell(t)$ in the collective coordinate model to be described below, and can be considered as a linear interaction of the kink with the Klein Gordon wake.

The slope at the center of a sine-Gordon kink of Eq. 6 is determined by ℓ , which equals the Lorentz factor γ^{-1} if it is freely propagating, and reflects the Lorentz contraction of the kink - a large velocity implying a large γ and therefore a small kink with a large slope at the origin. If a sine-Gordon kink solution, which cannot support an excited state, is put in with a slope at its center that is not given by $\ell = \gamma^{-1}$, the kink will emit a short burst of radiation and begin teetering. The continuum modes with $\omega > m = 1$ are able to radiate away, while those with $\omega < m = 1$ are the evanescent wake modes which travel at very low velocities and diminish as $\exp(-kz)/z$. These two components can be clearly seen in the expression for the Klein Gordon Green's function

$$G_j(z,t) = \frac{\delta(t - |z|)}{|z|} + \frac{1}{\sqrt{t^2 - z^2}} J_1(\sqrt{t^2 - z^2}) \Theta(t - |z|) \quad (17)$$

(the sine-Gordon Green's function has very similar asymptotic behavior¹²). If a sine-Gordon kink is put in the path of the wake of a distant disturbance, it will begin teetering indicating that this motion can be considered as a superposition of the Klein Gordon wake and the kink.

While the coupled system is not exactly integrable in general⁴, a reasonably good description of interactions between single kinks can be obtained using the collective coordinate model (CCM) used by Rice¹³ in the case of the perturbed sine-Gordon equation. Thus we start with the solutions for K_1 and K_2 written as

$$\phi_1 = 4 \tan^{-1} \exp[(z - \zeta(t))/\ell(t)]$$

$$\phi_2 = 4 \tan^{-1} \exp[(z - \zeta(t))/\ell(t)] \quad (18)$$

where $\zeta(t)$ is a collective coordinate representing the kink positions, while $\ell(t)$ is an internal coordinate to describe kink internal excited states. The Lagrangian for a K_1 - K_2 collision is then obtained by inserting the exact initial state $\phi = \phi_1 + \phi_2$ into the Lagrangian of Eq. 13 and integrating over z . This yields the effective Lagrangian

$$L_{KK}[\zeta(t), \ell(t)] = T_{KK}[\zeta, \dot{\zeta}] - V_{KK}[\zeta, \dot{\zeta}], \quad (19)$$

where T and V are given by

$$\begin{aligned} T_{KK}[\zeta, \dot{\zeta}] &= \frac{8(1 + \eta)}{\gamma} \left[\frac{\pi^2 \dot{\gamma}^2}{12\gamma^2} \dot{\zeta}^2 \right] + \eta \left[\frac{8}{\gamma} (\dot{\gamma} \dot{\zeta} + \dot{\zeta}^2) \right. \\ &\quad \left. - \frac{2\dot{\gamma}^2}{3\gamma^3} (4\gamma^2 \dot{\zeta}^2 + \pi^2) \right] \left(\frac{\zeta}{\text{sh}(\zeta)} \right), \\ V_{KK}[\zeta, \dot{\zeta}] &= 8\gamma [1 + \eta(1 + \eta(1 - \zeta/\text{sh}(\zeta)))] + \frac{8}{\gamma} [1 + \eta(1 - \zeta/\text{sh}(\zeta))] \\ &\quad + \frac{2}{(\text{ch}(\zeta) + 1)} [\zeta \text{cth}(\zeta) - 1] \quad (20) \end{aligned}$$

with $\gamma(t) = 1/\ell(t)$ and $\zeta = 2\gamma\zeta$.

A contour plot for this potential is shown in Fig. 5.

To effect the collision, the initial conditions on $\zeta(0)$, $\dot{\zeta}(0)$, $\ell(0)$ and $\dot{\ell}(0)$ were taken as:

$$\zeta(0) = 5, \quad \dot{\zeta}(0) = -v, \quad \ell(0) = 1/\sqrt{(1 - v^2)}, \quad \dot{\ell}(0) = 0,$$

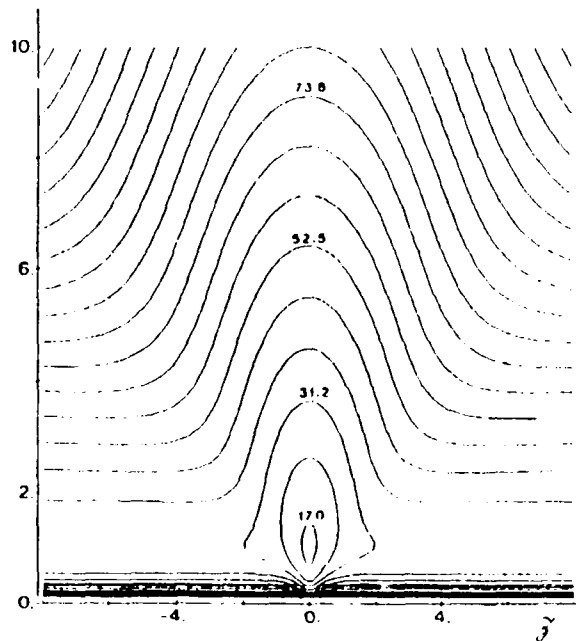


Fig. 5 Contour plot of $V_{KK}(Z)$.

where the initial separation $2 + Z(0)$ was chosen large enough to insure that the two kinks were virtually non-interacting at $t = 0$. For a range of initial velocities ranging from $v = -.999c$ to a threshold velocity at $v = -.325\bar{c}$, the kinks attract but will possess enough kinetic energy to prevent formation of a bound state. In Fig. 6 we have shown a K-K collision with $v = -.35\bar{c}$ where the collective coordinate $\ell(t)$ can be seen being set into motion at the moment of impact ($Z(t) = 0$).

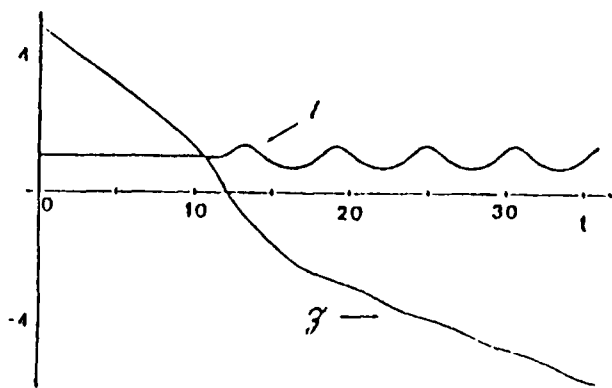


Fig. 6 Plot of collective coordinates $\ell(t)$ and $Z(t)$ for a $K_1 - K_2$ collision, $v = -.35$.

For velocities lower than $v = v_c$ as shown in Fig. 7 for $v = -.3\bar{c}$, it can be seen that after the first collision, the two kinks lose energy to the internal oscillation, attract and form a bound pair and after two or more repeated collisions, where en-

ergy can pass to or from the internal oscillation, gain enough kinetic energy from the internal oscillation to move apart. Upon collision, the internal coordinate is excited with a new amplitude that depends on its phase at the time of collision. A decrease in the initial velocity may then move the system into a region where the kinks are virtually never able to gain enough energy to separate and can thus be practically considered as a bound pair. Inclusion of radiation losses in the model would change this to a permanently bound pair.

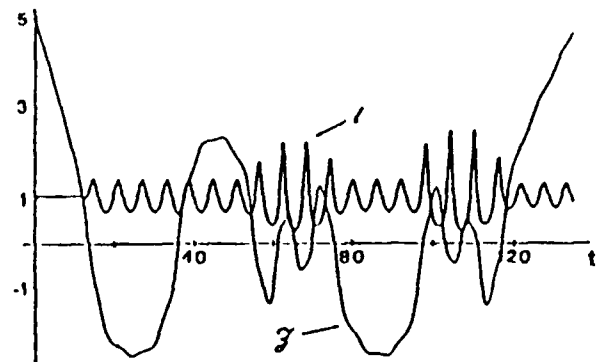


Fig. 7 Plot of collective coordinates $\ell(t)$ and $Z(t)$ for a $K_1 - K_2$ collision, $v = -.3$.

Similar behavior was found in the ϕ^4 and double sine-Gordon models by Campbell, Shonfeld, and Wingate¹⁴ who carried out a detailed study of "n bounce resonance windows" and developed a semi-phenomenological theory for various aspects of resonance scattering structure. A similar analysis can be carried out for the present model yielding for example an expression for $T(v)$, the time between the first and second impacts in the 2 bounce window as a function of incoming velocity

$$T(v) = \alpha / \sqrt{v_c^2 - v^2}, \quad \alpha \approx 2.64 \quad (21)$$

that agrees reasonably well with computed values as shown in Fig. 8.

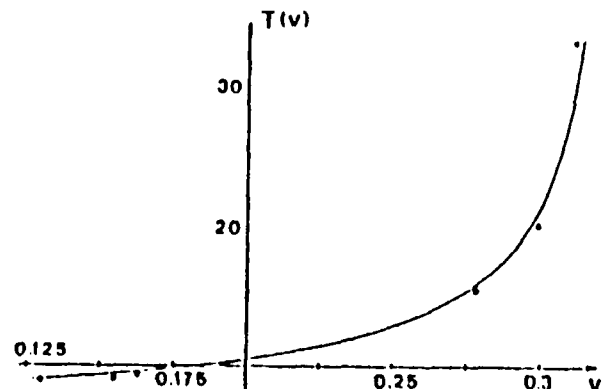


Fig. 8 Plot of $T(v)$, the time between two repeated collisions, versus initial velocity v , as given in Eq. 21. Plotted points are values computed using the CCM model.

As another way of viewing K-K collisions, we have plotted the orbits of the motion in $\mathcal{Z} - \ell$ space for the CCM potential Eq. 19 shown in Fig. 5. In Fig. 9, we show a parametric plot of the orbit in $\mathcal{Z} - \ell$ space for the K_1 - K_2 collision of Fig. 7. In Fig. 10 we have plotted a closed orbit with $E = 27.6$ and an average frequency of $\omega = .978$. Because there is no radiation mechanism in the simple CCM model, inclusion of radiation losses for a closed orbit like that of Fig. 10 will cause it to decay and become non-periodic.

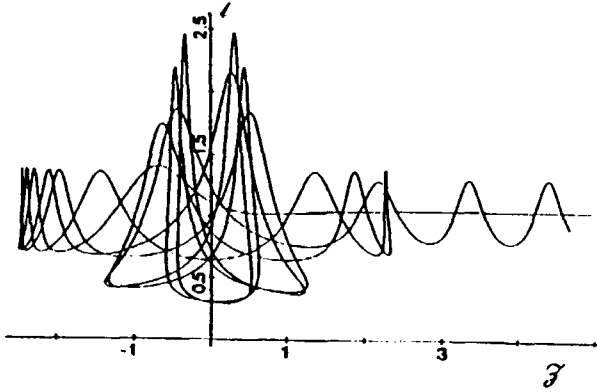


Fig. 9. Parametric plot of collective coordinate $\ell(t)$ (ordinate) versus $\mathcal{Z}(t)$ (abscissa) for $v = -.3$, $0 < t < 140$.

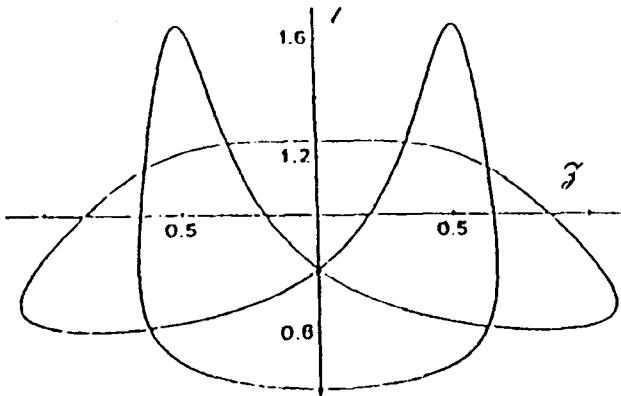


Fig. 10. Parametric plot of collective coordinate $\ell(t)$ (ordinate) versus $\mathcal{Z}(t)$ (abscissa) for $E = 27.6$, $0 < t < 600$.

For the case of a repulsive $K-\bar{K}$ collision, the effective kinetic and potential energy calculated using CCM are given by

$$\begin{aligned} \mathcal{T}_{K\bar{K}}[\mathcal{Z}, \ell] &= \frac{8(1+\eta)}{\gamma} \left[\frac{\pi^2 \dot{\mathcal{Z}}^2}{12\gamma^2} + \gamma^2 \dot{\mathcal{Z}}^2 \right] - \eta \left[\frac{8}{\gamma} (\dot{\mathcal{Z}}\dot{\ell} + \gamma\dot{\mathcal{Z}})^2 \right. \\ &\quad \left. - \frac{2\dot{\mathcal{Z}}^2}{3\gamma^3} (4\gamma^2 \mathcal{Z}^2 + \pi^2) \right] \left(\frac{\zeta}{\text{sh}(\zeta)} \right) \\ \mathcal{V}_{K\bar{K}}[\mathcal{Z}, \ell] &= 8\gamma [1 + \eta(1 + \zeta/\text{sh}(\zeta))] + \frac{8}{\gamma} [1 + j(1 - \zeta/\text{sh}(\zeta)) \left(\frac{\text{ch}(\zeta)+1}{\text{ch}(\zeta)-1} \right)] \\ &\text{with } \gamma = 1/\ell \text{ and } \zeta = 2\gamma\mathcal{Z}. \end{aligned} \quad (22)$$

For this case K and \bar{K} will collide and rebound for velocities $v < \bar{v}_c$, while for $v > \bar{v}_c$ they pass through each other. The CCM yields fairly good estimates for both v_c and \bar{v}_c compared with the values obtained using the full numerical model namely,

$$\{v_c(\text{CCM}) = -.235\bar{c}, \quad v_c(\text{Num}) = -.033\bar{c}\}$$

D. Kink Symmetries.

To investigate the other possible kink states available for the $N=3$ system we plot the effective potential

$$\mathcal{V}_{\Phi}[\phi_1, \phi_2] = -J(1 - \cos(\phi_1)) - J(1 - \cos(\phi_2))$$

$$-j(1 - \cos(\phi_1 - \phi_2 + 2\pi\Phi/\Phi_0)) \quad (23)$$

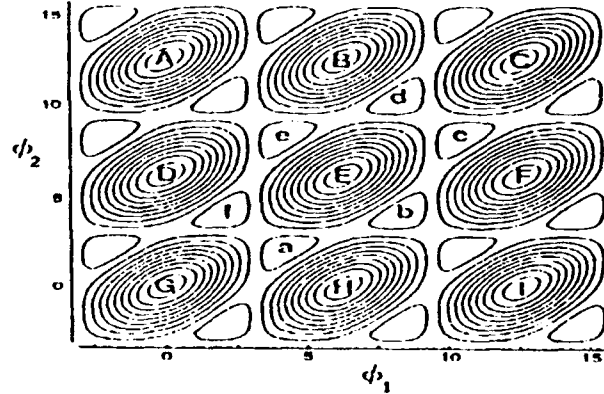


Fig. 11. Plot of the potential $\mathcal{V}[\phi_1, \phi_2]$ given in Eq. 23 with $J=j=1$.

as a function of ϕ_1 and ϕ_2 as shown in Fig. 11 for $\Phi = 0$. The possible kink states are those that connect adjacent peaks labeled as A, B, C etc. Thus the K_1 and K_2 kinks discussed above could be formed by motion of a Newtonian particle moving in $\mathcal{V}[\phi_1, \phi_2]$ from $E \rightarrow F$ and $F \rightarrow C$ respectively. The rest mass for both kinks is given by $E = 16$. There is a third series of sine-Gordon kinks that lie along the diagonal $\phi_1 = \phi_2$. Since the difference terms in the Lagrangian drop out for $\phi_1 = \phi_2$, the equations of motion reduce to a sine-Gordon equation on each line. Thus the EC kink will have the same energy as the EF and FC kinks and can be considered as a bound state of EF and FC with binding energy $E_b = 16$ supplied by the EF-FC attractive bond. In terms of flux loops it can be considered as a (negative) 2π flux loop around the third superconductor. This can be seen by exchanging the \bar{K}_1 antikink and its (negative) anticlockwise flux loop in Fig. 3 by a K_1 kink with a (positive) clock-

wise flux loop. The K_1 and K_2 flux loops will then cancel in the 3 junction and the resulting flux loop can thus be considered as an equivalent anticlockwise flux loop encircling superconductor 0.

It is clear that while the energies for the kinks EC, EF, and FC are equal, the topological invariants for the total magnetic flux defined by

$$\Delta\phi_i = \frac{\Phi_0}{2\pi} \int_{-\infty}^{\infty} \phi_{i,z} dz = [\phi_i(\infty) - \phi_i(-\infty)] \frac{\Phi_0}{2\pi} \quad (24)$$

are different for the three states. For the EC kink, $\Delta\phi_1 = 1$ fluxon and $\Delta\phi_2 = 1$ fluxon. For the EF kink $\Delta\phi_1 = 1$, $\Delta\phi_2 = 0$ while for the FC kink $\Delta\phi_1 = 0$ and $\Delta\phi_2 = 1$ fluxon. Since their energies are degenerate these three states may thus form a 3 representation for the SU(3) group while their antikinks CE, CF, and FE form a $\bar{3}$ representation. An indication of why this occurs can be given in terms of the connection of the present model with the bosonized SU(N) Thirring model to be discussed in the next section.

From the symmetry of $V[\phi_1, \phi_2]$ it can be seen that motion from A to E will lie along the line $\phi_1 + \phi_2 = 4\pi$. Inserting this as a constraint in the Lagrangian leads to the equation of motion for ϕ_1

$$\phi_{1,tt} - \phi_{1,xx} = -\frac{J}{1+2\eta} \sin\phi_1 - \frac{j}{1+2\eta} \sin(2\phi_1), \quad (25)$$

which is the double sine-Gordon equation. The AE kink is thus one of the known stable kinks of the double sine-Gordon equation [cf Condat Guyer¹⁵] that can be obtained by a simple integration of Eq 25 and is given for $\eta=1$ by

$$\phi_1 = 2 \tan^{-1} \left\{ \frac{1}{\sqrt{3}} \coth[\gamma(x-vt)/\sqrt{8}] \right\}, \phi_2 = -\phi_1. \quad (26)$$

As will be seen below however, in the context of the coupled JJ system, the AE kink is unstable.

The two kinks DC and GB are also double sine-Gordon kinks but it is not evident from the contour plot of $V[\phi_1, \phi_2]$ that a straight line connecting D to C would be the path taken by the motion of a particle moving from D to C since potential contours are not crossed at right angles. The origin of this problem is the cross term $\eta(\phi_{1,t} - \phi_{2,t})^2$ in the Lagrangian. By transforming to orthonormal coordinates $\{\psi_1, \psi_2\}$ that diagonalize the kinetic energy term

$$\psi_1 = (\phi_1 + \phi_2)/\sqrt{2}, \psi_2 = \sqrt{1+2\eta}(\phi_1 - \phi_2)/\sqrt{2}, \quad (27)$$

the Lagrangian may be reexpressed as

$$\mathcal{L}[\psi] = J_c \frac{\Phi_0}{2\pi} \left\{ \frac{1}{2} [(\psi_{1,t})^2 + (\psi_{2,t})^2 + (\psi_{1,z})^2 + (\psi_{2,z})^2] + V[\psi] \right\} \quad (28)$$

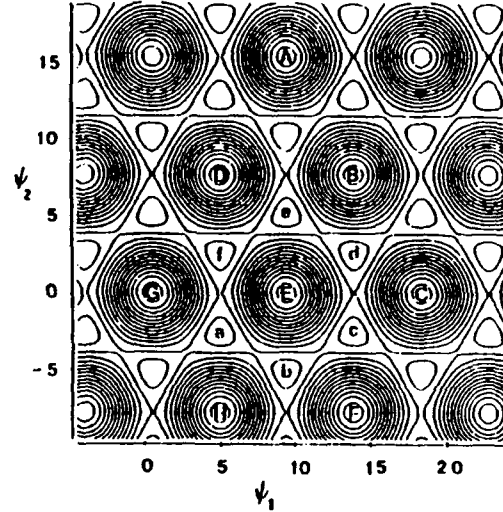


Fig. 12. Plot of the potential $V[\phi_1, \phi_2]$ in Eq. 23 as a function of $\{\psi_1, \psi_2\}$ where $\{\psi_1, \psi_2\}$ are related to ϕ_1, ϕ_2 by Eq. 27.

A plot of $V[\psi_1, \psi_2]$ as a function of ψ_1 and ψ_2 is shown in Fig. 12 indicates that the paths DC and GB are indeed straight lines, and by implication (since ϕ_i and ψ_i are linearly related) that the paths DC and GB in Fig. 11 are also straight lines. From the symmetry of $V[\psi_1, \psi_2]$ it can also be seen that AE, DC, and GB are simply rotated versions of the same state and a calculation of their energies shows them to be equal with $E[AE]=E[DC]=E[GB]=37$, which makes them potentially unstable against breakup into lower energy kinks.

A plot of the potential energy of any of the three double sine-Gordon kinks DC, GB, or AE using the CCM gives a potential that is confining in ℓ but non-confining in \mathcal{J} , with a saddle at $\mathcal{J}=0$, $\ell=4/3$. Numerical calculation of the evolution of these double sine-Gordon states bears out the CCM potential and shows them to be unstable as well.

3. $N=3$ COUPLED SUPERCONDUCTING

ELEMENTS ENCLOSING FLUX $\Phi = \frac{1}{2}\Phi_0$

We now assume that an external magnetic flux has been introduced along the z axis of the coupled JJ system by inserting a Bohm-Aharonov solenoid. For this section we shall choose $\Phi=\Phi_0/2$ which has the effect of shifting the origin to $\phi_1 = \pi$ and $\phi_2 = \pi$ and inverting $V[\phi]$, but otherwise leaving its

shape intact. This can be seen by changing the new coordinates reexpressing the phases ϕ_1 and ϕ_2 by $\phi'_1 = \phi_1 - \pi$ and $\phi'_2 = \phi_2 - \pi$ so that $V_{\Phi=\Phi_0/2}[\phi'_1, \phi'_2] = -V_{\Phi=0}[\phi_1, \phi_2]$. The static kink solutions are obtained by calculating the motion of a unit mass particle connecting the peaks of $V_{\Phi=\Phi_0/2}$ labeled by a,b,c... The solutions for the stable kinks (ab,bc,cd,de,ef,fa) are given below (for $\eta=J=j=1$), dropping primes henceforth as

$$(ab) \quad \phi_1 = 4 \tan^{-1} \left[\frac{\text{th}(\gamma(x-vt)/\sqrt{8})}{\sqrt{3}} \right] + \pi ;$$

$$\phi_2 = \phi_1/2 - \pi/2 ; \quad (29)$$

$$(bc) \quad \phi_1 = 2 \tan^{-1} \left[\frac{\text{th}(\gamma(x-vt)/\sqrt{8})}{\sqrt{3}} \right] ;$$

$$\phi_2 = 2\phi_1 + \pi ; \quad (30)$$

$$(cd) \quad \phi_1 = -2 \tan^{-1} \left[\frac{\text{th}(\gamma(x-vt)/\sqrt{8})}{\sqrt{3}} \right] ;$$

$$\phi_2 = -\phi_1 . \quad (31)$$

Each has energy $E = \sqrt{2}(6 - 2\pi/\sqrt{3})\gamma = 3.358\gamma$. The unstable (ac) and (ad) kinks have the solutions

$$(ac) \quad \phi_1 = 4 \tan^{-1} [c^{\gamma(x-vt)/\sqrt{2}}] + \pi/3 ;$$

$$\phi_2 = \phi_1 - 2\pi/3 . \quad (32)$$

$$(ad) \quad \phi_1 = -2 \tan^{-1} \left[\frac{\text{coth}(\gamma(x-vt)/\sqrt{8})}{\sqrt{3}} \right] ;$$

$$\phi_2 = 2\phi_1 - \pi ; \quad (33)$$

and their energies are respectively

$$E_2 = 8\sqrt{2}\gamma = 11.38\gamma ,$$

$$E_3 = \gamma\sqrt{2} \cdot 6 \cdot (1 + 2\pi/(3\sqrt{3})) = 18.75\gamma . \quad (34)$$

The energies of (fb), (fd), (ea), (ec), and (bd) are all equal to E_2 , while the energies of (eb) and (fc) are equal to E_3 , which is apparent from the symmetry of Fig. 12.

While each member of the multiplet of the six stable kinks and antikinks has the same energy as the others, they each have differing values for fluxon content indicating that they are related by a symmetry of the Lagrangian. Unlike the integer fluxon kinks for the $\Phi = 0$ case, the (ab), (ef), and (af) kinks have

topological invariants for the total magnetic flux in each junction that are fractional and equal to $1/3$ or $2/3$. Thus

	$\Delta\phi_1$	$\Delta\phi_2$	$\Delta\phi_1 - \Delta\phi_2$	$\Delta\phi_1 + \Delta\phi_2$	
(ab):	$2/3$,	$1/3$	$1/3$	1	
(ef):	$-1/3$,	$-2/3$	$1/3$	-1	
(af):	$-1/3$,	$1/3$	$-2/3$	0	(35)

The states [ab,bc,...fa] can be viewed in two ways: 1) They can be taken as the 3 and $\bar{3}$ representations of an $SU(3)$ symmetry. With this interpretation, ab, af, and ef could be designated as equivalent to $SU_f(3)$ (flavor $SU(3)$) u, d, and s quarks with "charge" given by the fractional fluxon number $\Delta\phi_1$. The corresponding particle physics designations of hypercharge Y and isospin component I_3 would be given by $Y = \Delta\phi_1 - \Delta\phi_2$ and $I_3 = (\Delta\phi_1 - \Delta\phi_2)/2$ yielding $Q = I_3 + Y/2 = \Delta\phi_1$. The kinks bc, de, and dc would then be the equivalents of the antiquarks \bar{s} , \bar{u} , and \bar{d} . Taking these as the fundamental fluxon quarks would then yield mesons like the π^+ meson $u\bar{d} = fb$, and the nucleon $\eta = ddu = (ae)$, both with energy E_2 . Since these fluxon quarks repel one another yielding unstable mesons and nucleons and moreover can have excited states, they are not appealing as fundamental units. 2) We can view {ab,bc,...fa} as 6 states of an octet of mesons (or nucleons) formed from fractional fluxon quarks. If we define a total fluxon number to be given by $\Delta\phi = \Delta\phi_1 + \Delta\phi_2$, then the kinks and antikinks of Fig. 11 will have integer total fluxon numbers and can be described as being formed from $1/3$ and $2/3$ fluxon number $SU(3)$ quarks. To define the fluxon quarks we represent the (ab), (bc), and (cd) kinks in terms of flux loops around each of the three conductors as shown in Fig. 13. In analogy with $SU_f(3)$ we can use the two param-

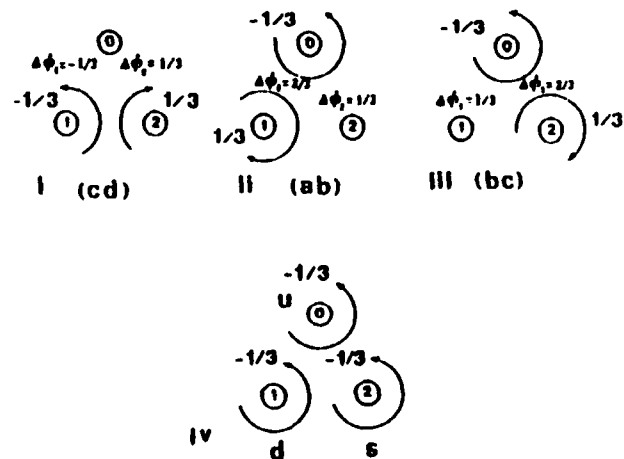


Fig. 13. i,ii,iii) Representation of the flux content of the (cd), (ab) and (bc) kinks respectively in terms of u, d, s. iv) The fundamental fluxon quarks u, d, s, in units of Φ_0 .

ters I_3 and Y instead of $\Delta\phi_1$ and $\Delta\phi_2$ to label the flux loop quarks namely $\Delta\phi_1=2I_3/3$ and $\Delta\phi_2=I_3/3+Y/2$ to yield $\Delta(\phi_1+\phi_2)=Q=I_3+Y/2$. We can then construct the 3 and $\bar{3}$ SU(3) weight diagrams and the table of I_3 and Y values for the flux quarks as shown in Fig. 14. Using these we may construct the $3 \times \bar{3} = 8 + 1$ representation¹⁶ for the "flux mesons" and "predict" that in addition to the 6 kinks and antikinks already considered, namely,

$$\begin{aligned}\pi^+ &= u\bar{d} \quad (ab) & \pi^- &= \bar{u}d = (dc) \\ K^+ &= u\bar{s} \quad (bc) & K^- &= \bar{u}s = (ec) \\ K^0 &= d\bar{s} \quad (cd) & \bar{K}^0 &= \bar{d}s = (fa)\end{aligned}$$

that there should be kinks corresponding to $\pi^0 = (u\bar{u}-d\bar{d})/\sqrt{2}$, $\eta^0 = (u\bar{u}+d\bar{d}-2s\bar{s})/\sqrt{6}$ and $\phi^0 = (u\bar{u} + s\bar{s} + d\bar{d})/\sqrt{6}$. We interpret the π^0 as being formed as an out of phase breather or bound state of (ab) and (ba) kinks with the η^0 and ϕ^0 being formed in a similar manner. The fact that the neutral K^0 meson (cd) has a distinct antiparticle (dc) while the π^0, η^0 and ϕ^0 do not, lends some consistency to this choice.

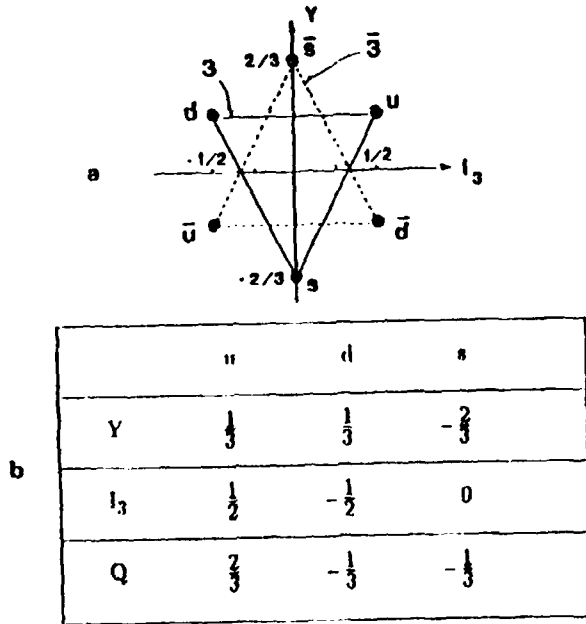


Fig. 14. a) Weight diagrams for the 3 and $\bar{3}$ representation of the SU(3) fluxon quarks (in units of 1 fluxon = Φ_0). b) Isospin, hypercharge and $Q = I_3 + Y/2$ values for the fluxon quarks u, d, s in fluxon units.

Nucleons can be formed from flux loop quarks in a manner similar to the mesons. Nucleons belonging to the lowest mass nucleon octet, such as $p=uud=(bc)$, will have the same fluxon content as the corresponding mesons because baryon number is not included in our model.

A. Relation to Gross Neveu Model

The source of this SU(3) symmetry can be traced to the relation between the present model and the bosonized Gross-Neveu model. We use the relations first pointed out by Coleman¹⁷ between the fermions of the zero charge sector of the 1 dimensional Thirring model with fermion field ψ and the sine-Gordon model

$$\begin{aligned}\bar{\psi}\psi &\leftrightarrow \cos(\phi) \\ i\bar{\psi}\gamma^5\psi &\leftrightarrow \sin(\phi) \\ \bar{\psi}\gamma^\mu\psi &\leftrightarrow d^\mu\partial_\mu\phi \\ \bar{\psi}\gamma^5\gamma^\mu\psi &\leftrightarrow \partial_\mu\nu^\mu\phi,\end{aligned}\quad (36)$$

where γ^μ and $\gamma^5 = \gamma^0\gamma^1$ are the Dirac matrices for one time and one space dimension ($\mu=0,1$).

The Lagrangian for the chiral invariant N= 3 Gross Neveu model with N fermion fields ψ^a ($a=1, \dots, N$)

$$\mathcal{L} = \sum_{a=1}^N i\bar{\psi}^a\gamma^\mu\partial_\mu\psi^a + \frac{g}{2} \left[\left(\sum_{a=1}^N (\bar{\psi}^a\psi^a) \right)^2 - \left(\sum_{a=1}^N (\bar{\psi}^a\gamma^5\psi^a) \right)^2 \right] \quad (37)$$

can then be written in bosonized form as⁵

$$\mathcal{L} = \sum_{a=1}^N \frac{1}{2} \partial_\mu\phi^a\partial^\mu\phi^a + g \sum_{a \neq b=1}^N \cos(\phi^a - \phi^b). \quad (38)$$

chiral invariance for the fermion Lagrangian implies invariance under the continuous transformation $\psi \rightarrow e^{i\beta\gamma^5}\psi$ for arbitrary β which for the bosonized Lagrangian amounts to invariance under translation of all the bose fields ϕ^a by the constant β , $\phi^a \rightarrow \phi^a + \beta$.

By performing a Fierz transformation of the N fermion fields of Eq 37 it has been shown by Ha⁵, that the Lagrangian may be cast into the form of the SU(N) invariant Thirring model⁴

$$\begin{aligned}\mathcal{L} = \sum_{\alpha=1}^N i\bar{\psi}^\alpha\gamma^\mu\partial_\mu\psi^\alpha - g \sum_{\Lambda=0}^{N^2-1} \sum_{a,b,c,d=1}^N (\bar{\psi}^\alpha\gamma^\mu\frac{1}{2}\lambda_{ab}^\Lambda\psi^b) \\ \cdot (\bar{\psi}^c\gamma_\mu\frac{1}{2}\lambda_{cd}^\Lambda\psi^d)\end{aligned}\quad (39)$$

where the λ^Λ are the (N^2-1) SU(N) matrices, and therefore by inference the bosonized Lagrangian of Eq. 38 is SU(N) invari-

ant as well. Furthermore it was shown in ref. [5] that an orthogonal transformation exists that can transform the N boson fields of a massless Gross Neveu model to a model of $N-1$ massive bosons having an interaction that is chiral invariant in terms of the original fields. Keeping in mind the form of a mass term for the bosonized Gross Neveu model given in Eq 36 i.e., $m\bar{\psi}\psi \leftrightarrow \cos\phi$, we can see that the Lagrangian for the system of Fig. 1b has been written in terms of the orthogonal variables ψ_1, ψ_2 as a massive Gross Neveu model for $N=2$ with an interaction term that is chiral invariant in terms of the original fields. Our finding that this system has an underlying $SU(3)$ symmetry is thus consonant with Ha's result. Using Ha's result we may thus in general infer $SU(N)$ invariance for the coupled JJ systems described by a massive $(N-1)$ chiral invariant Gross Neveu Lagrangian.

Another feature of the quark and Gross Neveu models that carries over to the present bosonized version with $\Phi = \frac{\Phi_0}{2}$ is confinement¹⁶. If we consider the effective potential for binding the fluxon subkinks in the (cd) kink using the CCM as a function of their separation $2+\zeta(t)$ and a common collective coordinate $\zeta(t)$, we obtain the potential

$$V_{cd}(\zeta, t) = \frac{2\sqrt{2}}{\ell} \left(1 - \frac{\pi}{3\sqrt{3}}\right) + \frac{3}{\sqrt{2}\ell} \mathcal{I}_0(\zeta) + \sqrt{2}\ell \left\{ \frac{2\pi}{3}(\sqrt{3}-1) + (3/2)(1 + 2\text{ch}(\zeta))\mathcal{I}_0(\zeta) \right\}$$

$$\text{where } \mathcal{I}_0(\zeta) = \frac{\zeta \cdot \text{sh}(\zeta) + 2\pi(1 - \text{ch}(\zeta))/(3\sqrt{3})}{2\text{ch}^2(\zeta) - \text{ch}(\zeta) - 1}$$

with $\zeta = \sqrt{2}\zeta/\ell$,

which is shown in Fig. 15. It can be seen that in the limit as $\zeta \rightarrow \infty$, the potential rises linearly with ζ as

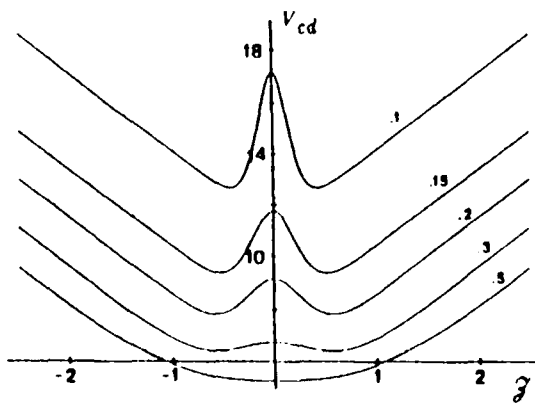


Fig. 15 Plot of $V_{cd}[\zeta, t]$ for $t=1, 15, 2, 3, 5$.

$$V_{cd}(\zeta, t) \xrightarrow{\zeta \rightarrow \infty} 3 \cdot \text{th}(\sqrt{2}\zeta/\ell) \cdot \zeta \quad (41)$$

which is the equivalent, for a potential well, of confinement in the field theory case.

In Fig. 16 we show the results of an attempt to separate a (cd) kink into its constituent subkinks by imposing the initial condition that $v = .99999\bar{c}$. The original (fa) kink is seen to be transformed into the set of topologically equivalent kinks reached by going around the hexagonal loop of Fig. 11 namely, (fc)+(ed)+(dc)+(cb)+(ba). The net result is a transformation of the (fa) kink into an equivalent excited (fa) kink (= (dc)*) and two kink antikink pairs [(ed)+(ba)] and [(fe)+(cb)]. Raising the initial energy to a threshold $v = .99999\bar{c}$ enables 2 hexagonal loops in the $\phi_1 = \phi_2$ direction to be encompassed as shown in Fig. 17. Reversing the initial velocities will excite the hexagonal loops below (fa). The net results of an attempt at arbitrar-

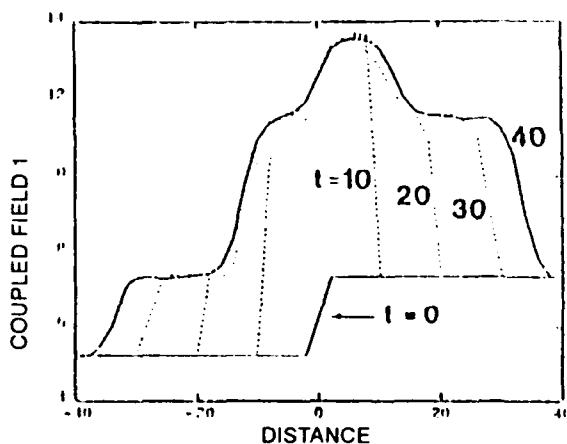


Fig. 16. Plot of $\phi_1(z)$ versus z , with initial conditions $v = .99999\bar{c}$, for times $t=0, 10, 20, 30, 40$ (with damping $= .1 \phi, t$).

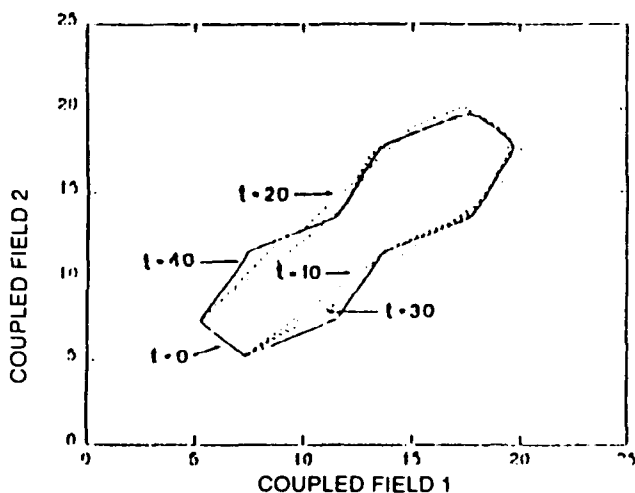


Fig. 17. Parametric plot of $\phi_2(t)$ versus $\phi_1(t)$, for times $t=0, 10, 20, 30, 40$, $v = .99999\bar{c}$, (with damping $= .1 \phi, t$).

ily large energy to separate the subkinks of the (fa) kink will thus be an excited (fa) kink and a string (2,4,6,...2N) of kink-antikink pairs, which is in qualitative agreement with the hadronic string picture of confinement¹⁶.

B. N= 3 system with $j < J$

We have mainly considered the symmetric case $J = j$, $\Phi = \Phi_0/2$, due to its connection with the Gross Neveu model, and the fact that the static solutions may be obtained by quadrature. For $1/2 < j < J$, the two adjacent maxima of V along the $\phi_2 = -\phi_1$ direction will move closer together, their positions being given by

$$\phi_1^* = \cos^{-1}\left(\frac{j}{J}\right) = -\phi_2^* \quad (42)$$

As an example, for the case $\phi_1^* = \pi/5$, $j = 2/(1+\sqrt{5}) = 0.618$, only the (ab) and (bc) kinks will have the same rest mass. The equation of motion for the (ab) kink is given by a quartic sine-Gordon equation as

$$\frac{d^2\psi}{d\zeta^2} = \frac{1}{(17+9\eta)} (4\sin(4\psi) - J\sin(\psi) - 3j\sin(3\psi)) \quad (43)$$

with $\phi_1 = 4\psi + \pi$, $\phi_2 = \phi_1/4 - \pi/4$, $\zeta = \gamma(z - vt)$, and

$$\{\phi_1, -\infty, \phi_2, -\infty\} = \{\pi/5, -\pi/5\} \rightarrow \{\phi_1, +\infty, \phi_2, +\infty\} = \{9\pi/5, \pi/5\},$$

and has a rest mass = 5.068. The equation of motion for the (cd) kink is given by the double sine-Gordon equation as

$$\frac{d^2\phi_1}{d\zeta^2} = -\frac{1}{(1+\eta)} \{J\sin\phi_1 - j\sin(2\phi_1)\} \quad (44)$$

with

$$\begin{aligned} \phi_2 &= -\phi_1, \\ \{\phi_1, -\infty, \phi_2, -\infty\} &= \{\pi/5, -\pi/5\} \rightarrow \{\phi_1, +\infty, \phi_2, +\infty\} = \{-\pi/5, \pi/5\} \end{aligned}$$

and has a rest mass = .612. The equation of motion for the unstable static (ad) kink is given by a triple sine-Gordon equation.

The fluxon content for the (ab), (cb), and (cd) kinks is then

	$\Delta\phi_1$	$\Delta\phi_2$	$\Delta\phi_1 - \Delta\phi_2$	$\Delta\phi_1 + \Delta\phi_2$
(ab)	3/10,	2/10	1/10	1/2
(cb)	-2/10,	-3/10	1/10	-1/2
(cd)	-1/5,	1/5	-2/5	0

The kinks (ab) and (cb) will thus form an SU(2) doublet with $I_3 = \Delta\phi_1 + \Delta\phi_2 = 1/2$ while (cd) will be a lower mass iso-singlet.

For $j = 1/2$, $\phi_1^* = 0$ and the c and d peaks will merge. The (cd) and (af) kinks will cease to exist. The kinks (ab) and (bc) will become integer fluxon kinks having the same rest mass and an SU(2) symmetry.

C. Relation to the coupled base-rotator model of DNA

The Homma-Takeno³ coupled base-rotator model for the dynamical properties of DNA molecules is described by the Lagrangian of Eq. 13 with $\eta = 0$, and $j/J = \eta_t$, where η_t is the ratio of hydrogen-bonding energy to local field energy for a base pair of DNA. For the exact B-form of DNA, this ratio is equal to 1/2 which makes this DNA model equivalent to the $j = 1/2$ integer kink SU(2) case mentioned above. The ratio η_t is not restricted to $\eta_t = 1/2$ however, so that for $\eta_t > 1/2$ fractional SU(2) kinks and SU(3) kinks for $\eta_t = 1$ are possible, with the confinement mechanism, discussed previously, operating for $\eta_t > 1/2$.

4. A SYSTEM OF N= 4 COUPLED SUPERCONDUCTING ELEMENTS

In the previous section we indicated that the N= 3 coupled JJ system could be considered either as an SU(2) massive Gross Neveu model or as a chiral invariant SU(3) massless Gross Neveu model. Using this equivalence we should be able to form an N= 4 system, that could be considered as a massive SU(3) Gross Neveu model or as a massless chiral invariant SU(4) Gross Neveu model, by adding a fourth superconductor to form JJ's with each of the superconductors of the N= 3 system (Fig. 1c). We may write the expression for the effective potential of the N= 4 system of 6 JJ's using the Bohm Aharonov constraints of Eq 8 for each of the three flux circuits of Fig. 1c, where each is assumed to contain flux Φ .

$$\begin{aligned} V(\phi_1, \phi_2, \phi_3) &= -J[(1 - \cos(\phi_1)) + (1 - \cos(\phi_2)) + (1 - \cos(\phi_3))] \\ &- j[(1 - \cos(\phi_1 - \phi_2 + 2\pi\Phi/\Phi_0)) + (1 - \cos(\phi_2 - \phi_3 + 2\pi\Phi/\Phi_0)) \\ &+ (1 - \cos(\phi_3 - \phi_1 + 2\pi\Phi/\Phi_0))] \end{aligned} \quad (45)$$

As in the previous system of three conductors, we transform to orthonormal coordinates so that the kinetic energy will be a sum of squared time derivatives, yielding paths of stable kinks that appear as straight lines in the new coordinates. For arbitrary positive values of η , the transformation to the new ψ coordinates is given by

$$\begin{aligned} \psi_1 &= (\phi_1 + \phi_2 + \phi_3)/\sqrt{3} \\ \psi_2 &= \sqrt{1+3\eta} \cdot (-\phi_1 + \phi_3)/\sqrt{2} \\ \psi_3 &= \sqrt{1+3\eta} \cdot (-\phi_1 + 2\phi_2 - \phi_3)/\sqrt{6} \end{aligned} \quad (46)$$

To give a graphical indication of what this potential looks like as a function of $\{\psi_1, \psi_2, \psi_3\}$, we have assembled in perspective the contour plots of $V[\psi_1, \psi_2, \psi_3]$ for $\eta = j = 1$ in the planes $\psi_1=0, \psi_2=0, \psi_3=24\pi/\sqrt{6}$, as shown in Fig. 18.

The centers of the large spherical contours are the peaks of $V[\vec{\psi}]$ as can be seen from the corner potential sphere B, while the disks in the $\psi_1=0$ plane represent cross sections of potential spheres that lie below the plane as represented by α_0 and above the plane, as represented by β_1 , with all other small disks repeating this alternate pattern. The minima of $V[\vec{\psi}]$ are the centers of the rounded rectangles in the three orthogonal planes.

$V[\vec{\psi}]$ can be easily seen to be invariant to rotations of $2\pi/3$ around an axis at the center of an absolute maxima in the $\psi_1=0$ plane (or equivalently by a rotation of $\pi/3$ plus a translation in the ψ_2 direction by $2\pi/\sqrt{3}$). There are further symmetry operations that are not immediately apparent such as a rotation of π around the ψ_2 axis. Since there are three symmetry axes in the $\psi_1=0$ plane separated by $2\pi/3$, this operation can be repeated in each of them to yield four equivalent orientations for the potential. The origin of this symmetry can be understood by remembering that $V[\vec{\psi}]$ is equally valid for a short junction, and that by lifting the central conductor of the short junction of Fig. 1c, one can make a tetrahedral JJ system as shown in Fig. 19a where it is assumed that small junctions have been placed half way along the 6 adjacent edges of the tetrahedron. Thus instead of the central superconductor having a privileged role, it can be seen that all four are equivalent, hence

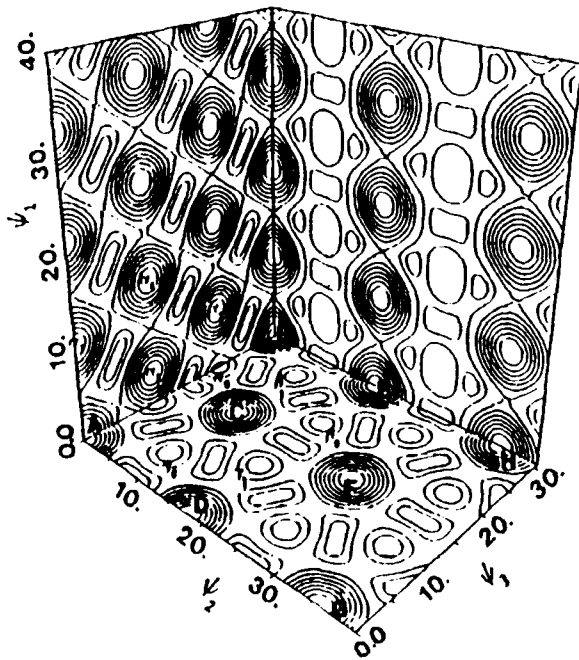


Fig. 18. Contour plots of $V[\psi_1, \psi_2, \psi_3]$ in the planes $\psi_1=0, \psi_2=0, \psi_3=24\pi/\sqrt{6}$, with $j=1$.

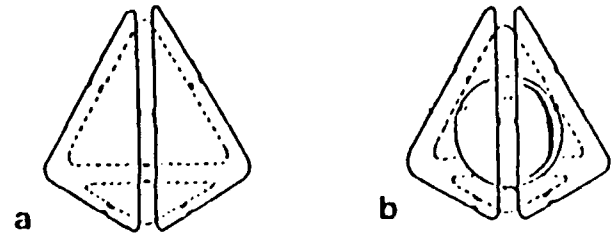


Fig. 19. a) 4 superconducting elements arranged as a tetrahedron with JJ's on each edge; b) same as a) plus an inner superconducting sphere forming JJ's with each tetrahedron face.

the fourfold symmetry of the potential. The elementary lowest energy kinks of $V[\vec{\psi}]$ are those connecting adjacent maxima of $V[\vec{\psi}]$ such as $A\alpha_1, A\alpha_3$ or $C\alpha_1$ with rest energy $E_1=24$. The next family of stable kinks are those that cross a rectangular minima at its narrowest width (α_1, α_3) or (γ_0, γ_1) . These kinks have a rest energy $E_2=32$ which makes them stable against breaking up into two $E_1=24$ kinks. If enough energy is supplied however, a kink such as $(\alpha_3\alpha_1)$ can be pulled apart into (α_3A) and $(A\alpha_1)$. The kinks that cross a rectangular minima lengthwise, AC or $A\alpha_4$, have energy $E_3=52$ and are unstable to breaking up into the adjacent $E_1=24$ kinks. A kink like AF which would be a triple sine-Gordon kink if confined to the $\psi_1=0$ plane, will immediately break up into the elementary kinks outside of the plane as $(A\gamma_0), (\gamma_0D), (D\gamma_1)$ and (γ_1F) .

As in the $N=3, \phi=0$ case, the elementary kinks can be put into a direct relation with flux loops around each of the superconductors. The $\vec{\phi} = (0,0,0) \rightarrow (2\pi, 0, 0)$ kink will have coordinates of $\vec{\psi} = [0,0,0] \rightarrow [2\pi/\sqrt{3}, -2\pi\sqrt{2}, -4\pi/\sqrt{6}]$ which is the $C\alpha_1$ kink. Similarly the $0 \rightarrow 2\pi \phi_2$ and ϕ_3 kinks are identified as $(C\beta_1)$ and $(C\gamma_1)$, while the kink $\vec{\phi} = [0,0,0] \rightarrow [2\pi, 2\pi, 2\pi]$ will have the coordinates of the $A\alpha_1$ or CC^1 kink, where C^1 (C^1) denotes the peak directly above (or below) C . The bound state of CC^1 and $C\alpha_1$ kinks has an energy $E_2=32$ and a binding energy of $E_b=16$ and is thus a rotated version of $(\alpha_1\alpha_3)$. The bound states of three and four elementary kinks have been calculated and are shown in Tab.1. From the table one can see that there is a simple fluxon bond chemistry, each fluxon-fluxon bond being associated with a binding energy of $E_b=16$. Thus the fully saturated case of a tetrad consisting of the four elementary kinks has a total binding energy equal to the sum of its rest masses. The fact that the total energy for the tetrad is zero with four fluxon present, indicates that the kinks composing the tetrad can form a 3 field breather.

Having described the $N=4$ potential of Fig. 18 we can now point out that the two tetrads $\{(C\alpha_1), (C\beta_1), (C\gamma_1), (CC^1)\}$ and $\{(C\alpha_0), (C\beta_0), (C\gamma_0), (CC^1)\}$ are the fundamental multiplets of $SU(4)^{18}$ and define weight diagrams analogous to Fig. 14. The 6 states with $E=E_2$ form a sextet representation of $SU(4)$. As in

Tab 1 Table of rest mass E_0 and binding energy E_b for 2, 3, and 4 fluxons.

	Rest Mass	Binding Energy
1 fluxon	$E_0 = 24$	$E_b = 0 \cdot 16$
2 bound fluxons	$E_0 = 32$	$E_b = 1 \cdot 16$
3 bound fluxons	$E_0 = 24$	$E_b = 3 \cdot 16$
4 bound fluxons	$E_0 = 0$	$E_b = 6 \cdot 16$

the previous case of $N=3$, $\Phi=0$, where the fundamental fluxons had integer flux number, the constituents of states with $E = E_2$ are not permanently confined.

The addition of an external flux $\Phi = \Phi_0/2$ will lead to an effective potential that is the inverse of $V[\vec{\phi}]$ in Eq 42 with $\phi_i \rightarrow \phi'_i = \phi_i + \pi$ as in the $N=3$ case. Unlike the $N=3$ case however, the maxima of the inverted potential are now lines in ψ_1, ψ_2, ψ_3 instead of isolated points. Thus on the plane defined by lines of potential maxima $\psi_1 = \sqrt{2}\psi_3 - 3\sqrt{3}\pi$, the potential looks like the grid of Fig. 20. Kinks can be formed by connecting any two points along adjacent or opposite ridge lines. Only kinks connecting opposite ridge lines at their midpoints will be stable. These have integer fluxon numbers and will not form a representation of the full $SU(4)$ group. This situation will be qualitatively the same for any combination j and J , mainly because the maxima of the inverse potential are not confined to

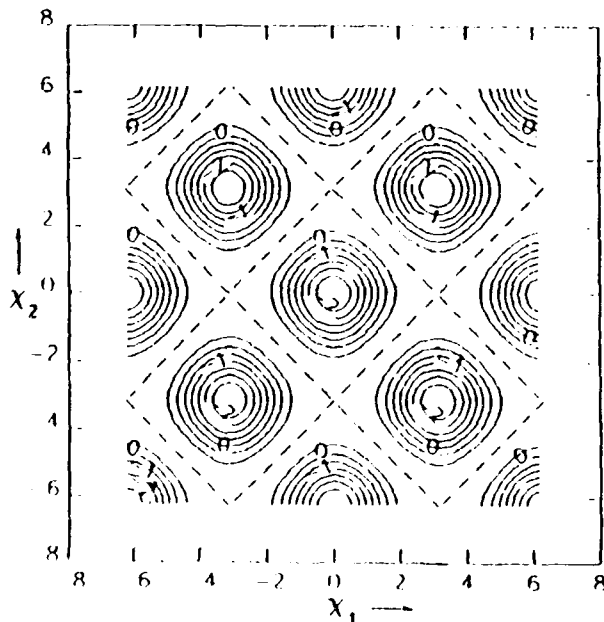


Fig. 20 Contour plot of $V[\psi_1, \psi_2, \psi_3]$ in the plane $\psi_1 = \sqrt{2}\psi_3 - 9\pi/\sqrt{6}$ for $j=1$ as a function of $\chi_1 = \psi_2/\sqrt{8}$ and $\chi_2 = \sqrt{3/8}\psi_3$.

isolated points. With the addition of an external flux $\Phi = \Phi_0/4$, isolated peaks exist that can lead to fractional fluxon subkinks. The masses, interactions, and symmetries of these kinks will be the subject of a future publication.

The process of increasing the symmetry of a coupled JJ system by adding one more superconductor can be carried only one half step further. We can add a fifth out of plane superconductor to the $N=4$ system of Fig. 1c. This is equivalent to putting a spherical shell (or an inverted tetrahedron scaled by $1/2$) inside the tetrahedron of Fig. 19a with junctions formed where the sphere touches the inside of the tetrahedron as shown in Fig. 19b. Each superconductor will have JJ contacts with each of the 4 other superconductors, yielding coupled JJ's with $SU(5)$ symmetry. Since a fifth JJ cannot be made to lie within the plane of the other four, we cannot translate this system parallel to itself to make an $N=5$ long coupled JJ.

5. CONCLUSIONS

We have investigated systems consisting of long coupled Josephson junctions formed from $N=3$ and 4 long superconducting elements. They can both be described by the bosonized Gross Neveu model. In both cases kink excitations having equal rest masses are observed to form groups having an $SU(N)$ internal symmetry. If all junctions are formed having the same critical current density J_c , the kinks will have integer fluxon content if the external magnetic flux $\Phi=0$. For the case $N=3$ with an external magnetic flux $= \Phi_0/2$ present, the subkinks on a given line have fractional fluxon content, while the total kink can be considered as being formed from permanently confined $1/3$ fluxon quarks. For non equal critical current densities ($j_c < J_c$), the symmetry is reduced from $Su(3)$ to $SU(2)$ for $N=3$. For the case $N=4$ with an external magnetic flux $= \Phi_0/4$ present, fractional fluxon kinks are possible.

6. REFERENCES

1. A. K. Jain, K.K. Likharev, J. E. Lukens and J. E. Sauvageau, "Mutual Phase Locking in Josephson Junction Arrays", *Phys. Rep.* 109, 309, 1984.
2. K.F. Lee and E. Goto, "D.C. Flux Parametron", World Scientific Publishing Co., 1986.
3. S. Homma and S. Takeno, "A Coupled Base-Rotator Model for Structure and Dynamics of DNA", *Prog. Theor. Phys.* 72, 679, 1984.
4. S. Ryang, "Free Boson Equivalence of the $SU(N)$ Massless Thirring Model", *Prog. Theor. Phys.* 77, 765, 1987.
5. Y.K. Ha, "Boson Formulation of Fermion Field Theories", *Phys. Rev. D*, 29, 1744, 1983, "Fermion-Boson Metamorphosis in a Chiral Invariant Theory", *Phys. Lett.*, 117B, 231, 1982.
6. R. Rajaraman, "Solitons and Instantons", North Holland Pub. Co. 1982.
7. K.K. Likharev, *Radio Eng. Elec. Physics (USSR)*, 20, 135, 1975.
8. P.N. Stenski and S. Doniach, "A System of Three Josephson Junctions", *J. Appl. Phys.*, 57, 867, 1985.

9. K.K. Likharev, "Dynamics of Josephson Junctions and Circuits", Gordon and Breach Science Publishers, 1986.
10. T.A. Fulton, "Equivalent Circuits and Analogs of the Josephson Effect", in "Superconductor Applications: SQUIDS and Machines", B. Schwartz and S. Foner eds., Plenum Press 1977.
11. M.J. Ablowitz, M.D. Kruskal, and J.R. Ladik, *SIAM J. Appl. Math.*, 36, 478, 1979.
12. R.J. Flesch and S.E. Trullinger, "Green's Functions for Nonlinear Klein-Gordon Kink Perturbation Theory", *J. Math. Phys.* 28, 1619, 1987.
13. M.J. Rice, "Physical Dynamics of Solitons", *Phys. Rev. B*, 28, 3587, 1987.
14. D.K. Campbell, J.F. Schonfeld, and C.A. Wingate, "Resonance Structure in Kink-Antikink Interactions in Theory", *Physica*, 9D, 1, 1983.
15. C.A. Condat, R.A. Guyer, and M.D. Miller, "Double sine-Gordon Chain", *Phys. Rev. B*, 27, 474, 1982.
16. T.P. Cheng and L.F. Li, "Gauge Theory of Elementary Particles", Clarendon Press, Oxford, 1984.
17. S. Coleman, "Quantum sine-Gordon Equation as the Massive Thirring Model", *Phys. Rev. D*, 11, 2088, 1975.
18. W. Ludwig, C. Falter, "Symmetries in Physics", Springer Verlag, 1987.

THE INFLUENCE OF DISLOCATION DENSITY ON ELECTRON MOBILITY IN InP FILMS ON Si

T.E. Crumbaker, M.J. Hafich, and C.Y. Robinson, Department of Electrical Engineering and the Center for Optoelectronic Computing Systems, Colorado State University

K.M. Jones and M.M. Al-Jassim, Solar Energy Research Institute

A. Davis and J.P. Lorenzo, Electromagnetics & Reliability Directorate, Rome Laboratory

Published in Applied Physics Letters, August, 1991

Abstract - The electron mobility and dislocation density have been measured as functions of the film thickness in InP films grown on Si substrates by gas-source molecular beam epitaxy. In a region extending about 2 μm from the Si interface, the density of dislocations was found to be very high and clustering of dislocations was observed by transmission electron microscopy. The corresponding mobility was very small. Beyond 2 μm , clustering was not observed, the density of dislocations decreased and the mobility increased with increasing film thickness. Thus, the threading dislocations created by the large InP/Si lattice mismatch can significantly degrade the free carrier mobility of the InP film.

The heteroepitaxial growth of III-V semiconductor films on Si substrates offers the possibility of combining, in a monolithic technology, high mobility GaAs or InP devices with complex VLSI Si circuitry. The primary materials problem in development of a III-V/Si technology is the formation of a high density of threading dislocations created by the large lattice mismatch between the III-V film and the Si substrate. In the GaAs/Si system (4% lattice mismatch), direct measurement using plan-view transmission electron microscopy (TEM) has shown that the dislocation density exceeds 10^9 cm^{-2} at the heterointerface and decreases into the GaAs [1-3]. In the InP/Si system (8% lattice mismatch), indirect evidence from cross-section TEM images [4] and x-ray diffraction measurements [5] indicate a similar distribution of dislocations. The high density of dislocations is expected to adversely affect the electrical properties of the GaAs or InP films, as evidenced by electron mobilities some 40% lower than bulk values in InP films 3-4 μm thick grown on Si by molecular beam epitaxy (MBE) [6] and metal-organic chemical vapor deposition [7]. We report here the direct measurement of both the dislocation density and electron mobility as functions of the film thickness in MBE InP-on-Si films, and a clear correlation is found between dislocation density and carrier mobility.

Three-inch diameter p-type Si substrates of 10-20 $\Omega\text{-cm}$ resistivity were etched in 5:1 $\text{H}_2\text{SO}_4\text{:H}_2\text{O}_2$ solution, then transferred to a N_2 atmosphere and briefly etched in a dilute HF solution before being loaded into the MBE system. All substrates were (100) misoriented 4° towards the [011]. The substrates were cleaned in vacuo at 700°C for 20 minutes prior to growth. Gas source MBE was used to grow the heterostructures with the In and Ga beams provided by conventional effusion cells

and a P_2 beam produced by thermal decomposition of gaseous PH_3 at 900°C in a low-pressure cracking oven. A buffer layer of 0.6- μm thickness was placed between the Si substrate and InP active layer and consisted of GaP followed by four strained-layer superlattices of $\text{In}_x\text{Ga}_{1-x}\text{P}/\text{In}_y\text{Ga}_{1-y}\text{P}$ ($x \neq y$). Details of this buffer layer have been described elsewhere [6]. The buffer layer was then followed by 2.6 - 4.9 μm of unintentionally doped InP grown at 480°C and 0.85 $\mu\text{m/h}$. The reflection high energy electron diffraction pattern of the InP surface during growth exhibited a well-defined P_2 -stabilized (2x4) reconstruction, very similar to that of high quality homoepitaxial InP grown under identical conditions. Using this method, films that are specular over the entire 3" wafer have been obtained and a full-width at half maximum (FWHM) of the (400) double crystal x-ray (DCXR) diffraction peak as low as 510 arc sec for an as-grown film has been measured.

The room temperature Hall mobility versus film thickness was determined by two depth profiling techniques. The first technique used anodic oxide layer stripping combined with Hall-van der Pauw measurements [8]. At each etch step, an anodic oxide was grown in a glycol:water electrolyte and then removed with a HF solution, resulting in the controlled removal of approximately 50 nm of InP. The mobility was determined and the etch step repeated. Ohmic contacts were made with Au/Ge/Ni.

The second profiling technique used iodic acid etching combined with Hall-van der Pauw measurements. InSn ohmic contacts were protected while 0.5-1.0 μm of the sample was removed in a 10:1 $\text{H}_2\text{O}:\text{HIO}_3$ solution. The resulting film thickness was measured using a surface profilometer. Hall measurements were then made and the entire process repeated 3-4 times until reaching the Si substrate.

The dislocation density as a function of film thickness was measured indirectly by DCXR diffraction and directly by plan-view TEM. Several wafers were grown in an identical manner. Then each wafer was divided into many samples, and each sample was etched with iodic acid to the desired film thickness. DCXR diffraction and TEM were then performed on each sample.

The unintentionally doped InP-on-Si films were n-type with residual carrier concentrations of $(1-10) \times 10^{15} \text{ cm}^{-3}$. Prior to depth profiling, the room temperature mobility of the as-grown films was as high as $2200 \text{ cm}^2 \text{ V}^{-1} \text{ s}^{-1}$ with typical mobilities in the range of $1000-1700 \text{ cm}^2 \text{ V}^{-1} \text{ s}^{-1}$. Depth profiling of the mobility was performed by the two above techniques on the same InP-on-Si film and the results are plotted in Figure 1(a), where the total film thickness is measured from the Si interface. The anodic oxide stripping technique was used to profile entirely through the $4.0 \mu\text{m}$ thick sample and clearly shows there is a very low mobility for the first $2 \mu\text{m}$ of growth followed by a steadily increasing mobility with increasing film thickness. Data at the Si interface was unreliable and is not shown. The four data points from the iodine acid etch technique show fair agreement with the extensive data from the anodic oxide stripping technique. Mobility profiles of another InP-on-Si film, which was $5.5 \mu\text{m}$ in thickness and grown under nearly identical conditions, were similar to Figure 1(a).

Plan-view transmission electron microscope images, obtained with a Philips CM-30 TEM at 300 KeV were used to observe the dislocations and to measure their density at a particular depth. Nominally $0.25 \mu\text{m}$ thick foils were prepared from the near surface region of films previously etched to the desired film thickness. Typical plan-view TEM images are shown in Figure 2. Films less than about $2 \mu\text{m}$ in total thickness exhibited clusters of dislocations and dislocation densities greater than $1 \times 10^9 \text{ cm}^{-2}$. Figure 2(a) shows a plan-view image at a film thickness of $1.5 \mu\text{m}$; here the dislocation density is so large and the distance between dislocations so small that the dislocations have become entangled, forming clusters. For films greater than about $2 \mu\text{m}$ in thickness, clustering was not observed and the dislocations appeared to be distributed laterally in a fairly uniform manner (Fig. 2(b)). Thus there appear to be two distinct regions in the InP-on-Si films: a region that extends to about $2 \mu\text{m}$ from the Si substrate where dislocations form clusters, and a region beyond about $2 \mu\text{m}$ where clustering of the dislocations does not occur.

The dislocation density as a function of film thickness determined from TEM measurements is shown in Fig. 1(b). Also shown is the dislocation density obtained from DCXR diffraction by measuring the FWHM of the (400) InP peak using $\text{CuK}\alpha$ radiation [6]. The equation from Hirsch [9], $D = (\text{FWHM})^2 / 9b^2$ where b is the Burger's vector, assumed to be 0.4 nm , was used to estimate the dislocation density D . In the region where the thickness is greater than $2 \mu\text{m}$ and clustering of the dislocations does not occur, TEM counts are accurate, and good agreement between the TEM and DCXR data can be seen in Fig. 1(b); thus, the Hirsch equation accurately predicts the dislocation density. In this region the dislocation density is

in the $10^8-10^9 \text{ cm}^{-2}$ range and decreases slowly with increasing film thickness, in a manner similar to that previously reported for GaAs-on-Si films of the same thickness [2,3]. In the region below $2 \mu\text{m}$, accurate determination of the dislocation density could not be obtained by TEM due to the clustering and thus only estimates of lower bounds are given in Fig. 1(b). Although we could not obtain independent confirmation that the Hirsch equation is accurate in this region, it is clear from the DCXR data that the apparent dislocation density decreases rapidly as the thickness increases to $2 \mu\text{m}$. Beyond $2 \mu\text{m}$, the dislocation density decreases very slowly with increasing film thickness. Hence, both the TEM and DCXR data indicate that there are two distinct regions in the InP-on-Si films.

A comparison of the two plots in Figure 1 shows a clear correlation between electron mobility and the distribution of dislocations. In the region within $2 \mu\text{m}$ of the Si substrate, the clusters of dislocations greatly increase free carrier scattering, producing a very low mobility. In the region beyond $2 \mu\text{m}$, the dislocation density is low enough that clusters do not form, and the mobility increases with film thickness as the dislocation density decreases. Since the measured mobility at all film thicknesses is much lower than the value of $3900-4200 \text{ cm}^2 \text{ V}^{-1} \text{ s}^{-1}$ obtained in our InP films grown on InP substrates under the same conditions, scattering due to dislocations appears to be the dominant scattering mechanism throughout the entire InP film.

Finally, we were concerned that the mobility profile of Fig. 1(a) may be an artifact of the Hall profiling technique, since the measured mobility in the outer $2 \mu\text{m}$ may be influenced by the underlying low mobility (inner) region. By modeling the sample as two uniform layers with fixed mobility and carrier concentration [10], a reasonable fit to the mobility profiles of Fig. 1(a) required the carrier concentration in the inner layer to be an order of magnitude greater than in the outer layer. The Hall measurements and electrochemical capacitance-voltage profiles of the films did not show evidence of the very high carrier concentration in the inner region needed to support the two-layer model. Thus the data in Fig. 1(a) is believed to accurately represent the variation of mobility with thickness.

In summary, in InP-on-Si films grown by MBE, the threading dislocations produced at the InP/Si interface significantly influence the electron mobility in the InP films. Within $2 \mu\text{m}$ of the interface, the dislocation density is very high, the average distance between dislocations is small, and the dislocations become entangled, forming clusters. The clusters greatly increase the scattering of carriers, resulting in very low mobility. Beyond $2 \mu\text{m}$, the clusters do not form, the density of dislocations decreases with increasing film thickness, and the electron mobility rises toward the expected value.

Achieving lower dislocation densities adjacent to the Si substrate could eliminate the formation of the dislocation clusters and the accompanying catastrophic drop in carrier mobility. However, even with the dislocation density in the 10^8-cm^{-2} range, the mobility will be less than that of homoepitaxial material. Thus the performance of devices requiring transport of carriers parallel to the InP/Si interface in thin InP epitaxial films or transport of carriers across the InP/Si interface could be adversely affected.

The authors would like to acknowledge the support of the Air Force Office of Scientific Research (Contract 89-0513) and the Air Force RL-Hanscom/DARPA (Contract F19628-89-K-0042).

REFERENCES

1. P. Sheldon, B. G. Yacobi, K. M. Jones, and D. J. Dunlavey, *J. Appl. Phys.* 58, 4186 (1985).
2. P. Sheldon, K. M. Jones, M. M. Al-Jassim, and B. G. Yacobi, *J. Appl. Phys.* 63, 5609 (1988).
3. M. Tachikawa and M. Yamaguchi, *Appl. Phys. Lett.* 56, 484 (1990).
4. T. E. Crumbaker, H. Y. Lee, M. J. Hafich, G. Y. Robinson, M. M. Al-Jassim, and K. M. Jones, *J. Vac. Sci. Technol.* B8, 261 (1990).
5. A. Yamamoto, N. Vehida, and M. Yamaguchi, *J. Cryst. Growth* 96, 369 (1989).
6. T. E. Crumbaker, H. Y. Lee, M. J. Hafich, and G. Y. Robinson, *Appl. Phys. Lett.* 54, 140 (1989).
7. M. Sugo, Y. Takanashi, M. M. Al-Jassim, and M. Yamaguchi, *J. Appl. Phys.* 68, 540 (1990).
8. J. P. Lorenzo, D. Eirug Davies, and T. G. Ryan, *J. Electrochem. Soc.* 126, 118 (1979).
9. P. B. Hirsch, in *Progress in Metal Physics*, edited by B. Chalmers and R. King (Pergamon, New York, 1956), Vol. 6, p. 236.
10. H. H. Weider, *Laboratory Notes on Electrical and Galvanomagnetic Measurements*, (Elsevier, New York, 1979), p. 170.

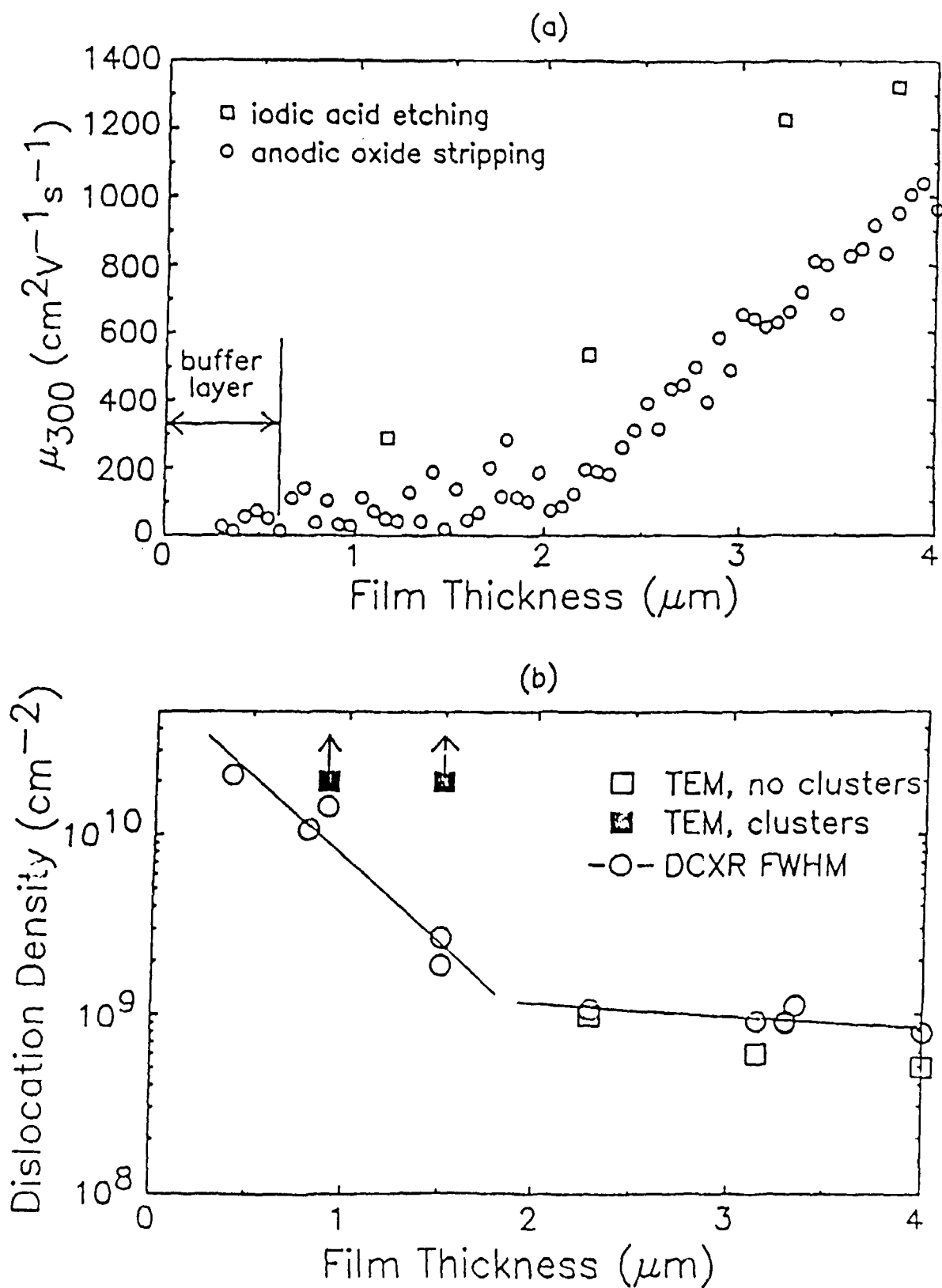
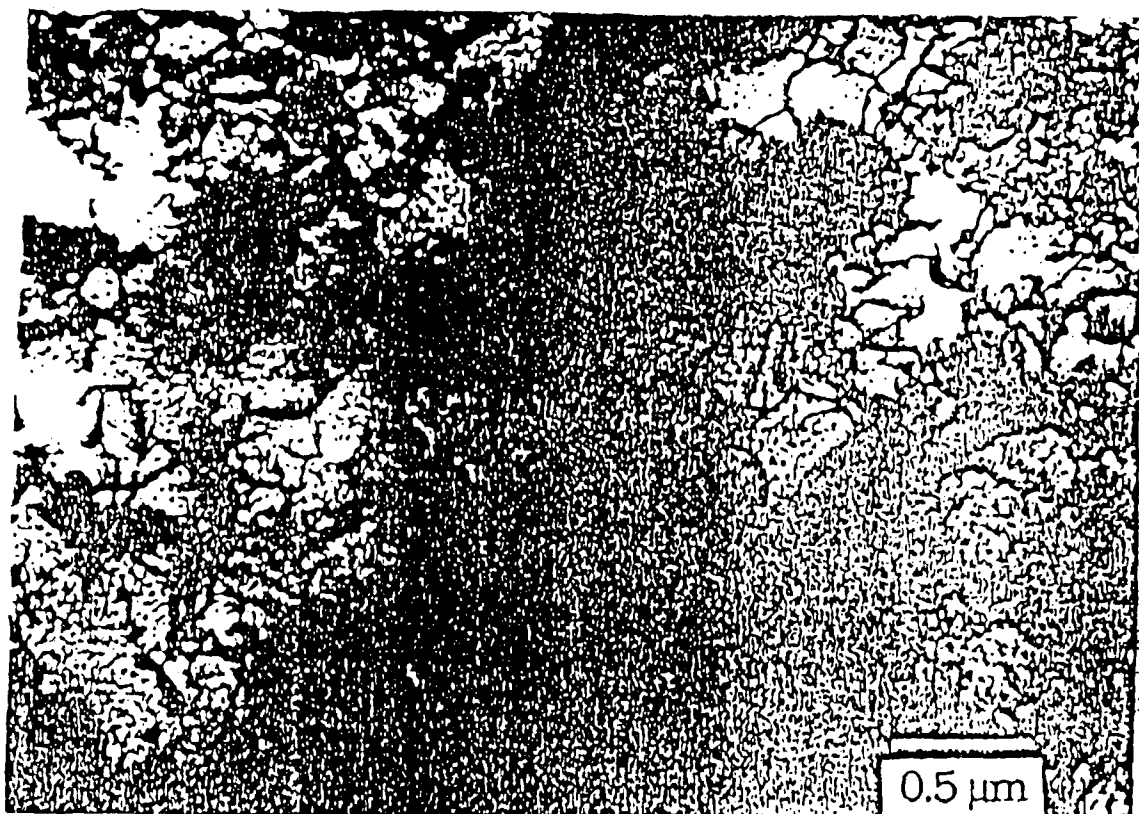


Fig. 1. Variation of (a) room temperature Hall mobility and (b) dislocation density versus film thickness for unintentionally doped InP on Si films with n -type residual carrier concentrations of $(1-5) \times 10^{15} \text{ cm}^{-3}$.

A



B

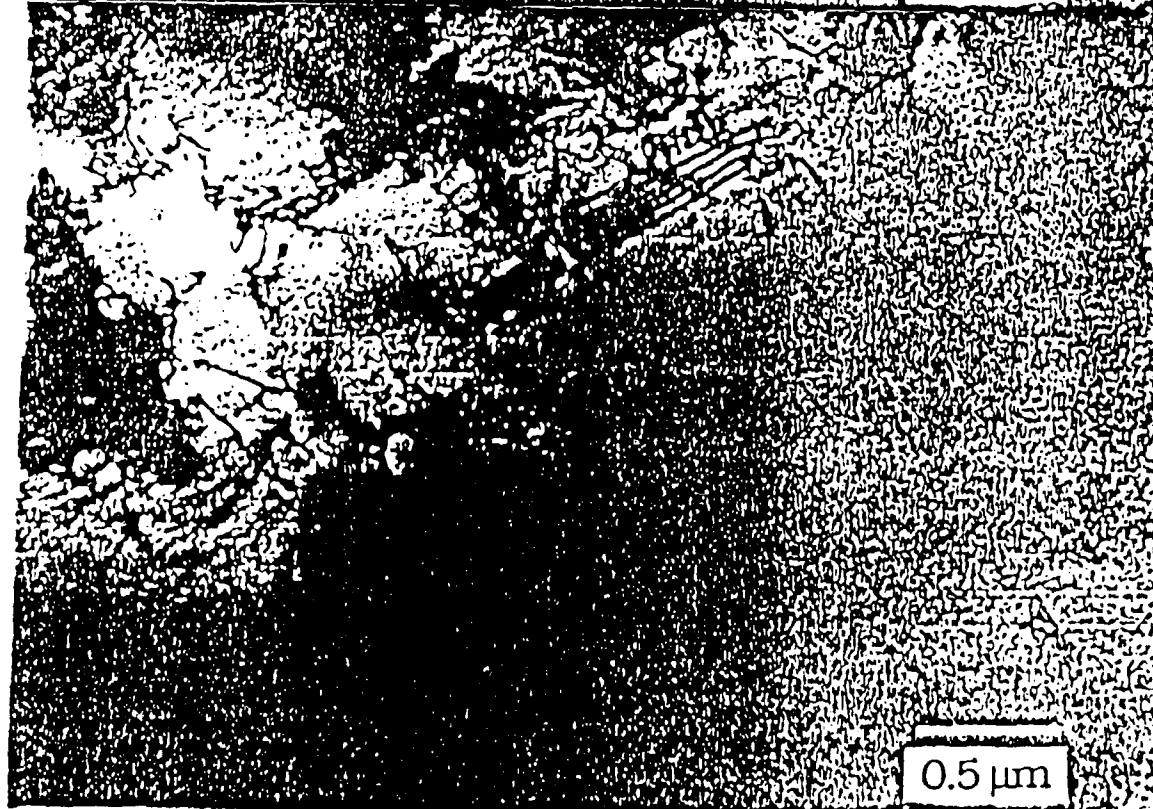


Fig. 2 Plan view TEM micrographs of two InP-on-Si films. (a) Film of 1.5 μm thickness exhibiting clusters of dislocations typical of films less than about 2 μm in thickness. (b) Film of 2.3 μm thickness with a uniform distribution of dislocation, a density of about $1 \times 10^9 \text{ cm}^{-2}$, and no clustering, typical of films greater than about 2 μm in thickness. Stacking faults are also visible in (a) and (b) and were discussed in a previous report [4]

SIGNAL-TO-NOISE POWER OR SIGNAL-TO-NOISE ENERGY FOR MAXIMIZING DECISION PERFORMANCE?

Vincent C. Vannicola, Surveillance & Photonics Directorate, Rome Laboratory

Published in Digital Signal Processing 1, 156-160 (1991)

1. INTRODUCTION

In the processing of waveforms for gaining information, we often find ourselves addressing a variety of issues from different points of view. Examples are signal power versus signal energy to noise ratio, theoretically derived optimum filtering versus heuristic (or seat-of-the-pants) approaches, the relation between independent noise sources and eigenvalues in a noise covariance matrix, and low-level versus high-level signal processing. In this series of articles, I will attempt to provide a better understanding of these subtle and sometimes confusing points.

Measured data which exist in a form unsuitable for the user must undergo certain transformations so that an intelligible outcome is attained. Transformations applied to measured data for the purpose of obtaining a set of observables in order to perform hypothesis testing, estimation, and classification constitute signal processing.

Front-end operations preamplify, downconvert (generally to base band), and often A/D the incoming waveform into data, compatible with the appropriate transformations that follow. The transformations may be linear or nonlinear and in general are performed across all domains or dimensions over which the data or signal may exist. These domains include time and space where samples of the signal/noise process are weighted, integrated, and subjected to decision-making criteria. The transformations, which include weighting and integration, are carried out through filters and equalizers in the time domain and through array beamformers and apertures in the spatial domain. In some cases, signals may be mapped from one domain to another when architecture, e.g., optical signal processors, in conjunction with the algorithm, finds it more suitable.

When processing has completed the transformation stage, the signal may be treated as a statistic where decisions, estimates, control parameters, and, at a higher level, inferences are generated. At such higher levels, modern signal processing makes use of numeric and symbolic methods in whatever combination necessary for completing the algorithm.

The three major phases of processing a signal/noise set of measured data are restated as preprocessing, transformation, and decision. Since my objective here is to bring about an understanding of the theoretical and practical aspects of signal-processing algorithms, I will restrict the preprocessing portion

of the presentation to a few comments regarding the effects it has on signal-to-noise ratio and overall processor performance. In reference to transformations, I will provide a general presentation on the approaches of correlation for optimizing performance through maximizing signal-to-noise ratio. Future articles will include the decision-making process using tests and estimation algorithms for both observation and generation of control parameters. Examples will focus on radar and communication signal processing and will include both adaptive and non-adaptive methods.

2. PREPROCESSING

A. Maintaining Signal-to-Noise Ratio

A waveform arriving at the front end of a sensor receiver must first of all have sufficient signal-to-noise ratio to maintain acceptable performance at the final decision stages of the system. Any processing losses which may further degrade the signal-to-noise ratio such that the ratio falls below this required minimum must be prevented by prior stages of sufficient gain.

The example shown in Fig. 1a illustrates a simple receiver front end where attenuation, L , precedes gain, G . Signal, $s(t)$, and noise, $n_0(t)$, are received at power (or energy) level, S and $n_0 = kT_0B$, respectively, where k is Boltzmann's constant, T_0 is the source temperature, and B is the noise bandwidth. The attenuator, $L > 1$, decreases the input signal, $s(t)$, as well as the input noise, $n_0(t)$, each by a factor of L . At the same time, additional noise, $n_a(t)$, is introduced (remember that the power, not the voltage of independent noise sources are summed), by the attenuator, at power level, $(1-1/L)n_1 = (1-1/L)kT_1B$, where T_1 is the temperature of the attenuator.

Letting the noise temperatures of the source and the attenuator be the same,

$$T_0 = T_1 = T,$$

it follows that the received noise power equals attenuator noise power (if L were infinite). Hence,

$$n_0 = n_1 = N.$$

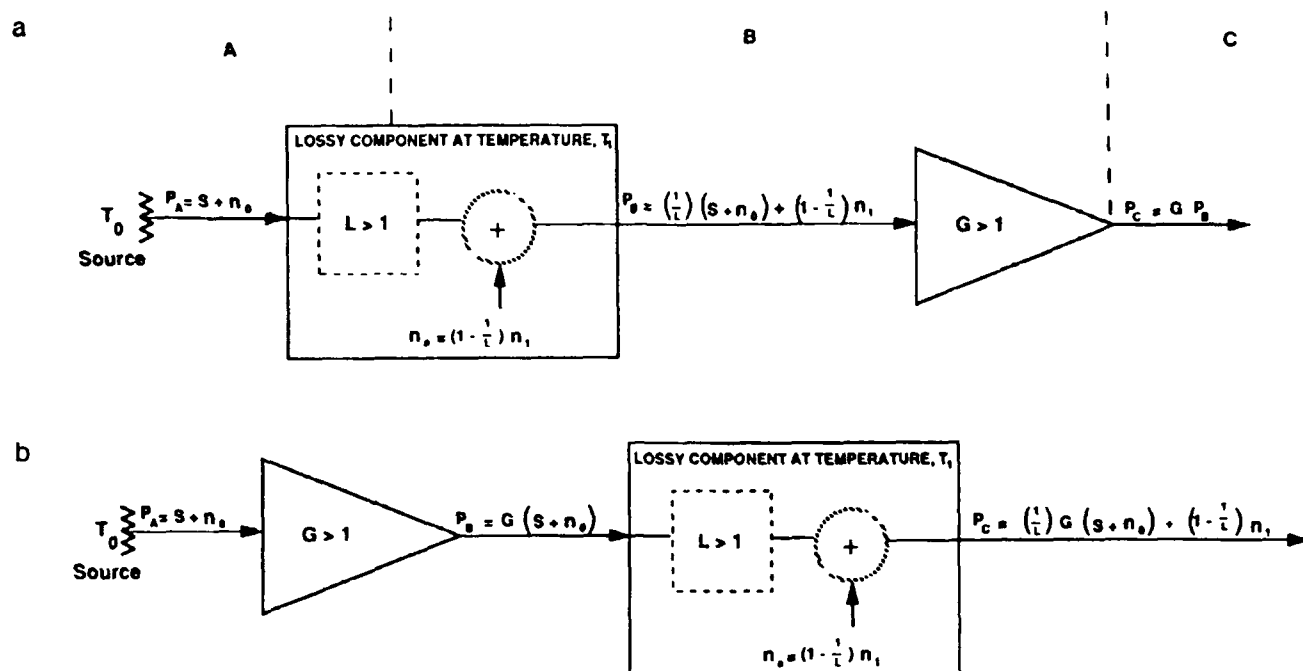


Fig. 1. Front-end receiver block diagrams. (a) Loss precedes gain. (b) Loss follows gain.

It is easily shown that the ratio of the input to output signal-to-noise ratios, i.e., the noise figure (the loss in signal-to-noise ratio across the channel), for Fig. 1a is

$$F_a = \frac{S/N(\text{input})}{S/N(\text{output})} = \frac{S/N}{(S/L)/(N[1/L + \{1 - 1/L\}])} = L. \quad (1)$$

In a similar manner, it can be shown that the noise figure for the channel shown in Fig. 1b, where the gain precedes the lossy component, is

$$F_b = \frac{S/N}{(1/L)GS/[(1/L)G + (1 - 1/L)]N} = 1 + \frac{L - 1}{G}. \quad (2)$$

Plainly, when gain precedes as well as dominates all stages of signal-to-noise loss, the system noise figure, F , is hardly affected. More details concerning noise figure may be found in Skolnik [1], Ziemer and Tranter [2], Gardner [3], and Haykin [4].

B. Correlation and Filtering

After appropriate gain, the signal and noise waveforms are generally downconverted, multiplexed, sampled, digitized, or subjected to whatever process appropriate to the data, information, and hardware requirements. Included along this path is a correlator which computes the energy contained within the signal waveform as well as the correlated part of the white or whitened noise. A correlator, matched to the signal waveform, also maximizes [3,4] the signal-to-noise ratio when the additive noise is white.

We show this by first expressing the energy, E , in the signal as the integral of the signal power over time. If $s(t) \neq 0: \{0 < t < T\}, = 0: \{t \text{ Otherwise}\}$ is the actual signal waveform and $s_0(t)$ is the signal waveform normalized to unit energy. That is, if

$$s(t) = E^{1/2}s_0(t) \text{ and } \int_0^T s_0^2(t)dt = 1,$$

then it follows that

$$E = \int_0^T s^2(t)dt = E \int_0^T s_0^2(t)dt. \quad (3)$$

A filter, $h(t)$, matched to the signal, $h(t) = s_0(-t)$, computes the square root of the energy contained in the actual signal, giving

$$\int_0^T s(u)h(t-u)du = E^{1/2}. \quad (4)$$

Next, consider a received waveform, $r(t)$, consisting of a signal, $s(t)$, contaminated by additive noise, $n(t)$, that is,

$$r(t) = s(t) + n(t). \quad (5)$$

In the most general case, the signal and noise may each be a Gaussian or non-Gaussian random process, be nonstationary, contain nonlinear parameters, be interdependent, and be characterized by correlation and covariance properties of their own. The derivation of the optimal signal processor algorithm, which provides the desired information from such a signal and noise environment, is extremely difficult and involves issues currently under investigation. We will confine our discussion to Gaussian, correlated, stationary, linear, and independent signal and noise processes.

Using such a model, we can, in many cases, visualize the signal and noise waveforms as vectors in a multidimensional space. The idea is to operate on the signal and noise such that we obtain, at the processor output, a projection (dot product) onto which the signal vector is maximized while the noise vector is minimized.

Let us consider a simple example. We assume that the received waveform, $r(t)$, consists of a deterministic signal, $s(t)$, contaminated by white Gaussian noise, $n(t)$, independent of the signal. The waveform is written in Eq. (5). In this case, the signal vector is fixed while the noise waveform is random and equally distributed in all dimensions (eigenvectors) of the space. We simply project the signal vector, $s(t)$, onto its unit vector, $s_0(t)$, through a dot product operation. This may be accomplished with the matched filter, $h(t)$, or modulator shown in

Fig. 2 and expressed in Eq. (4). The filter output (or vector projection) to the received signal, $s(t)$, turns out to be the square root of its energy, E .

For noise, $n(t)$, we must consider the random nature of its waveform. The filter, $h(t)$, output for the noise process, $n(t)$, is a random variable, n which is often characterized by its root mean square (rms) value. Its rms value is

$$\text{rms} \left[\int_0^T n(u)h(t-u)du \right] = \text{rms}(n) = \left[\frac{N_0}{2} \right]^{1/2}. \quad (6)$$

Equations (4) and (6) compute the square roots of the *energy* contained in the received signal waveform, $s(t)$, and the square root of that *average noise energy* contained in the noise waveform, $n(t)$, which is correlated with the signal waveform (the dot product of the noise vector with the normalized signal vector).

Without deviating much from the above special case, we may consider the signal waveform, $s(t)$, to also be a random process, having, at most, a Gaussian or Rayleigh distributed amplitude and a uniform phase distribution. As we did for the random noise case, above, we characterize the filter, $h(t)$, output for the random signal waveform, $s(t)$, as a random variable with rms value, $E^{1/2}$. Then, without loss of generality, the rms value of the filter output to the received waveform, $r(t)$, is, from Eqs. (4) and (6),

$$\text{rms} \left[\int_0^T r(u)h(t-u)du \right] = \text{rms}(s+n) = E^{1/2} + \left[\frac{N_0}{2} \right]^{1/2}. \quad (7)$$

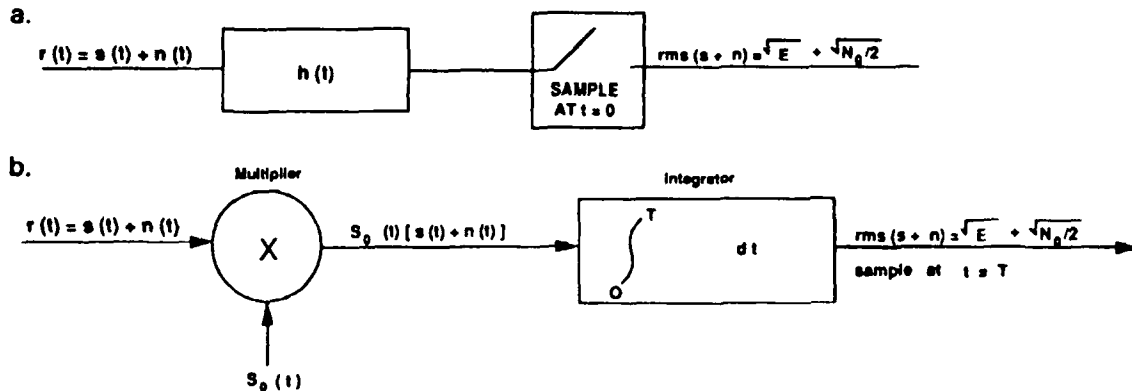


Fig. 2. Correlator realizations. (a) Matched filter, $h(t)$, realization of a receiver correlator. (b) Modulator/detector realization of a receiver correlator.

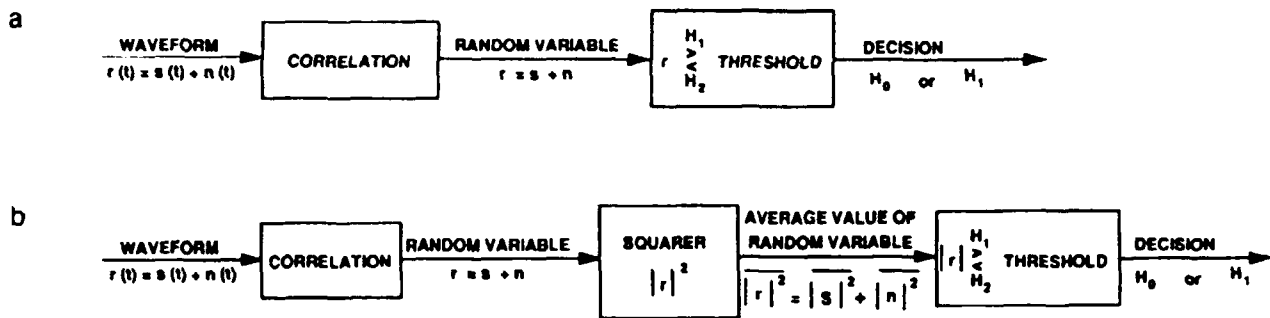


Fig. 3. Random variable processing from matched filter or correlator. (a) Signal having constant amplitude and phase. (b) Signal having zero mean random amplitude and uniform random phase.

The results of Eq. (7) give the sum of the square roots of the energy contained in the signal and noise components of the received waveform. For zero mean Gaussian received processes, the filter output is a bipolar random variable, $r = s + n$, whose mean square value (energy) is the variance. That is, for zero mean and independent processes,

$$\text{rms}\{s + n\} = [\text{var}\{s + n\}]^{1/2} = E^{1/2} + [N_0/2]^{1/2}. \quad (8)$$

It is desirable, from a theoretical and practical standpoint, that we convert the bipolar random variable into a unipolar random variable. We do this by passing the filter output through a squarer as shown in Fig. 3. This results in a nonnegative random variable which is used in threshold testing. In the case of multiple uncorrelated amplitude and phase samples of the waveform, we integrate (not shown) the squarer output to form a single desired random variable.

In a decision process (hypothesis testing), we simply compare the desired output of the filter or correlator to a predetermined threshold to test the condition whether or not the signal is present in the received waveform. Since the actual filter output is a random variable (the quantities on the right hand side of Eqs. (7) and (8) are merely averages), then there is a nonzero probability that noise alone will exceed the threshold and appear as signal plus noise. Also there is a nonzero probability that signal plus noise will not exceed the threshold and thus appear as noise alone. These conditions constitute probabilities of error, the determination of which forms the basis for evaluating processing performance. The larger the signal-to-noise energy ratio, the easier it is to set the threshold to minimize the error probability and maximize the probability of a correct decision.

The above discussion on correlation and filtering in linear systems holds for all types of waveforms including coded, pulse compression, and a train of pulses. The correlation and integration functions will differ depending on the nature of the wave-

forms and their statistical properties. Excellent presentations on this subject may be found in Van Trees [5] and DiFranco and Rubin [6].

3. SUMMARY

In our tutorial on preprocessing, we have provided insight into the importance of preamplification for combating system noise. We have also shown that it is the energy, and not necessarily the power, in the signal that determines the performance of a processor algorithm.

A future article will cover the whitening process when the noise has certain correlation characteristics, i.e., colored. There will also be a discussion on the difference between independent sources of noise and eigenvectors which show up in noise covariance matrices.

4. ACKNOWLEDGMENT

The author acknowledges Mr. David Sargrad for his review and comments.

5. REFERENCES

1. Skolnik, M. I. *Introduction to Radar Systems*. McGraw-Hill, New York, 1962, pp. 363-388; 2nd ed. pp. 343-353, 1980.
2. Ziemer, R.E., and Tranter, W.H. *Principles of Communications-Systems, Modulation, and Noise*. Houghton Mifflin, Boston, 1990, 3rd ed., pp. 752-781.
3. Gardner, W. A. *Introductions to Random Processes-with Applications to Signals and Systems*. McGraw-Hill, New York, 1990, 2nd ed., pp. 286-291 (Noise Figure), pp. 291-300 (Matched Filter).
4. Haykin, S. *Communication Systems*. Wiley, New York, 1983, 2nd ed., Appendix 3 (Noise Figure), Chap. 10 (Matched Filter).
5. Van Trees, H. L. *Detection, Estimation, and Modulation Theory - Part I*. Wiley, New York, 1968.
6. DiFranco, J. V., and Rubin, W. L. *Radar Detection*. Artech House, Dedham, MA, 1980.

MEASURING THE QUALITY OF KNOWLEDGE WORK

Anthony Coppola, Electromagnetics & Reliability Directorate, Rome Laboratory

Published in Quality and Reliability Engineering International, Vol. 7, 411-416, 1991

Abstract - There is a variety of ways to measure the quality of knowledge work. The best selection for a particular application depends on how the user defines quality and the intended use of the measure. This paper catalogues possible measures according to five different perspectives on quality and four different uses of quality measures. It concludes with some recommendations for measuring quality in a laboratory.

1. INTRODUCTION

Quality is of vital interest to the managers of knowledge workers such as the engineers and scientists of government research and development laboratories. These agencies are now in fierce competition for a shrinking amount of available funds. Like hardware producers, laboratories providing quality products and services have the best, perhaps only, chances for survival.

Although the multitude of quality 'gurus' do not agree on everything, they have some common ideas. One of these is that how one measures quality is of extreme importance. This paper will discuss the measurement of quality in knowledge work.

There is no universally accepted standard definition for quality. Indeed, Garvin¹ identifies five categories of definitions for quality. These are

1. Transcendent quality: a subjective feeling of 'goodness'.
2. Product-based quality: measured by attributes of the product.
3. Manufacturing-based quality: conformance to the specifications.
4. Value-based quality: 'goodness' for the price.
5. User-based quality: the capacity to satisfy the customer.

Each of these categories stems from definitions coined by analysts attempting to meet their particular quality needs. One should note that the categories are not mutually exclusive. In particular, no matter which definition is used, quality is always ultimately defined by the customer (i.e. user-based).

Any quality definition used must be compatible with the purpose of the measurement. Within the umbrella of measuring quality, one could be attempting to gauge customer satisfaction, appraise the agency's overall quality, appraise an individual's performance, or improve specific products, services and processes. This paper's objective can therefore be restated as filling in the blanks on the generic matrix in Table I.

Table I. Measures of knowledge work

Purpose:	Rate customer satisfaction	Appraise agency	Appraise individuals	Improve products and processes
Measure:				
Type of measure:				

2. TRANSCENDENT QUALITY MEASURES

'...Even though Quality cannot be defined, You know what it is', said Robert M. Pirsig in *Zen and the Art of Motorcycle Maintenance*. Pirsig's statement epitomizes the theory behind transcendent quality measures, which are merely means for capturing subjective opinions.

The most common tool for transcendent quality measurement is the rating scale. For example, cake mixes are tested by submitting their products to a panel which rates the taste of the cake on a scale from one to five, with five being the best possible. Knowledge workers sometimes use peer ratings in a similar manner. When an attribute is actually subjective, like taste, the transcendent cannot be challenged. In areas where other measures are possible, the more objective measures are generally preferable. Even then, subjective opinion may be useful, so long as it reflects the opinion of the customer. In fact, the transcendent opinion of the customer is the most important measure of one's quality.

In the author's opinion, a useful area for transcendent measures of quality is in the appraisal of individual performance. Dr. W. Edwards Deming, the most respected 'guru' of quality, condemns the use of annual appraisals for several reasons.² However, appraisal systems will probably be with us for a while. The use of transcendent measures may be one way to make them work. My recommendation is to use general categories (e.g. shows initiative) scored by the subjective opinion of the employee's supervisor, on the assumption that the supervisor's transcendent quality judgement of the employee is likely to be an accurate measure. (He will know quality work when he sees it.)

Finally, even when using more objective quality definitions, the transcendent can be useful as a 'sanity check'. If a measured quality value 'feels' too high or too low, perhaps one's intuition is calling for the re-evaluation of the selection of measures.

Transcendent definitions of quality are of no help in determining how to improve, and in measuring progress, except in a gross sense.

A summary of the above is shown in Table II.

3. PRODUCT-BASED QUALITY MEASURES

Product-based quality is measured by the amount of some desired ingredient or attribute. For example, the speed of a fighter plane (or of a computer). In knowledge work, one desired attribute may be innovation. The difference is, of course, that it is easy to measure speed and difficult to measure innovation.

Since innovation and other intangible features are desired not for themselves, but for their impact on the product, measurable units such as speed will reflect the quality of knowledge work once the work has made the transition into hardware or software. Under such circumstances, system parameters can be measured to establish the quality of the underlying knowledge work. This does not mean it is easy. For example, there are many parameters of an electronic system which represent desirable attributes. Unless a few dominate, the analyst can be swamped with measures. One can try to select the most meaningful measures, which should be the main interests of the product's user, and the main reasons the product was developed. To be effective as quality measures, however, the measured values must be referenced to some benchmarks. For example, the speed of a computer is useless for quality evaluation unless the analyst knows what previous machines delivered. Percentage improvement in a parameter over previous achievements is an appropriate measure of the quality of the improvement effort.

Besides selecting the critical parameters, a problem with attribute measures is that trade-offs may not be recognized. Speed

may be enhanced at the expense of payload which may or may not be an improvement overall. One way to evaluate this is the use of all-encompassing measures such as 'systems effectiveness'. Systems effectiveness can be defined as a function of a system's availability, dependability and capability against a specified threat.³ In the simplest case, availability is the probability of a system being operable when needed, dependability the probability that it will remain operable for the length of a mission and capability the conditional probability that, if operating, it will successfully complete the mission. For this simple case:

$$\text{System effectiveness} = (\text{Availability}) \\ \times (\text{Dependability}) \times (\text{Capability})$$

When one begins to consider degraded mission states, variations in the threat, ability to repair, etc., this simple formula expands to a problem in matrix algebra.³

An approach between the measurement of a few selected parameters and the calculation of system effectiveness is the use of indexes. Indexes are artificial, but supposedly not arbitrary, groupings of measures into an overall single measure. Examples are the consumer price index and the index of leading economic indicators. Similarly, a quality index can be created by identifying parameters of interest, establishing measures, weighing the measures and combining them into one. As a simple example, Gunning⁴ describes a 'fog index' for evaluating understandability of text. It is calculated by computing the average sentence length, adding this to the number of words of three syllables or more in 100 words, then multiplying by 0.4. Though Gunning claims his index corresponds roughly with the number of years of schooling a person would require to read the text with ease and understanding, an index figure is generally not meaningful in absolute terms. Rather, it shows trends, which is generally satisfactory. The results can be compared to benchmarks and can also be plotted on a control chart. Against these advantages, if its components are not chosen carefully, it can be an arbitrary number not particularly good as a measure of quality. Reference 5 describes a sophisticated indexing approach.

The more tangible the product, the better product-based measures work. However, in knowledge work the product is often intangible, such as a conceptual design or a set of recommendations, and product parameters cannot be measured as reflections of quality attributes. One way to overcome this situation is to use even more indirect measures so long as they also correlate with the attributes desired. For example, a large number of patents should indicate an innovative agency. Although this does not guarantee that any particular product of that agency will be

Table II. Transcendent quality measures of knowledge work

Purpose:	Rate customer satisfaction	Appraise agency	Appraise individuals
Measure:	Rating scales of customer opinions	Rating scales of customer or peer opinions	Rating scales of supervisor's opinions
Type of measure:	Subjective	Subjective	Subjective

produced with a high degree of innovation, it can provide a secure feeling to a potential customer and to the laboratory manager. Again, benchmarks are needed for accurate interpretation.

Some sample measures might be the ratio of in-house to contracted work, numbers of papers published, patents awarded, resources spent on education and training activities, advanced degrees earned, name requests for consulting committees received, and the amount of national/international professional activity among the knowledge workers. These are measures of the laboratory climate or environment favoring quality knowledge work.

One could also measure the climate opposing quality in knowledge work. Common measures indirectly showing unfavourable climates include absenteeism, turnover percentage, average sick days taken per employee, etc. Poor environments could perhaps be more directly measured by the number of approvals required to do work, the ratio of overhead to productive activity, the length of time required to obtain a part or a piece of test equipment, etc. These could be labelled 'hassle indexes'.

In summary, product-based quality measures are most useful when tangible products are available. Attributes such as the ability to innovate cannot be measured directly. Instead, product attributes and measures of environment can be used. Benchmarks are needed to evaluate the measures. Table III summarizes this information.

4. MANUFACTURING-BASED QUALITY MEASURES

Perhaps the best illustration of manufacturing-based quality definitions was proposed by Philip Crosby, who equated quality to compliance with specifications.⁶ This, of course presumes tangible products or services, which for knowledge work could include such items as technical reports and briefings as well as the more obvious hardware and software end-products.

Table III Product-based quality measures of knowledge work

Purpose:	Rate customer satisfaction	Appraise agency
Measure:	Product parameters, performance indexes, system effectiveness (against benchmarks)	Climate indicators, (a) favourable signs, (b) 'hassle indexes' (against benchmarks)
Type of measure:	Objective	Surrogate

The most commonly used manufacturing based quality measure is defect rate (i.e. the percentage of the product not in compliance with specifications). Defect rate is a universal quality measure and can be applied to knowledge work as well as manufacturing, though not as easily, by formulating an appropriate operating definition of defect. Besides percentage defects, there are other manufacturing-based measures of quality of varying utility to knowledge work. For example, yield is a common measure of product quality which really is not too useful in measuring knowledge work. On the other hand, cycle time is another widely used measure which is easily applied to knowledge work.

Product-based measures become manufacturing-based measures when acceptable limits are defined. For example, Gunning's 'fog index' can be used to specify a required value of understandability, which can then be evaluated by a manufacturing-based quality measure (e.g. percentage of reports exceeding a specified 'fog index').

Another manufacturing-based quality measure is the variation among products. All products will have some variation, and the greater this is, the more defects there will be. For illustration, suppose one did specify that all reports to a particular customer should have a fog index no higher than 12. If measurements show the average fog index of the reports to be 11.0, the writers are not necessarily doing well. They could be producing reports with fog indexes between 10 and 12, or between 9 and 13, or between 8 and 14, etc. The greater the variance, the more products which are out of specification, and the less predictable the quality of a given single product. Variance can be measured in various ways, such as by range (the difference between the highest and lowest values) or by standard deviation (a statistical measure). Assuming a normal or bell-shaped distribution of the parameter, 99.7 per cent of the product will have values no more than three standard deviations (σ) away from the mean value. The lower the value of σ , the more uniformity in the product.

Variance, however, is not the whole story. Suppose, for example, the mean fog index of our reports was 14.0 and 3σ was 0.2. The understandability of our reports is quite predictable, but that would be of no comfort to the customer who needs a fog index of 12 or less. Hence, both the mean and variance are important. A measure which considers both is called process capability (C_p). It compares the mean and variance of a product parameter to specified limits:

$$C_p = \frac{\text{upper specification limit} - \text{lower specification limit}}{6\sigma}$$

Thus a C_p of 1.0 means that 99.7 per cent of the product would be 'in spec', assuming that the mean of the product is

centered between the upper and lower control limits. To allow for means in other locations, a process performance (Cpk) index can be used:

$$Cpk = \frac{(\text{minimum distance between the mean and either control limit})}{3\sigma}$$

Using either measure, the higher the value, the better. Motorola's 'six sigma' programme strives for a Cp of 2.0 (6σ between the target mean and the specification limits) which, when the true mean is 1.5 σ off target, translates to a defect rate of 3.4 parts per million.

For non-structured work, the main issue with manufacturing-based quality definitions is determining what the 'specification' is. A specification for a study on computer technology may specify the format, perhaps even the type style, of the final report, which are all of secondary importance to a host of considerations such as responsiveness, innovation, realism, clarity, etc. With the exception of the fog index for understandability, the author has found no specifiable measures of these critical desires. If one assumes that meeting the specifications for a product reflects desired intangibles such as innovation, measuring conformance is adequate. Otherwise, the manufacturing-based measures simply will not work. One could specify that a product show innovation, but verification of compliance would require a subjective opinion, which is a transcendent, not a manufacturing-based quality measure.

Manufacturing-based quality figures do have an important place in knowledge work. A laboratory's operations include many processes and subprocesses. It is important to note that in knowledge work, as in any other, the final customer is only the last of a series. Each office involved in a process is the customer for some input and the provider of some output to another customer. Thus, even the process of creating innovations will include such processes as publishing reports, obtaining laboratory equipment, awarding contracts, etc., which can be evaluated by manufacturing-based quality measures. Improving these processes must improve the laboratory operations, even if we totally ignore intangibles such as innovation. For example, shortening the time to obtain a needed instrument yields more time for performing experiments with it, which in turn can produce more innovations.

Process improvement is the heart of total quality management (TQM). Improving the process can be accomplished by radical innovations or by accumulation of many small changes. Either way, it begins with an understanding of the process, and depends on the measurement of quality indicators. The process itself should tell you what to measure. If the process is proposal evaluation, for example, cycle times and/or the number of cor-

rections required (defects) may be compiled to establish a baseline against which proposed improvements can be compared.

One danger in measuring a process is that what you measure becomes the priority, and some ways of improving one parameter may deteriorate other critical parameters. Optimizing a process may therefore adversely affect a larger process in which it is embedded, or the quality of the process by other measures. For example, improvements in the cycle time for proposal evaluations can be made by taking less care in doing the work, for a loss in quality measured by the number of errors. As always, the test of value added is the overall impact on the customer.

This section's summary is given in Table IV.

5. VALUE-BASED QUALITY MEASURES

In value-based quality definitions, cost is a consideration. A low-cost automobile which provides dependable and reasonably comfortable transportation would be considered a quality vehicle even if it does not have the features of a Rolls-Royce. In fact, the Rolls-Royce may be considered too expensive for what it provides and hence not good value for the average consumer.

Quality is also not independent of schedule. As discussed above, cycle time is a measure of quality, but improving cyclic time can adversely affect other facets of quality such as product defect rates. Conversely, a good product delivered too late may be of no use to the customer.

The author's view of value-based quality is that every product, service or process can be measured in three dimensions: cost, time and some measure of 'goodness', such as percentage defects. Improvements which change one without detriment to the other two are always worth while. Other changes may or may not be worth while depending on the overall effect on the customer. Although the tradeoffs between cost, schedule and 'goodness' can be a subjective matter, all quality decisions should try to balance the three considerations. For example, contracting can be measured by cycle time (schedule), overhead man-hours (cost) and number of protests per contract (defects). Measuring only one of these invites sacrificing the others. For case of reference, a balanced combination of cost, schedule and 'goodness' measurements will be referred to in the Tables as a 'quality troika'.

Another approach to using value-based measures is to distinguish between effectiveness and efficiency. Effectiveness measures the 'goodness' of a product or service for its user, whereas efficiency considers the cost of making it happen. To illustrate the difference, consider the example of supplying integrated circuits meeting the customers needs by making much more than ordered and screening the output. The customer may be pleased with the product (high effectiveness), but the cost of

Table IV. Manufacturing-based quality measures of knowledge-work.

Purpose:	Rate customer satisfaction	Appraise agency	Improve products and processes
Measure:	Programme or product line: defect rates Cp or Cpk cycle times	Aggregates of: defect rates Cp or Cpk cycle times	Process parameters: defect rates Cp or Cpk cycle times
Type of measure:	Statistical	Statistical	Statistical

quality will be higher than it should be (low efficiency). Effectiveness can be measured perhaps by sales (or the laboratory equivalent: amount of external funding), market share or one of the product-based measures. Efficiency is measured by the cost of quality, overhead rates or one of the manufacturing-based measures.

The cost of quality is another concept, developed by Crosby.⁶ It includes the cost of preventing defects, the cost of inspection, the cost of rework and the cost of waste. As Deming notes,² it also includes immeasurable costs, such as the cost of a lost customer. Many companies look only at the first two costs, considering only the money spent by their quality professionals (in prevention and inspection) as the cost of quality. In reality, a typical company may be spending 25 per cent of its manufacturing costs on rework and scrap.

It is an axiom of TQM that more effort in preventing defects is repaid many times over in savings in the other cost areas for an overall lower cost of quality. One way of measuring quality, from the standpoint of efficiency, could therefore be the determination of the measurable components of the cost of quality. The lower the cost of quality, the higher the efficiency of the quality effort.

Still another approach is the Taguchi loss function, which considers any product not meeting the design centre to be of lesser quality as a function of its variation, even though it may still be within the specification limits.⁷ There are actually several loss functions, covering the cases where the product has a target value, where bigger is better, and where smaller is better. In all cases the calculated loss increases with the square of the deviation from the target. The loss can represent actual costs for repair of a defect, lost business, etc., or intangible losses such as the 'loss to society' because of poor quality.

One way to matrix this information is shown in Table V; Table VI organizes the information in the same format as Tables II-IV.

Table V.

To measure:	Effectiveness	Efficiency	Combinations
Use:	Sales Market share	Cost of quality Overhead rates Loss functions	Quality troikas

Table VI. Value-based quality measures of knowledge work

Purpose:	Appraise agency	Improve products and processes
Measure:	Cost of quality Overhead rates, Sales, Market share	Quality troikas Loss functions
Type of measure:	Financial	Hybrid

6. USER-BASED QUALITY MEASURES

As previously stated, all measures of quality must ultimately be user-based. The problem is translating user satisfaction to an appropriate quality measure. The most quoted user-based definition of quality is that of Juran,⁸ who defined quality as fitness for use. Juran divides fitness for use into two categories: features and freedom from deficiencies. Features, he stated, cost money and attract customers, whereas freedom from defects saves money and keeps customers. Knowledge work features could include innovations, responsiveness, ease of comprehension of ideas presented, etc. and freedom from defects includes accuracy, legibility of written reports, etc. Under this definition, product-based quality measures become user-based measures for evaluating features and manufacturing-based measures become user-based measures for evaluating freedom from defects. Transcendent and value-based quality measures may measure features, freedom from defects or overall fitness for use, depending on the application. Using Juran's definition of quality as the starting point, the various measures separate (roughly) as shown in Table VII. Table VIII recombines the information into the usual format, and summarizes all of the previous discussion.

7. CONCLUSIONS

Far from having no measures of the quality of knowledge work, there appears to be a plethora of choices. The author believes that a laboratory should measure effectiveness before ef-

Table VII

To measures:	Features	Freedom from defects	Overall fitness
Measure:	Rating scales Product parameters Performance indexes Systems effectiveness	Defect rates Cp or Cpk Cycle times Cost of quality Overhead rates Loss functions	Climate indicators Sales Market share Quality troikas

iciency and features before freedom from defects. Effectiveness makes a potential customer interested in the work. Efficiency makes the purchase more affordable, but the interest must be there before this is relevant. Features are more important than freedom from defects for similar reasons. For a laboratory, producing 'high tech' inefficiently is preferable to producing low tech efficiently. Of course, producing high tech efficiently is best and may possibly be the only way to survive.

The customer's transcendent evaluation of quality is of considerable importance. Hence, it is the first measure that should be obtained, followed by measures of overall effectiveness.

Needed next are efficiency measures to ensure competitiveness and help one remain competitive. All critical processes, such as contracting, should be measured for continual improvement of those things within the control of the agency which contribute to the customer's opinion of its quality or to the affordability of its products. Specific products and programmes should have appropriate quality measures developed by the appropriate managers in the laboratory, working with their specific customers. This adds up to a lot of measurements, but if a product, programme or process is important, it calls for quality measurement. In addition, one will need to establish benchmarks to compare against the measurements. The alternative is to bet the future without knowing where one stands.

8. REFERENCES

1. A. David Garvin, *Managing Quality*, The Free Press, NY, 1988.
2. W. Edwards Deming, *Out of the Crisis*, MIT, MA, 1986.
3. Weapon System Effectiveness Industry Advisory Committee, *Chairman's Final Report*, AFSC-TR-65-6. Air Force Systems Command, 1965, AD-467816.
4. Robert Gunning, *New Guide to More Effective Writing in Business and Industry*, Industrial Education Institute, Boston, 1964.
5. Robert D. Pritchard, Steven D. Jones, Philip L. Roth, Karla K. Stuebing and Steven E. Ekeberg 'Organization productivity measurement: the development and evaluation of an integrated approach', *AFHRL-TR-86-64*, Air Force Human Resources Laboratory, 1987, AD-A183 565.
6. Philip B. Crosby, *Quality is Free*, McGraw-Hill Book Co., NY, 1979.
7. Phillip J. Ross, *Taguchi Techniques for Quality Engineering*, McGraw-Hill Book Co., NY, 1988.
8. J. M. Juran, *Juran on Leadership for Quality*, The Free Press, N Y, 1989.

Table VIII User based quality measures for knowledge work

Purpose:	Rate customer satisfaction	Appraise agency	Appraise individuals	Improve products and processes
Measure:	Rating scales Product parameters Performance indexes Systems effectiveness Defect rates Cp or Cpk Cycle times	Rating scales Climate indicators Defect rates Cp or Cpk Cycle times Cost of quality Overhead rates Sales, Market share	Rating scales	Defect rates Cp or Cpk Cycle times Quality troikas Loss functions
Type of measure:	Subjective, objective or statistical	Subjective, surrogate, statistical or financial	Subjective	Statistical or hybrid
Definition of quality:	Transcendent, product-based or manufacturing-based	Transcendent, product-based, manufacturing-based or value-based	Transcendent	Manufacturing-based or value-based

BOUNDS ON THE SIZES OF IRREDUNDANT TEST SETS AND SEQUENCES FOR COMBINATIONAL LOGIC NETWORKS

Warren H. Debany, Jr., Electromagnetics & Reliability Directorate, Rome Laboratory
Carlos R.P. Hartmann, School of Computer and Information Science, Syracuse University

Published in Journal of Electronic Testing: Theory and Applications, Vol. 2, 325-338, 1991

Abstract - We present a method of determining lower and upper bounds on the number of tests required to detect all detectable faults in combinational logic networks. The networks are composed of AND, OR, NAND, NOR, and XOR gates. The fault model assumes that single stuck-at-zero faults occur on the lines of the networks, with the additional requirement that XOR gates be tested with all possible input combinations. The goal is to provide a simple and efficient implementation that processes the fanout-free subnetworks separately, and then combines the results without the need to consider the effects of reconvergent fanout. We introduce the concepts of irredundant test sets, where no test can be deleted regardless of the order of test application, and irredundant test sequences, where every test detects at least one additional fault when tests are applied in order. Identifying and differentiating between these types of collections of tests allows us to understand more precisely the mechanisms and expected performance of test generation and test compaction methods. We apply our test counting technique and two other published procedures to a set of benchmark circuits. Our bounds are shown to compare favorably to the results obtained by the other published approaches. We obtain "minimal" and "maximal" test sets and test sequences using a greedy optimization technique. Our bounds are shown to produce tight bounds for the smaller circuits; they grow more conservative as the size of the circuits increase.

1. INTRODUCTION

An important measure of the testability of a combinational logic network is the number of tests required to detect all detectable faults in the network. In this paper we consider the problem of determining, or at least estimating, bounds on the sizes of collections of tests that detect all faults in a digital logic network or circuit. Several new concepts are explored in this paper. We distinguish between the properties of *test sets* and *test sequences*, and we consider both *lower bounds* and *upper bounds* on sizes of irredundant collections of tests. This approach allows us to describe and bound the behavior of test generation and compaction techniques that are used in practical test generation schemes today.

The approach is a three-step process. First, a nonfanout-free combinational logic network is partitioned into fanout-free subnetworks. Second, the subnetworks are processed, as if they were standalone networks, to obtain bounds on test counts. At this point, the bounds are achievable. Third, the fanout-free subnetworks are treated as black boxes and their test counts are used to obtain bounds on the number of tests for the original, complete network. A goal is to develop a simple and efficient implementation that uses a minimum of knowledge about the

fanout structure of a circuit. This work is based on material first presented in [1].

This article is organized as follows. Section 2 presents preliminary definitions, the most critical of which concern the concepts of irredundant test sets and sequences. In Sections 3 and 4 lower and upper bounds are obtained on the number of tests required to detect all faults in fanout-free networks. In Section 5 these results are employed to obtain lower and upper bounds on the number of tests required to detect all detectable faults in nonfanout-free networks. Results of applying the test counting procedures to a number of logic circuits are presented in Section 6, and these bounds are compared with those obtained by other techniques. Conclusions are presented in Section 7.

2. PRELIMINARIES

The networks considered in this paper contain AND, OR, NAND, NOR (AONN), and exclusive-OR (XOR) gates. XOR "gates" are treated as indivisible elements, but are assumed to be realized in terms of an AONN network (such as all-NAND). XOR gates have two inputs, and all gates are single-output. Gates are connected by signal or logic lines. *Primary input lines* have logical values that are sourced externally. *Primary output lines* are the only lines whose logical values are directly observable.

A *node* is a set of connected lines and, in the class of networks considered in this article, every node is driven by exactly one line. A node that consists of more than one line is a *fanout node*, and it is assumed that fanout is from a single origin (i.e., fanout is ideal). The line that drives a fanout node is referred to as the *fanout origin* (often called a *fanout stem*) and the driven lines are the *fanout branches*.

A. Fault Model

Based on the stuck-at fault model, it has been shown that 2^n tests are necessary and sufficient to test any logically irredundant AONN realization of an n -input XOR Function [2]. Thus, every two-input XOR gate must be tested with all four possible input combinations. While any AONN network that realizes the XOR function must include lines that fanout, XOR gates are

considered to be indivisible elements in our approach so the fanout within XOR gates is not considered when categorizing a network as fanout-free or nonfanout-free. In Section 5 it is shown that it is desirable to identify AONN networks that realize the XOR function, and treat them as indivisible XOR gates, because it leads to better upper bounds on test counts.

We assume that in the presence of an internal stuck-at fault an XOR gate may exhibit any one of the $2^4 - 1 = 15$ possible faulty truth tables. This functional fault model for an XOR gate subsumes the stuck-at faults on the input and output lines of the XOR gate. We can now define the fault model used in this paper more precisely as follows:

Definition 1. A stuck-at fault in combinational logic network N is defined to be the event where exactly one of the following statements is true:

- a. exactly one logic line in N is permanently stuck-at-zero, or
- b. exactly one logic line in N is permanently stuck-at-one, or
- c. exactly one XOR gate in N exhibits a faulty truth table.

B. Irredundant Test Sets and Test Sequences

In this article a vector of logical values applied to the primary inputs during testing is referred to as a *test*. We constrain collections of tests so that each test in a collection contributes in some way to fault detection. We distinguish between collections of tests where the order in which tests are considered is significant, and where the order of the tests is not significant.

Definition 2. Irredundant test set T , for network N , is a set (an *unordered* collection) of tests in which every test in T detects at least one fault in N that is not detected by any other test in T .

Most fault detection procedures that can be applied to large networks involve a series of steps where test generation (targeting a fault or set of faults for detection) alternates with fault simulation (to determine which faults are actually detected). The resulting collection of tests is usually larger than necessary, and can be compacted either by taking advantage of *don't care* signal assignments or by eliminating tests that do not contribute to fault detection. Systematic test compaction techniques are known (e.g., [3], [4]) but such techniques are seldom used in practice because it is prohibitively-expensive to obtain what amounts to a "minimal cover."

It is well known that, if a collection of tests is fault-simulated in a different order, then some tests may be shown to be unnecessary [5], [6]. This provides the motivation to define a form of test irredundancy that is applicable to the process most often used in practice:

Definition 3. Irredundant test sequence U , for network N , is a sequence (an *ordered* collection) of tests in which every test u in U detects at least one fault in N that is not detected by any test that precedes u in U .

The problem of determining or estimating test set size has been considered by many authors (e.g., [2], [7]-[17]). The usual goal is to find the minimal cardinality of any test set, in which case the assumption is implicit that test sets are irredundant. Here, we systematically investigate the best and worst performances possible using any compaction or test elimination strategy.

Let the cardinality of test set T (the number of distinct tests in T) be denoted by $|T|$. Let the length of test sequence U (the number of tests in U , whether they are distinct or not) be denoted by $|U|$. In this article the term *size* is used for both set cardinality and sequence length where it is unnecessary to distinguish between the two terms.

Set irredundancy is stronger than sequence irredundancy in two important senses:

- Associated with each irredundant test set T there are $|T|!$ irredundant test sequences of length $|T|$ that can be constructed by taking all permutations of the $|T|$ tests in T . On the other hand, the $|U|$ tests that comprise an irredundant test sequence U do not necessarily constitute an irredundant test set.
- Let U be an irredundant test sequence such that its tests correspond to a redundant test set. In this case, there exists a reordering of the tests comprising U that results in a redundant test sequence, U' . Furthermore, although every test in U detects at least one fault not detected by any test that precedes it in U , one or more tests can be deleted from U yet the resulting test sequence U'' still detects all faults detected by U .

Sequences possess many properties that are analogous to those of sets [1]. A concept that is useful in deriving the results of this paper is that of a *subsequence*, which is analogous to the concept of a subset.

Definition 4. Sequence U' is a *subsequence* of sequence U if and only if all of the elements in U' are also in U and the relative order of the elements in U' is the same as that of the corresponding elements in U .

C. Irredundant Networks

Let F be a set of faults in network N . N is said to be *irredundant with respect to F* if and only if for each fault f in F there exists at least one test for f . Otherwise, N is said to be *redundant with respect to some fault in F* . In this paper F is taken to be the set of all stuck-at faults, unless otherwise stated. The general

problem of showing that a logic network is irredundant is known to be NP-Complete [8], [9].

Definition 5. For network N , denote by I_N the set of all irredundant test sets that detect *all faults* in N . Denote by I_N^d the set of all irredundant test sets that detect *all detectable faults* in N . Similarly, denote by R_N the set of all irredundant test sequences that detect *all faults* in N , and denote by R_N^d the set of all irredundant test sequences that detect *all detectable faults* in N .

I_N and R_N are always nonempty, but I_N^d and R_N^d are nonempty only if N is irredundant. If I_N and R_N are nonempty, then I_N and I_N^d coincide and, R_N and R_N^d coincide.

Definition 6. For network N , if I_N and R_N are nonempty, then denote by $\text{Min}(I_N)$ the minimal cardinality of any test set in I_N , and denote by $\text{Max}(I_N)$ the maximal cardinality of any test set in I_N . Similarly, denote by $\text{Min}(R_N)$ the minimal length of any test sequence in R_N , and denote by $\text{Max}(R_N)$ the maximal length of any test sequence in R_N . $\text{Min}(I_N^d)$, $\text{Max}(I_N^d)$, $\text{Min}(R_N^d)$, and $\text{Max}(R_N^d)$ are defined similarly, in terms of I_N^d and R_N^d .

It is clear that $\text{Min}(I_N)$ is equal to $\text{Min}(R_N)$. However, $\text{Max}(R_N)$ is generally greater than $\text{Max}(I_N)$. We demonstrate this by means of an example.

Example 1. Consider the smallest of the ISCAS '85 benchmark circuit, C17 [24]. All 34 stuck-at faults on the lines of C17 are detectable so I_{C17} and R_{C17} exist. It can be shown that I_{C17} contains 10 tests of cardinality 4, 308 of cardinality 5, 2,878 of cardinality 6, 1,848 of cardinality 7, and 252 of cardinality 8. Thus, $\text{Min}(I_{C17}) = \text{Min}(R_{C17}) = 4$, and $\text{Max}(I_{C17}) = 8$. It is more difficult to generate the entire set of irredundant sequences that comprise R_{C17} , but we were able to generate an irredundant test sequence of length 12. Thus, we know at least that $\text{Max}(R_{C17}) \geq 12$, which is 50% greater than the size of the largest test set in I_{C17} .

It has been shown that the problem of estimating the actual value of $\text{Min}(I_N)$ within any fixed percentage is NP-Hard, and thus its computational-complexity is comparable to those of the problems of fault detection and redundancy identification [14], [18], [19]. However, we present methods for determining close lower and upper *bounds* on test set and sequence sizes, that require computational time that can be shown to grow only linearly with network size.

D. Network Partitioning

The test counting procedure presented in this article is based on determining minimal and maximal test set and sequence

sizes for the individual fanout-free subnetworks of a logic network. The network is first partitioned into distinct maximal fanout-free subnetworks [1], [23]. A *maximal fanout-free subnetwork* is one that is not a subnetwork of any other fanout-free subnetwork but the maximal fanout-free subnetworks used in this article are further restricted to consist of either AONN gates only or XOR gates only. Our convention is to consider a fanout-free subnetwork that consists of only a line to be an AONN-type fanout-free network. It is important to note that the partitioning method of this paper is different from other approaches because of the special handling of XOR gates. It is convenient to define the following sets of lines in a network:

Definition 7.

- FX_N is the set of all lines in network N that are direct connections without fanout from an XOR gate to an AONN gate, or from an AONN gate to an XOR gate.
- FO_N is the set of all lines in network N that are fanout origins, primary outputs, or in FX_N .
- FB_N is the set of all lines in network N that are fanout branches, primary inputs, or in FX_N .
- $FD_{N(y)}$ is the set of all lines driven by line y , where y is in FO_N and y is excluded from $FD_{N(y)}$ unless y is in FX_N .

Each maximal fanout-free subnetwork in network N has all of its primary inputs in FB_N , and its primary output is in FO_N . Any nonfanout-free network N can be partitioned into n distinct maximal fanout-free subnetworks, where $n = |FO_N|$ and $n \geq 2$.

Definition 8. Let $n = |FO_N|$. For $i = 1, 2, \dots, n$, denote by N^i (note the superscript!) the i^{th} fanout-free subnetwork of N , and denote by N_i (note the subscript!) the identical fanout-free network as an independent, standalone network.

Example 2. Network N_α , shown in figure 1, has been partitioned into maximal fanout-free subnetworks. Lines $a-p$ are categorized as follows:

$$\begin{aligned} FX_{N_\alpha} &= \{n, o\} \\ FO_{N_\alpha} &= \{a, e, j, n, o, p\} \\ FB_{N_\alpha} &= \{a, b, c, d, f, g, h, i, k, l, n, o\} \\ FD_{N_\alpha(a)} &= \{b, c\} \quad FD_{N_\alpha(e)} = \{f, g\} \quad FD_{N_\alpha(j)} = \{k, l\} \\ FD_{N_\alpha(n)} &= \{n\} \quad FD_{N_\alpha(o)} = \{o\} \quad FD_{N_\alpha(p)} = \emptyset \end{aligned}$$

Since $|FO_{N_\alpha}| = 6$, network N_α has six maximal fanout-free subnetworks N^1, N^2, \dots, N^6 .

3. TEST COUNTING FOR AONN FANOUT-FREE NETWORKS

In this section lower and upper bounds are derived for the sizes of irredundant test sets and sequences for fanout-free networks consisting only of AND, OR, NAND, and NOR gates, but not XOR gates. Because Berger and Kohavi's method [10] is the starting point for this article's derivation of test sets and sequences with both minimal and maximal sizes, a brief review is presented of the essential elements of their method, and extensions of their work are given.

A. Sensitized and Desensitized Lines

In a fanout-free network, line x is said to be *sensitized* by test t if and only if t causes the primary output to be sensitized to a change in the value on x . Any line that is not sensitized by t is *desensitized* by t . Line x is said to be a *predecessor* of line y if and only if y is on the path from x to the primary output, and x and y are distinct; line y is then said to be a *successor* of line x . Every line is considered to be both a predecessor and a successor of itself.

The *parity* of a line is said to be even (odd) if and only if there are an even (odd) number of signal inversions between that line and the primary output. The parity of a line will be denoted by p , where $p = 0$ if the parity is even, and $p = 1$ if the parity is odd. Let $p \oplus z$ denote the sum (modulo 2) of p and a logical value z .

Berger and Kohavi showed that any test set T for AONN fanout-free network N can be partitioned into two test sets, T_0 and T_1 , for which the fault-free N has the output values 0 and 1, respectively. Thus, F , the set of all stuck-at faults in N , can be partitioned into two sets, F_0 and F_1 , where faults in F_0 are detected only by tests in T_0 and faults in F_1 are detected only by

tests in T_1 . Test set T_z , $z = 0$ or 1 , is said to be *irredundant with respect to F_z* if and only if every test in T_z detects at least one fault in F_z that is not detected by any other test in T_z .

Extending this concept to sequences, every test sequence U for an AONN fanout-free network N can be partitioned [1] into two subsequences, U_0 and U_1 , for which the fault-free network has the output values 0 and 1, respectively. Test sequence U_z , $z = 0$ or 1 , is said to be *irredundant with respect to F_z* if and only if every test u in U_z detects at least one fault in F_z that is not detected by any other test that precedes u in U_z .

Berger and Kohavi's method involves transforming a fanout-free network into two *characteristic graphs* for test counting and test vector generation. Characteristic graph G_0 (G_1) is used to count and generate tests in T_0 (T_1), with the goal of detecting all faults in F_0 (F_1). A characteristic graph is a directed graph consisting of lines and vertices. Every line in the network corresponds to a line in the characteristic graph and every gate corresponds to a vertex. Each vertex is either a *minivertex* or a *maxivertex*, depending on three factors: the corresponding gate's type, the parity of the vertex's output line, and the logical value of the faultfree network's output. Table 1 shows how this assignment is made. In table 1, "M" denotes a maxivertex, "m" denotes a minivertex, and "even" and "odd" refer to the parity of the gate output line with respect to the primary output. We adopt

Table 1. Maxivertex and minivertex assignments.

Gate Type	G_0		G_1	
	even	odd	even	odd
AND, NOR	m	M	M	m
NAND, OR	M	m	m	M

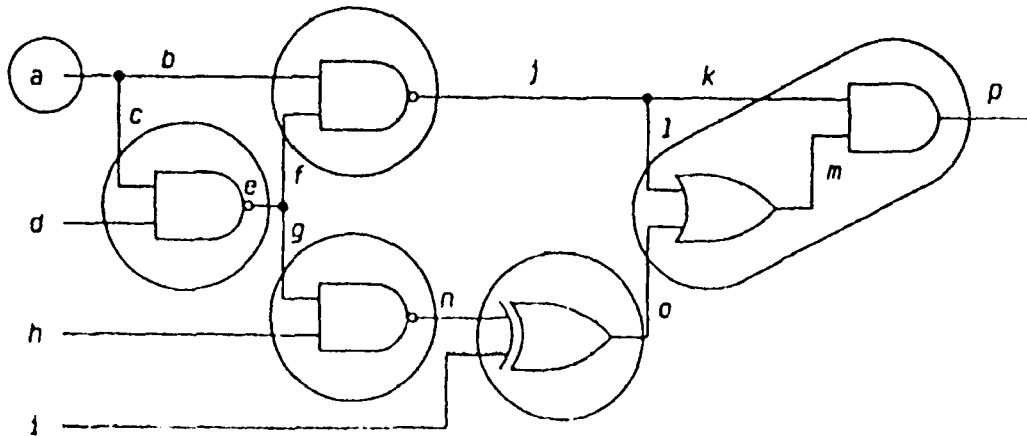


Fig. 1. Network N_1 partitioned into fanout-free subnetworks.

the convention that a single-input vertex is a maxivertex.

Example 3. Figure 2 shows network N_b and its corresponding characteristic graphs G_0 and G_1 .

The principles expressed in Lemma 1 and the (a) and (b) parts of Lemma 2 were used by Berger and Kohavi to achieve minimal cardinality test sets. The (c) part of Lemma 2 is a new observation and is the key principle that enables upper bounds on the sizes of irredundant test sets and sequences to be obtained:

Lemma 1. An input or output line connected to any maxivertex is sensitized (desensitized) if and only if all other lines connected to that maxivertex are also sensitized (desensitized).

Lemma 2. For any minivertex, exactly one of the following three conditions is true:

- a. the output is desensitized and all inputs are desensitized, or
- b. the output is sensitized and exactly one input is sensitized, or
- c. the output is sensitized and no input is sensitized

B. Lower Bounds

The test counting procedure derived in [10] obtains achievable lower bounds on $|T_0|$ and $|T_1|$ based on the properties of maxivertices and minivertices summarized in Lemmas 1 and 2. Since every minimal cardinality test set T for N is the union of a minimal cardinality T_0 and minimal cardinality T_1 , this procedure calculates $\text{Min}(\mathbf{I}_N)$ for AONN fanout-free networks. It is necessary to restate the simple procedure of [10] for obtaining minimal test counts for fanout-free networks in order to define

our notation:

Procedure BKA. Berger-Kohavi Algorithm (Test Counting Portion).

For characteristic graph G_z , $z = 0$ or 1 :

Step 1. Associate a test count of 1 with each input to G_z .

Step 2. Every *maxivertex*, for which all input test counts have been assigned, has associated with its output the *maximum* of its input test counts. Every *minivertex*, for which all input test counts have been assigned, has associated with its output the *sum* of its input test counts.

Step 3. If the output of G_z has not been assigned a test count, go to Step 2; otherwise, terminate.

Denote by $S_z(x)$ the test count given by the BKA for line x in characteristic graph G_z . Berger and Kohavi showed that $S_z(y)$, where y is the output of N , is an achievable lower bound on $|T_z|$. Therefore, $S_0(y) + S_1(y)$ yields a test count that is both $\text{Min}(\mathbf{I}_N)$ and $\text{Min}(\mathbf{R}_N)$.

Example 4. Characteristic graphs G_0 and G_1 of figure 2 are annotated with minimal test counts. For network N_b , $\text{Min}(\mathbf{I}_{N_b}) = \text{Min}(\mathbf{R}_{N_b}) = 6 + 3 = 9$ tests.

C. Upper Bounds

In [1] characteristic graphs were transformed into *reduced* characteristic graphs to aid in proofs concerning maximal test counts. We have simplified the earlier approach and now anno-

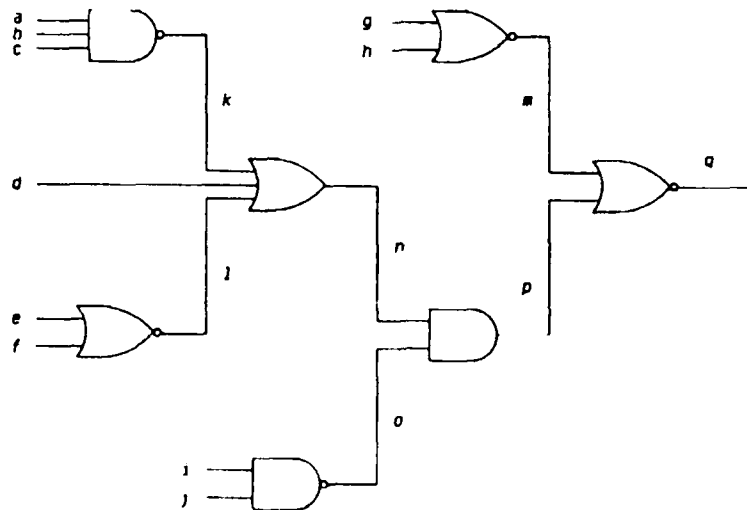


Fig. 2 AONN network N_b and its characteristic graphs G_0 and G_1 annotated with minimal test counts

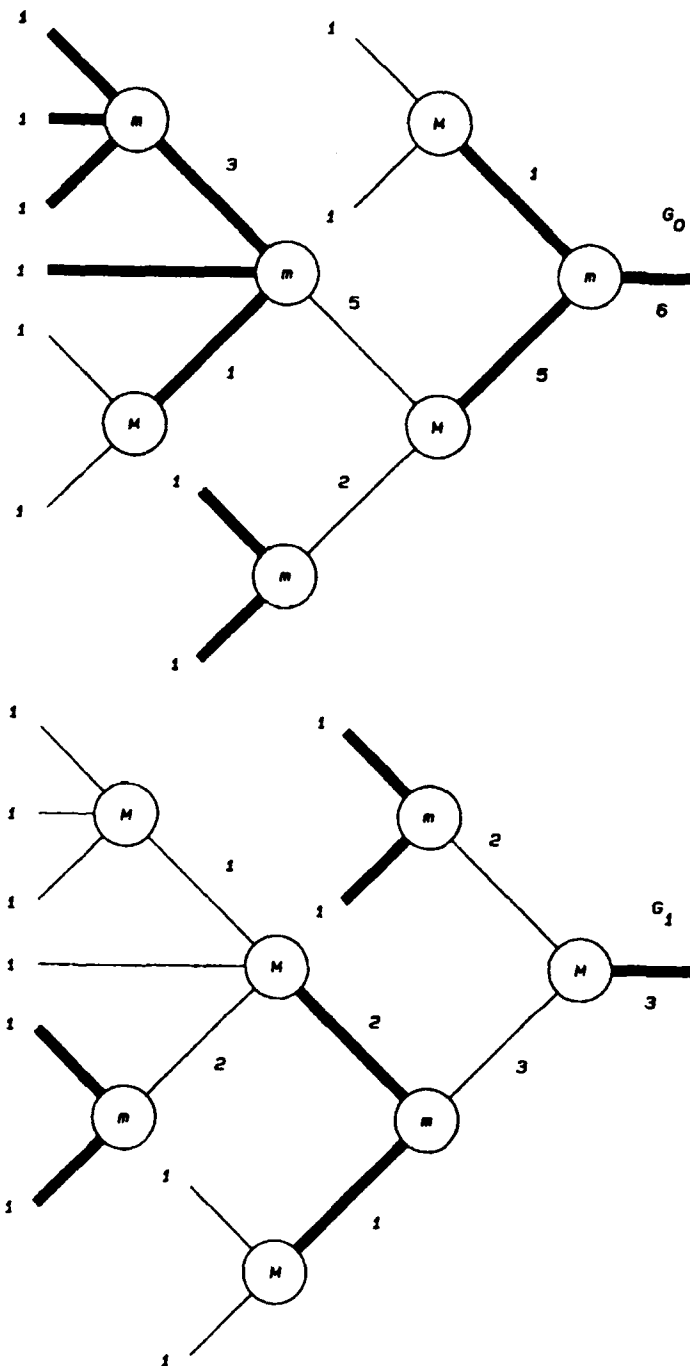


Fig. 2. (Continued)

tate (rather than modify) the characteristic graphs to denote critical lines that can be sensitized independently:

Procedure ILLP. Independent Line Labeling Procedure.

For characteristic graph G_z , $z = 0$ or 1 :

Step 1. Make every single-input vertex a maxivertex.

Step 2. Label as an *independent line* (IL) every line that is not an input to a maxivertex.

Step 3. Label as an *independent primary input* (IPI) every IL that is not a successor of another IL.

In the context of a characteristic graph labeled by the ILLP, necessary and sufficient conditions to detect all faults are sum-

marized in the following two lemmas [1]:

Lemma 3. Test set T_z (sequence U_z) detects all faults in F_z , $z = 0$ or 1 , if and only if T_z (U_z) sensitizes every IL in G_z at least once.

Lemma 4. Test set T_z (sequence U_z) detects all faults in F_z , $z = 0$ or 1 , if and only if T_z (U_z) sensitizes every IPI in G at least once.

Lemma 3 has a straightforward but lengthy inductive proof based on Lemmas 1 and 2, and Lemma 4 is an immediate consequence of it. They show that it is sufficient to consider only the ILs and IPIs of a characteristic graph to determine if a test set or sequence detects all faults and is irredundant. We now have enough information to prove the following theorems about maximal test counts for AONN fanout-free networks.

Theorem 2. Let N be an AONN fanout-free network with characteristic graphs G_0 and G_1 labeled by the *ILLP*. $\text{Max}(\mathbf{I}_N)$ is less than or equal to the sum of the number of IPIs in G_0 and G_1 .

Proof. Let T be an irredundant test set that detects all faults in F_0 and F_1 . Without loss of generality, consider only the subset of tests T_0 in T , because the proof for T_1 is similar and $|T| = |T_0| + |T_1|$. Since T_0 detects all faults in F_0 , by Lemma 4 T_0 must sensitize every IPI in G_0 at least once. Since T is irredundant so is T_0 . Now, assume that $|T_0|$ is greater than the number of IPIs in G_0 . Then there must exist a proper subset of tests in T_0 that also sensitizes every IPI in G_0 at least once, and thus by Lemma 4 this subset would detect all faults in F_0 as well. But this implies that T_0 is redundant, which is a contradiction.

The proof of Theorem 3 parallels that of Theorem 2, but is based on Lemma 3 and the properties of subsequences:

Theorem 3. Let N be an AONN fanout free network with characteristic graphs G_0 and G_1 labeled by the *ILLP*. $\text{Max}(\mathbf{R}_N)$ is less than or equal to the sum of the number of ILs in G_0 and G_1 .

The total number of IPIs in a fanout free network's characteristic graphs must be less than or equal to the total number of ILs. Therefore, $\text{MAX}(\mathbf{I}_N) < \text{Max}(\mathbf{R}_N)$ for any fanout free network N , as demonstrated in Example 2. In [1] it is shown by construction that the bounds stated in Theorems 2 and 3 are in fact achievable, and therefore their inequalities can be replaced by equalities.

Example 5. The shaded lines of the characteristic graphs for network N_b shown in figure 2 are the ILs and IPIs. Any IL that is not the successor of another IL is an IPI. Applying Theorems 2

and 3:

$\text{Max}(\mathbf{I}_{N_b}) = (\text{total number of IPIs}) = 8 + 5 = 13$ tests

$\text{Max}(\mathbf{R}_{N_b}) = (\text{total number of ILs}) = 11 + 7 = 18$ tests

D. Network Input Constraints

We have considered so far only the test counts associated with the output of the fanout-free network. Now we show that the BKA can be used to obtain additional constraints on signal assignments at the *inputs* of the network. This is motivated by the example of Akers and Krishnamurthy [15], [16]. Their approach involves repeated sweeps through the entire (nonfanout-free) network, but we restrict our analysis to information that can be obtained by processing only one fanout-free *sub* network at a time. Specifically, we show how the BKA can be used to obtain lower bounds on the number of times each input to a fanout-free network must take the values 0 and 1 in any minimal cardinality test set.

Lemma 5. Let g be a gate in an AONN fanout-free network and let p be the parity of the input lines of g . The logical value on each of input lines of g is given by $p \oplus z$ in both of the following cases:

- g is a maxivertex in characteristic graph G_z and its output is sensitized,
- g is a minivertex in characteristic graph G_z and its output is desensitized.

This lemma states that the same logical value *sensitizes* the inputs to a *maxivertex* in one characteristic graph and *desensitizes* the corresponding *minivertex* in the other characteristic graph. This interesting fact is the basis of a theorem that provides lower bounds on the number of times each input to a fanout-free network must take the logical values 0 and 1 based on its BKA test counts. Let $C_z(w)$ denote a lower bound on the number of times w , an input to fanout-free network N , must take the logical value z in any minimal cardinality test set for N .

Theorem 4. Let line w be an input to AONN fanoutfree network N . There are two cases:

Case (a): N contains at least one multiple input gate. Assign to z the logical value such that w is an input to a maxivertex in characteristic graph G_z . Let y be the first successor of w that is an IL in G_z . Let x be the successor of w that is the input to the maxivertex that sources y . Let p be the parity of w . Then

$$C_p \oplus z(w) = S_z(y) + S_{\bar{z}}(y) - S_{\bar{z}}(x) \\ C_{\bar{p} \oplus \bar{z}}(w) = 1$$

Case (b): N consists only of a line or a cascade of one or more single-input gates. Then

$$C_0(w) = C_1(w) = 1$$

Proof. If N is a line or a cascade of single-input gates the result is clear. Let us assume that N contains at least one multiple-input gate.

Consider first G_z , where line w is an input to a maxivertex. There is a cascade of one or more maxivertices between w and y , and any test that sensitizes y can be shown also to sensitize w (via Lemma 1 and induction on the number of maxivertices in the cascade). Therefore, w must be sensitized with the value $p \oplus z$ (Lemma 5) at least $S_z(y)$ times.

Now consider $G_{\bar{z}}$, where w is an input to a minivertex. There is a cascade of one or more minivertices between w and y . Let g be the minivertex that sources y . Line x (which is also line w if the cascade has only one minivertex) must be desensitized whenever any *other* input to g is sensitized. $S_z(y)$ is the sum of the minimal test counts of all of the inputs of g , so x must be desensitized at least $S_z(y) - S_{\bar{z}}(x)$ times. It can be shown that w must also be desensitized whenever x is desensitized (via Lemma 2 and induction). Therefore, it, must be desensitized with the value $p \oplus z$ at least $S_z(y) - S_{\bar{z}}(x)$ times. In total, w must be assigned the logical value $p \oplus z$ at least $S_z(y) + S_{\bar{z}}(y) - S_{\bar{z}}(x)$ times.

In $G_{\bar{z}}$, w must be sensitized at least once, and the logical value it must take is $\bar{p} \oplus \bar{z}$.

4. TEST COUNTING FOR XOR FANOUT-FREE NETWORKS

In this section lower and upper bounds are provided for the sizes of irredundant test sets and sequences for fanout-free networks consisting only of two-input XOR gates. It is shown in Section 5 that this approach leads to tighter bounds than if XOR gates were replaced by their AONN-gate equivalents.

We require that every two-input XOR gate must be tested by applying all possible input patterns to it: 00, 01, 10, and 11. These binary test patterns are referred to as *test symbols*. It has been shown that a test set detects all single faults in an XOR fanout-free network N if and only if the test set applies all four test symbols to every two-input XOR gate in N . For N , an XOR fanout-free network consisting only of two-input XOR gates, it

is an immediate consequence of Lemma 5 and Theorem 6 of [2] that $\text{Min}(\mathbf{I}_N) = 4$, and therefore $\text{Min}(\mathbf{R}_N) = 4$ as well.

The procedures for determining $\text{Max}(\mathbf{I}_N)$ and $\text{Max}(\mathbf{R}_N)$ for XOR fanout-free networks are simpler than those for AONN fanout-free networks, but the proofs are far more complex. Each test symbol applied to an XOR gate detects a set of (functional) faults associated with the gate. In order for test set T to be irredundant it is necessary and sufficient that each test apply at least one symbol to a gate that is not applied by any other test in T . In order for test sequence U to be irredundant it is necessary and sufficient that each test apply at least one symbol to a gate that is not applied by any test that precedes it in U . In order to prove the results stated in the following two theorems, the introduction of a substantial amount of new notation and terminology would be required. Furthermore, the proof of these theorems are lengthy and tedious since many cases must be considered. Therefore we state only the results and the interested reader is referred to [1].

Theorem 6. Let N be an XOR fanout-free network consisting of exactly G two-input XOR gates. $\text{Max}(\mathbf{R}_N) = 2G + 2$.

Theorem 7. Let N be an XOR fanout-free network consisting of exactly G two-input XOR gates, and having exactly G' gates with three neighboring gates (i.e., there are G' gates in N that have no inputs that are primary inputs of N and their outputs are not the primary output of N). If $G = 1$, then $\text{Max}(\mathbf{I}_N) = 4$; if $G \geq 2$, then $\text{Max}(\mathbf{I}_N) = 2G - G'$.

Example 6. Figure 3 shows XOR fanout-free network N_c . N_c contains eight XOR gates; hence $G = 8$. Two gates in N_c have three neighbors; hence $G' = 2$. Therefore:

$$\begin{aligned} \text{Min}(\mathbf{I}_{N_c}) &= \text{Min}(\mathbf{R}_{N_c}) = 4, \\ \text{Max}(\mathbf{I}_{N_c}) &= 2 \times 8 - 2 = 14 \\ \text{Max}(\mathbf{R}_{N_c}) &= 2 \times 8 + 2 = 18 \end{aligned}$$

In any test set for an XOR fanout-free network the output must take each of the logical values 0 and 1 twice; therefore $S_0(y) = S_1(y) = 2$ for output line y . Similarly, $C_0(x) = C_1(x) = 2$ for each input line x .

5. TEST COUNTING FOR NONFANOUT-FREE NETWORKS

In this section we use the easily-obtainable test counts for the individual fanout-free subnetworks to obtain bounds on test counts for general networks.

Definition 9. Let N^i be a subnetwork of N , and let T be any test set for N . A set of tests T^i , where $T^i \subseteq T$, that detects faults in N^i

is said to be a *subtest set* for N^i . A *subtest sequence* for N^i is defined similarly.

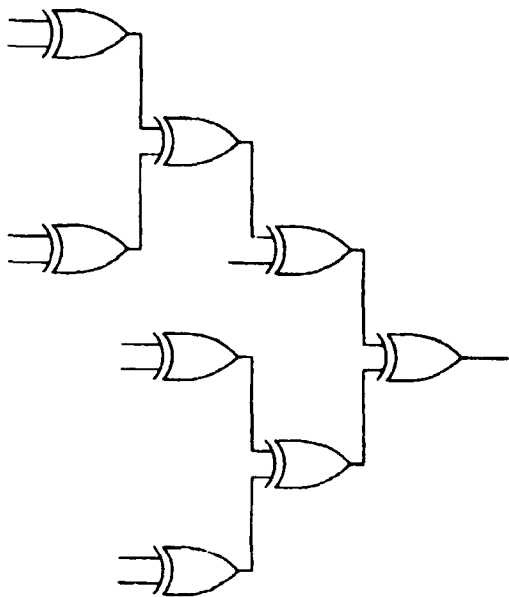


Fig. 3. XOR network for N_c .

The following two definitions apply to collections of tests that are applied to the inputs of a general network with the goal of detecting of faults in specific subnetworks:

Definition 10. Let N^i be the i th fanout-free subnetwork of network N . Define I_N^i to be the set of all test sets for N such that test set T is in I_N^i if and only if T is irredundant with respect to the set of all stuck-at faults in N^i , and T detects all stuck-at faults in N^i . That is, I_N^i consists of all irredundant subtest sets that detect all stuck-at faults in N^i . R_N^i , I_N^i , and R_N^i are defined similarly.

Definition 11. $\text{Min}(I_N^i)$ is the minimal cardinality of any subtest set in I_N^i . $\text{Max}(I_N^i)$, $\text{Min}(R_N^i)$, $\text{Max}(R_N^i)$, $\text{Min}(I_N^i)$, $\text{Max}(I_N^i)$, $\text{Min}(R_N^i)$, and $\text{Max}(R_N^i)$ are defined similarly.

The problem of obtaining the sizes of the subtest sets and sequences for its n fanout-free subnetworks N^1, N^2, \dots, N^n is of similar complexity to the original problem of test counting for N . On the other hand, obtaining the related minimal and maximal test counts for the corresponding *standalone* fanout-free networks N_1, N_2, \dots, N_n can be done using the methods presented in Sections 3 and 4. We present a theorem that expresses bounds on test counts for a general network in terms of these easily-obtained values.

In the following theorem it is understood that, for any lines w and y in N , " $C_z(w)$ " and " $S_z(y)$ " refer to the input constraint and test count, respectively, of the corresponding lines in the appropriate *standalone* fanout-free network.

Theorem 8. Let N be a nonfanout-free combinational logic network (irredundant or redundant) partitioned into n distinct maximal fanout-free subnetworks N^1, N^2, \dots, N^n . Let N_1, N_2, \dots, N_n be the corresponding *standalone* fanout-free networks.

a. Upper Bound on Irredundant Test Sequence Length:

$$\text{Max}(R_N^i) \leq \left[\sum_{i=1}^n \text{Max}(R_{N_i}) \right] - K + 1 \quad (1)$$

where K is the number of primary outputs of N .

b. Upper Bound on Irredundant Test Set Cardinality:

$$\text{Max}(I_N^i) \leq \sum_{i=1}^n [\text{Max}(I_{N_i}) - P_0(N^i) - P_1(N^i) - 2K^i] \quad (2)$$

where K^i is the number of primary outputs of N that are driven by a single-input fanout-free subnetwork that is driven by a fanout branch (such a subnetwork consists of only a line or a cascade of single-input gates). $P_z(N^i) = 1$ if N^i is AONN, and its output is in FX_N , and there is exactly one IL in G_z for N_i ; otherwise $P_z(N^i) = 0$.

c. Lower Bound on Irredundant Test Set and Sequence Size (if N is irredundant):

$$\text{Min}(I_N) \geq \max_{y \in FO_N} \{R_0(y) + R_1(y)\} \quad (3)$$

where for y , a line in FO_N ,

$$Q_z(y) = \begin{cases} \max_{w \in FD_N(y)} \{C_z(w)\} & \text{if } FD_N(y) \text{ is nonempty} \\ 0 & \text{otherwise} \end{cases}$$

and

$$R_z(y) = \max \{S_z(y), Q_z(y)\}$$

Proof. See Appendix.

The two upper bounds can be reduced further by considering additional special cases involving lines in FX_N and the fanout-

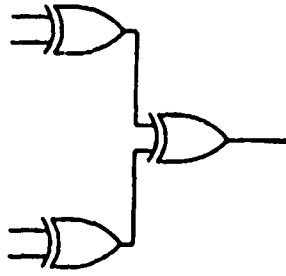


Fig. 4. XOR network N_d .

free subnetworks that drive the primary outputs. However, the improvements obtained in the bounds do not justify the additional complexity of the statements of those conditions.

Treating the XOR function as an indivisible gate has introduced additional complexity in the derivation of the test counting method that could have been avoided because XOR gates can be expressed in terms of AONN networks. The payoff is demonstrated by the following example that shows the considerable improvement of these bounds when the XOR function is recognized as an indivisible gate.

Example 7. XOR fanout-free network N_d , shown in figure 4, is expanded into the equivalent AONN network N_e shown in figure 5. Two different NAND realizations of the XOR function are used. After partitioning N_e and applying Theorem 8, it is concluded that:

$$\begin{aligned} \text{Min}(I_{N_e}) &\geq 4 \\ \text{Max}(I_{N_e}) &\leq 32 \\ \text{Max}(R_{N_e}) &\leq 40 \end{aligned}$$

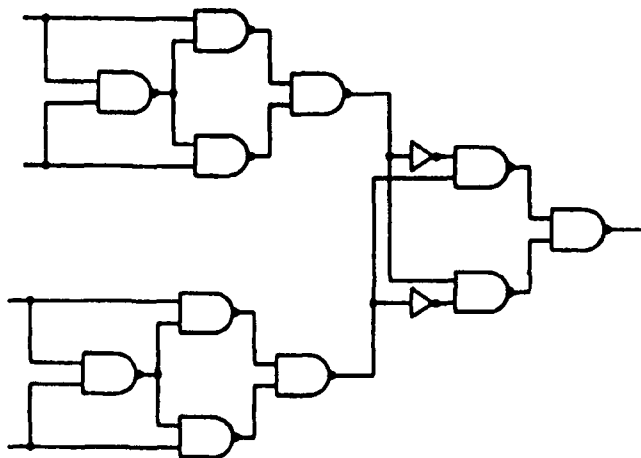


Fig. 5. AONN network N_e (NAND-equivalent of XOR network N_d).

By considering XOR gates to be indivisible elements the following achievable values are obtained for N_d :

$$\begin{aligned} \text{Min}(I_{N_d}) &= 4 \\ \text{Max}(I_{N_d}) &= 6 \\ \text{Max}(R_{N_d}) &= 8 \end{aligned}$$

It can be shown that N_d and N_e are irredundant, and also that $I_{N_d} = I_{N_e}$ and $R_{N_d} = R_{N_e}$. Therefore, the actual values of $\text{Min}(I_{N_e})$, $\text{Max}(I_{N_e})$, and $\text{Max}(R_{N_e})$ are 4, 6, and 8 as well. Although the lower bound is unaffected, the upper bounds are greatly improved by treating the XOR function as an indivisible gate.

6. RESULTS OF TEST COUNTING EXPERIMENTS

Table 2 summarizes the results of applying the test counting procedures developed in this paper to a set of logic networks. For comparison, estimates of the lower and upper bounds are obtained using test minimization and maximization techniques. We also apply Akers and Krishnamurthy's algorithm (AKA) [15], [16] to the same set of networks. There is minor typographical error in the version of the AKA presented in [16] (the sensitivity value for a fanout node should read " $\alpha^* \geq \max_{i \in T_N(t^*)}$ "). The AKA is correct as it appears in [15].

Table 2. Results of test counting experiments.

Network	LB on	UB on	UB on	AKA [16]	Greedy Min Set size	Greedy Max Seq Size
	Min(I_w)	Max(I'_{N_e})	Max(R'_{N_e})	LB on Min(I_w)		
N_f	18	22	25	14	18	22
54LS181	10	206	254	11	12	107
54LS182	8	74	79	8	11	53
54LS85	11	120	135	11	23	59
Am25SO5	10	228	276	10	10	79
C17	4	16	21	4	4	12
C432	15	425	500	16	36	209
C499	9	498	599	11	52	185
C880	11	743	917	11	39	330
C1355	9	1210	1543	12	82	263
C1908	20	1566	1855	27	99	339
C2670	38	2211	2608	38	53	276
C3540	27	2786	3407	30	131	575
C5315	11	4390	5228	13	97	796
C6288	4	5824	7713	5	17	221
C7552	16	6020	7443	17	109	583

A. Networks and Experiments

A number of logic circuits were used to compare the bounds on test counts to the sizes of some actual test sets and sequences. Network N_f is the 17-input logic circuit shown in figure 6. The

54LS181 is a 4-bit ALU, the 54LS182 is the look-ahead carry circuit used to cascade ALUs, and the 54LS85 is a 3-bit comparator [20]. This version of the ALU is expressed entirely in terms of NAND gates. The Am25S05 is a two's-complement multiply/accumulate circuit [21]. These circuits are available as MSI and LSI devices, and they are common logic blocks used in large VLSI designs today. The remaining 11 networks are the ISCAS '85 combinational benchmark set [24].

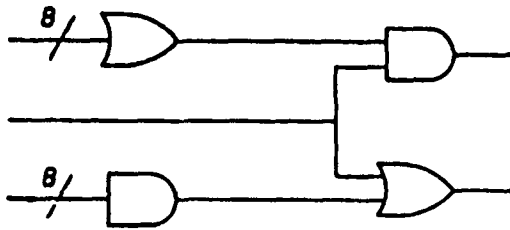


Fig. 6. AONN network N_f .

Table 2 shows the lower bound (LB) on $\text{Min}(I_N)$ and upper bounds (UBs) on $\text{Max}(I'_N)$ and $\text{Max}(R'_N)$ given by Theorem 8. In giving a lower bound for $\text{Min}(I_N)$ the tacit assumption is made that I_N is nonempty for each network (i.e., that all faults are detectable in each network). In fact, only six of these 16 networks are irredundant. However, the largest percentage of undetectable faults in any of these circuits is only 4.26% (which occurs in the case of C2670) so "nearly all" of the faults are detectable. This same assumption is implicit in the AKA as well.

The lower bound on $\text{Min}(I_N)$ obtained by the AKA is shown in the table. In addition, some actual test set and sequence sizes are listed. The actual values are given for the minimum for the 54LS181 [16] and the minimum and maximum for N_f . For the remaining values, a "greedy" optimization procedure [22] was used to provide empirical estimates of $\text{Min}(I_N)$ and $\text{Max}(R'_N)$ by finding actual irredundant test sets and sequences for the designs. No computationally tractable method of empirically estimating $\text{Max}(I'_N)$ is known to us.

The input to the greedy optimization procedures is the *complete* set of faults detected by each test in a set of tests. A limit of 2,000 randomly-generated tests was set for the Am 25S05 and the ten largest ISCAS '85 circuits. This approach is consistent with standard practices (e.g., [5]); the small limit on the number of tests was necessary to keep both the CPU times and data storage requirements manageable. These test sets, in most cases, failed to detect a few of the known detectable faults in the circuits. The consequence of limiting the number of tests available to the greedy optimization procedure in this case was that the resulting *smallest* test sets were larger, and the *largest* test sequences were smaller, than would have resulted if the optimi-

zation procedure had had a greater selection of tests with which to work.

B. Discussion

Our lower bounds produce the exact minima for N_f , Am25S05, and C17, and compare very favorably to the sizes of the greedy minima for 54LS181 and 54LS182. The lower bounds for the remaining circuits show greater departures from the greedy minima.

Although our method is substantially easier to understand and implement than the AKA, our lower bounds on $\text{Min}(I_N)$ coincide with, or are very close to, those of the AKA in every case. There is one case shown in table 2 where the AKA exceeds our bound by seven tests (C2670), but circuit N_f demonstrates that it is possible for our lower bound to improve on theirs. By increasing the fanin of the two first level gates in N_f the improvement obtained using our method can be made arbitrarily large.

Comparison of our upper bounds with the sizes of the test sequences resulting from the greedy maximization procedure shows that a great deal of merging of the subtest sets for the fanout-free subnetworks is unavoidable. Our upper bounds grow more conservative as the sizes of the circuits increase. As mentioned earlier, the greedy optimization procedure, as applied here, do not produce the actual minimal and maximal results. Therefore, comparison of our lower and upper bounds to the sizes of actual test sets and sequences is pessimistic, and the actual results can only be better.

A method given by Hayes [11] was applied to the 54LS181. This technique determines an upper (rather than lower) bound on $\text{Min}(I_N)$ based on the assumption that single path sensitization is sufficient for fault detection. This method requires exhaustive enumeration of input/output paths. The value of 1,858 tests was obtained by this method. Hayes' bound is very high because it accounts for *every possible* consequence of reconvergent fanout. Our bounds on $\text{Max}(I'_N)$ and $\text{Max}(R'_N)$ take into account *no* information about the fanout structure of the general networks and are substantially better than those of Hayes.

7. CONCLUSION

A number of new concepts have been presented in this article that include differentiating between the properties of irredundant test sets and sequences, and obtaining maximal as well as minimal test counts. Maximal test counts place upper bounds on the sizes of test sets and sequences where collections of tests are constrained such that every test is required to contribute to fault detection. The problem of test counting has been a,

proached by considering only the fanout-free substructure of a network and ignoring the effects of fanout. The minimal test counts obtained in this paper are tighter by orders of magnitude than those of a method by Hayes that explicitly considers every consequence of reconvergent fanout. The problem of determining maximal test counts has not previously been systematically addressed.

Test counting has been applied to a set of benchmark networks and a greedy optimization technique has been used to produce actual test sets and sequences for comparison. The greedy optimization procedures do not necessarily produce the actual minima or maxima (the difference being greater for the larger circuits) so the comparison is pessimistic. Our lower bound is equal to or very close to the greedy minima for the small circuits. Our procedure consistently produces a lower bound that is equal to or slightly less than that provided by a far more complex algorithm presented by Akers and Krishnamurthy; in one case we demonstrate that our procedure can improve on their results. Our upper bounds are more conservative in relation to the greedy maxima.

8. ACKNOWLEDGMENT

The authors wish to thank Dominick Aiello and Eve Wallace for their assistance in artwork preparation. This work was supported in part by the New York State Center for Advanced Technology in Computer Applications and Software Engineering (CASE) at Syracuse University.

APPENDIX

Proof of Theorem 8:

Part (a): Upper Bound on $\text{Max}(\mathbf{R}'_N)$

It is easily shown, by contradiction, that neither \mathbf{R}_N nor \mathbf{R}'_N contains a subtest sequence of length greater than $\text{Max}(\mathbf{R}_N)$.

For $i = 1, 2, \dots, n$,

$\text{Max}(\mathbf{R}'_N) \leq \text{Max}(\mathbf{R}_N)$, if N^i is irredundant,

$\text{Max}(\mathbf{R}'_N) < \text{Max}(\mathbf{R}_N)$, if N^i is redundant.

It is also easily shown, by contradiction, that $\text{Max}(\mathbf{R}'_N)$ is less than or equal to

$$\sum_{i=1}^n \text{Max}(\mathbf{R}_N) \quad (4)$$

Consider two fanout-free subnetworks in N , N^i and N_j . Let U be an irredundant test sequence for N , and let U' and U'' be the first subtest sequences that appear in U such that $U' \in \mathbf{R}_N$ and $U'' \in \mathbf{R}_N$. The upper bound on $|U|$ given by (4) is achievable

only if

$$u' \neq u'' \text{ for } : \forall u' \in U', \forall u'' \in U'', \forall i, j : i \neq j$$

However, the first test in U is also the first test in each of the subtest sequences for the K fanout-free subnetworks that drive the primary outputs. Therefore, (4) can be reduced by $K - 1$ to account for the overlap of the subtest sequences, resulting in (1).

Part (b): Upper Bound on $\text{Max}(\mathbf{I}'_N)$

It is easily shown, by contradiction, that neither \mathbf{I}_N , nor \mathbf{I}'_N contains a subtest set of cardinality greater than $\text{Max}(\mathbf{I}_N)$. For $i = 1, 2, \dots, n$,

$\text{Max}(\mathbf{I}'_N) \leq \text{Max}(\mathbf{I}_N)$, if N^i is irredundant,

$\text{Max}(\mathbf{I}'_N) < \text{Max}(\mathbf{I}_N)$, if N^i is redundant.

It is also easily shown, by contradiction, that $\text{Max}(\mathbf{I}'_N)$ is less than or equal to

$$\sum_{i=1}^n \text{Max}(\mathbf{I}_N) \quad (5)$$

Consider two fanout-free subnetworks in N , N^i and N_j . Let T be an irredundant test sequence for N . The upper bound on $|T|$ given by (5) is achievable only if

$t' \neq t''$ for:

$$\forall t' \in T', \forall t'' \in T'', \forall T' \in \mathbf{I}'_N, \forall T'' \in \mathbf{I}'_N, \forall i, j : i \neq j$$

which is a far more restrictive condition than the corresponding one for test sequences.

Let N^i be an AONN fanout-free subnetwork that drives XOR fanout-free subnetwork N^j via a line y in FX_N . Any irredundant subtest set of N^j involves placing both of the logical values 0 and 1 on y . If G_z for N_j contains only one IL (which, therefore, is an IPI), then the logical value z cannot be placed on y without having a test in some set in \mathbf{I}'_N coincide with a test in some set in \mathbf{I}'_N . Therefore, (5) can be reduced by $P_z(N^j)$ for $i = 1, 2, \dots, n$ and $z = 0$ and 1.

Any fanout-free subnetwork N^i that consists of a single line (or cascade or single-input gates) that drives a primary output, but is not driven by a primary input, is driven by a fanout branch of a fanout-free subnetwork N^j , where N^j consists of at least one multiple-input gate. Both tests in any subtest set in \mathbf{I}'_N must coincide with two tests in each subtest set in \mathbf{I}'_N . Therefore, (5) can be further reduced by $2K$, resulting in (2).

Part (c): Lower Bound on $\text{Min}(I_N)$ and $\text{Min}(R_N)$

This bound has meaning only if N is irredundant. The approach is based on determining the minimum number of times each node in the circuit must be assigned the logical values 0 and 1. Consider the node driven by y , the output of N^i . $Q_z(y)$ is a lower bound on the number of times that any line driven by y must take the logical value z , based on the input constraints of each of the subtest sets for the fanout-free subnetworks driven by y . $R_z(y)$ is a lower bound on the number of times y must take the logical value z that refines $Q_z(y)$ by accounting also for the number of times y must take the value z in minimal cardinality subtest sets that involve y . Since the tests that assign 0 to y are distinct from the tests that assign 1 to y , the number of tests needed to detect all faults in N cannot be smaller than the largest value of $R_0(y) + R_1(y)$ for any N^i , resulting in (3).

REFERENCES

1. W.H. DeBany, "On using the fanout-free substructure of general combinational networks," Ph. D. Dissertation, Syracuse University, Syracuse, NY, December 1985.
2. J.P. Hayes, "On realizations of Boolean functions requiring a minimal or near-minimal number of tests," *IEEE Transactions on Computers*, vol. C-20, pp. 1506-1513, December 1971.
3. M.A. Breuer and A.D. Friedman, *Diagnosis & Reliable Design of Digital Systems*, Rockville, MD, Computer Science Press, 1976.
4. M. Abramovici, M.A. Breuer, and A.D. Friedman, *Digital Systems Testing and Testable Design*, Computer Science Press, NY, 1990.
5. J.L. Carter, S.F. Dennis, V.S. Iyengar, B.K. Rosen, "ATPG via random pattern simulation," *Proceedings, International Symposium on Circuits and Systems (ISCAS)*, pp. 683-686, 1985.
6. J.H. Aylor, J.P. Cohoon, E.L. Feldhausen, B.W. Johnson, "Compacting randomly generated test sets," *Proceedings, International Conference on Computer Design (ICCD)*, pp. 153-156, 1990.
7. S.M. Reddy, "Easily testable realizations for logic functions," *IEEE Transactions on Computers*, vol. C-21, pp. 1183-1188, November 1972.
8. C.D. Weiss, "Bounds on the length of terminal stuck-fault tests," *IEEE Transactions on Computers*, vol. C-21, pp. 305-309, March 1972.
9. S.B. Akers, "Universal test sets for logic networks," *IEEE Transactions on Computers*, vol. C-23, pp. 835-839, September 1973.
10. I. Berger and Z. Kohavi, "Fault detection in fanout-free combinational networks," *IEEE Transactions on Computers*, vol. C-23, pp. 908-914, October 1973.
11. J.P. Hayes, "Path complexity of logic networks," *IEEE Transactions on Computers*, vol. C-27, pp. 459-462, May 1978.
12. M.G. Karpovsky, "Universal tests detecting input-output faults in almost all devices," *Proceedings, 1982 IEEE International Test Conference*, pp. 52-57.
13. M.G. Karpovsky and L.B. Levitin, "Universal testing of computer hardware," in *Spectral Techniques and Fault Detection*, M.G. Karpovsky (Ed.), Academic Press, Orlando, FL, 1985.
14. B. Krishnamurthy and S.B. Akers, "On the complexity of estimating the size of a test set," *IEEE Transactions on Computers*, vol. C-33, pp. 750-753, August 1984.
15. S.B. Akers, and B. Krishnamurthy, "Test counting: An analysis tool for VLSI testing," Technical Report CR-86-55, Tektronix Computer Research Laboratory, November 1986.
16. S. D. Akers and B. Krishnamurthy, "Test counting: A tool for VLSI testing," *IEEE Design & Test of Computers*, vol. 6, pp. 58-77, October 1989.
17. J. P. Hayes and A. D. Friedman, "Test point placement to simplify fault detection," *IEEE Transactions on Computers*, vol. C-24, pp. 727-735, July 1974.
18. O.H. Ibarra and S. K. Sahni, "Polynomially complete fault detection problems," *IEEE Transactions on Computers*, vol. C-25, pp. 242-249, March 1975.
19. H. Fujiwara and S. Toida, "The complexity of fault detection problems for combinational logic circuits," *IEEE Transactions on Computers*, vol. C-31, pp. 555-560, June 1982.
20. *The TTL Data Book for Design Engineers*, 2nd Ed., Texas Instruments (TI), 1976.
21. *Bipolar Microprocessor Logic and Interface Data Book*, Advanced Micro Devices (AMD), 1985.
22. A.V. Aho, J.E. Hopcroft, J.D. Ullman, *Data Structures and Algorithms*, Addison-Wesley, Reading, MA., 1983.
23. J. P. Hayes, "A NAND model for fault diagnosis in combinational logic networks," *IEEE Transactions on Computers*, vol. C-20, pp. 1496-1506, December 1971.
24. F. Brglez and H. Fujiwara, "A neutral netlist of 10 combinational benchmark circuits and a target translator in FORTRAN," *Proceedings, International Symposium on Circuits and Systems (ISCAS)*, 1985.

AN EXTENSION OF PROBABILISTIC SIMULATION FOR RELIABILITY ANALYSIS OF CMOS VLSI CIRCUITS

Farid N. Najm (Member IEEE) and P. Yang (Senior Member IEEE), Semiconductor Process and Design Center, Texas Instruments, Inc.
Ibrahim N. Hajj (Fellow IEEE), Coordinated Science Laboratory, University of Illinois at Urbana-Champaign
This work was supported by Texas Instruments, Inc. and by the U.S. Air Force Rome Laboratory

Published in IEEE Transactions on Computer-Aided Design, Vol. 10, No. 11, November 1991 (IEEE Log Number 9144598)

Abstract - The probabilistic simulation approach [1] is extended to include the computation of the variance waveform of the power/ground current, in addition to its expected waveform. To provide the motivation for doing this, we focus on the problem of estimating the median time-to-failure (MTF) due to electromigration (EM) in the power and ground buses of CMOS circuits. New theoretical results are presented that quantify the relationship between the MTF and the statistics of the stochastic current. This leads to a more accurate estimate of the MTF that requires both the expected and variance waveforms. A novel technique is then presented to compute the variance waveform for CMOS circuits, which has been incorporated into the probabilistic simulator CREST [1]. We show results of this implementation, demonstrating efficiency and accuracy on a number of circuits. We also use these results to study the importance of the variance waveform by estimating its contribution to the MTF relative to that of the expected waveform.

1. INTRODUCTION

RELIABILITY, already a major concern in integrated circuit design, can only become more important in the future. As higher levels of integration are used, metal linewidth and line separation will continue to decrease, thereby increasing a chip's susceptibility to failures resulting from line shorts or opens.

While the results to be presented can be used to study a variety of reliability problems, we will illustrate their utility by focusing on the problem of *electromigration* (EM) [2], [3]. EM is a major reliability problem caused by the transport of atoms in a metal line due to the electron flow. Under persistent current stress, EM can cause deformations of the metal lines which may result in shorts or open circuits. The failure rate due to EM depends on the current density in the metal lines and is usually expressed as a median time-to-failure (MTF). There is a need for CAD tools that can predict the susceptibility of a given design to EM failures.

In [1] we presented a novel technique for MTF estimation based on a *stochastic current waveform* model. The implementation of this technique in the program CuRent ESTimator (CREST) has proven to be very effective both in terms of accuracy and speed. In the interest of clarity, we will review some of the basic concepts behind this approach. The reader is referred to [1], [4] for a more detailed description.

We focus on the power and ground buses and derive currents for them to be used for MTF estimation. The argument presented in [1] is that the desired current waveform in any branch

of the bus is one that combines the effects of all possible waveforms at the circuit primary inputs. By considering the set of logical waveforms allowed at the circuit inputs as a *probability space* [5], the current in any branch of the bus becomes a *stochastic process*. CREST derives the *expected* (or *mean*) waveform (not a time average) of this process, which we call an *expected current waveform*, $E[i(t)]$. This is a waveform whose value at any given time is the weighted average of all possible current values at that time. CREST uses *statistical* information about the inputs to directly derive $E[i(t)]$. The resulting methodology is what we call a *probabilistic simulation* of the circuit. In general, it can be slightly more time consuming than a single timing simulation run, but it needs to be applied only once, resulting in significant speedup.

While the feasibility of performing probabilistic simulation was established in [1], the justification for using $E[i(t)]$ to estimate the MTF was based mainly on qualitative arguments. In Section 2 of this paper we quantify these arguments and present new theoretical results that specify the relationship between the MTF and the statistics of the stochastic current. This leads to an efficient and more accurate technique for deriving the MTF which requires the *variance waveform*, $V[i(t)]$, of the stochastic current in addition to its expected waveform. $V[i(t)]$ is a waveform whose value at any given time is the variance of the current values at that time, $V[i(t)] = E[(i(t) - E[i(t)])^2]$. It is an indication of the spread of the real current waveforms around their expected waveform.

In Section 3 we present a novel technique for deriving the variances of the individual gate currents in CMOS circuits. This has been implemented in the probabilistic simulator, CREST [1]. Section 4 and the Appendix contain a discussion of how the bus current variance waveforms may be obtained from those of the individual gates. In Section 5, we present some results of our implementation, and use them to study the importance of the variance waveform. This is done by estimating its contribution to the MTF relative to that of the expected waveform. The Appendix also presents several approximations that can be used when handling large chips to simplify the variance computations, and thus make it possible to handle VLSI circuits.

Several simplifying assumptions and/or approximations will be made in the following sections to make the problem com-

putationally tractable. Whenever possible, we will attempt to justify these assumptions. However, because of lack of space, this will not always be possible, and the reader will be referred to the appropriate references. Nevertheless, we will offer a verification of the overall approach on a *global* scale, by comparing the end result of the simulation (variance waveform) from CREST with that derived using SPICE. The extended CREST program, with the variance computation built in, maintains its excellent performance compared to traditional approaches: we demonstrate a speedup (over SPICE) of over 11 500X on a 648 transistor CMOS parallel multiplier circuit. Preliminary results of this research have appeared in [6], [7].

2. STOCHASTIC CURRENT WAVEFORM AND THE MTF

Consider a metal line of uniform width and thickness carrying a *constant* current. Due to EM, the line will fail after a period of time. The time required for 50% of a large population of such lines to fail is called MTF, also denoted by t_{50} . Due to the nature of the distribution (log normal) of EM failure times, it turns out that the MTF is also approximately equal to the mean-time-to-failure. The two names are used interchangeably in the EM literature. The relationship between the MTF, t_{50} , and the current density j in the line has been extensively studied, and shown to be a complex nonlinear function [8], as shown in Fig. 1. We will consider the MTF to be $t_{50} \propto 1/f(j)$ where j is in amperes per square centimeter, and f is the dimensionless nonlinear function shown in Fig. 2.

If a metal line carries a varying current, of density $j(t)$, then the MTF is $t_{50} \propto 1/J_{\text{eff}}$, where J_{eff} depends both on f and on the waveform $j(t)$. It has been suggested [9] that, if the waveform is periodic, with period T , and if every period consists of a train of pulses $p = 1, \dots, m$ of heights j_p and duration t_p ,

then $J_{\text{eff}} = \sum_{p=1}^m (t_p/T) \hat{f}(j_p)$, where $\hat{f}(j)$ is chosen to be one of the

three dotted line approximations to $f(j)$ in Fig. 2, depending on the value of j_p , as follows. If $j \leq 10^5$ A/cm² then $\hat{f}(j) = j$, if 10^5 A/cm² $\leq j \leq 10^6$ A/cm² then $\hat{f}(j) \propto j^{3/2}$, and if $j \geq 10^6$ A/cm² then $\hat{f}(j) \propto j^2$. A more accurate expression, however, can be written in terms of f itself, as follows:

$$J_{\text{eff}} = \sum_{p=1}^m \frac{t_p}{T} f(j_p). \quad (2.1)$$

For a general periodic waveform, we take the summation to the limit and write

$$J_{\text{eff}} = \frac{1}{T} \int_0^T f(j) dt. \quad (2.2)$$

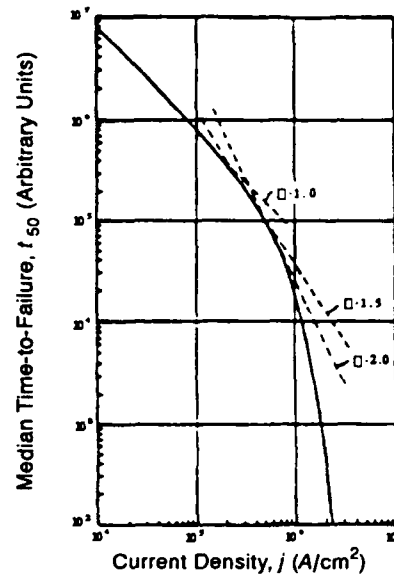


Fig. 1. The dependence of MTF on current density, reproduced for convenience from [8]. The dashed lines show the results of the approximation $t_{50} \propto j^{-n}$ for $n = 1, 3/2$, and 2.

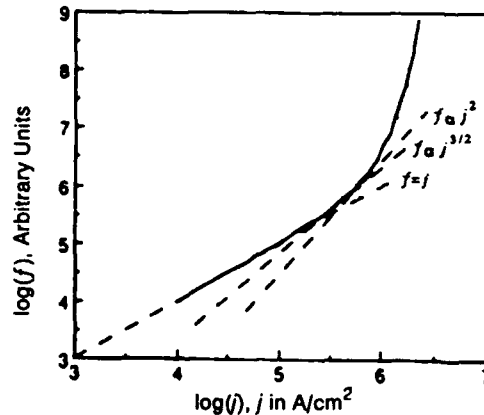


Fig. 2. A plot of $f(j)$, obtained from Fig. 1 by inverting and appropriately scaling the ordinate axis.

If the current waveform is not periodic, then better estimates of J_{eff} are obtained by using larger values of T so that more features of the waveform are included. Therefore, one can write:

$$J_{\text{eff}} = \lim_{T \rightarrow \infty} \frac{1}{T} \int_0^T f(j) dt. \quad (2.3)$$

Now suppose that the current waveform is *stochastic*, i.e., it is a stochastic process $j(t)$, that represents a family of deterministic (real) current waveforms $j_k(t)$, with associated probabilities P_k , $k = 1, \dots, N$, over the (finite) interval $(0, t_0]$. Based on this information, we can build a (nonstochastic) current waveform $j(t)$, over $[0, T]$ as $T \rightarrow \infty$, that is indicative of the current during the typical operation as follows. Consider a random sequence of the waveforms $j_k(t)$, each being shifted in time, span-

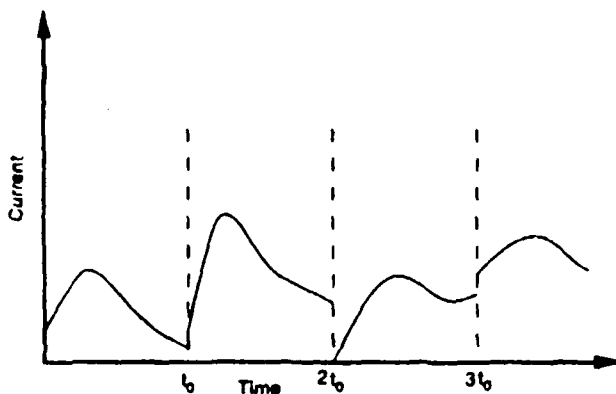


Fig. 3. A (nonstochastic) current waveform, $j(t)$, built as a sequence of the waveforms $j_k(t)$, each occurring with its assigned probability P_k .

ning an interval of length t_0 , and occurring with its assigned probability P_k , as shown in Fig. 3. Let $n_k(T)$ be the (integer) number of occurrences of the waveform $j_k(t)$ in $[0, T]$, and let $n_T = \lfloor T/t_0 \rfloor$. If $J_k = 1, \dots, N$ are defined as follows:

$$J_k \triangleq \frac{1}{t_0} \int_0^{t_0} f(j_k) dt \quad (2.4)$$

then

$$\begin{aligned} J_{\text{eff}} &= \lim_{T \rightarrow \infty} \frac{1}{T} \int_0^T f(j) dt \\ &= \lim_{n_T \rightarrow \infty} \sum_{k=1}^N J_k \frac{n_k(T)}{n_T} = \sum_{k=1}^N J_k \lim_{n_T \rightarrow \infty} \left[\frac{n_k(T)}{n_T} \right]. \end{aligned} \quad (2.5)$$

By the law of large numbers [5], $\lim_{n_T \rightarrow \infty} [n_k(T)/n_T] = P_k$, which leads to

$$\begin{aligned} J_{\text{eff}} &= \sum_{k=1}^N \left[\frac{1}{t_0} \int_0^{t_0} f(j_k) dt \right] P_k \\ &= \frac{1}{t_0} \int_0^{t_0} \left[\sum_{k=1}^N f(j_k) P_k \right] dt \end{aligned} \quad (2.6)$$

and finally:

$$J_{\text{eff}} = \frac{1}{t_0} \int_0^{t_0} E[f(j)] dt \quad (2.7)$$

where $E[\cdot]$ denotes the expected value operator. Therefore, the MTF due to a stochastic current depends only on the expected waveform of a nonlinear function of the current density.

Since f is nonlinear, $E[f(j)]$ is not easy to evaluate. At low current density values, where f is linear (Fig. 2), $E[f(j)] = f(E[j])$. In this case, the expected current waveform $E[j]$ derived in [1] is indeed the correct waveform for MTF estimation.

In general, f is nonlinear, and a generalized approach will be developed in the following.

At any time t , the process $j(t)$ is a random variable j with mean $\eta_j \triangleq E[j]$, and variance $\sigma_j^2 \triangleq E[(j - \eta_j)^2]$. In general, the p th moment of j is $\mu_{j,p} \triangleq E[(j - \eta_j)^p]$. To estimate $E[f(j)]$, a Taylor series expansion of f gives [5]

$$E[f(j)] \approx f(\eta_j) + f'(\eta_j) \frac{\sigma_j^2}{2} + \dots + f^{(p)}(\eta_j) \frac{\mu_{j,p}}{p!}. \quad (2.8)$$

When f is linear, this reduces to

$$E[f(j)] = f(E[j]) \quad (2.9)$$

as observed above. Therefore, using the expected current waveform for MTP estimation [1] amounts to making a first-order approximation in (2.8). Naturally, higher order approximations would lead to better results. In particular, if f is approximated by a quadratic in the neighborhood of η_j , then

$$E[f(j)] \approx f(\eta_j) + f'(\eta_j) \sigma_j^2 \frac{1}{2}. \quad (2.10)$$

This approximation becomes exact if $f(j)$ is represented by the straight lines corresponding to j^1 and j^2 in Fig. 2. It is more accurate than (2.9) since it covers a wider range of currents. As a result, (2.10) and (2.7) offer a new, more accurate technique for computing the MTF. In order to make use of this technique, we need to derive the variance of the waveform in addition to its expected value. As pointed out in the introduction, the estimation of the expected current waveform has already been described in our previous work [1]; the following sections discuss the derivation of the variance waveform.

3. DERIVATION OF THE GATE VARIANCE WAVEFORM

We will briefly review the probabilistic simulation approach [1], which follows an event-driven simulation strategy. Probability waveforms, which represent a large number of logic waveforms, are applied at the primary inputs and propagated through the circuit as a sequence of probabilistic events. A probabilistic event embodies a number of possible logical transitions. Whenever a gate is simulated, the events at its inputs are used to derive an event at its output and an expected current pulse $E[i(t)]$, to be added to the global expected current waveform. This pulse is modeled as a triangular pulse that starts with a peak value $E[I]$ at the time of transition and decays linearly to zero after a time interval called the time span. The variance

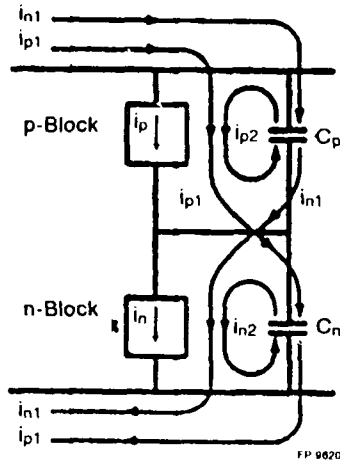


Fig. 4. A generic CMOS gate structure.

waveform can be derived with little modification to the overall simulation strategy. Whenever an expected pulse is derived for a gate, a *variance pulse* will be derived as well.

Fig. 4 shows a generic CMOS gate. The p-block or p-part (n-block or n-part) of a gate refers to the p (n)channel transistor mesh between its output node and the power supply (ground). A gate will be assumed to have *independent* inputs. While this may be true at the primary circuit inputs, it is not true in general. However, the general case is handled using the concept of a supergate [1], with the independent-inputs-gate-solver used as a subroutine.

As in [1], we only consider the *charging* component of the power supply or ground currents. The output node capacitance is split into two lumped capacitors C_p to V_{dd} and C_n to V_{ss} . Similarly, each internal gate node n_i has two capacitors C_{in} and C_{ip} . Capacitance values are derived from the circuit description and the transistor model parameters. On a low-to-high transition, the currents flowing through C_n and C_p at the output node are i_{p1} and i_{p2} , respectively, as shown in the figure. The corresponding i_{n1} and i_{n2} for a high-to-low transition are also shown. The currents i_{p2} and i_{n2} are discharging currents that redistribute locally, and we are interested in $i = i_{p1} + i_{n1}$, which is the current associated with the output node. The total gate current i_{tot} will be larger than i since it also contains the currents needed to charge/discharge the C_{in} and C_{ip} capacitors at the internal nodes. However, the output current plays a central role in the derivation.

The variance waveforms for the gate total and output currents will be modeled by triangular pulses $V[i_{tot}(t)]$ and $V[i(t)]$, respectively, with peak values of $V[i_{tot}]$ and $V[i]$. If an event occurs at the gate input at time t , then we denote by t^- and t^+ the instances of time immediately before and after the event, respectively. Focusing for now on the output current pulse, its

variance starts with a peak of $V[i] = V[i(t^+)]$ at time t and decays linearly to zero at time $t + \tau$. Since $V[i] = E[i^2] - E[i]^2$ [5], and since CREST already derives the expected pulse peak $E[i]$, we will concentrate here on the derivation of $E[i^2]$.

Let $i_p = i_{p1} + i_{p2}$ and $i_n = i_{n1} + i_{n2}$. It is easy to verify that $i_{p1} = i_p \times C_n / (C_p + C_n)$, and $i_{n1} = i_n \times C_p / (C_p + C_n)$. Therefore:

$$E[i^2(t)] = E[i_p^2(t)] \left(\frac{C_n}{C_p + C_n} \right)^2 + E[i_n^2(t)] \left(\frac{C_p}{C_p + C_n} \right)^2. \quad (3.1)$$

The term containing $E[i_p(t)i_n(t)]$ is omitted (it is zero) since at least one of the charging currents is zero at any given time. In particular, the value at the peak is

$$E[i^2] = E[i_p^2] \times \left(\frac{C_n}{C_p + C_n} \right)^2 + E[i_n^2] \times \left(\frac{C_p}{C_p + C_n} \right)^2. \quad (3.2)$$

The values of $E[i_p^2]$ and $E[i_n^2]$ are derived as follows. For $E[i_p^2]$, consider the p-part of the gate, and let every transistor T_k be represented by a switch of on-conductance $g_{on,k}$ [1]. Based on this switch-network model of the pblock, let $G_p(t)$ be the random conductance between the output node and V_{dd} . G_p is a function of the individual transistor random conductances g_k , where g_k is 0 if the transistor is off and $g_{on,k}$ if it is on. If an event occurs at a gate input at time t , then the value of $G_p(t^-)$ and the previous state of the output node, $V_0(t^-)$, will determine i_p . Formally, we have $E[i_p^2] = E[(V_{dd} - V_0(t^-))^2 \times G_p^2(t^+)]$, which becomes

$$E[i_p^2] = V_{dd}^2 \times E[G_p^2(t^+) | G_p(t^-) = 0] \times P(G_p(t^-) = 0) \quad (3.3)$$

where $P(A)$ is the probability of the event A , and $E[A | B]$ denotes the *conditional expected value* [5] of A given B . The formula is correct because if $G_p(t^-) = 0$ ($\neq 0$) then $V_0(t^-) = 0$ (V_{dd}). Similarly for the n-part of the gate, we obtain

$$E[i_n^2] = V_{dd}^2 \times E[G_n^2(t^+) | G_n(t^-) = 0] \times P(G_n(t^-) = 0). \quad (3.4)$$

To derive the conditional expectations, consider a graph representation of the p block (or n block), where every edge in the graph is labeled with $E[g_k^2(t^+) | G_p(t^-) = 0]$, $E[g_k(t^+) | G_p(t^-) = 0]$, and the gate node probabilities of its corresponding transistors. The details of how these quantities can be derived for every transistor can be found in [4]. Then perform a *graph reduction* operation [1], [4], which, simply stated, involves a number of series/parallel combinations and node eliminations that reduce the graph to a single edge, whose labels are the required statistics $E[G_p^2(t^+) | G_p(t^-) = 0]$ and $E[G_p(t^+) | G_p(t^-) = 0]$. Similar

work can be done for the n-block. As a result, we have the peak value, $V[i] = E[I^2] - E[I]^2$, of the output current variance pulse.

The time span τ is found by first solving for the area under the $V[i(t)]$ pulse. Notice that, if $i(t)$ is a triangular pulse of height I and area q , then:

$$\int_0^\infty i^2(t) dt = \frac{2}{3} Iq. \quad (3.5)$$

In this case, q is equal to the charge delivered to (or from) the output node capacitors. From this it follows that

$$\int_0^\infty E[i^2(t)] dt = \frac{2}{3} E[Iq],$$

and

$$\int_0^\infty E[i(t)]^2 dt = \frac{2}{3} E[I] E[q]. \quad (3.6)$$

The second equation follows since $E[i(t)]$ is a triangular pulse of height $E[I]$ and area $e[q]$. Therefore, the variance pulse has an area

$$\frac{V[I] \times \tau}{2} = \int_0^\infty V[i(t)] dt = \frac{2}{3} (E[Iq] - E[I] E[q]). \quad (3.7)$$

The value of $E[Iq]$ can be written as:

$$E[Iq] = E[(I_{p1} + I_{n1}) \times (q_{p1} + q_{n1})] \quad (3.8)$$

where $I_{p1}(I_{n1})$ is the peak of $i_{p1}(t)$ ($i_{n1}(t)$), and $q_{p1}(q_{n1})$ is the charge delivered by $i_{p1}(t)$ ($i_{n1}(t)$). Since $q_{p1}(q_{n1})$ is equal to $V_{dd} C_p$ ($V_{dd} C_n$), if $i_{p1}(t)$ ($i_{n1}(t)$) is nonzero, and is otherwise zero, then:

$$E[Iq] = \frac{V_{dd} C_n^2}{C_p + C_n} E[I_p] + \frac{V_{dd} C_p^2}{C_p + C_n} E[I_n]. \quad (3.9)$$

The time span of the gate output current variance pulse is, therefore

$$\tau = \frac{4}{3} \left(\frac{E[Iq] - E[I] E[q]}{V[I]} \right). \quad (3.10)$$

An expression similar to (3.7) can be written for the gate total current, $i_{tot}(t)$, as follows:

$$\int_0^\infty V[i_{tot}(t)] dt = \frac{2}{3} (E[I_{tot} q_{tot}] - E[I_{tot}] E[q_{tot}]). \quad (3.11)$$

Unfortunately, $E[I_{tot} q_{tot}]$ does not have as simple an expression as was found for $E[Iq]$. We have chosen to use a conservative estimate based on the following assumption: whenever a

node in the p-block (n-block) is charged to V_{dd} (V_{ss}), then every other node in the p-block (n-block) is also charged to V_{dd} (V_{ss}). This assumption is true for simple gates, and may overestimate the current-charge product in more complex cases. Based on this assumption, one can show [4] that

$$E[I_{tot} q_{tot}] \approx \frac{E[q_{p,tot}]}{E[q_p]} \frac{Q_p C_n}{C_p + C_n} E[I_p] + \frac{E[q_{n,tot}]}{E[q_n]} \frac{Q_n C_p}{C_p + C_n} E[I_n] \quad (3.12)$$

where $E[q_p]$ and $E[q_n]$ are available as [1, eqs. (3.12), (3.13)], $E[q_{p,tot}]$ and $E[q_{n,tot}]$ are, respectively, the first and second summations in [1, eq. (3.10)] and

$$\begin{aligned} Q_p &= \sum_{i \in N_{block}} V_{dd} C_{in} \\ Q_n &= \sum_{i \in N_{block}} V_{dd} C_{ip} \end{aligned} \quad (3.13)$$

As was assumed for the expected current pulse [1], we let the time span of the gate total current variance pulse be equal to that derived for the gate output current. Therefore:

$$V[I_{tot}] = \left(\frac{E[I_{tot} q_{tot}] - E[I_{tot}] E[q_{tot}]}{E[Iq] - E[I] E[q]} \right) \times V[I]. \quad (3.14)$$

4. ESTIMATING THE VARIANCE CURRENT WAVEFORMS IN THE BUS

In the two previous sections, we presented the motivation for computing the variance waveform, and a procedure for computing the variance pulse for a CMOS gate. Ultimately, the variance waveform (of the current density) in every branch of the power/ground bus is required. In this section we present a technique for deriving the bus variance waveforms from those of the individual gates. Since the current density $j(t)$ in any branch of the power or ground bus is directly proportional to the current $i(t)$ in that branch, we will discuss the derivation of $\sigma_i^2(t)$ (i.e., $V[i(t)]$) rather than $\sigma_j^2(t)$ (i.e., $V[j(t)]$). Furthermore, we will only discuss the power bus since the ground bus analysis is similar.

We assume that gates are tied to the bus at certain points, called *contacts*. Several gates may be tied to the same contact. The current in a branch of the bus, $i(t)$, is a function of the currents being drawn off the contacts, $i_j(t)$, $j = 1, \dots, n$. Each of these is, in turn, simply the sum of the individual gate currents tied to that contact:

$$i_j(t) = i_{j1}(t) + \dots + i_{jk}(t). \quad (4.1)$$

In the framework of our probabilistic simulation technique, the process of deriving the variance waveforms consists of three steps.

- 1) Using the probabilistic events at the inputs to each logic gate, derive its variance pulse.
- 2) Combine the pulses at each contact point to derive the variances of the contact currents.
- 3) Using the bus topology and the variances of the contact currents, derive the variances of the bus branch currents.

Step 1) has been described in Section 3; the other two steps will be described in the following.

A critical issue in computing the variance is the correlation between the different current waveforms. Since such correlation is too expensive to derive for VLSI circuits, we will occasionally be making conservative approximations to simplify the problem. Our experience with the probabilistic simulation approach [1] suggests that neglecting the correlation between different current waveforms gives good results in most cases, especially for large circuits. In general, there will be cases where this becomes a poor assumption, as in clocked circuits, for example, where different parts of the circuit may switch in unison in response to a central clock. However, since the variance is of secondary importance in (2. 10), and since keeping track of the correlation is too expensive for large VLSI circuits, we have opted to make this accuracy efficiency tradeoff.

Based on this, we assume that the gate currents tied to the same contact are *uncorrelated*. This immediately provides a simple solution for step 2), using (4. 1), as follows:

$$\sigma_{ij}^2(t) = \sigma_{ij1}^2(t) + \dots + \sigma_{ijk}^2(t). \quad (4.2)$$

Thus the variance pulses from the individual gates are simply added to provide the contact current variance waveform (step 2)). The implementation and results presented in the next section are based on (4.2).

Step 3) is considerably more complex, and is left to the Appendix, where a number of approximations are also proposed to make possible an efficient implementation. The present implementation of CREST provides the user with the expected and variance waveforms for the contact currents (steps 2) and 3)). The proper place for the implementation of step 3) is in the SPIDER [10] program, which takes the currents generated by CREST and uses the bus layout information to estimate the MTF.

5. IMPLEMENTATION AND RESULTS

The variance calculation technique outlined above has been implemented in CREST. We present in the following the results

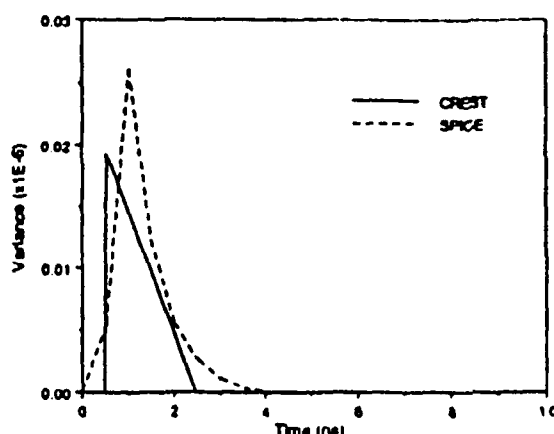


Fig. 5. CREST variance pulse result for a 2-input CMOS NAND gate, compared to SPICE.

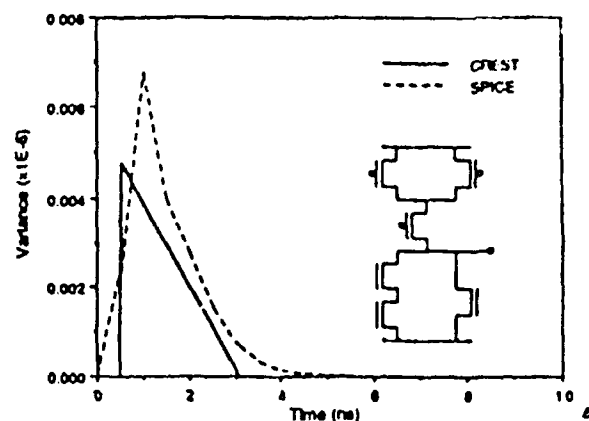


Fig. 6. Variance results for a 3-input CMOS complex gate (inset).

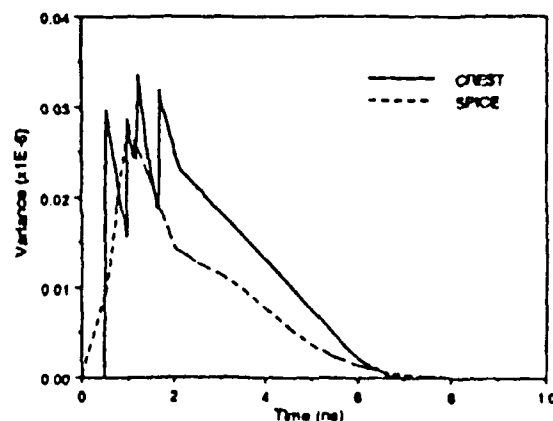


Fig. 7. Variance results for a 16-MOSFET exclusive-OR (XOR) CMOS circuit.

of CREST runs on a variety of circuits, showing both waveform comparisons and timing performance.

To assess the accuracy of the results, it is important to make a fair comparison with a variance waveform derived using a valid simulation tool. To do so, we have generated the variance waveform for a variety of examples by running SPICE for every set of input voltage signals allowed by the probability vectors (see

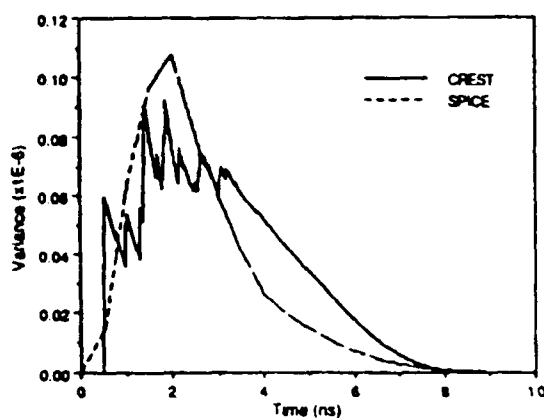


Fig. 8. Variance results for a 54-MOSFET 2-b ripple adder CMOS circuit.

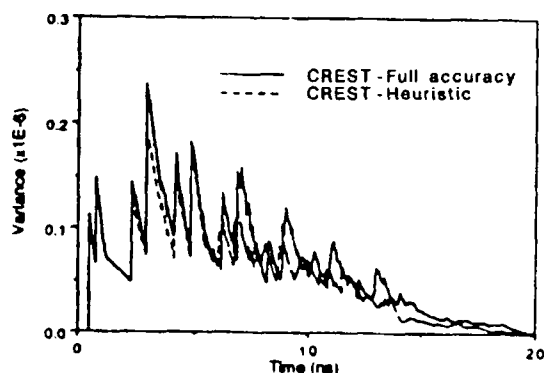


Fig. 9. Variance results for a 648-MOSFET 4-b parallel multiplier CMOS circuit.

[1, section II-2.1)], deriving the expected current waveform $E[i(t)]$ by doing a time-point averaging of the results, and then using that to find the variance as the time-point average of $(i - E[i(t)])^2$. Since EM models for non-dc waveforms are still controversial, it makes little sense to shoot for perfect accuracy in the current waveforms. Furthermore, it is important to make a tradeoff between accuracy and efficiency to make possible the solution of large circuits. Hence, our objective has been to derive, in a very short time, a waveform that matches reasonably well the peak and general shape of the SPICE waveform. Since the number of required SPICE simulation runs grows exponentially with the number of circuit inputs, the comparisons to be presented will necessarily be limited to medium sized circuits. There is no reason to suspect, however, that the accuracy observed on these circuits will deteriorate on larger ones.

Waveform comparisons are shown in Figs. 5 and 6 for a single NAND gate and a complex gate, respectively. The comparisons for two larger circuits are shown in Fig. 7 (for an exclusive-OR circuit) and Fig. 8 (for a 54-MOSFET 2-b ripple adder circuit).

For our next example, we consider a 648 MOSFET 4-b parallel multiplier. This circuit is too big to make the 2^{16} required

SPICE simulations. We will, therefore, show the results of two different CREST runs on this circuit. In Fig. 9 we compare a full accuracy CREST run and a heuristic [1] CREST run in which all internal nodes of the multiplier were assumed independent (uncorrelated). The excellent agreement demonstrates that the correlation between different current pulses in large circuits may indeed be neglected.

These results can be used to assess the significance of the contribution of the variance waveform to the MTF, i.e., to see whether the gain in accuracy is worth the effort. Recall that the expected and variance waveforms combine to provide a J_{eff} effective current density value for MTF estimation, according to (2.10) and (2.7). We have measured the variance contribution as the increase in J_{eff} due to the variance waveform, divided by J_{eff} using only the expected waveform, as follows:

$$\Delta \frac{J_{eff}}{J_{eff}} \triangleq \frac{J_{eff}(\text{using } E[J] \text{ and } V[J]) - J_{eff}(\text{using only } E[J])}{J_{eff}(\text{using only } E[J])}$$

$$= \frac{\int_0^{t_0} \frac{f''(E[J])}{2} V[J] dt}{\int_0^{t_0} f(E[J]) dt} \quad (5.1)$$

This expression depends on current *density* and not simply on current. Consequently, the expected and variance waveforms have to be augmented with metal line *width* information in order to evaluate (5.1). Table I shows the results for all the test cases presented above, for different values of linewidth, with a line thickness of 0.3 μm throughout. Note that (5.1) has been tabulated as a percentage.

For a given circuit, the variance contribution increases with a decrease in linewidth. The two width values used in the table for each circuit are meant to demonstrate that the variance contribution to the MTF can vary from insignificant to very important. For the types of circuits, and technology that we have examined, it seems that one can use a practical lower limit of 1 μm

Table I. Variance Contribution (with Relevant Linewidth). Size Refers To The Number of Transistors. μm Stands For Micrometer

Circuit	Size	$\Delta J_{eff}/J_{eff}$ (width)	
NAND	4	110% (0.067 μm)	0.00% (1.0 μm)
Complex	6	185% (0.033 μm)	0.00% (1.0 μm)
XOR	16	236% (0.067 μm)	0.00% (1.0 μm)
Adder	54	107% (0.17 μm)	0.43% (1.0 μm)
Multiplier	648	219% (0.25 μm)	3.70% (1.0 μm)
Multiplier*	648	200% (0.25 μm)	3.40% (1.0 μm)

* Heuristic CREST run, all others are full accuracy CREST.

Table 2. Execution Time Comparisons. Time is in CPU Seconds on a VAX-11/780. Size Refers to the Number of Transistors

Circuit	Size	SPICE	CREST	Speedup
NAND	4	41.75	0.90	46X
Complex	6	244.15	1.09	224X
XOR	16	356.00	3.13	116X
Adder	54	32 620.42	21.33	1529X
Multiplier	648	697 530.88†	1871.99	373X
Multiplier*	648	697 530.88†	60.16	11 595X

* Heuristic CREST run, all others are full accuracy CREST.

† Estimated (2^8 times the cost of a typical SPICE run)

on linewidth, and do without a variance waveform. However, in cases where such limits cannot be guaranteed (as in manual layout with unlimited designer freedom) and/or where the circuit and metal technologies involve high enough current density, the variance waveform can be as important (or more) than the expected waveform.

In any case, and regardless of the significance of its contribution to the MTF, the variance waveform is important in its own right. Its relevance for studying other reliability problems will be briefly discussed in the next section.

Finally, we illustrate the speed performance of CREST with the variance estimation built in. Table 2 shows the speed comparisons between CREST and SPICE for all the examples presented above. The speedup is excellent, and becomes much better for larger circuits (1529 X for the adder and 11 595 X for the multiplier). In fact, the speedup grows exponentially, because an exponential number of deterministic simulation runs are replaced by a single probabilistic simulation run. We point out the case of the multiplier circuit (the largest circuit in the table) with the heuristic CREST run (last row in Table 2). The excellent waveform comparison in Fig. 9, along with the speedup of 11 595 X and execution time of 1 min in Table 2, establishes the feasibility of solving large VLSI chips.

6. SUMMARY AND CONCLUSIONS

We have extended the probabilistic simulation approach [1] to include the computation of the variance of the power/ground current waveform, in addition to its expected waveform. To provide the motivation for this, we have focused on the problem of estimating the MTF due to EM in the power and ground buses of CMOS circuits. This requires knowledge of the current density in these buses.

In previous work [1], we presented a novel technique for MTF estimation based on a *stochastic current waveform* model. We derived the expected waveform of this current

model and gave a qualitative argument suggesting that it is the appropriate waveform to be used for MTF estimation. In this paper, we have quantified that argument by presenting new theoretical results which show the exact relationship between the MTF and the statistics of the current. Equation (2.7) relates J_{eff} , required for estimating the MTF, to the mean waveform of a nonlinear function of the stochastic current. Coupled with (2.10), it provides an efficient and more accurate technique for computing the MTF, which requires both the expected and variance waveforms. A novel technique was then presented to compute the variance waveform for CMOS circuits, which has been incorporated into the probabilistic simulator CREST [1].

The results of several CREST runs were presented, demonstrating good waveform agreement with SPICE, as well as excellent speedups over traditional approaches: a speedup of over 11 500X was demonstrated on a 648 transistor circuit.

Using these results, we have studied the significance of the variance waveform by evaluating its contribution to the MTF, $\Delta J_{eff}/J_{eff}$. We have found this to be highly dependent on whether a minimum metal linewidth can be guaranteed, in which case, this contribution may be neglected. Otherwise, and/or if a high current density technology is used, then the variance contribution can be as important (or more) than the expected waveform.

In any case, and regardless of the significance of its contribution to the MTF, the variance waveform is important in its own right as a measure of the spread of the real current waveforms. Such information may be useful for studying voltage drop (glitches) on the power/ground lines. If stochastic techniques are to be used for this purpose, then it seems definite that the expected current by itself will not be sufficient.

APPENDIX

In this Appendix, we are concerned with the problem of deriving the variance waveforms in the power/ground bus branches given those at the bus contacts. The bus can be modeled as a *linear* time-invariant (LTI) system with inputs x_j and outputs y_i . The inputs $x_j(t)$, $j = 1, \dots, n$ represent the contact currents and carry the stochastic processes $i_j(t)$ of known variance waveforms $\sigma_{i_j}^2(t)$. The outputs $y_i(t)$, $i = 1, \dots, m$ represent the bus branch currents at which the variance waveforms, $\sigma_{y_i}^2(t)$, are required. Let $h_{ij}(t)$ be the impulse response function relating $y_i(t)$ to $x_j(t)$:

$$y_i(t) = \sum_{j=1}^n h_{ij}(t) * x_j(t), \quad i = 1, \dots, m \quad (A.1)$$

where "*" denotes the convolution operation.

It is well known (see [5, p. 209]) that the variances of the system inputs are not enough to derive the variances of its outputs. The autocorrelation of each input, $R_{x_j x_j}(t_1, t_2) \triangleq E[x_j(t_1) x_j(t_2)]$, is also required. Since the input processes are not *wide-sense stationary* [5], an exact analytical solution can be quite complex, even if the autocorrelations were known. Therefore, as is often necessary, we will make certain simplifying assumptions about the structure of $R_{y_j y_j}$.

We assume that the correlation between $x_j(t)$ and $x_j(t + \tau)$ goes to zero as $\tau \rightarrow \infty$. In terms of the autocovariance, $C_{x_j x_j}(t_1, t_2) \triangleq R_{x_j x_j}(t_1, t_2) - \eta_{x_j}(t_1)\eta_{x_j}(t_2)$, where $\eta_{x_j}(t) \triangleq E[x_j(t)]$, this is formulated as

$$\begin{aligned} C_{y_j y_j}(t_1, t_1) &= \sigma_{y_j}^2(t_1) \\ C_{y_j y_j}(t_1, t_2) &= 0 \quad \text{for } |t_1 - t_2| \geq T \end{aligned} \quad (\text{A.2})$$

where T is a (typically small) time interval.

Consider the *discrete time* system obtained by sampling, with period T , the continuous time system defined by (A.1). If $x_j[k] \triangleq x_j(kT)$ are the discrete processes at the inputs, and $y_i[k] \triangleq y_i(kT)$ are the discrete output processes, then:

$$y_i[k] = \sum_{j=1}^n h_{ij}^{(d)}[k] * x_j[k], \quad i = 1, \dots, m \quad (\text{A.3})$$

where $h_{ij}^{(d)}[k]$ is the discrete impulse response function relating $y_i[k]$ to $x_j[k]$. As shown below, the discretized output variance waveforms can be derived irrespective of the shape of $C_{y_j y_j}(t_1, t_2)$ for $|t_1 - t_2| < T$. The continuous variance waveforms can then be obtained by interpolation. Strictly speaking, therefore, the sampling period T should be small: $1/T$ should be larger than the largest frequency component of the inputs. However, since fine waveform details are not of paramount importance in this work, we need only restrict T to be small enough so that waveform features in that small an interval are inconsequential.

To simplify the notation, define $y_{ij}[k] \triangleq h_{ij}^{(d)}[k] * x_j[k]$. Furthermore, as pointed out above, we will neglect the correlation between the contact currents. Hence, the x_j inputs are uncorrelated, and

$$\sigma_{y_i}^2 = \sum_{j=1}^n \sigma_{y_{ij}}^2[k], \quad i = 1, \dots, m. \quad (\text{A.4})$$

We have thus reduced the problem to analyzing a single-input, single output discrete LTI system:

$$y_{ij}[k] = h_{ij}^{(d)}[k] * x_j[k] = \sum_{\kappa=0}^{\infty} h_{ij}^{(d)}[\kappa] x_j[k - \kappa]. \quad (\text{A.5})$$

Let $\bar{x}_j[k] \triangleq x_j[k] - \eta_{x_j}[k]$ and $\bar{y}_{ij}[k] \triangleq y_{ij}[k] - \eta_{y_{ij}}[k]$. Then $\sigma_{y_{ij}}^2[k] = E[\bar{y}_{ij}[k]^2]$ and $\bar{y}_{ij}[k] = h_{ij}^{(d)}[k] * \bar{x}_j[k]$, hence:

$$\begin{aligned} \sigma_{y_{ij}}^2[k] &= E \left[\left(\sum_{\kappa=0}^{\infty} h_{ij}^{(d)}[\kappa] \bar{x}_j[k - \kappa] \right)^2 \right] \\ &= \sum_{\kappa_1=0}^{\infty} h_{ij}^{(d)}[\kappa_1] \sum_{\kappa_2=0}^{\infty} h_{ij}^{(d)}[\kappa_2] \\ &\quad \cdot E[\bar{x}_j[k - \kappa_1] \bar{x}_j[k - \kappa_2]]. \end{aligned} \quad (\text{A.6})$$

Furthermore, it is easy to see that $E[\bar{x}_j[k_1] \bar{x}_j[k_2]] = C_{x_j x_j}(k_1, k_2)$, which, using (A.2), gives

$$\begin{aligned} \sigma_{y_{ij}}^2[k] &= \sum_{\kappa=0}^{\infty} |h_{ij}^{(d)}[\kappa]|^2 \sigma_{x_j}^2[k - \kappa] \\ &= |h_{ij}^{(d)}[k]|^2 * \sigma_{x_j}^2[k]. \end{aligned} \quad (\text{A.7})$$

Finally, the variance waveforms for the system output are, using (A.4):

$$\sigma_{y_i}^2[k] = \sum_{j=1}^n |h_{ij}^{(d)}[k]|^2 * \sigma_{x_j}^2[k], \quad i = 1, \dots, m. \quad (\text{A.8})$$

In other words, *the variances of the system outputs (bus branch currents) can be obtained from the convolution of the variances of its inputs (contact currents) with the squares of its discrete impulse response functions*. This discrete convolution can be easily performed once the discrete impulse response functions are found. Of course, the summation need not be taken to infinity, and may be conveniently truncated after $|h_{ij}^{(d)}[\kappa]|$ is less than some small value. To obtain the discrete impulse response functions, note that if a unit-step input current is applied at contact j , with all other contact currents held at zero, and if the resulting outputs $y_i(t)$ are monitored, then:

$$\begin{aligned} h_{ij}^{(d)}[k] &= y_i(kT) - y_i((k-1)T) \\ &= \int_{(k-1)T}^{kT} h_{ij}(\tau) d\tau, \quad i = 1, \dots, m. \end{aligned} \quad (\text{A.9})$$

This suggests two methods for deriving $h_{ij}^{(d)}[k]$. The first uses a simulation program such as SPICE to simulate the bus with unit-step input currents applied at each contact (one at a time), while monitoring the bus branch currents. This gives the *mn* functions $h_{ij}^{(d)}[k]$ using (A.9). Another (approximate) method would be to make use of the second equality in (A.9): if the continuous impulse response functions are approximated using some RC time constant analysis of the bus, then the discrete impulse response functions can be obtained from them.

For very large chips, it may be prohibitively expensive to perform the required convolutions. One can simplify the calculations by making an additional assumption as follows. If the bus is known to be "fast," i.e., if $h_{ij}^{(d)}[k]$ dies down faster than changes in $\sigma_{ij}^2[k]$, then (A.7) reduces to:

$$\sigma_{y_{ij}}^2[k] \approx \sigma_{x_j}^2[k] \sum_{\kappa=0}^{\infty} |h_{ij}^{(d)}[\kappa]|^2. \quad (\text{A.10})$$

So the convolutions in (A.8) can be replaced by simple multiplications, and the constants $\sum_{\kappa=0}^{\infty} |h_{ij}^{(d)}[\kappa]|^2$ can be derived in a preprocessing step from the impulse response functions and stored in a single $m \times n$ constant matrix.

If the chip is too big to even derive $h_{ij}^{(d)}[k]$, then one further simplification can be made as follows. If $h_{ij}^{(d)}[k]$ dies down faster than changes in $x_i[k]$ then (A.5) reduces to $y_{ij}[k] = x_j[k] \sum_{\kappa=0}^{\infty} h_{ij}^{(d)}[\kappa]$, and so:

$$\sigma_{y_{ij}}^2[k] \approx \sigma_{x_j}^2[k] \left[\sum_{\kappa=0}^{\infty} h_{ij}^{(d)}[\kappa] \right]^2. \quad (\text{A.11})$$

The constants $(\sum_{\kappa=0}^{\infty} h_{ij}^{(d)}[\kappa])^2$ can be very easily obtained as follows. Notice that $\sum_{\kappa=0}^{\infty} h_{ij}^{(d)}[\kappa]$ is the *steady-state* current in branch *i* in response to a unit-step input current at contact *j*, with all other contact currents held at zero. If the bus is modeled as a resistive network, then the steady-state node voltages in response to such inputs are the entries of the driving point impedance matrix. So if the node admittance matrix is built by simple inspection of the bus and then inverted to produce the driving point impedance matrix, the steady-state currents are immediately available.

REFERENCES

1. F. Najm, R. Burch, P. Yang, and I. Hajj, "Probabilistic simulation for reliability analysis of CMOS VLSI circuits," *IEEE Trans. Computer-Aided Design*, vol. 9, pp. 439-450, Apr. 1990.
2. F. M. d'Heurle, "Electromigration and failure in electronics: An introduction," *Proc. IEEE*, vol. 59, pp. 1409-1418, Oct. 1971.
3. J. R. Black, "Electromigration failure modes in aluminum metallization for semiconductor devices," *Proc. IEEE*, vol. 57, pp. 1587-1594, Sept. 1969.
4. F. Najm, "Probabilistic simulation for reliability analysis of VLSI circuits," Ph.D. dissertation, Dept. Elec. Comput. Eng., Univ. of Illinois at Urbana-Champaign, June 1989.
5. A. Papoulis, *Probability, Random Variables, and Stochastic Processes*, 2nd ed. New York, NY: McGraw-Hill, 1984.
6. F. Najm, I. Hajj, and P. Yang, "Electromigration median time-to-failure based on a stochastic current waveform," in *Proc. IEEE Int. Conf. Computer Design*, Cambridge, MA, Oct. 2-4, 1989, pp. 447-450.
7. - "Computation of bus current variance for reliability estimation of VLSI circuits," in *Proc. IEEE Int. Conf. on Computer-Aided Design*, Santa Clara, CA, Nov. 6-9, 1989, pp. 202-205.
8. J. D. Verables and R. G. Lye, "A statistical model for electromigration induced failure in thin film conductors," in *Proc. 10th Ann. IEEE Reliability Physics Symp.*, Las Vegas, NV, Apr. 5-7, 1972, pp. 159-164.
9. J. W. McPherson and P. B. Ghate, "A methodology for the calculation of continuous dc electromigration equivalents from transient current waveforms," in *The Electrochemical Society. Proc. Symp. on Electromigration of Metals*, New Orleans, LA, Oct. 7-12, 1984, pp. 64-74.
10. J. E. Hall, D. E. Hocevar, P. Yang, and M. J. McGraw, "SPIDE-R: A CAD system for modeling VLSI metallization patterns," *IEEE Trans. Computer-Aided Design*, vol. CAD 6, pp. 1023-1031, Nov. 1987.

APPLICATION OF AUDIO/SPEECH RECOGNITION FOR MILITARY REQUIREMENTS

Edward J. Cupples, Intelligence & Reconnaissance Directorate, Rome Laboratory
Bruno Beck, Asce Corporation

This article is Chapter 8 of a book entitled "Application of Audio/Speech Recognition for Military Requirements," published by Kluwer Academic Publishers, Norwell MA in December 1991. The book is based on lectures which were sponsored by AGARD/NATO and delivered by Mr. Cupples in several NATO countries.

1. INTRODUCTION

Increases in the functional capabilities of military systems have made these systems increasingly more difficult to operate. Increased operator workload in modern workstations and aircraft have produced operator stress and fatigue, resulting in degraded operator performance, especially in time critical tasks. One reason for this problem is that both data entry and system control functions are often controlled via the systems keyboard. In some systems functions are nested many layers deep making the system inefficient and difficult to use. For this reason technology to improve the interface between the system and its operators is of high interest. Many efforts and several technologies are being pursued in speech recognition and synthesis, multimodal interface techniques, and voice interactive concepts and methods. Such work is being pursued to satisfy the requirements for modern communication, collection, analysis, identification, resource management, and control.

Interest in potential uses of Automatic Speech Recognition (ASR) technology is steadily increasing in both military and civilian communities. Much of this interest is due to advances in electronics and computers rather than in new techniques for speech recognition. Despite its current limitations, ASR promises to aid in a variety of military applications by increasing the effectiveness and efficiency of the man-machine interface. Indeed, military organizations have long been, and continue to be, one of the main sources of support of research and development of ASR technology.

This chapter discusses some recent applications of ASR technology. It is not intended to be exhaustive but rather presents a representative perspective of the military uses of this technology. Four major categories of applications are discussed: Audio Signal Analysis, Voice Input for Command and Control, Message Sorting by Voice, and Automatic Gisting.

2. AUDIO SIGNAL ANALYSIS

Speech enhancement and interference reduction technology to improve the quality, readability and intelligibility of speech signals that are masked and interfered with by communication

channel noise has high interest and many applications. This interest in speech enhancement is not only in improving the quality, readability and intelligibility speech signals for human listening and understanding but to improve speech signals for machine processing as well. Speech technology such as speaker identification, language recognition, narrowband communications, and word recognition being developed requires good quality signals in order to provide effective results. The development of automatic real-time speech enhancement technology is therefore of very high interest to military users.

There are a large number of applications for speech enhancement. Many systems that perform silence or gap removal and/or speech compression have difficulty with the processing of noisy communications data. In many instances gap removal is completely ineffective and compression schemes completely degrade speaker identity and cause large reductions in intelligibility. These systems require speech enhancement to be operationally effective. The use of Automatic Speech Recognition (ASR) in noisy environments such as the Cockpit is of very high interest. Although there has been some success in using restricted and well structured ASR in the cockpit, difficulties with acoustic noise in the airborne environment is much more troublesome for larger vocabulary continuous speech recognition systems. The successful use of enhancement for ASR can offer performance improvements that will make voice control and data entry operationally acceptable for many airborne applications.

Another area in which the noise generated in an aircraft causes problems is the use of vocoders for narrowband jam resistant communications. Vocoder technology use is restricted in many airborne applications because the acoustic noise generated by the aircraft degrades the intelligibility of the vocoder system to an unacceptable level. Speech enhancement to reduce the aircraft noise offers the capability to make a variety of vocoder technology available for airborne use.

A. Speech Enhancement

Speech Enhancement is the capability to remove frequently encountered communication channel interferences with mini-

imum degradation to the speech signals. The types of interferences or noises removed can be classed into three groups (1) impulse noise such as static and ignition noise, (2) narrowband noise which includes all tone like noise, and (3) wideband random noise such as atmospheric, receiver electronic noises, and aircraft noise. Impulse noise removal processes are usually a time domain process. The process is very effective for removing impulses up to 20 milliseconds in length. Narrowband noise removal processes are usually a frequency domain process. Techniques are required to remove both high level and low level tones of which there may be several hundred. The tones may be fixed or moving. Such a capability is extremely useful in removing power converter hums and heterodyne signals found on communication channels. Wideband noise removal processes frequently use cepstrum subtraction processes. The only successful process developed by the United States Air Force at Rome Laboratory, Griffiss AFB NY is a subtractive process that is accomplished in the spectrum of the square root of the amplitude spectrum. While this function is not the same as the cepstrum (the cepstrum is the spectrum of the log amplitude spectrum), since it resembles the cepstrum it is referred to as the root-cepstrum. In this method of noise reduction the average root-cepstrum of the noise in the input signal is continually updated and subtracted from the root-cepstrum of the combined speech and noise. Because the random noise concentrates disproportionately more power in the low region of the root-cepstrum than does the speech, the subtracted reconstructed time signal produces an enhanced speech signal. A picture of a prototype, the VLSI, and the VHSIC enhancement units is shown in Figure 1.

Other enhancement processes have been developed for unique interferences and noises and have been shown to be effective for their specific use. New enhancement methods are continually sought. Some examples currently being pursued by research and development laboratories are technologies such as Hidden Markov models, Neural Networks, and Artificial Intelligence.

B. Speech Enhancement Testing

How to determine the value of a speech enhancement capability or technique has been a never ending debate. Test methods are subjective and test procedures not well established making comparisons of systems and techniques difficult to impossible. However, proper testing is critical to successfully applying and fielding a capability in a military or commercial application. As a result, several test methods and procedures were developed by Rome Laboratory through necessity. Since the Rome Laboratory Speech Enhancement Unit (SEU) is cur-

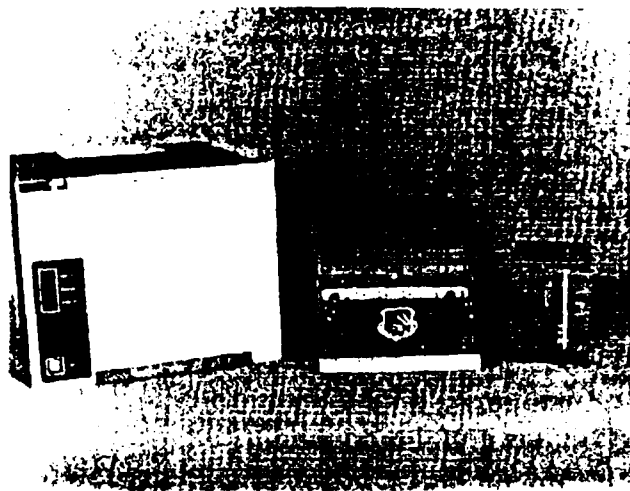


Fig. 1. Evolution of Speech Enhancement Hardware. From left to right Prototype, VLSI, VHSIC.

rently the only process that has been thoroughly tested in the laboratory and in field military applications, and since many of the test methods have been endorsed by other agencies, the discussion on testing and on enhancement capabilities will use the SEU as an example.

The SEU has been tested in two areas. They are (1) the reduction of communication channel noise to improve the recognition performance of human listener and (2) the reduction of wideband random noise and aircraft cockpit noise to improve the performance of automatic speech recognition (ASR) systems. Improvements in performance have been demonstrated in other areas.

The first test conducted on the SEU determined the effect of processing radio frequency voice communication channels containing a variety of off-the-air noises on the monitoring per-

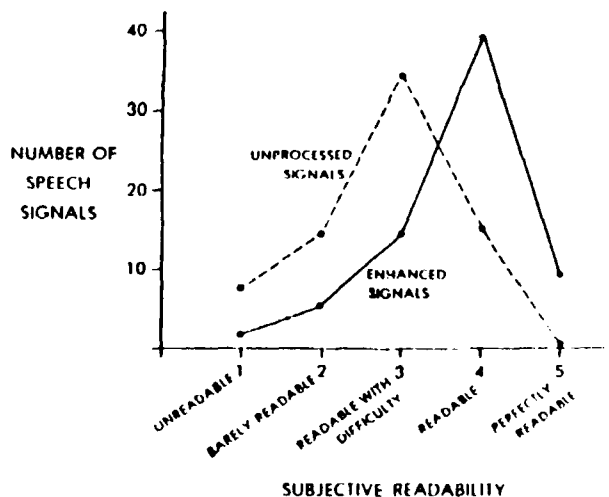


Fig. 2. Speech Enhancement Operational Results

formance of humans. The signals were monitored by equally skilled trained Air Force operators both before and after enhancement by the SEU. The data was controlled so that no operator heard the same data before and after enhancement. The readability of the signals was rated before and after enhancement. The readability of the signals is as shown in Figure 2. Note the shift in the readability of the signals after enhancement. The results clearly show an improvement in readability. However, not only was there a significant improvement in the readability of the signals but operator fatigue was reduced, intelligibility improved, and very importantly, the enhancement process was found to be capable of being operated in an entirely automatic mode. Also important was the uncovering of events that were not recognized before enhancement. These results appear to agree with equipment laboratory tests which showed the narrowband and impulse noise to be attenuated as much as 40dB. Measurements on the wideband removal process showed a signal-to-noise ratio improvement of from 15 to 21dB.

The second set of tests were conducted to determine the effect of using the SEU as a preprocessor to automatic speech recognition systems. Several speech recognizers were used with good results.

The results of a test conducted at an Air Force flight laboratory with the SEU acting as a preprocessor to an LPC-based recognizer showed substantial recognition improvements. The tests were conducted in a facility where the acoustic environment of the F-16 cockpit was simulated. The tests were conducted using the Advanced Fighter Technology Integration (AFTI) 36-word vocabulary. Training was accomplished without the SEU and in 85dBa sound pressure level (SPL). Six subjects were tested; four military pilots and two Lear Siegler personnel. The two subjects used for the enhancement tests were the lowest scoring military pilots in the tests. Enhancement was used only during the 109dBa and 115dBa noise level tests. At

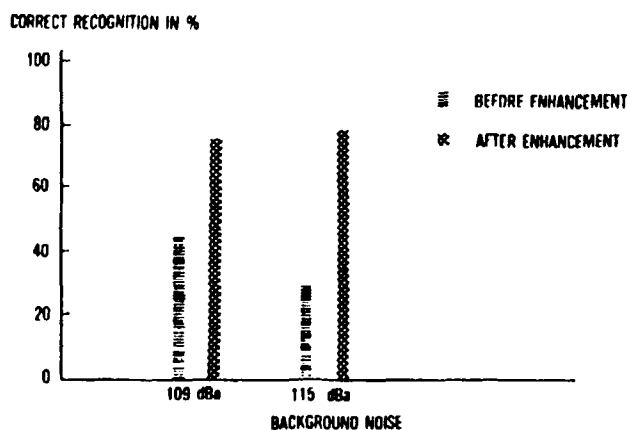


Fig. 3. SEU/LPC Based Recognition Performance

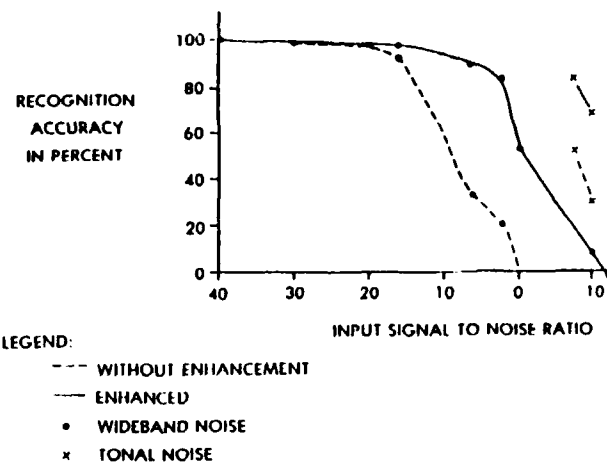


Fig. 4. Recognition Performance of Filter Bank Word Recognizer

109dBa noise level recognition performance increased from 46% without SEU processing to 75% after enhancement. Performance jumped from 30% to 79% after enhancement for the 115dBa noise level condition, Figure 3.

Other tests using the SEU or a preprocessor have shown varying degrees of improvement. Test results without training the recognizer through the SEU show digit recognition improvements of 20% correct recognition to 83% after enhancement for an input S/N of 3dB using wideband random noise, Figure 4.

Better performance was obtained by training the recognizer through the SEU under no noise conditions. The results obtained for this condition show an improvement from 21% to 100% correct recognition after enhancement at a 10 dB S/N.

C. Co-Channel Interference Reduction

Another type of interference that is often encountered in military operations is co-channel interference. This voice on voice interference occurs when there are two or more transceivers transmitting at the same time on the same frequency channel. As an example, co-channel interference occurs when two aircraft attempt to communicate with the control tower at the same instant in time which most often results in unintelligible speech at the tower.

Techniques to reduce co-channel interference have been applied to the radio frequency, the intermediate frequency and the demodulated audio signals. Radio frequency methods attempt to reduce the interference by creating antenna peaks and nulls to separate signals by spatial filtering. This method is limited by the physical size of the antenna array. This method is not effective for signals having the same line of bearing.

Intermediate frequency techniques which have had some success use signal amplitude and frequency to discriminate between the co-channel signals. The techniques are effective for separating frequency modulated (FM) signals from other FM signals and amplitude modulated signals (AM) from FM signals but are not effective for separating AM from AM signals.

Separating the co-channel signals in the audio band is attractive because it is independent of the geometry of the emitters and the signal modulation. Many techniques have been developed but generally all these techniques are based on separating voiced speech segments only. Therefore these techniques must rely on separating the pitch of the talkers and using this information to extract the desired talker or suppress the interfering talker. Some of the techniques that have had some success on signals where the ratio of the talkers strengths are large (-12 to -25 dB reference to the stronger talker) are pitch tracking comb-filters and harmonic magnitude suppression algorithms. Both require accurate pitch tracking and hence have difficulty where the pitches of the talkers cross, where the pitch changes rapidly and where the pitches are close in frequency. Analysis techniques that provide high resolution to resolve small differences in the pitch of the talkers are not able to track rapid changes in pitch. Therefore trade-offs are generally made between frequency and time resolution to satisfy both tracking speed and frequency resolution requirements.

Techniques that rely on eliminating the pitch components of one talker by removing the components entirely have not had success in improving the intelligibility of the desired talker. The suspected reason is that some components of the desired talker are also eliminated and the holes in the frequency spectrum generate masking noise. The only techniques that have improved intelligibility of co-channel speech are those that have suppressed the larger interfering talker to a level near to the desired talker. This places the burden of separating the talkers on the listener. Results for a method called Harmonic Magnitude Suppression (HMS) which uses this technique show an absolute improvement in intelligibility of 6.3% for a ratio of -6 dB reference stronger talker and 7.2% for a ratio of -18 dB for the same reference. It should be remembered that this improvement was made by processing only the voiced speech.

Unvoiced speech was left for the listener to interpret. Based on the continuous speech of two English talkers simultaneously talking, the percent of the time voiced speech falls on voiced speech is approximately 35%. Hence, if the HMS process provided perfect separation of voiced-on-voiced speech, the maximum improvement in intelligibility can be no greater than 35%. Larger improvements will require research in the separation of unvoiced speech from both the voiced and unvoiced speech of another talker.

3. VOICE INPUT FOR COMMAND AND CONTROL

There are many man-machine interface (MMI) problems associated with the modern communication stations, battle management workstations and the advanced aircraft cockpit. Several factors have led to the MMI problems and the subsequent thrust of military development of MMI technologies. They are:

- Adding on new capabilities to existing systems
- New systems with many combined capabilities
- Increased complexity of the environment
- Reduced time to complete tasks
- Increases in the number of time critical tasks

Many of these factors are the direct result of reduced manpower (accomplish more with fewer operators), and the increased speed of events caused by higher speed aircraft and advanced weaponry.

New ASR and speech synthesis technology forms the basis for voice input/output (I/O) systems. Such systems can improve man-machine interaction for modern communications, collection, analysis, identification, resource management and control. Speech communication with machines can offer advantages over other modes of communication such as manual methods, especially when humans are engaged in tasks requiring hands and eyes to be busy. Speech offers the most natural, and potentially the most accurate and fastest mode of communication, but is susceptible to environmental interference, and restricted by speaker and training requirements. Researchers are currently investigating speech recognition techniques which would permit a more natural, continuous form of speaking style and which would require a minimum amount of training by the speaker.

The workload of the military flight crew is becoming more demanding, due to increases in the amount of complex equipment crew members must monitor and control. Hence, there are constant demands on crew members for manual, visual and aural attention in order to perform vital mission functions, such as navigation, controlling weapons and monitoring sensors. At present, most critical functions are performed via manual operation of switches and keys. The increase in the number of manual tasks, as well as information processing demands, has made it difficult for the crew member to perform all the necessary functions while maintaining control of the aircraft. ASR technology can aid in relieving this information and motor overload by allowing the use of voice to control manual functions.

An airborne environment presents serious problems for any speech recognition device. These problems include high ambi-

ent noise, high g-forces, vibration, effects of oxygen masks, and extremes of altitude, pressure, temperature and humidity. Yet there is no doubt that military organizations see ASR technology as an integral part of future airborne cockpit avionics if the challenge of operating in the harsh air environment can be met.

Currently efforts are being made for the development of MMI concepts and testbeds for test and evaluation of those concepts. The overall purpose of the research is to determine the requirements to provide efficient interfaces for the advanced cockpits and workstations. The voice interface goals are to develop the rudiments of an overall philosophy for verbal interaction with these systems.

In order to develop the philosophy and subsequent techniques, detailed scenarios for the cockpit and workstations are analyzed in terms of tasks, workload types, type and amount of information to be transferred, time constraints, criticality, of the information, and environmental conditions. Using the scenarios information, experiments are conducted to determine fundamental relationships such as:

- the effects of S/N in terms of time and accuracy on the completion of an audio task at various audio workloads.
- the effects of various visual, manual, and oral workloads on various audio (listening) tasks and vice versa.
- the effects of injecting audio messages (both voice and sound) into a system under various audio, visual, and manual workloads.

Knowing these interrelationships narrows the number of interface modalities for a given task under a given set of conditions and allows an estimation of a performance level. Based on the results from the experiments, designs for MMI testbeds are developed, and evaluated. Tests are generally conducted using the communications scenarios.

A. Voice Verification

A different type of voice command system is used to control entry to secure areas and computer systems. There is significant military interest in the use of automated systems based on personal attributes (such as speech) to verify the identity of individuals seeking access to restricted areas and systems (such as flight lines, weapon storage areas, classified record storage areas, command posts, computers, workstations, aircraft, etc.). In this application, ASR technology is employed for automatic speaker verification, which identifies who is doing the talking rather than the words being spoken. Techniques based on both amplitude spectral information and Linear Predictive Coding (LPC) have proved successful.

In discussing the accuracy of speaker verification and other ASR systems, it is important to note the tradeoffs that can be made which affect system's performance. The two most commonly recorded error types are: rejection (a legitimate utterance is falsely rejected) and substitution (an incorrect utterance of falsely substituted for the legitimate utterance). In evaluating speaker verification performance, rejections are called "Type I" errors and result when an authorized user has been incorrectly denied access to a secure area. Substitutions are called "Type II" errors and are a consequence of an imposter succeeding in gaining access as an authorized user. The tradeoff between the two error types are illustrated in Figure 5.

Most ASR systems (including speaker verification) incorporate a variable threshold which can be adjusted to control the

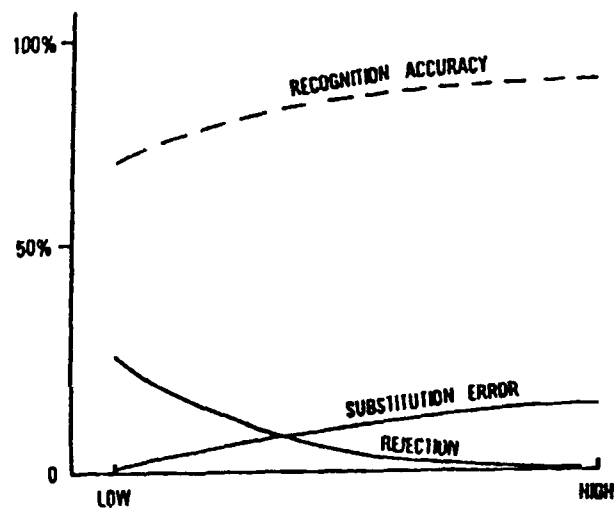


Fig. 5. Speaker Verification Performance

balance between error types. Lowering the threshold tightens the requirements for acceptance of an utterance and thus lowers the Type II error, but with an increase in the Type I error. Also shown in Figure 5 by the dotted curve is a Receiver Operating Characteristic, which is a graph of the overall recognition accuracy as a function of threshold.

Recognition accuracy may be increased by threshold adjustment, with however, a penalty of additional substitution errors (Type II errors).

In one test of an automatic speaker verification system intended for military use, the average Type I and Type II error rates were both on the order of one percent. The test included over 100 talkers, over a several month test period (which included occasions when speakers had colds or other voice ailments), and for an environment with a high signal-to-noise ratio (SNR). This system was able to perform successfully even when several professional mimics attempted to imitate selected target speakers. Recent results obtained in a speaker verification test using 100 male and 100 female speakers, show a 1% Type

I error for 7300 verification attempts and a 0.07% Type II error for 28,000 verification attempts.

It is important when using ASR technology for military command and control applications that the total system be considered, not just the voice component. A thorough analysis of the human job tasks and a complete understanding of the system and environment to which ASR technology is interfaced are necessary.

4 MESSAGE SORTING/AUDIO MANIPULATION

Listening to radio broadcasts is a time-consuming, manpower-intensive and tedious task for military operators. This is due to the high density of received signals and the poor signal quality, which causes operator fatigue and reduced effectiveness. A potential solution to the problem is the use of ASR technology to automate part of the listening process. There are several recognition technologies being pursued that address the message sorting and routing problem, these include speaker identification, language recognition and keyword recognition.

Figure 6 shows how a typical message-sorting system might

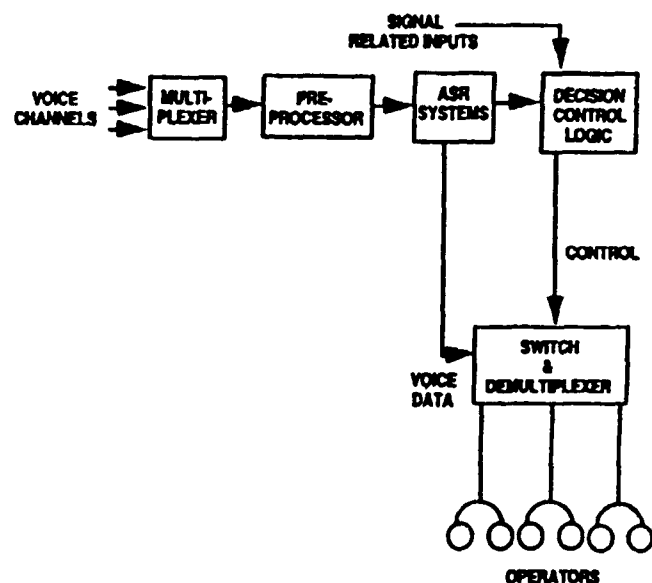


Fig. 6. General Message Sorting System

operate. A number of voice channels are multiplexed into a pre-processor. The preprocessor performs initial signal processing such as noise and interference removal as well as co-channel interference reduction. Subsequently, several automated ASR systems such as speaker authentication, language recognition, etc. determine important characteristics of the speech in the channels being monitored. Based on these results, a decision

processor then combines the information from the ASR system with signal related inputs such as signal-to-noise ratio, time, etc., and provides a correlated input to a switching demultiplexer which provides the messages to an operator, or an automatic gisting system.

In order to satisfy military operational needs these recognition technologies must handle several operational constraints.

An ASR system must

- Be context independent for speaker and language identification
- Handle uncooperative speakers
- Be robust to band-limited and noisy channels
- Handle dynamic channel conditions
- Operate on-line and in real-time
- Perform recognition on very short messages

A. Speaker Authentication

Speaker authentication is one method of message sorting that can be used to reduce the number of signals a communications operator must handle. Such systems must identify unknown talkers on multiple channels in real time using a small sample of their speech and under the above operational constraints. The operator can specify those talkers who are of interest at a particular time, and the system will route to the operator only speech that it identifies as spoken by the specified talkers.

Prior to executing a recognition task, a speaker authentication system is trained using one to two minutes of speech from each of the talkers who may later be recognized. The major requirement for the system is that it identify speakers using as little as two to five seconds of their speech since messages are often short but critical. Very few systems have been field tested.

One Speaker Authentication System developed by Rome Laboratory uses two techniques, a multiple parameter algorithm using the Mahalanobis metric and an identification technique based on a continuous speech recognition (CSR) algorithm. The multiple parameter algorithm uses both speech and non-speech frames. The speech frames are used to characterize the talker for recognition, and the non-speech frames to detect possible changes in talkers.

Recognition is performed by comparing the current average parameter vector with each of the active speaker models. Once per second the identity of the three models that are closest to the speech being recognized are output with their corresponding scores. Each second, the frames from the last second are accumulated and added to the average. The distance is then computed using the Mahalanobis metric.

The recognition module also monitors nonspeech frames to detect pauses in the input speech that are associated with possi-

ble changes in talkers. When non-speech frames are input, the recognition module ignores the frame, but increments the silence-frames-in-a-row counter. If the silence-frames-in-a-row counter exceeds a silence threshold (user selectable, default value of 0.5 seconds), the recognition module signals a possible change in talker.

A second approach uses small sub-word templates to model a person's voice characteristics, rather than the long term spectral statistics that are used in the multi-parameter technique. The test results, using a CSR speech recognition system, show a very significant improvement in recognition accuracy over the first approach. The recognition accuracy exceeded 95% for clean speech segments of 2 seconds or longer duration, as compared to 75% for the multiparameter technique. Speech enhancement as a noise removal preprocessor to speaker identification is required if automatic message sorting by speaker is to be effective in field operations.

B. Audio Management

Increases in the functional capabilities of modern workstations have made them increasingly more difficult to manage and operate. Increased operator workload has produced operator stress and fatigue, which has resulted in degraded operator performance, especially in time critical tasks. Military research and development continues to investigate and develop methods for audio handling, routing, and prioritization.

Rome Laboratory developed the first Advanced Speech Processing Station (ASPS) in the late 1970's. The concept of the

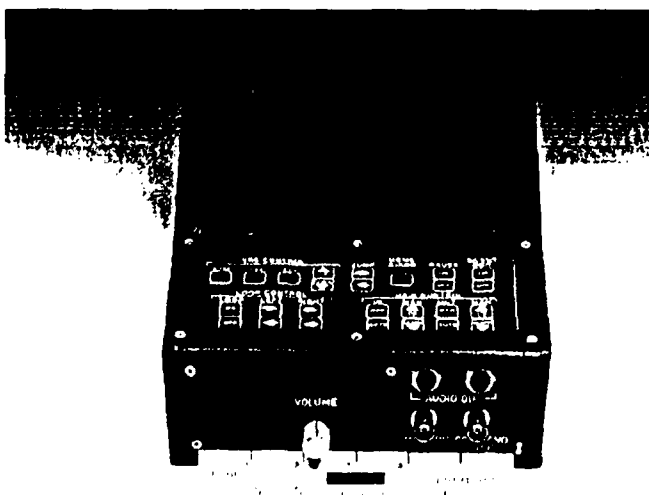


Fig. 7 Stand Alone Low Cost Audio Manipulation Unit

ASPS was to alleviate the problems associated with analog recording methods by utilizing digital techniques. These techniques were the first to allow an operator to playback pre-re-

corded speech while still recording incoming speech. Utilizing a two minute buffer, digital techniques allowed the operator to manipulate the audio signal in the following ways: jump backwards or forwards, speed-up or slow-down while retaining frequency information, repeat or loop speech segments, tag speech for instant recall and remove silence or non speech gaps.

New systems improved both the audio and text capabilities, provided better operator interfacing, and reduced workstation size, weight and cost. Tests on these systems have demonstrated improved performance/productivity (speed and accuracy), reduced operator fatigue and improved comprehension of the audio data.

Because of the success of these techniques, modern workstations containing many of the capabilities are commercially available. Audio manipulation capabilities are also available in a stand alone unit, Figures 7 and 8.

- **FIVE MINUTES OF DIGITAL AUDIO STORAGE**
- **SIMULTANEOUS RECORD/PLAYBACK**
- **JUMP FORWARD/BACKWARD**
- **LOOP** - variable size
- **VARIABLE RATE PLAYBACK** - 0.65 - 2 X's real-time
- **SILENCE/GAP REMOVAL ON PLAYBACK** - selectable
- **AUTOMATIC PITCH NORMALIZATION**
- **BANDWIDTH** - 100 - 3700 Hz
- **SENSITIVITY** - 1 millivolt
- **DELAY/RESPONSE TIME** - 300 millisec. maximum
- **COMPACT IN SIZE** - 3"H x 7"W x 10"D
- **LIGHT WEIGHT** - 10 lbs

Fig. 8. Specifications of the Audio Manipulation Unit in Figure 7

5. AUTOMATIC GISTING

There is high interest in the military in automatic gisting (understanding the major intent of a message) technology. The goal of automatic gisting is to automatically gist voice traffic in real-time for the updating of databases and to produce in-time reports. Such a capability will significantly increase the ability to collect and process large amounts of voice traffic and reduce the data to its most meaningful kernel, i.e., "gist."

However, to develop a gisting technology requires advanced technology in the following areas:

- Continuous Speech Recognition
- Keyword Recognition
- Speaker Identification

- Speaker Adaptation/Normalization
- Natural Language Processing
- Speech Understanding/Artificial Intelligence
- Noise Reduction Techniques

Although much research is being conducted in several of these technology areas independently for commercial and military applications, much less research is being conducted to combine these technologies. Due to the harsh military environment, keyword/phase recognition performance has been very poor. It is, therefore, essential to combine these technologies to obtain a robust gisting capability. The technology is being applied to air traffic control voice communications.

The goal of the research is to extract information from the communication that takes place between the aircraft and the control tower. The system would be capable of producing a gist of the dialog and would compile the information about the transactions and activities that occurred. Some of the desired capabilities are:

- Separate the speech between pilots and controllers
- Determine the airline and flight number
- Identify both the pilot and controller
- Determine the activity underway such as takeoff, landing, etc.

A final goal of the research is to develop a real-time testbed system to perform the extensive testing necessary to assess the current technology as well as provide future direction for research and development to address military field operations.

	<u>TODAY</u>	<u>CHALLENGE</u>
<u>SPEECH RECOGNITION</u>		
VOCABULARY SIZE	300	1000
TYPE OF SPEECH	ISOLATED	CONTINUOUS
ACCURACY	97%(CLEAN)	95%(COCKPIT)
<u>SPEAKER IDENTIFICATION</u>		
ACCURACY	94%(CLEAN)	98% (NOISY)
<u>SPEECH ENHANCEMENT</u>		
NOISE REDUCTION	18 dB	30 dB
<u>SPEECH COMPRESSION</u>		
BITS PER SECOND	2400	50-400
JAM RESISTANT FACTOR	2	10 TO 100

Fig. 9. Speech Technology Capabilities Today & the Challenge for the Future

6. FUTURE DIRECTION

The use of speech technology for military applications has been shown to increase the effectiveness of a variety of operational tasks. Figure 9 shows some basic speech processing technologies along with the current capabilities and future challenges for these technologies. Speaker identification current performance is given for small numbers of speakers while the challenge is to obtain this performance for a hundred or more speakers. Several new techniques are being pursued to meet the speech enhancement challenge. However, it is crucial that the speech signal not be degraded by the process. Measurement techniques for speech enhancement are not standardized making performance comparison of techniques difficult. New laboratory measurement techniques that better estimate field performance are required. The figure also shows the speech compression jam resistant factor referenced to a four kilohertz bandwidth. The challenge here is to obtain the jam resistant factor and meet intelligibility requirements when the acoustic environmental noise is high such as in the cockpit of an aircraft or in a ground vehicle. It must also be pointed out that minimizing both adaptation and training time is an important and challenging issue for many military applications.

Significant progress has been made in the development of audio signal analysis, voice input, message sorting and automatic gisting technologies. Although several technologies look promising for providing automatic sorting and gisting capabilities for military applications, these technologies can not meet today's requirements. However, the use of these technologies in combination offers a potential solution to improving performance to an acceptable level for use in the field.

In order to provide these speech processing capabilities to the field for test, evaluation, and operation, an increase in processing power per size, weight and cost is required. Therefore, the development of very high speed speech processors that can provide the processing power to support multiple speech functions and channels is essential if these technologies are to meet military requirements and be economically transitioned to both airborne and ground operations.

7. REFERENCES

1. Beck, Dr.B., and Cupples, E.J., et al. "Trends and Application of Automatic Speech Technology." S.D. Harris (ed.) *Symposium on Voice-Interactive Systems: Applications and Payoffs*, Dallas, TX, 1980.
2. Beck, Dr.B., and Neuberg, E.P., Hodge, D.C. "An Assessment of the Technology of Automatic Speech Recognition for Military Applications." *Acoustic, Speech, and Signal Processing*, Aug 1977.
3. Cupples, E.J., and Foelker, J.L. "Air Force Speech Enhancement Program." *Military Speech Tech '87*, Vol 1, No. 2, Media Dimensions, Inc., NY, NY, 1987.

4. Cupples, E.J. "Speech Research and Development at Rome Air Development Center." *Military Speech Tech '87*, Vol 1, No. 2, Media Dimensions, Inc., NY, NY, 1987.
5. Desapio, R.G., and Fry, E. "Avionics System Plays 'Ask and Tell' With Its Operator." *Speech Technology*, Vol 1, No. 4, 1983.
6. Lea W.A. "The Value of Speech Recognition Systems." W.A. Lea, (ed.). *Trends In Speech Recognition*, Prentice-Hall, Englewood Cliffs, NJ 1980.
7. Levinson, A.E., and Liberman, M.Y. "Speech Recognition by Computer." *Scientific American*, Vol 244, No. 4, 1981.
8. Naylor, Dr. J., Wrench, Dr. E., and Wohlford, R. "Multi-Channel Speaker Recognition." *RAIDC Technical Report Number TR-85-280*, 1986.
9. Simpson, C.A., Coler, C.R., and Huff, E.M. "Human Factors of Voice I/O for Aircraft Cockpit Controls and Displays." D.S. Pallet (ed.). *Workshop on Standardization for Speech I/O Technology*, NBS, Gaithersburg, MD, 1982.
10. Vonusa, R., Cupples, E.J., et al. "Application, Assessment and Enhancement of Speech Recognition for the Aircraft Environment." *Advanced Avionics and the Military Aircraft Man/Machine Interface*, AGARD Proceedings No. 329, France.
11. Weiss M., and Aschkenasy, E. "The Speech Enhancement Advanced Development Model." *RAIDC Technical Report Number TR-78-232*, 1978.
12. Weiss, M., and Aschkenasy, E. "Wideband Speech Enhancement Addition." *RAIDC Technical Report Number TR-81-53*, 1981.
13. Woodard, J.P., and Cupples, E.J. "Selected Military Applications of Automatic Speech Recognition Technology." *IEEE Communications*, Vol 21, No. 9, NY, NY, Dec 1983.
14. Howard, J.A., "Flight Testing of the A1T1/F-16 Voice Interactive Avionics System," *Proc. Military Speech Tech 1987*, (Media Dimensions), Arlington, VA, November 1987.
15. Hale, M., and Norman, O.D., "An Application of Voice Recognition to Battle Management," *Proc. Military Speech Tech 1987* (Media Dimensions), Arlington, VA, November 1987.
16. Naylor, J.A., and Boll, S.F., "Techniques for Suppression of an Interfering Talker in Co-Channel Speech," *IEEE Proc. ICASSP '87*, pp. 205-208, April 1987.
17. Weinstein, C.J., "Opportunities for Advanced Speech Processing in Military Computer-Based System" to be published in *DARPA Speech and Natural Language Workshop*.

NOTE: RAIDC (Rome Air Development Center) was renamed Rome Laboratory during November 1990.

III. Abstracts of Publications

A. SURVEILLANCE

TERRAIN-SCATTERED JAMMING CANCELLATION EXPERIMENT - JUNE 1991

C. R. Clark, D. N. Woods, Technology Service Corporation
D. Hildebrand, K. Zyga, Rome Laboratory, Surveillance &
Photonics Directorate

Abstract - Lookdown airborne radars are highly susceptible to deliberate or inadvertent ground-scattered jamming into the radar mainbeam, a threat against which spatial nulling techniques are ineffective. Algorithms have been proposed to cancel the scattered jamming via its correlations with the direct path signal. This paper reports on a ground-based experiment conducted to collect scattered jamming data for the validation of the canceller algorithms. Results of measurements and canceller performance are presented.

37th Annual Tri-Service Radar Symposium, 25-27 Jun 1991,
Boulder CO.

THE CART CONFORMAL ARRAY DEMONSTRATION

J. J. Schuss, J. Child, E. Geyh, A. Glickman, J. Upton, Raytheon
Company
G. Plotz, Rome Laboratory, Surveillance & Photonics Directorate

Abstract - Presented here is the design of the CART (Conformal Array Radar Technology) demonstration array being built to prove out the technology necessary for thin, conformal, low sidelobe phased arrays suitable for integration into the skin of an aircraft. This array is based upon several novel features, including a combined radiator/module ("antennule") architecture, a phase amplitude compensating rf beamformer, a high performance dual polarized patch radiator, and a control system that permits individual access and calibration of each T/R module. The combining of these elements into an antenna that addresses key conformal array issues will be discussed.

37th Annual Tri Service Radar Symposium, 25-27 Jun 1992,
Boulder CO.

BROADBAND MULTISPECTRAL PASSIVE SURVEILLANCE/TARGET ID

Robert F. Ogradnik, Rome Laboratory, Surveillance & Photonics Directorate

Abstract - This paper will address the development of an adaptive passive sensor system and its technologies which are founded on all spectrum awareness noncooperative bistatics which employs full spectrum monitoring of both the electromagnetic environment (ambient noncooperative illuminators, clutter and ECM spectrums) and broadband target signal spectrums which have the potential for supporting target identification. This sensor technology adaptively responds to the exploitable environment for optimized illuminator selection/bistatic hosting, interference cancellation/rejection and extended performance for small target detection/tracking in a multiple-mixed target and complex ECM environment. This adaptive multimode bistatic technology will automatically adjust to the changing spectral environment by sensing environmental changes and reacting through modifications in frequency, beam angle and time domain processing, and, illuminator selective switching, adaptive processing and interference nulling techniques. These developments will create a broadband, automatically response sensor system self contained in the bistatic receiver/processor on adaptive broadband passive phased array antenna, exploiting external noncooperative illuminators by employing full spectrum awareness monitoring and spectrum pulse sorting. These developed techniques will be implemented in the ESM/Bistatic Testbed which resides in the RADC/OC Surveillance Laboratory. This implementation will allow the collection of a test database for techniques develop purposes. It will also support performance validation testing against noncooperative illuminators, environments and target flight sorties. Test validations will be based on performance model, test plans, and evaluation criteria developed in this program.

4th National Symposium on Sensor Fusion, Apr 91, Orlando FL.

SINGLE-FREQUENCY TWO DIMENSIONAL DOPPLER IMAGING

Uve H. W. Lammers, Richard A. Marr, Rome Laboratory, Electromagnetics & Reliability Directorate

Abstract - Using a unique form of target action, two dimensional images of the target are generated by a single-frequency CW radar. This plus the limited range of aspect angles required for imaging places fewer constraints on the target than other known methods. Doppler shift induced by target rotation has been widely studied in the literature for its imaging potential.

Rather than rotation, we investigate here a target motion reminiscent of the precession of a rotating body. If target images are generated with the radar looking along the precession axis, the following benefits accrue: a single wavelength radar imaging a target at multiple angles between precession axis and target axis is equivalent to a multi wavelength radar imaging at a single angle only; two dimensional targets suffer no shadowing; scatterers need only be isotropic reradiators over a limited range of angles; target restrictions due to linear polarization of the radar signal are alleviated. These and other features of the method are demonstrated by imaging simulated point target scenes.

Antennas and Propagation Society Symposium Digest, June 1991, University of Western Ontario, London Ontario Canada.

OPTIMAL SUBPIXEL-LEVEL IR FRAME-TO-FRAME REGISTRATION

M. Fernandez, A. Aridgides, and D. Randolph, G.E. Ocean and Radar Systems Division

D. Ferris, Rome Laboratory, Surveillance & Photonics Directorate

Abstract - Current image registration approaches tend to operate independently on each of the frames of data that are to be registered, significantly degrading performance. In our approach, however, all the frames are matched simultaneously to a reference frame, thus utilizing in a global manner the information contained in all of them. It is shown that this approach, optimal in the minimum-variance sense, provides important registration gains over current procedures. The problem of registering multiple frames of data, ideally at the subcell or subpixel level, can be encountered in applications spanning the whole industrial, medical, and military worlds. For example, image quality is improved by removing the jitter introduced by the motion of the imaging platform. Likewise, precise alignment of frames of data collected over time or across sensors enables the effective extraction of the information they contain. Finally, the registration parameters themselves provide the ability to obtain large data compression gains by enabling the storage of a number of data frames in terms of a set of mappings affecting only one of them. An excellent overview of the importance and applicability of effective data registration algorithms continues to be Huang's¹.

SPIE Signal and Data Processing of Small Targets 1991

ACCURACY OF THE REFLECTED IR SIGNATURE COMPONENTS IN OPTASM

Jon S. Jones, Rome Laboratory, Surveillance & Photonics Directorate

Dr. Charles Acquista, PAR Government Systems Corp.

Abstract The Optical Target Signature Model (OPTASM) is a first principles computer code written in FORTRAN 77 for predicting the apparent radiance of military vehicles (e.g., aircraft, missiles, surface ships, tanks, etc.) in infrared, visible, and laser spectral bands. OPTASM was designed to allow accurate computations of the energy reflected from and emitted by the outer surfaces of a target vehicle, including reflected sunshine, earthshine, skyshine, and laser illumination. It has been applied to optimize the design of controlled signature vehicles, and to guide the design of IR surveillance systems for detecting dim targets.

This paper addresses the algorithms used to manipulate the Bidirectional Reflectance Distribution Function (BRDF) that describes the reflectance properties of the outer surfaces of target vehicles. Techniques for extending measurements to form a complete BRDF data base, and using this data base to predict the IR signature of aircraft and missiles will be discussed.

OPTASM is one of the first signature models that attempt to introduce surface curvature into the computation of IR radiance. The algorithms geometrical algorithms for computing curvature from a flat facet model, and the optical algorithms for the efficient computation of reflections from the curved surfaces will also be described.

IRIS Symposium on Targets, Backgrounds and Discrimination, Sandia National Laboratories, Albuquerque, NM, 29, 30, 31 January 1991

INFRARED SENSOR SIMULATION

Jon S. Jones, Rome Laboratory, Surveillance & Photonics Directorate

Abstract An infrared sensor simulation is currently being used to provide a stand alone sensor analysis capability for evaluation of infrared sensor concepts. The simulation encompasses a broad range of electro optical sensors including search and track systems. The simulation requires a wide range of inputs including information on the scenario, target, sensors, and the atmospheric conditions. It takes all this information and performs an end to end engagement. The type of calculations performed by the simulation are based on first principle models. Many valid assumptions have been made in the development of

this computer program so as to easily perform sensors scenario type engagements without taking hours of CPU time. The program is written in FORTRAN and is currently in operation on a PC AT computer using the DOS operating procedures. This paper will focus on the basic principles used in the simulation along with a description of how each input is described. A sample computer run will be developed and typical outputs will be presented. A description of support programs used to develop inputs to this simulation will also be described.

1991 Summer Computer Simulation Conference (SCSC 91)
Baltimore, MD July 22-24, 1991

OPTASM MULTICOLOR SPATIAL IR SIGNATURES FOR INPUT TO SENSOR FUSION PROCESSORS

Jon S. Jones, Rome Laboratory, Surveillance & Photonics Directorate

Abstract - Rome Lab has undertaken the research leading to the development of an infrared sensor system to perform detection and track of targets at long ranges. The infrared sensor system is expected to be a dualband (multicolor) sensor system focusing on the mid-wave and long-wave infrared bands and sub-bands thereof. Multicolor data fusion involves the fusion of several infrared wavebands. This process may be performed either at the infrared sensor system processor level, or at a central fusion processor, fusing many sensor results together. This paper will focus on predicting the hardbody (no plume) infrared signatures of threat targets using the Optical Target Signature Model (OPTASM) code. Infrared target signatures for three different targets using four separate wavebands will be developed. Both source and apparent signature measurements will be made at several target aspect angles. The target signatures will then be analyzed and unique features will be sought.

OPTASM has been developed for calculating the signature of targets such as missiles and aircraft in either infrared or visible bands. OPTASM addresses only the "hard body" components of a vehicle signature. It requires inputs concerning the shape and optical properties of the target, the parameters of the sensor, the geometry of the engagement (including the position and velocity of the target, the sensor, and any external source of illumination like lasers), and the state of the atmosphere. These inputs are used to perform detailed calculations for five signature components: thermal skin emission, reflected sunshine, laser reflections, reflected earthshine and reflected skyshine. An IR Target Signature Database (IRTSD) has been developed to provide the IR target signatures required to accomplish the research being performed in support of the mission. The IRTSD allows fast access to accurate high spatial resolution images of

threat targets. The operation of OPTASM will also be addressed in the paper along with associated database of target vehicles.

4th National Symposium on Sensor Fusion, 3 April 1991, Orlando, FL

OPTASM SPATIAL IR SIGNATURES OF TACTICAL TARGETS FOR AIR DEFENSE MISSIONS

Jon S. Jones, Rome Laboratory, Surveillance & Photonics Directorate

Abstract - The Optical Target Signature Model (OPTASM) has been developed for calculating the infrared signature of targets such as missiles and aircraft. OPTASM addresses only the "hard body" components of a vehicle signature. The OPTASM computer code along with plume and atmospheric computer codes have been used to generate a data base for sensor analysis. This data base called the Infrared Target Signature Database (IRTSD), has been used for clutter rejection and signal processing algorithm development.

IRIS Symposium on Targets, Backgrounds and Discrimination,
30 Jan. 1991 Albuquerque, NM

SIMULATION OF BISTATIC RADAR

Stanley E. Borek, Rome Laboratory, Surveillance & Photonics Directorate

Abstract - This paper discusses a simulation and modelling of bistatic radar, i.e., a transmitter and a receiver that are not collocated. The focus is on the inherent flexibility necessary to allow the simulation tool to adequately address any reasonable number of bistatic radar configurations/concepts that are of interest to the analyst. These include ground-based, airborne, spaceborne systems and any combination thereof.

The driving requirement of such a simulation capability is the development of an accurate design tradeoff/analysis tool to assess the performance of these systems with respect to such areas as target and clutter scattering of RF (radio frequency) energy due to the varying observation geometries that are possible. Thus exacting consideration is given to modelling of these scattering phenomenologies, along with the concerns of target coherence effects and bistatic radars functioning in the pulse doppler mode.

The simulation tool that addresses these concerns is the Bistatic Radar Simulation (BRADS). The main features of this simulation are flexibility and generality. Discussion shall center

around the parameters available in BRADS to define a surveillance scenario for simulation via computer software. These parameters, and their options, allow for varying degrees of parametric analysis to be accomplished. Bistatic radar parameters to be discussed will address: clutter spectra due to representation of clutter by different models, ambiguity functions, waveform selection, detection probability, antenna patterns/models, processing errors, target attributes, jamming (if applicable), trajectories, types/methods of resultant data presentation/output, etc. The capability of BRADS will be illustrated by means of a generic example for an airborne transmitter/airborne receiver bistatic radar configuration with parametric analysis results presented/discussed for several selected parameters of interest in the radar community.

Proceedings of the 1991 Summer Computer Simulation Conference, 22 - 24 July 1991, Baltimore, Maryland.

AIRBORNE BISTATICS

Robert F. Ogrodnik, Rome Laboratory, Surveillance & Photonics Directorate

Abstract - This paper addresses the technical issues and solution approaches for noncooperative coherent airborne bistatics. The presented technology and designs have been validated, in part, by either field tests or test validated simulation studies, thereby establishing credible solutions for this difficult look-down, moving surveillance application. Paramount technical challenges which are addressed include lookdown noncooperative illuminator selection and bistatic synchronization from a moving reference frame system, motion modulated clutter cancellation techniques and their controls, spurious multipath/anomalous target return discrimination and rejection, and target registration/track maintenance during multiple illuminator static exploitation and switching.

The technical approach achieved in these developments is based on coherent noncooperative bistatics, employing novel detection and signal processing which insures target registration instantaneously at the signal detection level, with target registration established for three simultaneously independent observables, which are; range, velocity, and angular position. The cross-correlation signal processing approach, which exploits direct path sampling of a noncooperative bistatically hostable illuminator, provides match filter waveform processing which insures pulse compression signal processing gain even in variable illuminator switching selection conditions. A broadband multioctave passive phased array antenna is employed in support of signal sampling/exploitation diversity over an extreme carrier frequency domain. This same antenna supports bistatic space-time processing technology for clutter suppression and minimization of motion induced processing losses. The bistatic space-time techniques employed, as well as clutter cancellation results will be included. These approaches are unique and provide significant clutter suppression in a varying bi static sur

veillance geometry situation. Simulated results for target detection/tracking, which performance measures such as Minimal Discernible Velocity (MDV) and Minimal Detectable Signal (MDS) in the ambiguity surface (range-doppler) domain are also given for different design/approach strategies. The application of this technology to Airborne Early Warning platforms is included in the final section.

37th Annual Tri-Service Radar Symposium, Jun 91, Peterson AFB, Colorado Springs, CO

RECONFIGURABLE RADAR

Robert F. Ogrodnik, Rome Laboratory, Surveillance & Photonics Directorate

Abstract - This paper addresses the technical approach and performance merits of a sensor with the features of reconfigurable operation. The range of reconfigurability is passive operation to active operation. In the passive mode, the sensor operates in either a coherent noncooperative bistatic manner or an ESM/ELINT manner. In this active mode the sensor is waveform and angle agile, with agility parameters selected for optimized clutter rejection and energy on target enhancements for improved monostatic detection/tracking performance. Mode selection is based on monitoring the environment on a sector-to-sector basis where clutter/jammer interference monitoring can initiate counter waveform operation or passive frequency-angle evasive operation. The monitoring element at all times is an ESM sensor which is integrated into the system by sharing a common phased array antenna with the passive/active subsystems. The signal processor continually reconfigures doppler processing methods and range processing algorithms (such as adaptive constant false alarm ratio (CFAR) algorithm) for waveform match filter processing and processing gain optimization. The clutter cancellation CFAR is adaptive to clutter discrete environments. In the bistatic mode, the signal processor involves coherent cross-correlation exploiting a direct path sample of the bistatically exploited noncooperative illuminator/cross-correlation against target echo returns. This approach insures match filter operation for any noncooperative waveform selected. The ESM monitor chooses bistatic illumination based on blind speed and ambiguous range criteria, as well as bistatic geometry impacts on target doppler visibility and bistatic tracking performance factors.

This paper presents results of field tests and several design options, as well as application ideas in support of survivable tactical sensor performance.

37th Annual Tri Service Radar Symposium, Jan 91, Peterson AFB, Colorado Springs, CO

ABSOLUTE PHASING OF SEGMENTED MIRRORS USING THE POLARIZATION PHASE SENSOR

Herbert W. Klumpe III, Barbara A. Lajza-Rooks, Rome Laboratory, Surveillance & Photonics Directorate
James Blum, W. J. Schafer Assoc.

Abstract - The Polarization Phase Sensor (PPS) is a white light polarization shearing interferometer which has successfully demonstrated absolute mirror segment alignment in the Rome Laboratory Optical Systems Engineering Laboratory. Operating at the center of curvature, the PPS demonstration has been configured to perform closed-loop phasing of a three segment spherical mirror. The PPS may be adapted for use with other optical systems, including aspheric surfaces. PPS device simulation and testing have verified this. This paper will address the optical layout of the device, experimental testing, and the results of subsequent analysis.

Analysis of Optical Structure, July 1991, San Diego, CA. Proc. SPIE 1532.

ABSOLUTE PHASING OF SEGMENTED MIRRORS USING THE POLARIZATION PHASE SENSOR (summary of presentation)

Herbert W. Klumpe III, Barbara A. Lajza-Rooks, Rome Laboratory, Surveillance & Photonics Directorate
James Blum, W. J. Schafer Assoc.

Abstract - The Polarization Phase Sensor (PPS) is a white light polarization shearing interferometer which has successfully demonstrated absolute mirror segment alignment in the Rome Laboratory Optical Systems Engineering Laboratory. Operating at the center of curvature, the PPS demonstration has been configured to perform closed-loop phasing of a three segment spherical mirror. The PPS may be adapted for use with other optical systems, including aspheric surfaces. PPS device simulation and testing have verified this. This summary will review the operation and performance capabilities of the PPS.

Technical Digest on Space Optics for Astrophysics and Earth and Planetary Remote Sensing, 1991, Optical Society of America, Nov. 1991, Williamsburg, VA, Vol.19.

ABSOLUTE PHASING OF SEGMENTED MIRRORS USING THE POLARIZATION PHASE SENSOR

Herbert W. Klumpe III, Barbara A. Lajza-Rooks, Rome Laboratory, Surveillance & Photonics Directorate
James Blum, W. J. Schafer Assoc.

Abstract - The purpose of this paper is to discuss a unique optical instrument which uses polarized white light to accomplish absolute mirror segment phasing. The Polarization Phase Sensor (PPS) is a polarization shearing interferometer which uses two Wollaston prisms to create and shear two wavefronts of orthogonal polarizations. A third Wollaston prism creates a known tilt between these wavefronts. By modulating the set of interferometric fringes formed by the reflection of these wavefronts off a test optic (segmented mirror), an analysis of the segment misalignment can be performed. A closed loop control experiment has demonstrated that this device is capable of actively phasing a three segment spherical mirror. This paper describes the instrument, the proof of concept demonstration, the results of this experiment, and how this instrument may be used with different types of mirrors, such as aspheres.

Technical Digest on Space Optics for Astrophysics and Earth and Planetary Remote Sensing, 1991 (Optical Society of America, Washington, D.C., 1991), Vol. 19

ADAPTIVE MULTIBAND POLARIZATION PROCESSING FOR SURVEILLANCE RADAR

Russell D. Brown, Rome Laboratory, Surveillance & Photonics Directorate
Hong Wang, Department of Electrical Engineering, Syracuse University

Abstract - Frequency diversity is shown to improve detection performance of adaptive radar processing in the polarization domain. Multiband processing increases the quantity of data available for covariance estimation of clutter which is often inhomogeneous in range. The diversity improvement under an equal transmit energy constraint is greater for adaptive processors than that obtained in optimal processors which operate with known statistics.

IEEE International Conference on System Engineering, Aug 91, Dayton, OH.

B. COMMUNICATIONS

PERFORMANCE OF A DEMONSTRATION SYSTEM FOR SIMULTANEOUS LASER BEACON TRACKING AND LOW DATA RATE OPTICAL COMMUNICATIONS WITH MULTIPLE PLATFORMS

Paul J. Oleski, Rome Laboratory, Command, Control, & Communications Directorate

R. C. Short, M. Cosgrove, and D. L. Clark, Kodak

Abstract - A high speed area array detector has been used as the basis for a proof-of-concept system which simultaneously tracks and receives data from multiple asynchronously modulated laser beacons. Such a system has applications in space optical communications network management, in which a terminal needs to track and maintain status information on several satellites to facilitate rapid switching of a high data rate optical link among those satellites.

The proof-of-concept system tracks 3 laser diode beacons using sophisticated windowing, centroiding and Kalman filtering algorithms. Simultaneous tracking and communications are achieved with as little as 1 picowatt of power on the detector even in the presence of high and non-uniform backgrounds. The tracking as well as clock and data recovery algorithms are implemented with a combination of specially developed digital signal processing electronics and software. Performance has exceeded program goals. With beacon powers of 1 picowatt or less on the detector, the system tracks with fractional pixel accuracies and recovers data at 1 kilobit/sec with low bit error rates. Tracking is maintained for beacon images which pass arbitrarily close together. Much of the tracking error is systematic and correctable with additional signal processing.

SPIE Proceedings of Free-Space Laser Communication Technologies III, 21 January 1991, Los Angeles, California.

A SOLID STATE AMPLIFIER FOR V-BAND SPACE COMMUNICATIONS

Joseph A. Mancini, Rome Laboratory, Command, Control, & Communications Directorate

Abstract - Three-terminal (transistor) solid state device technology has reached a level of capability and performance where

realistic alternatives to traveling wave tube (TWT) and IMPATT diode based amplifiers now exist at V band frequencies. Available device technologies such as MESFET, PHEMT, and HBT can be complimented by various power combining techniques such as chip level, module level planar, corporate, radial, and spatial to realize solid state alternatives. It can be shown that combinations of such technologies and techniques can produce 5 watt, class A and AB amplifiers intended for driving communication links at 60 gigahertz. Rome Laboratory (RL) is currently sponsoring the development of one such PHEMT based, radially combined 5 watt, 60 gigahertz solid state amplifier advanced development model (ADM) for utilization in future military command, control and communications (C3) space crosslinks.

LOW COST/VOLUME SHF/EHF RECEIVERS

William G. Cook, Rome Laboratory, Command, Control, & Communications Directorate

Abstract - A desire for more man-portable satellite terminals has arisen from the conflict in the Persian Gulf. Of particular interest is the development of affordable EHF manpack terminals to support tactical users with high AJ/LPI requirements. The Air Force is also interested in reducing the cost and volume associated with their airborne EHF terminals. For the Space segment, DARPA is currently developing a lightweight, cost affordable EHF technology base for implementation on "small" satellites and MILSTAR is considering upgrades to the hardware for their Restructuring program. The Strategic Defense System (SDS) is looking at fairly high production numbers for their Space platforms and the communications payload has severe weight limitations.

This paper provides descriptions of a 20 GHz receiver, x4 up-converter (with output at 44 GHz), and a 44 GHz spacecraft receiver which support the low volume and cost objectives discussed above. This is accomplished through the use of advanced MMIC/MIC components and low volume packaging techniques. The tradeoffs involved with the various levels of MMIC and/or MIC integration and packaging approaches as a function of system requirements, mitigation of cost, and overall terminal/payload construction are discussed. New technology and design alternatives are put forth in the paper as recommendations for future programs for the hardware presented.

Published in GOMAC '91 Proceedings, 7 Nov 91

A RULE-BASED ANALYZER WITH TEMPORAL REASONING FOR COMMUNICATION PROTOCOLS

Charles Meyer, Rome Laboratory, Command, Control, & Communications Directorate

Abstract - With data networks growing and serving less sophisticated users, there is a need for tools which facilitate or automate diagnosis of network failures. In this paper we describe a rule-based system for analyzing communication protocols. This system employs an architecture which allows the diagnostic knowledge for a particular protocol to be separate from the reasoning mechanism. The protocol-specific knowledge is held in a structure we refer to as the Protocol Diagnostic Model, or PDM, and consists of a set of associations between patterns and actions. A diagnosis of a network failure can be made by recognizing certain symptoms from observed protocol events. These symptoms are detected by matching representations of the temporal relationships between observed events against the patterns in the PDM.

"A Rule-Based Analyzer with Temporal Reasoning for Communication Protocols", Charles Meyer, November 1991, MILCOM '91, McLean, VA.

ENHANCED MULTINET GATEWAY: SURVIVABLE MULTI-LEVEL SECURE DATA COMMUNICATIONS

Wladimir Tirenin, Rome Laboratory, Command, Control, & Communications Directorate

Abstract - The Enhanced Multinet Gateway (EMG) is a Multi-Level Secure (MLS) packet-based gateway being developed by Falcon Communications Corporation under contract to Rome Laboratory, formerly Rome Air Development Center. It will provide secure flow of data from a single or multilevel host or network to another host or network operating at an equal or higher security level. The EMG will interface to commercial and DDN x .25- based Wide Area Networks (WANs), Ethernet/802.3 Local Area Networks (LANs), and several types of point-to-point transmission equipment including TRI-TAC. This paper describes the functions, capabilities, and security features of the EMG.

"Enhanced Multinet Gateway: Survivable Multi-Level Secure Data Communications", Wladimir Tirenin, November 1991, MILCOM '91, McLean, VA.

MACHINE INTELLIGENCE FOR SURVIVABLE COMMUNICATIONS NETWORK MANAGEMENT

Nick Kowalchuk, Rome Laboratory, Command, Control, & Communications Directorate

Abstract - The development of communications networking technologies that increase the survivability of services provided to military users has been an important goal in Air Force programs over the past several years. This enhanced survivability is a result of work that has focused on two areas: the development of more robust communication equipment, and the development of a management system that coordinates the use of that equipment. This paper will discuss the role of machine intelligence in the design of such a network management system. Emphasis will be placed on the intelligent network management decision making capabilities that are required in a military environment, and the design trade-offs which must be made in developing a system that can optimize the system-wide use of resources without the need for human intervention.

"Machine Intelligence for Survivable Communications Network Management", Nick Kowalchuk, 13-16 May 91, AGARD Symposium, Lisbon, Portugal.

ADVANCED HP DIGITAL NETWORKS

Nelson Robinson, Rome Laboratory, Command, Control, & Communications Directorate

Abstract - This paper covers ongoing work in the area of networking technology enhancements in HF communications that are currently being developed by Rome Laboratory under contract with Harris Corporation. The primary focus for this work that applies to both military and civilian use is application of a totally decentralized, distributed network architecture for digital voice and data communications in the 2-30 MHz band. Small nets of 400 mile radius comprise one large network of 4000 mile radius, with up to 100 network members at any time. Described in this paper are improved HF networking, LQA techniques, LPD/LPE waveforms for OPSEC, and frequency management in a frequency hopping (FH) environment. A PC portable simulation (INS), user manuals, and technical report with an appendix covering the cooperative work done with USA CECOM, Ft Monmouth, NJ, will result from this effort. The INS allows a user to specify and configure any network to meet their needs, see how it operates, and receive a printout of the results.

"Advanced HF Digital Networks", Nelson Robinson, 4-6 September 1990, Conferences on Electrical and Computer Engineering, Ontario, Canada.

SURVIVABILITY OF TACTICAL COMMUNICATIONS NETWORKS AGAINST AN INTELLIGENT ADVERSARY

John B. Evanowsky, Ph.D., Rome Laboratory, Command, Control, & Communications Directorate

Abstract - Work in the United States Air Force to develop survivable communications networks builds upon a foundation of assessment techniques designed to quantify their vulnerability to an intelligent adversary based on susceptibility, interceptibility, accessibility, and feasibility analyses. An architecture is being developed based on the inherent survivability of distributed processing techniques. This architecture will map the services required by theater and tactical users to the available communications infrastructure available to them using a fully integrated voice, data, and message switching fabric. A robust protocol suite is being defined which can perform under the bandwidth, mobility, multi-transmission media, jamming, destruction, and interoperability constraints that characterize the tactical environment.

1991 IEEE Military Communications Conference, Nov 1991, McLean, Virginia

EXPERIMENTAL EVALUATION OF INTELLIGENT RECEIVER DESIGN TECHNIQUES

Ernst K. Walge, Rome Laboratory, Command, Control, & Communications Directorate

Jeffrey S. Yalowitz, SRS Technologies

Abstract - The intelligent receiver concept combines heuristic methods with conventional decision/estimation theory and modern control systems methods. Its objectives are to incorporate awareness of electromagnetic and mission environments into communications receivers and to produce robust adaptive receiver control strategies in real time. An automated laboratory testbed system was constructed. Measurements made using the testbed have demonstrated enhancements in radio receiver adaptation to radio channels that contain fading and interference.

Proceedings, 1991 MILCOM 91 (Journal Proceedings)

COMPUTER MODELING OF SPREAD SPECTRUM NON-LINEAR PROCESSORS

John J. Patti, Stephen C. Tyler, and Robert M. Husnay, Rome Laboratory, Command, Control, & Communications Directorate

Abstract - This paper describes results obtained with a computerized modeling program. The program is designed to generate, modulate, channel emulate, adaptively process, despread and demodulate spread spectrum communication signals. The adaption refers to the process of digitally computing, by statistical estimation techniques, the channel characteristics consisting of interference and multi-path channel distortion terms. The processor employs both time and frequency domain techniques. The paper will present our initial results obtained in an effort to combine linear and non-linear adaption techniques as an approximation to the generally non-linear ideal solution, and other methods of approximation to the ideal solution.

Proceedings, 1991 MILCOM Conference

HIGHLY INTEGRATED RECEIVERS FOR EHF SPACE COMMUNICATIONS

William G. Cook, Rome Laboratory, Command, Control, & Communications Directorate

Abstract - Descriptions of a 20 GHz ground/airborne terminal receiver for downlinks, a 44 GHz receiver for spacecraft uplinks, and a 60 GHz receiver for crosslinks are presented. The tradeoffs involved with the various integration and packaging approaches as a function of overall hardware construction and system requirements is discussed. The device technologies of choice are examined as well as comparisons between MMIC and hybrid design approaches. Also, new technology and design alternatives to the receivers presented are put forth as recommendations for future enhancements.

Proceedings, 1991 MILCOM Conference

C. COMMAND AND CONTROL

RADC'S ADVANCED SIMULATION ENVIRONMENT (RASE).

Craig S. Anken, Rome Laboratory, Command, Control, & Communications Directorate

Abstract - RADC's Advanced Simulation Environment (RASE) is an object-oriented toolset designed to facilitate rapid development of simulations needed to support Air Force Command and Control. RASE currently consists of an object-oriented simulation language (ERIC), a cartographic database system (CARTO), an object-oriented Map Display system (MDS), and several other development support tools (RACK, HIER, and CLOCK Viewer). A tactical simulation, Land Air Combat in ERIC (LACE), is being developed within the RASE framework and will be utilized in a testbed environment aimed at the validation and verification of decision aid results (i.e., expert system testing).

Society for Computer Simulation (SCS) Simulation Series, Jan. 1991, Anaheim, California.

HEURISTIC ROUTE OPTIMIZATION: A MODEL FOR FORCE LEVEL ROUTE PLANNING

Lt Janet L. Barboza, Rome Laboratory, Command, Control, & Communications Directorate

Abstract - Effective route planning is essential to mission accomplishment and pilot/aircraft survivability, yet many factors inextricably associated with flying a route through a defended area are not or cannot be considered by techniques currently being used, whether manual or automated. Heuristic Route Optimization, or HERO, is an exploratory development project managed by the Advanced Concepts Branch of the Rome Air Development Center (RADC), undertaken to produce a model for automated force level route planning. It uses Object Oriented Programming techniques to make the aid more flexible and dynamic than other aids or manual techniques. HERO pursues detailed analysis of multiple planning variables to produce the most effective, survivable route for a mission.

HERO produces more realistic routes because it considers specific airframes and configurations, as well as taking into account the implications of force level tactics. HERO considers

the effects of multiple sorties, threat connectivity and alert status, environmental variables, and other route planning factors that are not or cannot be considered by techniques currently available. HERO can be modified to reflect current threat information, changes in mission configuration, or future user requirements. The dynamic nature of HERO (due to the use of object-oriented techniques), combined with the type and amount of information used in planning routes, allows HERO to suggest flyable, survivable routes that more closely approach the optimum path than if other planning methods had been used.

The paper discusses why the Air Force needs HERO, how HERO was developed, the lessons learned in its development, and its future potential for operational applications.

AGARD Conference Proceedings 499, Pub Sept 91, 13-16 May 1991

AIR FORCE TEST RANGE COMMAND & CONTROL SYSTEM REAL TIME DATA INTEGRATION & DISPLAY

Jeffrey T. Carlo, Scott M. Bolen, Capt Chris Belson, Rome Laboratory, Surveillance & Photonics Directorate

Abstract - Located at Tyndall Air Force Base (AFB) is one of the nation's premiere air-to-air combat training and weapons systems evaluation centers. Tyndall AFB is located near Panama City, Florida in the state's panhandle region. The Tyndall AFB Test Range covers an extensive area over the Gulf of Mexico and includes a smaller area over land. The US Air Force Air Defense Weapons Center (USAFADWC) currently maintains a manual range control system that coordinates the air operations over the Test Range. Operators of the 81st Range Control Squadron currently use analog radar scopes, voice communications, and overhead projectors as a means to gather and present critical information for analysis, evaluation, and control of aircraft. A requirement has been levied by the Tactical Air Command to upgrade the present command & control system to take advantage of modern data integration and display techniques. The new system would automatically gather, process, display, and record information from multiple sensors to form a complete unambiguous air & sea situation picture. Human observations from aircraft would also be reported to the new system for inclusion into the air situation data base. Rome Laboratory was selected as the lead Air Force agency to develop and construct the new range control system for the USAFADWC. The key technologies are data integration and information display processing. The range control system must be able to track multiple aircraft in a dense clutter environment and process data from multiple sensors automatically. Data

must be integrated and displayed in an accurate and timely fashion to operators for evaluation and use in real-time control of aircraft on the range. Rome Laboratory in cooperation with the 475th Weapons Evaluation Group at Tyndall AFB, and ASD at Eglin AFB has begun working on the design, development, and implementation of the new range control system. Completion of the new system is scheduled for March 1993. This paper will discuss the project status, architecture issues, and design considerations for implementing the range control system including the sensor data integration feature.

1991 Data Fusion Symposium Oct 91

AN AIR/LAND COMBAT SIMULATOR AND SCENARIO GENERATION ASSISTANT

Craig S. Anken, Rome Laboratory, Command, Control, & Communications Directorate

Abstract - This paper describes an air / land combat simulator and Scenario Generation Assistant (SGA) developed by Rome Laboratory (RL) and Advanced Decision Systems (ADS) Inc. The simulator was built using an environment consisting of an object-oriented language, EPIC, created specifically for writing simulations, an object-oriented cartographic Map Display System, and various other support tools.

SCS International Simulation Technology Proceedings 1991, Oct, 1991, Orlando, Florida

A DISTRIBUTED COOPERATION ENVIRONMENT FOR INTEGRATION AND TESTING OF EXPERT SYSTEMS.

Craig S. Anken, and Jeffrey D. Grimshaw, Rome Laboratory, Command, Control, & Communications Directorate

Abstract - Rome Laboratory has embarked on the development of a distributed environment that will support the testing of and cooperation between multiple decision aids (or expert systems). This environment is called the Advanced Artificial Intelligence Technology Testbed (AAITT). This paper discusses some of the previous approaches in this area that include both decentralized and centralized approaches, as well as the approach taken in the AAITT research.

World Congress on Expert Systems Proceedings, Dec. 1991, Orlando, Florida

A METHODOLOGY FOR AIR DEFENSE OPERATOR LEVEL C3 FUNCTIONAL DEVELOPMENT

David A. Griffith, Rome Laboratory, Command, Control, & Communications Directorate

Abstract - A Methodology has been determined and implemented in a laboratory environment to conduct the full spectrum of activity associated with person, hardware and software in-the-loop operator level functional development. A simulation has been developed to model the threat, sensors, communications and weapons systems associated with North American air defense. This simulation, combined with live real-time operational data, establishes a credible range of problems to be solved by the C3 operators. A network of high performance color graphic workstations has been configured to assist the surveillance, identification, weapons control, resource management, weather, communications, logistics and other operators in single or group decision making processes to present options to the battle commander for execution. A functional analysis has been completed which decomposed the human and computer processes to the lowest level functions. These functions can be recombined in a variety of ways and allocated across the workstations to evaluate and optimize operator and overall system performance. This paper presents the philosophy, approach and infrastructure of the laboratory environment. Following papers will provide detail on particular aspects of the process.

8th Annual Conference on Command and Control Decision Aids, June 1991, National Defense University, Ft. McNair, Washington, DC.

REQUIREMENTS CAPTURE, AUTOMATION AND UTILIZATION

Neil S. Marples, Rome Laboratory, Command, Control, & Communications Directorate

Abstract - This Rome Laboratory presentation describes the evolutionary parallel approach to develop the future Air Defense system to replace the existing Sector Operations Control Centers (SOCC). It documents the results of the recently completed ADI Functional Analysis which allotted particular operational functions to a recommended functional position and defines the inputs/outputs and processes required to accomplish the function. Requirements were captured using PSL/PSA while Network II.5 was used to identify and eliminate system bottlenecks. The paper also discusses the approach being followed to automate and implement the current SOCC functions. Initial emphasis has been placed on the fusion of data from multiple

types of sensors and the automation of the weapons control function using Nexpert expert system application.

8th Annual Conference on Command & Control Decision Aids, June 1991, National Defense University, Ft McNair, Washington D.C.

REQUIREMENTS CAPTURE, AUTOMATION AND UTILIZATION

Neil S. Marples, Rome Laboratory, Command, Control, & Communications Directorate

Abstract - This Rome Laboratory presentation describes the evolutionary parallel approach to develop the future Air Defense system to replace the existing Sector Operations Control Centers (SOCC). It documents the results of the recently completed ADI Functional Analysis which allotted particular operational functions to a recommended functional position and defines the inputs/outputs and processes required to accomplish the function. Requirements were captured using PSL/PSA while Network II.5 was used to identify and eliminate system bottlenecks. The paper also discusses the approach being followed to automate and improve the current SOCC functions. Initial emphasis has been placed on the fusion of data: from multiple types of sensors and the automation of the weapons control function using Nexpert expert system application.

8th Annual Conference on Command & Control Decision Aids, National Defense University, Ft. McNair, Washington D.C., 26-27 June 1991

BATTLE STAFF DECISION SUPPORT (BSDS)

Bill Brennan, Rome Laboratory, Command, Control, & Communications Directorate

Abstract - The overall intent of the decision aids in the Battle Staff Decision Support System (BSDS) is to stress the storage, analysis, and display of information to Battle Staff decision making personnel. The decision aids will support the direction of Battle Staff operations including the implementation of operational plans, support of DEA/US Customs tasks, fusing of intelligence data, planning and directing of engagement actions. The monitoring of sector resources and supporting the Battle Commander (BC) in sector maintenance functions will also require decision aids to assist in the implementation of these responsibilities. The design will be flexible enough to support the easy integration of expert systems at a later date.

8th Annual Conference on C² Decision Aids, Fort McNair, Virginia, 27 June 1991

FORCE LEVEL EXECUTION DEMONSTRATION

Thomas A. Clark, Georganne deWalder, Lt. Sally McCullers, Gerald C. Ruigrok, and Capt. Michael Shoop, Rome Laboratory, Command, Control, & Communications Directorate

Abstract - Rome Laboratory has undertaken a program to solve a variety of force level problems identified across the Tactical Air Force (TAF). The first major effort to address some of these problems is currently underway, called the Advanced Planning System (APS). The APS will provide automated support in constructing an Air Battle Plan (ABP) for the Combat Plans Division of the Tactical Air Control Center (TACC). The APS effort has successfully combined in-house and contractual work to produce several prototype versions of a fielded capability. Drawing upon the development accomplishments of the APS, Rome Laboratory will continue its activity at the force level in a follow-on effort entitled the Force Level Execution Demonstration.

The Force Level Execution Advanced Development Program will demonstrate automated support for the functions performed by the Combat Operations Division within the TACC. Leveraging the Open Systems Architecture, lessons learned, and baseline system processes of the APS, Rome Laboratory will develop and demonstrate an initial capability for the Duty Officers of the Combat Operations Division to perform ABP monitoring, status updating, and plan changing functions.

This paper will present the current status of the APS and the efforts to integrate it into the TAF's force level systems. Also, a brief description of the APS in-house/contractor relationship will be discussed. The remainder of the paper will concentrate on the activities of the Force Level Execution effort. This will include the establishment of an in-house Execution Testbed and will focus on the method of rapid prototyping as used in APS and how it can be extended to evolutionary prototypes for the Execution effort. It will be shown how the Research & Development community can effectively capture the true requirements of the users by producing evolutionary prototypes.

Automated Mission Planning Society, Crystal City, Virginia, July 1991

APPLYING GRAPHICAL TECHNIQUES TO TAF PLANNING

Earl C. LaBatt, Jr., Rome Laboratory, Command, Control, & Communications Directorate

Abstract - This paper reveals graphical techniques that help facilitate the transfer of information between a planning system and its operator. Rudimentary examples of how these techniques could be applied to the Tactical Air Force (TAF) planning domain have been developed in the areas of resource allocation, resource scheduling, force level planning, weapon engineering, and the effects of weather.

Expert systems, blackboards, and framebased systems are examples of some of the advanced concepts that are incorporated

into many decision aid applications. However, the user interface to these advanced applications resembles the manual process. What hinders these traditional text based interfaces is the inability to visualize cause and effect relationships within a system.

Part of the inability of these interfaces is a result of automating a paper process that was not designed to show calculation intensive relationships (relationships between complex variables). By combining graphical techniques with the interface, both the user and the machine can perform tasks that they excel at; man in understanding pictorial data and the machine in manipulating vast amounts of data.

Planning Desert Storm Symposium and Exhibition, Crystal City, Arlington, Virginia, 16 - 18 July 1991

D. INTELLIGENCE

RESULTS OF THE NEURAL NETWORK INVESTIGATION (NND)

Lee A. Uvanni, Rome Laboratory, Intelligence & Reconnaissance Directorate

Abstract - Rome Laboratory has designed and implemented a neural network based Automatic Target Recognition (ATR) system under contract F30602-89-C-0079 with Booz, Allen & Hamilton (BAH), Inc., of Arlington, Virginia. The system utilizes a combination of neural network paradigms and conventional image processing techniques in a parallel environment on the IE-2000 SUN 4 workstation at Rome Laboratory. The IE-2000 workstation was designed to assist the Air Force and DoD to derive the needs for image exploitation and image exploitation support for the late 1990's - year 2000 time frame. The IE-2000 consists of a developmental testbed and an applications testbed, both with the goal of solving real-world problems on real-world facilities for image exploitation. To fully exploit the parallel nature of neural networks, 18 Innos T800 transputers were utilized, in an attempt to provide a near-linear speed-up for each subsystem component implemented on them. The initial design contained three well-known neural network paradigms, each modified by BAH to some extent: the Selective Attention Neocognitron (SAN), the Binary Contour System/Feature Contour System (BCS/FCS), and Adaptive Resonance Theory 2 (ART-2), and one neural network designed by BAH called the Image Variance Exploitation Network (IVEN). Through rapid prototyping, the initial system evolved into a completely different final design, called the Neural Network Image Exploitation System (NNIES), where the final system consists of two basic components: the Double Variance (DV) layer and the Multiple Object Detection And Location System (MODALS). A rapid prototyping neural network CAD Tool, designed by Booz, Allen and Hamilton, was used to rapidly build and emulate the neural network paradigms. Evaluation of the completed ATR system included probability of detections and probability of false alarms among other measures.

Presented at the SPIE's 20th AIPR Workshop, Oct 1991

FUTURE UNMANNED AERIAL VEHICLE (UAV) RECONNAISSANCE FORCE STRUCTURE

Ronald B. Haynes, Rome Laboratory, Intelligence & Reconnaissance Directorate

Arnold H. Lanckton, Synectics Corporation

Abstract - The Air Force's Rome Laboratory is currently providing support to the Unmanned Aerial Vehicle Joint Program Office to provide a system architecture and specific interfaces which will allow for a total interoperable reconnaissance force structure. Rome Laboratory has contracted with the Synectics Corporation to assist in the development of this future reconnaissance force structure. The objective is to provide an Imagery Interoperability Architecture between any collection platform and any surface station. The implementation of this architecture will greatly reduce the number of redundant aerial vehicles and provide for deployment of the "common surface station." Under this program, standard data structures, interfaces, interoperable data links, and other interoperability issues are defined. This program is based upon several defined industry standards and parallels NATO and ongoing U.S. reconnaissance interoperability efforts. This paper discusses the overall architectural approach to achieving total reconnaissance interoperability, the current status of reconnaissance interoperability efforts, and several new standards that are being proposed such as: an image format specification, data link architectures, definition of common surface station components, and establishment of standard performance evaluation.

The Eighteenth Annual Association for Unmanned Vehicle Systems (AUVS) Technical Symposium and Exhibit, 13-15 Aug 1991, The Sheraton Washington Hotel, Washington DC.

ARC DIGITAL RASTER IMAGERY (ADRI) OVERVIEW

Mr. James A. Sieffert, Rome Laboratory, Intelligence & Reconnaissance Directorate

Abstract - HQ USAF has validated the Statement of Need (SON) 002-87 for a Precise Geopositioning Capability (PGC) to support intelligence applications and aircraft mission planning and targeting requirements on a worldwide basis. Rome Laboratory (formerly Rome Air Development Center - RADC) has developed the technology for precise geopositioning, but no worldwide digital databases are currently available. The Defense Mapping Agency (DMA) plans to begin production of a Digital Point Positioning Database (DPPDB) in the mid 1990s but it will not be worldwide and it will be classified (limited distribution). Based on this situation and the urgency of the AF requirement for mission planning support data, the Rome Laboratory/IRRP and HQ USAF/INTBR have jointly developed the concept of an Air Force Standard geocoded image product as a solution to the worldwide database problem to support mission planning applications within the Air Force. The Air Force chosen format for this product, ARC Digital Raster Imagery (ADRI), has been derived from the DMA ARC Digitized Raster Graphics (ADRG) standard product for maps and charts.

Second Air Force Spatial Data Conference 23 - 25 July, 1991,
Ann Arbor, Michigan.

ROME LABORATORY MAPPING CHARTING GEOPOSITIONING & IMAGERY PROGRAM

Joseph J. Palermo, Rome Laboratory, Intelligence & Recon-
naissance Directorate

Abstract - The paper discusses the Advanced Cartographic Ap-
plications Program, The Precise Geopositioning Program, the
development of Common Mapping Program (CMP) software

versions 1 and 2 via the Advanced Planning System Program
and the Air Force Mission Support System Program and the
Rome Laboratory expansion of the CMP versions 1 and 2 capa-
bilities to address the Air Force Command, Control and Intelli-
gence systems Mapping, Charting, Geopositioning and Imag-
ery support requirements (CMP 3). This evolution of CMP is
being addressed under two FY 1991 Rome Laboratory efforts,
the Air Force Geographic Information Handling System
(AFGIHS) and the Cartographic Support to Intelligence (CSI).
Future Rome Laboratory R & D in the area of automatic spatial
database update techniques is discussed.

Second Air Force Spatial Data Conference 23 - 25 July, 1991,
Ann Arbor, Michigan

E. ELECTROMAGNETICS

BLOCH-VECTOR MODEL FOR DRESSED STATES OF RESONANT RAMAN INTERACTION

M. S. Shahriar, Massachusetts Institute of Technology
P. R. Hemmer, Rome Laboratory, Electromagnetics & Reliability Directorate

Abstract - It is well known that the resonant Raman interaction optically pumps atoms into a nonabsorbing dressed-state.¹ When this state is long-lived compared to the optical Rabi frequencies and the decay rate of the intermediate state, many interesting dynamics arise. These dynamics are significant in applications such as Raman clock AC-Stark shifts, micro-wave phase sensitive optical absorption,² and Raman cooling. By using appropriate approximations, we show that these dynamics can be well described with a Bloch-vector model, which involves only ground-state populations and coherence. This ground-state Bloch-vector model resembles the Bloch-vector model of two-level system, but it has subtly different dynamics. Furthermore, we construct a novel dressed-state Bloch-vector that clearly shows the analogy between conventional optical pumping and coherent Raman trapping. In this model, one dressed state is a nonabsorbing state, and the other is an absorbing state. We use the dressed-state Bloch vector to show how Raman AC-Stark shift arises and how it depends on experimental parameters. We also show how the microwave phase-sensitive optical absorption can be quantitatively calculated in a simple way.

References

1. H. R. Gray, R. M. Whitley, and C. R. Stroud, Jr., Opt Lett 3,218 (1978).
2. M. S. Shahriar, P. R. Hemmer, XVIII QEC Technical Digest, 286 (1990).

Proceedings, 1991 Annual Meeting, Optical Society of America

MULTIGROUP- S_n BENCHMARK COMPARISON FOR ELECTRON TRANSPORT

B. D. Ganapol, University of Arizona, Department of Nuclear and Energy Engineering
S. Woolf, ARCON Corporation
J. C. Garth, Rome Laboratory, Electromagnetics & Reliability Directorate

Abstract - A set of benchmark calculations is described for the one-dimensional, multigroup discrete ordinates method as applied to electron transport. An analytical representation of the group scalar flux is obtained by application of the Fourier transform operator to the transport equation, expansion of the transformed equation in terms of the flux moments, and re-inversion of the transformed scalar flux moments. The results of S_n calculations, with both the linear discontinuous and diamond difference algorithms, are compared with benchmark calculations for a plane isotropic source of 200 keV electrons in infinite aluminum. The degree of scattering anisotropy is allowed to vary from isotropic to third-order anisotropic. Analysis of spatial discretization error is also discussed.

Conf. proceeding of American Nuclear Society, Topical Meeting on "Advances in Mathematics, Computations, and Reactor Physics," Apr. 28 - May 1, 1991, Pittsburgh, PA. Vol. 5, pages: 30.1 (9-1 to 9-11)

AMORPHOUS HYDROGENATED SILICON (a-Si:H) PHOTOVOLTAIC THIN FILMS DEPOSITED ONTO ULTRA-LOW DENSITY AEROGELS

S. P. Hotelling and E. P. Proni, Rome Laboratory, Surveillance & Photonics Directorate

Abstract - Amorphous Hydrogenated Silicon (a-Si:H) photovoltaic thin films have been deposited onto ultra low density (ULD) silica aerogel substrates using plasma enhanced chemical vapor deposition (PECVD). The techniques and results of ULD aerogel fabrication, surface treatment, thin film deposition and photovoltaic (PV) characterization are discussed. DC photocurrent and transient time of flight measurements were performed for the PV characterization, while ellipsometry, transmission optical spectrophotometry, scanning electron microscopy (SEM) and low magnification optical microscopy (x64) were used to obtain qualitative and quantitative surface morphology, microstructure and film thickness data. This research indicates that ULD aerogels may be used as substrates for dielectric and metallic thin films which have electrical, optical and mechanical properties comparable to films deposited onto conventional substrates such as glass, metals or plastics. These data taken together with the lightweight of the ULD aerogels may be of interest to the space based sensor community as a possible route to large, lightweight photonic sensors or PV arrays. These results thus indicate that ULD aerogels could be used as substrate materials for other thin films of interest to the PV community, for example, we have produced ultra lightweight reflective optics using this fusion of solgel and thin film technologies.

Materials Research Society Symposium Proceedings, Vol. 219, 30 Apr-3 May 91, Anaheim, California

RADIATION TESTING OF AlInAs/InGaAs AND GaAs/AlGaAs HBTs

S. B. Witmer, AT&T Bell Laboratories

S. Mittleman and D. Lehy, Rome Laboratory, Electromagnetics & Reliability Directorate

F. Ren, T. R. Fullowan, R. F. Kopt, C. R. Abernathy, S. J. Pearton, D. A. Humphrey, R. K. Montgomery, and P. R. Smith, AT&T Bell Laboratories

J. P. Kreskovsky and H. L. Grabin, Scientific Research Associates

Abstract - The radiation hardness of small geometry ($\sim 2 \times 4 \mu\text{m}^2$), state of the art AlInAs/InGaAs and GaAs/AlGaAs HBTs to ^{60}Co γ -rays has been investigated up to a dose of 100 MRad. The former devices showed a small change in I_c and gain for 20 MRad, with essentially no change in I_B . At 40 MRad, the gain of the devices had decreased to unity. By contrast, for GaAs/AlGaAs HBTs, the current gain actually increased up to a dose of 75 MRad. At 100 MRad, none of our devices were still operational. This was ascribed to degradation of the base-collector contact metallization (TiPtAu) and in particular to the presence of Au. Carbon- and beryllium-doped base devices showed the same response to ^{60}Co γ -ray doses. No long transient responses in either base or collector currents were observed during irradiation of the GaAs/AlGaAs devices with 120 nsec pulses of 10 MeV electrons at rates up to $2.7 \times 10^{10} \text{ Rad} \cdot \text{sec}^{-1}$. Results of a 2-dimensional modelling study suggest that both GaAs and InP based HBTs are relatively immune to damage by transient radiation effects up to a dose rate of $10^{11} \text{ Rad} \cdot \text{sec}^{-1}$, with GaAs based devices being more resistant to radiation than InP due to their shorter recombination times.

Materials Research Society, Fall Meeting, 1991

MELT AND HYDROTHERMAL GROWTH OF BISMUTH SILICATE

John J. Larkin, Meckie T. Harris, J. Emery Cormier, and R. N. Brown, Rome Laboratory, Electromagnetics & Reliability Directorate

A. F. Arrington, Park Mathematical Laboratory

Abstract - Bismuth Silicate (BSO) in the sillenite structure Bi_2SiO_5 , is a non-linear optical material which has many applications including four wave mixing and optical memories. As obtained by melt growth methods, at approximately 900°C , it is orange-brown in color and exhibits the photorefractive effect. Hydrothermal growth of this material has been accomplished at the Rome Laboratory hydrothermal facility. Spectra cut from crystals produced by this method are colorless, transparent, free of inclusions and strain and thus might provide

a starting point to engineer materials superior to commercial crystals produced by growth methods such as Czochralski (CZ) and gradient freeze. The hydrothermal process may permit "tailoring" of the properties of this material since growth takes place at a relatively low temperature and properties regarded as intrinsic in melt grown materials may be the result of a high temperature defect absent at the hydrothermal processing temperature ($\sim 400^\circ\text{C}$). Growth conditions will be described for this material. Some electrical and optical characteristics and chemical analyses will also be presented. Preliminary results on doped materials will be described.

Sagamore Conf, 10-12 Sep 91

SIMULATION OF ELECTROMAGNETIC ENVIRONMENTAL EFFECTS (E3) ON PHASED ARRAY RADAR PERFORMANCE USING THE GENERAL ELECTROMAGNETIC MODEL FOR THE ANALYSIS OF COMPLEX SYSTEMS (GEMACS)

Timothy W. Blocher, Rome Laboratory, Electromagnetics & Reliability Directorate

Abstract - The United States Air Force has been actively pursuing the development of phased array radar systems over the last several years for wide area C3I surveillance. The incentive for this technology development is the Air Force's requirement to detect smaller or "stealthy" targets in increasingly noisy environments. The capabilities of these phased array radars must include the generation of ultralow sidelobes and high radiated power in order to fulfill their mission. The strict radar specifications increase the sensitivity of the entire system, aircraft and subsystems, to electromagnetic environmental effects (E3). This paper illustrated the General Electromagnetic Model for the Analysis of Complex Systems (GEMACS) software as a tool for analyzing the response of a phased array radar to various electromagnetic environments. Other topics discussed included future modifications to GEMACS for phased array simulations and a comparison of run times on a DEC VAX 8650, a 33 MHz 386 based PC and the Alliant FX/80 parallel processor.

Proceedings 1991 Summer Computer Simulation Conference, July, 1991, Baltimore, MD

PHASED ARRAY SIMULATION WITH NON-ISOTROPIC AND ISOTROPIC RADIATING ELEMENTS

John C. Cleary, Rome Laboratory, Electromagnetics & Reliability Directorate

Michael J. Callahan, Robert J. Denton, Jr., Rome Laboratory, Surveillance & Photonics Directorate

Abstract - Computerized simulation of phased array performance provides a cost-effective means to investigate antenna designs before hardware is actually built. The inherent flexibility of the simulation approach and the ease of data entry allows an antenna designer to iterate through an antenna optimization design, evaluation, and redesign process fairly quickly, and many times if necessary.

A description of such a simulation tool and a brief demonstration of its capabilities will be presented in this paper. A generic corporate-fed phased array system with two different types of radiating elements will be simulated.

Antenna patterns for a generic phased array were generated at various scan angles (boresight and thirty degree E-plane and H-plane beam steering). Transmit/receive (T/R) module multiplicative amplitude (± 1 dB Gaussian distribution) errors and additive phase (± 5 degree uniform distribution) errors will be incorporated into the simulation. The quantization effects of four bit phase shifters were included. The array factor at the above scan angles will be generated for the antenna and then multiplied by the appropriate element pattern in each case to produce far field patterns for the antenna. This was demonstrated for two representative types of radiating elements, the first one being a microstrip patch and the second one a thin strip dipole. The patterns were compared to those obtained with isotropic radiating elements (the array factor) to demonstrate the importance of having the capability to include element pattern effects in the simulation runs.

Proceedings 1991 Summer Computer Simulation Conference, July, 1991, Baltimore, MD

MODELING ELECTROMAGNETIC ENVIRONMENTAL EFFECTS IN MULTI-PORT MMICS

Daniel J. Kenneally, Timothy W. Blocher, Rome Laboratory, Electromagnetics & Reliability Directorate

Abstract - Monolithic microwave integrated circuits (MMICs) are currently of interest for many aerospace radar applications. Active aperture, phased array antennas use MMICs in trans-

mit/receive (T/R) modules which are integral parts of the array face. In addition to the digital circuits used for beam synthesis and steering, the modules also use linear circuits for both transmit and receive signal enhancements. For example, there are low noise preamplifier and power amplifier MMICs in modules covering L-band up to X-band frequencies.

These circuits and modules must operate and survive in wideband, electromagnetic spectral environments that are intense, degrading and sometimes, damaging. Ambient signals from these environments seriously effect the performance and reliability of susceptible MMICs by causing functional upset and waveform distortion. These and other induced effects reduce the array performance and, subsequently, the radar effectiveness.

MMIC device susceptibility to the unwanted signals is determined during CAD usually by simulating test ambient signals added to the desired signals at the input signal port and then computing the contaminated, degraded response at the output signal port. This conventional way of characterizing the electromagnetic susceptibility of a device is scalar and involves only two ports, input and output. In contrast, MMICs are typically multiport devices with several RF, digital, ground and bipolar DC bias ports and would seem to warrant a vector characterization.

This paper presents a computer simulation methodology for determining electromagnetic environmental effects' susceptibility in multiport MMICS. A LIBRA* circuit simulator computes nonlinear (susceptibility) responses in models of contemporary low noise amplifiers and power amplifiers. Circuit drivers which simulate the environmental signals are modeled as Thevenin and Norton equivalent sources at the accessible MMIC ports, including the signal, bias and ground ports.

The nonlinear models simulate the mixing of desired and undesired signals present at the input port or at any other port or combination of ports, and crosscoupling those contaminated signals to the output port or to any other port or combination of ports. These include signal, bias and ground ports in power dependent, combinations to form a matrix or vector "susceptibility" function similar to a linear transfer function. This matrix of effects includes susceptibility data from the accessible ports (or pin pairs) for most MMIC designs used in radar T/R modules. The resulting intermodulation and crossmodulation vectors are described.

Proceedings 1991 Government Microcircuit Applications Conference (GOMAC '91), November, 1991, Orlando, Florida

*LIBRA is a registered trademark of Elisof Inc., 5601 Lindero Canyon Road, Westlake Village, CA 91362-4020

NON INVASIVE MEASUREMENT OF HPM SHIELDING EFFECTIVENESS

J. P. Quine, K. E. Larson, and G. A. Wellence, Rome Research Corporation

A. J. Pesta, M. F. Seifert, Rome Laboratory, Electromagnetics & Reliability Directorate

Abstract - This paper describes a simple and practical method for measuring HPM Shielding Effectiveness (SE) without the use of internal probes. The method can be implemented if the enclosure has at least one hole on its outer surface that is larger than approximately one quarter wavelength in diameter, the limitation being measurement sensitivity. Leakage holes are measured two at a time, and can be connected to a network analyzer by standard waveguide to coaxial line transitions butted against the outside surface of the enclosure. The magnitudes of the scattering parameters S_{11} , S_{22} , and S_{12} are measured, and used to calculate SE. Good agreement was obtained between the scattering method and the conventional method which employs internal and external B-dot probes.

In this preliminary proof-of-principle experiment, choke joints were employed with the waveguide to coaxial line transitions to insure stable contact with the relatively flat enclosure surface. Thin-sheet absorbers can also be employed for stable contact. Practical methods for obtaining reliable contact with curved enclosure surfaces and for coupling to larger holes will also be discussed.

1991 IEEE International Symposium on EMC, Aug 91, Cherry Hill, NJ

CONDUCTED SUSCEPTIBILITY TEST TECHNIQUES FOR ADVANCED TECHNOLOGY INTEGRATED CIRCUITS

Michael F. Seifert, Rome Laboratory, Electromagnetics & Reliability Directorate

John K. Daher and John P. Rohrbaugh, Georgia Tech Research Institute

Abstract - In general, conducted susceptibility tests are performed on IC's to determine the upset and/or damage thresholds at specified pins and also to determine the upset/damage mechanisms that occur. This paper will focus on test techniques for characterizing IC upset thresholds and mechanisms. Upset

mechanisms include RF rectification, stuck-at or latch-up conditions, and timing or phase shifts. Upset thresholds are needed to determine circuit hardening requirements. The basic conducted susceptibility test method for both digital and analog devices involves: (1) summing an interference signal with a functional test signal and coupling these signals to the pin-under-test in a controlled manner and (2) monitoring for changes in functional performance as the interference power is increased.

Various signal combiner networks are required to sum the interference and functional test signals. Key characteristics of signal combiners are high isolation between input ports, wide bandwidth, insensitivity to varying output load impedance, low loss, minimal propagation delay, and high power handling capability. Combiner networks which have been successfully employed in the past include dc bias tees, dual quadrature hybrids, diplexers, and summing op amp combiners.

The definition of upset varies depending on the device-under-test, the device application, and the performance parameter(s) of concern. For digital devices, the selection of upset criteria is normally straightforward. Logic state changes and timing variations are common examples. For analog devices, however, the selection of upset criteria is not as clear and is frequently application dependent. Examples of upset criteria used with analog devices include deviations in critical performance parameters such as gain, noise figure, input impedance, compression point, and third-order intercept point.

Susceptibility measurements are performed at input, output and power/bias pins. In general, input pins (such as clock or analog/digital control pins) are the most susceptible. Measurements are usually performed on packaged IC's. However, measurements can also be performed at the wafer or module levels of development provided that controlled impedance paths are maintained to the device pin- or pad-under-test and bias conditions are similar at each level of fabrication. In many cases, package de-embedding can be used to either remove the effects of the device package or add the effects of the package depending on what level of fabrication measurements are performed.

General descriptions of conducted susceptibility test techniques and procedures were presented that are applicable to digital (including VLSI) and analog (including MMIC) IC's. Emphasis in the paper was tailored to Aerospace applications.

Proceedings EMC Expo, 1991, June, 1991, Orlando, FL

MINIATURE ELECTROMAGNETIC FIELD SENSORS

John P. Rohrbaugh, and Ron C. Alford, Georgia Tech Institute
Rolfe E. Ferrara, Rome Laboratory, Electromagnetics & Reliability Directorate

Abstract - This paper describes the results of a program to assess the feasibility of developing a miniature electromagnetic (EM) field monitoring system, referred to as an Electromagnetic Performance Monitor (EMPM). The EMPM would be used to monitor peak EM field strength over a broad frequency range (300 MHz to 18 GHz) in flight and ground tests of aircraft. Microwave interference in this frequency band can cause upset or damage to sensitive silicon or Gallium Arsenide electronics.

The EMPM, once developed, would consist of miniature 3-axis resistive dipole antennas with built-in detectors, a summing preamplifier, an analog-to-digital converter, a fiber optic digital data transmitter, and a fiber optic power receiver less than 2 cubic inches in volume. A data processing module (EMPM Signal Processing Module) capable of receiving, preprocessing, and storing information from four antennas, occupying less than 2 cubic inches (not including batteries) was also determined to be feasible. The EMPM Signal Processing Module would also include a laser used to provide power to the four antennas. The EMPM could be operated alone or in conjunction with RADC's (now Rome Laboratory's) Time Stress Measurement Device (TSMD). The TSMD is designed to monitor environmental stresses on or within an aircraft and provide a real time stamp of the occurrence of the environmental stresses. The TSMD is not designed to monitor high frequency electromagnetic interference.

Proceedings 1991 Government Microcircuit Applications Conference (GOMAC-91), November, 1991, Orlando, FL

INFRARED/MICROWAVE CORRELATION MEASUREMENTS

J. D. Norgard, D. W. Metzger, and M. Sega, University of Colorado

J. C. Cleary, and M. F. Seifert, Rome Laboratory, Electromagnetics & Reliability Directorate

Abstract - An Infrared (IR) measurement technique for determining two-dimensional (2D) and three-dimensional (3D) microwave field distributions is presented. This IR technique is used to verify predictions made by various numerical electromagnetic (EM) codes. The experimental technique is based on IR thermal measurements of the Joule heating induced in a

lossy dielectric or resistive material used as a calibrated IR detection screen when microwave energy is absorbed by the screen. An IR scanning system records the thermal radiation from the screen. The intensity of the microwave field is related to variations in the surface temperature distribution. The detection screen material is of a thin, planar construction and, thus, produces a 2D map of the microwave field. By moving the screen along the normal to its plane, samples of the 3D field are obtained. This experimental approach has been applied to several 2D and 3D scattering and coupling problems. Comparisons are made between the theoretical and experimental results for various hollow slit cylinder configurations. The advantages, disadvantages and limitations of this IR thermal technique for validation of EM theoretical predictions are discussed.

Proceedings, 1991 Society of Photo-Optical Instrumentation Engineers (SPIE) International Symposium, 26 Jul 91, San Diego, CA

ANTENNA MEASUREMENTS FOR ADVANCED AIRBORNE T/R MODULE ARRAYS

John S. DeRosa, Rome Laboratory, Electromagnetics & Reliability Directorate

Abstract - Advanced airborne surveillance radar antennas will consist of precision arrays of thousands of individual T/R modules and radiating elements. Brassboard arrays in both conformal and nonconformal configurations on the aircraft are currently being developed. In order to provide adequate clutter rejection for our future needs, the antenna must exhibit ultra low sidelobe performance as mounted on the aircraft platform. The detrimental effects of the aircraft structure on the antenna performance becomes increasingly important for ultra low sidelobe antennas. On-aircraft measurements for these antennas represents a major challenge to the antenna measurement community. Large aperture, high fidelity antenna test facilities will be required which have characteristics which challenge the current state-of-the-art. In this paper, the characteristics of these facilities are discussed and general requirements for T/R module array testing are considered. An antenna measurement program which was conducted at the Rome Laboratory on an experimental 104 element, X-band T/R module array mounted on top of a 1/10th scale RC-135 aircraft is also described.

Proceedings of the 1991 Antenna Measurements Techniques Association, 7-11 Oct 91, Boulder, CO.

MOLECULAR ENGINEERING BY LASER CHEMICAL VAPOR DEPOSITION OF A NONLINEAR INTERFACE SWITCH

J. Chaiken, Syracuse University

J. Osman, Rome Laboratory, Surveillance & Photonics Directorate

Abstract - Devices which have as inputs two light pulses and output a third pulse depending on whether one or both of the two inputs is present are *optical switches*. Although a wide variety of design criteria must also be met to allow construction of large scale optical computers and switching networks, discrete optical switches and smaller scale devices constructed using them as components, e.g. multiplexers and spatial light modulators, would find immediate application in optical computing and communications. Originally proposed by Kaplan in 1972, proof of principle research for the class of optical switches known as *nonlinear interfaces* was completed over the last several years. Development of practical devices based on those principles currently involves designing extremely specialized materials using thin film inorganic / organometallic photorefractive materials. I will first give a little background and then explain how the switches work. I will then describe the current state of our research and give a near term prognosis.

Proceedings, 4th Chemical Congress of North America, August 26, 1991

AN OPTICAL MEMORY ELEMENT FOR AN INTEGRATED OPTICAL COMPUTER

M. Parker, S. Libby, Rome Laboratory, Surveillance & Photonics Directorate

P. Swanson, Cornell University, Photonics Center

Abstract - The design and test results of an integrable optical RS flip flop is presented for use as an optical memory element in an optical processor. Logic and memory devices consisting of lasers, waveguides, saturable absorbers and detectors have been integrated onto a wafer of GaAs AlGaAs multiquantum well heterostructure. The laser based memory element to be integrated uses laser quenching for the *reset* operation and the saturation of absorption in multiquantum well material for the *set* operation. The monolithic development of this device should serve as a key component for optical computing in future Air Force technology.

Proceedings, OSA OPTCON 91, Nov 3-8, 1991, San Jose

SPOT ARRAY GENERATION AND OPTICAL INTERCONNECTION USING BIREFRINGENT CRYSTALS

T. Stone, Rutgers University

J. Battiatto, Rome Laboratory, Surveillance & Photonics Directorate

Abstract - The use of cascaded slabs of birefringent materials is investigated for spot array generation and optical interconnects. Experimental results and performance limitations are presented. Cascaded slabs of birefringent crystals or prisms may be used to generate arrays of spots or to interconnect emitting, receiving, or modulating devices. The input light for each slab can be unpolarized, circularly polarized, or polarized linearly at 45° to the reference plane which is defined as a plane which contains both the ordinary and extraordinary rays. The output light for a given stage is then resolved into two linearly polarized orthogonal component polarizations. The crystal in the next stage is rotated by 45° so that each linearly polarized wave from the output of the previous stage has components parallel and perpendicular to the new reference plane. This process may be repeated with each stage doubling the number of spots to be formed. The thickness of each crystal slab stage controls the displacement of the spots it creates. All the stages may be optically contacted or cemented to greatly reduce reflections and scatter. This technique may be particularly useful for sub-array generation where a sparse regular array of beams (e.g. as produced by a microlaser array with relatively wide element spacings) can be transformed into a much denser spot array with approximately the same lateral extent.

Proceedings, OSA OPTCON 91, Nov 3-8, 1991, San Jose

OFF-AXIS BINARY OPTIC REFLECTIVE FOCUSING GRATINGS FOR FREE SPACE OPTICAL INTERCONNECTS

D. Mikolas, H. Craighead, and D. Brown, Cornell University

E. Haas, D. Honey, Rome Laboratory, Surveillance & Photonics Directorate

Abstract - We present results of the design, fabrication, performance prediction and testing of high quality off axis binary optic reflective focusing gratings for interwafer optical interconnects. Free space optical interconnects can provide the fast, highly parallel data channels needed for interwafer communication. High quality optical elements enable the use of high density source/detector arrays. We have fabricated and tested multilevel reflective gratings in Si. We present the theoretical and experimental performance of reflective off axis binary optical elements, and a scenario for the integration of these de-

vices into current hybrid wafer-scale computers. $\lambda/2$ and $\lambda/4$ constant phase surfaces are computed, and then approximated by short line segments which form polygons. We will discuss the methods of dealing with patterning curved grating structures using what are inherently rectilinear lithography tools. We will also discuss the sensitivity to overlay misalignment between the phase surfaces and other unavoidable fabrication errors. Measured radiation patterns for fabricated binary optic reflective focusing gratings are compared to the calculated patterns. Possible integration into current hybrid-scale packaging schemes are discussed.

Proceedings, OSA OPTCON 91, Nov 3-8, 1991, San Jose

MEASUREMENTS OF LIGHT EMISSION DURING THE CHARGE-2 ELECTRON BEAM EXPERIMENT

Neil B. Myers, Rome Laboratory, Electromagnetics & Reliability Directorate
W. John Raitt, Physics Department, Utah State University

Abstract - The CHARGE-2 electron beam sounding rocket experiment carried two photometers capable of measuring 3914 Å light emission. One photometer viewed the region through which the electron beam propagated away from the rocket. The second photometer was located opposite to the electron gun aperture and viewed along the vehicle skin to observe light emission in the sheath due to electrons accelerated by the vehicle potential. Photometer measurements were obtained during electron emission from 115 km to 262 km. The release of cold neutral nitrogen gas increased the light emission in both the beam and the sheath often by more than an order of magnitude. The light emission measured by the beam photometer was linearly dependent on the beam current, indicating that no beamplasma discharge occurred. The sheath photometer measurements decreased as the flight time increased, showing a presumed dependence on the outgassing from the rocket.

American Geophysical Union Spring Meeting, Baltimore, MD, May 31, 1991

RECENT PROGRESS TOWARDS DEVELOPING A SUPERCONDUCTING MAGNET FOR MAGNETIC BALANCE SYSTEMS USING HIGH-TC CERAMIC SUPERCONDUCTORS.

R. J. Andrews, Rome Laboratory, Electromagnetics & Reliability Directorate

Abstract - Chemical Spray pyrolysis has the potential to synthesize good quality large area films on irregularly shaped substrate at extremely low cost. In this process soluble salts, (nitrates, acetates, or oxylates), of the metallic precursors are dissolved in solution and sprayed onto a heated substrate. The surface residue from the spray contains salt complexes which, after thermal cycling, are then converted into metal oxides. In the first phase of this research Ba-Ca-Cu-O films were prepared and thallous oxides were diffused into the films to form superconducting phases of the Tl-Ba-Ca-Cu-O system. In that research it was found that glycerol could be used as a chemical binder in the solution to tie all three metallic salts into a single chemical complex and later fused into microcrystallites. Although these initial films were reproducible, (one exhibited a phase transition ($T_c(\rho=0)$) of 111.5K), and demonstrated preferential c-axis orientation in the plane of the substrate, phase stability and low critical current densities remain a problem.

This research will focus on resolving these problems by examining experimental methods to improve the process, from the perspectives of solution chemistry, deposition parameters, thermal conversion and annealing. Materials issues related to the design and construction of a "flexible" superconducting tape will also be discussed. Finally, the relative advantages of using other ceramic materials, such as the highly anisotropic Bi-Sr-Pb-Ca-Cu-O or $(Nd,Ce)_2Cu_{4-x}$ systems, which can be sprayed and thermally cycled in a single process step and recently discovered $(Ba,K)BiO_3$ system, which has superconducting properties but lower temperature phase transitions, ($T_c(\rho=0) \leq 30K$), will also be contrasted and assessed.

International Symposium on Magnetic Suspension Technology, NASA Langley Research Center, Hampton, Va. 23665 August 19-23, 1991

PROCESSING- AND RADIATION-PRODUCED DEFECTS IN InP SOLAR CELLS

P. J. Drevinsky and C. E. Cafer, Rome Laboratory, Electromagnetics & Reliability Directorate
C. J. Keavney, Spire Corporation

Abstract - This report describes the detection, characterization, and determination of the stability of processing- and radiation-produced defects in p-type indium phosphide by means of Deep Level Transient Spectroscopy (DLTS). Samples consisted of chips of solar cells and portions of wafers from which solar cells were fabricated. Irradiations with 1-MeV electrons were at room temperature. Comparison of defects detected in cells with junctions fabricated by ion implantation and by epitaxial techniques reveals major differences. For samples with implanted

junctions, prominent defects are present in as-fabricated cells and are hole traps at $E_v + 0.46$ eV and $+ 0.49$ eV. Upon electron irradiation, the concentration of the shallower level decreases and that of the deeper one increases. Samples with epitaxial junctions, however, showed no DLTS peaks before irradiation. After 1-MeV electron irradiation, two dominant defects are observed along with two deeper levels in smaller concentrations. The dominant defects have activation energies of $E_v + 0.30$ eV and $+ 0.38$ eV. No minority carrier traps were detected. Studies were mainly on samples with epitaxial junctions. The carrier removal rate after a fluence of $1.0E+16$ electrons/cm² was 3.4. Effects of thermal and injection anneal on DLTS samples and companion solar cells will be presented. Defects were correlated with critical parameters of solar cells.

Third International Conference on Indium Phosphide and Related Materials, April 1991, Cardiff, Wales, U.K.

EVIDENCE FOR PHASE SEPARATION IN Bi-Ca-Sr-Cu-O SYSTEM

Osama H. El-Bayoumi, Rome Laboratory, Electromagnetics & Reliability Directorate

Abstract - A glass-crystallization route has been widely used to fabricate superconductors in the Bi-Ca-Sr-Cu-O system. The microstructure of a glass is important because it affects the nucleation and crystallization processes during the crystallization of a glass. Glasses were prepared by mixing appropriate powders, melting and splash quenching. The resulting glass showed phase separation by XRD, DTA, and TEM. The results of a detailed study of phase separation will be presented. In addition, the effect of phase separation on crystallization will also be discussed.

American Ceramic Society Annual Meeting, Cincinnati, OH, April 28-May 2, 1991

MICROSTRUCTURE DEVELOPMENT OF Bi-BASED HIGH T_c SUPERCONDUCTORS FROM A GLASS CERAMIC ROUTE

Osama H. El-Bayoumi, Rome Laboratory, Electromagnetics & Reliability Directorate

Abstract - The fabrication of high T_c materials in the Bi-Ca-Sr-Cu-O system with oriented microstructure via glass-ceramic route is limited by inhomogeneities in the melt-quenches glasses due to phase separation and unmelted CaO-rich phase. Homogeneous glass is necessary for controlled nucleation and unidirectional crystallization of a desired phase. In this report, we present our recent efforts in the Pb-doped Bi-Ca-Sr-Cu-O

system w.r.t. homogeneity of the glass, phase development and microstructure control

American Ceramic Society Annual Meeting, Cincinnati, OH, April 28-May 2, 1991

SURFACE IMPEDANCE MEASUREMENTS OF THIN FILM SUPERCONDUCTORS AT MILLIMETER WAVE FREQUENCIES

J. S. Derov, C. Chin, A. Drehman, and R. J. Andrews, Rome Laboratory, Electromagnetics & Reliability Directorate
E. Cohen, ARCON Corporation

Abstract - The surface impedance of thin superconducting films has been measured at millimeter wavelengths. The copper cavities were used to measure the temperature dependence of the superconducting thin films at 35, 52, and 56 GHz and niobium cavities at the same frequencies were used to measure the frequency dependence at 4 K. The 4 K measurement was used to establish a lower limit for the surface resistance of the temperature dependence. A f^2 model was used to fit the frequency dependence of the measurements. Superconducting films varying in thickness from 1.7 to 0.3 microns were measured. When the film thickness and the penetration depth are on the same order magnitude radiation leakage occurs through the sample. This causes an increase in the measured value of the surface resistance. The measured surface resistance data has been corrected for radiation loss. This data will be presented and discussed, along with the surface reactance measurements made at 35 GHz.

* This work supported by the RADC Laboratory Director's Fund.

American Physical Society Meeting, March 1991, Cincinnati Ohio

Y-Ba-Cu-O S-N-S JUNCTIONS

A. J. Drehman, B. L. MacDonald and R. J. Andrews, Rome Laboratory, Electromagnetics & Reliability Directorate
P.M. Tedrow*, Francis Bitter National Magnet Laboratory.

Abstract - In order to make practical SQUID's and related circuitry, it is necessary to be able to make Josephson weak links in a reproducible manner without having to rely on substrate defects. We have made trilayer S-I-S structures which exhibit a high resistivity ($> 10^9$ ohm-cm at 200 K) for a 20 to 200 nm insulating layer. By utilizing an ion milled via through the insulator, the superconducting layers are connected with a thin film of

gold to form an S-N-S junction. This technique permits the study of the insulating layer's quality prior to device fabrication. These junctions support a supercurrent through the gold. The electrical properties of these junctions will be presented.

*Air Force University Research Fellow at Rome Air Development Center.

American Physical Society Meeting, March 1991, Cincinnati, Ohio

PERFORMANCE MEASUREMENTS OF AN ACTIVE APERTURE PHASED ARRAY ANTENNA

Livio D. Poles, Edward Martin, and James Kenney, Rome Laboratory, Electromagnetics & Reliability Directorate

Abstract - Transmit and receive modules (T/R) utilizing GaAs monolithic microwave integrated circuit (MMIC) technology for amplifiers, attenuators, and phase shifters are becoming integral components for a new generation of radars. These components, when used on the aperture of low sidelobe electronically steerable antennas, require careful alignment and calibration at multiple stages along the RF signal path. This paper describes the calibration techniques used to measure the performance of an active 64 element S-band phased array antenna that employs TR modules at every element. RF component performance and phased array sidelobe characteristics are presented and discussed.

Proceedings of the fourteenth Antenna Measurement Technique Association, October 1991, Boulder, Colorado

INTEGRATED C3I OPTICAL PROCESSOR

Robert L. Kaminski, Rome Laboratory, Command, Control, & Communications Directorate

Abstract - This paper will discuss the integration of optical/optoelectronic processing functions capable of operating on multiple C3I signals/data such as, surveillance, Electronic Support Measures (ESM), communication, intelligence, imaging. The processor will operate on a broad spectrum of signals (HF to IR) provided by multispectral passive sensors, bistatic ESM, IR cameras, and multi-mode/band radar. The developed processor will support processing requirements for multifunction airborne surveillance and advanced space sensor systems. In addition, this paper will examine optical processors for adaptive null steering, adaptive beamforming, signal excision, and general purpose computation.

The design of this processor will be based on utilizing the massive parallelism provided by optical interconnects and switches in addition to all optical memory for high volume but small size. Rapid access and interconnection of memory to the processor and its attendant effect will be critical to the design. The processor, as envisioned, will be capable of delivering greater than one trillion operations such as content addressable memory comparisons, per second throughput and will utilize three-dimensional optical memory and optical interconnects in the implementation. The processor will be hybrid, marrying digital electronic modules enhanced by optical interconnects, optical switches and optical memory to achieve a highly interactive, rapidly reconfigurable machine. This high performance optical processor will be able to integrate the following C3I systems: Automatic Signal Identification, Null Steering in high density jammer environments, Low Observable Target Signals Processing, and Imagery.

"Integrated C3I Optical Processor," Robert L. Kaminski, July 1991, Proceedings of the International Society for Optical Engineering, Volume 1564

F. PHOTONICS

OPTICAL PHASE CONJUGATION WITH A SODIUM RAMAN LASER

J. Donoghue, Tufts University

J. S. Kane and P. R. Hemmer, Rome Laboratory, Electromagnetics & Reliability Directorate

Abstract - Recently, there has been increased interest in the use of resonant atomic systems for performing optical-wavefront conjugation. This interest has arisen because resonant systems are inherently fast, with response times in the nanosecond range. However, resonant systems tend to have lower efficiencies and greater optical power requirements than do photorefractive crystals, such as BaTiO₃. In this paper, we explore the possibility of using a highly efficient Raman laser in a sodium vapor cell to obtain efficient phase conjugation at greatly reduced optical power densities. In this demonstration we use a self-pumped (linear cavity) conjugator for simplicity. With this setup, we have achieved phase conjugate reflectivities of 2% with input powers of only 20 W/cm². This is only 2% of the optical power density previously reported to obtain comparable reflectivity with a self-pumped scheme in sodium vapor.

Proceedings, 1991 Annual Meeting, Optical Society of America

IMPACT OF SECONDARY CENTERS ON THE WAVELENGTH DEPENDENCE OF THE PHOTOREFRACTIVE EFFECT IN BARIUM TITANATE

George A. Brost, Rome Laboratory, Surveillance & Photonics Directorate

Abstract - We discuss the impact of secondary centers on the wavelength dependence of the photorefractive effect in BaTiO₃. The presence of those traps can lead to such results as a wavelength dependent effective empty trap concentration.

Conference on Lasers & Electro Optics (CLEO), 12-17 May '91 in Baltimore, MD, 1991 *Technical Digest Series Volume 10, Conference Edition*.

PHOTOREFRACTIVE DEAMPLIFICATION FOR ARTIFACT NOISE REDUCTION

Jehad Khoury and Mark Cronin-Golomb, Electro Optics Technology Center, Tufts University

Charles L. Woods, Rome Laboratory, Electromagnetics & Reliability Directorate

Abstract - Many optical image processing operations such as edge enhancement may be performed by suitable linear spatial filters. A broader class of operations is made available by extending this technique to nonlinear filters. An example of this is the use of a logarithmic nonlinearity for conversion of multiplicative to additive noise. In this work, we demonstrate that phase preserving thresholding in the Fourier plane which linearly transmits signals above a certain intensity, reduces additive signal dependent noise, such as noise from coherent artifacts, image defects and uniformity noise.

Published in OSA Topical Meeting on Photorefractive Materials and Devices Conf. Proceedings, July 1991 (Conf. Beverly, MA)

MULTIPLICATIVE TO ADDITIVE SPECKLE NOISE CONVERSION VIA PHASE CANCELLATION WITH PHOTOREFRACTIVE PHASE CONJUGATORS

J. A. Khoury and M. Cronin-Golomb, Tufts University, Electro Optics Technology Center

A. M. Biernacki, Charles Stark Draper Laboratory, Inc.

Charles L. Woods, Rome Laboratory, Electromagnetics & Reliability Directorate

Abstract - A new technique for dealing with multiplicative complex speckle noise on coherently imaged amplitude objects is presented. This technique uses phase cancellation via quadratic nonlinearity to convert the multiplicative noise into additive noise on the Fourier spectrum. This is accomplished using a noisy image as the pump and a clean planar reference beam as the probe in a degenerate four-wave mixing phase conjugator. The counterpropagating pump is provided by the phase conjugate of the noisy image from a total internal reflection self-pumped phase conjugator whose input is the noisy image transmitted through the first crystal. The phase conjugate output is read off from the clean probe; the remaining noise on the Fourier spectrum of the output image is additive and can be removed by nonlinear filtering in the Fourier plane.

Published in OSA Topical Meeting on Photorefractive Materials and Devices Conf. Proceeding, July 1991 (Conf. Beverly, MA)

FORCES ON THREE-LEVEL ATOMS INCLUDING TRAPPED-STATE CONTRIBUTION

M. S. Shahriar, Massachusetts Institute of Technology, Research Laboratory of Electronics

P. R. Hemmer, Rome Laboratory, Electromagnetics & Reliability Directorate

N. P. Bigelow and M. G. Prentiss, AT&T Bell Laboratories

Abstract - In this paper we present a new calculation of the force on a stationary three-level atom in a bichromatic standing-wave light field. Contrary to other theoretical treatments, which ignore optical pumping into the trapped state, we find that a stationary atom experiences no force when there is no difference frequency detuning (i.e., when $\Delta = 0$). However, when there is a nonzero differential detuning ($\Delta \neq 0$) there can be force components that vary in both the wavelength of the optical fields and their beat wavelength. This stimulated force can be much larger than the maximum spontaneous force associated with this system. To obtain a simple physical interpretation of this force, the problem is treated in a basis that is formed from symmetric $|+\rangle$ and antisymmetric $|-\rangle$ linear combinations of the atomic ground states.

Proceedings, 1991 Annual Meeting, Optical Society of America

HIGH-PERFORMANCE OPTICAL DISK SYSTEM FOR TACTICAL APPLICATIONS

Mr. Fred Haritatos, Rome Laboratory, Intelligence & Reconnaissance Directorate

Abstract - Optical disk storage offers several advantages which are critical to tactical military applications. These advantages include: high data storage capacity, immunity to head crashes and data loss due to vibration and shock, fast random data access, removable recording media and reduced susceptibility to nuclear radiation effects. In order to fully develop and demonstrate these inherent features, an R&D program was initiated entitled: Tactical Optical Disk System (TODS). Under this program, a suite of three Advanced Development Models (ADM) will be developed, flight tested and transitioned to the Air Force. A rewritable storage material, based on magneto-optics (M-O) technology, was selected since it provides a user with the ability to read, write and erase digital data. Currently, the TODS equipment suite will use both 5.25 and 14-inch diameter recording material on a glass substrate for better performance under military conditions.

SPIE Conference on Optical Data Storage '91, Vol. 1499, 25-27 Feb 91.

THE BERYLLIUM SCATTER ANALYSIS PROGRAM

J. L. Behlau, E. M. Granger, J.J. Hannon and M. Baumler, Eastman Kodak Company, Federal Systems Division

J. F. Reilly, Rome Laboratory, Surveillance & Photonics Directorate

Abstract - Many groups today are researching the characteristics of beryllium, in an attempt to find ways of producing high quality (low scatter) stable beryllium optics. This paper discusses a two part study in which 1) an attempt is being made to determine the best, raw beryllium mixture and preparation, machining and polishing processes, test and analysis methods, and 2) a proposed model for the prediction of scatter from beryllium surfaces (based on a knowledge of surface and subsurface interactions with incident wavelengths) will be refined against empirical data. We discuss design of the experiment, the model, and some of the early results.

218 / SPIE Vol. 1530 Optical Scatter: Applications, Measurement, and Theory (1991)

NON-LINEAR OPTICAL BEHAVIOR OF GLASSES AND QUANTUM CLUSTERS IN GLASS

Osama H. El-Bayoumi, Rome Laboratory, Electromagnetics & Reliability Directorate

Abstract - Optical non-linear behavior in solids results from a variety of processes which affect their local polarizability. This paper reviews 3 major sources of non-linear optical behavior based on the 3rd order susceptibility in glasses and glasses containing semiconductor quantum clusters, and one source of electro-optical behavior based on the second order susceptibility. Recent measurements on silica-germania glasses which support the formation of permanent optical gratings, on heavy cation and anion glasses with large Kerr effect, on doped glasses with notable two photon absorption and on semiconductor quantum dots in glass are reported. The mechanisms of optical non-linearity and the relative change in the refractive index and absorption coefficient associated with each process are discussed.

5th International Conference On Ultrastructure Processing 17-21 February 1991, Orlando, Florida

AN APPLICATION OF OPTICAL SIGNAL PROCESSING: FINGERPRINT IDENTIFICATION

Kenneth H. Fielding, Joseph L. Horner, and Charles K. Makekau, Rome Laboratory, Electromagnetics & Reliability Directorate

Abstract - We describe an optical fingerprint identification system that optically reads a latent fingerprint for correlation using a binary joint transform correlator. The fingerprint is read using the total internal reflection property of a prism. The system was built, tested, and the experimental results are presented.

SPIE Proceedings, 1991

VARIABLE TIME DELAY FOR RF/MICROWAVE SIGNAL PROCESSING

Edward N. Toughlian, Rome Laboratory, Surveillance & Photonics Directorate
Henry Zmuda, Stevens Institute of Technology, Department of Electrical Engineering

Abstract - This paper addresses the problem of dynamic optical processing for the control of phased array antennas. The significant result presented is the demonstration of a continuously variable photonic RF/microwave delay line. Specifically, it is shown that by applying spatial frequency dependent optical phase compensation in an optical heterodyne process, variable RF delay can be achieved over a prescribed frequency band. Experimental results which demonstrate the performance of the delay line with regard to both maximum delay and resolution over a broad bandwidth are presented. Additionally, a spatially integrated optical system is proposed for control of phased array antennas. The integrated system provides mechanical stability, essentially eliminates the drift problems associated with free space optical systems, and can provide high packing density. This approach uses a class of spatial light modulator known as a deformable mirror device and leads to a steerable arbitrary antenna radiation pattern of the true time delay type. Also considered is the ability to utilize the delay line as a general photonic signal processing element in an adaptive (reconfigurable) transversal frequency filter configuration. Such systems are widely applicable in jammer/noise canceling systems, broadband ISDN, spread spectrum secure communications and the like.

SPIE Vol. 1476 Optical Technology for Microwave Applications V (1991)

BINARY PHASE ONLY FILTER ASSOCIATIVE MEMORY

Jonathan S. Kane, Phil Hemmer, and Charles Woods, Rome Laboratory, Electromagnetics & Reliability Directorate
Jehad Khoury, Electro-Optics Technology Center, Tufts University

Abstract - An associative memory is implemented using a Binary Phase Only Filter as the memory element. In the current architecture, if the input contains any part of the set of stored memories, then the entire set is retrieved at the output. In addition, the sharp autocorrelation peak and the high signal to noise ratio allows operation without necessitating a thresholding device.

SPIE Vol. 1564 Optical Information Processing Systems and Architectures III (1991)

SILICON-GERMANIUM AND SILICON-ON-INSULATOR INTEGRATED OPTICS

R. A. Soref, Rome Laboratory, Electromagnetics & Reliability Directorate
F. Namavar, Spire Corporation

Abstract - Silicon-based opto-electronics is an important emerging area of integrated optics with military applications. The guided wavelength range is 1.2 - 20 μm . We believe that SiGe-on-Si and Si-on-SiO₂-on-Si are practical waveguide "strategies". SOI offers tight confinement of optical modes, sharp waveguide bends, and < 5 db/cm loss when the Si defect density is kept low. SiGe/Si offers loose-to-tight mode binding (depending upon the Ge concentration) and < 3 db/cm loss. SiGe/Si also opens a range of heterostructure strategies. Optical modulation and switching are provided by the free-carrier plasma effect in Si and SiGe (not including the new effects in Si-Ge superlattices). Modulation is proportional to the electrical depletion, accumulation, or injection of electrons and holes. The thermo-optic effect can also be applied to modulation and switching.

We have obtained 1.3 μm guiding in a 1500 Å CVD layer of Ge_{0.18}Si_{0.82} buried 2 μm beneath the surface of a Si wafer, and we simulated the operation of a 1.55 μm waveguided *npn* Si/GeSi/Si heterojunction bipolar transistor, finding that a 400 μm -long device would give 10 dB of intensity modulation at 10^{19} electrons/cm³ injected into the GeSi base. We also investigated vertical coupling and 3D integration of Si waveguides in a 6-layer SiO₂-Si-SiO₂-Si-SiO₂-Si structure fabricated by SIMOX and epitaxy. Independent 1.3 μm guiding on two Si

levels was observed when the intervening oxide was 3600 Å thick; but the guided modes became coupled between Si levels for a 1200 Å oxide separation. Currently, we are combining SOI with SiGe by growing a selective-area $\text{Si}_{0.5}\text{Ge}_{0.5}$ layer on an SOI waveguide for 1.3 μm photodetection.

Workshop on Integrated Optics for Military Applications, Huntsville, Alabama, 8 May 1991

ELECTROMECHANICAL OPTICAL SWITCHING AND MODULATION IN MICROMACHINED SILICON-ON-INSULATOR WAVEGUIDES

R. Watts and A. L. Robinson, Solid State Electronics Laboratory, University of Michigan
R. A. Soref, Rome Laboratory, Electromagnetics & Reliability Directorate

Abstract - Novel monolithic waveguide structures are proposed for optical modulation, switching and opto-mechanical transduction using silicon-on-insulator technology. With etched well techniques, the silicon core of a silicon-on-silicon dioxide channel waveguide is formed into active optical devices which use mechanical deflection to alter the guided wave. Two basic devices, the micro-cantilever beam and the micro-bridge have been modelled and analyzed. This paper is a theoretical evaluation of the voltage-controlled optical modulation and switching properties of these two devices.

1991 IEEE Silicon-on-Insulator Workshop, Vail, Colorado, October 1991

NEAR IR AND VISIBLE PHOTOLUMINESCENCE STUDIES OF POROUS SILICON

C. H. Perry and F. LU, Northeastern University
F. Namavar and N. M. Kalkoran, Spire Corporation
R. A. Soref, Rome Laboratory, Electromagnetics & Reliability Directorate

Abstract - We report photoluminescence emission and photoluminescence excitation studies of porous silicon obtained from *p*-type Si(111) wafers over the range of 0.9-3.0 eV (~ 400-1400 nm). Strong IR emission above and below the bulk silicon band gap at ~ 1.09 eV (1135 nm) at 300 K was observed. This luminescence due to intrinsic band-to-band recombination, was found to be enhanced by two orders of magnitude or more over the IR spectrum from an unanodized wafer. The visible luminescence peak that has been attributed to quantum confinement effects in porous silicon was located at ~ 1.8 eV (689 nm). We

studied the high intensity IR and visible PL in detail as a function of temperature (4-700 K), laser excitation energy (1.96-3.80 eV), and laser power (0.1-1000 mW). The measured shift in the bulk silicon band gap was approximately linear from 300-700 K (~ -0.22 meV/K), while the visible peak, red-shifted by ~ -1.24 meV/K over the same range. Below 300 K they both had comparable temperature dependences. The visible PL was investigated at room temperature in magnetic fields up to 15 T; no discernible shift in the peak position or change in the peak intensity was observed.

Symposium AA of the 1991 Fall Meeting of the Materials Research Society, Boston, MA, December 3, 1991

CARRIER INDUCED CHANGE IN REFRACTIVE INDEX OF Si, SiGe, InGaAsP AND APPLICATIONS TO LOW-LOSS PHASE MODULATORS AND SWITCHES

Richard Soref, Rome Laboratory, Electromagnetics & Reliability Directorate

Abstract - Electrical "manipulation" of charge carriers is a promising way to get electrooptical modulation and switching in semiconductors. The prospects for devices are "good" in group IV semiconductors (Si, Ge, SiGe alloys) and "better" in III-V semiconductors. The advantage of GaAs and InP materials stems from their direct gap compared to the indirect gap of Si and Ge. Although the free-carrier plasma effect is sizeable in both Group IV and III-V materials, this effect is augmented in III-Vs by bandfilling and bandgap renormalization effects. However, the plasma effect stands virtually alone in Si and Ge. The properties of bulk semiconductors differ from their quantum-confined counterparts, and the features of superlattice and multiple-quantum-well structures are both unique and powerful in applications. However, since other speakers will deal extensively with quantum-confined structures, I shall focus on what can be done with bulk materials. I will review the carrier-induced changes in the complex index ($\Delta n + i \Delta k$) of Si, Ge, SiGe, InP, GaAs, and InGaAsP in the 1.3 - 1.6 μm fiberoptic wavelength range, presenting mainly theoretical predictions and a few experimental results. The real index of refraction was obtained from Kramers-Kronig inversion of differential absorption spectra. I shall illustrate the application of these index changes to optical modulation and switching in channel-waveguide structures such as the interferometric Mach-Zehnder intensity modulator and the 2 x 2 balanced-bridge switch. The waveguided Si/SiGe/Si heterojunction-bipolar-transistor is another promising electrooptic device.

Mini-Symposium on Optical Modulation using Semiconductor Plasmas, Grasmere, England, September 17, 1991

NON-LINEAR OPTICAL PROCESSES IN GLASSES AND GLASS-BASED COMPOSITES

Osama H. El-Bayoumi, Rome Laboratory, Electromagnetics & Reliability Directorate

Abstract - Optical non-linear behavior in solids results from a variety of processes which affect their local polarizability. This paper reviews major sources of non-linear optical behavior based on the 3rd order susceptibility in glasses and glasses containing semiconductor clusters, giving examples from our own studies. The mechanisms of optical non-linearity and the relative change in the refractive index and absorption coefficient associated with each process are discussed.

VII International Conference On The Physics Of Non-crystalline Solids; 5 August 1991; Cambridge, England

ADVANCES IN FABRICATION AND PROCESSING OF BULK OPTICAL COMPONENTS

Osama H. El-Bayoumi, Rome Laboratory, Electromagnetics & Reliability Directorate

Abstract - Extensive research in recent years has resulted in novel and/or improved materials and fabrication processes for reflective and transmissive optical component substrates. While specific requirements for materials and fabrication processes depend on the application, typical goals include enhanced dimensional stability, surface quality (figure and roughness), mechanical integrity, lightweighting, reproducibility and fabricability (rapid fabrication in few stages as possible). This paper reviews selected advances in optical component substrate materials-for example, chemical vapor deposited ceramics and sol gel derived glasses; substrate fabrication techniques-for example spin casting, hot isostatic pressing and deposition on precision mandrels; and surface finishing-for example, ion beam milling and multiply actuated membrane laps.

Symposium On Solid State Optical Materials, American Ceramic Society Annual Meeting, Cincinnati, OH, April 28-May 2, 1991

G. SIGNAL PROCESSING

PHASED ARRAY SIMULATION WITH NON-ISOTROPIC AND ISOTROPIC RADIATING ELEMENTS

Michael J. Callahan, Robert J. Denton, Jr., John C. Cleary,
Rome Laboratory, Surveillance & Photonics Directorate

Abstract - Antenna patterns for a generic corporate-fed phased array antenna were generated and analyzed at various scan angles (boresight and thirty degree E-plane and H-plane beam steering angles). Transmit/receive (T/R) module multiplicative amplitude and additive phase error effects, as well as the quantization effects of four bit phase shifters, were taken into account. The array factor for the antenna at each of the above scan angles was generated and then multiplied by an element pattern to produce a far field pattern. This was done for two cases: 1) an antenna having microstrip patch radiating elements; and 2) the same antenna, only having thin strip dipole radiating elements in place of the microstrip patches. The patterns generated were compared to those obtained for the same antenna having isotropic radiating elements instead of realistic ones to demonstrate the importance of having the capability to include element pattern effects in phased array simulation runs.

Proceedings of Computer Simulation Conference, 17 July 1990, Calgary, Alberta, Canada.

"ADAPTIVE MAINBEAM NULLING"

Robert Purpura, Rome Laboratory, Surveillance & Photonics Directorate
Robert Benson, General Electric

Abstract - Adaptive mainbeam nulling experiments have been performed for the purpose of reducing to practice certain theoretical techniques for minimizing the effects of a jammer in the mainlobe of a radar. Rome Laboratory has built a 5120 dual polarized phased array radar for the purpose of measuring the performance, in a free space environment, of nulling algorithms developed to adaptively create mainlobe spatial and polarization and sidelobe spatial nulls in the presence of a jammer. These experiments also determined performance limitations and the major contributors to these limitations.

Multiple experiments have been conducted using ground based jammers and various antenna configurations and canceller algorithms. This test data was processed off-line and analyzed and compared to theoretical performance levels for each exper-

iment. The ground based jammer tests have been supplemented by flight tests using a jammer aircraft (Little Crow) and a target to introduce realistic dynamics to the nulling problem. This flight data has also been processed off-line to minimize computer throughput requirements and to allow for fine tuning. As proof that the technology is translatable to the real world an array processor was programmed to implement mainbeam ECCM in real time.

Record of the Thirty-Sixth Annual Tri-Service Radar Symposium Record. WRDC-TR-90-1146.

SDI PROCESSING TECHNOLOGY

Frederick D. Schmandt, Rome Laboratory, Command, Control, & Communications Directorate

Abstract - This presentation details the real time signal processing program being conducted at Rome Laboratory under SDIO sponsorship. This multifaceted program addresses hardware, software and architectural aspects, relating them to near and far term Strategic Defense System (SDS) requirements. The focus is on pushing relevant technology to obtain at least an order of magnitude improvement, more typically 2 to 3 orders, in relevant parameters. On-going efforts in distributed processing architectures, scalar and vector processors, special purpose processors and waferscale integration (WSI) packaging are summarized. Their interrelationships are indicated within the context of overall SDS processing needs.

Conference of the American Defense Preparedness Association, April 1990, University of Texas, Austin, TX.

RADIATION HARDENED VECTOR PROCESSOR - A HIGH PERFORMANCE PROCESSOR FOR SPACE APPLICATIONS

Frederick D. Schmandt, Rome Laboratory, Command, Control, & Communications Directorate

Abstract - The Radiation Hardened Vector Processor (RHVP) is a versatile, high performance, programmable, scalar-vector processor capable of performing 150 million floating-point operations per second (150 MFLOPS). Its flexible architecture, rich instruction set and Ada programmability enable the RHVP to address a wide range of signal processing problems. This paper begins with an overview description of the RHVP architecture and brassboard implementation. Brassboard performance obtained for a multiple target tracking scenario is presented and contrasted with a scalar only implementation. The paper concludes with a discussion of enhancements to the ar-

architecture and implementation that are currently underway to evolve the RHVP into a space qualifiable product.

First Annual Fire Control Symposium, Oct 1990, U.S. Air Force Academy, Colorado Springs, CO.

FUSION AND PRESENTATION OF MULTI-SENSOR DATA

Todd P. Humiston, Rome Laboratory, Command, Control, & Communications Directorate

Abstract - Command and control centers are continually receiving newly developed or previously unavailable sensor information. This information must be made available to several workstations in the command and control environment based on that workstation's application. The collective volume of this data can, at times, overload the workstation and/or the operator. Therefore, data reduction techniques such as fusion and filtering must be employed. Sensible presentation of this information can also expedite the performance of the command and control function.

8th Annual Conference on C2 Decision Aids, Ft. McNair, Washington D.C., 26 June 1991

ASSESSING PERFORMANCE OF STANDARD EVALUATION CIRCUITS FOR RADIATION HARDENED 32 BIT PROCESSOR

Nancy A. Koziarz, Rome Laboratory, Electromagnetics & Reliability Directorate

Abstract - As part of the Rome Laboratory's Radiation Hardened 32 Bit Processor development program there was a need to evaluate the four phase I contractors to insure they possessed the ability to accurately design, model and fabricate devices capable of meeting the requirements of the final 32 bit processor chip set. To facilitate comparisons between contractors a Standard Evaluation Circuit (SEC) was selected. This was used as a gauge to evaluate the contractors wafer yield level, reliability and performance in a normal and radiation environment on the final product. The contractors were required to deliver four lots of product over a four month time period.

This paper will discuss the testing performed on the devices and the methodology used to complying and comparing the data from the four contractors to allow valid comparisons. The calculation for final product yield from the SEC yield data had to be tailored for this study. The Poisson estimate of yield was

used to minimize factors between manufacturers and allow better comparisons. The gamma yield function is more common and represents a more accurate prediction for yield of complex microcircuits, however, the coefficient of variance contained within the equation varied greatly between the different manufacturing processes and was not easily obtainable. If the contractor could meet the yield requirements using the Poisson equation which was a very pessimistic estimate, then the probability of yielding sufficient production devices was high. The problems encountered and lessons learned during the evaluation will also be discussed. For example the electrical test data from the ring oscillator and delay Johnson counter was to be compared to simulation data obtained from the contractors. The fixturing and loading of the devices remained constant for all four contractors during electrical testing, however, the simulation conditions varied with each of the contractors. It was difficult to determine the loading schemes used in the simulations. Therefore only general comparisons between simulation results and electrical test data were possible.

University/Government/Industry Microcircuit Symposium, June 1991

KNOWLEDGE-BASED TRACKING ALGORITHM

Allan F. Corbeil and Linda Hawkins, Technology Service Corporation
Paul Gilgallon, Rome Laboratory, Surveillance & Photonics Directorate

Abstract - This paper describes the Knowledge-Based Tracking (KBT) algorithm that was recently demonstrated in real-time flight tests conducted at the Air Force's Rome Laboratory (AFRL). In KBT processing, the radar signal in each resolution cell is thresholded at a lower than normal setting to better detect low observable (LO) targets. Additional signal processing, including knowledge-based spectral and spatial acceptance tests and Technology Service Corporation's (TSC) Track-Before-Detect (TBD) algorithm, were then applied to the measured data to detect target tracks. The TBD algorithm, which was originally described in the 1986 Tri-Service Symposium Record, uses knowledge of the sensor noise environment and target kinematics to sort LO target tracks from random false alarm events. It consists of (1) forming tentative track templates for each threshold crossing, (2) applying knowledge-based association rules to the range, Doppler, and azimuth measurements from successive scans, and (3) using an M-association-out-of-N-scan rule to declare a detection. This scan-to-scan integration enhances the probability of LO target detection while maintaining a low output false alarm rate.

For a real-time demonstration of the KBT algorithm, the L-band radar at AFRL was used to illuminate small Cessna 310 and Seneca II test aircraft. The received radar signal was digitized and processed by a ST-100 Array Processor and a pair of VAX computers. In these tests, the KBT algorithm provided 9 to 10 dB of improvement relative to single scan performance, with a nominal real time delay of less than one second between illumination and display.

37th Annual Tri-Service Radar Symposium, Jun 91, Peterson AFB, Colorado Springs, CO

ARCHITECTURE FOR SURVIVABLE SYSTEM PROCESSING (ASSP)

Richard J. Wood, Rome Laboratory, Surveillance & Photonics Directorate

Abstract The ASSP Program is a multiphase effort to implement DOD and commercially developed high-tech hardware, software and architectures for reliable space avionics and ground based systems. System configuration options provide processing capabilities to address Time Dependent Processing (TDP), Object Dependent Processing (ODP) and Mission Dependent Processing (MDP) requirements through Open System Architecture (OSA) alternatives that allow for the enhancements, incorporation and capitalization of a broad range of development assets. High technology developments of hardware, software, networking models address technology challenges of long processor life times, fault tolerance, reliability, throughput, memories, radiation hardening, size, weight, power (SWAP) and security.

Proceedings, GOMAC '91

DESIGNING A WAFER-SCALE VECTOR PROCESSOR USING VHDL

Richard W. Linderman and Ralph L. Kohler, Jr., Rome Laboratory, Surveillance & Photonics Directorate

Abstract The Wafer Scale Vector Processor (WSVP) is a flexible, high performance, multi element superscalar vector processor architecture being developed by the Air Force Rome Laboratory and the Air Force Institute of Technology under SDIO sponsorship. The WSVP addresses a wide range of high performance computing requirements from real time, embedded, based signal processing to floating point coprocessors attached to desktop workstations solving classes of supercomputing problems. In between, there are many applications to ground based and airborne systems requiring high throughput.

By employing stacked hybrid wafer scale integration and a new memory packaging approach, the WSVP achieves very low size, weight, and power, while the super-scalar vector architecture sustains high throughput on important signal processing problems. Since the basic element of the WSVP requires only about one square inch of area within a hybrid wafer scale substrate, a wide variety of multi-element WSVP architectures can be considered for any particular application.

The WSVP development has closely relied upon the family of advanced computer-aided design (CAD) tools which surround the IEEE Standard 1076, VHSIC Hardware Description Language (VHDL). The central elements of the VHDL toolset include the descriptive language itself, the analyzer (i.e. compiler), and the simulator. The basic tools are available from several vendors and primarily support design modeling and hierarchical simulation. These tools are supplemented with an ever growing list of peripheral CAD tools which interface to the IEEE standard language to support functions like high level architectural assessment, design verification, design synthesis, and Ada compiler generation.

Proceedings, GOMAC '91

MULTI-SPEAKER CONFERENCING OVER NARROWBAND CHANNELS

T. Champion, Rome Laboratory, Electromagnetics and Reliability Directorate

Abstract - A technique for digital conferencing over narrowband channels is proposed which allows for the representation of multiple simultaneous speakers. The technique takes advantage of the properties of multi-rate parametric vocoders (which includes a Sinusoidal Transform Coder and a Multi-Band Excitation Vocoder, as well as embedded coders). The technique described herein performs signal summation in a manner similar to analog conferences, however, signal summation is deferred to the terminal. To maintain quality for a single speaker while allowing multiple speakers, the technique adaptively allocates channel bandwidth based on the number of speakers to be represented. Development is in progress on a system that allows two simultaneous speakers, although three simultaneous speakers is achievable.

Published in the Proceedings of the IEEE Workshop on Speech Coding for Telecommunications, September 1991

MULTI-RATE STC AND ITS APPLICATION TO MULTI-SPEAKER CONFERENCING

R. J. McAulay and T. F. Quatieri, Lincoln Laboratory, M.I.T.
T. Champion, Rome Laboratory, Electromagnetics & Reliability Directorate

Abstract - It has been shown that speech of very high quality can be synthesized using a sinusoidal model when the amplitudes, frequencies, and phases are derived from a high-resolution analysis of the short-time Fourier Transform. Several techniques for parameterizing the amplitudes, frequencies, and phases to allow for effective coding at bit rates between 2.4 and 8.0 KBPS are discussed. In particular, the amplitudes are coded using a cepstral envelope, the frequencies are coded using a harmonic model of speech, and the phases are derived from a voicing measure and the minimum phase envelope. Since the same model is used at all bit rates, translation between bit rates can be done in the parameter domain independent of the original speech waveform. This feature is exploited in the Rome Laboratory (RL) multi-speaker conferencing system, where rate-conversion at a conferencing bridge is performed to accommodate multiple speakers during collisions.

Proceedings of the IEEE MILCOM 91 Conference, November 1991

MULTICHANNEL DETECTION USING A MODEL-BASED APPROACH

J. H. Michels, Rome Laboratory, Surveillance & Photonics Directorate
P. Varshney and D. Weiner, Syracuse University

Abstract - This paper considers the Gaussian multichannel binary detection problem. A multichannel generalized likelihood ratio is implemented using a model-based approach when the signal is assumed to be characterized by an autoregressive (AR) vector process. Detection performance is obtained for the special case where the underlying processes are assumed to have known autoregressive process parameters. Specifically, results for two-channel signal vectors containing various temporal and cross-channel correlation are obtained using a Monte-Carlo procedure. These results are compared to known optimal detection curves.

1991 International Conference on Acoustics, Speech, and Signal Processing, 14-17 May 1991, Toronto, Ontario, Canada

H. COMPUTER SCIENCE

A DISTRIBUTED ENVIRONMENT FOR TESTING COOPERATING EXPERT SYSTEMS

Capt Jeffrey D. Grimshaw and Craig S. Anken, Rome Laboratory, Command, Control, & Communications Directorate

Abstract - This paper discusses the Advanced Artificial Intelligence Technology Testbed (AAITT) being sponsored by Rome Laboratory. The purpose of this testbed is to provide a powerful environment for integrating dissimilar software systems including expert systems, conventional software, databases, and simulations distributed over a network. In addition, this testbed will provide measurement and analysis tools for evaluating the results of the various user-supplied software components.

AGARD Conference Proceedings 499, May 1991, Lisbon Portugal

SOFTWARE LIFE CYCLE SUPPORT ENVIRONMENT (SLCSE) PROJECT MANAGEMENT SYSTEM (SPMS): NOT JUST ANOTHER PROJECT MANAGEMENT TOOL

James R. Milligan, Rome Laboratory, Command, Control, & Communications Directorate

Abstract - The paper describes the Software Life Cycle Support Environment (SLCSE) Project Management System (SPMS). SLCSE (pronounced "slice") is a computer-based framework for the instantiation of Software Engineering Environments (SEEs) that are tailored to accommodate the specific needs of software development projects. SPMS is an extension of SLCSE that provides advanced project management capabilities.

Since SPMS is an extension of SLCSE, section I begins with an overview of SLCSE. The process of project management is then discussed in terms of its interrelated activities (i.e., planning, tracking, monitoring, assessment, adjustment, and reporting).

Section II begins with a discussion of the purpose, intended users, operational concept, modes of operation, and the various automated tools of SPMS. Special features of SPMS, particularly in the context of SLCSE, are then described.

Section III provides a brief summary, and section IV provides a list of references which were used in the preparation of the paper

AIAA (American Institute of Aeronautics-Astronautics) Conference Proceedings, 24 Oct 91

DISTRIBUTING OBJECT-ORIENTED SIMULATION LANGUAGES

Clifford D. Krumvieda (Sponsored by the Air Force Office of Scientific Research/AFSC)

James H. Lawton, Rome Laboratory, Command, Control, & Communications Directorate

Abstract - The object-oriented computer simulation language ERIC, developed during an in-house project at the Rome Air Development Center (RADC), was studied to determine its applicability to distributed programming. Recent published results in distributed object-based languages and distributed object-based simulations were studied. These results suggest that speedups obtained by distributing object-oriented simulation languages are not easy to realize. A distributed version of ERIC, called DERIC, was implemented at the Center, showing that extending an object-oriented simulation language into the distributed paradigm is feasible.

1991 Summer Computer Simulation Conference, Baltimore, Maryland, 22-24 July 1991

TAGALOG: A NULL SUBJECT LANGUAGE WITH VARIANT MORPHOLOGY

Michael L. Mc Hale and Leticia S. Mc Hale, Rome Laboratory, Command, Control, & Communications Directorate

Abstract - The last decade has seen a lot of discussion on those languages that allow null subjects, the so called pro-drop languages. This discussion started based on data from Spanish and Italian. The first explanation for these data was a rich morphology, since these languages are highly morphological in nature. Huang's work in Chinese however, demonstrated that null subjects can be found in languages with no morphology. This resulted in a dichotomized approach. Subsequent changes to the theory were the result of numerous exceptions to the then current model. Among languages considered in this stage were German, Dutch, Portuguese, Japanese and Irish. The final result of all this iterative polishing was Jaeggli and Safir's proposal that null subjects are licensed by a uniform morphology (i.e., either all of the forms are morphologically complex or none of them are).

This paper presents Tagalog as a counter example to this model. A member of the Philippine group of Austronesian languages, Tagalog is a configurational language with variant morphology that allows numerous kinds of null subjects.

The paper starts with an overview of Tagalog inflectional morphology and then contrasts this basic inflectional paradigm with some non uniform features of the language. Then the types of null subjects allowed in Tagalog are examined. These include expletive deletion, persona adjectives, PRO drop, and sentences with non nominal topics

Numerous examples are given throughout the paper. The examples given stand as a counter example to the current formulation of the null subject theory. While this paper posits no new proposal for the null subject parameter, some possible explanations of the phenomenon for Tagalog are considered.

First SouthEast Asian Linguistics Conference, May 9-12, 1991, Wayne State University, Detroit, MI

NEW METHODOLOGIES FOR VERIFICATION AND VALIDATION (V&V) IN EVOLUTIONARY ACQUISITION

Kenneth B. Hawks, Rome Laboratory, Command, Control, & Communications Directorate

Abstract The author presents the problems associated with traditional V&V in the context of rapid prototyping and evolutionary acquisition; namely: timeliness of reporting, application of resources in a highly dynamic environment, selection of resources, tool selection and payoff, and depth and breadth of coverage. A paradigm being applied to current Command and Control programs is examined. The new technologies are described and the concept of veracity in concert with verification and validation is introduced

AIAA Computing in Aerospace 8 Symposium, Baltimore, Maryland, 21-24 Oct. 1991

FEA TECHNIQUES FOR DESIGNING RELIABILITY INTO ELECTRONIC SYSTEMS

Edward J. Jones, William J. Bocchi, Jr., Douglas J. Holzhauer, and Peter J. Rocci, Rome Laboratory, Electromagnetics & Reliability Directorate

Abstract Rome Laboratory has pioneered the use of finite element analysis (FEA) as a computer-aided engineering tool to design reliability into new and emerging electronic technologies. Rome Lab has applied FEA to a wide variety of electronic devices. This paper presents two unique examples. The first example shows how FEA is used to design highly reliable gallium arsenide (GaAs) monolithic microwave integrated circuits (MMIC) for use in phased array radar modules. The second example shows how FEA is used to evaluate the thermal management system in the so called 3-D computer which utilizes the stacking and interconnecting of whole silicon wafers together into a high speed parallel processor.

Design Productivity International Conference, February 1991, Honolulu, Hawaii.

FINITE ELEMENT ENHANCEMENT OF CRYOGENIC TESTING

Clare D. Thiem, Rome Laboratory, Electromagnetics and Reliability Directorate
Douglas A. Norton, Rome Laboratory, Surveillance & Photonics Directorate

Abstract - Finite element analysis (FEA) of large space optics enhances cryogenic testing by providing an analytical method by which to assure that a test article survives proposed testing. The analyses presented in this paper were concerned with determining the reliability of a half meter mirror in an environment where the exact environmental profile was unknown. FEA allows the interaction between the test object and the environment to be simulated to detect potential problems prior to actual testing.

FEA was applied in house at Rome Laboratory to determine the amount of time required to cool the mirror to its desired test temperature. It was also determined that the proposed mirror mount would not cause critical concentrated thermal stresses that would fracture the mirror. FEA and actual measurements of the front reflective face were compared and good agreement between computer simulation and tests were seen. Evaluating design approaches by analytical simulation, like FEA, verifies the reliability and structural integrity of a space optic during design prior to prototyping and testing

SPIE Proceedings of the Analysis of Optical Structures Conference, 23-24 July 1991, San Diego CA

FMECA, THE RIGHT WAY

Barry T. McKinney, Rome Laboratory, Electromagnetics & Reliability Directorate

Abstract - Submitted as "in-depth" and "fully compliant", an isolated and untimely "Block-Checking" exercise is all that could truly describe the Failure Modes, Effects and Criticality Analysis (FMECA) that lay before me. Required in conjunction with the development of an advanced approach radar system, the FMECA was supposed to identify all failure modes within the system. However, a FMECA's primary contribution is the early identification of all catastrophic, critical, and safety related failure possibilities so they can be eliminated or minimized through design changes.

In addition to being untimely and isolated, seven major deficiencies were identified, five will be shown to be common among FMECA efforts. These deficiencies are the shared responsibility of the government and contractors:

- Lack of defined failure causes.
- Reckless and improper severity classification.
- No Data Sources
- Failure to recognize deficiencies and failure modes of earlier systems of similar design.
- Lack of recommendation pertaining to the operation and support of the system.
- Narrow scope of analysis.
- Untimely submission.

It is the intent of this paper to: clearly address the above deficiencies; show, through the use of simple examples, how these requirements should be addressed (the right way); and, demonstrate how the information may be effectively utilized in the system design and planning of operational and supporting tasks.

Annual RAMS 1991, Orlando FL, Jan 91.

A DESIGNED APPROACH TO ACCELERATED RELIABILITY TESTING

Barry T. McKinney, Rome Laboratory, Electromagnetics & Reliability Directorate
F. Michael Speed, Jr., Aeronautical Systems Division

Abstract - Engineers at the Air Force's Rome Laboratory and Aeronautical Systems Division (ASD) have begun software development that automates the design and set-up of accelerated reliability tests. Test designs and resulting analysis will comply with standard validation requirements and economic considera-

tions. Through significant user interactions, the software will progressively develop component unique reliability verification procedures, as well as perform a complete data reduction and final estimation of the component's operational reliability.

The approach being considered is an environmentally stressful, factorial split-plot experimental design. This technique provides a means to quantify the relationships of various stresses and their individual effect on the component's failure rate. Once quantified, these relationships will be combined to form a cumulative stress, failure rate acceleration model. This model establishes the operational reliability of the component.

IES Annual Conference, San Diego CA, May 91.

DESIGNING THROUGH TEST

Barry T. McKinney, Rome Laboratory, Electromagnetics & Reliability Directorate
F. Michael Speed, Jr., Aeronautical Systems Division

Abstract - Engineers at the Air Force's Rome Laboratory and Aeronautical Systems Division (ASD), in an effort to extend the design process through the entire procurement cycle, have begun software development that automates the design and analysis of accelerated reliability tests. Test designs and resulting analysis will comply with standard validation requirements and economic considerations. The software will progressively develop component unique, experimentally designed, reliability quantification procedures, as well as perform a complete data reduction and final estimation of the component's inherent operational reliability.

AIAA Conference, Baltimore MD, Oct 91.

C³I GRAPHICAL APPLICATIONS

Earl C. LaBatt Jr., Rome Laboratory, Command, Control, & Communications Directorate

Abstract - Past research efforts in the field of Command, Control, Communications, and Intelligence (C³I), have concentrated on the application and refinement of advanced Artificial Intelligence (AI) concepts. However, the man-machine interface to these advanced applications has experienced little improvement and does not adequately reflect some of the AI concepts embedded within these systems.

The development of more advanced computing techniques requires a more sophisticated interface to the system. These enhancements cannot be adequately conceived by a user using traditional display techniques.

This paper reveals the underlying AI concepts that help facilitate the transfer of information between acquired C³I data and an operator. Many of these concepts are discussed in regard to their application in current Tactical Air Force research projects. In addition, the paper discusses the limitations of previous program Interfaces and the current advances in graphical interface techniques

AGARD Conference Proceedings 499

USER INTERFACE MODELING

Carla L. Burns, Rome Laboratory, Command, Control, & Communications Directorate

Abstract The requirements specifications for the user interface of a system are often ambiguous, imprecise, inconsistent and incomplete. Consequently, when the system is developed, the user interface does not live up to the end user's expectations. Rapidly prototyping the user interface during the requirements phase of the lifecycle aids in improving the user interface requirements specifications. The Rapid Prototyping System (RPS) contains a collection of tools to prototype the user interface of Command, Control, Communications, and Intelligence (C³I) systems. The purpose of the RPS user interface modeling tools is to quickly generate a demonstration of what the end user would see on the display when the system was developed. Once the user interface prototype has been developed, the end user of the system is brought in to confirm the requirements. The implementor goes through a scenario with the end user, who provides comments along the way. Typical comments might include: objects are a different color, objects should be located in a different area on the display, or additional capabilities are required. Changes are likely to be made to the prototype as a result of running the demonstration for the end user. These changes can be incorporated into the prototype at a relatively low cost. Once the changes have been incorporated, the end user can be brought back again for his assessment. This is an iterative cycle and is typically how the final user interface requirements for the system can be identified and verified. There are several advantages of using the RPS tools. First, the prototype may be created without the need for writing any software. The RPS does not require extensive knowledge of hardware specifics or a particular programming language to allow a non-programmer to develop user interface prototypes. The RPS tools generate the source code automatically. Another advantage is that the way in which the source code is generated allows a programmer to add any additional capabilities to the demonstration by simply coding and linking into the automatically generated source code. Finally, a great amount of time is saved by having the source code automatically generated. In order to determine the usefulness and overall quality of the RPS tools, the development of a user interface prototype for a large C³I

system was performed. The Granite Sentry Program Office was in the process of developing the requirements for updating the Air Defense Operations Center computer system displays. From a set of 14 baseline slides depicting the user interface requirements, RADC developed a scenario based on these slides consisting of 53 unique displays. It took RADC 6 person weeks to generate the prototype. Approximately, 10,000 lines of code were generated. The Granite Sentry Program office was already in the process of prototyping the user interface requirements. It took them 1 person year using regular programming techniques. Many of the ambiguities and inconsistencies in the requirement specifications were brought out from developing this demonstration. Prototyping is a very useful technique for improving user interface requirements.

Chapter 19, "Interface for Information Retrieval and Online Systems," American Society for Information Sciences, 1991

RAPIDLY PROTOTYPING THE USER INTERFACE OF A C³I SYSTEM

Elizabeth S. Kean, Rome Laboratory, Command, Control, & Communications Directorate

Abstract - Requirements specifications of large command, control, communications and intelligence (C³I) systems are often ambiguous, inconsistent and incomplete. Rome Laboratory is involved in the evolutionary development of a Requirements Engineering Environment (REE) and methodology to support prototyping the requirements of large C³I systems. One important prototyping activity is the prototyping of a system's user interface. The REE's interface prototyping tool provides the user the ability to rapidly construct user interface characteristics of C³I systems. User interface prototypes can be developed so rapidly because there is no computer programming required. In order to verify the feasibility of user interface prototyping, a prototype of the user interface of a C³I system was developed using an existing prototyping system called the Rapid Prototyping System (RPS). Rome Laboratory requested the baseline slides of the upgrades to the Air Defense Operations Center Command and Control System from the Granite Sentry Program Office who was responsible for implementing the updates. Based upon these slides, a user interface prototype, called the Granite Sentry Prototype, was developed. The purpose of this paper is to describe a requirements engineering process model, the results of prototyping activities following the process model, and the development of the REE.

Proceedings, AIAA Computing in Aerospace 8, Oct 1991

C3 MODELING USING EXPERT SYSTEMS

James L. Sidoran, Rome Laboratory, Command, Control, & Communications Directorate
Jerry H. Shelton, Computer Sciences Corporation

Abstract - The value of having a model of a Command, Control, and Communication system early in the system development life cycle is considered. An approach to modeling a Command, Communication, and Control problem within the NORAD domain using co-operating expert systems is described. By allowing for the identification and manipulation of relevant objects and issues of concern early in the system development life cycle, such a model can serve as an aid in flushing out system requirements and capabilities, providing a tool to assist analysts in defining and testing specifications and key behavioral portions of such a complex system.

Expert Systems World Congress Proceedings, Vol. 1, Dec 1991, Orlando, FL

SYSTEM CONCEPT MODELING

James L. Sidoran, Rome Laboratory, Command, Control, & Communications Directorate
Jerry H. Shelton, Computer Sciences Corporation

Abstract - Concept modeling is an abstract representation of a system or domain that is as close to the human conceptualization of the problem as possible [Mylopoulos]. This can be a useful tool in identifying objects and relationships between objects within a complex domain. The problem lies in scoping the model and representing it at the appropriate level of abstraction, and translating these abstract representation into an automated environment. This activity is a methodological process that takes time, experience, and access to domain knowledge. Once there is a process and method for articulating concept level models, various tools and techniques can assist the model builder in designing and implementing a concept model. The objective of this summary is to present some of the ideas for analyzing domains, method and tool support for concept modeling, initial design alternatives, and give a few examples of how concept modeling can contribute to clarity and understanding, and articulation of requirements at system conception into requirements, and perhaps throughout system development.

2nd International IEEE Workshop on Rapid Systems Prototyping, June 1991

PARALLEL PROTO - A SOFTWARE REQUIREMENTS SPECIFICATION, ANALYSIS & VALIDATION TOOL

Carla Burns, Rome Laboratory, Command, Control, & Communications Directorate

Abstract - Studies have shown that the more costly problems of software development arise in the definition of software requirements, not in the actual production of code. Software prototyping is one approach which may be used early on in the software lifecycle to identify errors in requirements. Software prototyping refers to the quick development of executable software supporting critical attributes of a system's software components such as the user interface, complex algorithms or performance. Rome Laboratory has recently developed a prototyping tool, called Parallel Proto, for specifying, analyzing and validating functional software requirements which are targeted to either sequential, parallel or distributed architecture environments. The tool provides facilities for graphically representing the software functional requirements and parallel and distributed hardware architecture environments, associating the software functions with the hardware components and interactively executing the functional prototype. Using Parallel Proto, parallelism can be explicitly identified and modeled in the requirements and high level design stages of software development. Such a capability supports the early analysis of high level software and hardware architecture trade-offs. This paper discusses the capabilities of Parallel Proto along with an associated methodology for using the tool. The Parallel Proto facilities used to construct and execute the functional prototype are also presented in detail.

Proceedings, AIAA Computing in Aerospace 8 Conference, Oct. 1991

PARALLEL PROTO - A PROTOTYPING TOOL FOR ANALYZING AND VALIDATING SEQUENTIAL AND PARALLEL PROCESSING SOFTWARE REQUIREMENTS

Carla Burns, Rome Laboratory, Command, Control, & Communications Directorate

Abstract - Software prototyping is one approach which may be used early on in the software lifecycle to analyze and validate software requirements. Parallel Proto is a software prototyping tool for analyzing and validating functional requirements which are targeted to either sequential, parallel or distributed architecture environments. Currently, most parallel processing com-

puter-aided software engineering (CASE) tools focus on the identification and simulation of parallelism during the coding stage of the software lifecycle. Such an approach does not take into account any explicit specification of parallelism inherent in the application or an associated parallel-oriented design. Using Parallel Pro^o, parallelism can be explicitly identified and modeled in the requirements and high level design stages of software development. The tool provides facilities for graphically constructing data-flow-like software functional specifications and parallel and distributed hardware architectures, associating

the software functions with the hardware components and interactively executing the functional prototype. Performance modeling statistics are available after prototype execution. Such capabilities support the early analysis of high level software and hardware architecture trade-offs. This paper discusses the capabilities of Parallel Proto along with an associated methodology for using the tool.

Proceedings, 2nd International IEEE Workshop on Rapid Systems Prototyping, June 1991

I. RELIABILITY SCIENCE

MEASURING THE COVERAGE OF BRIDGING FAILURES BY INTERNAL ACCESS METHODS

Warren H. Debany, Rome Laboratory, Electromagnetics & Reliability Directorate

Abstract - A method is presented that determines the coverage of shorts (bridging failures) by internal access techniques that provide node observability. These techniques include CMOS *Ipp* monitoring, CrossCheck, voltage contrast, bed-of-nails, guided probe, and boundary scan. Only good circuit simulation is required. It obtains the exact sets of nodes that potentially can be shorted without being detected by a given test vector sequence. The method does not require the universe of bridging failures to be explicitly listed.

Proceedings, IEEE VLSI Test Symposium, April 1991, pp 215-220

VLSI PACKAGE RELIABILITY

P. S. Speicher, Rome Laboratory, Electromagnetics & Reliability Directorate

Abstract - The challenge presented by advanced package development in the past five years has further accentuated the constant need for package quality and reliability monitoring through extensive laboratory testing and evaluation. As pin counts and chip geometries have continued to increase, there has been additional pressure from the military and commercial sectors to improve interconnect designs for packaged chips, including chips directly attached to the printed wiring board (PWB). One of the options employed has been tape automated bonding (TAB). However, this assembly technique also presents new standardization, qualification and reliability problems. Therefore, at Rome Air Development Center (RADC), there is regular assessment (through in-house failure analysis studies) of parts destined for military and space systems. In addition, Department of Defense (DoD) high tech development programmes, such as very high speed integrated circuits (VHSIC), have utilized all present screening methods for package evaluation, and have addressed the need for development of more definitive non-destructive tests. To answer this need, two RADC contractual efforts were awarded on laser thermal and ultrasonic inspection techniques.

Through these package evaluations, a number of potential reliability problems are identified and the results provided to the specific contractors for corrective action implementation. Typical problems uncovered are lid material and pin corrosion, damage to external components and adhesion problems between copper leads and polyimide supports, hermeticity failures, high moisture content in sealed packages and particle impact noise detection (PIND) test failures (internal particles). Further tests uncover bond strength failures, bond placement irregularities, voids in die attach material (potential heat dissipation problems), and die surface defects such as scratches and cracks.

This presentation will review the specific package level physical test methods that are employed as a means of evaluating reliable package performance. Many of the tests, especially the environmental tests-e.g., salt atmosphere and moisture resistance- provide accelerated forms of anticipated conditions and are therefore applied as destructive tests to assess package quality and reliability in field use. In addition to a manufacturer's compliance with designated qualification procedures, the key to package quality lies in utilizing good materials and well-controlled assembly techniques. This practice, along with effective package screen tests, will ensure reliable operation of very large scale integration (VLSI) devices in severe military and commercial environment applications.

Hybrid Circuits Magazine (Journal of International Society for Hybrid Electronics - Europe), Sep 1991

ON THE EQUIVALENCE BETWEEN SIMILARITY AND NON-SIMILARITY SCALING IN ROBUSTNESS ANALYSIS

Haniph A. Latchman, University of Florida-Gainesville
Robert J. Norris, Rome Laboratory, Electromagnetics & Reliability Directorate

Abstract - In the analysis of multivariable systems in the presence of structured uncertainties, similarity scaling and non-similarity scaling techniques have been independently proposed as methods for obtaining nonconservative robustness measures. In order to fully exploit the unique advantages of each method, it is desirable to obtain the required non-similarity scaling matrix, and vice versa, without the need for separate optimizations. In this paper an explicit relationship is developed between the similarity and non-similarity scaling matrices which enables the direct computation of the non-similarity scaling matrices from the similarity scaling. Several applications of the results are also presented.

1991 American Control Conference, June 1991, Boston, MA.

A NEW LOWER BOUND FOR THE STRUCTURED SINGULAR VALUE

Haniph A. Latchman, University of Florida-Gainesville
Robert J. Norris, Rome Laboratory, Electromagnetics & Reliability Directorate

Abstract - In this paper, we examine some geometric issues related to the Major Principal Direction Alignment (MPDA) principle and propose a new and unified algorithm for computing the structured singular value $\mu(M)$.

1991 American Control Conference, June 1991, Boston, MA.

AT-SPEED VERIFICATION TECHNIQUE FOR LRMs AND PCBs

James M. Nagy, Rome Laboratory, Electromagnetics & Reliability Directorate

Abstract - Current board testers are mainly used as a functional tester to allow diagnostic testing down to the component level. Board testers are satisfactory for that function but do not have the capability to perform at-speed verification of Line Replaceable Modules (LRMs) or Printed Circuit Boards (PCBs) and cannot perform parametric evaluation testing of these device types. This paper presents a method to perform at-speed verification and parametric evaluation of a LRM by testing the module on a VLSI component tester and treating the LRM as a component. The LRM demonstration was conducted on two distinct VLSI test systems, a GenRad GR-180 located at Sacramento ALC at McClellan AFB, CA and a Teradyne J953 located at Rome Laboratory, Griffiss AFB NY. The LRM demonstration will be explained from the capturing of test requirements in IEEE proposed data format standards of TRSL and WAVES, the formation of an automatically generated test program using a generic ATE postprocessor (IN-STEP), and the results of the LRM testing.

Proceedings of the Automatic Test Conference, Sept. 1991, Anaheim, CA

A NEW METHODOLOGY FOR TEST PROGRAM SET GENERATION AND RE-HOSTING

James P. Hanna and Willis J. Horth, Rome Laboratory, Electromagnetics & Reliability Directorate

Abstract - This paper discusses a new methodology for significantly improving the consistency, reliability, and transportabil-

ity of Test Program Sets (TPS). This methodology utilizes proposed IEEE tester independent data standards and resource-independent, standardization test methods to automate the TPS development process. Automating this process greatly reduces the costs associated with TPS development and provides a highly cost effective method for re-hosting existing TPSs to new tester environments.

IEEE Systems Readiness Technology Conference, Anaheim, California, 24-26 September 1991

MILITARY BURN-IN REQUIREMENTS - ONE PERSPECTIVE

Daniel J. Burns, Rome Laboratory, Electromagnetics & Reliability Directorate

Abstract - This workshop position paper reviews military burn-in requirements, acknowledges current industry concerns, and highlights issues relating to specifying and running effective, efficient burn-in tests. Military burn-in requirements and options are referenced, and the trend toward process monitoring and improvement is noted.

It is pointed out that where a low density of point defects dominate early life fallout, it is essential that each individual product die be exhaustively tested and screened. References are given which discuss current difficulties, including incomplete test vectors, uneven stressing, inappropriate test generation strategies for spot defect coverage and delay fault testing, stress voltage limitation by process, and insensitivity of accepted electrical measurements to degradation. Innovative solutions are also referenced, including powerful new built-in test modes, built-in burn-in screen test modes, and in-process screening techniques. The value of a Field Return failure analysis program to validate screening effectiveness is noted.

Proceedings of the IEEE International Test Conference, Oct. 1991, Memphis, TN.

EFFECT OF DEPOSITION TECHNIQUE ON THE AS-DEPOSITED MICROSTRUCTURE OF COPPER THIN FILMS

Lois Walsh, Rome Laboratory, Electromagnetics & Reliability Directorate

N. Feilchenfeld, IBM Corporation

J. Schwartz, Syracuse University

Abstract - Copper metallization is an ideal choice for use in semiconductor devices and packages. The metal's desirable properties are low resistivity, good electromigration resistance,

solderability, and low cost. Microstructural differences in copper deposited by four techniques commonly used in the microelectronics industry are presented. These differences were measured using optical microscopy, X-ray diffraction, scanning electron microscopy, Auger electron spectroscopy, and secondary ion mass spectroscopy. The results were correlated to clearly define the differences in microstructure among the different copper films providing a basis for interpreting the effects of copper film deposition method on film microstructure and those physical properties influenced by microstructure. The final result is that the microstructural differences can be measured and used to predict the reliability and performance of resulting films.

38th Annual Symposium and Topical Conferences of the American Vacuum Society, 11-15 Nov 1991, Seattle, Washington

VOID GROWTH AND ELECTROMIGRATION

Lt. J. B. Mattila, J. V. Beasock, Y. J. Kieme, (AFOSR Associate), and L. H. Walsh, Rome Laboratory, Electromagnetics & Reliability Directorate

Abstract - Studies are being pursued which center on device reliability as influenced by materials. Our research is focused on understanding the fundamental cause/causes of electromigration in order to eliminate its contribution to device failures and miniaturization limitations.

The research task uses surface analysis techniques, Auger electron spectroscopy (AES), and Secondary Ion Mass Spectroscopy (SIMS), to characterize how materials and material interfaces influence solid state microelectronic device reliability. Electronic structure modeling is being pursued as a possible method for investigating how changing materials and interfaces influence electromigration. To this end Atomic Force Microscopy (AFM) and Electron Spectroscopy for Chemical Analysis (ESCA) will be used to confirm theoretical hypothesis with actual experimental results.

Initially the results of previous time lapse void growth experiments are being examined using digital image analysis equipment. Typical data consists of several series of scanning electron microscope (SEM) micrographs of voids produced at elevated current density. We are most interested in characterizing how a void grows as a function of time, current density, temperature, and location. For aluminum lines on silicon at a current density of 7×10^5 amps per cm^2 , observed initial void growth rates (< 100 minutes) range from 0.04 to 0.20 square micron per minute. The shape of the void is tracked by calculating the ratio of area to perimeter squared. Preliminary results will be shown.

First International Workshop on Stress Induced Phenomena in Metallizations, Ithaca, New York, 11-13 September 1991

DESIGN VERIFICATION USING LOGIC TESTS

Warren H. Debany, Heather B. Dussault, Kevin A. Kwiat, Mark J. Gorniak, Anthony R. Macera, and Daniel E. Daskiewicz
Rome Laboratory, Electromagnetics & Reliability Directorate

Abstract - Design verification is the process of assuring that a design is error-free. Empirical design verification involves the running of test cases against the design. To be effective, "sufficient" testing must be performed. But to be cost-effective as well, testing must be terminated when that point is reached. There is a lack of quantifiable metrics to guide the development of tests for digital logic design verification. This paper reports on the results of experiments that indicate that fault simulation, which parallels the well-known mutation testing approach used in software design verification, can be used to grade the coverage of test cases used for hardware design verification.

Proceedings, IEEE Rapid System Prototyping Workshop, June 1991.

A METHOD FOR THE CONSISTENT REPORTING OF FAULT COVERAGE

Warren H. Debany and Kevin A. Kwiat, Rome Laboratory, Electromagnetics & Reliability Directorate
Sami A. Al-Arian, University of South Florida

Abstract - A standard procedure has been developed for fault coverage measurement. This paper outlines the methods prescribed in Procedure 5012 of MIL-STD-883. This procedure governs the reporting of fault coverage for digital microcircuits for military applications. It describes requirements for the development of the logic model for an IC, fault universe, fault simulation, and reporting of results. Procedure 5012 provides a consistent means of measuring fault coverage for an integrated circuit regardless of the specific logic and fault simulator used. It addresses the testing of complex, embedded structures that are not implemented in terms of logic gates, such as RAMs, ROMs, and PLAs. Fault coverages for gate-level and non-gate-level structures are weighted by transistor counts to arrive at an overall fault coverage value. The procedure addresses built-in-self-test based on the use of linear feedback shift registers for output data compaction. Two fault sampling procedures are permitted. A Fault Simulation Report documents the fault coverage level obtained, as well as the assumptions, approximations, and methods used.

COMPARISON OF RANDOM TEST VECTOR GENERATION STRATEGIES

Warren H. Debany, Rome Laboratory, Electromagnetics & Reliability Directorate

Carlos R.P. Hartmann, Kishan G. Mehrotra, and Pramod K. Varshney, Syracuse University

Abstract - A number of random test strategies have been proposed in the literature, or are currently being used in automatic test vector generation systems. In this study four random test

generation strategies were compared to determine their relative effectiveness: equiprobable 0s and 1s; two weighted random pattern generation algorithms; and the maximum output entropy principle. The test generation strategies were compared at a variety of target fault coverages. Two statistically-based metrics were used to evaluate the techniques: a large-sample test of the difference of means and an upper confidence limit. It was found that the two weighted random test pattern generation strategies were generally superior to equiprobable 0s and 1s and maximum output entropy, although both of the latter techniques were optimal in some cases. For a given logic circuit, the same technique is not necessarily optimal at every fault coverage.

Proceedings, IEEE International Conference on Computer-Aided Design (ICCAD-91), November 1991.

IV. PATENTS

NORMAL INCIDENCE OPTICAL SWITCHES USING FERROELECTRIC LIQUID CRYSTALS

Richard A. Soref, Rome Laboratory, Electromagnetics & Reliability Directorate

Patent Number: 4,989,941

Date of Patent: Feb. 5, 1991

Abstract - This invention comprises a new group of fiber optic switching devices that use layers of surface-established ferroelectric liquid crystals (FLCs) as the switching media. In each of the devices light impinges upon the ferroelectric liquid crystal at an angle of 90° (normal incidence) with the surface plane. Each FLC gives 0° or π° optical rotation, depending upon the polarity of the electric voltage applied. A series of polarizing beam splitters are used to separate unpolarized light into its s and p polarization components. After ferroelectric liquid crystal switching, other polarizing beam splitters are used to direct the s and p light to output optical paths. The switches discussed below are voltage controlled 2×2 , 1×4 , 1×6 , 1×8 , 4×4 , or $N \times N$ devices that use one or more layers of surface stabilized ferroelectric liquid crystals.

METHOD FOR MEASURING LARGE ANTENNA ARRAYS

Peter R. Franchi, and Harvey Tobin, Rome Laboratory, Electromagnetics & Reliability Directorate

Patent Number: 4,998,112

Date of Patent: Mar. 5, 1991

Abstract - A method for measuring the far field antenna pattern of a large phased array antenna on a conventional far field range by applying a correction factor to the antenna phase shifters. As the antenna is electronically steered to each of its scan angle, a particular correction factor is applied to each radiating elements to correct the far field antenna pattern to the shortened far field range.

LOW LOSS SEMICONDUCTOR DIRECTIONAL COUPLER SWITCHES INCLUDING GAIN METHOD OF SWITCHING LIGHT USING SAME

Richard A. Soref, Rome Laboratory, Electromagnetics & Reliability Directorate

Patent Number: 5,004,447

Date of Patent: Apr. 2, 1991

Abstract - In multiple quantum well directional couplers, non-centralized input and output legs, occupying major portions of the switches, are continuously forward biased, to produce sufficient gain in light intensity therein to overcome losses in the centralized portions, to in turn provide a transparent (ODB loss) two-by-two coupler switch. Short segments of the centralized coupling portion occupying minor portions of the switches, are switched between forward bias states and zero bias states to provide light beam switching. Thus these switches employ both carrier gain and carrier refraction. The large changes in the index of refraction enable extremely short, low loss, switches to be fabricated and cascaded if desired. A second group of less preferred switches employ solely the carrier refraction effect, by injecting carriers into the waveguides at high levels, preferably equal to or greater than $1 \times 10^{18}/\text{cm}^3$.

MECHANICALLY ROTATED DOPPLER FREQUENCY SHIFTER

John B. Morris, Uve H. W. Lammers, and Richard A. Marr, Rome Laboratory, Electromagnetics & Reliability Directorate

Patent Number: 5,007,721

Date of Patent: Apr. 16, 1991

Abstract - A mechanical Doppler shifting device for a high frequency radiated beam comprises a rotating helical reflector having its axis of rotation parallel to the beam and a plane stationary mirror mounted parallel to the axis. The helix has a smooth reflective surface which is at a 45 degree slope with respect to the axis so that the distance to the surface from the source of the beam varies with the rotation of the helix. The beam is reflected from the helix to the plane stationary reflector and back upon itself to the source at a Doppler shifted frequency. Also disclosed is a system using 2 helical reflectors, the second being a mirror image of the first and being oppositely rotated synchronously therewith for reflecting the beam to a receiver spaced from the source of the beam.

WAFER CLEANING METHOD

Mark W. Levi, Rome Laboratory, Electromagnetics & Reliability Directorate

Patent Number: 5,009,240

Date of Patent: Apr. 23, 1991

Abstract - A wafer cleaning system which cleans semiconductor wafers by sand blasting them with ice particles is disclosed. In this system a stream of gas is conducted by a conduit to the semiconductor wafer while a spray of water is frozen into the

ice particles by a number of cooling coil systems which protrude into the conduit. After the semiconductor wafer is sand blasted with ice, any residual ice is removed simply by evaporating it. This results in a clean wafer without the contamination that can accompany chemical solvents of other semiconductor cleaning and etching systems.

LOSSLESS NON-INTERFEROMETRIC ELECTRO-OPTIC III-V INDEX-GUIDED-WAVE SWITCHES AND SWITCHING ARRAYS

Richard A. Soref, Rome Laboratory, Electromagnetics & Reliability Directorate

Patent Number: 5,013,113

Date of Patent: May 7, 1991

Abstract - Lossless guided-wave switches with more than 30 dB of crosstalk-isolation are comprised of branched channel waveguides with laser-like cross-sections. Optical gain, sufficient to overcome power-splitting losses, is provided by carrier-injection currents. Due to its low-noise properties, the single-quantum-well structure is found to be optimum for cascading switches into a multi-stage network. A lossless 1 X N network with 1024 switched outputs should be feasible.

MODIFIED COMPACT 2F OPTICAL CORRELATOR

Joseph L. Horner, Belmont; Kenneth H. Fielding, and Charles K. Makekau, Rome Laboratory, Electromagnetics & Reliability Directorate

Patent Number: 5,016,976

Date of Patent: May 21, 1991

Abstract - A modified 2f Fourier transform optical correlator combines a collimation and first Fourier Transform lens into one thin lens. The resulting correlator thus utilizes one less lens relative to the unmodified 2f optical correlator.

AMPLITUDE ENCODED PHASE-ONLY FILTERS FOR OPTICAL CORRELATORS

Joseph L. Horner, Rome Laboratory, Electromagnetics & Reliability Directorate

Patent Number: 5,024,508

Date of Patent: Jun, 18, 1991

Abstract - Method allows a first phase-only optical correlator filter function to be written on an amplitude modulating device such as a spatial light modulator (SLM) by applying a bias term to the phase only filter function great enough to obtain a second amplitude encoded filter function, for use with a more economical amplitude responsive SLM.

EXTENDED DYNAMIC RANGE ONE DIMENSIONAL SPATIAL LIGHT MODULATOR

Stephen T. Welstead, Huntsville, Alabama, and Michael J. Ward, Rome Laboratory, Surveillance & Photonics Directorate

Patent Number: 5,039,210

Date of Patent: Aug. 13, 1991

Abstract - An optical information system which uses a liquid crystal television (LCTV) as a one dimensional spatial light modulator (SLM) is presented. An optical carrier-wave is generated by polarizing and collimating the output of a laser. The liquid crystal television modulates the optical carrier wave with a digital modulating signal to output thereby a modulated optical signal. An array of photodetectors electrooptically connects the modulated optical signal into a modulated electrical signal which is displayed on an oscilloscope. The use of an LCTV as a one dimensional SLM yields higher numerical accuracy and extended dynamic range than two dimensional SLM applications of the same equipment.

SINGLE SLM JOINT TRANSFORM CORRELATORS

Joseph L. Horner, Rome Laboratory, Electromagnetics & Reliability Directorate

Patent Number: 5,040,140

Date of Patent: Aug. 13, 1991

Abstract - A simple, low cost, high performance joint Fourier transform correlator, which requires only a single spatial light modulator, is disclosed. Input and reference images are recorded upon a single phase modulating SLM, and a lens produces a first joint Fourier transform of the images upon an electro-optic sensor. The first Fourier transform is binarized and recorded upon the single SLM electronically, and the same lens produces a second Fourier transform to form an image correlation signal at a correlation plane. Also, recordation of the input and reference images and recordation of the joint Fourier transform upon the single SLM may be performed optically rather than electronically.

NON-CONTACT POLISHING

Brian S. Ahern, Rome Laboratory, Electromagnetics & Reliability Directorate

Patent Number: 5,040,336

Date of Patent: Aug. 20, 1991

Abstract - A non-contact polishing apparatus is used for polishing semi-conductor planar substances. The substrate is set back from any surface and is held by a chuck fixed within a collar. This substrate holder assembly is placed within an enclosed container that has a non-abrasive solution therein. The container is mounted to a high speed rotating table that provides random motion to the holder assembly. This action provides isotropic polishing with no polishing created defects on the substrate surface.

FIBER OPTIC CALIBRATION STANDARD APPARATUS

David D. Curtis, Rome Laboratory, Electromagnetics & Reliability Directorate

Patent Number: 5,056,915

Date of Patent: Oct. 15, 1991

Abstract - A fiber optic calibration standard apparatus having a fiber optic cable pair which have difference in length of one quarter the wavelength of the applied modulated signal and are coupled to a mirrored reflecting surface to provide reflection reference signals that are utilized to generate error correction signals. A matched termination has one end of an optical fiber sealed in a vial of index matching fluid to absorb the optical power incident to the fiber.

HYBRID CLUTTER CANCELLATION METHOD AND SYSTEM FOR IMPROVED RADAR PERFORMANCE

Russell D. Brown, Donald D. Weiner, and Michael C. Wicks, Rome Laboratory, Surveillance & Photonics Directorate

Patent Number: 5,061,934

Date of Patent: Oct. 29, 1991

Abstract - A system is disclosed for use with radar systems so as to reduce the dynamic range requirement of the analog to

digital converter through analog clutter cancellation prior to digitization. Clutter return estimates are formulated via modern digital signal processing techniques, converted to analog representation, and subtracted from the received waveform. Typically, the MTI cancellation is performed on the quadrature components of the received signal. The complex residue is then processed for target detection. This quadrature processing is not illustrated in the figures. In practice, sampling the received waveform prior to baseband down conversion, at an intermediate frequency, is also feasible. Digital synchronous detection and coherent MTI processing are then implemented in the digital signal processor. Rather than employ a radar signal processor which is either all analog or all digital it is beneficial to utilize hybrid schemes which capitalize on the advantages of both. A hybrid system is disclosed in which the acoustic delay line, which fundamentally limits analog MTI canceller performance, is replaced by a digital delay line. In effect, the transmitter crystal, delay medium, and receiver crystal are replaced by the analog to digital converter, digital delay, and digital to analog converter. The hybrid clutter canceller with digital processor and analog waveform synthesizer utilizes modern signal processing techniques to estimate the clutter return which is subtracted from the incoming analog signal. The full dynamic range of the received signal is not presented to the analog to digital converter, reducing the number of bits required for target detection in clutter. In effect, application of the hybrid clutter canceller reduces the A/D converter probability of saturation for a given A/D converter.

ORTHOGONALLY POLARIZED QUADRAPHASE ELECTROMAGNETIC RADIATOR

Michael C. Wicks and Paul Van Etten, Rome Laboratory, Surveillance & Photonics Directorate

Patent Number: 5,068,671

Date of Patent: Nov. 26, 1991

Abstract - A broadband multi-element antenna having desirable phase, standing wave and polarization characteristics is disclosed. The antenna is arranged as a plurality of airfoil shaped elements located in radial planes about a central axis with the element peripheries collectively defining a horn shaped surface centrally disposed of which is a ground plane member of preferably truncated conical shape which includes electrical feeding arrangements having in phase and out of phase element coupling. The antenna is suitable for radar, satellite, and other precision uses including military applications.

COMPACT 2F OPTICAL CORRELATOR

Joseph L. Horner and Charles K. Makekau, Rome Laboratory,
Electromagnetics & Reliability Directorate

Patent Number: 5,073,006

Date of Patent: Dec. 17, 1991

Abstract - A 2f Fourier transform optical correlator uses two simple, single element lenses, with the second lens performing both quadratic phase term removal and the inverse Fourier transform operation in a compact two-focal-length space. This correlator performs correlations quite well and uses three less lens elements than a prior 2f system, is shorter by a factor of two compared to the standard 4f system, and uses one less lens than the 3f system, while still retaining the variable scale feature.

V. ROME LABORATORY TECHNICAL REPORTS

TECH. REPORT NO.	ACCESSION NUMBER	TITLE	AUTHOR
RL-TR-91-6	A234123	Digital Logic Testing and Testability	Warren H Debany Jr
RL-TR-91-8		Mutual Coupling in a Random Array of Mono- pole Elements: Experiment Results	1Lt Randy J Richards
RL-TR-91-9		The Mean and Variance of Diffuse Scattered Power as a Function of Clutter Resolution Cell Size	Robert J Papa Margaret B Woodworth
RL-TR-91-10	A234309	RADC Cathode Life Test Facility	Mark E. Novak Edward J Daniszewski Dirk T Bussey
RL-TR-91-11	A236327	Proceedings of the Fifth Conference on Knowl- edge-based Software Assistant	Louis J Hoebel Douglas A White (editors)
RL-TR-91-21	B154058	Calibration of an Actively Controlled Segmented Mirror	Herbert W. Liunpe III Janes D. Blum
RL-TR-91-26	B154144L	Maximal Bandwidth Expansion	Joseph A Mancini
RL-TR-91-29	A233855	An RADC Guide to Basic Training in TQM Anal- ysis Techniques	Anthony Coppola
RL-TR-91-43		Practical Considerations Relative to the Design and Manufacture of Microstrip Antennas	Daniel A Mullinix Capt, USAF
RL-TR-91-44		Vehicle Potential Measurements During Electron Emission in the Ionosphere	Dr Neil B Myers
RL-TR-91-46	A235353	A Users Guide to the Texplan System	Michele Kubis Colleen A McAuliffe
RL-TR-91-47	A235604	Optical Performance Analysis of the Precision Optical Research and Tracking Laboratory (PORTL)	Paul L Repak
RL-TR-91-48	A235354	Measuring the Quality of Knowledge Work	Anthony Coppola
RL-TR-91-49		Low-frequency Scattering from Two-dimensional Perfect Conductors	Thorkild B Hansen Arthur D Jaghjian
RL-TR-91-65	B157577	Performance of X.25 Lapb on Simuiated Radio Links and Type-of-service Routing Issues for Tac- tical Gateways	Bradley J Harnish
RL-TR-91-71		Large Angle Bistatic Cross Sections of Birds and Targets	James L Schmitz J Leon Poirier

<u>TECH. REPORT NO.</u>	<u>ACCESSION NUMBER</u>	<u>TITLE</u>	<u>AUTHOR</u>
RL-TR-91-80	A247350	Improvement in Radar Detection Under Scan to Scan Processing and Scan Rate Reduction	Dr Donal D Weiner Dr Joon Song
RL-TR-91-85		A Statistical Model of Radar Bird Clutter at the DEW Line	John Antonucci
RL-TR-91-87	A236148	A Survey of Reliability, Maintainability, Supportability, and Testability Software Tools	Joseph A Caroli
RL-TR-91-88		Material Effects In Photoconductive Frozen Wave Generators	Robert M OConnell J B Thaxter Capt Richard E Bell
RL-TR-91-113	B156344	Post Conference Report 3rd Annual Electro-optical Space Surveillance Conference	Richard W Carman
RL-TR-91-114		Scattering Experiments at the Ipswich Electromagnetic Measurements Facility: Swept Bistatic Angle Measurement System	Robert V McGahan
RL-TR-91-115		Electromagnetic Scattering From Dielectrics - A Two Dimensional Integral Equation Solution	Marian Silberstein
RL-TR-91-124		Linear Phased Array of Coaxially-fed Monopole Elements in a Parallel Plate Waveguide	Boris Tomasic Alexander Hessel
RL-TR-91-136	B155804	ANDVT Tactern Voice Interface Unit	Joseph A Mancini
RL-TR-91-138		Development Of A Liquid Phase Epitaxial Growth System for Fabrication of Indium Phosphide Based D	Michael Gregg Kenneth Vaccaro
RL-TR-91-139		Dual-surface Magnetic-field Integral Equation Solution for Bodies of Revolution	James L Schmitz
RL-TR-91-149, Vol I	B156765	2nd Annual Large Optics Conference	N/A
Vol II	B156766	2nd Annual Large Optics Conference	N/A
RL-TR-91-156		Proceedings of the 1990 Antenna Applications Symposium	Paul Mayes, et al
RL-TR-91-159		Serial Signal Breakback (u)	Cpt Martin J Mersinger
RL-TR-91-169	A239572	Intelligence Analyst Associate (IAA): A Preliminary Analysis & Specification	Carrie G Pine
RL-TR-91-208	C958515L	Image Processing Support for JSTARS (U)	Todd B Howlett Peter J Costianes

TECH. REPORT NO.	ACCESSION NUMBER	TITLE	AUTHOR
RL-TR-91-248	B158104L	Adaptive Nonlinear Processing for Interference Mitigation in a Spread Spectrum System	Stephen C Tyler John J Patti
RL-TR-91-249	B161083	The Air Force Maui Optical Station Air and Space Technical Symposium: Conference Proceedings	Deborah D Harden
RL-TR-91-250	B158127	The Air Force Maui Optical Station Air And Space Technical Symposium: Workshop Proceedings	Deborah D Harden
RL-TR-91-269	A241331	Multichannel Detection Using The Discrete-Time Model-based Innovations Approach	Dr James H Michels
RL-TR-91-270	A241535	Adaptive Optical Processor	Capt Michael J Ward Capt Christopher W Keefer Dr. Stephen T. Welstead
RL-TR-91-275	A244 635	A Visual Programming Methodology For Tactical Aircrew Scheduling and Other Applications	Capt Douglas E Dyer
RL-TR-91-286		Charge - 2B Diagnostic Free-flyer Pneumatic Payload Ejector Test and Calibration Report	James Ernstmeier
RL-TR-91-305	A242594	Total Quality Management (TQM), An Overview	Anthony Coppola
RL-TR-91-306	B159 778L	Evaluation of the 128 X 128 Element Cellular Logic Image Processor (CLIP)	Lee A. Uvanni
RL-TR-91-307	A242 838	A Performance Model of Thermal Imaging Systems (TISs) Which Includes the Human Observers Response "State of the Art" Displays	Denise M Blanchard
RL-TR-91-309	B159 805L	RCS Analysis of a Tactical Target	Edward M Starczewski
RL-TR-91-316	A242 837	Room-temperature Carrier Lifetimes and Optical Nonlinearities of GaInAs AlInAs and GaAlInAs	Steven T Johns
RL-TR-91-319	B159 824	Research and Development for Intelligence Data Handling	John M Pirog
RL-TR-91-338		Analysis of the HF Antenna Performance for the Ducted Satellite Experiment	Capt Randy J Richards
RL-TR-91-347	B160 010L	Back Propagation Neural Network Generator	Jeffrey L Fordon
RL-TR-91-351		Analytical Characterization of Bistatic Scattering from Gaussian Distributed Surfaces	Lisa M Sharpe

<u>TECH. REPORT NO.</u>	<u>ACCESSION NUMBER</u>	<u>TITLE</u>	<u>AUTHOR</u>
RL-TR-91-357	B160 148L	Contingency Support System (CSS)	Joseph D Stooks John F Vona
RL-TR-91-359	A248 602	Variable Hold Time In Dynamic Random Access Memories	Daniel J Burns Mark W Levi Wilmar Sifre
RL-TR-91-386	B163 186	Predelivery Testing of the Deployable	John F Vona Joseph D Stooks Michael J Corelli
RL-TR-91-392		Microwave Studies of High TC Copper Oxide Super Conductors and NBN	Chi-Chung Chin
RL-TR-91-400	B160 985	A Prediction Model of a Metal CDTE-INSB Eta- lon	Jacqueline Dacre Smith Chi Luen Wang Prasanta K Ghosh Ju-Tah Jung Philipp Kornreich
RL-TR-91-404	B160949	Measurement of Contrast Ratios for a Ferroelec- tric Liquid Crystal Spatial Light Modulator	D C H Stanchfield II J D Smith Dr P Kornreich
RL-TR-91-420	B161439	LSP Component Characterization & Development	Jacqueline Dacre Smith
RL-TR-91-421 same as 91-360		Optimization of the Elliptically Polarized Diffuse Power Scattered from a Rough Surface with Two Scales of Roughness	Robert J Papa Margaret B Woodworth
RL-TR-91-432	B-161 568	Evaluation of Space Communications Networks	Gregory J Hadynski
RL-TR-91-438	B161 848	Calibration of a Wavefront Sensor	R J Michalak M A Getbehead P Repak K M Magde
RL-TR-92-45	A250435	Forty Years of Research and Development at Griffiss Air Force Base	John Q Smith David A Byrd, SSgt, USAF